ECRIS 2008

18th International Workshop on ECR Ion Sources

Chicago, Illinois USA – September 15 -18, 2008

Hosted by Argonne National Laboratory

International Advisory Committee

A. Drentje, KVI, Netherlands
S. Gammino, LNS, Italy
H. Koivisto, JYFL, Finland
T. Lamy, LPSC, France
D. Leitner, LBNL, USA
R. Leroy, GANIL, France
C. Lyneis, LBNL, USA
T. Nakagawa, RIKEN, Japan
P. Spadtke, GSI, Germany
H. Zhao, IMP, China

Local Organizing Committee

R. Pardo, Co-Chairman
R. Vondrasek, Co-Chairman
J. Bergman
J. Brunsvold
C. Pardo
M. Power
R. Scott

Topics

ECR ion sources – normal, superconducting, and next generation
Charge breeders
Radioactive ion beams
Applications and diagnostics
Beam extraction and transport
Source plasma studies and models

Contact Information

R. Pardo, pardo@phy.anl.gov
R. Vondrasek, vondrasek@anl.gov
J. Bergman, Workshop Secretary, ECRIS08@phy.anl.gov
Web site: www.phy.anl.gov/ECRIS08/

Workshop Site

Chicago History Museum
1601 N. Clark Street
Chicago, Illinois 60614
www.chicagohistory.org

Argonne National Laboratory
Physics Division
9700 S. Cass Avenue
Argonne, Illinois, 60439 USA

Contents

International Advisory Committee

* A. Drentje, KVI, Netherlands
* S. Gammino, LNS, Italy
* H. Koivisto, JYFL, Finland
* T. Lamy, LPSC, France
* D. Leitner, LBNL, USA
* R. Leroy, GANIL, France
* C. Lyneis, LBNL, USA
* T. Nakagawa, RIKEN, Japan
* P. Spadtke, GSI, Germany
* H. Zhao, IMP, China

Local Organizing Committee

* R. Pardo, Co-Chairman
* R. Vondrasek, Co-Chairman
* J. Bergman
* J. Brunsvold
* C. Pardo
* M. Power
* R. Scott

PAPER NOT RECEIVED

STATUS REPORT AND RECENT DEVELOPMENTS WITH VENUS

D. Leitner#, J.Y. Benitez, D. R. Dietderich, M. Leitner, T.J. Loew, C.M. Lyneis, S. Prestemon, G. Sabbi, D.S. Todd, X. Wang, LBNL, Berkeley, CA 94720, U.S.A.

Abstract

Since the superconducting ECR ion source VENUS started operation with 28 GHz microwave heating in 2004 it has produced ion beam intensities such as 860 eμA of Ar^{12+}, 200 eμA of U^{34+}, or with respect to high charge state ions, 270 eμA of Ar^{16+}, 1 eμA of Ar^{18+} and .4 eμA of Xe^{42+}. In August of 2006, VENUS was connected to the 88-Inch Cyclotron as the third injector ion source extending the energy range and available heavy ion beam intensities from the 88-Inch Cyclotron. This paper will highlight recent developments and results.

In addition, the paper will discuss recent modifications to the VENUS superconducting lead design, which became necessary after an unexpected quench damaged a superconducting lead. Following a quench in January of 2008, the VENUS sextupole coils could not be energized. The lead quenched due to the loss of liquid helium in the upper cryostat. This resulted in localized heating, which vaporized a section of the lead wire. Analysis of the quench scenario, which is discussed in the paper, revealed design flaws in the original lead support and cooling design. The major undertaking of repairing the magnet leads and rebuilding the VENUS cryostat is described.

INTRODUCTION

The VENUS ECR ion source (shown in Fig.1) at the Lawrence Berkeley National Laboratory (LBNL) is a 3rd generation source. The fully superconducting magnet structure has been designed for optimum fields for operation using 28 GHz plasma heating frequency. As a prototype ECR ion source for the Facility for Rare Isotope Beams (FRIB) the emphasis of the R&D is the production

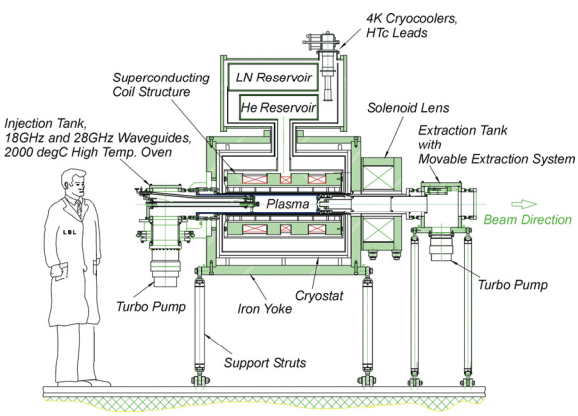

Figure 1: Mechanical layout of the VENUS ion source and cryogenic systems

of medium high charge states such as U^{33+}. As an injector into the 88-Inch Cyclotron the emphasis is on the production of high charge state ions. VENUS has been operated routinely using 28 GHz as its main heating frequency since 2004 and has produced many record beams. Besides 28 GHz, 18 GHz can be injected as a second frequency for double frequency heating or used for single frequency heating ($B_{ECR,18\ GHz}$=0.64T). Table 1 shows a summary of the VENUS ECR ion source performance[1-4].

Two main magnetic confinement and heating configurations are typically used in the VENUS ECR ion source. In the single frequency heated plasma mode a minimum B field of .64 to .75 T is used, which results in a shallow magnetic field gradient at the 28 GHz resonance zone. Up to 6.5 kW of 28 GHz power has been coupled into VENUS using this mode of operation. In the double frequency mode a minimum B field of .45 T is used. This field profile results in a combination of a shallow gradient (for 18 GHz heating) and a steeper gradient (for 28 GHz heating) at the resonance zone. Up to 9kW of combined 18 and 28 GHz power (a power density of about 1kW/liter for the about 9L big plasma chamber) has been coupled into the VENUS plasma chamber so far. The ion source performance continues to improve as we couple more power into the plasma chamber. For typical 28 GHz operation in single or dual frequency mode, the sextupole magnet is energized to produce slightly above 2 Tesla at the plasma chamber wall.

Table 1: Recent VENUS Results

VENUS 28 GHz or 18 GHz +28 GHz							
CS	^{16}O	^{40}Ar	CS	^{84}Kr	^{129}Xe	^{209}Bi	^{238}U
6^+	2850		25^+	223		243	
7^+	850		26^+			240	
8^+			27^+	88		245	
12^+		860	28^+	25	222	225	
13^+		720	29^+	5	168	203	
14^+		514	30^+	1	116	165	
16^+		270	31^+		86		
17^+		36	33^+		52		205
18^+		1	34^+		41		202
			35^+		28.5		175
			37^+		12		
			38^+		7		
			41^+			15	
			42^+				.4
			47^+			2.4	5
			50^+			.5	1.9

In September of 2006 the first ion beam from VENUS was injected and accelerated by the 88-Inch Cyclotron.

#Corresponding author: dleitner@lbl.gov

So far the Cyclotron has accelerated Ar, Kr, Xe and U beams from VENUS. Substantial gains in both intensity and energy were demonstrated for the heavy masses and very high charge states. For high charge state uranium beams such as U47+ 11 times more beam was extracted from the cyclotron using the VENUS ECR ion source than using the 14 GHz AECRU injector ion source. The ion beam intensities provided by the VENUS ECR ion source for high charge state uranium extends its energy range to the Coulomb barrier range for nuclear physics experiments. Another important application for the VENUS injector is the production of high charge state xenon to extend the mass range of the 16 MeV/nucleon heavy ion cocktail to xenon [4]. Figure 2 shows beam developments conducted with high charge state Xe beams in comparison with the beam intensities achieved using the AECRU injector ion source. 80 to 100 times more beam intensities could be extracted using the VENUS ECR ion source. For the first time neon-like xenon (Xe44+) could be extracted from the cyclotron. Using Glovanisvky's diagram[5] of the (neτi)Te criteria, this result indicates that in the VENUS source the (neτi) product has reached 2·1011sec/cm3.

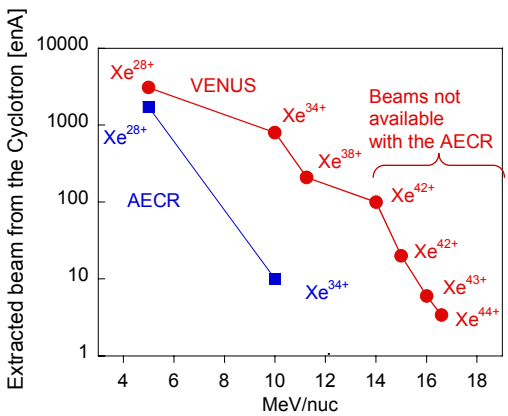

Figure 2: Cyclotron using the AECRU injector in comparison to the VENUS injector at various MeV/nuc and high charge state ions.

VENUS LEAD QUENCH AND STATUS OF THE REPAIR

In January 2008, while the magnet was fully energized to 28 GHz fields, an unexpected quench occurred after which the sextupole coils could not be energized. Analysis of the event suggests that a leak in the pressure relief system lead to a slow loss of liquid helium by evaporation. The liquid level dropped below the service tower level. Consequently, localized heating at the solder joint between the superconducting vacuum feedthrough and the charge lead of the sextupole (see figure 3) initiated a lead quench.

These solder joints are non superconducting and have a resistance of several tens of nOhm. If those joints are insufficiently cooled, they can heat up and initiate a lead quench, which will lead to further heating and consequently burn out. In the case of the NbTi VENUS sextupole wires[3], assuming an adiabatic heating model, it takes about 1.7 sec for the wire to reach 1300 K (melting point of copper) at the sextupole operational current of 465A. However, if the NbTi wire is heated beyond 600K the wire will have irreversible damage and altered superconducting properties.

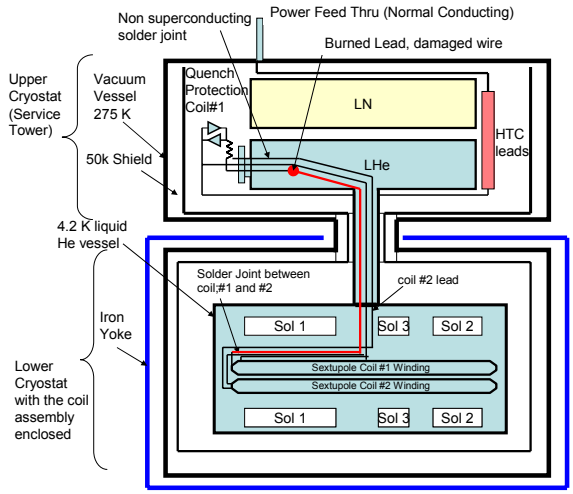

Figure 3: A schematic of the VENUS cryostat and upper service tower. The location of the burned lead is indicated.

The VENUS upper service tower was opened and it was found that about 10 cm of the VENUS sextupole charge lead had been vaporized during the quench. Most likely the 10 cm missing wire was vaporized in the plasma discharge caused by the high voltage build up in the coil during the quench.

As expected from simple thermal calculations, analysis of the remaining wire in the upper service tower showed that the wire was overheated sufficiently to degrade its superconducting properties. The adjacent wire, which was guided in the same insulating sleeve and contacted the quenching lead was also damaged and needed to be replaced as well. Figure 4 shows a cross section of the damaged wire in comparison with an original sample. It can be easily seen how the NbTi wires have melted and fused with the Cu matrix surrounding the conductor.

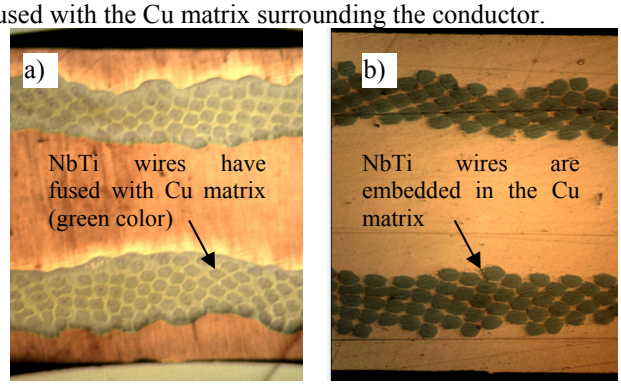

Figure 4: A polished cross section of the VENUS sextupole wire for a) the overheated damaged wire and b) the original sample.

As we analyzed samples further away from the burned section, the wire properties improved. Figure 5 shows the

result of the I_s short sample test .5 m from the burned section and .9m from the burned section.

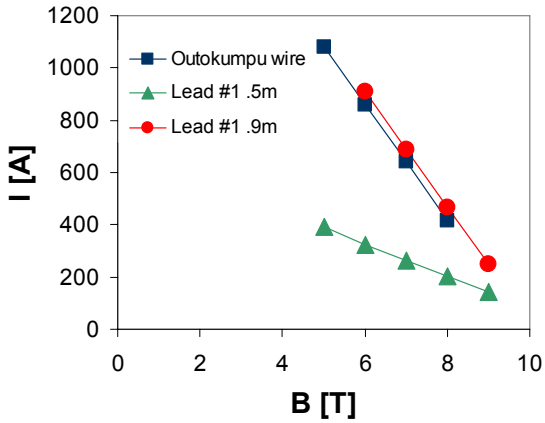

Figure 5: Short sample tests for two sections of the burned lead wire .5m and .9m away from the burned section.

While the first section (closer to the burned lead) clearly showed degradation of the superconducting properties, the second section is well within the specification of the original sextupole wire [3]. Therefore, the remaining lead wire was used for splicing. The magnet system was reassembled and prepared for cool down in a test cryostat. Figure 6 shows a picture of the VENUS cold test assembly and Figure 7 a detailed view of the quench protection system and the diagnostic's wiring.

Figure 6 The VENUS magnet assembled for the cold test at the LBNL superconducting magnet test facility.

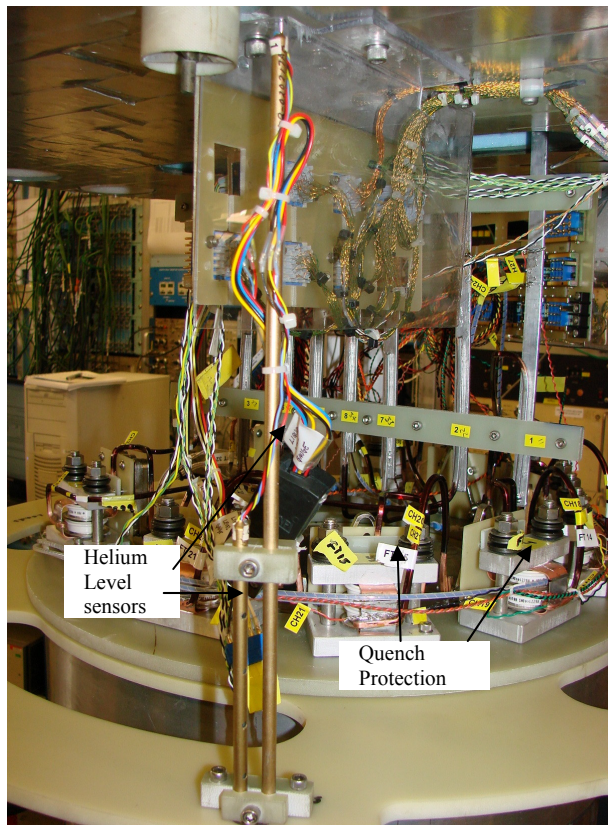

Figure 7: A detail view of the quench protection system, the vapor cooled leads and the diagnostic wiring.

VENUS Cold Test

The VENUS magnet was cooled down using the cryostat of the Superconducting Magnet Test Facility at LBNL and energized to full excitation (4.1T, 3.2 T and 2.1 T) without quenches in three ramps. First the solenoids were energized and ramped down, then the sextupole was energized and ramped down, and finally all magnets were ramped up together to full fields. Figure 8 shows the last ramp for the full system. The sextupole magnet was ramped to 493A (110% of its design value), typical operational current values for 28 GHz are 465A to 475A.

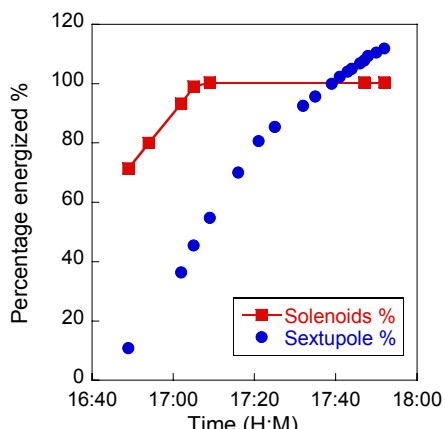

Figure 8: Ramp up of all VENUS magnets during the cold test.

During the ramping of the sextupole, small conductor movements were observed in the sextupole coils. The slippage occurred with and without solenoid field. Figure 9 shows an example of such a slippage event. The terminal voltages across each individual sextupole (A to F) and the whole sextupole coil were recorded by a chart recorder with a sampling frequency of 125 kHz. The $V(t)$ traces shown in Figure 9 were processed by the following two steps: 1) normalized by subtracting the average of the first ten data points so each trace starts at 0V and 2) shifted by an interval of 2 V from coil A to the whole sextupole voltage for better readability.

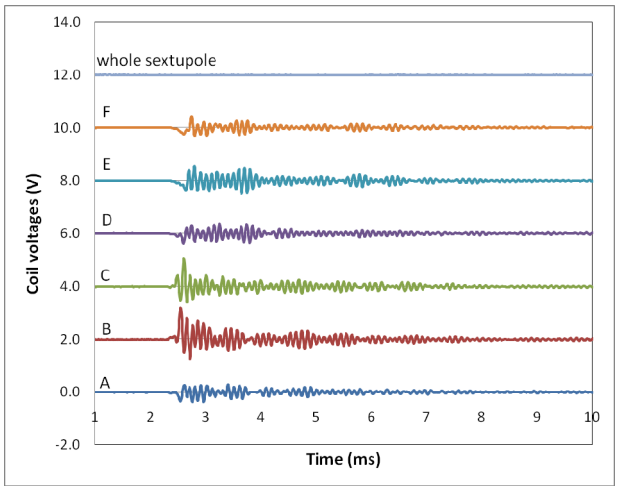

Figure 9: An example sextupole coil slippage during the ramp. Terminal voltages across each individual sextupole coil (A to F) and the whole sextupole are shown.

The voltage spikes had a typical frequency of around 9 kHz but with damping amplitudes. The whole ringing lasts around 5.7 ms. In the example shown, the slippage was initiated by a movement in coil B at 2.33 ms, accompanied by a movement in coil C at 2.39 ms. The peak voltage change was around 1.2 V in coil B, which was the highest of all the slippage events recorded. An examination of the recorded slippage events shows that the slippage did not concentrate in one particular coil indicating that neither a particular coil or part of the structure in the assembly are defective. Since the total flux in the whole sextupole must be conserved, no voltage spike was observed across the whole sextupole. No voltage spikes were observed in the solenoids during the test.

Even though many slippage events were observed when the sextupole current was higher than 400 A (90% of design current) with full solenoid field, none of these slippages with energy release led to any quench, as mentioned above. The high Cu/SC ratio of the VENUS NbTi conductor could be one of the reasons that the small movements of the coils during the ramping do not lead to quenches, but are damped in the system.

Consequences of a lead quench versus a coil Quench

During the training phase and testing phase in 2000 the VENUS magnet quenched about 15 times. However, none of those quenches caused any damage to the magnet. So what is the difference between a lead quench and quenches initiated in the middle of the coil?

Quench inside the coil

The VENUS sextupole magnet coil assembly has an inductance of 1.2H and therefore a stored energy of 150kJ at full excitation current of 500A. The relationship is described by

$$E = \frac{L \cdot I^2}{2}, \qquad [1]$$

where L is the coil inductance and I the drive current.

During the quench process, this stored electromagnetic energy is converted into heat and the rising coil resistance causes the current to decay. The critical value is the maximum temperature inside the coil during the quench. The quench propagates through the coil from the point of origin, driven by resistive heating and heat conduction. It propagates in a three dimensional process along and transverse to the windings. In the VENUS sextupole coil this propagation is sufficiently fast to dissipate the energy over the whole coil. This prevents overheating of the wire at the origin of the quench.

Using the program QUENCH[6,7] for the VENUS sextupole magnet, it can be estimated that the maximum temperature inside the coil in this case reaches less than 120K, a conservative and reasonable value. Two scenarios were simulated. In the first case only one coil was considered, assuming that each coil is quenched independently. Therefore, the stored energy is dissipated over all coils evenly. In the second scenario it was assumed that the stored energy of all six coils would be dissipated in one coil. The reality lies in between these two extreme scenarios since the adjacent sextupole coils will quench also as the quench progresses and dissipate some of the stored energy.

Figures 10, 11 and 12 show the dynamics of a coil quench. The internal voltage build-up across the coil triggers the quench protection causing the power supply to be shut off within 50ms and the current to be shunted through the quench protection diodes. However, very little energy can be dissipated through the quench protection circuit. Most of the power needs to be dissipated in the coil itself, which contains sufficient specific heat in the copper to safely absorb the stored energy of the magnetic field. The collapsing field and rising temperature causes the adjacent coils to quench. The current decays within 1 sec to less than 200 A preventing any damage to the coil or the lead wire.

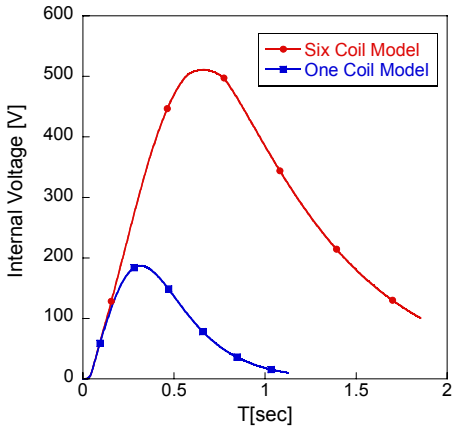

Figure 10: QUENCH Model Calculations for the sextupole magnet, the internal coil voltage is plotted for the two extreme scenarios.

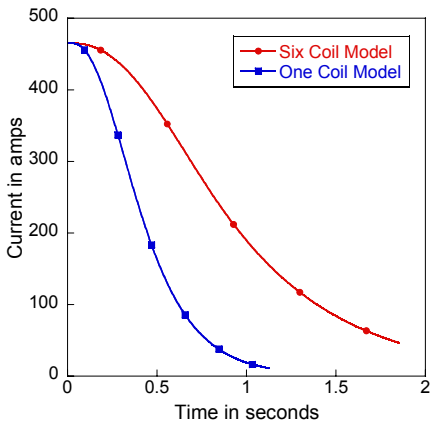

Figure 11: QUENCH Model Calculations for the current decay following a quench.

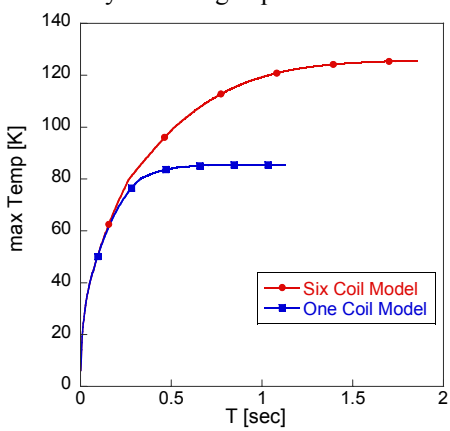

Figure 12: QUENCH Model Calculations of the maximum temperature inside the sextupole coil.

Lead Quench

During a lead quench the quench propagation dynamics is dramatically altered. The VENUS lead-quench started about 1 m above the sextupole coil at the normal conducting solder joint between two superconducting wires due to insufficient cooling. In this particular case, the quench propagation is only linear along the wire and is further slowed down once the quench reaches the liquid helium level. Assuming a longitudinal quench propagation of 5-20 m/sec[8]. It takes 50 to 200 ms for the quench to reach the coil. Although the wire heats up very quickly, the voltage built up is rather low until the quench reaches the coil. The quench protection detection does not engage, resulting in continued full current flow while the quench is propagating through the lead wire (Figure 13). Once the lead wire opens, the inductively-driven internal voltage in the coil sustains a helium plasma arc between the burned out wire-section, which further damages the wire.

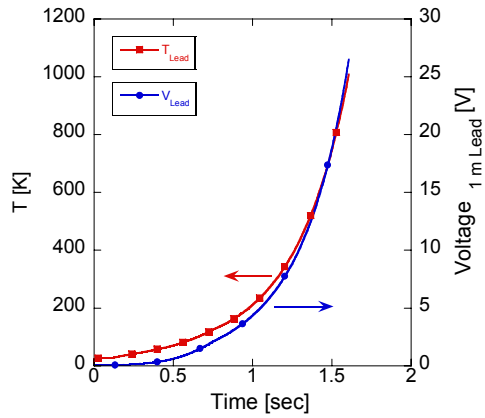

Figure 13 Worst case temperature rise for a 1m long single wire sextupole lead (465 A, .9mm x 1.8mm, 3:1 Cu/sc ratio) and voltage built up in the lead.

An adiabatic model of the temperature rise inside a 1m long wire (not cooled) predicts that in about 1.4 seconds the NbTi wire reaches temperatures above 600K at which point the superconducting properties deteriorate irreversibly, and in about 1.7 seconds the wire reaches 1300K at which point the copper melts. Although this model is simple, it describes a fairly realistic scenario since the VENUS magnet leads were wrapped in shrink tubing which prevented any possibility of vapor cooling of the leads.

Design options available to avoid lead burn-out

A failure as experienced with VENUS causes a severe interruption of the ion source operation, since the repair takes many months. Therefore it is very important to consider lead quench scenarios during the design phase of a superconducting ECR ion source. There are several strategies that can be pursued to avoid this kind of damage.

One possibility is to design the leads to be cryogenically stable. In this case the wire must be heavily reinforced with copper to avoid the risk of reaching elevated temperatures. However, this solution is somewhat cumbersome and carries the risk that in the case of a quench the quench propagation would be very slow and could lead to a coil edge quench, which could damage the first turns of the superconducting coil.

Another design possibility would be to pursue an active quench protection system, which would be a preferred solution for a new magnet system. An active quench protection system could include a) external dump resistors

that divert the energy away from the magnet as soon as the quench is detected, and b) heaters in contact with the superconducting coils that spread the quench as quickly as possible once a quench is detected. In addition, the leads must be further protected by adding voltage taps across the normal conducting splicing section, which would enable to detect a lead quench quickly, and would activate the active quench protection before the wire would be damaged.

However, one of the most important diagnostics for the cryogenic system must be reliable and redundant liquid helium sensors, which are interlocked with the magnet power supplies.

VENUS repair

Several improvements are currently being incorporated in the VENUS magnet system to protect it from lead quenches in the future. Most importantly, the liquid helium level will be monitored with two independent liquid helium sensors, which are included in the magnet interlock chain. The current carrying leads have been doubled to increase the superconducting margin of the charge leads. This will reduce the likelihood of initiating a quench in the lead. In addition, doubling the cross section will reduce the current density by a factor of four, without reducing the quench propagation speed too much. In addition, the original shrink-tubing insulation around all lead wires has been replaced with a Teflon spiral insulation, which allows active vapor cooling and liquid helium penetration. Finally, an additional thermal link between the normal conducting solder joint and the liquid helium level will be installed to improve the cooling of this solder joint. Together, these design changes will substantially reduce the probability of a similar failure in the future.

REPAIR SCHEDULE

After the successful cold test the VENUS cold mass will be reinstalled into the helium vessel. The lower cryostat has to be rewelded and the sealed. The service tower will be reconstructed, welded to the lower cryostat and the insulation and the wiring restored. Once the cryostat is reconstructed and inserted into the iron yoke, the VENUS ECR ion source can be reinstalled on the vault roof of the 88-Inch Cyclotron. The present time schedule estimates that these final steps will need four to six months, meaning that this repair will have required more than 12 months until VENUS is fully operational again.

ACKNOWLEDGEMENTS

The authors would like to thank the main mechanical shop at LBNL for the excellent and dedicated work during the VENUS repair. In additional we would like to thank the LBNL Supercon group for taking on the task of analyzing the failure, repairing the VENUS magnet, and allowing us to use of the superconducting magnet test facility. In particular we would like to thank Jim Swanson and Paul Bish for their technical support in the repair of the VENUS wires and the preparation for the cold test.

This work was supported by the Director, Office of Energy Research, Office of High Energy and Nuclear Physics, Nuclear Physics Division of the U.S. Department of Energy under Contract DE AC03-76SF00098

REFERENCES

[1] D. Leitner, M L Galloway, T.J. Loew, C.M. Lyneis, I. Castro Rodriguez, D.S. Todd, and J.Y. Benitez, RSI **79** (02A316), (2008).

[2] C. M. Lyneis, D. Leitner, O. Tarvainen, D. Todd, S. Virostek, T. Loew, and A. Heinen, Rev. Sci. Instrum. **77** (03A342), 1-5, (2006).

[3] C. E. Taylor, S. Caspi, M. Leitner, S. Lundgren, C. Lyneis, D. Wutte, S.T. Wang, and J.Y. Chen, IEEE Transactions on Applied Superconductivity **10** (1), 224, (2000).

[4] D. Leitner, J.Y. Benitez, M L Galloway, T.J. Loew, C.M. Lyneis, and D.S. Todd, Proceedings of the 18th International Conference on Cyclotrons and Their Applications (CYCLOTRONS 2007), Giardini Naxos, Messina, Italy, 2008

[5] K.S. Golovanivsky, Instrumentations and Experimental Techniques **28** (5), 989, (1986).

[6] M. N. Wilson, Oxford University Press, in *Superconducting Magnets*, edited by Oxford University Press (1983), p. 218.

[7] M. N. Wilson, Report No. RHEL/M151, 1968.

[8] M. N. Wilson, Oxford University Press, in *Superconducting Magnets*, edited by Oxford University Press (1983), p. 206.

NEW 28GHZ SC-ECRIS FOR RIKEN RI BEAM FACTORY PROJECT

T. Nakagawa ,J. Ohinishi, H. Higurashi, M. Kidera, H. Okuno, K. Kusaka, Y. Sato, O. Kamigaito, M. Kase, A. Goto, and Y. Yano, RIKEN Nishina Center, Wako, Saitama, Japan
T. Minato, Mitsubishi Electric Corporation, Kobe, Hyogo, Japan

Abstract

To increase the intensity of U ion beam for RIKEN RI beam factory project, we started to construct new SC-ECRIS. The main features of the ion source is as follows 1)the ion source has a large size of ECR surface 2) field gradient and surface size at ECR zone can be changed independently to study these effects on the ECR plasma. Six sets of solenoid coils and hexapole coil are used for making the magnetic field. The maximum magnetic field of RF injection side (B_{inj}), beam extraction side (B_{ext}) and radial magnetic field at the plasma chamber surface (B_r) are 3.8, 2.4 and 2.1T respectively. The construction began at Mitsubishi Electric Corporation in October 2007. After all the coils were wound and assembled, the excitation tests were performed in June 2008. After excitation test, we obtained the 85~90% of designed value. In the excitation test, we recognized that it is necessary to reinforce the structure at the coil ends of the hexapole. After the test, we started to modify the structure of the hexapole coil end. In September 2008, we will start the second excitation test.

INTRODUCTION

Since middle of 1990s, RIKEN has undertaken construction of new accelerator facility so-called Radio Isotope Beam Factory (RIBF) [1] and successfully produced 345MeV/u U beam (~4 nA on target) in 2007.[2] However, to meet the requirement of the RIBF (primary beam intensity of 1pμA on target), we still need to increase the beam intensity of the heavy ions. For this reason, we started to construct the new superconducting ECR ion source (SC-ECRIS) which has an operational frequency of 28 GHz.

Before construction, we intensively studied the effect of the key parameters (magnetic field, RF power, gas pressure bias disc etc) on the plasma and beam intensity for optimizing the structure of the ECRIS. During the investigation, we obtained several interesting results.[3-5] Based on these results, we designed the ion source and made a first excitation test of SC-coils.

In this paper, we report the structure, progress of the new RIKEN SC-ECRIS construction

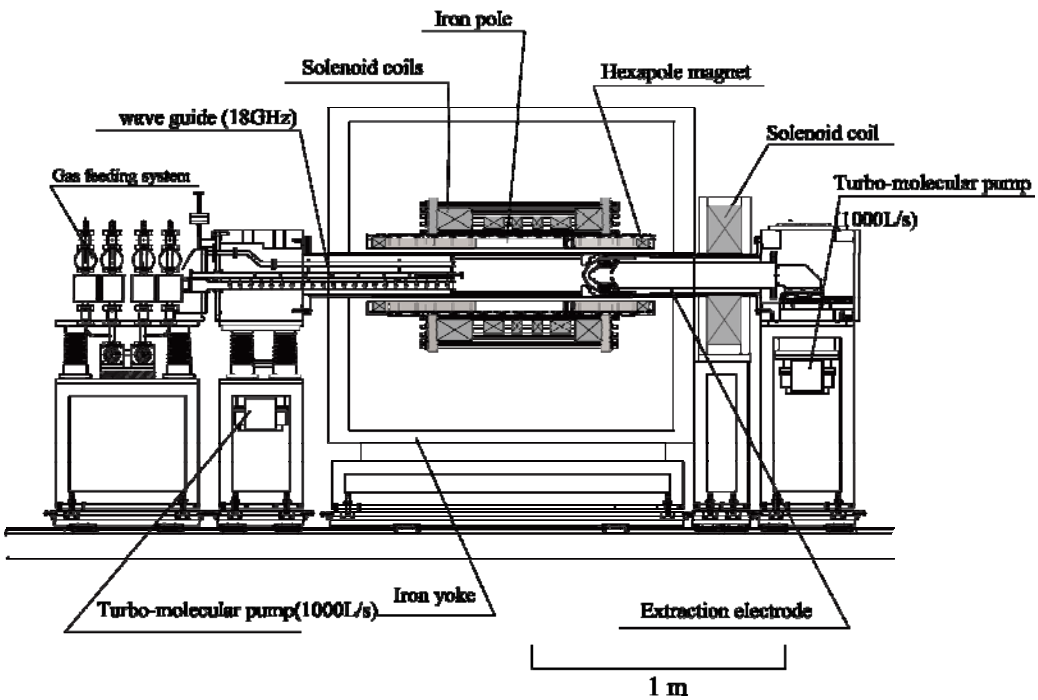

Fig.1 Schematic drawing of the RIKEN SC-ECRIS

SOURCE DESGIN

Figure 1 shows the mechanical layout of the RIKEN SC-ECRIS. As described in ref.3, we used the six solenoid coils to choose the resonance surface size and field gradient at resonance zone, independently. Using this system, we can test the effect of field gradient and zone size on the beam intensity. Figure 2 shows the ECR zone size vs. B_{min}.

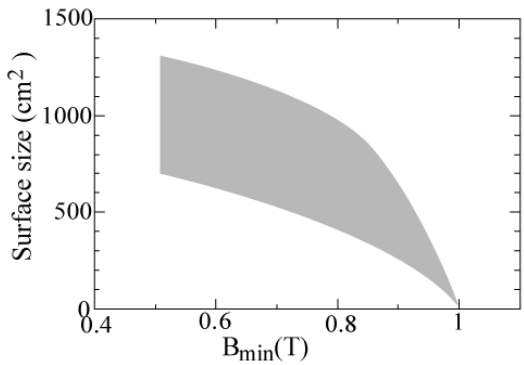

Fig.2. ECR zone size vs. B_{min}.

Superconducting coils and cryostat

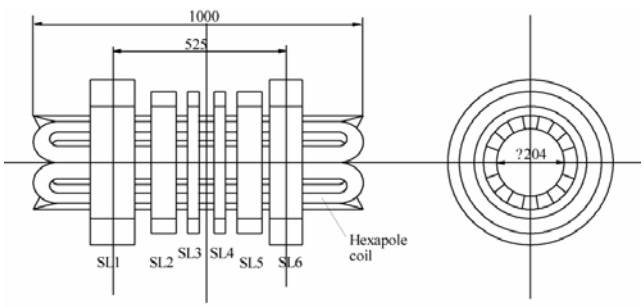

Fig.3. Schematic drawing of the superconducting coils

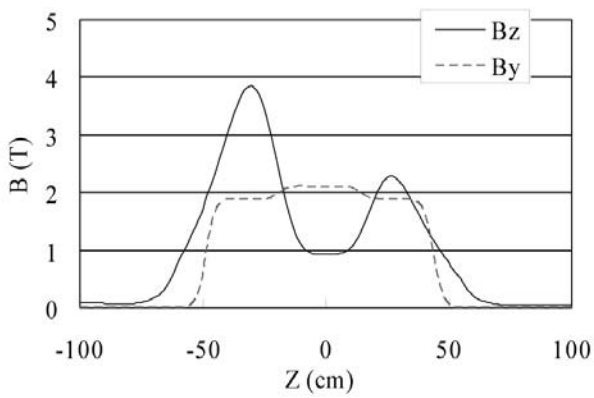

Fig.4. Axial and the hexapole magnetic field distributions along the beam axis

A schematic drawing of the superconducting coils is shown in Fig.3 [7]. Figure 4 shows the designed axial and the hexapole magnetic field distributions along the beam axis. The maximum axial magnetic fields are 3.8 T at the RF injection side (B_{inj}) and 2.2 T at the beam extraction side (B_{ext}). Inside radii of the hexapole and solenoid coils are 102 mm and 170 mm, respectively. Four coils (SL2 ~SL5) are used for making a flat magnetic field region between the mirrors. The maximum hexapole magnetic field is 2.1 T on the inner surface of the plasma chamber (r = 75 mm). The hexapole magnetic field in the central region is increased by using iron poles, which is same structure as the VENUS.[6] A NbTi-copper conductor is used for coils and these are bath-cooled in liquid helium. Parameters of the coils are shown in Table 1. A conductor with a round shape of φ1.09(a NbTi/Copper ratio of 6.5) is used for SL3 and 4. A conductor with a rectangular shape of 0.82 mm x 1.15 mm (a NbTi/copper ratio of 1.3) is used for the other solenoid coils and the hexapole. Figure 5 shows the Ic performance of the conductor with a rectangular shape and the load points for the solenoid SL1 and the hexapole. Although the maximum field on the hexapole coil windings is 7.4 T, the component perpendicular to the current direction is 6.5 T. The magnetic stored energy is 830 kJ with all coils at the design current.

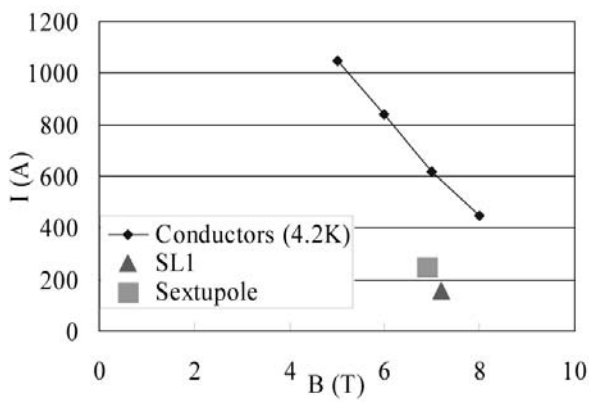

Fig.5. I_c performance of the conductor with a rectangular shape and the load points for the solenoid SL1 and the hexatupole

The longitudinal distributions of the magnetic force acting on the straight region of the hexapole coils are shown in Fig. 6. Because the expansion magnetic force in the azimuth direction is generated by their self-field as well as the radial magnetic field of the solenoids, its magnitude changes according to the longitudinal position and the polarity of the hexapole coil. It is clearly seen that the magnetic force becomes strongest in the region between the SL1 and the SL2. The six hexapole coils are assembled using titanium spacers with a triangle cross section and fixed with four layers of φ0.65 mm stainless steel wires wound with very high tension of about 580 MPa. A stainless steel disk with outer diameter

of 250mm and a thickness of 30 mm are inserted between the SL1 and the SL2 to fix the hexapole coils more tightly because the magnetic force in the azimuth direction is strongest there. 3D calculations of the deformation of the coil assembly were performed with ANSYS [7]. The coils were treated as orthotropic material where the elastic coefficients are 97 GPa in the direction of conductors and 16 GPa in the orthogonal. Assuming that a shrinkage factor of the coils is 0.5% in the cooling down to the LHe temperature, the tension of the binding wire was calculated to decrease by 25% and the coils to shift inward by 0.16 mm at the maximum due to the remaining compressive force. Each of the hexapole coils was dry-wound to work for turn transitions and was vacuum impregnated with epoxy. The percolation of the epoxy into the inside of the windings was inspected to be successful by cutting a trial winding. On the other hand, each solenoid coil was wet-wound with warm epoxy and cured. Figure 7 shows the final assembly of the hexapole coils and six solenoids. The ends of the hexapole coils are fixed with a stainless steel ring to support the large radial magnetic force acting on the current return sections. The six solenoids were assembled with stainless steel spacers and tightened with sixty-four long aluminum-alloy bolts that support a repulsive force of approximately 800 kN at the maximum.

Table 1. Parameters of the superconducting coils

	SL 1	SL 2	SL 3	SL 4	SL 5	SL 6	Sextupole
Inner radius (mm)	170	175	175	175	175	170	102
Outer radius (mm)	250	220	220	220	220	250	142
Length (mm)	135	75	35	35	75	100	1073
Conductor size (mm)	0.82 x 1.15	0.82 x 1.15	φ1.09	φ1.09	0.82 x 1.15	0.82 x 1.15	0.82 x 1.15
Cu/NbTi ratio	1.3	1.3	6.5	6.5	1.3	1.3	1.3
No. turns	9124	2778	1305	1305	2778	6830	1216
Current (A)	162	182	109	109	155	132	271
Bmax (T)	7.2	5.2	3.1	3.0	4.8	5.4	7.4 (6.5)
Ic (A)	203	298	229	233	278	223	349
Iop/Ic	0.80	0.61	0.47	0.47	0.56	0.59	0.78
Inductance (H)	34.0	4.0	1.0	1.0	4.0	20.0	6.9

Amount of the liquid-He is assumed to be ~500 L. The cryostat is equipped with two small GM refrigerators for 4 k and 70 K stages and operated without supplying liquid He after poured once. In addition, to increase the cooling power at 4K, we will use two GM-JT refrigerators, which have total cooling power of 10W at 4K. The nine current leads made of high temperature superconducting material are used to minimize the heat load to 4 K stage. The heat load to 70 K stage is 160 W caused by copper current leads, supports of a cold mass and radiation through the multi-layer insulation.

The maximum electromagnetic force between the magnetic shields and the cold mass is estimated to be 8 tons in axial direction. The cold mass is supported with the belts from an outer tank in room temperature. Four belts with a cross-section of 300 mm^2 are used for the axial direction to support the axial force up to 10 tons. On the other hand, eight belts with a cross-section of 80 mm^2 are used for each of the vertical and horizontal directions to support up to 5 tons. The six solenoids and the hexapole coils are excited individually with seven power supplies. The solenoid coils are excited through seven high temperature superconducting current leads. The current lead between two adjacent solenoids is used to reduce the heat load. The diodes are placed in the liquid He vessel to protect the coils when any of the high Tc current leads breaks.

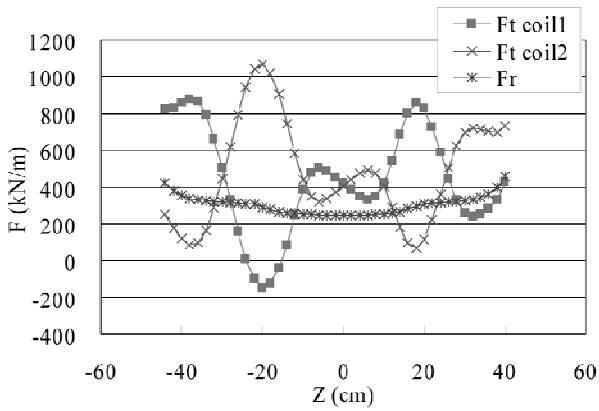

Fig.6. Longitudinal distributions of the magnetic force acting on the straight region of the hexapole coils

Excitation test

After the solenoid and hexapole coils were assembled, the excitation tests were performed in a cryostat. Both ends of all coils of the solenoids and the hexapole were connected with clamp diodes placed in liquid helium for the quench protection. Each solenoid coil achieved the design current without a quench.

Next, the hexapole coils was tested. Table 2 shows the currents when a quench occurred in the

hexapole. The hexapole also achieved the design current (271A) after two quenches (189A, 255A) when no solenoids were excited.

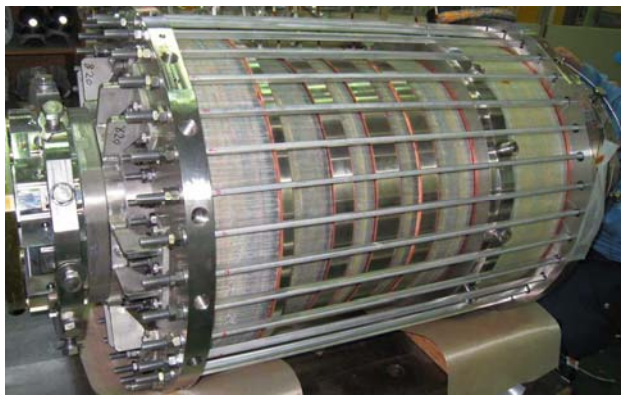

Fig.7. Picture of SC-coils

Table 2. Coil currents (A) when the sextupole quenched.

run #	sextupole	SL1	SL2	SL5	SL6
design	272	162	182	155	132
1	189				
2	255				
3	90	136	183		
4	65	136	183		
5	73	136	183		
6	114	136	183		
7	70	136	183		
8	77	136			
9	109				132
10	220				92
11	204			155	132
12	230			132	112
13(NQ)	272				
14	258	146	164		
15	234			135	114
16	238			136	116
17	235	127	143		
18	256	137	154		

In the combination tests in which the hexapole and one or two of the solenoids were excited at the same time, the hexapole coils quenched in all cases. The hexapole quenched at low currents ranging from 65 A (24%) to 115 A (42%) when the SL1 and the SL2 were excited at their design currents in advance (run #3~#7). The hexapole coils also quenched similarly when the SL6 was excited in advance (run #9, #11). A cause of these quenches was presumed to be a coil motion at the ends of the hexapole coils from the voltage signals, which observed in some of these runs. In run #10, the SL6 was ramped after the hexapole coils was excited at 220 A.

In run #12 and #14~#17, the solenoids and the hexapole coils were excited simultaneously keeping a ratio of the currents. In this case the direction of the force acting on the hexapole coils did not change during the excitation. The quench current of the hexapole increased to more than 85% of the design value in this way. It, however, was difficult to reach the design current. We have thus concluded that it is necessary to reinforce the structure at the ends of the hexapole coils.

PLASMA CHAMBER

Two turbo-molecular pumps (1100L/sec) are placed at the RF injection side and beam extraction side to keep the high vacuum of the plasma chamber (~10^{-8} Torr). The maximum extraction voltage is 40kV. The position of extraction electrode is remotely controlled. The high temperature oven is inserted from the RF injection side. To set the oven on the optimum position, the position of oven is also remotely controlled. The negatively biased disc is placed in the axial direction and its position is remotely controlled with the accuracy of 0.1 mm.

The inner diameter and outer diameter of the plasma chamber are 150 and 162 mm, respectively. The chamber is made of double wall stainless steel tube with the water cooling channel in between. To keep the high voltage (40kV max), the kapton sheet (total thickness of 2mm) covers the plasma chamber. For high voltage test, we could easily supply 40kV to the plasma chamber and kept it for 1hour without high voltage break.

LBL group demonstrated that the temperature of the cryostat increases with increasing the RF power in case of 28GHz.[9] It is due to the high energetic X-ray form the ECR plasma. To minimize the X-ray effect when using 28GHz microwave, the plasma chamber is covered by the 2mm thick Ta sheet.

LEBT for SC-ECRIS

Although we planed to construct a new injector system for injecting the U beam into the RIKEN ring cyclotron, we will start for construction in 2009 at the earliest and it takes several years. In order to supply the intense U beam to the experimentalist as soon as possible, we will install the SC-ECRIS on the existing high voltage platform of RIKEN heavy ion linac, which was used for injecting the heavy ion beam into the linac, before construction of the new injector. For injecting U^{35+} beam into the linac, we need the acceleration voltage of ~130kV.

After the extraction of the beam at 30kV, the solenoid coils is used for focusing the beam. Design of the 90-degree analyzing magnet is based on the LBL one [10]. The vertical gap and bending radius are 150 mm and 510 mm, respectively. The ion source, solenoid coil, and bending magnet will be installed on the high voltage platfrom. The U^{35+} beam (energy of 130qkeV)

will be transported from high voltage terminal to the first acceleration tank of Riken heavy ion linac.

These ion beams are accelerated by accelerator complex of RIKEN RIB factory project up to 345MeV/u.

PLANED SCHEDULE

The excitation test after modification of sc-coils will be done in middle of September 2008. After second text experiment, the superconducting coils will be installed in the cryostat. Final acceptance test of the magnet will be concluded by beginning of December 2008. The ion source assembling will be done in December 2008. 90deg. analyzing magnet is constructed by end of January 2009. After assembling, the ion source and analyzing magnet will be installed on the high voltage plat home.

The first plasma will be obtained in spring 2009 using two 18GHz microwaves power supply (total output power of 3kW)

ACKNOWLEGDEMENT

Authors wish to thank Dr. Lyneis and Dr Leitner for their variable information of the X-ray shielding method, design of the analyzing magnet, etc for designing the SC-ECRIS.

REFERENCES

[1] Y. Yano, NIM A261 (2007)1009.
[2] A. Goto el al., 18th Int. Conf. Cyclotron and Their Applications, Giardini Naxos, Sep. 2007, p. 3.
[3] T. Nakagawa et al., Rev. Sci. Instr. 79 (2008) 02A327.
[4]M. Imanaka et al, NIM B237(2005)647
[5]H. Arai et al, NIM A491(2002)9
[6] D. Leitner et al., 18th Int. Conf. Cyclotron and Their Applications, Giardini Naxos, Sep. 2007, p. 265.
[7] J. Ohnishi et al., High Energy Physics and Nuclear Physics 31, suppl. 1, 37 (2007).
[8] http://ansys.com.
[9]D. Leitner et al, RSI 79(2008)033302.
[10] M. Leitner et al, Proc. of 15th International workshop on ECR ion sources, Jyvaskila, Finland, June 2002, p32

PAPER NOT RECEIVED

COMMISSIONING RESULTS OF THE 18GHZ FULLY SUPERCONDUCTING ECR ION SOURCE SUSI

G. Machicoane, D. Cole and P. Zavodszky

National Superconducting Cyclotron Laboratory, Michigan State University, East Lansing, MI48824, USA

Abstract

The construction of SUSI the 3rd generation ECR ion source from NSCL/MSU has been completed. After an initial period marked by problems with its coil system, SUSI has now reached stable operation at 18GHz. Excellent performances have been obtained during the commissioning of the ion source for various elements including: ^{40}Ar, ^{129}Xe and ^{208}Bi. Some early results regarding beam transport are also discussed and in particular the choice of not using a focusing element between the ion source and the bending magnet.

INTRODUCTION

The coupled cyclotron at the National Superconducting Cyclotron Laboratory (NSCL) at Michigan State University (MSU) can accelerates heavy ion beams up to 200 Mev/u. This primary beam is then used to produce radioactive ion beams by fast fragmentation on a beryllium target. In order to respond to the experimental program in nuclear science, a wide range of primary beam has been developed since 2001 from ^{16}0 to ^{238}U. Beams are initially produced by an ECR ion source and then transported at low energy before injection in the K500. Final acceleration is made into the K1200 and in recent years large gain in beam intensity have been achieved for most beams. In particular more than a 1kW of primary beam power can now be extracted from the K1200 for ^{48}Ca and ^{40}Ar. These gains in beam intensity were not achieved by increasing the ion current extracted from the ECR ion sources but instead reflect a strong effort to improve the beam transport in particular from the ECR to the K500 [1]. However it is clear and in particular for heavier ion beams, that the gains that can be ultimately achieved through the coupled cyclotron largely rely on the choice of the ECR ion source used to inject the beam. SUSI the most recent ECR ion source from NSCL is a fully superconducting ECR source designed to operate primarily at 18GHz. Large gains in beam intensity are therefore expected compare to our 6.4 GHz SC-ECR or 14GHz ARTEMIS. In addition a flexible axial magnetic field described previously [2] provides the capability to modify the length and the position of the resonant zone and also to adjust the gradient of the axial magnetic field near the resonance. Finally, the injection baffle can be moved providing an additional knob that allow for example to adjust the volume of the plasma chamber. These innovative features in the SUSI design should help to not only maximize the intensity of the extracted ion beam current but more generally to optimize the brightness of the extracted ion beam.

MAGNET TESTS AND QUENCHES

However, to achieve an ion source with a flexible axial magnetic field requires the design and construction of a complicated coil system. The axial magnetic field of SUSI is defined using 6 solenoids. Two large solenoids at the injection with an outer diameter of 460mm, and four smaller ones with two at the extraction of the source plus an additional two more in the middle. These fours smaller solenoids have an outside diameter of 400 mm and the two solenoids in the middle are running with opposite polarity. All six solenoids have an inner diameter of 300 mm and a length of 80 mm. A field of 2.6T/1.5T can be reached at the injection/extraction side by powering either coil with 290A/210A. The hexapole coils are also superconducting and are 743 mm long. The ends of the sextupole are far from the central field of the solenoids, to minimize the interaction forces. Based on a similar design developed at LBNL for the construction of VENUS, these coils were wound around a three-piece core, which includes a central piece made of steel to enhance the field. The sextupole coils can provide 1.5T at the plasma chamber walls with 390A.

All coils were wounded at NSCL and then tested individually. During these tests, the solenoids were taken beyond 400A without training. On the other hand the sextupole coils experienced a few training quenches but eventually reached more than 700A each. These current values are well beyond the values needed for operation of the ion source at 18GHz and in fact would correspond to the current needed to operate the ECR ion source with a 28GHz microwave frequency transmitter. After the tests with the individual coils were completed, the assembly of the full coil system took place. The sextupole coils were assembled around the bore of the helium vessel tube, banded together and then inserted into the solenoid bobbin. Bladders installed between each sextupole and inflated with an Indium alloy were used to restraint the sextupole coils from moving radially. A very detailed and complete description of the design, construction and assembly of the coils can be found elsewhere [3]. Once the assembly was complete the coil system was cooled down in a large Dewar and tested. Because the number of current leads on the Dewar was limited, only four solenoids plus the sextupole could be energized at any given time. Additionally, the two large solenoids at the injection were serially connected and depending on the

tests either the middle coils or the extraction coils were also connected in series. In this configuration the sextupole was first ramped up and underwent some training quenches. After 10 quenches, the sextupole could reach 567A and was then ramped down to zero without a quench. With no current going to the sextupole, the solenoids were then energized and quenched once at 365A before reaching 400A without any further problems. However it was found that it was not possible to reach a configuration with both the sextupole and the solenoids energized while ramping them sequentially. This situation always resulted in a quench and no improvement was observed over time. Measurements with an oscilloscope showed that the quench always occur first in the sextupole. This behavior did not improve by trying to train the sextupole to higher current or by decreasing the ramp rates of the power supplies used. Also improving the restrain on the leads did not help. Fortunately, a solution was found by ramping together both the solenoids and the sextupole. Although initially, this configuration also resulted in a few quenches, it was found that the coil assembly energized in this way could be trained and in a short time the solenoids reached close to 400A and additional training allowed the sextupole to reach 585A. These tests confirmed earlier findings made with the individual coils that the magnet system can be run with currents high enough to provide a magnetic field suitable for operation at 28GHz. Once done with these tests, the coil system was installed inside the SUSI cryostat. By the end of 2006, the assembly of the ion source was complete and after installation of the injection and extraction hardware the first plasma was ignited.

Unfortunately at that point, new unexplained quenches occurred. These quenches would not appear while ramping the field but instead some period of time after reaching the desired field. The length of time the magnetic field would stay up was found to be extremely random and was measured to be as little as a few minutes or as long as several days. In addition stronger magnetic field did not seem to quench sooner. Careful monitoring of different sources parameters (Power supplies voltage, current and also strain gauges for the support links), showed that the first sign of a quench is always a strong decrease in current in the hexapole then followed by the current in the solenoid at injection. Various tests were made to explain the situation but none provided a satisfactory explanation. At last, the situation improved dramatically in September 2007. Two changes are worth noting that might have caused this sudden change. First the polarity of the sextupole was reversed and also soon after, the forces applied to the support links were adjusted. In a configuration where the magnetic field on the injection side of the ion source is produced by the coil located at the far end, no quenches have occurred since these changes were made. Also, with the same configuration, a magnetic field corresponding to the operation of the ion source at 24 GHz was run continuously for 24 hour without a quench. Finally, the commissioning results shown below correspond to more than 250 hours of operation without any problems. It should be mentioned however that, although the solenoids at the extraction of the source and the ones in the middle have been adjusted over a wide range while tuning the ion source, changes in the magnetic field at the injection of the source by trying to move the peak inward still result in a quench.

COMMISSIONING RESULTS AT 18GHZ

SUSI was directly connected to the 90-degree analyzing magnet without a focusing element in between. An einzel lens was used right after the bending magnet to help reach a smaller beam waist at the analyzing faraday cup. The ion source high voltage was about 24kV. After initial conditioning of the ion source, the base pressure at the injection reached about 6.10^{-9} Torr and about $1.3.\ 10^{-8}$ Torr at the extraction. 2 kW of microwave power was available from an 18GHz klystron. Additional power was used from a 14 GHz transmitter but was not find to help improving the production of Highly charged ions beyond a few hundred watts. Following some uncertainty remaining with the stability of the coil system, no attempt was made to tune the field in the injection region of the ion source and a field of 2.5T was kept constant using the most outward coil. Also, the sextupole during these tests was kept around 370A therefore producing about 1.5T at the plasma chamber walls. However both the current in the middle and extraction coils were adjusted to optimize the intensity of the extracted beam current. Very good performances from SUSI have been obtained for various ions. For Argon, about 550 euA of Ar11+ was reached with more than 1.5kW of microwave power and an additional 300 W from the 14GHz transmitter. For lower charges more than a 1mA was obtained for Ar8+. However a limited time was spent optimizing the charge state distribution for higher charge state and only about 145 euA was obtained for Ar14+.

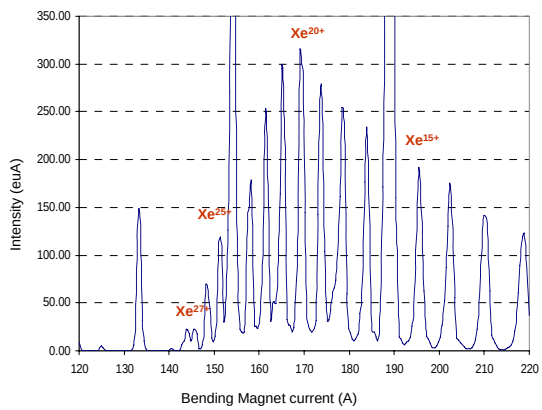

Figure 1: Xenon distribution optimized on Xe^{20+}

Figure 1 shows the distribution optimized for the production of Xe20+. About 335 euA was obtained for this charge state with 1.7kW microwave power. The same distribution but optimized for higher charge state is shown in figure 2 below. About 180 euA was obtained for

Xe27+, with essentially the same microwave power but with a lower Xenon pressure and more Oxygen.

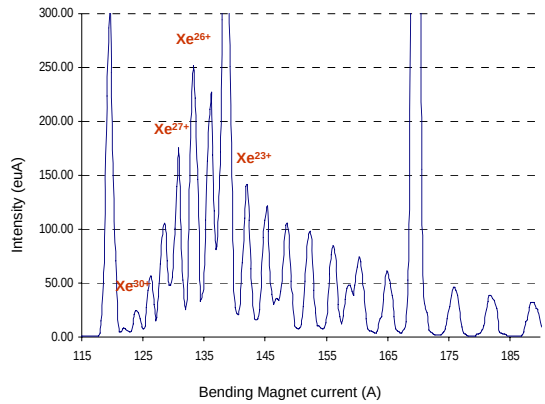

Figure 2: Xenon distribution optimized on Xe^{27+}

The microwave transmitter could not deliver more power reliably and it is expected that better performance could be reached if more microwave power at 18GHz is available. Some commissioning results have been obtained for Bismuth with a resistive oven, which can go up 1300 C. More than 150euA of Bi 28+ was obtained with 1.4kW of microwave power.

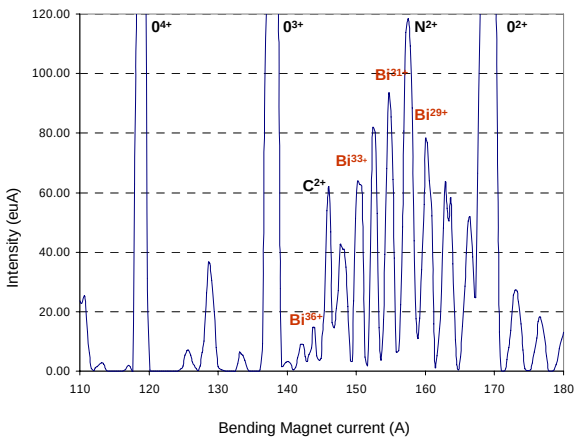

Figure3: 208 Bismuth distribution optimized for Bi^{33+}

Figure 3 shows the bismuth spectra optimized for high charge states. Up to 65 euA of Bi 33+ was produced and 15euA of Bi 36+. This time the microwave power was increased to the maximum available from the transmitter (1.7-1.8kW). It is interesting to note that these results were obtained before complete conditioning of the resistive oven and some significant amount of carbon are still present. It is expected that better results could be obtained if more time is devoted to the production of bismuth. In the present case the ion source was only run for a few days.

BEAM TRANSPORT

Some preliminary studies were made with the beam extracted from SUSI. The beam extraction consists of a plasma electrode (12mm in diameter) followed by an accel-decel system. The gap at extraction can be changed remotely over a range of 5 cm. The bending magnet provides double focusing with pole faces presenting an angle of 27.3 degree. This bending magnet has a large 18 cm gap and actively correct for higher order aberrations. The design was essentially based on the bending magnet developed for the VENUS ion source at LBNL. An initial test was conducted to check the linearity of the bending magnet. First a pencil beam was defined using a very small aperture. Then the beam was deflected horizontally and vertically using a magnetic steerer located 90 cm before the bending magnet and then finally the beam centroid position was recorded on a beam viewer located about 50cm after the magnet for each steerer settings. Provided that the deflection of the steering magnet has been calibrated (in this case 12mrad/A) the position of the beam at the entrance of the bending magnet can be known. The results indicated a central region of the bending magnet extending over 7cm in both directions, which provided an excellent linear response on the beam viewer.

An interesting feature of SUSI is the possibility to bias negatively the beamline between the ion source and the bending magnet to try to take advantage of a higher longitudinal energy when transporting the multi-component beam before charge selection. After a few weeks of conditioning, the beam line could effectively be biased to –20kV while maintaining +24 kV on the ion source reliably. Past experience at NSCL has shown that using a solenoid to provide the initial focusing of a beam extracted from an ECR ion source can lead to significant emittance degradation [4]. To mitigate space charge problem with the beam before charge selection it was decided to try to have the bending magnet right after the ion source without any focusing element in between. Of course, in this situation, the test with the bending magnet described above is important because the beam size is expected to be large inside of it. In this configuration, the distance between the plasma electrode and the edge of the bending magnet pole faces is 90cm. An einzel lens was added right after the bending magnet to improve the beam waist at the faraday cup. This latter was located 75 cm after the bending magnet. Finally an Allison emittance scanner was installed 30 cm after the faraday cup. Two cases were investigated using a ^{40}Ar beam and some preliminary results are shown here: an extracted beam current of about a 1mA obtained with a low microwave power (100W) and a 4mA beam current obtained with higher power (800W) and higher gas pressure. The beam transmission in the first case was close to 85 % and would increase slightly when a -20kV bias was applied on the beamline. In the second case, the transmission would reach 68% with the beamline grounded and increase to 83% with -20kV applied to the beamline. Then the emittance of Ar^{8+} was measured for both cases. Figure 4 shows the phase space distribution for (xx') and (yy') in the case of the 1mA (Top) and 4mA (Bottom) argon beam. The distributions obtained with the 1 mA beam show only little aberrations and mostly in the vertical plane.

Although it is unlikely that the bending magnet produce sextupole aberrations, the test done with the steering magnet needs to be cross check with computer calculations. The other explanation is that these tails originated at the extraction of the source. The emittance measurements for the case with a higher total extracted beam current (Bottom), reflects stronger aberrations due, most likely, to space charge. No improvement was observed when the beam line was biased at –20kV for the 1mA case which would reinforce the idea that the bending magnet is not contributing to the observed tails. On the other hand, some improvement was observed for the case at higher current.

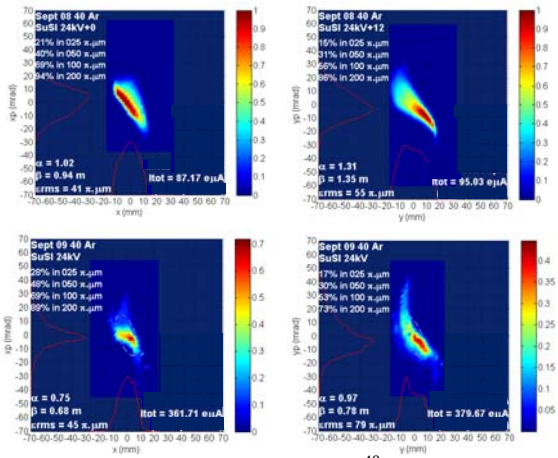

Figure 4: Emittance distribution for ^{40}Ar. Left to right are (xx') and (yy') respectively. Top pictures correspond to a 1mA beam extracted while the distributions at the bottom were obtained with a 4 mA beam current.

CONCLUSION

After a period marked with difficulties with its coil system, SUSI has now reached stable and reliable operation at 18GHz. A stronger magnetic field was also obtained for a short period of time that would make the ion source capable to operate at higher frequency (24GHz). Very good performances have already been obtained with SUSI for the production of high charge state ions of Xenon and Bismuth. Better performance could be obtained with more microwave power. More development will be done with metallic beams such as ^{40}Ca and using our inductively oven: ^{58}Ni, ^{76}Ge and ^{238}U. Also a systematic study needs to be made regarding the flexible axial field and will be reported soon. Finally, although, early results regarding the beam transport without a focusing element between the ion source and the bending magnet are encouraging, more work from both simulations and experiments is needed to validate this configuration. Plans are being made to move SUSI from the development Lab to the ECR area where it will be used for injection into the cyclotron next year.

REFERENCES

[1] M. Doleans "Optics Improvements of the K500 Axial Injection Line", 18th International Conference on Cyclotrons and their Applications, Giardini Naxos, Messina, Italy, September 30-October5, 2007

[2] P.A. Závodszky et al., Rev. Sci. Instr. 77, 03A334 (2006)

[3] P.A. Závodszky et al., Rev. Sci. Instr. **79** 02A302 (2008)

[4] G. Machicoane et al., "Experimental Evidences for Emittance Degradation by Space Charge Effects when using a focusing Solenoid below an ECR ion Source," Proceedings of ICIS2007, Jeju, South Korea, August 2007

ION BEAM RESEARCH AND DEVELOPMENT WORK AT JYFL

H. Koivisto, T. Ropponen, V. Toivanen and M. Savonen, JYFL, Jyväskylä, Finland

Abstract

During the last year the main focus of the JYFL ion source group has been on the studies of the beam transmission, time evolution of Bremsstrahlung (will be presented elsewhere in this same proceedings by T. Ropponen) and on the development of metal ion beams. Comprehensive studies of the beam transmission efficiency at the Department of Physics, University of Jyväskylä have shown several problems concerning the injection line of the K-130 cyclotron. The experiments have shown strongly non-uniform and elliptical beam shape, which limits the beam transmission efficiency. The durability of the inductively heated oven has successfully been improved and it has been tested with the 14 GHz ECRIS for the production of titanium and chromium ion beams. The intensity level of about 20 μA was reached for the medium charge states, which is adequate for most of the nuclear physics experiments at JYFL.

INTRODUCTION

According to operation experience with the K130 facility at JYFL (University of Jyväskylä, Department of Physics) the beam transmission efficiency decreases when the beam intensity extracted from the ECRIS increases [1]. In some cases the available beam intensity after cyclotron even decreased when the beam intensity from the ECRIS was increased. As a result of this behavior the beam transmission project was initiated in order to over come the problem and to meet the beam intensity requirements. The extensive beam transmission measurements were started in 2007 with the beam line simulations in collaboration with NSCL/MSU. As a result of the simulations several bottlenecks concerning the beam transmission were found. As a next step the beam transmission experiments were started in order to confirm the results obtained by the simulations.

The most of the beams needed for the nuclear physics experiments are produced with the JYFL 14 GHz ECRIS. Figure 1 shows the beam line components used for the focusing and steering of the ion beams from the ECRIS to the cyclotron. In this case the beam is transported via three different dipole magnets: DJ1 is used as a mass spectrometer, SWI1 is used to select the ion source for the experiment (i.e. light ion source, 6.4 GHz ECRIS or 14 GHz ECRIS) and DI2, which is used to bend the beam into the vertical injection of the cyclotron. As the figure shows the focusing of the beam is carried out with solenoids, which generates different focus points for different q/m-ratios. The beam diagnostics includes Faraday cups, beam viewers and an Allison-type emittance scanner.

BEAM TRANSMISSION EFFICIENCY

The objective of the beam transmission experiments was to define the losses of different beam line sections including the K130 cyclotron. The beam intensities were measured from several locations: FCJ2, FCI5, inflector, outer radius of cyclotron, after deflector and finally from PFC. The Faraday cup FCJ2 is located after the analysing magnet, FCI5 in the vertical beam line before the cyclotron injection and PFC is the first Faraday cup after the cyclotron.

Figure 2 shows the tendency of the transmission efficiency as a function of the beam intensity extracted from the 14 GHz ECRIS. Here the efficiency is calculated from the ion beam currents measured by FCJ2 after the first dipole magnet (DJ1) and by PFC after the cyclotron. The transmission studies were carried out using $^{40}Ar^{8+}$ ion beam, which corresponds to the q/m-ratio normally needed for the nuclear physics experiments. The voltage of 9.66 kV was used for the extraction of ion beam from the ECRIS and the beam current was varied by changing the microwave power. The experiments were carried out with the second harmonic acceleration.

According to the experiments the transmission efficiency decreases strongly when the beam intensity extracted from JYFL 14 GHz aECRIS increases. As Fig. 2 shows the total transmission efficiency has the value of about 15 % for the beam intensities less than 25 μA (drain current ≈ 0.5 mA). The efficiency degrades almost linearly when the beam intensity increases being only about 6 % for the beam intensities above 100 μA (drain current ≈ 1 mA or higher). The corresponding drain current of high voltage power supply is presented in the same figure. The drain current roughly corresponds to the total beam current extracted from the ECRIS if secondary electrons from the puller are excluded.

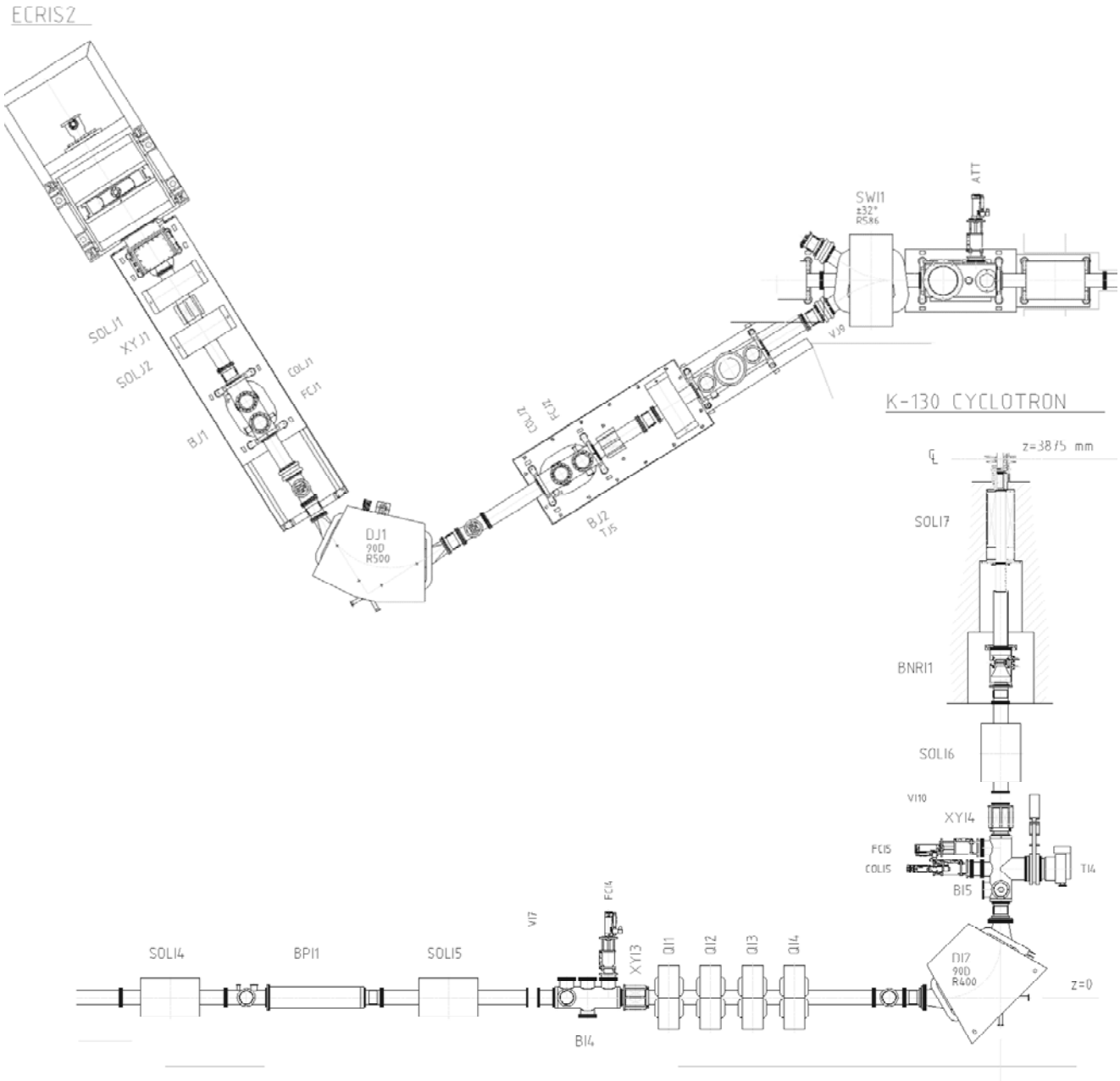

Figure 1: The JYFL beam line from the 14 GHz ECRIS (ECRIS2) to K130 cyclotron.

From Fig. 2 it can be estimated that about 6 μA of the $^{40}Ar^{8+}$ ion beam can be extracted from the K130 cyclotron when 50 μA is available from the ECRIS. Approximately the same accelerated beam current is available if the beam intensity from the ECRIS is doubled. Consequently, there is no ambition to improve the performance of the ECRIS before the reason for the behavior has been found.

As was mentioned earlier the beam currents were measured from different sections of the beam line. It was found that the tendency shown in Figure 2 can be seen only in the section between FCJ2 and FCI5 (see Fig. 3). The other sections have practically constant transmission efficiency or the intensity effect is of the order of 10 % or less. This indicates that the main problem in the case of the second harmonic acceleration exists before FCI5. As a next step it has to be defined if the main problem is the ECR ion source or the beam line.

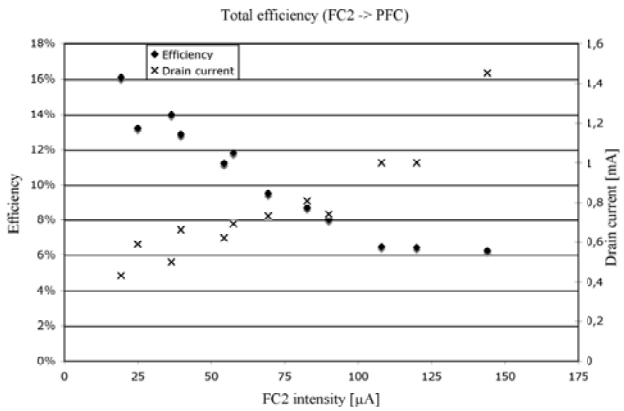

Figure 2: Total transmission efficiency of K130 cyclotron facility, i.e. (PFC/FC2), in the 2nd harmonic acceleration.

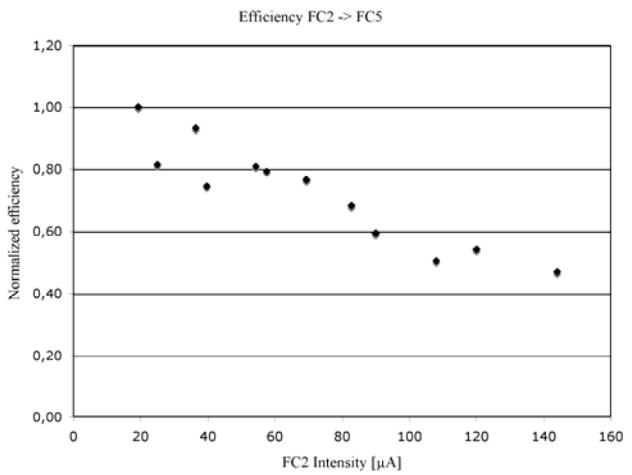

Figure 3: Transmission efficiency between FCJ2 and FCI5 (see Fig.1).

BEAM STRUCTURE

The beam line simulations were carried out by DIMAD code [2]. According to simulations the entrance and exit angle of dipoles in the beam line are not exactly correct (DJ1 and DI2). As a consequence, the focusing properties in different planes are not same, which results in an asymmetric beam profile. The 2D emittance of asymmetric beam can increase remarkably when focused by the solenoids making the beam injection into the cyclotron more inefficient.

In order to confirm the beam line simulations KBr beam viewers were installed before and after the analysing magnet (DJ1). As upper picture of Fig. 4 shows the beam profile after the analysing magnet is elliptical as was anticipated from the DIMAD simulations. In this case the $^{40}Ar^{9+}$ beam intensity was only 33 μA. In addition to elliptical shape a hollow beam structure (lower picture of Fig. 4) is present when the beam intensity exceeds the value of about 70 μA or strong solenoid focusing is used. This certainly decreases the beam quality and transmission efficiency. The hollow beam structure tends to be more pronounced when the beam intensity and the strength of the focusing power increases.

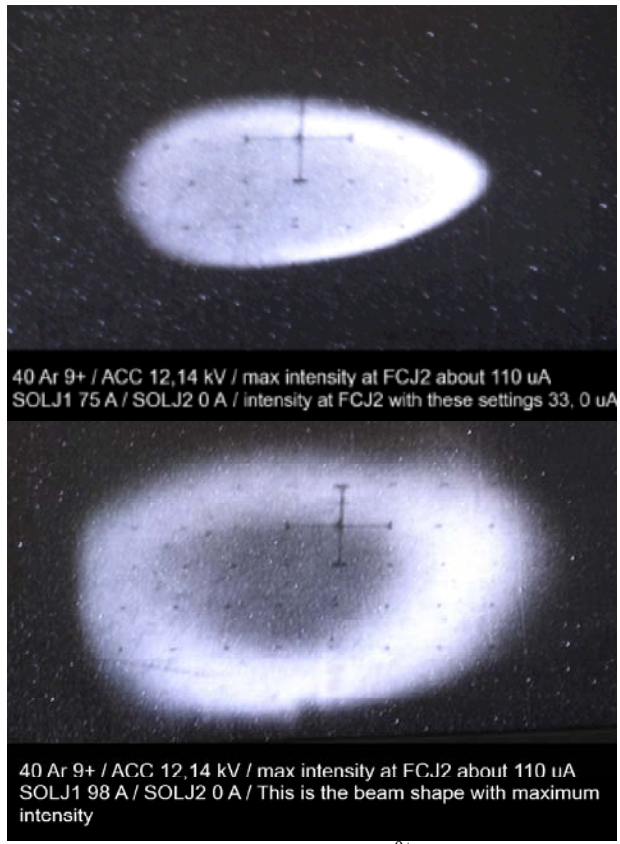

Figure 4: The beam profiles of Ar^{9+} ion beam after the analysing magnet.

TRANSMISSION EFFICIENCY WITH HIGHER INJECTION VOLTAGE

The effect of injection voltage on transmission efficiency was tested with Ar^{9+} ion beam using 9.75 kV and 12.14 kV. The injection voltage needed for the cyclotron operation is defined by the energy required for the nuclear physics experiments. Typical energy is slightly above the Coulomb barrier, i.e about 5 MeV/nucleon, which requires the injection voltage of about 10 kV. The use of higher injection voltage would then require geometrical changes into the central area of cyclotron in order to make the acceleration of ions possible.

According to Child-Langmuir law the improvement of about 40 % can be anticipated when the injection voltage is increased from 9.75 kV to 12.1.4 kV. However, the improvement of about 100 % was obtained (see Fig. 5). This indicates that the beam intensity within the acceptance of the cyclotron increases drastically with the injection voltage. A possible explanation is that the effect of the hollow beam structure shown in Fig. 4 decreases dramatically with the injection voltage. This can be due to decreased space charge effect. The same effect can

possibly be obtained with the lower beam intensity (i.e. lower space charge effect). This will be studied later.

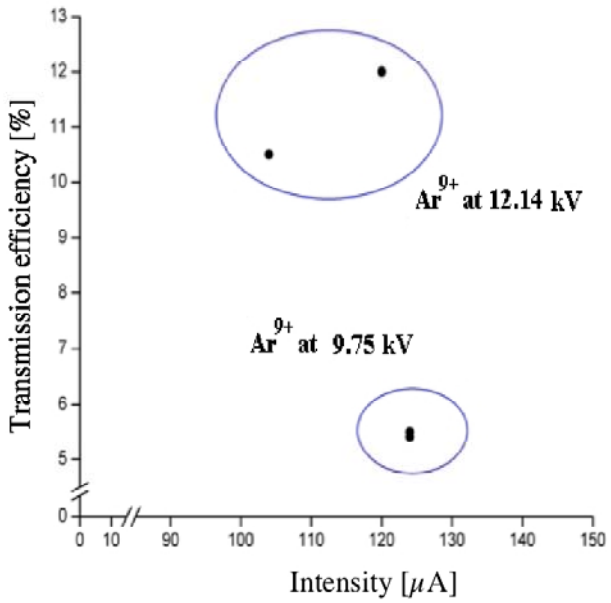

Figure 5: The effect of injection voltage (= extraction voltage of ECRIS) on the beam transmission efficiency.

TESTS WITH QUADRUPOLES

Quadrupole magnet focuses ion beam in one plane and defocuses it in the perpendicular plane. Thus it is possible to alter the shape of the beam profile by using quadrupole magnets. An experiment was carried out to determine if the beam quality at JYFL could be improved by reshaping the beam profile this way. To achieve this, a quadrupole doublet was temporarily installed before the analysing magnet (DJ1) of JYFL 14 GHz ECRIS and the beam shape was observed with a beam viewer after the analysing magnet. The beam was focused through a 20 mm aperture after the beam viewer and its intensity was measured with Faraday cup (FCJ2). Just after the FCJ2 (see Fig. 1), the beam emittance was measured with Allison-type emittance scanner.

The quadrupole magnets proved to be effective in the reshaping of the beam, especially in the case of fixing a strong elliptical profile to a more circular one. Reshaping of the beam caused considerable increase in the beam intensities measured in FCJ2. These changes are probably caused by the 20 mm aperture in the beam line. Previously the aperture had caused more beam losses because of the elliptical shape of the beam. With quadrupole magnets it is possible to focus more beam through the collimator. The measured intensities after the analysing magnet increased on average over 14 % when quadrupole magnets were used. Intensities after the cyclotron increased on average almost 10 %.

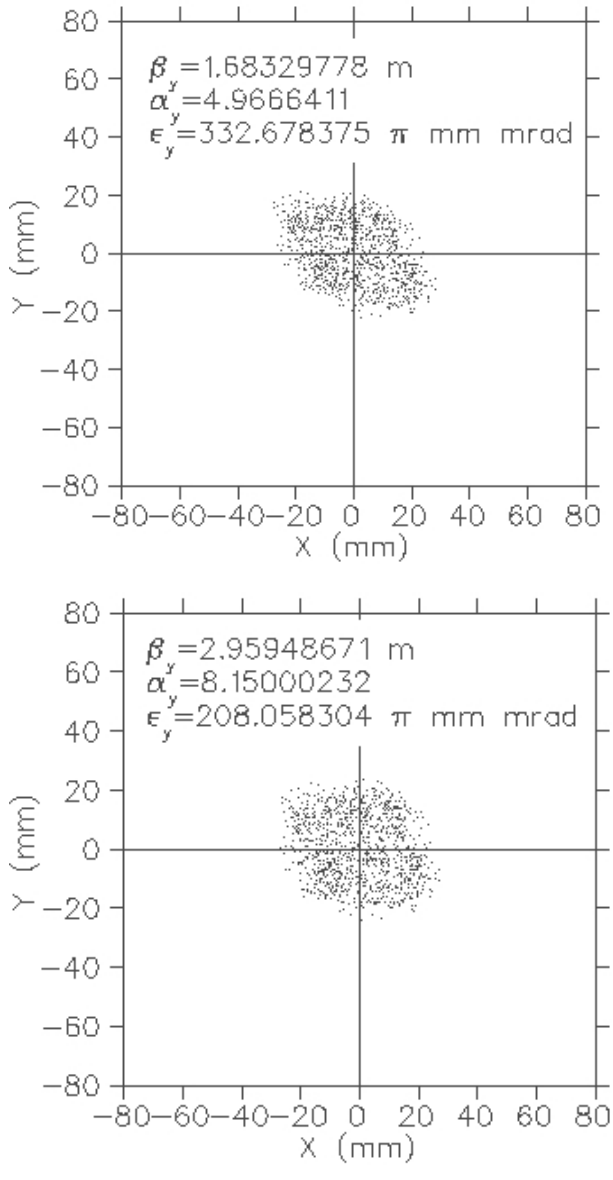

F

Figure 6: Upper picture: Beam profile and emittance without the quadrupoles. Lower picture: Beam profile and emittance with the quadrupoles.

Reshaping of the beam had a significant impact on the beam emittance. The emittance decreased with the use of quadrupole magnets over 25 % on average. Aberrations, which can be seen as 'S'-shape in the emittance phase space plots, were reduced. A similar decrease of emittance was also seen in computer simulations (see Fig. 6). According to the results of these simulations, the beam is more symmetric at the emittance scanner due to the use of quadrupole magnets. This results in a smaller value of beam emittance.

Although it was assumed that the reshaping of the beam would improve the beam transmission efficiency, this was not observed. It is possible that the beam quality degrades during the remaining transmission line so much that there

is no clear improvement in the transmission efficiency even if the starting conditions have become better. With higher intensities the beam also becomes hollow which further decreases the beam quality and transmission efficiency. This may hide some improvements, which otherwise could be gained from reshaping the profile of a higher intensity beam. It is also possible that the beam intensity within the acceptance of cyclotron does not increase although the emittance has decreased (i.e. only some aberrations have decreased due to more circular shape of the beam).

METAL ION BEAMS

The titanium and chromium ion beams have been developed with the inductively heated oven [3]. The oven can reliably be operated at the temperature of 1700 ˚C, which is needed for the production of Ti ion beam (the oven has been tested up to 2000 ˚C). In the case of $^{nat}Ti^{10+}$ the intensity of 20 μA and 1 μA were extracted from the JYFL 14 GHz ECRIS and the K130 cyclotron, respectively. During the experiment the consumption rate was slightly less than 2 mg/h. Oxygen was used as a buffer gas and clear getter effect was seen in operation. The intensity level after the ECRIS was about 20 μA for the medium charge states like Ti^{10+}. After the test a clear degradation of ECRIS performance was found. The other experiment was carried out using helium as a buffer gas. In this experiment the same intensities and consumption rates as with oxygen plasma were achieved. In the case of chromium similar intensities were obtained as with titanium. However, the consumption rate was remarkably lower (≈ 0.5 mg/h) and a clear effect in the subsequent performance was not seen.

FUTURE PLANS

The main focus of the work of the JYFL ion source group will be in the beam formation and transmission. According to measurements the main problem is the hollow beam structure, which is more visible with higher beam intensities. Several different solutions will be considered and tested. The higher injection voltage would certainly be the most effective solution. However, in this case a new central area for the cyclotron has to be designed and constructed. The higher injection voltage decreases the space charge effect. A smaller charge density can easily be achieved with a smaller extraction aperture of ECRIS, which will be tested at JYFL. This decreases the total beam current but probably the decrease is more pronounced for the low charge states as is indicated by some experimental results (for example by the LBNL ion source group [4]). However, the beam quality can improve faster than the beam intensity decreases due to the smaller extraction aperture, which can result in a higher ion beam current after the cyclotron.

The simulations in order to see the effect of Wien-filter have been started. The first results indicated that the size of the filter might be too large to be installed in the extraction area of ECRIS. However, the simulations will be continued. The Wien-filter would be beneficial because it would make it possible to remove all unwanted elements – i.e decreases the total current - from the extracted beam. In addition, focus points of different q/m-ratios before the analysing magnet can be avoided. The relocation of the JYFL ECRIS closer to analysing magnet will be considered. It is also possible that the successful project concerning the electrostatic focusing performed at the NSCL/MSU [5] will be carried out at JYFL. The Bremsstrahlung experiments will be continued.

ACKNOWLEDGEMENTS

This work has been supported by the EU 6th programme “Integrating Infrastructure Initiative – Transnational Access”, Contract Number: 506065 (EURONS) and by the Academy of Finland under the Finnish Centre of Excellence Programme 2006-2008 (Project No. 213503, Nuclear and Condensed Matter Programme at JYFL).

REFERENCES

[1] H. Koivisto, et. Al., Rev. Sci. Instrum., 79, (2008), p. 02A303.
[2] R. Servranckx, K. Brown. L. Schachinger, D. Douglas, Users Guide to the Program DIMAD, SLAC report 285 UC-28 May 1985.
[3] H. Koivisto et. al., High Energy Physics, and Nuclear Physics, Vol. 31, Supp. I, Jul., (2007), p. 41.
[4] D. Wutte, M.A. Leitner and C.M. Lyneis, Physica Scripta, T92, (2001), p. 247.
[5] X. Wu, et. al., High Energy Physics, and Nuclear Physics, Vol. 31, Supp. I, Jul., (2007), p. 196.

THE HIGH CHARGE STATE ALL-PERMANENT MAGNET ECRIS OPERATED ON 320 KV HV PLATFORM*

L. T. Sun#, J. Y. Li, Y. C. Feng, Y. Cao, P. Z. Wang, S. Sha, X. Z. Zhang, H. Wang, B. H. Ma, M. T. Song, X. W. Ma, H. W. Zhao, Institute of Modern Physics (IMP), Chinese Academy of Sciences, Lanzhou, 730000, P. R. China

Abstract

An all-permanent magnet ECR ion source named LAPECR2 (Lanzhou All-permanent magnet ECR ion source No. 2) has been built and tested at IMP. This ion source is designed and operated to produce intense ion beams of both low charge states (such as H+, He2+, Xe3+…) and high charge states (such as Ar14+, Xe30+…) for the 320 kV high voltage (HV) platform at IMP. Many good results have been obtained on LAPECR2, such as 1emA O6+, 130 eμA O7+, 166 eμA Ar11+, 2 eμA Ar16+, 0.33eμA Ar17+, 85 eμA Xe20+, 24eμA Xe27+, 2eμA Xe31+. This ion source was designed to fulfill the various requirements of all of the experimental terminals, such as the delivery of metallic ion beams. A high temperature micro-oven has been fabricated and installed on the source to produce stable metal vapor. This HV platform has been successfully biased to 390 kV without ion beam. And ion beams with the energy up to 340 keV/q have already been delivered to the successive experimental terminals. After a brief introduction of the source LAPECR2, the operation status on the HV platform is discussed. The typical performance of the source of both gaseous and some metallic ion beams will be given in this paper.

INTRODUCTION

As the most efficient machine to produce stable intense high duty factor high charge state ion beams, ECR ion sources have been widely adopted as the injectors of multiple charge state ion beams for different purposes [1]. With the development of the techniques of ECRISs, many high performance ECRISs have been built around the world, such as GTS [2], VENUS [3], SECRAL [4], etc. These ion sources can provide very intense high charge state ion beams for the successive accelerators or experimental terminals. Besides the demands of high performance room temperature or superconducting ECRISs, there is great demand of all permanent magnet ECRISs, because of their typical characteristics such as large electricity free, strong cooling water free, easy handling and operation, simple structure, etc. With the advancement of NdFeB techniques, high remanence and high coercivity materials are now comercially available, which enables the realization of high magnetic field with comparably reasonable cost. The Nanogan series [5] and the BIE series [6] are all successful candidates of all permanent magnet ECRISs.

With the development of heavy ion beam associated research, we notice that there is an energy margin between the ion beams delivered by an ordinary ECRIS platform and the ion beams accelerated by SFC accelerator at IMP (K=69), which covers many interesting fields concerning heavy ion beams. To promote the studies in these fields, a 320 kV HV platform had been set up by the end of 2006. Five experimental terminals of this HV platform are dedicated to the research activities of highly charged ion physics, atomic physics, material physics, biophysics, and astrophysics respectively. These research activities inquire the platform to deliver ion beams of both light and heavy elements from low charge states to high charge states. Thus, the project of building a high performance all permanent magnet ECRIS LAPECR2 was started from the beginning of 2004. In this paper, the commissioning results of LAPECR2 and the operation status on the HV platform are presented.

LAPECR2 ION SOURCE

The physical goals of the 320 kV HV platform inquire that LAPECR2 should be a high charge state ECR ion source that can deliver both gaseous and metallic ion beams. This indicates that high B, high rf frequency and high rf power modes should be taken into consideration in this design. However, one of the biggest drawbacks of all permament magnet ECRISs is the inflexibility of the magnetic field and insufficient field strength. Thus, the designed magnetic field configuration should be optimized for the desired operation mode. The latest semiempirical scaling laws of ECRIS [7] can be an important reference in the conceptual design. In our design, three big 24-segmented axial magnetic rings at the source injection side provide the injection magnetic field peak up to about 1.3 T, and three 24-segmented axial magnetic rings at the extraction side provide the extraction field up to about 1.1 T. A single central axial magnetic ring increases the Bmin field up to 0.42 T. And the radial magnet is a 36-segmented Halbach structure hexapole which provides a 1.2 T radial field at the inner wall of a Ø67 mm ID plasma chamber. These key parameters are designed to optimize the operation of the source at 14.5 GHz. To have sufficient radial confinement to the plasma and also to keep the axial field high enough, the hexapole, one of the injection magnetic rings and also one of the extraction magnetic rings are specially shaped to satisfy the physical requirements (as shown in figure

* Work supported by National Scientific Fund for Outstanding Youth through the contract of 10225523 and National Natural Science Foundation of China for Young Scientists through the contract No. 10405026

sunlt@impcas.ac.cn

1). According to the simulation with TOSCA 3D, the total field |B|= 1.05 T= 2Becr contours are well close inside the plasma chamber.

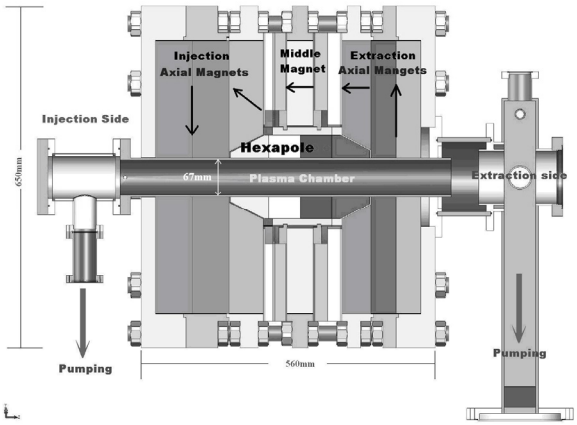

Figure 1: Schematic of LAPECR2 ion source

After about one year's fabrication, the magnetic body was then ready for source commissioning. The measured magnetic field is very close to the designed values. A double wall water-cooling SS plasma chamber is installed to have better cooled chamber in order to avoid thermal demagnetization of the permanent magnet and to minimize the outgassing of the inner surface of the chamber at high rf power injection. 14.5 GHz microwave power is injected into the plasma chamber through a WR62 microwave guide. A simple diode extraction system is adopted to let intense ion beams extraction at HV=25 kV. The total magnetic body and some of the accessorial components are floated at the extraction HV potential.

COMMISSION RESULTS

LAPECR2 was firstly ignited at the middle of 2005 with oxygen plasma at 14.5 GHz with a 350 W TWT microwave generator. But because of HV platform setup, the source could only give the first results at the middle of 2006 [8]. Since LAPECR2 has adopted a plasma chamber whose ID dimension is comparable to that of a room temperature ECRIS, 350 W microwave power feeding is not sufficient to achieve the best performance. A 14.5 GHz klystron microwave generator with the maximum microwave power output of 1.1 kW is adopted as the microwave power generator, with the sacrifice of the alteration of the microwave frequency. RF power coupling, ion beam extraction and transmission are always the spiny aspects in the field of ECRIS. The condition becomes even more severe for an all permanent magnet ECR ion source. For most ECR ion sources, rf power direct feeding through rectangular waveguide is always adopted because of its simple structure and comparably better rf power coupling efficiency. While for a permanent magnet ECR ion source, the injected rf power before being fed into the plasma chamber, it will encounter several parasitic resonances under vacuum (as illustrated in figure 2), which may lead to power absorption inside the waveguide if the vacuum inside the waveguide is not good enough. As for the case of LAPECR2 source, many Ø2 mm holes are drilled at the both H sides of the WR62 waveguide inside the vacuum to help vacuum evacuation inside the waveguide. In this way, the rf power feeding efficiency is improved a lot. The positive and negative magnetic fields (as shown in figure 2) at the ion beam extraction and transmission region of a permanent magnet ECR ion source give much trouble to ion beam extraction and transmission. For LAPECR2, the negative field at the extraction region is -0.87 T, which has the effect of a permanent magnet Glaser lens to the ion beam transmission. Some ion beam mismatching problem might occur during the optical design for the ion beam transmission system. The negative stray field should be considered in the corresponding simulations. For LAPECR2, a solenoidal lens after the source has been adjusted in position to minimize the effect of the negative stray field and also to reduce the magnetic force between the source body and the Glaser lens which is caused by the magnetization of stray field to iron yoke of the Glaser lens. It is worth mentioning that the beam loss caused by ion beam transmission mismatching will be catabatic when the HV platform is biased to hundreds of kV.

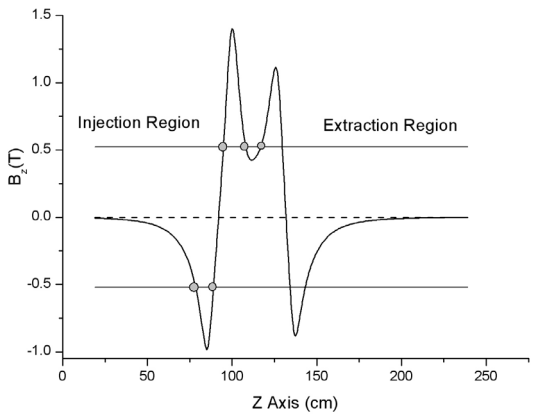

Figure 2: Magnetic field configuration of LAPECR2 and the stray field at injection and extraction sides

By proper solution of the problems of vacuum, extraction HV, microwave power injection efficiency and so on, very promising results of gaseous ion beams have been obtained on LAPECR2 [9]. Figure 3 presents the typical xenon ion beam intensities in comparison with those of other high performance ECRISs. These results are mostly obtained under the condition of 1.1 kW microwave power feeding and an extraction HV of 25 kV. With the power density of about 1.0 kW/l inside the plasma chamber, the typical performance of LAPECR2 is very promising and can even be comparable with those obtained on some room temperature ECR ion sources working at 14.5 GHz, such as LECR2 [10] and 14.5 GHz Caprice [11].

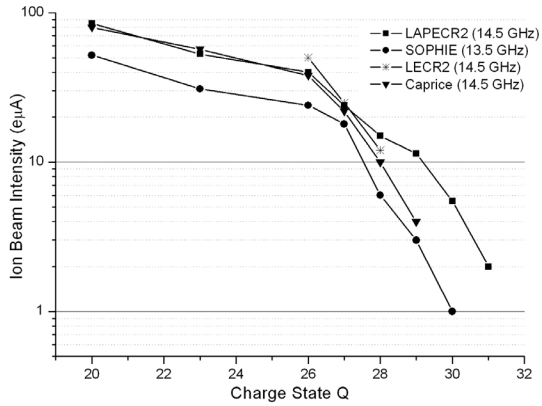

Figure 3: Typical xenon ion beam results in comparison with other high performance ECRISs at 14.5 GHz

METALLIC ION BEAM PRODUCTION

The 320 kV HV platform at IMP is a versatile tool for different physical studies. Gaseous element ion beams are always demanded, however, metallic ion beams are also very important. While the designing of LAPECR2, metallic ion beam production has been taken into consideration. Micro-oven evaporation, plasma sputtering and MIVOC are the possible choices. For low melting point metals, micro-oven is a very suitable method. We have fabricated a medium temperature micro-oven suitable for the accurate handling of the temperature at 300□~1000□. Figure 4 illustrates the temperature evolution vs. electric power of the oven. By heating the plasma with a 14.5 GHz TWT microwave generator, the first obvious bismuth spectrum was observed when 9.0 W electric power was applied on the micro-oven, but most of Bi ion beam peaks on the spectrum were very small. By increasing the electric power up to 11.2 W, the beam spectrum peaked at Bi19+. And higher charge state bismuth ion beams such as Bi28+, Bi31+ can be clearly observed in the spectrum as indicated in figure 5. When Poven was enhanced to 12.6 W, 24 eμA Bi21+ was detected. During the tuning, high charge state bismuth ion beams were also detected at the Faraday cup. 17 eμA Bi28+ and 5 eμA Bi31+ are the typical results. As the plasma of LAPECR2 was just recovered from carbon ion beam production, the inner surface of the plasma chamber was severely contaminated. That is why the carbon ion beam peaks are so high in the spectrum when optimizing bismuth ion beam production. For unknown reasons, the bismuth material inside the oven was dissipated very fast. Within about 72 hrs, 900 mg bismuth material was totally evaporated. The possible reason might be that the increment of the temperature in the oven was too fast. And the working condition was not well optimized. This experiment is just a preliminary test. A further experiment with an aluminium chamber is scheduled.

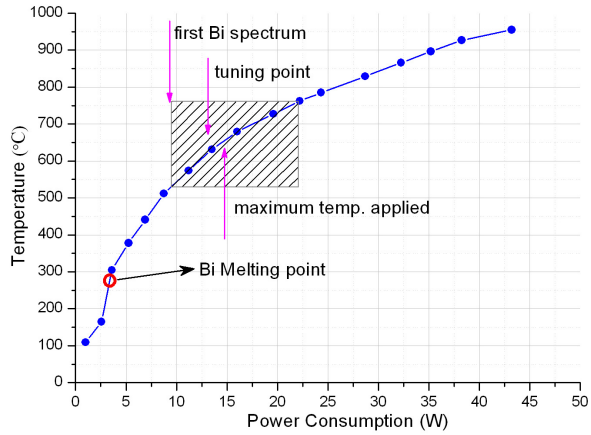

Figure 4: Oven temperature vs. oven electric power

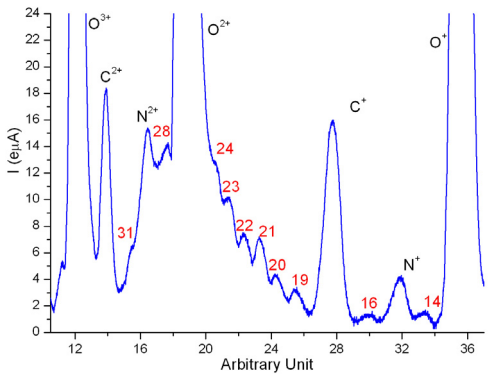

Figure 5: One of the spectra optimized for Bi

THE 320 KV HV PLATFORM

The IMP HV platform is designed to be operated in the energy range of 20~320 kV/q, which covers most of the energy range that interests the researchers of the five experimental terminals. The LAPECR2 ion source, a Glaser lens, a 90º analyzer magnet, a three-column electrostatic lens and the accessories (include power supplies, etc.) are situated on the HV platform. Since many units on the platform need low pressure water cooling, Water pipe with maximum 4.0 kg/cm2 output water pressure is connected to the platform. The maximum drain current of the 400 kV HV power supply is 2.5 emA, which demands that the total drain current from the water pipes should be as low as possible. The electrical resistivity of the cooling water is about 1 MΩ·cm. The single cooling water pipe is about 25 m, which is twisted on an insulator column. During the operation, a 0.8 emA drain current can be observed when ion beam is off. And when ion beams are accelerated, the total drain current increment is around 0.1~0.2 emA. These results are well up to the functioning margin of the HV power supply. All the units on the HV platform are powered through a 400 kV HV insulating transformer. An Ø180 mm ID acceleration column which has a 45-electrode structure has been adopted to connect the HV platform and the vacuum tube at ground potential. In the commissioning procedure of the HV platform, the

platform has been biased to 390 kV with the acceleration column installed. The control of all the units on the HV platform is realized by a RF remote control system. According to the more than 3000 hrs operation, this system is quite reliable and stable.

Ion beams extracted from LAPECR2 are analyzed by a 90º double-focusing 67 mm gap analyzer. A Glaser lens mounted between the ion source and the analyzer is a very useful tool for the ion beam transmission adjustment. After been analyzed, ion beam experiences an electrostatic lens which is used to adjust for better ion beam transmission coupling between the HV platform and the acceleration column. At ground potential, the accelerated ion beam is delivered to the straight experimental beam line through a 90º double-focusing deflection magnet. There are totally 5 experimental terminals, which include one straight line terminal and 4 terminals with the ion beam distributed by 120º defection magnets from the straight line. Series of quadrupole magnets are used for ion beam focusing to each terminal. Figure 6 presents the envelope calculation to the first order with Trace 3D [12] for terminal No. 2. And the incident ion beam is 625 keV Xe25+ beam, and the acceleration column voltage is 400 kV.

When the HV platform is at ground potential, the available energy of the ion beams delivered for experiments are normally from 10 keV to 600 keV and the beam intensities vary from pA to μA. Taking Xe beam for example, the ion charge state available is varying from 2+ to 30+ and the extraction HV can be varied from 4.5 kV to 25 kV. Within such a big extraction HV range, it is very important to know how to have very good beam transmission efficiency, stability and beam quality to satisfy the requirements of the experiments. During the tests, we found that the transmitting efficiency of higher charge state heavier ion beams was higher than that of the lower charge state lighter ion beams. For example, at experiment terminal No. 3, the transmission efficiency of Xe22+ beam is 58% and 65 % for Xe27+, but under the same condition, the transmission of He+ is only 5%. It is also found that with lower extraction HV, the quality of the ion beam obtained at the experimental terminal was much worse than that obtained at higher extraction HV.

Since the December 2006, 320 kV HV platform has been operated for more than 11500 hrs for the commissioning of the HV platform and several physical experiments which covered 9000 hrs. The ion beams of Ar, Xe, Ne, He, O, C, H with various energies and different charge states have been produced. The on-line operation status of the all-permanent magnet source LAPECR2 is quite good. Even with a TWT microwave generator with maximum output rf power of 350 W, very promising ion beam intensities have been produced, such as 200 eμA Ar8+, 60 eμA Ar11+, 50 eμA Ne8+, 70 eμA Xe20+, 17 eμA Xe27+, etc. The operation time with the platform HV biased is up to about 5000 hrs. The highest on-line operation HV applied is 320 kV, which means the HV platform at IMP has the capacity of deliver multiple charge state ion beams with the energy in the range of 4.5 keV/q ~345 keV/q.

CONCLUSION

A high charge state all permanent magnet ECR ion sources have been successfully fabricated at IMP. After more than one years' modification and commissioning, some promising results have been obtained. Typical results like 1.0 emA O6+, 166 eμA Ar11+, 2 eμA Ar16+, 85 eμA Xe20+, 24 eμA Xe27+ and 5.5 eμA Xe30+ are close to or even better than some room temperature ECR ion sources working at 14.5 GHz. The good performances of LAPECR2 owe much to the optimum designed magnetic field configuration, some auxiliary tricks to enhance the plasma density and realize better confinement to higher charge state ions, effective solutions to some intractable problems such as effective rf power feeding, sparking, etc, and also sufficient source conditioning. LAPECR2 has already been dedicated to routine operation for the 320 kV platform. Many MCI beams, such as H+, He+, He2+, O4+, N5+, Ne9+, Ar12+, Xe20+, Xe29+, have already been delivered to the corresponding experimental terminals with the projectile energy in the range of 4.5 keV/q to 345 keV/q. Metallic ion beam production with Bi has also been tested on LAPECR2. Preliminary results show that LAPECR2 has the capability to produce intense high charge state metallic ion beams with the proper methods. More are expected with an aluminium chamber to be installed.

REFERENCES

R. Geller, Electron Cyclotron Resonance Ion Sources and ECR Plasmas (Institute of Physics, Bristol, 1996).

D. Hitz et al., Rev. Sci. Instrum. 75, 1403 (2004).

D. Leitner, M. L. Galloway, T. J. Loew, C. M. Lyneis, I. Castro Rodriguez, and D. S. Todd, Rev. Sci. Instrum. 79, 02C710 (2008).

H. W. Zhao et al., Rev. Sci. Instrum. 79, 02A315 (2008).

C. Bieth, J. L. Bouly, J. C. Curdy, S. Kantas, P. Sortais, P. Sole, and J. L. Vieux-Rochaz, Rev. Sci. Instrum. 71, 899 (2000).

Dan. Z. Xie, Rev. Sci. Instrum. 73, 531 (2002).

S. Gammino, G. Ciavola, L. Celona, D. Hitz, A. Girard, and G. Melin. Rev. Sci. Instrum. 72, 4090 (2001).

L. T. Sun et al. Rev. Sci. Instrum. 77, 03A319 (2006).

L. T. Sun et al. Nuclear Instruments and Methods in Physics Research B 263 (2007), p. 503–512.

H. W. Zhao, B. W. Wei, Z. W. Liu, Y. F. Wang, and W. J. Zhao, Rev. Sci. Instr. 71 (2000), p. 646-650.

D. Hitz, F. Bourg, P. Ludwig, G. Melin, M. Pontonnier, T.K. Nguyen, Proceedings of the 12th International Workshop on ECR Ion Sources, April 25–27, 1995, RIKEN, Japan, p. 126.

AccelSoft Inc., P. O. Box 2813, Del Mar, CA 92014 USA, 858-677-0133. Available from: accelsoft@ghga.com, www.ghga.com/accelsoft.

THE BIO-NANO-ECRIS PROJECT: A NEW ECR ION SOURCE AT TOYO UNIVERSITY TO PRODUCE ENDOHEDRAL FULLERENES*

T. Uchida#, H. Minezaki, Y. Yoshida, Toyo University, Saitama, Japan
S. Biri, ATOMKI, Debrecen, Hungary
A. Kitagawa, M, Muramatsu, NIRS, Chiba, Japan
Y, Kato, Osaka University, Suita, Japan
T, Asaji, K, Tanaka, Tateyama Machine Co Ltd., Toyama, Japan

Abstract

We are developing a new electron cyclotron resonance ion source (ECRIS) for the synthesis of endohedral fullerenes, which have potential in medical care, biotechnology and nanotechnology. So this ion source is called Bio-Nano ECRIS. It has been reported that ions of fullerenes and carbons-loss fullerenes, such as C_{60}^+, C_{58}^+, …, are easily produced in ECRISs. Such carbons-loss fullerenes might have an advantage for the production of various endohedral fullerenes. The Bio-Nano ECRIS is designed for the production of endohedral fullerenes. In this paper, the recent progress is briefly summarized; i) Bio-Nano ECRIS project, ii) design aspect of the Bio-Nano ECRIS, iii) results of the initial experiments on the production of the ions of fullerenes and carbons-loss fullerenes.

BIO-NANO ECRIS PROJECT

Endohedral fullerenes

Fullerenes have a unique type of inner empty space with their unusual cage-like structures [Fig. 1(a)]. A variety of atoms may reside in this space [1] and form endohedral fullerenes [Fig. 1(b)]. Endohedral fullerenes have novel physical and chemical properties that are very important for their potential applications such as magnetic resonance imaging agents, biological tracing agents, organic ferromagnets and superconductors etc.

Endohedral fullerenes are generally produced by arc discharge and laser vaporization methods [1]. These methods are originally for the synthesis of fullerenes. The soot, which contains fullerenes, is generated by arc discharge or laser vaporization of the pure graphite target. These methods are applied for the synthesis of endohedral fullerenes. By using the encapsulating elements-graphite mixed target in place of the pure graphite target, we can synthesize the endohedral fullerenes. However the atomic species and fullerene species, which can form endohedral fullerenes, are still limited for arc discharge and laser vaporization methods. For example, the production of iron-encapsulated fullerenes has not been successful so far. But it can be applied as magnetic resonance imaging agents. Thus, we aim the production of Fe@C_n using the Bio-Nano ECRIS, where @ means that the atoms listed to the left of "@" are encapsulated into C_n, C_n means fullerenes or carbons-loss fullerenes.

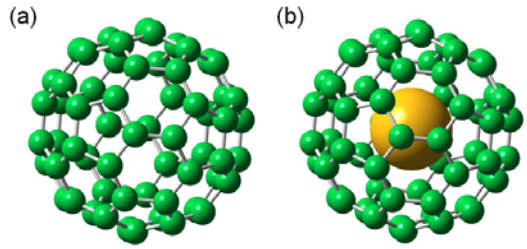

Figure 1: Illustration of (a) C_{60} molecule and (b) endohedral C_{60} molecule.

Recently the organic chemical synthesis of H_2@C_{60} has been reported by Komatsu et al. [2]. They demonstrated the synthesis of the open-cage C_{60}, which has a large orifice (13-membered ring), by an organic chemical reaction. And they synthesized open-cage fullerene incorporating hydrogen. They showed the availability of the open-cage fullerenes, which has a large orifice on their surface, for the production of endohedral fullerenes.

Fullerenes in ECRIS

Fullerene plasmas and beams have been produced in ion sources, such as electron impact, Nielsen-type, Nier-type, Kaufman-type, radio-frequency and ECR ion sources, for various scientific and practical reasons and purposes [3]. In particular, by using an ECRIS, collision reactions of fullerenes have been studied so far [4]. In a ECR plasma, fullerenes are ionized and fragmented; C_{60}^+, C_{58}^+, C_{56}^+, … are generated. Fullerene fragments (so-called carbons-loss fullerenes) are generated by eliminating C_2 units. We expect that carbons-loss fullerenes might have an orifice (7-membered ring or higher), even though such structure is unstable and transient. Therefore, carbons-loss fullerenes might have an advantage for encapsulating atoms into their inner spheres.

Our early study

In Institute of Nuclear Research of the Hungarian Academy of Sciences (ATOMKI), the encapsulation of gas atoms into fullerenes in ECR plasma has been studied using the ATOMKI-ECRIS, which is designed for the production of multiply charged ions [5]. In 2006, a prototype magnetic structure (the ATOMKI-ECR-B,

* Part of this study has been supported by a Grant for the 21st Century Center of Excellence Program since 2003 and a Grant for the High-Tech Research Center Fund since 2006. Both funds were organized by the Ministry of Education, Culture, Sports, Science and Technology (MEXT), Japan.
# uchida_t@toyonet.toyo.ac.jp

which is equipped with a large plasma chamber and a weak hexapole around it. This ECRIS is specialized for the production of large-sized, low-ionized plasmas and provided the fullerene beams for a number of experiments.) was tested to produce fullerene and iron ions [6]. In 2007, an evaporator using induction heating was tested to produce iron ions, and it demonstrated that this heating method was suitable for operation in the good vacuum [7]. Consequently, a mechanical design for optimum operation to produce endohedral fullerenes in ECR ion source was developed. At present, we have started the investigation of the basic property and the initial experiments of the production of ions of fullerenes or carbons-loss fullerenes by using a mostly completed apparatus. And the manufacturing of an induction heating iron evaporator is in progress.

DESIGN ASPECT OF THE BIO-NANO ECRIS APPARATUS

Overview

The Bio-Nano-ECRIS apparatus is designed for the synthesis of the endohedral fullerenes. In other words, this apparatus is specialized to produce the low-charged and large-mass ions and the deposition of the ion beam. The main features of this apparatus are as follows.

- Several evaporation sources (fullerene evaporation and Fe evaporation,…)
- Large plasma chamber to reduce the wall loss of low-charged large-mass ions and to mount several evaporation sources
- Relatively weak magnetic field in order to reduce the synthesis of high-charged ions
- Low extraction voltage and large sector magnet to analyze the ion beam with high mass-to-charge ratio
- Beam deceleration system and substrate holder to do the ion beam deposition

Figure 2 shows the schematic diagram of the Bio-Nano ECRIS apparatus. This apparatus is composed of four main parts; (1) an ECRIS, (2) an ion beam extraction electrode and focusing lens, (3) a beam analyzing magnet, (4) beam detectors and a deceleration electrode.

The ECRIS (Fig. 3) equips large plasma chamber, two microwave waveguides, fullerene evaporating oven, and gas inlet. The diameter and length of the plasma chamber are 14 cm and 34 cm, respectively. In particular, the diameter of the chamber is larger than that of ECRIS which is for the synthesis of the multiply charged ions. Two microwave sources are an 8 - 10 GHz travelling wave tube (TWT) amplifier and a 2.45 GHz magnetron source. At present, only 8 - 10 GHz microwave is available. 2.45 GHz microwave will be operative in 2009. The fullerene vapor is provided with a resistance heating oven based on the RIKEN micro-oven [8]. The Fe vapor is provided with an induction heating oven. This is now manufacturing In addition, the optional processing chamber is mountable between the plasma chamber and the extraction electrode. The first tests of these items in the Bio-Nano-ECRIS will be done soon. The magnetic

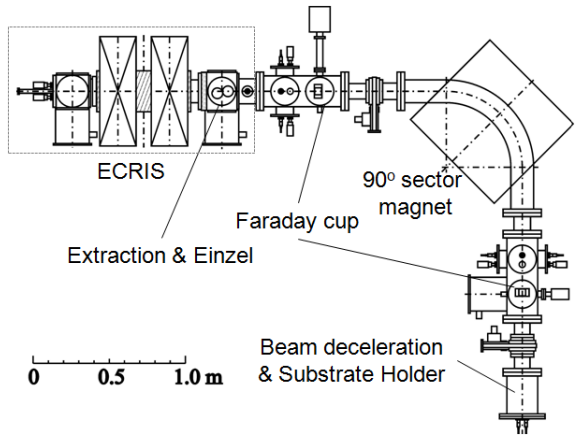

Figure 2: Schematic diagram of the Bio-Nano-ECRIS apparatus.

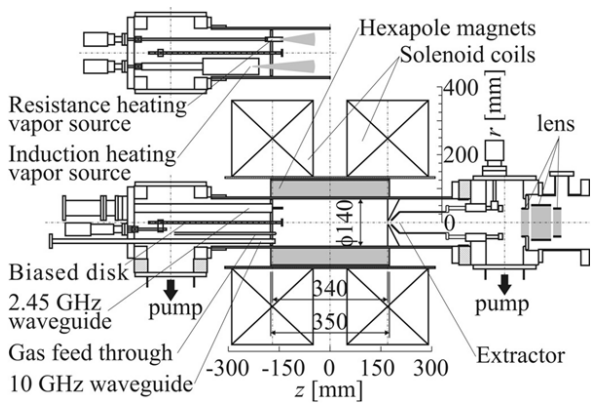

Figure 3: Schematic diagram of the ECRIS.

system for the confinement of the charged particles in the plasma chamber is provided with the mirror coils (axial direction of the chamber) and the hexapole permanent magnet (radial direction of the chamber). The details about the magnetic system are shown in the next section.

Ions generated in the plasma chamber are extracted and focused by electrostatic systems; a movable extraction electrode and an einzel lens. The extraction gap (distance between the plasma aperture and the extraction electrode) is 1 - 6 cm. The extraction voltage is 0.5 – 5 kV. Simulations of the ion beam extraction and focusing are now in progress.

The extracted and focused ion beam is analyzed by a 90° sector magnet according to mass-to-charge ratio. The curvature radius of this magnet is 50 cm. The magnetic field of the sector magnet can be controlled from 0 to 0.8 T. Thus, we can get the mass-to-charge spectrum by sweeping the magnetic field or separate specific ions according to mass-to-charge ratio. This system can transport the 5 kV beams with mass-to-charge ratio of around 800, which corresponds to C_{60}^{+} and C_{70}^{+}.

The detection of ion beam is done by the faraday cups, which are mounted before and after the sector magnet. At the end of this beam line, a beam deceleration electrode, which can hold a substrate, is mounted. Maximum deceleration voltage is 5 kV.

All these ECRIS and following beam line are evacuated by three turbo molecular pumps (450 l/sec). The pressure in the chamber is monitored by a cold cathode ionization gauge just above each pump.

The specification and normal operating parameters of the Bio-Nano ECRIS apparatus is shown in Table 1.

Table 1: Specification and normal operating parameters of Bio-Nano ECRIS apparatus

Mirror magnets	Solenoid coils
Axial magnetic induction peak (500 A)	0.442 T
Minimum field strength (500 A)	0.165 T
Mirror ratio (500A)	2.68
Hexapole Magnet	Nd-Fe-B
Maximum radial magnetic induction in chamber	0.72 T
Microwave (1)	TWT amplifier
Frequency (1)	8 – 10 GHz
Microwave (2)	Magnetron
Frequency (2)	2.45 GHz
ECR magnetic field for 2.45 GHz	0.0875 T
8 GHz	0.29 T
10 GHz	0.36 T
Plasma chamber diameter	14 cm
Plasma chamber length	34 cm
ECR zone diameter (500 A, 10 GHz)	10 cm
ECR zone length (500A, 10GHz)	23 cm
Fullerene evaporation	Resistance heating oven
Temperature (normal use)	400 – 500 °C
Extraction gap	1 – 6 cm
Extraction voltage	0.5 – 5 kV
Diameter of Extraction electrode	1 cm
Diameter of plasma aperture	1 cm
Analyzing magnet	Solenoid coil, 90° sector, r = 50 cm
Magnetic field strength	0 – 0.8 T
Deceleration voltage	0 – 5 kV
Vacuum system	Turbo molecular pump (450 l/sec × 3)

Magnetic system

As mentioned above, the confinement field of the charged particles is provided with mirror coils and a hexapole permanent magnet. Figure 4 shows the axial magnetic field distribution at the coil current of 500 A. The ECR magnetic field strength for 10 GHz microwave is also shown in the figure. For the coil current of 500 A, the maximum and minimum field strengths are 0.442 T and 0.165 T, respectively. In this case mirror ratio is 2.68. Figure 5 a), b) show the two dimensional contour plot of the hexapole magnetic field (cross-sectional view of the plasma chamber) and the magnetic field distribution along

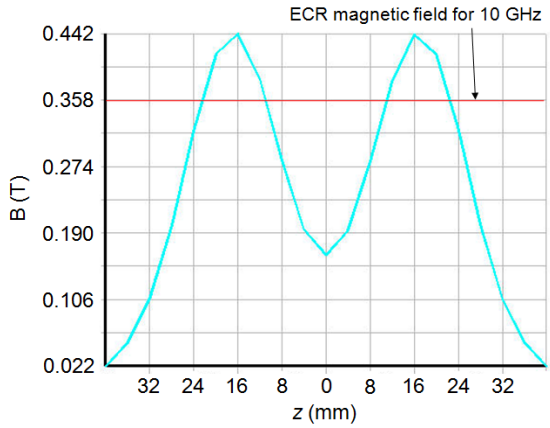

Figure 4: Axial magnetic field distribution at the coil current of 500 A.

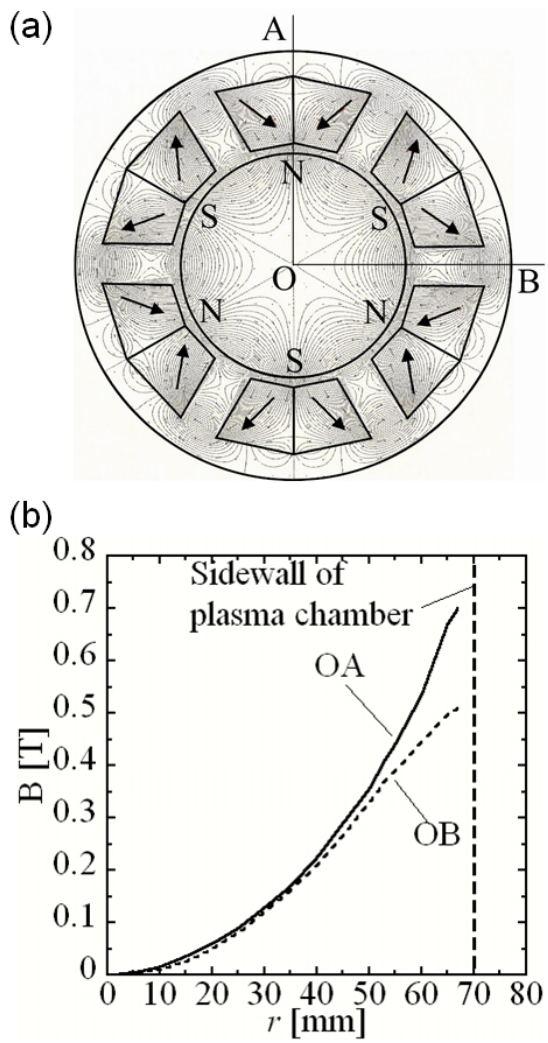

Figure 5: (a) Two dimensional contour plot of the hexapole magnetic field (cross-sectional view of the plasma chamber) and (b) magnetic field distribution along the OA and OB axes.

the OA and OB axes, respectively. Figure 6 is the contour plot of the calculated magnetic field (longitudinal sectional view of the plasma chamber) at the coil current of 500 A. In this case, the ECR magnetic field for 10 GHz microwave is 0.36 T. The corresponding ECR zone for 10 GHz is also shown in the figure. The diameter and the length of the ECR zone at the coil current of 500 A is 10 cm and 23 cm, respectively.

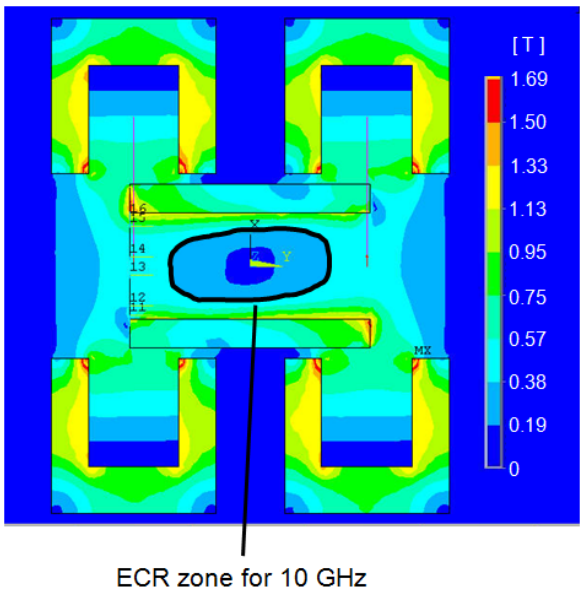

Figure 6: Contour plot of the calculated magnetic field (longitudinal sectional view of the plasma chamber) at the coil current of 500 A.

RESULTS OF THE INITIAL EXPERIMENTS

Fullerene ion beam

As an initial experiment of the production of fullerene ion beam, we have generated the pure fullerene plasma and measured the fullerene ion beam spectra. We used pure C_{60} powder (99.5%, nanom purple, Frontier Carbon Corporation) and pure C_{70} powder (98 %, nanom orange, Frontier Carbon Corporation) as sources. Figure 7 (a), (b) show the C_{60} ion beam spectrum and C_{70} ion beam spectrum, respectively. In case of the C_{60} ion beam spectrum [Fig. 7 (a)], the measurement conditions are as follows; mirror coil of 500 A, microwave frequency of 9.75 GHz, microwave power of 5 W, extraction voltage of 5 kV, and plasma chamber pressure of 5×10^{-5} Pa. We could generate the C_{60} plasma without the assist gas (Ar, N_2, …). The single-, double- and triple-charged ions of C_{60} are observed in this figure. In addition, the single- and double-charged ions of carbons-loss C_{60} are also observed. For the ions with *m/q* value less than ~200, it is difficult to analyze because of the complex structure of high-charged fullerene ions and single-charged small carbons-loss fullerenes (< C_{20}) ions. The beam intensities of C_{60}^{+}, C_{60}^{2+} and C_{60}^{3+} are 400 nA, 800 nA and 170 nA, respectively. It should be noticed that these values are almost as high as those obtained by using the ATOMKI-ECRIS even though the operating conditions are not optimized.

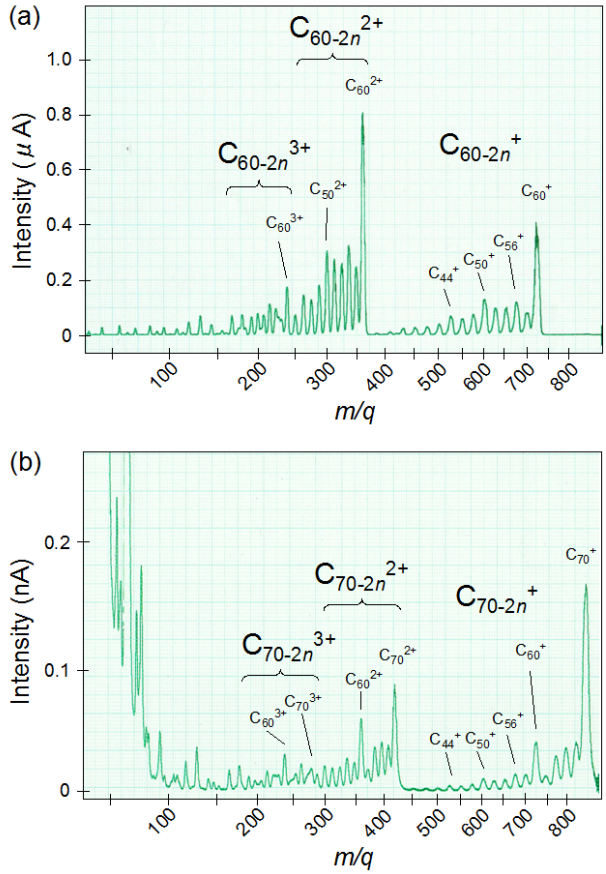

Figure 7: (a) C_{60} ion beam spectrum and (b) C_{70} ion beam spectrum.

In case of the C_{70} ion beam spectrum [Fig. 7 (b)], the measurement conditions are almost same except for the microwave power. The microwave power is 10 W. Basically, C_{70} ion beam spectrum shows the similar tendency to C_{60} ion beam spectrum. But the beam intensity for C_{70} spectrum is much lower than that for C_{60} spectrum. The reason of this low beam intensity is unclear. We guess that this is due to the lower vapor pressure of C_{70} than C_{60}.

For both C_{60} and C_{70} ions beam spectra, ion beam currents of C_{70}, C_{60}, C_{56}, C_{50} and C_{44} are the (local) maximum in both C_{60} and C_{70} ion beam spectra. It is thought that this is because such carbons-loss fullerenes are stable [9]. As mentioned above, we could obtain very clear C_{60} and C_{70} ion beam spectrum using a new ECRIS apparatus. We should optimize the operating conditions, such as beam extraction and focusing and examine the beam deposition.

SUMMARY AND FUTURE PLAN

We have developed the large part of the ECRIS apparatus for the production of endohedral fullerenes. We

have finished the initial experiments of fullerenes (C_{60} and C_{70}) ion beam extraction. We could synthesis the ions of fullerenes and carbons-loss fullerenes and separate them according to the mass-to-charge ratio. In particular, high beam intensity was obtained for C_{60} ions even though the operating conditions were not optimized. We think that there is still room for improvement of the beam intensity. In the future, we are planning to do following things; i) optimization of the beam extraction, ii) production of iron ions using induction heating oven, iii) production of iron-encapsulated carbons-loss fullerenes

REFERENCES

[1] R. Kitaura and H. Shinohara, Jan. J. Appl. Phys 46, 881-891 (2007).
[2] K. Komatsu, M. Murata and Y. Murata, Science 307, 238-240 (2005).
[3] S. Biri, IEEE Transactions on Plasma Science 36, 1489 (2008).
[4] E. E. B. Campbell, *Fullerene Collision Reactions*, Springer, (2003).
[5] S. Biri, A. Valek et al., Rev. Sci. Instrum. 73, 2 (2002).
[6] S. Biri, É. Fekete et al., Rev. Sci. Instrum. 77, 03A314 (2006).
[7] Y. Kato, T. Kubo et al., Rev. Sci. Instrum. 79, 2 (2008).
[8] M. Kidera, T. Nakagawa et al., Proc. of the 15th International Workshop on ECRIS, 74-76 (2002).
[9] S. Díaz-Tendero et al., Int. J. Mass Spectrom. 250, 133-141 (2006).

EXPERIMENTS WITH HIGHLY CHARGED IONS AT THE PARIS ECR ION SOURCE, SIMPA*

C. I. Szabo, D. Attia, A. Gumberidze, P. Indelicato, E.-O. Le Bigot, S. Schlesser (LKB, Paris, France),
E. Lamour, J. Merot, C. Prignet, J.-P. Rozet, M. Trassinelli, D. Vernhet (INSP, Paris, France),
S. J. Coelho do Carmo (Coimbra University, Coimbra, Portugal)

Abstract

In this paper recent achievements will be reported at the SIMPA ion source in Paris that include the first use of an electrostatic ion trap for trapping highly charged ions on the beam line of an ECR ion source and electron temperature and density measurements with the help of the observation of the bremsstrahlung spectrum of the electrons in the ECR plasma of the source. Also a new vacuum double crystal spectrometer is under construction in our lab that will allow us to measure the very narrow inner shell transitions of highly charged ions produced in the ECR plasma and provide new x-ray standards with this method for the atomic physics community.

THE SIMPA ION SOURCE

The full permanent magnet "supernanogan" type Electron Cyclotron Resonance (ECR) ion source, SIMPA (Source d'Ions Multichargés de Paris = Paris highly charged ion sourcs) has been jointly operated by LKB (Laboratoire Kastler Brossel) and INSP (Institut des NanoSciences de Paris) since 2004. Since this time numerous projects have been started to use the extracted beam in atomic physics and surface physics experiments and the x-ray radiation of the ECR plasma for plasma and atomic physics investigations. The ion source has a fully permanent magnet setup with a microwave line of 14.5 GHz attached into the plasma chamber. The extraction is made possible by raising the whole ion source to a high voltage platform between 0 kV to 35 kV potential, leaving the beam line at ground potential. The beam line has a solenoid magnet for beam focusing. Charge state selection and scan is possible with a dipole magnet. Figure 1 shows a general setup of the SIMPA ECR ion source laboratory in Paris.

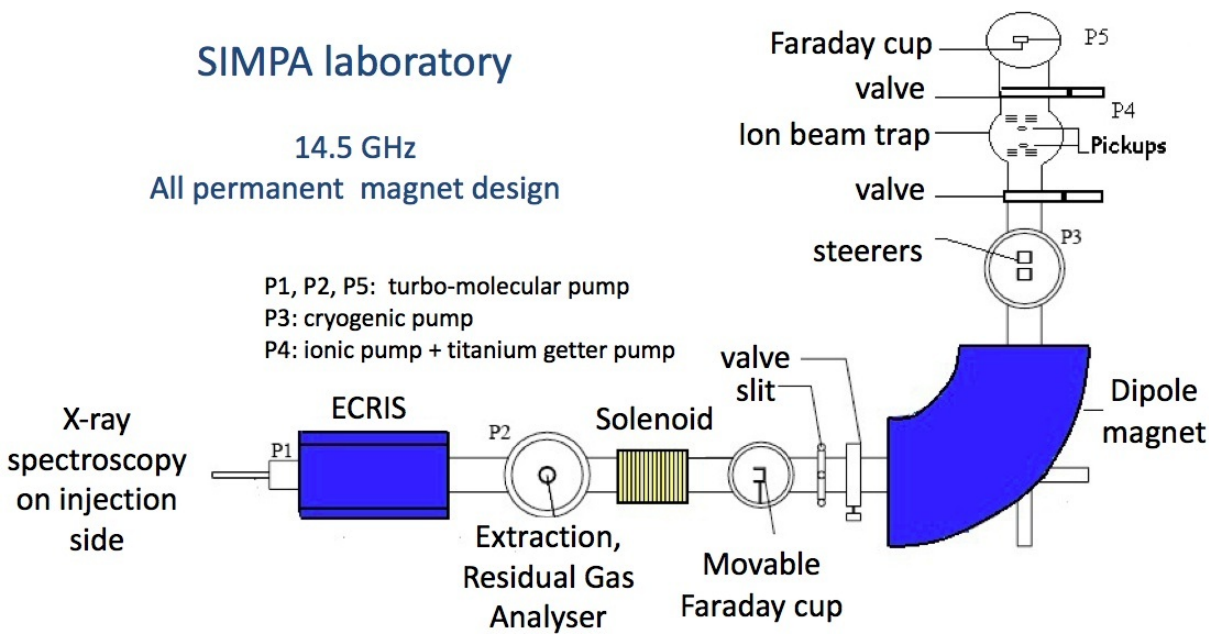

Figure 1: The SIMPA ECR Ion Source laboratory in Paris. The 14.5 GHZ all permanent magnet SUPERNANOGAN type ECR ion source is connected to a beam line with a solenoid and dipole magnet feeding the ion beam trap. A Be window on the injection side allows x-ray spectroscopy

THE ELECTROSTATIC ION BEAM TRAP

The development and applications of ion traps and heavy-ion storage rings have a significant impact on many branches of physics. These devices enable the storage of ions for a relatively long time, with meV to eV kinetic energies, in ion traps and to GeV kinetic energies, in heavy-ion storage rings. Ion traps are able to trap charged particles for a long time, and they have been successfully applied in several areas of physics. Recently,

a novel type of ion traps has been developed [1, 2], in which ions oscillate between a pair of electrostatic mirrors, much like photons in an optical resonator. The trapped ions have kinetic energies of a few keV per charge in the central part of the trap while inside the mirrors they have only a few meV near their turning points, where they are also subject to radial focusing forces. This means that this ion trap uses only electrostatic fields to trap a beam of ions, hence the name: electrostatic ion beam trap (EIBT). Several experiments have already been performed with these devices; such as lifetime measurements of singly charged ions [3, 4] and charge transfer dissociation of molecules [5]. Following a design from the Weizmann Institute [1], we have constructed an electrostatic ion beam trap and attached it to the beam line of SIMPA. Fig. 1 shows the ion trap on the beam line of the ion source. A schematic drawing of the trap together with a photo of the trap electrodes is displayed in Fig. 2.

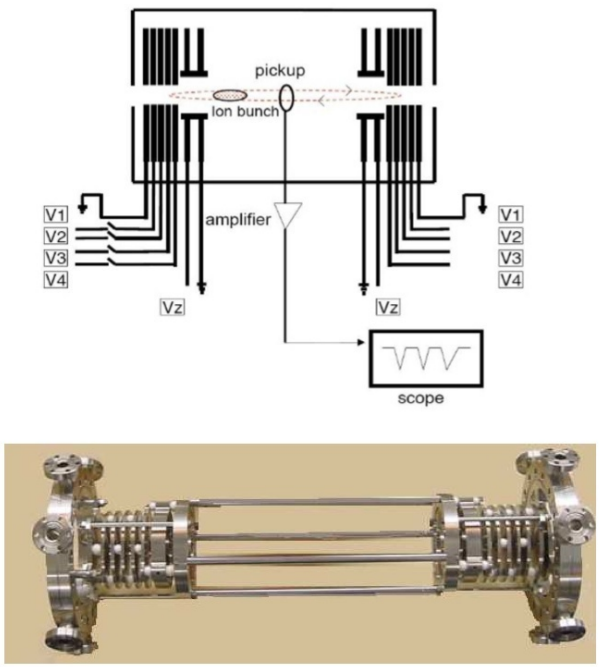

Figure 2: schematic view and a photo of the electrostatic ion trap on the beamline of SIMPA

The ion trap consists of two coaxial electrostatic mirrors, each composed of a stack of eight cylindrical electrodes. The configuration of the trap is characterized by the potentials on five of these electrodes, V1, V2, V3, V4, Vz (see Fig. 2), the other three electrodes are grounded. Provided that the field generated by these potentials fulfils certain criteria, ions can be trapped oscillating between the two mirrors [1]. A cryopump and an ion pump is pumping the trap to a pressure of about $5 \cdot 10^{-10}$ mbar. Injection of an ion bunch into the trap is performed by grounding all the entrance electrodes. The electrodes on the other side are kept at high potential so that the bunch is reflected toward the entrance. Before the ion bunch returns to the entrance mirror, the potentials of its electrodes are rapidly (<100 ns to 200 ns) raised and the ion bunch is thus confined between the mirrors. The highly charged ions are produced in the SIMPA ECR ion source and are extracted and accelerated by the extraction voltage of 4.2 kV. After extraction the ions are focused and analyzed by the solenoid and the dipole magnets and run into the electrostatic steerer where an electrostatic chopper creates bunches of ions with a temporal extension of 80 ns to 500 ns. (see fig. 1). The closure of the entrance of the trap is synchronized with this electrostatic chopper providing an adjustable delay making optimization possible. Also steering of the ions is possible with the other two electrostatic deflectors in the steerer region. The evolution of ion bunches during storage was monitored with a cylindrical pickup electrode with a length of 7 mm and an inner diameter of 18 mm located at the center of the trap (see fig. 2). The amplified pickup signal was recorded on a digital oscilloscope and a spectrum analyzer.

Experimental data and simulations for the electrostatic ion beam trap

With the help of the pick up electrode in the linear center of the trap we have proved trapping for tens of milliseconds in the case of a variety of high charge states of O, Ar, Kr and Xe ions (up to O^{5+}, Ar^{13+}, Kr^{21+} and Xe^{20+}). Using a low (< 20 V) radio frequency voltage with frequencies close to the oscillation frequency of the ions in the trap we were able to observe trapping times up to 50 ms. Running the ion trap in the so called ”bunching” or synchronization mode [2] in the time domain of the pickup signal we observed a strange oscillation on the millisecond scale superposing the ion oscillation in the trap on the microsecond scale. This is shown in Figure 3 for the case of Ar^{8+}.

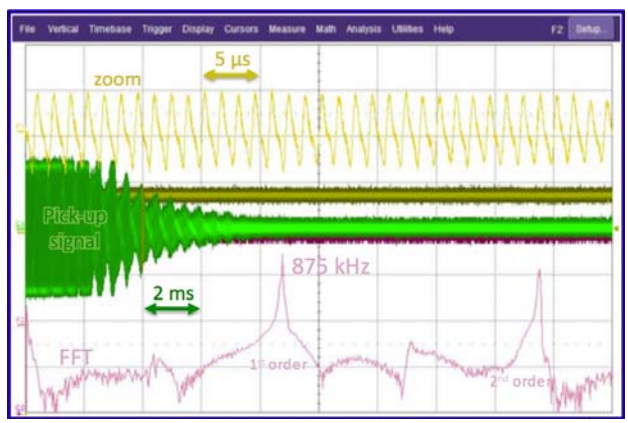

Figure 3: The screen of a digital oscilloscope showing trapping of Ar^{8+} ions. A zoom of a 20 µs region in time is shown on the top of the screen at 4 ms of trapping. The FFT of the oscillation (shown on the bottom) provides the trapping frequency: 875 kHz for Ar^{8+} at 4.2 keV kinetic energy per charge.

Our goal is to explain the observed oscillations with computer simulations. We mainly use two types of simulations for this purpose. The first method is based on

a 1D model described by Pedersen et al [6], where the behavior of a test ion close to a bunch of ions in the trap is investigated. The estimate for the bunch size dynamics can be obtained from observing variation of the distance between the test ion and the ion cloud as a function of time. This is shown in figure 4a, where millisecond scale oscillations of the bunch size is clearly visible. This could in principle, be considered as a possible reason for the observed oscillations in the experiment because the change in the bunch size could affect the pickup signal.

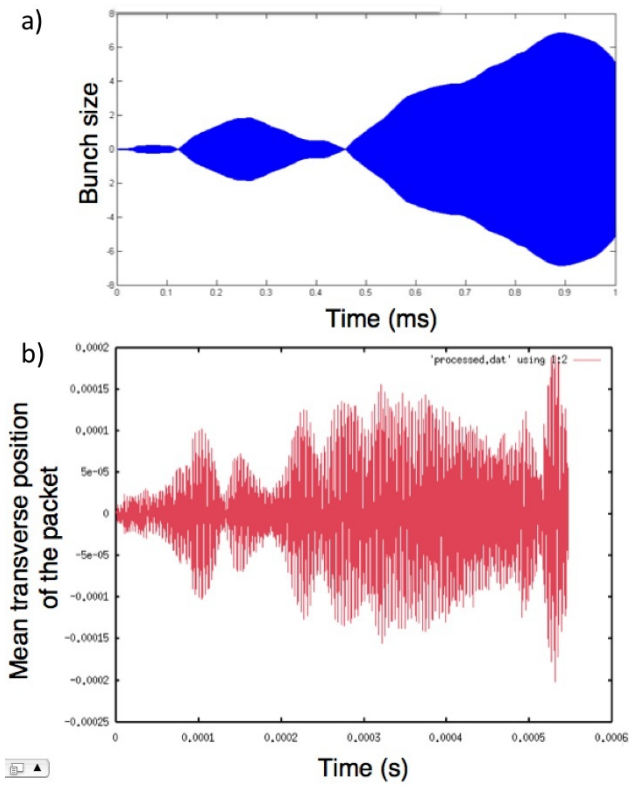

Figure 4: a) 1D simulation showing variation of the distance between the test ion and the ion cloud as function of time (bunch-size dynamics); b) N-particle 3D simulation of the bunch radial position as function of time.

In addition to the 1D model, we are developing an N-particle 3D simulation where we include the interaction between the ions fully and observe dynamics of all the particles in the potential of the trap. First results of this simulation are shown in fig 4b. Here, we show that if there is a slight misalignment during the injection of the ion beam in the trap, the radial velocity given to the bunch leads to radial oscillations of the packet. These radial oscillations could perturb the signal of the pickup as well because it depends on the distance from the charge. Further checks for various effects and consistency are underway. Now that we have proven trapping of highly-charged ions, we plan, as a next step, to utilize the ion trap for measurement of the life times of metastable states in highly charged ions.

ELECTRON TEMPERATURE MEASUREMENTS

We have used a silicon x-ray detector to observe bremsstrahlung radiation from the ECR ion source. The plasma was observed through the hollow polarization electrode on the injection side of the source, at a typical distance of 1 m. A 1 cm thick Pb collimator was used right in front of the detector with a 1 mm hole on it allowing x rays from the ion source to the detector. Pure aluminum filters were set in order to keep the rate on the Si(Li) detector on a reasonable level to avoid pile-up and high dead times. Different gases were injected into the ion source: argon, krypton and xenon, as well as oxygen rare-gas mixture. Other components typically present in the source were nitrogen and water. The x rays emitted by the source had to traverse a 250 µm thick Be window and 29 cm of air and when necessary a variable thickness (2 mm to 20 mm) Al filter. The absolute efficiency of the detector as a function of energy has been carefully measured previously. The measurement has been extended to higher energies with the help of an ^{241}Am radioactive source using known line intensity ratios up to 60 keV [9]. The detector efficiency corresponds very closely to that of a 5.755± 0.350 mm thick crystal, with no dead zone and a 26.5± 0.5 µm thick Be window, which is close to the manufacturers' specification. Efficiency and absorption through filters and windows are corrected for, using a Mathematica code interpolating data from the NIST x-ray mass absorption coefficients [10]. The energy scale was calibrated using the same ^{241}Am radioactive source. On Figure 5 we present typical spectra obtained for Xe plasmas at different injected microwave powers, after correction for detector efficiency and filter absorption.

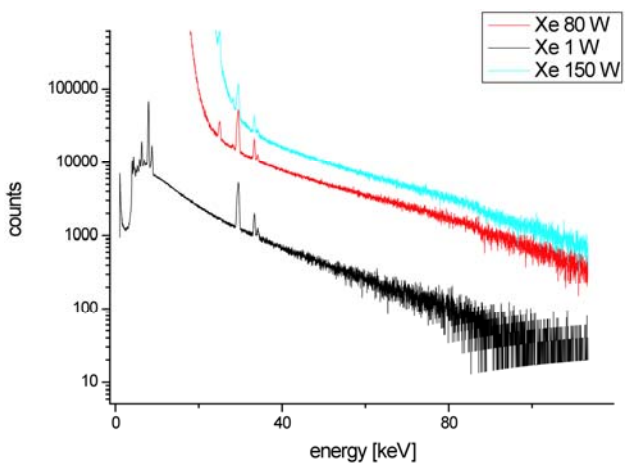

Figure 5: Examples of Xe x-ray spectra obtained with different microwave powers applied to the source. Each spectrum is corrected for detector efficiency, air, filter and window absorption. All spectra have been normalized by the acquisition time. Energy scale was obtained using an ^{241}Am source.

The bremsstrahlung tail clearly appears up to energies of 110 keV. To obtain the average electron temperature, we do a weighted fit of an exponential *AExp(-e/T)* to the spectra, for a range of energy between 40 keV and 110 keV.

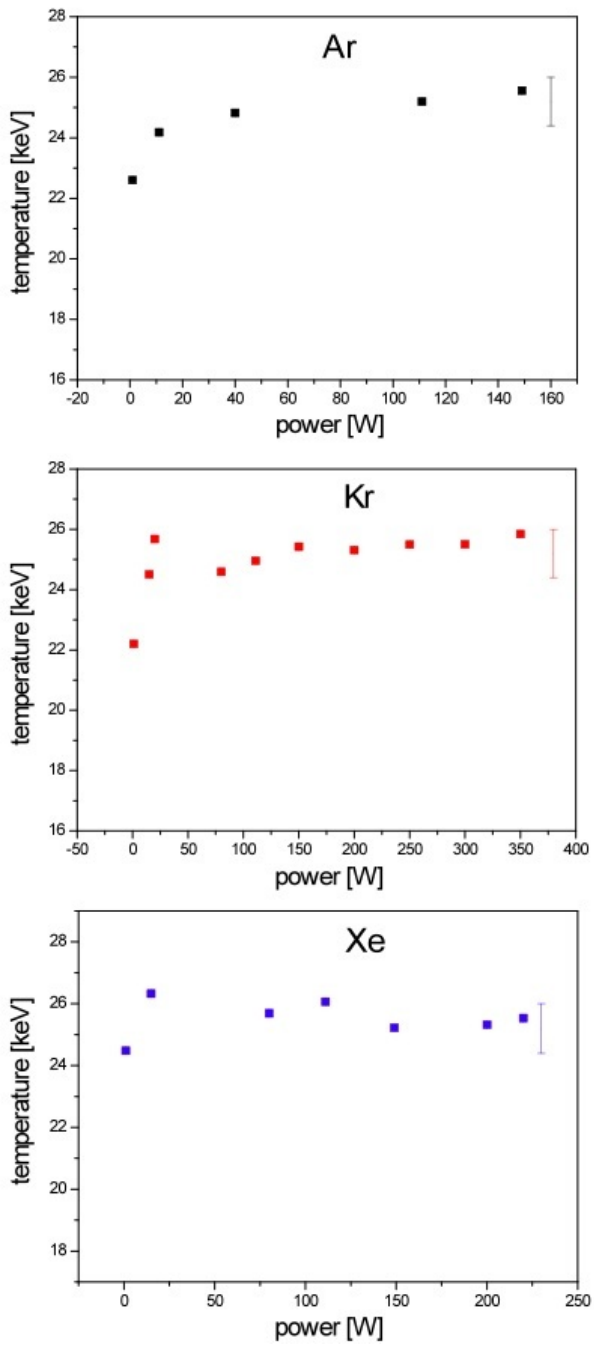

Figure 6: Maxwellian temperatures kT_{Mw} in keV, as a function of the microwave power in SIMPA in the case of different gases injected in the source.

The weighted fit is using the square root of the measured intensities in each point. A lower end for the fit was determined because the low energy part of the spectra after efficiency and absorption corrections is very intense. Even with filters that should cut the low energy part of the spectrum, one can observe an increase of the intensities after corrections. This increase is due to Compton scattering following escape of high-energy photons from the crystal, which leads to only a partial deposition of the original photon energy in the detector. These events produce high count-rates in the low energy part of the spectra that would modify the exponential fit if included. The upper limit of the fit corresponds to the place where the detector efficiency becomes too small and statistical uncertainty becomes too large. We have noticed that the correction for absorbers based on [10] did not completely consistently compensate for the absorber effect for different thicknesses and the calculated electron temperature values deviated from each other by up to 10%. A corresponding correction was applied based on the comparison of measurements for different Al absorber thicknesses with the one without an absorber, all of them carried out at 1 W (because for higher powers the photon rate was too high without absorbers). It was found that the effect increases with increasing absorber thickness. We attribute this effect to the fact that we do not have a "narrow" photon beam (=collimation is not ideal). This allows photons to get scattered in the absorber and the scattered photons hit the detector producing counts that are not taken into account when applying the corresponding absorber correction. A Monte Carlo simulation based on our experimental geometry has confirmed that this effect can for thick absorbers lead to the observed deviation of the resulting temperature. This deviation is included in the experimental error. On figure 6 we present the extracted spectral temperature as a function of microwave power for different gases (Argon, Krypton, Xenon). The error bars indicate systematic uncertainty due to the detector efficiency and the absorber corrections. The temperature changes initially at very low power and then practically saturates at about 25±1 keV average Maxwellian electron temperature. The starting temperature for Ar and Kr is around 22 keV and the saturation temperature of 25 keV is reached at powers around 100 W. For Xe however, the temperature is more or less constant. The saturation happens at lower power for lower-Z elements.

DOUBLE CRYSTAL X-RAY SPECTROMETER FOR X-RAY STANDARDS

A good way to understand the specific mechanisms that lead to the different charge state production and level populations in different ions is by the observation of the x-ray lines emitted by the ECR plasma, under different conditions, with a very high resolution. The K ($2p \rightarrow 1s$) x-ray spectra of highly charged ions, emitted by an ECRIS, have been studied in a limited number of cases, on S, Cl, Ar, Co and Kr. [11]

Observation of x rays from 1+ to helium-like ions in S, Cl and Ar where performed with a spherically-bent, high-efficiency, Johann-type x-ray spectrometer, on the PSI

ECRIT [12] with a resolution ranging from 0.3 eV to 0.45 eV [13-17]. This increase in resolution, efficiency, and improvement in the background have lead to both high-accuracy x-ray measurements of few-electron highly-charged ions and to the observation of many unidentified lines, that should shed more light on the excited level population mechanisms, once the necessary analysis has been performed. Kα x rays from elements like argon are good probe of their ionization level in a plasma, because the electron undergoing the transition to the K shell for q>8 is in the same shell as the electron removed by the ionization process. Thus the shift in energy is large between charge states. The typical good resolution spectra from an Ar plasma contains an unresolved group of lines containing Kα lines from Ar^{+} to Ar^{9+} (i.e., ions with one K hole and 0 to 8 M holes), and then well resolved features from Ar^{10+} to Ar^{17+}, depending on the conditions of the plasma. Figure 7 shows good resolution (~3 eV) spectra of argon-oxygen mixture plasma, observed with a mosaic-graphite crystal spectrometer at the SIMPA source.

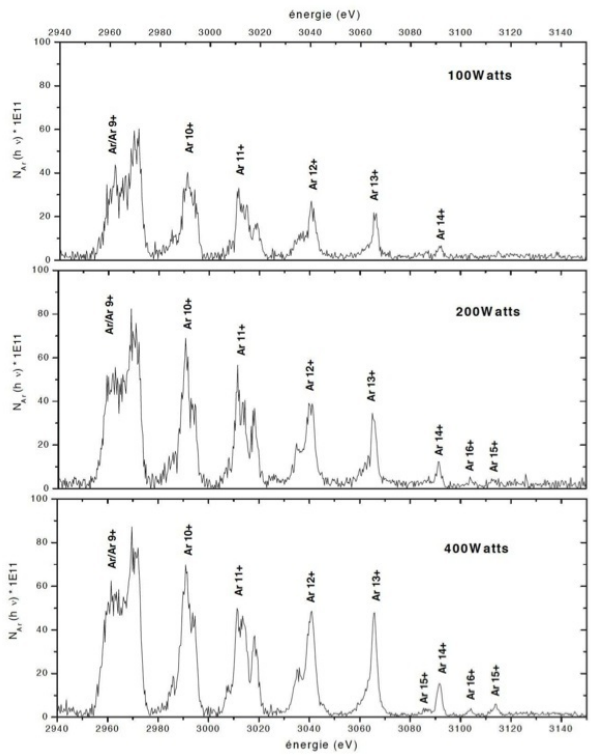

Figure 7: Normalized X-ray spectra of Ar ions in the plasma, as a function of microwave power, measured with a mosaic-crystal X-ray spectrometer.

These sample spectra are normalized and show clear change of the charge state distribution of the plasma with changing microwave powers. These spectra could be acquired in a typical time of two hours.
The resolution of the spectrometer is not high enough to give a more detailed analysis but it can show the variation of the spectra as a function of the injected power and identify the Ar lines.

At 400 W, the structure labeled Ar^{13+} is the most prominent of the highly-charged ion lines, and would certainly be a good candidate for a first attempt of high-resolution x-ray spectroscopy. The relativistic M1 line in He-like argon would be the ideal candidate for high-precision, high-resolution spectroscopy, but it is probably too weak at this stage to be observed. It should be noted that the spectrometer used in the experiment shown on Fig 8 observed the plasma through a ~500 µm diameter pinhole, as it required an entrance slit, and also a reduction of rate. A double-flat crystal instrument [17], although very inefficient, would make use of the full polarization electrode aperture, which represents a 570 fold increased intensity. Figure 8 shows the operation principle of the double crystal instrument under development in our group.

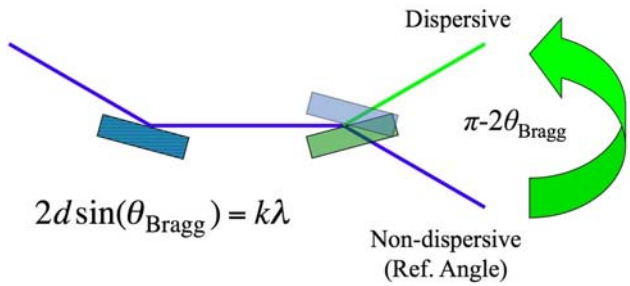

Figure 8: Operation principle of a double crystal instrument. The first crystal (left) acts like a monochromator, and by measuring the angle difference between the two positions of the second crystal the wavelength of the chosen transition can be absolutely determined.

With this instrument x-ray wavelength can be absolutely measured by angle difference measurement. The new double crystal spectrometer dedicated to x-ray measurements at ECR ion sources has the ability to rotate the whole optical table supporting the rotational stages of both crystals inside the vacuum chamber. With this the first crystal can be aligned to accept the x rays at the right Bragg angle for the line under investigation. With absolute wavelengths measurements of the lines from HCI with great accuracy these lines can serve as new x-ray standards with their very narrow features in high precision x-ray spectroscopy.

SUMMARY

We have shown our first results with the new electrostatic ion beam trap (EIBT) installed at the beam line of the SIMPA ion source. With this device we have proven trapping of highly charged ions up to O^{5+}, Ar^{13+}, Kr^{21+} and Xe^{20+}. We have also made progress with computer simulations explaining oscillations on the millisecond scale on the trapping signal.
From x-ray spectroscopic studies we have defined an average electron temperature based on the bremsstrahlung radiation that is in good agreement with other measurements at other ECRIS laboratories.

We also have reported on the progress of our double crystal spectrometer project that will provide new x-ray standards through high precision absolute wavelength measurements using highly charged ions in an ECRIS.

ACKNOWLEDGMENTS

This work has been supported by a grant from "Agence Nationale pour la Rechcherche (ANR)" number ANR-06-BLAN-0233. The Authors would like to acknowledge the assistance and encouragement from colleagues and the special work of the technical staff.

REFERENCES

[1] Zajfman D, Heber O, Vejby-Christensen L, Ben-Itzhak I, Rappaport M, Fishman R, and Dahan M 1997 Phys. Rev. A **55** R1577

[2] Dahan M, Fishman R, Heber O, Rappaport M, Altshtein N, van der Zande W J and Zajfman D, 1998 Rev. Sci. Instrum. **69** 76

[3] Wester R, Bhushan K G, Altstein N, Zajfman D, Heber O, and Rappaport M L 1999 J. Chem. Phys. **110** 11 830

[4] Knoll L, Bhushan K G, Altstein N, Zajfman D, Heber O, and Rappaport M L 1999 Phys. Rev. A **60** 1710

[5] Strasser D, Bhushan K G, Pedersen H B, Wester R, Heber O, Lafosse A, Rappaport M L, Altstein N, and Zajfman D 2000 Phys. Rev. A **61** 060705

[6] Pedersen H B, Strasser D, Heber O, Rappaport M L, and Zajfman D 2002 Phys. Rev. A **65** 042704

[7] C.Barué, M. Lamoureux, P. Briand, et al., J. Appl. Phys. **76**, 2662 (1994).

[8] R. D. Deslattes (1967) Rev. Sci. Instrum. **38** pp. 616-620

[9] C. D. Cohen, Nucl. Instrum. Meth. A **267**, 492 (1988)

[10] J J. Hubbell, S.M. Seltzer, Tech. Rep. NISTIR 5632, National Institute of Standards and Technology (1995), http://physics.nist.gov/PhysRefData/XrayMassCoef/cover.html

[11] G. Douysset, H. Khodja, A. Girard, J.P. Briand, Phys. Rev. E **61**(3), 3015 (2000)

[12] S. Biri, L. Simons, D. Hitz, Rev. Sci. Instrum. **71**, 1116 (2000)

[13] D.F. Anagnostopoulos, S. Biri, D. Gotta, A. Gruber, P. Indelicato, B. Leoni, H. Fuhrmann, L.M. Simons, L. Stin- gelin, A. Wasser et al., Nuc. Instrum. Methods A **545**, 217 (2005)

[14] D.F. Anagnostopoulos, S. Biri, V. Boisbourdain, M. Demeter, G. Borchert, J. Egger, H. Fuhrmann, D. Gotta, A. Gruber, M. Hennebach et al., Nucl. Instrum. Methods B **205**(1-4), 9 (2003)

[15] M. Trassinelli, S. Boucard, D.S. Covita, D. Gotta, A. Hirtl, P. Indelicato, O.L. Bigot, J.M.F.d. San- tos, L.M. Simons, L. Stingelin et al., Journal of Physics: Conference Series **58**, 129 (2007) http://stacks.iop.org/1742-6596/58/129

[16] P. Indelicato, S. Boucard, D.S. Covita, D. Gotta, A. Gruber, A. Hirtl, H. Fuhrmann, E.O.L. Bigot, S. Schlesser, J.M.F.d. Santos et al., Nucl. Instrum. Meth. A **580**, 8 (2007)

[17] J. W. M. DuMond, A. Hoyt, Phys. Rev. **36** p.1702 (1930)

ECRIS ON HIGH VOLTAGE PLATFORM FOR ENGINEERING AND MODIFICATION OF MATERIALS

P. Kumar, G. Rodrigues, P.S. Lakshmy and D. Kanjilal
Inter University Accelerator Centre, New Delhi 110067, INDIA

Abstract

An all permanent magnet electron cyclotron resonance ion source (ECRIS) along with the associated components like 10GHz UHF transmitter, vacuum pumps, vacuum gauges, vacuum pump controllers, gas handling systems with gas bottles, local command and controls systems, etc are set up on a 200kV platform for providing various ion beams having energy in the range of a few tens of keVs to a few MeVs. Understanding of charge transfer processes during collision with molecules and dissociation of molecules are discussed. The capability of ECRIS in producing multiply charged ions is being used for engineering and modification of materials. The beam currents available from the first few charge states are mainly used for these studies. The 10 GHz all-permanent-magnet ECR ion source on high voltage platform at Inter University Accelerator Centre (IUAC) has been in regular operation since 2000 for delivering various ion beams for research in materials science, atomic and molecular physics. The salient features of ECRIS based Low Energy Ion Beam Facility (LEIBF) at IUAC, operational experience of the ion source for producing some of the special beams and some of the experimental results are presented.

INTRODUCTION

To get the operational experience of ECR ion source [1] on high voltage platform and to provide the low energy ion beams from gaseous and solid species, the LEIBF [2] has been been set up at IUAC. The most important feature of the facility (LEIBF) is that the ECR ion source and all its peripheral components including electronics (power supplies, RF power amplifier, etc.) and vacuum systems are placed on a high voltage (200 kV) platform. The various parameters of the source are controlled through fiber optics communications at 200 kV isolation. The regular operation of this facility provided us experience and expertise to design and build the world's first High Temperature Super-conducting ECR Ion Source (PKDELIS) [3] for use on a high voltage (400 kV) platform. The ion source has been tuned to get optimum intensities of gaseous, semi metallic and metallic ion beams which are being used for research in emerging fields like nano science and spintronics. To engineer the optical, electrical and structural properties of materials via ion implantation and ion irradiation, first few charge states of beam and moderate beam intenisty (~ 1μA) are mainly required. Nanostructured materials play an important role in technology as they exhibit different, and quite often, unique physical properties relative to their macroscopic counter parts. These composites have drawn a lot of attentions due to their applicability for fast switching devices, single electron transistors, gas sensors and nano-electronics in one dimensional molecular wire. In comparison of other methods, ion implantation allows us to obtain well controlled nanostructures by choosing suitable ion implantation conditions and subsequent thermal annealing. In this paper, development of Ni and Si beams using ECR ion source and fabrication of their nanocomposites in different matrices are presented.

DEVELOPMENT OF NICKEL AND SILICON BEAMS

For the development of Ni beam, Metal Ions using VOlatile Compound (MIVOC) method was used. In order go get enough throughput required for high intensities of lower charge states, the pellet (6mm in diameter and 3 mm thick) of nickelocene was prepared and placed into the source inside the bias tube (a negatively polarized copper tube placed axially into the source from the injection side to reflect the electrons back into the ECR plasma to increasing electron density for ionization) for the development of the ion beams. A mesh of metal wires was used at the open end (towards the plasma) of the bias tube to avoid falling of the volatile compounds from the tube during initially pumping of the source for vacuum. With this technique, we got enough intensities (of the order of l μA) of the beams. The analysed charge state distribution (CSD) of Ni is shown in figure 1.

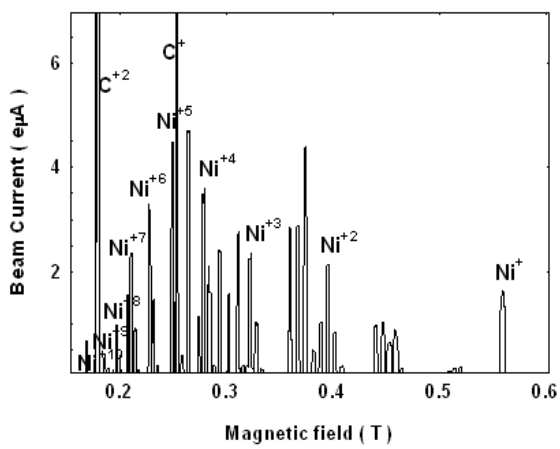

Figure 1: Charge state distribution of Ni optimized for +1 charge state

The optimized source parameters for the extraction of nickel beam are listed in table 1.

Table 1: The optimized source parameters for the extraction of Ni ion beam from the ECR plasma

Source parameters	Values
E/q (Total potential difference)	100 kV
Beam	$^{58}Ni^{+}$
Einzel lens voltage	7.0 kV
Source pressure	5.0 x 10^{-6} mbar
Microwave power	20 W
Bias voltage	130 V
Beam current	1.63 μA

200 keV silicon ion beam was developed successfully using tri-methylchlorosilane liquid volatile compound. For introducing vapors of liquid compound into plasma chamber, the gas feed network (mainly used for introducing gas into plasma chamber from lecture bottles) was modified. The CSD of Si optimized on +3 is shown in figure 2.

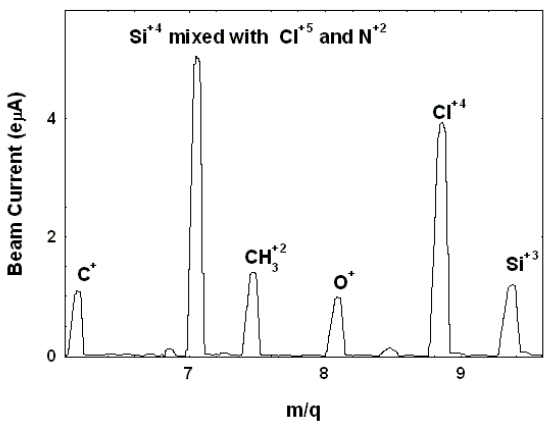

Figure 2: Charge state distribution of Ni optimized for +2 charge state

The total potential difference of 66.6 kV was set for the extraction of 200 keV Si^{+3} ion beam. The source was operated at a pressure of 4.2 x 10^{-7} mbar and input microwave power was 5 W.

EXPERIMENTAL

The implantation of 100 keV Ni ions was performed in quartz matrix at room temperature at fluences ranging from 5x10^{15} ion/cm^2 to 2x10^{17} ion/cm^2. The typical beam size on the target was ~ 5 mm. The analyzed beam current on the target was 1.63 μA. The beam was scanned on the target (scanning area = 10 mm x 10 mm). Implantation was performed in a vacuum chamber having a pressure of the order of 5 × 10^{-7} mbar. The implanted samples were post annealed at 600^{0}C and then characterized by UV-Visible Absorption Spectroscopy, Magnetic Force Microscopy (MFM), Atomic Force Microscopy (AFM), X-Ray Absorption Spectroscopy (XAS), Zero Field Cooled (ZFC) and Field Cooled (FC) magnetization measurements.

200 keV Si beam was implanted (at room temperature) in optical grade fused silica (SiO_2) at an ion fluence of 2.5 x10^{16} ion/cm^2. The samples were annealed at high temperature as well as using swift heavy ions (athermal annealing). The samples were characterized using UV-visible spectroscopy, photoluminescence and transmission electron microscopy.

RESULTS AND DISCUSSION

Charge state analyzed beams of Nickel and silicon at desired energies were produced successfully using ECRIS on high voltage platform (figures 1 and 2) for implantation. The UV-visible spectra of the annealed samples (for all ion fluences) are shown in figure 3.

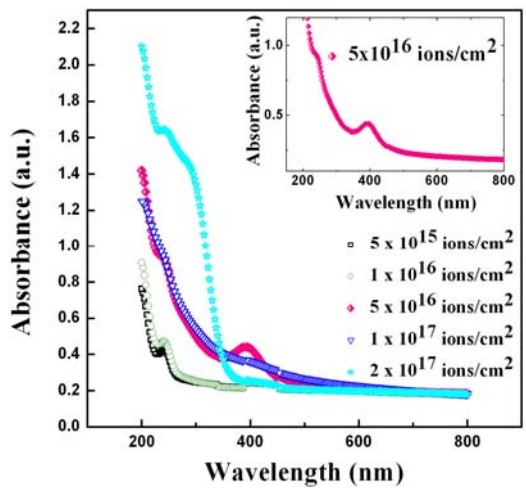

Figure 3: Optical absorption spectra of Ni implanted and annealed (at 600^{0}C) quartz samples at different fluences

The AFM and corresponding MFM images of the sample implanted at ion fluence of 5x10^{16} ion/cm^2 are shown in figure 4.

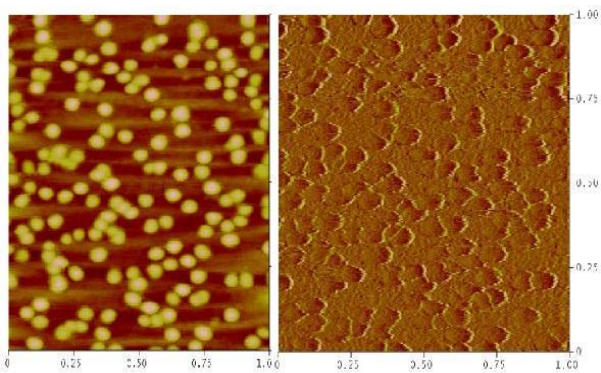

Figure 4: AFM image and corresponding MFM contrast of the quartz implanted at 5x10^{16} ions/cm^2

For the same ion fluence, field cooled and zero field cooled magnetization measurements are shown in figure 5. With these measurements, development of uniformly distributed Ni nanoparticles (4.8 nm in diameter) in quartz is accomplished for optimum ion fluence of $5x10^{16}$ ion/cm^2 [4].

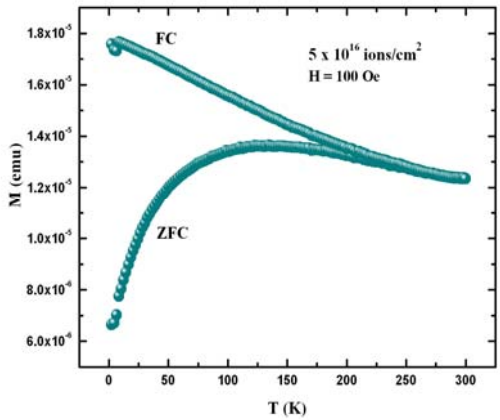

Figure 5: Variation of M vs T for zero field cooled and field cooled measurements of the sample having ion fluence of $5x10^{16}$ ions/cm2

The annealing of Si implanted fused silica leads to the formation of Si nanocrystals in the matrix which is confirmed by absorption and photoluminescence (PL) analysis. The typical PL spectra are shown in figure 6 [5].

Figure 6 : Photoluminescence spectra of (a) Si-implanted

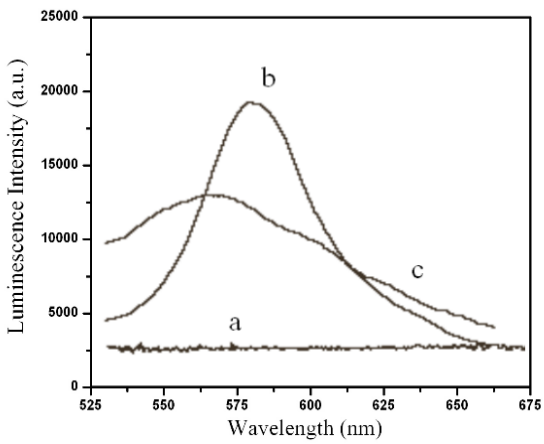

and unannealed SiO_2 (b) Si-nanoparticles grown in SiO_2 due to thermal annealing at 1050^0C and (c) Si nanoprecipitates grown in SiO_2 due to 70 MeV Si-irradiation-induced annealing.

CONCLUSION

ECRIS based LEIBF is in regular operation and is being used by a large number of research groups from various universities for conducing experiments mainly related to materials engineering and modifications. For material engineering, beam energy in the range of a few keV to a few MeV (i.e, beam of first few charge states for ECRIS on HV platform), moderate beam intensities, multi-element beams and long term beam stability are mainly required. ECR ion sources on high voltage platform can meet these requirements and can find applications in this emerging area of science and future technology.

REFERENCES

[1] R. Geller, Electron Cyclotron Resonance Ion Sources and ECR Plasmas, IOP, Bristol, (1996).

[2] D Kanjilal, T Madhu, G O Rodrigues, U K Rao, C P Safvan and A Roy, Ind. J. of Pure and Appl. Phys. **39**, 25 (2001).

[3] D. Kanjilal, G. Rodrigues, P. Kumar, A. Mandal, A. Roy, C. Bieth, S. Kantas, P. Sortais, *Rev. Sci. Instrum.* **77**, 03A317 (2006).

[4] P. Kumar, Ravi Kumar, D. Kanjilal, M. Knobel, P. Thakur, and K.H. Chae, *J. Vac. Sci. Technol.* B, **26(4)**, L36-L40 (2008).

[5] T. Mohanty, A Pradahan, S. Gupta, and D. Kanjilal, Nanotechnology **15**, 1620 (2004).

APPLICATION OF THE ATOMKI-ECRIS FOR MATERIALS RESEARCH AND PROSPECTS OF THE MEDICAL UTILIZATION*

S. Biri#, I. Iván, Z. Juhász, B. Sulik, Institute of Nuclear Research (ATOMKI), Debrecen, Hungary

Cs. Hegedűs, A. Jenei, S. Kökényesi, J. Pálinkás, University of Debrecen, Debrecen, Hungary.

Abstract

In the ATOMKI ECRIS Laboratory long-term projects were initiated to use heavy ion beams and plasmas for materials research and to explore the possibility of industrial or medical applications of such ions. In the paper four applications are shown. (1) A new ECR-device was developed in collaboration with Japanese institutes to produce endohedral fullerenes, namely caged Fe in C_{60}. (2) Titanium bio-implants are covered with fullerene ions to form an intermediate layer between the metal and the organic tissues in order to shorten the time of the cell growth and to improve the properties of the connection. (3) Laser and electron irradiations showed that the structure and properties (volume, refractive index) of certain amorphous thin films can be effectively modified. We extend these investigations using heavy ion beams, focusing on the effect of the ion charge. (4) Highly charged slow ions were found to be efficiently guided by insulating nano-capillaries even at large tilt angles. This phenomenon is investigated for different kinds of capillary arrays and materials.

INTRODUCTION

In the history of the ECRIS workshops majority of the talks, posters and papers dealt with the technical features of ECR ion sources. During their operation lifetime most sources undergone several minor or major modifications or upgrades. The main goal is usually to increase the beam intensity and/or the charge of the extracted ions. Another large volume of the papers discussed the physics of the ion sources, both experimentally and theoretically. In these fields excellent results were achieved and presented in the ECR workshops and in ion source conferences.

Nowadays a continuously increasing demand is detected for the application of heavy ion beams in industry and medicine. The application of plasmas and ion beams produced by ECR ion sources is normally published in other conferences or in independent papers. These contributions usually do not show the details of the ion sources or the "beam-making" itself. However, a specific application of a heavy ion beam frequently requires the modification of the ion source itself or, at least, unusual plasma formation or ion extraction.

* This work was supported by the Hungarian National Science Foundation OTKA (Grant No's: K46454, K73703 and PD050000), the RET-GENOMNANOTECH project of the Debrecen University (4.3.3 and 4.2.1 sub-projects) and in part by the Bio-Nano Electronics Research Center (Kawagoe, Japan) and the National Institute of Radiological Sciences (NIRS, Chiba, Japan).

#biri@atomki.hu

In this paper we show a few possible, promising applications of heavy ion beams. Each of these projects just started at the ATOMKI ECRIS Laboratory, some of them in collaboration with other institutes. The first results already appeared, but the major achievements are expected within the next 1-5 years.

NEW MATERIALS IN ECR DISCHARGE

Fullerene plasmas and beams have been produced in ECR ion sources for various scientific and practical reasons and purposes [1]. High intensity singly and multiply charged beams are needed for collision experiments. The endo- and exohedral fullerenes are getting more and more important for materials research and, in some cases, for medical applications. Endohedral means that an alien atom or molecule is encapsulated inside the carbon cage. The most known endohedral fullerene is the $N@C_{60}$ molecule (here the @ sign means that the atom at left locates inside the molecule at right). It has been investigated to develop a sensitive indicator to measure molecular distortions, molecular motions etc. and in conjunction with quantum computing [2].

At the ATOMKI-ECRIS fullerene plasmas have been produced since 2000 by using filament ovens to evaporate fullerene. One of our goals has been the production of high intensity singly and multiply charged fullerene ion beams. Another research topic is the investigation of mixture plasmas (C_{60} + X, where X is N, O, Fe or other atoms). In C_{60}+N mixture plasmas endohedral $N@C_{60}$ was observed in the beam spectra and in macroscopic quantity in the soot deposited on the wall of the plasma chamber [2].

The fullerene encapsulated iron would be another promising new material if one could produce it first in a beam then in bulk quantity. In the past years we made some efforts in this direction. The composition of C_{60}+Fe mixture plasmas was studied by extracting ions from it. The iron component of the plasma was obtained from ferrocene powder or using high-temperature filament ovens to melt pure iron rods [3,4]. These and other results and demands led us to a major modification of the ATOMKI-ECRIS. Since 2006 it has been operating in two modes ("A" and "B") [5]. In "B"-mode the ion source is equipped with a large plasma chamber and a weak hexapole around it. This mode is specialized for the production of large-sized, low-ionized plasmas and provided the fullerene beams for a number of experiments.

The ATOMKI-ECRIS-B source was selected as a prototype for an other new ECRIS just built in Toyo

University, Kawagoe, Japan [6]. The new ion source was designed to produce iron encapsulating fullerene ions in beam and in deposited layer form. The details of the technical solutions and the latest beam results are presented in a separated paper at this workshop [7]. Here we list only the basic features of the source.

- Geometry: plasma chamber diameter is 14 cm, length is 35 cm.
- Microwave: 8-10 GHz and optionally 2.45 GHz, as second frequency.
- Mirror field: two identical room-temperature coils, peak fields max. 0.64 Tesla.
- Hexapole: NdFeB, modified AECR-U design, field at poles is 0.72 Tesla. The magnet borders at radial positions were calculated to form parallel slits for a future easier radial approach to the plasma (see Figure 1.).
- Fullerene gas: using simple filament oven or evaporation boat.
- Iron gas: by induction oven (under development).
- Extraction: grounded, movable puller, einzel triplet.
- Beamline: bending magnet to transport upto 5 KV beams with M=800.
- Other: an optional processing chamber is under construction to be connected at the extraction side. It will be equipped with biased meshes and cooled electrodes to help the iron-fullerene synthesis.
- Name: because the ion source is being built at the Bio-Nano Electronics Research Center of the Toyo University and it is aimed to produce new materials useful for physical, biological and medical research and application, it is called Bio-Nano-ECRIS.

The Bio-Nano-ECRIS delivered the first gaseous and fullerene plasmas and beams in 2008. Further details and results are in [7].

BONE CELL GROWTH ON TITANIUM COATED WITH FULLERENE

Current clinical implant therapy includes microscopic modification of bone formation on machined titanium implants. This concept is called “osseointegration” and now is widely accepted in clinical dentistry and surgery. Efforts have been and still are being made to accelerate and increase bone formation around dental and orthopedic implants and to improve lifetime and mechanical stability. Nanotechnology offers physicists, engineers and biologists new ways of interacting with relevant biological processes. Nanoscale modification of titanium implant surfaces can alter cellular and tissue responses that may benefit osseointegration and dental implant therapy. The biological usefulness of the titanium implants can be improved either if their surfaces are modified or if they are coated.

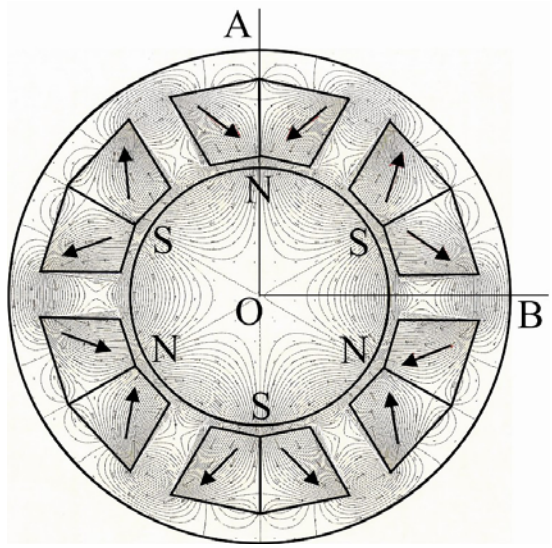

Figure 1. The structure of the hexapole of the Bio-Nano-ECRIS. Nd-Fe-B magnet material: NMX-S45SH. Note the parallel slits at gap positions.

To our knowledge fullerene (C_{60}) coating has never been tried yet as an intermediate layer between the metal and the organic tissue in order to increase the cells growth speed and to improve the properties of the cells connection. C_{60} molecules, if ionized, can be shot to the metal surface with any required velocity. Depending on this velocity, the carbon balls may remain intact or may be partly or fully damaged by hitting the metal surface. The strength of the connection is obviously depends on the projectile velocity which is needed to be explored experimentally. On the other side, fullerene molecules can be very reactive, hydroxyl and other group of atoms and molecules are connected to them likely and easily. Such derivatised fullerenes can be medically useful [8]. Therefore, in collaboration with the Faculty of Dentistry of the Debrecen University, we have started a research program in order to coat titanium surfaces by fullerenes with various velocity and thickness. Then biological tests will be carried out on the covered samples by growing bone cells on them.

For an ion source point of view the task was to irradiate simultaneously 10 pieces of identical Ti samples (size is approx. 10x10 mm, thickness is 0.5 mm) with as homogenous fullerene beam, as possible. An irradiation facility was built in the primary (zero degree) beamline. The Ti samples located approx. 50 cm distance from the plasma electrode. The analyzed (90 degrees) beamline was used only to check the composition of the beam, before and after the irradiation. The ATOMKI-ECRIS-B source [5] can produce “pure enough” fullerene beam in two point of views: around 90% of the beam is single-charged, and more than 80% of the extracted beam is fullerene. The rest less than 20% is mostly H_2O and N_2/CO. The necessary energy (extraction voltage) of the fullerene beam was chosen with the help of published data [9]. The structure of carbon films, deposited from

ionized fullerenes accelerated to different energies, depends on the deposition energy. Below 300 eV fullerenes are deposited preserving the molecular identity while above 800 eV the deposited material can be considered already almost as amorphous carbon [9]. In our experiments we aimed to make half of the samples covered with "intact" fullerenes and the other half with "partly-broken" fullerenes. Therefore U=250 V and U=500 V acceleration energies were chosen to get 250 eV and 500 eV beam energy, respectively. Composition of a typical analyzed beam: H_2O+: 10 nA, (N_2/CO)+: 10 nA, C_{60}^{3+}: 3 nA, C_{60}^{2+}: 30 nA, C_{60}^{+}: 100 nA. These currents were measured in the Faraday-cup after the bending magnet, the extraction voltage was U=250 V. At U=500 V all these currents were higher about 2-3 times. A vertical sample holder together with a 5-segments beam profile monitor was designed and constructed. This device enabled us to set a 50 mm diameter fullerene beam (see Fig. 2). Due to the radial multipole magnets ECR-beams always have a specific, well-known structure. Nevertheless, we could always set a beam where the 5 current values on the 5 segments differed from each other by less than 10%. The beam current impacted the samples was about 300 and 800 enA at U=250 V and U=500 V, respectively. The rate was calculated to produce the Ti-surfaces to be covered with 1 C_{60} molecular layer and others with 5 layers.

After building the ATOMKI-ECRIS-B mode we tested both our 14.3 GHz klystron and 12.2 GHz TWTA, as microwave sources – without any remarkable difference in this experiment. The applied microwave power was varied between 4 and 20 W. The solenoid field was much lower, than normally, the two magnetic peaks just surpassed the resonance values. No mixing gas was used. The fullerene source was the simple filament oven we used earlier many times [3]. We placed 10 Ti-samples to the copper holder and altogether 4 irradiations were done during 4 days. The Table 1 summarizes the main characteristics of the irradiations (columns 2-5).

The irradiation of the titanium with fullerenes was followed by biological experiment. Human embryonic bone cells (type: palatal mesenchymal pre-osteoblast, HEPM 1486, ATCC) were cultured onto the Ti substrates for 48 hours, followed by a fixing in formaldehyde for 10 minutes. Then the cells were dual labeled with special markers (FITC-falloidin) for 45 minutes at 4º C to make the actine and vinculine parts more visible. The confocal imaging was performed on a laser scanning microscope (LSM 510, Carl Zeiss). The morphology of the cells is different compared to the control substrate (pure glass), but remarkable differences between the four series could not be observed so far. The control cells on glass are quite spread showing an interconnected morphology. The cells grown on the Ti substrates are more spindle-like shape showing denser actine and vinculine structure. In Figure 3. confocal images of the bone cells grew on glass and titanium substrates (latter covered with C_{60}), are shown.

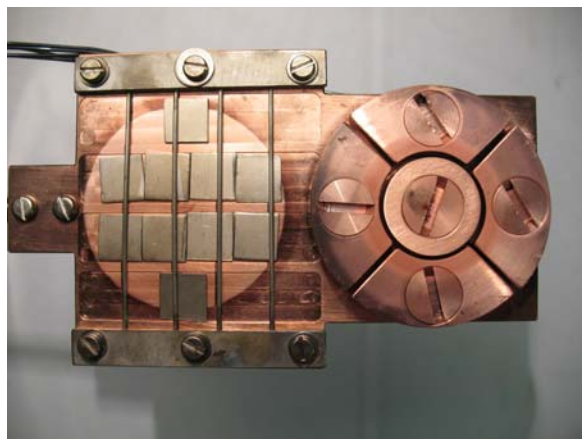

Fig. 2. The 5-segments copper beam profile monitor (right) and the sample holder with 10 Ti samples (left). This device is mounted on a vacuum feedthrough with 100 mm longitudinal run.

The last column of Table 1 shows the number of the grown bone cells (result of averaged microscope counting) on the fullerene layer. While these numbers show some tendency, it is too early to draw conclusions from them for the optimal beam energy or ion dose.

Table 1. Titanium irradiation with fullerenes. One series contained 10 Ti-samples.

Ti sample series	C_{60} fraction in beam (%)	Beam energy (eV)	Number of C_{60} layers on Ti	Time of irradiation (min)	Number of bone cells (10^5/ml)
1	80	500	4.3	90	8.0
2	93	500	1.2	23	3.4
3	74	250	4.9	87	6.6
4	84	250	1.1	32	8.9

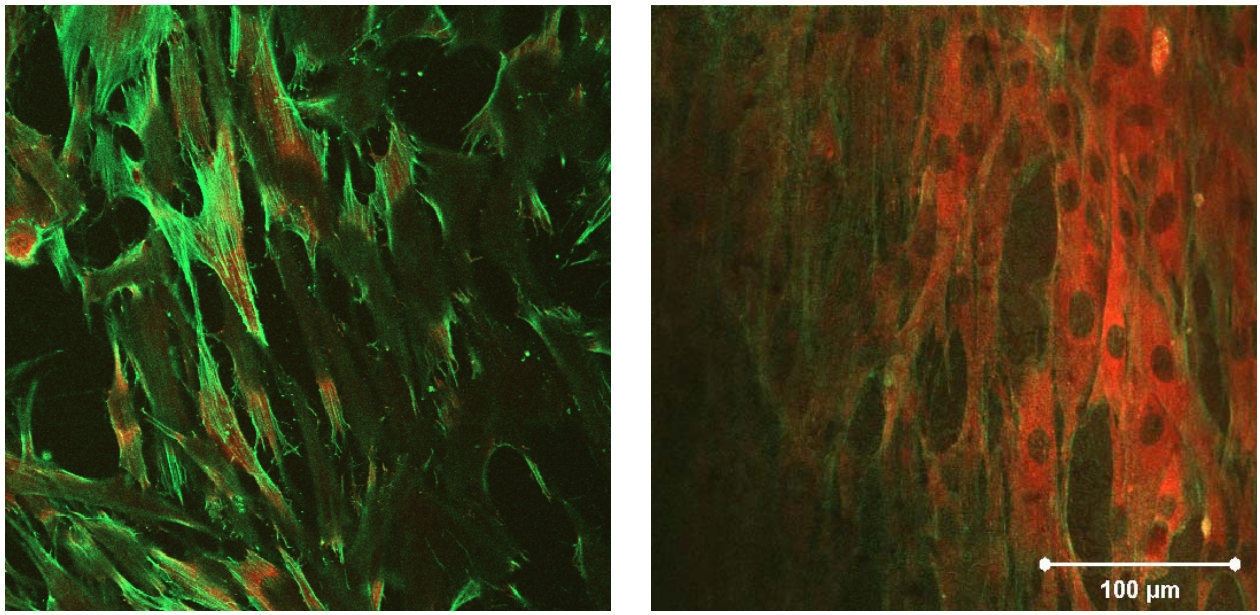

Fig. 3. Confocal laser scanning microscope images of bone cells grown on glass (left) and on Ti surface covered with 250 eV C_{60} layer (right).

This first experiment obviously ended with success in the sense that it was clearly proved the C_{60} coating does not prevent bone cells grows. Further experiments however are necessary to explore the optimal beam properties (energy, dose, density, composition) to improve both the physical (Ti-C_{60} connection) and biological (C_{60}-cells) properties of the connections.

OPTICAL CHANGES IN THIN FILMS

Ion bombardment and ion implantation are versatile tools for modification of properties of thin near-surface layers of solid materials. In case of singly charged ions and a large variety of materials this effect is rather well understood and widely used in different branches of the modern industry. The effect of the bombardment of multiply and highly charged ions has been studied only in a few materials, such as HOPG (highly oriented pirolytic graphite), mica, Al_2O_3, SiO_2 and Se [10-13]. These studies concentrated on the nanohillock and crater formation caused by impact of single ions depending on the ion charge state and on the materials properties. There have not been studies on the effects caused by ions while traveling through and stopping inside the solid, since the charge state dependence was thought to be too small to detect experimentally [14,15].

However, we have observed significant charge state dependence in darkening of amorphous AsSe thin films bombarded with Ne^{q+} (q=4..8) ions. Previous ion irradiation experiments with 80-180 keV protons and deuterons have shown [16,17] that the ion bombardment causes structural rearrangements in AsSe and in similar amorphous chalcogenide thin films, which in turn result in optical band gap decrease (i.e. decrease of optical transmission at certain wavelengths). The relative transmission change during bombardment with Ne^{q+} (q=4..8) ions (measured at 600 and 640 nm) versus ion fluence plots are shown in Fig. 4. The total kinetic energy of all ions was set to 120 keV, therefore the ion source extraction voltage was from 15 to 30 KV. The thickness of the AsSe films was 800 nm which is about three times as large as the expected thickness of the modified layer (SRIM [18] calculations gave 196 nm range and 116 nm longitudinal straggling). In Fig 4 one can see the optical transmission decreasing with the ion fluence while reaching saturation value at about ~$3\cdot10^{14}$ ion/cm^2 in this particular case. The saturation value of the relative transmission depends on the thickness of the modified layer (see l in the equation) and on the depth distribution of the induced absorbance $\Delta\alpha(z)$:

$$\left(\frac{T}{T_0}\right)_{sat} \propto \exp\left(-\int_0^l \Delta\alpha dz\right).$$

Our experiment shows that the $(T/T_0)_{sat}$ is larger for the sample irradiated with Ne^{8+} ions than for the one irradiated with Ne^{4+} ions. Since the $\Delta\alpha(z)$ is proportional to the total energy/volume deposited in the material by the ions (i.e. the higher the deposited energy the larger the $\Delta\alpha$) [16, 17] and the ions with higher charge are expected to have higher specific energy loss [15], the observed difference in the $(T/T_0)_{sat}$ values by necessity means that thickness of the modified layer is smaller for the Ne^{8+} ions than for Ne^{4+} ions by 25%. As the modified layer thickness is in strong correlation with the stopping range of the ions, the above stated relation is true also for the range of the ions.

This result has impact on our knowledge of charge equilibration processes of ions traveling in solids and also on a number of basic scientific and technical problems,

which along with the details of the experiment will be discussed in detail in a forthcoming paper [19].

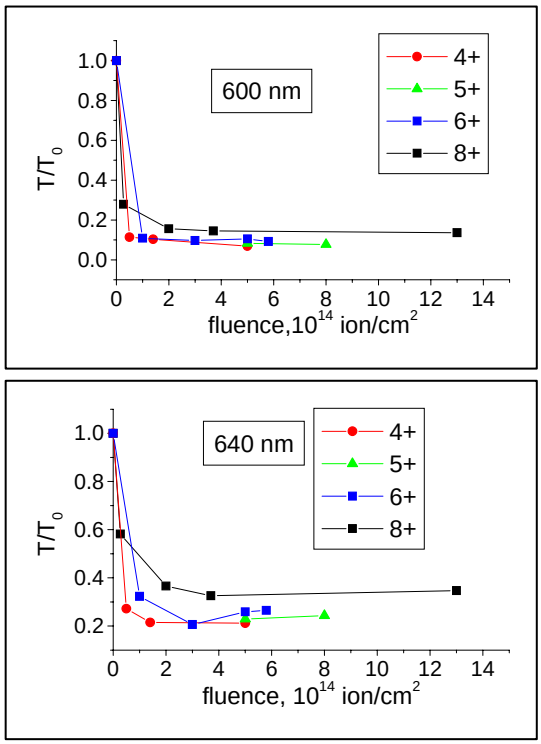

Fig 4. The change of optical transmission (T) of a 800 nm thick AsSe film measured at 600 and 640 nm relative to its initial value (T_0) during bombardment with Ne^{q+} (q=4..8) ions versus the ion fluence.

CAPILLARY GUIDING

Charging up of insulating surfaces during irradiation by ion beams involves mesoscopic or long range interaction of the ions and the charged surfaces. Insulating nanocapillaries have attracted considerable attention since the discovery of capillary guiding caused by the self-organizing charging up of the inner capillary walls [20]. Ions with a few keV kinetic energy are efficiently transmitted through the capillaries of thin insulating foils mostly in their initial charge state, and the transmitted ions are directed along the capillaries with a narrow angular distribution. There is significant transmission even if the capillaries are tilted by large angles, i.e., when there is no geometrical transparency for straight line trajectories. Due to these properties, insulating nanocapillary arrays might find numerous applications, e.g., in guiding, directing and focusing slow ion beams in nanoscale devices. They might be used for irradiating single cells and writing on charge sensitive surfaces.

In order to collect more data with different kinds of capillaries that is useful for the full understanding of this self-organizing phenomenon, experiments were carried out on the 90 degree beamline of the ATOMKI-ECRIS-A source. Neon (6+, 7+) and argon (8+, 9+) beams were transported into the capillaries. The extraction voltage was usually 500 V and a collimator set of two 1 mm diaphragms at a distance of 205 mm restricted the beam divergence to ±0.3 degrees from axis at the end of the beamline. The beam intensity on the targets fall in the pA or nA range. The typical beam current for 3 keV Ne^{6+} was about 300 pA. For 6 keV Ne^{6+}, it was 500 pA.

The sample holder with the capillaries was mounted in the middle of a vacuum chamber with three axial and one rotational freedom. Separately, a spectrometer was mounted on a rotating table to measure the charge and currents of the transmitted ions at different observation angles. The incidence angle of the ions was changed by tilting the target samples. Two dimensional angular distributions were recorded by the multi-channel-plate (MCP) detector placed behind the target samples. The ion spectrometer and the MCP were used alternatively.

Most of the target samples were prepared of membranes of nanochanneled Al_2O_3. The thickness of the samples was about 15 μm and the capillaries were ordered in a honeycomb structure. The average inner capillary diameters of the different samples used in the experiments were about 140 and 260 nm. In order to prevent macroscopic charging up of the samples, niobium layer of about 20 nm thickness was deposited on both sides of the membranes by dc-sputtering. Macroscopic sized single capillaries were also investigated. Those capillaries were made of glass and had an inner diameter of a few tenth of mm.

The angular and charge state distribution of Ne^{6+} and other ions transmitted through Al_2O_3 capillary samples were measured by different methods. The major outcome of these experiment was that the ions have been efficiently guided by the capillaries up to a few degrees tilt angle, similarly to the earlier investigated polyethylene terephthalate [20] and SiO_2 [22] capillary samples. Most of the transmitted ions preserved their initial charge as it can be seen in Fig. 5. The results obtained by the ion spectrometer were compared with those studied by the MCP array. The details of the experiment and some of the results have been published in other papers [21,22], others are to be published. Preliminary experiments have shown that under certain conditions macroscopic glass capillaries can guide slow ions as well.

COMPARISON

The Table 2 gives a simple overview of the four different applications of heavy ions detailed in the preceding chapters. The tasks and beam requirements are very different, but the ECR source proved to be versatile enough to fulfill all these requirements and serves as a real multi-purpose facility.

Table 2. Summary and comparison of the projects require heavy ion beams from the ion source point of view.

Project short name	Endohedral fullerenes	Ti implants coating	Thin layer modification	Capillary guiding
Ion source	ATOMKI-ECRIS-B and Bio-Nano-ECRIS	ATOMKI-ECRIS-B	ATOMKI-ECRIS-A	ATOMKI-ECRIS-A
Plasma/beam	Fe^{+}, C_{60}^{+}	C_{60}^{+}	$Ne^{4+...8+}$	$Ne^{6+,7+}$, $Ar^{8+,9+}$
Beam diameter (mm)	10-20	50	4	1
Extraction voltage (V)	500-5000	250-500	15000-30000	500-1000
Microwave frequency (GHz)	8-12	12-14	14.3	14.3
Microwave power (W)	1-50	4-20	200-400	200-600
Specification	Synthesis in plasma or on surface	Irradiation in the zero-degree beamline	Beams with same total energy	Puller on high negative voltage

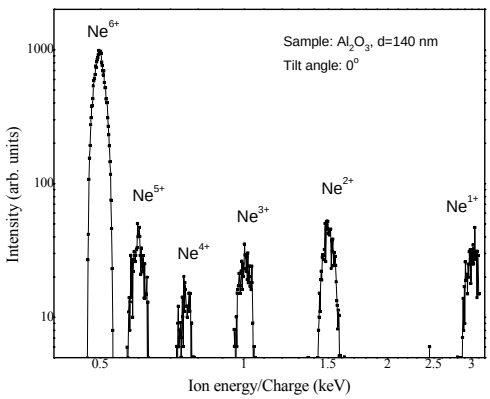

Fig. 5. Charge state distribution of the ions transmitted through 140 nm long capillaries at 0° tilt angle. The incident beam was of 3 keV Ne^{6+} ions.

REFERENCES

[1]. S. Biri, IEEE Transactions on Plasma Science 36(4) (2008) 1489.

[2]. S. Biri, A. Valek, L. Kenéz, A. Jánossy, A. Kitagawa, Rev. Sci. Instrum. 73 (2002) 2:881

[3] S. Biri, É. Fekete, A. Kitagawa, M. Muramatsu, A. Jánossy, J. Pálinkás. Rev. Sci. Instrum 77 (2006) 3A314.

[4] É. Fekete, S. Biri, I. Iván, Fullerenes, Nanotubes, and Carbon Nanostructures 15 (2007) 249.

[5] S. Biri, É. Fekete, I. Iván, I. Gál, High Energy Physics and Nuclear Physics - Chinese Edition Supplement 31 (2007) 156.

[6] K. Tanaka, M. Muramatsu, T. Uchida, S. Biri, T. Asaji, K. Shima, T. Hanajiri, A. Kitagawa, Y. Kato and Y. Yoshida, In Proc. 17. Int. Conf. on Ion Implant. Technol. (ITT2008), Monterey, California, USA, June 8-13, 2008.

[7] T. Uchida, H. Minezaki, Y. Yoshida, S. Biri, A. Kitagawa, M. Muramatsu, Y. Kato, T. Asaji, K. Tanaka, See this proceedings (ID: 1065 - MOCO-C01).

[8] L. J. Wilson, The Electrochemical Society's Interface, Winter 1999, pp. 24-28. http://www.electrochem.org/dl/interface/

[9] H. Huck et al., Applied Surface Science 211 (2003) 379.

[10] T. Meguro, Y. Yamaguchi, H. Fukugawa, H. Takai, N. Hanano, Y. Yamamoto, K. Kobashi, T. Ishii, Nucl. Instrum. Methods B235 (2005) 431.

[11] I. C. Gebeshuber, S. Cernusca, F. Aumayer, H. P. Winter, International Journal of Mass Spectrometry 229 (2003) 27

[12] S. Kökényesi, I. Iván, E. Takács, J. Pálinkás, S. Biri, A. Valek, Nucl. Instrum. Methods B233 (2005) 222.

[13] S. Kökényesi, I. Iván, V. Takáts, J. Pálinkás, S.Biri, I. A. Szabó, Journal of Non-Crystalline Solids 353 (2007) 1470.

[14] J. P. Biersack, Nucl. Instrum. Methods B80/81 (1993) 12.

[15] T. Schenkel, M. A. Briere, A. V. Barnes, A. V. Hamza, K. Bethge, H. Schmidt-Böcking, D. H. Schneider, Phys. Rev. Lett. 79 (1997) 2030.

[16] I. Iván, S. Szegedi, L. Daróczi, I. A. Szabó, S. Kökényesi, Nucl. Instrum. Methods B229 (2005) 240.

[17] S. Kökényesi, J. Csikai, P. Raics, I.A. Szabó, S. Szegedi, A. Vitéz, Journal of Non-Crystalline Solids 326&327 (2003) 209.

[18] Downloaded from www.srim.org

[19] I. Iván, S. Biri, S. Kökényesi, to be published.

[20] N. Stolterfoht, J.-H. Bremer, V. Hoffmann, R. Hellhammer, D. Fink, A. Petrov, B. Sulik, Phys. Rev. Lett. 88 (2002) 13320.
[21] S. Mátéfi-Tempfli, M. Mátéfi-Tempfli, L. Priaux, Z. Juhász, S. Biri, É. Fekete, I. Iván, F. Gáll, B. Sulik, Gy. Víkor, J. Pálinkás, N. Stolterfocht, Nanotechnology 17 (2006) 3915.
[22] Z. Juhász, B. Sulik, S. Biri, I. Iván, K. Tőkési, É. Fekete, S. Mátéfi-Tempfli, M. Mátéfi-Tempfli, Gy. Víkor, E. Takács, J. Pálinkás, Nucl. Instrum. Methods B (accepted for publication).

DEVELOPMENT OF ECR HIGH PURITY LINERS FOR REDUCING K CONTAMINATION FOR AMS STUDIES OF ^{39}Ar

Chris Schmitt, Matt Bowers, Philippe Collon, Daniel Robertson, University of Notre Dame, Notre Dame, IN 46556, U.S.A.

Dale Henderson, Cheng-Lie Jiang, Richard Claude Pardo, Ernst Rehm, Robert Scott, Richard Vondrasek, ANL, Argonne, IL 60439, U.S.A.

Frank Calaprice, Ernst de Haas, Cristiano Galbiati, Princeton University, Princeton, NJ 08544, U.S.A.

Michael Paul, Hebrew University of Jerusalem, Jerusalem, 91904, Israel

Walter Kutschera, Vienna Environmental Research Accelerator, Institut fuer Isotopenforschung und Kernphysik, Universitaet Wien, Austria

Abstract

The first application of ^{39}Ar Accelerator Mass Spectrometry (AMS) at the ATLAS linac of Argonne National Laboratory (ANL) was to date ocean water samples relevant to oceanographic studies using the gas-filled magnet technique to separate the ^{39}K-^{39}Ar isobars. In particular the use of a quartz liner in the plasma chamber of the Electron Cyclotron Resonance (ECR) ion source enabled a ^{39}K reduction of a factor ~130 compared to previous runs without liners and allowed for our current lowest detection limit of ^{39}Ar/Ar = 4.2x10^{-17} [1]. We are currently working on improving the AMS method for ^{39}Ar by following two development paths to allow for higher beam currents while lowering ^{39}K rates. The first option is to modify the design of the quartz liner to provide active water cooling. The second option is to use a thick walled liner of high purity aluminum constructed with an interference fit to the plasma chamber wall. The overall driving force for this AMS project is to search for a source of argon that has a low concentration of ^{39}Ar. Such a source of argon would be useful for new liquid argon detectors that are being developed for detecting dark matter WIMPs (Weakly Interacting Massive Particles).

INTRODUCTION

Commercial argon is obtained from the atmosphere and contains ^{39}Ar, which is produced by cosmic ray interactions with ^{40}Ar in the atmosphere. The ^{39}Ar decays by beta emission with an end-point energy of 560 keV and a half-life of 269 years. The atmospheric concentration of ^{39}Ar relative to ^{40}Ar is 8.1 × 10^{-16}, corresponding to a beta decay rate of ~1 Bq/kg of argon [2].

Argon can also be found as a trace component in gas that comes from deep underground wells. Shielded from cosmic rays it should have lower than atmospheric levels of ^{39}Ar though there are nuclear reaction mechanisms that can produce ^{39}Ar in underground sites. For example, the neutron induced reaction ^{39}K(n, p)^{39}Ar will occur if there is uranium and thorium together with potassium, since the alpha particles of the U and Th chains produce neutrons by (α, n) reactions on light nuclei [3, 4].

The challenges to detect ^{39}Ar at natural levels are great with ^{39}Ar/Ar (= 8.1 × 10^{-16}) being a thousand times smaller than that of ^{14}C/C (=1.2 × 10^{-12}). One liter of "modern" ocean water, i.e. water in equilibrium solubility with the atmosphere, contains only ~6500 atoms of ^{39}Ar, requires very high overall detection efficiency [5].

Since argon does not form negative ions, tandem accelerators, the traditional AMS tool, are unsuitable and positive-ion accelerators must be used and a very high background of ubiquitous ^{39}K, the interfering stable isobar (ΔM/Q = 1.55 × 10^{-5}) must be separated.

The difficulty in this experiment is also evident in a mechanical sense. From ECR II to the spectrograph there is over 120m of equipment that must maintain relatively good stability for long periods of time (see figure 1). Factors that come into play range from: the output of the ion source, the tune of the beam provided by the accelerator, beam line elements like magnets that can drift

as the temperature fluctuates, and thin windows that separates gas filled regions from vacuum that can tear, potentially ruining the vacuum in the beam line.

Another aspect of this overall difficulty is the estimated ^{39}Ar count rate. The highest beam current from the ion source during the last run was between 130-133 eμA so assuming 20% transmission from ECR II to the spectrograph focal plane we get:

- 100% atmospheric Argon ≈ one ^{39}Ar count per minute
- 10% atmospheric Argon ≈ one ^{39}Ar count in 10 minute
- 1% atmospheric Argon ≈ one ^{39}Ar count in 1.7 hours
- 0.1% atmospheric Argon ≈ one ^{39}Ar count in 17 hours.

The standard experimental time for attempting measurements is a week. This quantifies the necessity for stability and the need for an ultra pure liner that can provide high source output and low background to allow for the measurement of a "representative" sample.

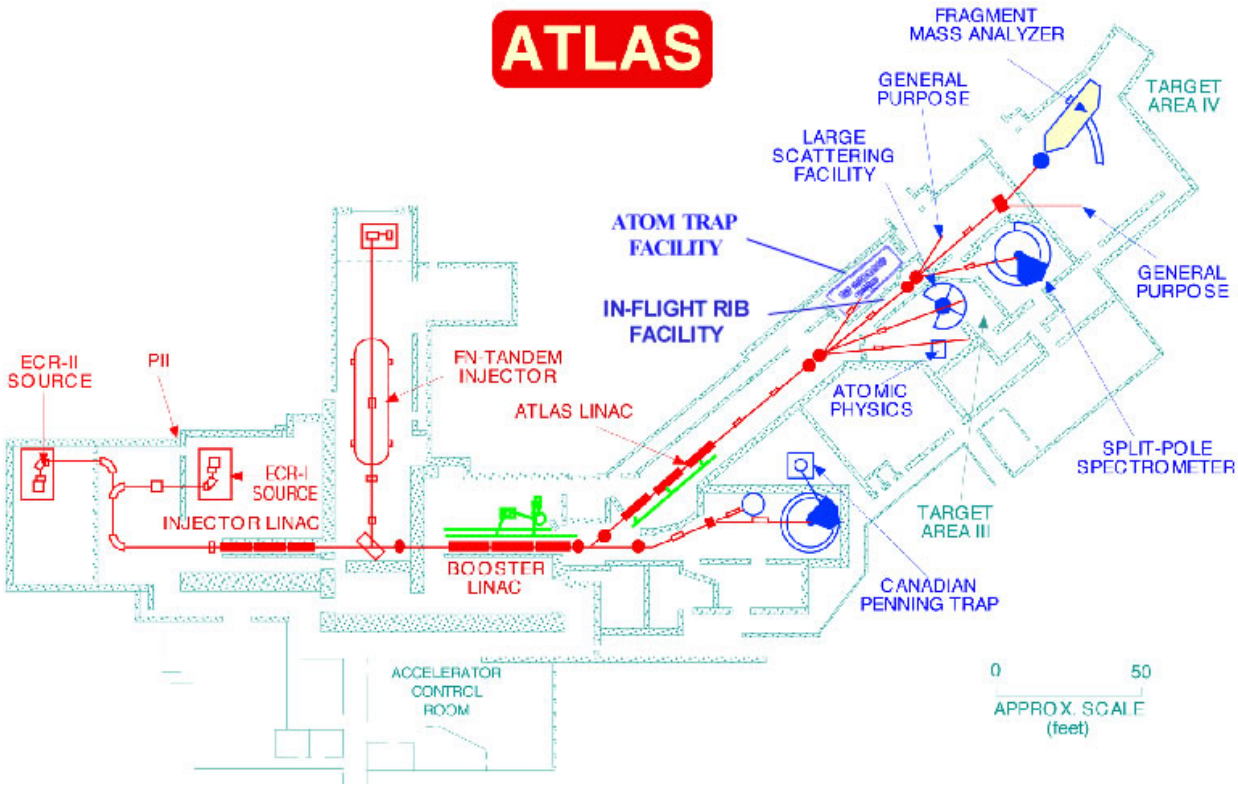

Figure 1: ATLAS facility floor plan at Argonne National Laboratory. From ECR II to the Split-Pole Spectrometer is approximately 400 feet (120 m).

One of the initial goals of our research was to develop and to improve the AMS technique to the stage of obtaining reasonably precise ^{39}Ar measurements from 20 liter water samples for oceanographic studies (see next section) [6, 1]. In the case of ^{39}Ar analysis using AMS, the isobaric separation from ^{39}K was achieved using the gas-filled spectrograph technique [7] (see figure 2). The two key effects combined in this technique, the bending of the ions trajectory in the magnetic field and the loss of ion energy in the gas, have different relations to the charge and mass of the ion, thus allowing the separation of both isotopes and isobars. In particular, in the gas-filled region of the magnet, the discrete trajectories of each of the charge states of the ions coalesce around a trajectory defined by the mean charge state of the ion in the gas [8]. The development of this method and the ^{39}Ar/Ar measurements that followed were performed at ANL using the ATLAS accelerator facility.

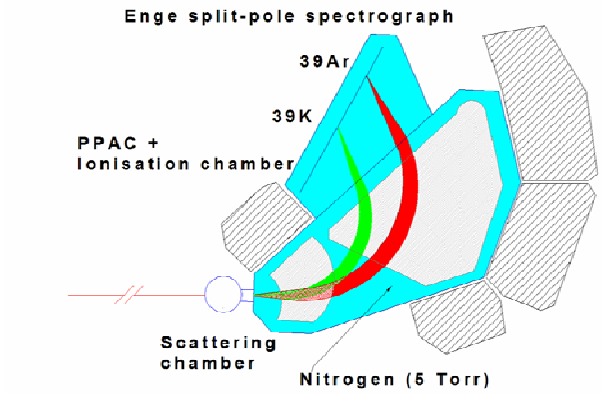

Figure 2: In the gas-filled magnetic region, the discreet charge states coalesce around a trajectory defined by the mean charge state of the ion in the gas.

$^{39}Ar^{8+}$ ions were alternately produced in ECR I and ECR II sources, accelerated to 232MeV by the linac, separated from their isobar $^{39}K^{8+}$ ions in the gas-filled spectrograph, and detected using a position sensitive parallel plate avalanche counter (PPAC) followed by an ionization counter [7, 9] (see figure 3).

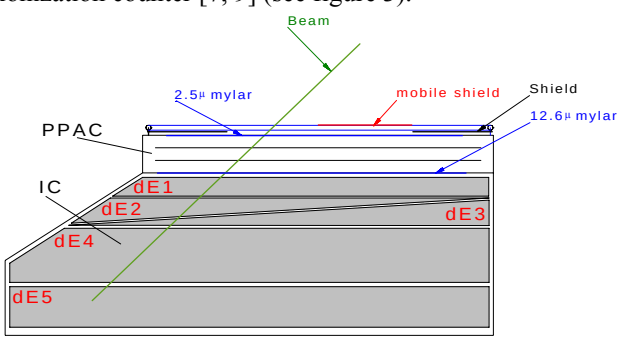

Figure 3. Typical detector setup with a position sensitive PPAC on top and below an ionization chamber.

Although experiments previous to May 2002 obtained a clear separation between the ^{39}K and ^{39}Ar peaks, the intensity of the ^{39}K count rate created signal pile-up in the detector. This pile-up became a major problem when trying to measure samples with lower than atmospheric concentrations and making it impossible to consider increasing the overall beam intensity for AMS measurements as the ^{39}K isobaric background scales with the $^{40}Ar^{8+}$ beam intensity. A series of experimental runs were initiated to try various plasma chamber liner configurations in order to reduce the amount of potassium coming from the source.

MOTIVATIONS

Oceanographic Applications

With the atmospheric concentration of ^{39}Ar/Ar = 8.1 × 10^{-16}, the practical use of ^{39}Ar as a tracer represents a major technical challenge: 1 L of modern ocean water produces ~17 ^{39}Ar decays per year. As long as large ocean water samples for ^{14}C analysis (~250 L) were routinely collected, low level counting (LLC) of ^{39}Ar extracted from five large volume samples (~1000 L) water samples was feasible [5]. However, with the advent of AMS, only 1 L samples were required for ^{14}C measurements, reducing the routine availability of large water samples. As a consequence, the LLC method for oceanographic ^{39}Ar measurements was practically put on hold and no data have been obtained during the past decade. Therefore it became vital to develop an AMS technique for ^{39}Ar measurements at facilities such as the ATLAS linac facility of ANL.

The first applications of ^{39}Ar AMS at ATLAS to date ocean water samples relevant to oceanographic studies (May 2002, October 2003) were most successful. In particular the use of a quartz liner in ECR II made it possible to reduce the ^{39}K background intensity by a factor of ~130 compared to previous runs. This opened the door to measuring the ^{39}Ar content of actual ocean samples and our measurement demonstrated an excellent detection limit of ^{39}Ar/Ar = 4.2×10^{-17}, corresponding to more than 4 “equivalent half-lives” [1, 6]. However to achieve the original program goal, i.e. to develop a technique that would allow to perform ^{39}Ar/Ar isotope ratio measurements with an uncertainty of the order of 5% using no more than 20 L of ocean water samples, it was necessary to increase the source beam current as well as to improve the overall detection sensitivity while keeping the ^{39}K background at acceptable levels [4]. This has been the focus of the October 2003 run as well as subsequent tests by the ECR group at ANL.

Dark Matter Searches

Recently work done by Frank Calaprice and Cristian Galbiati from Princeton University has opened up a new motivation to develop this AMS technique for ^{39}Ar in groundwater [10]. The driving force for the use of AMS is to search for a source of argon that has a low concentration of ^{39}Ar. Such a source of argon would be useful for new liquid argon detectors that are being developed for detecting dark matter WIMPs.

Standard liquid argon, which is obtained from atmospheric argon gas, has a small but important component of ^{39}Ar owing to cosmic ray reactions. Argon gas is also found underground in natural gas and CO_2 gas wells. Because the cosmic ray flux is suppressed, underground argon may be low in ^{39}Ar. However, underground processes can also produce ^{39}Ar by a sequence of (α,n) and ^{39}K(n,p)^{39}Ar reactions in rock with high concentrations of U, Th, and K. A mantle source of argon may fit these requirements. We therefore propose a set of measurements on argon gas samples from different sites to search for a suitable source. A source of argon with ^{39}Ar at <1% the atmospheric concentration would be highly desirable for WIMP searches.

If WIMPs do exist they will collide with ordinary nuclei and the collisions may be detected by observing the recoil atoms. The recoils will have a continuous energy spectrum ranging up to ~100 keV. The event rate expected could be as low as a few events per ton per year with a projected cross section of $3x10^{-45}$ cm^2. Detecting WIMPs therefore requires a large detector with low background and a low energy threshold.

The rare gas atoms- neon, argon, and xenon - have excellent properties for detecting rare WIMP-induced nuclear recoils. The rare gasses can detect nuclear recoils down to a few keV by scintillation and/or ionization. Moreover, the beta and recoil signals differ, which provides powerful discrimination for separating events due to recoil atoms from ubiquitous gamma and beta events. The difference in the stopping power between recoils and betas leads to significant difference in the ratio of ionization charge to scintillation light detected and also produces different scintillator pulse shapes that are quite significant in argon. It is also expected that the technology can be scaled up to detectors with a mass of hundreds of kilograms.

For a liquid argon detector, the beta-recoil discrimination is particularly important because of background from the atmospheric ^{39}Ar. Preliminary studies of the beta-recoil discrimination with the WARP 2.3 kg liquid argon detector indicate that the discrimination is marginally sufficient to permit a sensitive WIMP search with a 100 kg liquid argon detector produced from atmospheric argon. Argon with a concentration of ^{39}Ar at or below 1% the atmospheric concentration would permit a very sensitive search for dark matter.

The AMS technique developed at ANL for measuring ^{39}Ar was well suited for the original oceanographic applications however the proposed measurements on underground argon related to WIMP searches requires improved sensitivity. The limiting factor to the AMS sensitivity is the background beam of K. Reducing the K background beam is therefore part of the goal of the proposed measurements.

PRESENT STATUS OF THE ^{39}K BACKGROUND REDUCTIONS

The successful use of a quartz liner in the plasma chamber to significantly reduce the amount of K background has been demonstrated. However, this is linked to a limitation of beam intensity. The October 2003 run, as well as more recent tests by the ion source group, strongly indicate that the use of a quartz liner limits the argon beam intensities to a present maximum achieved current around 80eμA. Previous tests using metal liners or silicon oxide coatings of the plasma chamber showed significantly higher $^{40}Ar^{8+}$ currents but were always hampered by extremely high levels of ^{39}K.

The Princeton group is involved in the Borexino solar neutrino experiment and has extensive experience in low background counting. Measurements of the naturally occurring radioactive elements K, U, and Th have been made on a number of materials and a data base has been accumulated that will be helpful for choosing materials to eliminate bulk sources of K in the ECR source. Precision cleaning of critical parts of the ECR source to eliminate surface contamination is also important. Precision cleaning methods with suitable low K cleaning agents have been developed for Borexino and can be applied to reduce the K background in the ECR source.

We are currently pursuing the development of the ^{39}Ar AMS technique at ATLAS using a powerful cleaning technique using detergents with very low metal content (i.e. potassium) developed for removing both particulates and other materials from surfaces, largely driven by the semiconductor industry. Additionally, at Argonne and other labs working on RF superconductor technology, high pressure ultra-pure water rinsing techniques have also been developed. This technique has been used very successfully with the ATLAS resonators to remove surface particulates and improve surface fields. A number of these cleaning techniques have been adopted for low-level counting chambers with particular attention to potassium.

We adapted these techniques to carry out a series of tests to determine if the potassium background in the ECR II ion source can be significantly reduced. A first

experiment using these techniques was run June 2007 where we tested a cleaned ultra pure Al liner in ECR II resulting in a $^{40}Ar^{8+}$ output of 210 eμA, a clear improvement over the quartz liner case. Without a liner in place, the available beam intensity has been demonstrated up to 340 eμA of $^{40}Ar^{8+}$. These tests were hampered however by extremely high levels of $^{34}S^{7+}$ which made it through the accelerator and spectrograph. These were probably due to the thin ultra pure Al liner having lost thermal contact with the chamber wall. The loss of thermal contact resulted in the melting of part of the aluminum liner during the run (see figure 4). During the June 2007 tests using the high purity Al liner plus cleaning technique resulted in a ^{39}K count rate as low as: $3.6x10^4$ cps, which showed the promise of using Al liners.

Figure 4: The ultra pure aluminum liner after losing thermal contact from the plasma chamber wall.

This opens up the possibility of combining increased argon beam intensity, associated with the use of a more robust high purity aluminum plasma chamber liner or coating, with a suppressed K background resulting from the above mentioned cleaning techniques.

The April 2008 tests with ECR II were dedicated to further investigate techniques using ultra pure aluminum from Hydro Aluminium Deutschland GmbH. Testing both the ultra pure aluminum coated wall to avoid the thermal contact problem previously encountered and then in combination with open quartz liners to try and achieve the coupled outcome of increased Ar beam intensity with lower levels of ^{39}K background.

The spare plasma chamber from ECR II was sent to Princeton for cleaning, using the techniques they have developed, as well as coating the wall with ultra pure Al, which has K at less than 1ppb. These tests were made to avoid the thermal contact problems from the previous run. In addition to this, a new extractor cathode, bias disk, and injector snout were fabricated out of this ultra pure Al material and were used during the run.

Overall the results were very promising. During this run we initially used the open-ended quartz liner in combination with the Al coated chamber. However later on, this liner was removed and the source was run in an "ultra-pure Al plasma chamber configuration" alone. In both configurations no significant ^{34}S contamination was detected. This is a "first" as during previous runs when no liners were used there was always a detectable ^{34}S component.

Background suppression in the ECR ion source

The use of the ultra pure Al coated chamber also showed marked improvements in ^{39}K levels, both in combination with the open quartz liner as well as without any liner using only ultra pure materials in the plasma chamber.

The levels of ^{39}K using an open ended quartz liner during the August 01 run were: ^{39}K count rate: $1.3x10^6$ cps with an ion source currents of 80eμA. During this run ^{39}K count rates in identical conditions were $3.6x10^5$ cps with a clean separation between the ^{39}K tail and the ^{39}Ar peak. The lowest levels of ^{39}K were achieved during the May 2001 run (Closed quartz liner): ^{39}K count rate: 9800 cps. It is clear though that closed quartz of that configuration is limited to extracted currents of ~80eμA $^{40}Ar^{8+}$. Many subsequent tests have shown that increasing this beam current is not possible with closed quartz. The count rate of ^{39}K without any liner, but using only the high-purity Al coated chamber and end-pieces made from the same material was $1.5x10^6$ cps only hours after the source had been opened twice over a 6 hour period. This is similar to the lowest count rate achieved with open-ended quartz in August 01 and is the lowest level ever detected without a quartz liner. Though some beam line alignment issues prevented us from making reliable measurements to lower levels. We have strong evidence that the ^{39}K count rate was significantly decreasing over time (a factor of 10 over 9 hours) to levels where measurements below our current level would be possible.

Improved sensitivity in the detector

The use of higher gas pressures both in the spectrograph and in the Ionization Chamber allowed us to optimize the separation between the tail end of the ^{39}K peak and the ^{39}Ar peak due to their specific ranges in the detector (see figure 5). Slight modifications to the detector (i.e. different Mylar window support grids) will allow us to further increase this and thereby improve our sensitivity.

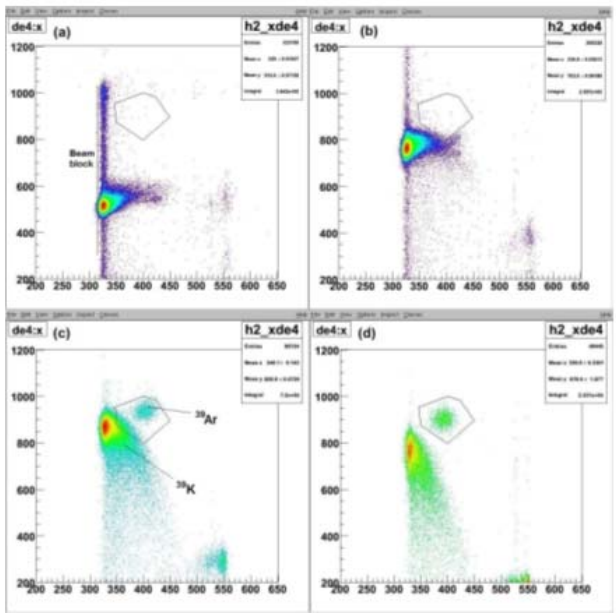

Figure 5. Position vs dE_4 spectrum taken for varying IC and spectrograph pressures. The 232MeV ^{39}Ar + ^{39}K beam was unchanged in these runs. A beam block was placed to block most of the ^{39}K peak and only the tail-end of the peak is observed. In (a) and (b) ionization pressure is changed and data collected for a couple of minutes. P_{IC} = 14.8 torr and P_{IC} = 20.8 torr, respectively. In (c) the pressure is change to P_{IC} = 24.7 torr, but the data collection time is longer approximately an hour. Here we see ^{39}Ar separated from ^{39}K, but there is some signal pile-up. In (d) the N_2 pressure (P_{SPEC}) increased from 12 to 13 torr and the separation between the peaks is made much clearer.

DEVELOPMENT PATHS

There are two development paths that will be pursued. The first is a quartz liner that is aluminum coated and actively water cooled. The best results have always come with the closed ended quartz liner and the hope is that the Al coating will allow us to increase the source output (see figure 6).

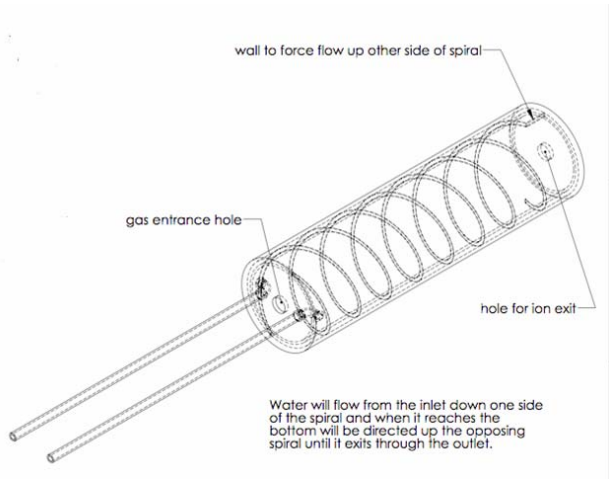

Figure 6: A schematic of the closed quartz liner that is actively cooled.

A several mm thick ultra pure Al liner will be constructed with an interference fit. The chamber will be heated and the liner chilled with liquid nitrogen. When the liner warms up it will make maximum surface contact to ensure continuous cooling.

CONCLUSION

The application of AMS toward ^{39}Ar at ANL began as a way to date ocean water samples relevant to oceanographic studies and now a new motivation for dark matter WIMP searches. There is currently active development to increase the detection sensitivity to improve the AMS method for ^{39}Ar. The principal, though not the only, difficulty is the high ^{39}K background. To reach our goal we need to be able to reduce the background and increase the ion source output.

There are two development paths to allow for higher beam currents while lowering ^{39}K rates. The first option is to modify the design of the quartz liner to provide active water cooling and the other path is to use a thick walled liner of high purity aluminum constructed with an interference fit to the plasma chamber wall. The present results show great promise as is summarized in Table 1.

Table 1: Summary of Results.

	Date	**^{39}K full peak**	**I_{ECR} ($^{40}Ar^{8+}$)**	**Comments**
^{39}K no treatment	June 07	$4.2x10^6$ cps	83 eμA	Baseline (a)
Open Quartz	Aug 01[5]	$1.3x10^6$ cps	83 eμA	Factor 3.2
Closed quartz	May 01 [5]	9800 cps	83 eμA Max output	Factor 430, best ever but limited in current
Open ultra-pure Al	June 07	$4.5x10^4$ cps	98 eμA	Factor 110, higher beam
	June 07		210 eμA	Max beam output in these conditions
Ultra-pure Al coated chamber	April 08	$1.5x10^6$ cps	55 eμA	Factor 1.8 (normalized to 83eμA)
	April 08		130 eμA	Max beam output in these conditions

(a) In the above table this run was used as the baseline for ^{39}K count rate.

REFERENCES

[1] P Collon et al., Nucl. Instr. and Meth. B 223-224 (2004) 428-434.

[2] H. H. Loosli, Earth Planet. Sci. Lett. **63**, 51 (1983)

[3] Loosli etal., Geochim. Cosmochim. Acta 53, 1825 (1989).

[4] Andres et al., Geochim. Cosmochim. Acta 53, 1803 (1987).

[5] M. Gaelens, M. Loiselet, G. Ryckewaert, R.C. Pardo, R. H. Scott, R. Vondrasek, Ph. Collon, W. Kutschera, Rev. Sci. Instrum. **75**, 1916 (2004).

[6] P. Collon, Z-T. Lu, W. Kutschera, Annu. Rev. Nucl. Part. Sci. (2004) 54:39-67.

[7] M. Paul et al. Nucl. Instr. Meth. B. 273, 403 (1998)

[8] H. Betz, Rev. Mod. Phys. 44, 465 (1972).

[9] K.E. Rehm and F.L.H. Wolfs, Nucl. Instr. Meth. A 273, 262 (1988).

[10] D. Acosta-Kane et al. Nucl. Instr. & Meth. A 587 (2008) 46-51.

USE OF AN ECR ION SOURCE FOR MASS SPECTROMETRY

D. Button and M.A.C. Hotchkis
ANSTO, PMB 1, Menai, NSW 2234, Australia.

Abstract

At ANSTO we have developed an Electron Cyclotron Resonance (ECR) ion source to investigate new concepts for mass spectrometers designed to measure isotopic ratios of elements such as carbon, nitrogen and oxygen. The low pressure ECR plasma presents particular challenges when used for mass spectrometry. The elements we are interested in measuring are typically present as residual gas in vacuum systems and hence we need to achieve ultra-high vacuum throughout our system. Also ECR plasmas generate highly reactive species of these elements which can then bond to internal surfaces. A number of measures have been taken to combat these difficulties. We have shortened the plasma bottle length to minimise the surface area. In making this change we have also discovered that the useful plasma volume is much less than expected. Originally the source was designed with a mirror ratio of around 2.1. With the restricted bottle size, our effective mirror ratio is 1.8 and yet the performance of the source is unaffected. This and other design modifications will be discussed.

INTRODUCTION

At ANSTO we are developing an Isotopic Ratio Mass Spectrometer (IRMS) system utilising an Electron Cyclotron Residence Ion Source (ECRIS) [1]. The ECRIS properties have two main advantages over traditional systems based on electron impact ionization. Firstly the ionization efficiency which can be 2 orders of magnitude greater than electron impact ionization at converting the sample to an ion beam for measurement. Secondly the process of creating charge states greater than 1+ breaks up molecules which cause molecular interferences in mass spectrometry of the single charge state. For this reason our IRMS system typically makes measurements of 2+ charge state ions, and thus the name adopted for our system is the IRMS++.

Initial testing of the system has verified the ability of our ECRIS to generate 2+ and greater charge states free of molecular interference at a sample efficiency >10%. Other characteristics that are not desirable for the operation of a mass spectrometer have also been discovered. This has included high backgrounds, high levels of background beams and retention of the sample in the ion source (ion source memory effect). We describe below methods used to minimise these effects and modifications that have been made to the ion source to reduce them, while avoiding any negative impact on the performance of the ECRIS.

EXPERIMENTAL ARRANGEMENT

The configuration of the IRMS++ instrument developed at ANSTO is shown in Figure 1, including an electrostatic analyser which has been installed since the work shop report ref[1]. The system incorporates an in house developed cost effective ECR ion source to produce low to medium charge state ions. The source is described briefly below; a more detailed description of it can be found in a recent paper [2].

Microwave power to the ECR ion source is provided by a 100 watt microwave amplifier and oscillator, which is tuneable within 64 channels across a frequency range of 6.85 – 7.15GHz. The microwave generator is coupled to the ion source chamber via a wave guide. Normally the microwave generator is operates at 10-25W, and frequency of 7.115GHz.

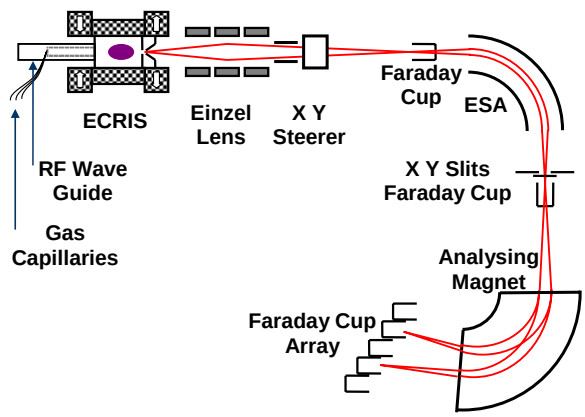

Figure 1: The configuration of the ANSTO IRMS++ instrument.

The magnet field is achieved by permanent magnets, consisting of 2 ring magnets to form the axial field, and a hexapole to from the radial field.

The plasma bottle is constructed from a 48mm ID closed end quartz tube, with the closed end transitioning to a 9mm OD tube as to deliver gas to the plasma chamber. The quartz plasma bottle is transparent to microwaves enabling the capping of the end, and provides electrical isolation to ground for the plasma electrode and the plasma itself. The support, and sample gases are delivered to the 9mm OD quartz tube via 3 polymer coated silica capillaries of different lengths and diameters, allowing delivery of gases from chambers at pressures ranging from 5 to 1000 Torr. These utilise the poor conductance to transition between laminar gas flow in the sample section, to molecular flow of the Ultra High

Vacuum (UHV) ion source without fractionating the sample.

The plasma electrode has a 2.5mm diameter aperture, and was constructed from stainless steal which was later electroplated with gold to ensure an inert surface. Efficient utilisation of the sample gas is enhanced by an aluminium foil seal between the circumference of the plasma electrode and the quartz wall of the plasma bottle. Post extraction the system incorporates an einzel lens, followed by X and Y steerers. Beams are energy-analysed with the electrostatic analyser and separated according to their mass to charge ratio in the analysing magnet. Multiple beams can be measured simultaneously by the Faraday Cup array.

The UHV system is oil free, and consists of 2 150 l/sec turbo molecular pumps (both have 2 greased bearings) backed by a 14m^3/h 5 stage roots blower pump, which itself backed by a 2 stage diaphragm pump. The first Turbo pump is located on the einzel lens chamber directly after the source, and the second on the electrostatic analyser chamber. A 60l/sec triode ion pump is located on the Faraday cup array chamber. This configuration allows use to regularly achieve base pressures $<4\times10^{-6}$ Pa.

HIGH BACKGROUNDS AND CONTAMINATION

As the IRMS++ system is intended for the measurement of isotopic ratios of oxygen, carbon, and nitrogen in substances such as water carbon-dioxide, nitrogen gas, etc. it is imperative that the residual sources of these species be minimized in the system. In our earlier paper [2], we showed results where low backgrounds were achieved, with total contamination beams at around 0.2% of the total beam. However, this level proved to be very hard to achieve on a routine basis. Figure 2 show a typical mass spectrum captured from 5N (99.999%) purity helium. The spectrum indicates oxygen, hydrogen, and carbon peaks of the order of hundreds of nanoamps, compared to just over 10μA of helium beam. The relatively low level of nitrogen beams shows that air leaks are not a major factor in this instance. Possible sources of the contamination include water vapour, oxygen, hydrocarbons, hydrogen and carbon from stainless steel, and others. Possible processes leading to the release of contaminants include outgassing, permeation, diffusion through capillaries, desorption, and others. While some of these effects relate simply to the technicalities of vacuum practice, there are also significant effects peculiar to the use of a plasma. The plasma may both cause deposition on the walls and strip and recycle materials from the chamber walls. Such effects are well known in a number of areas of technology (see for example, ref [3]). However, the ECR ion source is an unusual environment and our requirements are particularly stringent.

Surface deposits and the cleaning process for the ion source bottle

The background was firstly considered to originate from residual contaminants from the cleaning of the quartz ion source bottle.

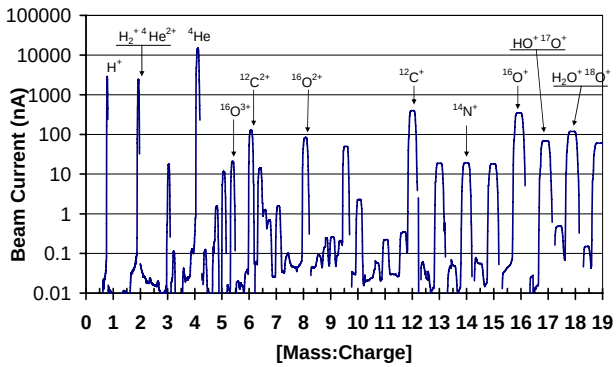

Figure 2: Above is a typical mass spectrum generated from running helium support gas.

In one attempt to remove oxide layers from the internal surfaces of the plasma chamber, cyclohexane (C_6H_{12}) vapour was introduced into the plasma. However, perhaps not surprisingly, this led to undesirable and persistent residual carbon beams. The source was opened to clean it. Figure 3(a) shows the pattern of contamination on the plasma bottle, including obvious carbon deposits. The pattern, while quite familiar to ECR ion source users, demonstrates how the plasma has a strong cleaning effect in the principal electron loss zones, but leaves deposition areas just adjacent to this zone. We believe this evidence provides an important clue as to the deposition/desorption processes occurring in the chamber with all types of sample gases.

It is also worth noting our cleaning procedure for the quartz bottle.

Hydrofluoric acid etching was our original preferred method of cleaning. However, preferential etching at imperfections in the surface of the quartz leaves an undesirably roughened surface finish. Internally, this can increase the surface area for deposition. Externally, the roughening can make it more difficult to achieve a vacuum seal at the ends

As a result of the surface finish from the etching, the procedure was changed to the following 4 step process.

1. Visible deposits are abrasive removed from bottle inner surface.
2. Bottle is cleaned in Aqua regia *(1:3 nitric acid to hydrochloric acid)* then rinsed with high purity water.
3. The bottle is ultrasonic cleaning in ethanol.
4. Finally the bottle is vacuum baked at 150°C.

The Aqua regia was selected as it dissolves gold and rhodium which could be sputtered from the plasma electrode, as well as other metals. However, some kinds of deposits, eg carbon, are not removed effectively by this method leaving a surface staining.

(a)

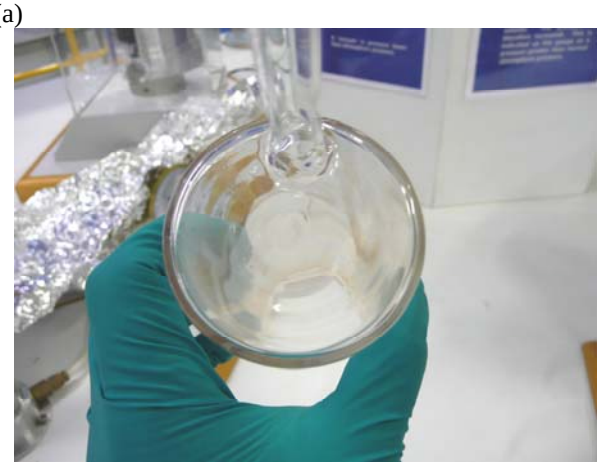

(b)

Figure 3: Image (a) shows the residual surface contamination within the plasma bottle after running Cyclohexane (C_6H_{12}) vapour. Image (b) shows the bottle after atmospheric baking at 1000°C for 2 hours.

Carbon 14 sample preparation for accelerator mass spectrometry requires extremely clean glassware during the chemistry preparation process as to minimise the introduction of modern carbon. At ANSTO this is achieved in the final stage by baking the glassware in a furnace to burn off any carbon residue. For this reason a similar process was introduce as the final step in the ion source bottle cleaning process. This was the baking of the plasma bottle at 1000°C in an atmospheric furnace for 2 hours. Figure 3 (b) shows the plasma bottle after this baking has been preformed. This visually restored the surface to a pristine condition, and gave a visually cleaner surface than the previous methods. This was also evident in the reduction in the conditioning time to achieve base background levels.

Sources of oxygen contamination

As initial intended of the instrument is for the measurement of oxygen ratios we focused on the sources of oxygen in the system via various processes. Table 1 lists the processes of oxygen contribution that were investigated as background sources. Out of those listed in the table 1, the sources that were found to have a significant contribution are discussed below.

Table 1

	Possible Source of Oxygen Contamination	**Effect**
1	Oxygen or water vapour contamination in the helium carrier gas.	Significant
2	Oxygen or water vapour contaminant diffusing in through capillaries from sample chambers.	Negligible to None
3	Outgassing of stainless steel fittings at UHV end of capillaries.	Negligible to None
4	Outgassing of ferrules used to seal capillaries.	Significant
5	Outgassing or permeation of elastometer (FKM 'Viton') seal used to join stainless steel fittings to quartz inlet tube on the plasma chamber.	Significant
6	Sputtering of oxygen from quartz surface inside vacuum chamber	Negligible to None
7	Oxygen, water, or oxide layer on the inside of the plasma chamber. This layer is probably created by the action of the plasma, and is only released through the action of the plasma.	Very Significant
8	Diffusion of oxygen or water vapour from residual gas in vacuum in the beam extraction region into the plasma chamber.	Negligible to None

Oxygen or water vapour contamination in the helium carrier gas. The gas flow from the 99.999% helium cylinder was passed through a high surface area stainless steel vacuum bellows, submerged in liquid nitrogen before entering the sample system. This would freeze out any water vapour, carbon dioxide, and possibility liquefy O_2 also. The result was a significant decrease in the overall contamination level. As a result of these finding, a new manifold system for the cylinder gases is under construction, and incorporates Alltech All-Pure gas specific filtering columns [4] for helium and hydrogen, as used in gas chromatography, to remove CO, CO_2, O_2, H_2O, and sulphur compounds to <1ppb..

Outgassing of ferrules used to seal the capillaries. The heating of the original Vespel [5] ferrules showed a constant out gassing level suggesting a permeation or leak due to the applied heat. Retightening of the ferrule made no impact on this rate. An alternative all metal sealing product for capillaries namely Siltite [5] ferrules were installed in place of the Vespel. Baking of these fittings showed a distinctive outgassing cycle with no sign of an ongoing leak, or permeation.

Outgassing or permeation of elastometer (FKM 'Viton') seal used to join stainless steel fittings to quartz inlet tube on the plasma chamber. This was assessed by baking the fitting to 180°C. It was found that the o-ring of the Swagelok Ultratorr 3/8" fitting would show a standard bake-out curve, which after 24h would have an improved performance. Although after the baking over a week the contamination would show signs of increase. If re-baked the o-ring would again show signs of out gassing demonstrating a standard out gas curve with quite a high initial outgas rate. It was considered that the o-ring was absorbing water from the lab air, and permeating it through to the vacuum side. To verify this process the system was run logging $^{16}O^{2+}$ currents and the o-ring fitting was wet with water. Figure 4 shows the logged data and the rate at which the oxygen levels increased. To prevent this process the stainless steel fitting was modified and adhered to the quartz with Torr Seal [6] epoxy. This gave an improved performance over the elastometer seal and can also be baked to 120°C. After initial baking of the Torr Seal bond and fitting, the vacuum base pressure doesn't respond again to later heating.

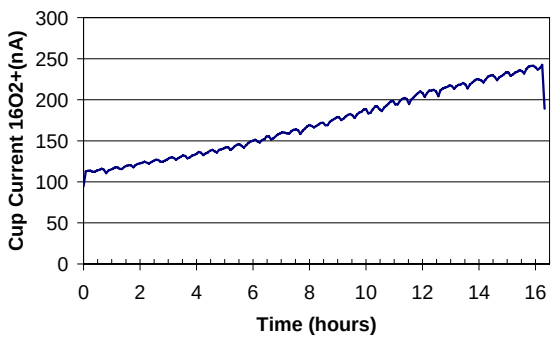

Figure 4: This chart show the increasing $^{16}O^{2+}$ background over 16 hours due to the wetting of the FKM 'Viton' o-ring of the Ultratorr fitting. The fitting couples the quartz gas delivery tube of the ion source bottle to stainless steel fittings which interfaces the capillaries from the sample from the sample chamber.

Oxygen, water, or oxide layers on the inside of the plasma chamber. Such layers are probably created by the action of the plasma, and are only released through the action of the plasma. To establish that these layers are generated by the plasma, the ion source was run continuously with helium to burn out contaminants to normal background levels. As the magnet array on the ECR ion source is mounted on liner bearings, the location of the ECR zone and associated loss zones of the ion source are able to be moved relative to the plasma chamber. Utilising this ability the magnet array was moved 5-10mm after achieving base background levels, the source showed an immediate increase in contamination levels. Leaving the array in the offset position, the source was once again left to burn out the contaminants to background levels. The array was relocated to the original position once again, with the background contamination levels once again immediately elevating. As the contaminants may tend to deposit out around the plasma bottle as like those shown in figure 3(a), it was considered that an in situ surface cleaning process was required.

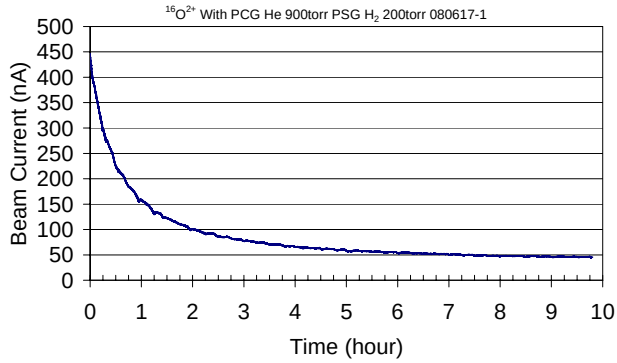

(a)

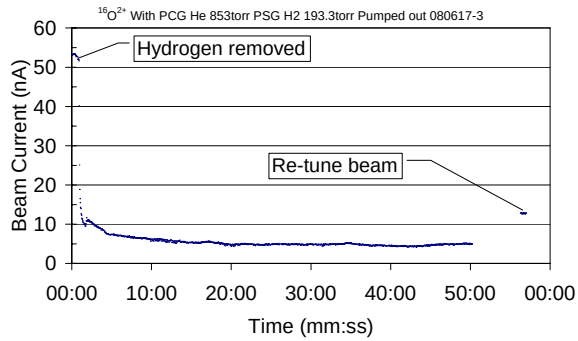

(b)

Figure 5: Chart (a) shows the reduction in the $^{16}O^{2+}$ beam over a period of 10 hours after the introduction of hydrogen into the ion source. Chart (b) shows the reduction in the $^{16}O^{2+}$ over 1 hour after the removal of the hydrogen.

Hydrogen gas was chosen for this purpose, as it may be expected that hydrogen atoms or ions can bonds with contaminants mobilising them as gasses molecules. Once liberated from the surface the contaminant can re-enter the plasma or be pumped away. Figure 5(a) shows the decay of the $^{16}O^{2+}$ beam after the introduction of hydrogen in addition to the helium in the ion source. Figure 5(b) shows the $^{16}O^{2+}$ beam after the hydrogen was removed from the sample system, which further reduces the level of $^{16}O^{2+}$ in the beam. Note after an hour the beam optics were retuned to show the true $^{16}O^{2+}$ level. The drop in the $^{16}O^{2+}$ beam after the removal of the hydrogen further demonstrates the dependence of the hydrogen at liberating the contaminant. There is clearly a very considerable reduction to the oxygen surface contamination of the plasma bottle. Although this was not the first time that hydrogen had been run in the ion source, the effectiveness for cleaning was not noticeable

until the before mentioned background reduction modifications had been made.
Figure 6 shows the resulting spectrum against the original spectrum after the above modifications and cleaning processes.

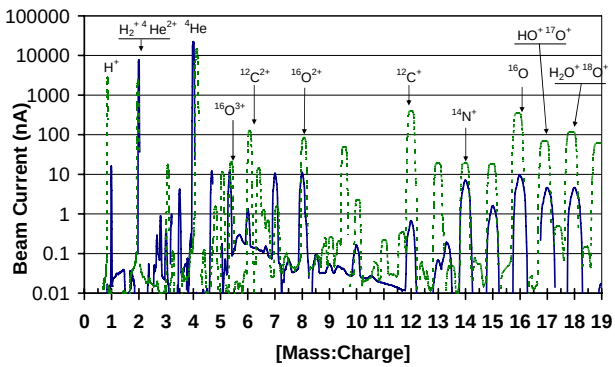

Figure 6: This chart show the background after the modifications, and cleaning of the system.

ION SOURCE RETENTION

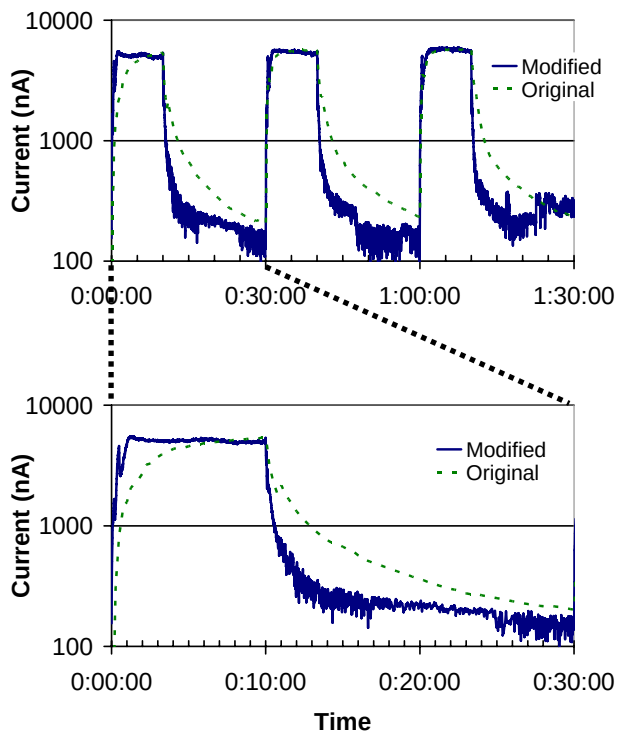

Figure 7: The chart shows the original, and modified ions source rise and delay characteristics of $^{14}N^{2+}$ beam over 3 cycles of nitrogen gas introduced for 10 minutes, then pumped away for 20 minutes.

Initial testing of the instrument indicated that there was a significant rise and decay time during the introduction and removal of sample gases [2]. This can be seen in Figure 7, demonstrating this effect within a $^{14}N^{2+}$ beam. It was also found that the instrument vacuum, as measured in the flight tube after the einzel lens, also reflected the same rise and decay characteristic over the same period. It was considered that the capillary lines after transferring the gas to the ion source from the sample section, can act as a storage volume that releases slowly due to the low conductance of the capillary. Varying the length of the capillaries thus their volume, had no impact on the rise and decay rates of the beam.

Dummy runs of the sample pulses into the source, with the microwave unit turned off thus plasma extinguished, showed that the vacuum of the system responded at a much faster rate, coming to equilibrium within 10 seconds of introduction and removal of sample gases. It was also found that when the source was ignited after the dummy run, that there was no residual background in the ion source due to the recently introduced sample gas.
During both the rise and decay portion of a sample cycle, the RF source was turned off to allow the vacuum level to reach the peak and base values before restarting the RF. When the plasma was reignited, in both cases the vacuum and beam currents returned to the previous point in the rise and decay cycle. This indicated that the sample gas is stored and removed form the source by the action of the plasma.

Operation of the source with inert gases showed a much faster rise and decay cycle taking 10s of seconds to peak and reduce to background as opposed to the 10s of minutes for the reactive gases. For this reason it was thought that there maybe a reactivity problem with the walls of the plasma chamber. To change the plasma chamber wall reactivity, the plasma bottles inner cylinder surface was gold plated by evaporation. The result of this coating did not have a significant effect on the rise and decay period.

An axial sample gas delivery tube was installed in the ion source to try and deliver the gases to the rear edge of the ECR zone. This was to maximise likelihood of the first interaction of the sample gas to be ionization as opposed to molecular interaction with the surfaces of the plasma chamber. This did not show any benefit to the rise and decay rate, but did show that we were able to place a surface beyond the B_{max} point of the axial field towards the ECR zone without degrading the operation of the ion source.

As the retention process appeared to be an effect that takes place between the plasma chamber surface and the plasma, it was consider that reducing the available surfaces in the ion source chamber could reduce the effect. Figure 3(a) also shows that there is a cleaning effect from bombardment of the inner quartz surfaces at the loss zones, this can be seen as the transparent area surrounded by the carbon residue, this feature is also found on the plasma facing electrode. Thus an increase in the ratio of area interacting with the lose zones, to those inactive areas outside of them is desirable.

To achieve a reduced inactive surface area in the ion source, the plasma facing electrode was moved toward the ECR zone within the hexapole between the resonance field of 0.25T and the B_{max} of 0.456T, residing at 0.390T.

The length of the plasma bottle was also reduced so that the back of the plasma bottle finished at the geometric symmetrical location to the hexapole with an axial field strength of 0.425T. These modifications can be seen in figure 8, which shows the relative source component locations to the axial field strength.

This modification didn't inhibit the operation of the source, but effectively altered the mirror ratio (B_{max} / B_{min} on the axis) at the inlet and extraction ends of the ion source. The extraction end reduced from 2.10 to 1.81, and the inlet end reduced from 2.4 to 1.98. As a larger mirror ratio is conventionally considered to facilitate the generation of higher charge state ions, it was of importance to verify the effect of this modification on the charge state distribution performance.

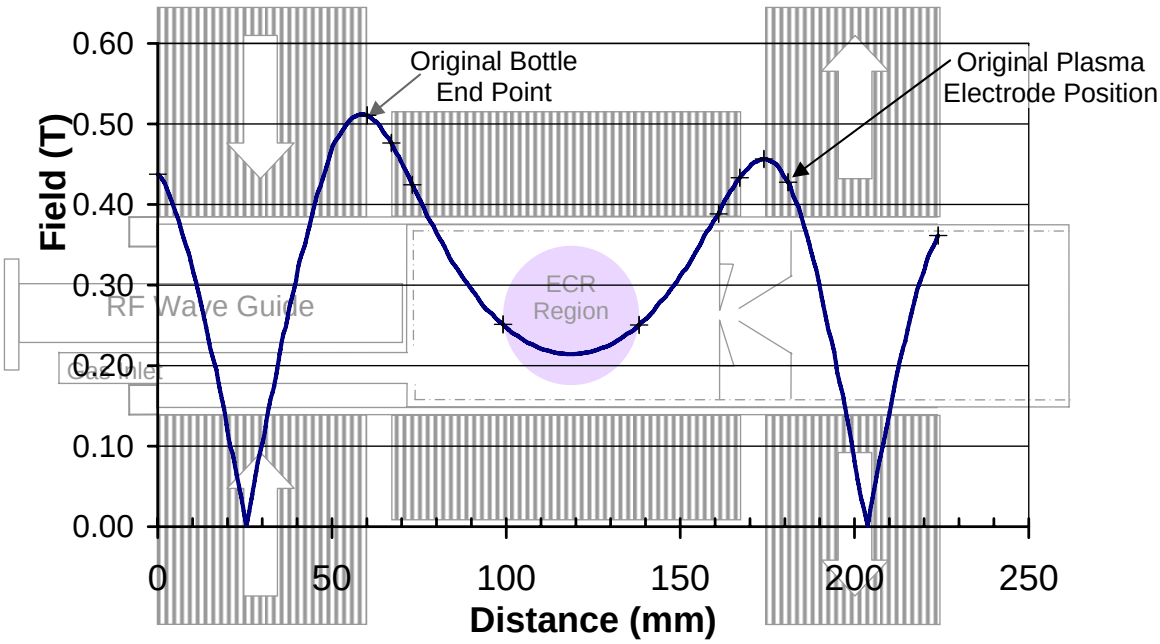

Figure 8: The above is a plot of the axial field of the ECR magnet array. The relative positions of the various elements of our ion source are can be seen with respect to the field structure. Note that the plasma facing electrode, and end of the quartz plasma bottle are located on the ECR zone side of their respective B_{max}.

Figure 9 shows the charge state distributions of the nitrogen ion charge states for both helium supported, and pure nitrogen for both the original source geometry, and modified geometry. The chart shows that there is little effect on the distribution, and no degrading of the 2+ charge state which is utilised for the measurement of oxygen isotopic ratios.

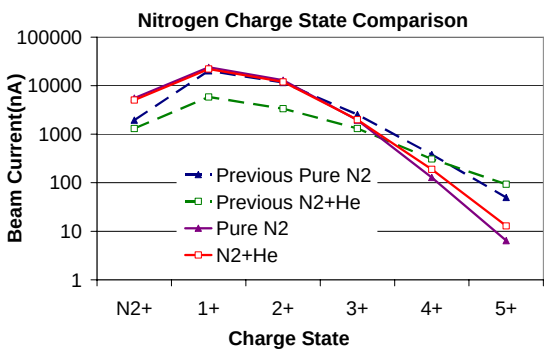

Figure 9: Plot shows the beam current of each of the charge states of nitrogen produced by the ion source with the original geometry, and the compacted geometry.

REFERENCES

[1] M.A.C. Hotchkis, D. Button, C.L. Waring, Rapid Comm. Mass Spectrom. 22 (2008) 1408.
[2] M.A.C. Hotchkis, Buckley D, Button D. Rev. Sci. Instrum. 79 (2008) 02A304.
[3] K. S. A. Butcher, Afifuddin, P. P.-T. Chen, and T. L. Tansley, phys. stat. sol. (c) 0 (2002) 156.
[4] Supplied by http://www.discoverysciences.com
[5] Supplied by SGE http://www.sge.com/
[6] Supplied by Varian http://www.varianinc.com

BEAM-PROFILE/-EMITTANCE MEASUREMENTS AT THE FRANKFURT ECRIS

K. E. Stiebing, S. Enz, Th. Kruppi,
Institut für Kernphysik der Johann Wolfgang Goethe-Universität, Frankfurt am Main,
Max-von-Laue-Straße 1, 60438 Frankfurt am Main.

Abstract

The off -line analysis of the Frankfurt Emittance and Profile Monitor (FProM) has been improved to allow better (direct) access to the calibrated profile and emittance representations. With the new system profile and emittance scans can be performed and directly interpreted at measuring times of 2-3min per full scan. With this significantly improved working performance a series of measurements has been carried out, where we have pursued the issue of beam filamentation in the extraction region of the 14GHZ Frankfurt ECRIS. The new program development will be presented together with results from the measurements.

.

INTRODUCTION

The determination of the beam parameters distinctly beyond the mere measurement of extracted beam currents has become an important issue for the development of new ion sources. In particular the development of newest generation ECRIS sources with their extremely high magnetic fields, extending far into the extraction area, have to be based on detailed measurements not only the beam emittance but also of the lateral beam profile, in order to carefully tailor the beam transport system. We have upgraded the “Frankfurt online scanning system”, which initially was developed as a simple and easy to install monitor to control position and integrated lateral profiles of the beam from the Frankfurt 14Ghz ECRIS. This system had already been turned into an emittance / and profile monitor by adding an automated moving-slit system [1]. For a better usability of this system, an offline data-analysis system has been supplemented, which allows direct access to the normalized and calibrated beam profiles and emittance distributions. For the determination of Twiss parameters a converter allows the use of the EAS code [2] for further processing of the measured data.

THE FProM-SYSTEM

A detailed description of the scanner hardware is given in Ref. 1. The idea behind the scanning system is to shadow the current, measured in a (in principle in any) Faraday cup in the beam line by moving a trapezoidal Aluminium screen, mounted on a wheel which rotates around the Faraday cup. In this way the primitive function of the beam profile is measured in two orthogonal directions. Derivation of these two profiles delivers the lateral density distributions of the beam profile (x/y-profiles). A typical online screen of FProM is displayed in Fig. 1. In the left upper corner the original profile (primitive function) is displayed, whereas in the bottom windows the derivatives of the two slopes (rising and falling) are plotted, allowing the online control of form and position of the beam in the two orthogonal scanning directions. The panels in the upper right of the screen are controls for the stepping motors of altogether 3 moving slit systems, which can be added to the hardware in order to transform the scanner into a high resolution profile and emittance monitor. In this way up to 3 systems can be controlled by the online program.

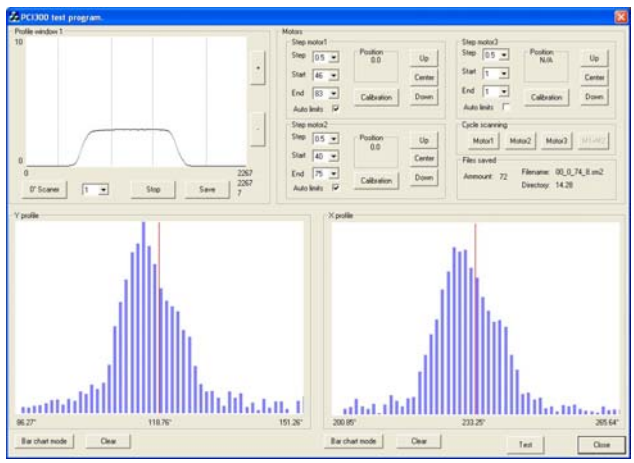

Figure 1: on line scree of the Franfurt Profile and Emittance Monitor (FProM)

Altogether three such systems have been installed in Frankfurt now, two in the ECRIS beam line (one at 0°; one at the injection into the RFQ). The third system has been installed in the injection line to the new Frankfurt Low Energy Storage Ring (FLSR) in order to match the injected beam to the ring acceptance. All systems are equipped with at least one slit system, the ECRIS 0° beam monitor has two slit systems allowing to measure emittances in both lateral directions (x-x´ and y-y´). Additionally, by controlling the joint movement of such a pair of orthogonal slits, the 4-dimensional information (x,x´,y, y´) can be measured like in a “pepper pot” measurement. Since the two orthogonal directions are scanned by only one rotating shadow, the scanning edges of the shadow have to be oriented at 45° to the axis of rotation. This implies that a mounting of the system e.g. into a spare port opposite to the mounting flange of the Faraday cup, which normally is mounted in a way that it is aligned to the accelerator based x or y direction, results

in a scanning frame of reference which is rotated relative to the accelerator-fixed system by 45°. This can easily be compensated by mounting the diagnose box (with Faraday cup and Scanner) under 45° degrees relative to the accelerator frame of reference (see Fig. 2 of the FProM-system in the FLSR-injection line).

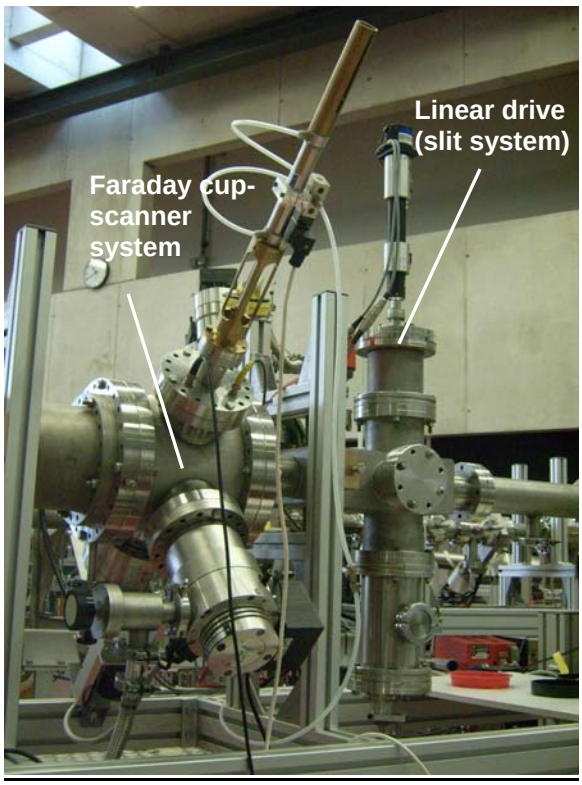

Figure 2: One of three systems installed at the IKF accelerator centre (Injection line to the Frankfurt low energy storage ring FLSR)

DATA PROCESSING AT FProM

The principle of an FProM emittance measurement is essentially a slit-grid measurement, however, in contrast to a slit-grid system, where the grid's zero position is usually moved together with the slit, in FProM the scanning system is fixed and the measured emittance profiles are rotated by 45° relative to the x´/y´= 0 axis. Additionally it may be skewed due to the constructive details of the respective scanner. Hence the interpretation of online data is aggravated and a further processing of the data is necessary. In order to keep the speed and universality of the online processing, this analysis in done in an offline program, containing all calibration parameters and constructive details of the scanner. This is not really a drawback since the program scans with a speed of 1Hz (data taking, online display and data storage).

It is an advantage of FProM that it always performs two scans in orthogonal direction. Therefore any profile scan perpendicular to the slit (emittance) is supplemented by a profile scan along the slit (high-resolution scan of the lateral density distribution). In Fig. 3 a screen of the offline analysis system for a very wide (divergent) beam in the 0° Faraday cup of the ECRIS beam line is displayed. This system calibrates and displays the online data in the accelerator based coordinate system (Profile, lower left screen) and in the normal emittance representation (lower right screen). The vertical lines on the profile are regions shadowed by the wires from the electron suppression grid (see the description in Ref 1). These are wires of 1mm thickness with 6 mm spacing. Due to the limited length of the active slit motor drive, only a total length of 35mm could be scanned, resulting in a range on the x and y axes of 49mm, not sufficient to show the full beam. The emittance profile is truncate as well but clearly points to a divergent beam.

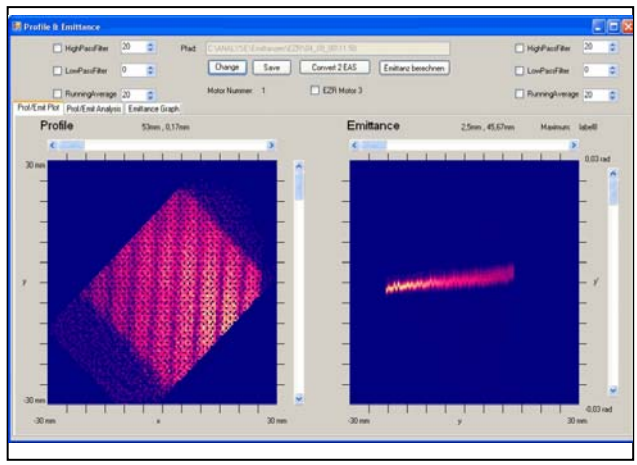

Figure 3: screen of the offline program for FProM

In order to suppress noise and to cut spurious signals, different filters in the offline program (upper part of the panel) allow modification of the data. Finally the data can be stored in a format directly compatible with the input of the emittance analysis software EAS [2] for further processing (e.g. determination of the Twiss parameters).

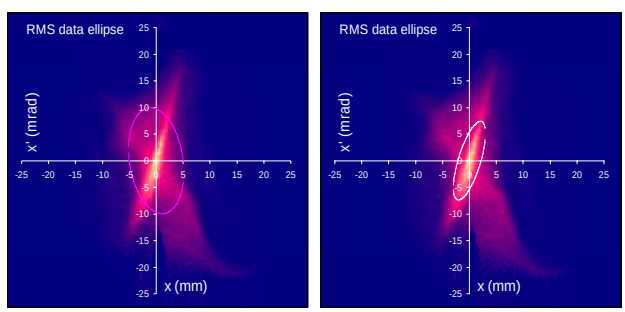

Figure 4: RMS emittance of a profile measured at the 0°-Faraday cup using EAS. **left picture:** no filters applied**; right picture:** a data-filter ellipse(EAS) was used to discard the aberrations.

An example of the data analysis with EAS is displayed in Fig. 4 for a measurement of the ECRIS -0° beam where substantial aberrations are present. The 85% area emittance (15%cut off level) determines to 392 mm mrad (EAS) and 287 mm mrad (offline program) respectively

MEASUREMENTS AT THE ECRIS

One motivation to upgrade the scanner system was to investigate the obvious losses of beam in the low energy bam transport system (LEBT) of the Frankfurt ECRIS. If the beam is well focussed onto the Faraday cup directly after the analysing magnet only a very small fraction of this beam could be detected in the next Faraday cup (3m downstream at the entrance of the RFQ post accelerator. On the other hand if focussing was optimized on the second Faraday cup, substantially larger beam currents could be measured there the same intensity was measured in FC90-1 also. One explanation of this unexpected behaviour could be the extraction of filament beams as a consequence e.g. of the radial magnetic confinement by means of the hexapole field inside the source. In fig. 5 a preliminary result of a scan at the 90° beam line scanner is displayed. The source was optimized for the production of Ar 8+ the beam transport was optimized in FC90-2. Clearly two centres can be isolated in the 90° profile as well as in the emittance distribution (upper panel of fig.5). The distributions measured for the same beam tuning in the 0°beam line show a well focussed beam without inner structures (no voltage was applied to the 0°-Quadrupole triplet for this particular tuning).

It is obvious that in particular the unfavourable positioning of the 0° scanner does not allow really deciding on this question. It is a long standing plan to redesign the LEBT of the Frankfurt ECRIS installation. Before doing so, it was meaningful to have the full performance of the FProM systems available. In particular, the position of the 0° scanner will be shifted upstream, to allow mounting of a new 0°-electrostatic quadrupol triplet with larger aperture (100mm) downstream from the Scanner (the presently used system has an aperture of 60mm and is installed between slit- and scanner system. It has to be switched off for FProM scans).

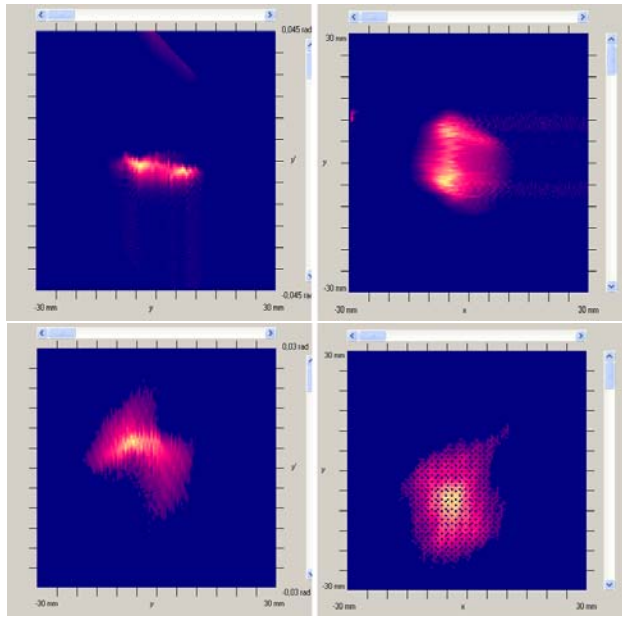

Figure 5: Ar^{8+} optimized in the Faraday cup of the 90°-ECRIS FProM); **upper panel:** emittance scan (left) and Profile scan (right) in the 90°-FProM; **lower panel:** emittance scan (left) and Profile scan (right) of the identical beam tuning in the 0°-beam scanner

The 90° degree scanner will be equipped with a larger-area Faraday cup to allow a wider scanning area. After upgrade the system is ready for systematic measurements of beam parameters as a function of different source tunings and manipulations.

REFERENCES

[1] K. E. Stiebing, M. S. Kaiser, J. D. Meyer, L. Schmidt, H.Schmidt-Böcking, O.Strekalovskij, V. Alexandrov, A. Kayukov, M. Koryevkina, G. Shirkov
Rev. Sci. Instrum., Vol. 75, No. 5, May 2004;

[2] Emittance Analysis System (EAS), Accelerator PhysicsGroup Codes Spallation Neutron Source (SNS) ; <www.sns.gov/APGroup/Codes/Codes.htm >

CONCEPTUAL DESIGN OF A SPUTTER-TYPE NEGATIVE ION SOURCE BASED ON ELECTRON CYCLOTRON RESONANCE PLASMA HEATING

O. Tarvainen and S. Kurennoy, Los Alamos National Laboratory, Los Alamos, NM 87545, U.S.A.

Abstract

A design for a negative ion source based on electron cyclotron resonance plasma heating and ionization by surface sputtering is presented. The plasma chamber of the source is an rf-cavity designed for TE_{111} eigenmode at 2.45 GHz. The desired mode is excited with a loop antenna. The ionization process takes place on a cesiated surface of a biased converter electrode (cathode). The ion beam is further "self-extracted" through the plasma region. The magnetic field of the source is optimized for both, plasma generation by electron cyclotron resonance heating, and beam extraction. The source can be used for a production of a variety of negative ions ranging from hydrogen to heavy ions. The potential users for the source concept range from large scale accelerator facilities, utilizing H^- ion beams, to dc tandem accelerators for heavy ions. The benefits of the source concept compared to widely used filament- and inductively coupled rf-driven sputter-type sources are the lack of consumable parts and low neutral pressure minimizing the stripping losses of negative ions. In this article we will focus on the H^- production scenarios with the novel source. The benefits and drawbacks of higher frequency operations are also discussed.[*]

INTRODUCTION

The focus of the H^- ion source development program at Los Alamos Neutron Science Center (LANSCE) has recently been on improving the performance of the filament-driven surface conversion ion source (see for example ref. [1]) and developing an rf-driven surface conversion ion source operated with helicon wave mode [2]. The main problems associated with these ion sources are the presence of consumable parts and high neutral gas pressure causing stripping losses, respectively.

In this article we propose a design for a novel H^- ion source based on electron cyclotron resonance plasma heating and surface ionization. The source is expected to operate within a neutral gas pressure range of 0.1-1 mTorr i.e. order of magnitude lower than the helicon discharge [2]. This helps to mitigate the H^- losses due to collisions with neutrals and reduces the volume formation of H^- preventing undesired increase of emittance, sometimes observed with surface converter ion sources [1].

[*] Work supported by the US Department of Energy under contract DE-AC52-06NA25396

PHYSICS ASPECTS OF H^- ION BEAM PRODUCTION

Modern H^- ion sources are based on two important ion formation processes, the volume [3] and the surface [4] production. The relative importance of these processes depends on the detailed design of the ion source.

The volume production of H^- is generally accepted to be due to dissociative attachment (DA) of low energy electrons to rovibrationally (v'') excited molecules. Two electron populations are needed in order to optimize the volume production process: hot electrons (few eV) creating the excited molecular states i.e. $e_{hot} + H_2 \rightarrow e + H_2^{v''}$ $(v'' > 5)$ and cold electrons (less than 1 eV) responsible for dissociative attachment i.e. $e_{cold} + H_2^{v''}(v'' > 5) \rightarrow H + H^-$. Therefore, the ion sources based on this process are typically optimized by separating the plasma chamber in two parts by a filter (electrostatic or magnetic) decoupling the plasma heating zone from the H^- production zone (see for example ref. [5]).

The surface production mechanism in negative ion sources is so-called resonant tunneling ionization: the electron affinity level of a hydrogen atom adsorbed on a metal surface shifts and broadens. If the electron affinity level shifts below the Fermi energy of the (cesiated) metal surface, electrons have a finite probability to tunnel through the potential barrier forming an H^- ion when the surface is subjected to heavy ion (Cs) bombardment [7].

The work function of the surface affects the probability of the electron tunneling, which is the other beneficial effect of cesium i.e. Cs deposition lowers the work function. If the bias-voltage of the converter electrode is on the order of hundreds of volts (like in the case of LANSCE converter source) the sputtering of the metal becomes an important issue. This aspect favors the use of converter materials such as molybdenum and rhenium with low sputtering yields under proton bombardment.

In a converter-type ion source the H^- ions created on the cesiated surface have to propagate through the plasma in order to become extracted from the ion source. Three types of loss processes of H^- due to collisions with other particles within the propagated distance need to be considered:

(1) $H^- + e \rightarrow H + 2e$: The H^- mean free path can be calculated from the electron mean free path by taking into account the average velocities (energies) of the particles, $\lambda_{H^-} = \sqrt{\frac{m_e E_{H^-}}{m_{H^-} E_e}} \lambda_e$. This equation was used for estimating the H^- losses due to collisions with electrons for the proposed ion source design.

(2) $H^- + H_2 \rightarrow H^0$ (it is assumed that the neutral hydrogen is in molecular form): A typical neutral gas pressure in an ECR-heated plasma (at 2.45 GHz) is 0.1-1 mTorr. Based on cross section data from ref. [8] it can be calculated that the H^- losses in this pressure range are less than 10% within a propagated distance of < 10 cm.

(3) $H^- + Cs^0 \rightarrow H^0$*:* The calculation for H^- losses in collisions with neutral cesium atoms (based on the reported cross section [9]) for an H^- energy of 300 eV suggests that if the neutral pressure of cesium exceeds 0.7 mTorr the loss rate of H^- due to collisions with neutral cesium atoms exceeds the loss rate due to collisions with neutral hydrogen molecules at pressure of about 1 mTorr (of H_2). The cesium vapor pressure in the surface converter ion sources is typically much less than 0.7 mTorr.

Therefore, it is plausible to claim that collisions between H^- and neutral H_2 is the dominant loss mechanism. Reducing the neutral gas pressure in the ion source plasma chamber (compared to existing converter sources) is the most efficient way to increase the extracted H^- beam current. In fact, the ability to reduce the neutral gas pressure (from 5-10 mTorr which is typical for the LANSCE helicon source producing 12 -13 mA of H^- [10]) is the greatest motivation for the novel source design.

Due to the negative bias of the converter electrode the H^- beam is formed in the plasma sheath adjacent to the converter surface and is "self-extracted" from the ion source. The beam is focused to the outlet aperture by shaping the surface of the converter. The formation mechanism of the beam explains the relatively small emittance values typically obtained with a LANSCE-type surface conversion ion sources. The trajectories of the H^- ions are affected by the magnetic field in the region between the converter and the outlet aperture. The magnetic field of the ECR-driven ion source can be optimized for both plasma production and beam extraction.

CONCEPTUAL DESIGN OF THE SPUTTER-TYPE ECR SURFACE CONVERSION ION SOURCE

Negative ion sources (for H^-) based on ECR plasma heating have been designed and built earlier. The approach of Tuske *et. al* has been to separate the main plasma from the H^- production region by a filter magnetic field reducing the electron temperature and, consequently, mitigating stripping losses of negative ions near the outlet aperture. H^- ion beam currents on the order of 5 mA have been obtained with this type of an ion source relying on the volume production mechanism of H^- [5]. The main drawback of this approach is the drop of plasma density, imposed by the filter field, between the two stages of the ion source. This limitation can be overcome with a converter-type ion source. Takagi *et al.* have designed and tested an ECR-driven plasma sputter ion source equipped with a converter electrode [11]. In that source design the converter electrode was used also as an antenna coupling the microwave power with the plasma. Negative ion beam currents of 7 mA were obtained with that source. However, the extracted ion beam contained almost 30 % of impurities (O^- and OH^-) due to required microwave power level (3-4 kW) and subsequent heating of vacuum seals. In order to understand the origin of these problems and to avoid them we used MicroWave Studio [12] to simulate the mode structure excited into the plasma chamber. According to our simulations it seems likely that the plasma chamber of the source described in reference [11] is in fact a multimode cavity. In addition, the resonant frequencies closest to 2.45 GHz deposit significant amounts of energy at the microwave window, which could explain the observed heating of vacuum seals near this location. In order to optimize the ionization process we designed (with MicroWave Studio, MWS eigensolver) the plasma chamber to be a single-mode resonant cavity for TE_{111} eigenmode at 2.45 GHz, which should significantly improve the coupling efficiency of the microwaves compared to the source by Takagi. Variation of this design is used at CERN (ISOLDE) for ionization of noble gas radioisotopes (positive ions) [13].

A schematic drawing of the new ion source is presented in Figure 1. Details such as vacuum seals and water cooling channels or subsystems such as cesium oven are not presented.

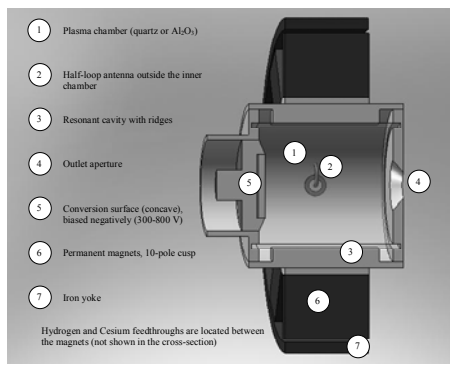

Figure 1. A schematic of the proposed ECR-driven surface conversion ion source.

The plasma chamber of the source is a quartz tube (or aluminum nitride tube for high power, high duty factor operation) located inside a resonant cavity. The quartz tube prevents the plasma to be directly in contact with the antenna and allows the main plasma volume and the remaining cavity volume to be in different vacuum conditions. Two metal ridges with gaps near the end walls are inserted 180 degrees apart on the inner wall of the cavity to allow the magnetic field of the TE_{111} eigenmode at 2.45 GHz, corresponding to a frequency of a cheap commercial magnetron, to complete its loop and to separate it from the unwanted modes, including TM_{010}. The cavity dimensions can be listed as follows: Cavity inner radius 45 mm, cavity length 80 mm, quartz-tube outer radius 37.5 mm, quartz-tube wall thickness, 3.175

mm, ridge width 20 mm, ridge height 7.5 mm, and ridge-end-wall gap length 8 mm.

The desired eigenmode can be exited with a simple loop antenna inserted in the cavity mid-plane, with the loop plane oriented vertically, and connected to a 50-Ω coaxial cable. The magnetic field of the mode is well coupled to the antenna. Figure 2 shows the electric and magnetic fields of the TE_{111} eigenmode excited in the cavity. The presented field normalization is the MWS default, i.e. the field total energy is 1J, which means that the presented values do not correspond to the cavity fields of the operating source.

The effects of the end wall (outlet and biased converter electrode) holes, gaps and shapes were also studied and taken into account in the preliminary design. It was observed that these features had a small effect on the resonant frequency. Also plasma loading of the cavity will slightly affect the resonant frequency. Effects of both kinds can be compensated by tuning the cavity length by moving the converter electrode acting as a tuner.

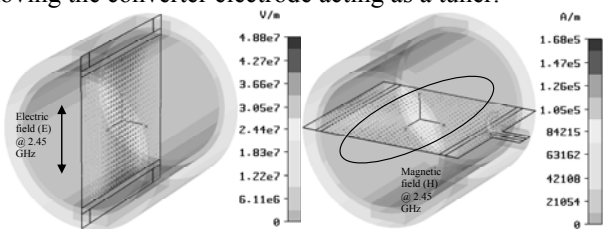

Figure 2. Electric field (left) and magnetic field (right) of the TE111 eigenmode (at 2.45 GHz) excited in the cavity of the proposed ECR-driven surface conversion ion source.

For 2.45 GHz the corresponding resonance magnetic field is 0.0875 T (875 G). The required magnetic field can be generated either with solenoids or permanent magnets. Magnetic field design based on permanent magnets is favorable for two reasons: it makes the source more compact and helps to maximize the extraction efficiency of the H^- ions. In our design ten rows of permanent magnets (NdFeB, grade 50 MGO, 1 inch by 1.5 inch cross section, and length of 2 inches) are placed around the cavity forming a typical 10 pole cusp structure. The resulting resonance surface (B = 0.875 T) is illustrated in Figure 3. The magnetization direction of the permanent magnets is indicated by arrows. The spatial location of the resonance can be varied by moving the magnets in radial direction.

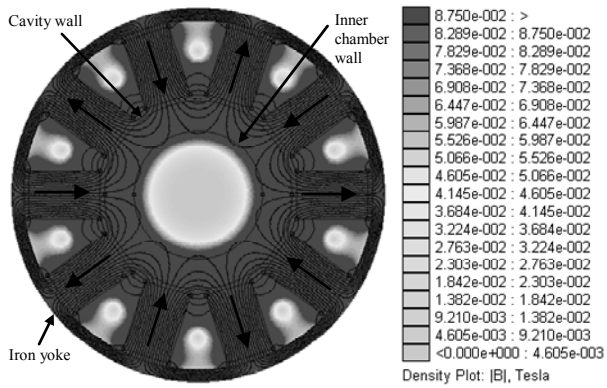

Figure 3. The cusp magnetic field and corresponding resonance surface of the proposed ECR-driven surface conversion ion source. Simulation with FEMM [14].

The magnetic field on the source axis is zero, which is favorable for the beam extraction and for attaining a more uniform plasma density due to $F = -\mu \nabla B$ force "pushing" the electrons (and ions) towards the center of the plasma chamber (cusp confinement). The extraction efficiency was studied with an ion tracking code written with Mathematica. The magnetic field for the ion tracking was simulated with Radia3D [15]. The calculated beam spot at the outlet electrode is presented in Figure 4. The parameters used in this example of ion tracking calculation are: distance from the converter to the outlet 90 mm, converter voltage -500 V, converter radius of curvature 127 mm (concave), converter radius 19 mm. The geometry of the magnetic field is reflected into the shape of the beam spot i.e. number of cusps on the beam spot is half of the number of magnetic poles. Reducing the number of magnetic poles makes the extraction of the H^- more problematic due to increasing magnetic field near the source axis. However, the maximum number of poles that can be used is 10 since for higher number of poles the resonance surface is outside the quartz chamber.

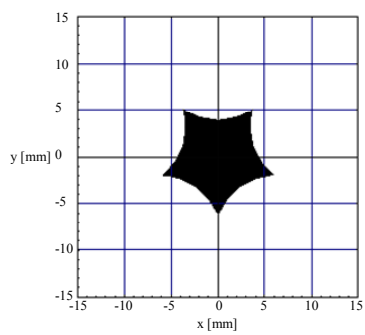

Figure 4. The results of the ion tracking calculation. The "star" represents the predicted beam spot at the outlet aperture.

The energy of the electrons in an ECR heated plasma depends on the neutral gas pressure, microwave frequency and applied power. The electron energy can be reduced by increasing the neutral gas pressure. However, it is desirable for the H^- source application to keep the

pressure under 1 mTorr, which not only minimizes the losses due to collisions with neutral particles but also helps to minimize the volume production of H^-. The electron energy distribution is typically a double Maxwellian. It can be expected that the temperature of the dominant electron population is in the order of few eV. The cross section for H^- losses due to collisions with electrons peaks at about 10-20 eV reaching a maximum value of $3 \cdot 10^{-15} cm^2$. However, the converter electrode voltage can be raised in order to increase the H^- velocity and therefore reduce the losses in collisions with electrons.

The drawback of the design is modest electron confinement, which means that in order to achieve plasma densities on the order of 10^{12} cm^{-3}, relatively high microwave power, on the order of kilowatts, needs to be applied to operate the source in overdense mode.

The deposition of cesium and sputtered material (from the converter) on the quartz tube can have an adverse effect on the coupling of the microwave power with the plasma. This can be mitigated by choosing the right converter material. Rhenium seems to be favorable due to low sputtering yield and high skin depth (compared to other metals). In the worst case if the metal deposition on the quartz tube presents a problem, the tube can be omitted. In this case the antenna needs to be covered by an insulator preventing a direct contact with the plasma. Furthermore the antenna-insulator assembly needs to be shielded from metal deposition. This can be realized with a metal (or dielectric) shield. It is important to isolate the metal shield from the cavity wall in order to prevent the formation of a surface current loop canceling the magnetic field in the antenna region and therefore preventing the coupling of the microwave power to the plasma.

Based on the experience gained with both the LANSCE filament- and helicon-driven surface conversion ion sources we can estimate the expected H^- output for the microwave-driven source presented in this article. Taking into account differences in plasma density, electron temperature and beam dynamics (propagation through the plasma) *we estimate that the H^- ion beam current extracted from the microwave source can be 25-30 mA*. The emittance of the ion beam is mainly defined on the converter surface (sputtering energy of the ions) and, therefore, it can be expected that the emittance of the H^- ion beams extracted from the ECR-driven surface conversion ion source does not differ significantly from the emittance of the LANSCE filament-source (typically 0.15-0.25π mmmrad, 95 % norm.-rms). The expected duty factor of the ECR-driven source is at least 12 %.

Based on the conceptual design and the afore-mentioned estimations we are planning to start construction of the Negative ECRIS (NECRIS) at LANSCE. The goal of the program is to support the ongoing development efforts with the filament- and helicon-driven ion sources and eventually develop a reliable ion source for future missions of LANSCE.

DISCUSSION

The source design presented in this paper can be used for producing other negative ions as well. The converter can be transformed into a cathode manufactured from a material to be ionized. The heavy ion induced sputtering of the cesiated surface will result into emission of negative ions (as in a typical sputter-type ion source based on cesium ionization on hot surfaces). For this purpose the source could be operated in continuous mode. In addition the source concept could be used for the production of intense proton ion beams.

The cusp-ECRIS design could be operated at higher frequency in order to reach higher plasma densities at lower neutral gas pressures. However, the magnetic field design needs to be revisited for this purpose. Using a Halbach-array (with an opening for a coax-input for the antenna) is probably desired if higher frequency operations are pursued. The drawback of using higher frequencies is increased production of X-rays, which requires heavy shielding.

REFERENCES

[1] J. Sherman et al., Proceedings of the 10th International Symposium on Production and Neutralization of Negative Ions and Beams, AIP Conference Proceedings, 763, (2005), p. 254.
[2] O. Tarvainen, G. Rouleau, R. Keller, E. Geros, J. Stelzer and J. Ferris, Rev. Sci. Instrum. 79, 02A501, (2008).
[3] M. Bacal, E. Nicolopoulou and H.J. Doucet, Proc. Symp. on the Production and Neutralization of Negative Hydrogen Ions and Beam (BNL, Upton, NY, USA), (1977), p. 26.
[4] Y.I. Belchenko, G.I. Dimov and V.G. Dudnikov, Nucl. Fusion 14, 113, (1974).
[5] O. Tuske *et al*., Proceedings of the 11th International Symposium on Production and Neutralization of Negative Ions and Beams. AIP Conference Proceedings, Volume 925, p. 114, (2007).
[6] M. Rasser, J.N.M. Wunnik and J. Los, Surf. Sci.,118, p 697, (1982).
[7] C.F.A. van Os and P.W. van Amersfoort, Appl. Phys. Lett. 50 (11), p. 662, (1987).
[8] H. Tawara, Y. Itikawa, Y. Itoh, T. Kato, H. Nishimura, S. Ohtani, H. Takagi, K. Takayanagi and M. Yoshino, Nagoya University Report No. IPPJ-AM-46, (1986).
[9] F.W. Meyer, J. Phys. B: Atom. Molec. Phys. 13, p. 3823, (1980).
[10] O. Tarvainen *et al.* to be published in the proceedings of 1st Intl Conference on Negative Ions, Beams and Sources, Aix-en-Provence (2008).
[11] A. Takagi and Y. Mori, Rev. Sci. Instrum., 71, (2000), p. 1042.
[12] Microwave Studio, v.2006B, CST GmbH, 2007. www.cst-world.com
[13] F. Wenander and J. Lettry, Rev. Sci. Instrum., 75, 5, p. 1627, (2004).
[14] D. Meeker, http://femm.foster-miller.net/
[15]http://www.esrf.eu/Accelerators/Groups/InsertionDevices/Software/Radia

STATUS OF NEW ELECTRON CYCLOTRON RESONANCE ION SOURCES AT ITHEMBA LABS

R. W. Thomae, P. J. Celliers, J. L. Conradie, J. L. G. Delsink, J. G. de Villiers, H. du Plessis, D.T. Fourie, M. Sakildien

iThemba LABS, P.O. Box 722, Somerset West 7130, South Africa USA

Abstract

iThemba Laboratory for Accelerator Based Sciences (iThemba LABS) is a multi-disciplinary accelerator facility. One of its main activities is the operation of a separated-sector cyclotron (SSC), which provides beams of various ion species at energies ranging from 5 to 220 MeV/amu. These beams are used for fundamental nuclear physics research in the intermediate energy region, radioisotope production and medical physics applications. During the last 16 years the heavy ion beams at iThemba LABS were produced in a 10 GHz Minimafios Electron Cyclotron Resonance Ion Source (ECRIS). In 2006 the decision was made that, due to the requirements of nuclear physics for new ion species and higher particle energies, a new 3rd generation ECRIS should be procured. Therefore a source, based on the design of the Grenoble Test Source (GTS), is under construction. It is a room temperature source that uses two microwave frequencies, 14.5 GHz and 18 GHz, to deliver highly-charged ions of sufficient intensity to be accelerated in the separated-sector cyclotron to energies in the GeV range. At the same time a 14.5 GHz ECRIS4 with its beam line elements that were designed and constructed by Grand Accelerator National d'Ions Lourds (GANIL) and originally built for the Hahn-Meitner-Institute (HMI) in Berlin was donated to iThemba LABS and has recently been installed. The status of the projects and future plans will be discussed.

INTRODUCTION

iThemba LABS is operated by the National Research Foundation (NRF) of South Africa. It provides accelerator and ancillary facilities for: research and training in the physical, biomedical and material sciences; treatment of cancer patients with energetic neutrons and protons and related research; production of radioisotopes and radiopharmaceuticals for use in nuclear medicine, industry and related research. At the heart of the iThemba LABS accelerator complex is the variable-energy, separated-sector cyclotron, which provides beams with a maximum energy of 200 MeV for protons. Beams are directed to vaults for the production of radioisotopes, proton and neutron therapy and nuclear physics experiments as shown in Fig. 1. Light ions, pre-accelerated in the first solid-pole injector cyclotron (SPC1) with a K-value of 8 are used for therapy and radioisotope production. For radioisotope production and neutron therapy a high-intensity 66 MeV proton beam is used, while a low-intensity 200 MeV beam is used for proton therapy. The second solid-pole injector cyclotron (SPC2) with a K-value of 10 is used for pre-acceleration of light and heavy ions as well as polarized protons from the two external sources shown in Fig. 2. With the 3:1 available RF frequency range and the different harmonic numbers that can be used, the particle energy of all three cyclotrons can be varied over a wide range for a large variety of ion species. Beams are delivered to the different user groups for 24 hours per day and seven days per week. The 66 MeV proton beam is available for radionuclide production and neutron therapy from Mondays until midday on Fridays. Patients are treated during daytime and between treatments the beam is switched to the radionuclide production vaults within seconds, and the intensity increased to 250 μA. During weekends a 200 MeV beam is used either for proton therapy or nuclear physics research using beams of light and heavy ions, as well as polarized protons [1, 2].

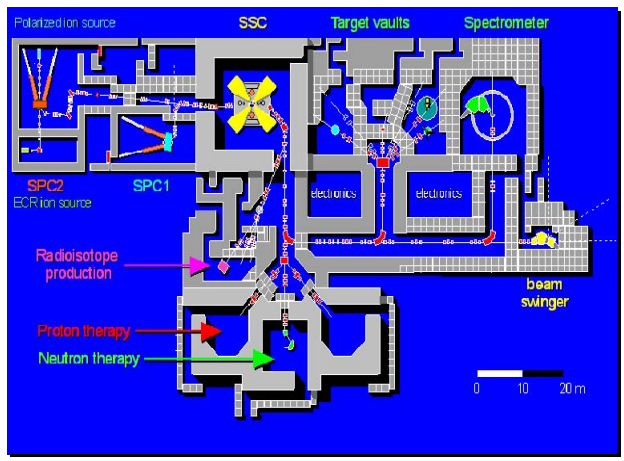

Figure 1: Layout of the accelerators at iThemba LABS.

ACCELERATORS AT ITHEMBA LABS

The Injector Cyclotron for Heavy Ions

The solid pole injector cyclotron SPC2 with a K-value of 10 has four radial magnet sectors and an extraction radius of 48.6 cm. Beams are accelerated with two 90º-dees operated at a maximum voltage of 60 kV. The RF-system can be tuned over the frequency range 8.6 MHz to 26 MHz with movable short-circuit plates in quarter-wave transmission lines. Harmonic numbers 2 and 6 are used. The beam is extracted with an electrostatic channel and two active and one passive magnetic channel. The ion sources are external and the beam is injected axially with three spiral inflectors corresponding to the three orbit geometries that are being used. At present heavy ions with mass numbers up to that of xenon are delivered by our

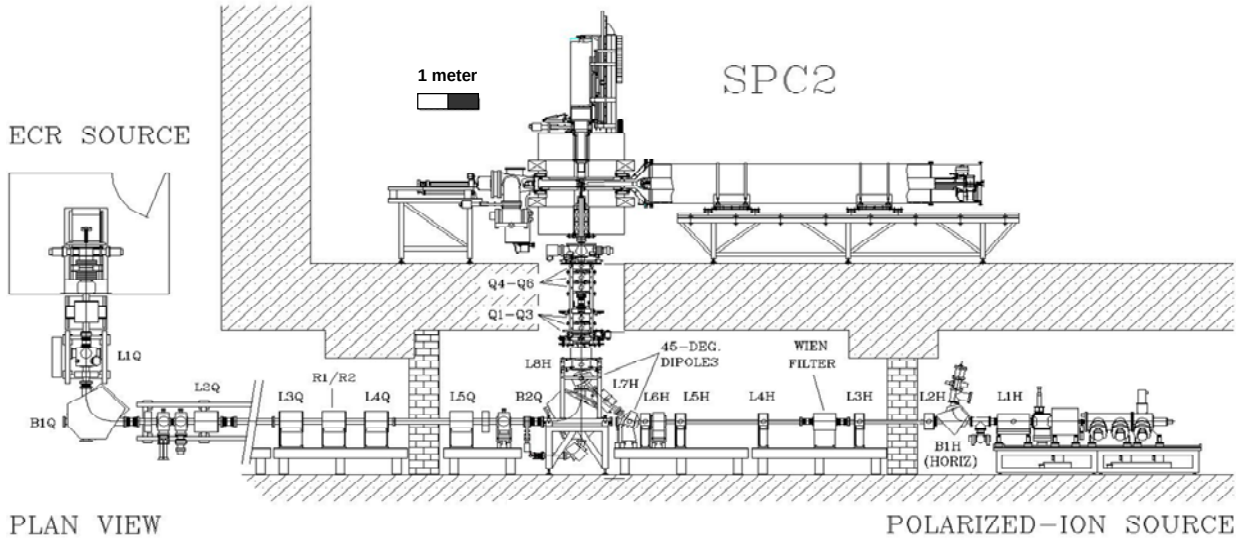

Figure 2: The beam lines that transport beams from the Minimafios and polarized proton ion source to the SPC2.

Minimafios ECRIS. Proton beams from an atomic beam polarized ion source are also accelerated with this injector cyclotron. Beams have been delivered since 1994 [3]. The position of the two sources and the beam lines towards SPC2 are shown in Fig. 2.

The Separated-Sector Cyclotron

The SSC has four separate magnet sectors with an overall diameter of 13 m with a sector angle of 34°. The RF-system consists of two vertical half-wave resonators that operate in the frequency range 7 MHz to 26 MHz. The maximum dee voltage is 220 kV at a power level of 80 kW per resonator [4]. The beam is inflected with two bending magnets and a magnetic inflection channel. Beam extraction is obtained with an electrostatic extraction channel and two septum magnets. A flat-topping system, operating at the third harmonic, has been installed in one of the valley vacuum chambers. Typically, the cyclotron delivers a 250 μA beam of 66 MeV protons for radioisotope production with 99.8% transmission through the machine.

The Minimafios Ion Source

A MINI Machine for Ion Stripping (Minimafios) Electron Cyclotron Resonance Ion Source (ECRIS) [5] was purchased in 1987 from the Centre d'Etudes Nucleaires (CEN) Saclay. This source operates at a RF frequency of 10 GHz with an RF power of up to 1 kW. Typical values for the injection and extraction coil currents are around 1000 A at 50 V to obtain a magnetic induction of approximately 0.8 T. The operating pressure varies for different ion species from 10^{-6} mbar to 10^{-5} mbar. Supporting gases like helium or oxygen are sometimes used. The extraction voltage applied to the source varies from 10 to 20 kV. For electron density enhancement a biased disc at -50 V is introduced to the injection side of the plasma chamber. Examples for beam currents in eμA (not necessarily optimized for intensity) obtained with the source are: up to 800 for H^+, 800 for He^{2+}, 18 for N^{5+}, 16 for O^{6+}, 40 for Ar^{8+}, 4 for Kr^{15+} and 3 for Xe^{22+}. Table 1 lists the beam energies for particle species which have been required by users and accelerated with the SSC, using the internal PIG (Penning or Philips Ion Gauge) source of SPC1 and the Minimafios ECR ion source of SPC2.

Table 1: Beams delivered at iThemba LABS.

Element	**Mass**	**Energy range (MeV)**	
		From	To
H	1	11.5	227
He	4	25	200
B	11	55	60
C	12	58	400
C	13	75	82
N	14	140	400
O	16	73	400
O	18	70	110
Ne	20	110	125
Ne	22	125	125
Al	27	150	349
Si	28	141	141
Cl	37	205	250
Ar	40	280	280
Zn	64	165	280
Kr	84	450	530
Kr	86	396	462
I	127	730	730
Xe	129	750	790
Xe	136	750	750

THE ECRIS4 SOURCE OF THE HAHN MEITNER INSTITUTE

This ECRIS4 with its beam line, shown in Fig. 3, that was originally built by GANIL for the Hahn Meitner Institute (HMI) [6, 7], was recently installed at iThemba LABS and linked up to the existing Q-line. This source consists of a water-cooled plasma chamber (length 18cm, diameter 7 cm) surrounded by FeNdB permanent magnets which produce a hexapole field of 1T (at the wall of the chamber) for radial plasma confinement. Two solenoid coils produce an axial field which confines the plasma axially. The field on the axis typically varies from 0.4 to 1.1 T. The microwave power is coupled into the source via a wave guide. The generator can deliver up to 2 kW of microwave power at a frequency of 14.5 GHz. The source is designed to operate with an oven and sputter target techniques, but was used in Berlin mainly for the beam production from noble gases, hydrogen and nitrogen. Typical values of intensities and charge states for argon are: 25, 6 and 3 eμA for Ar^{11+}, Ar^{13+}, and Ar^{14+} respectively. These values demonstrate the advantages of this source when compared with the existing ECR source at iThemba LABS. Not shown in the picture is the second diagnostic chamber which connects this beam line to the existing Q beam-line.

Figure 3: The Hahn-Meitner-Institute ECRIS4 source and the new beam-line, consisting of a solenoid, a diagnostic chamber and 90º-degree bending magnet.

Because of the different beam heights at iThemba LABS and the HMI a new support structure was designed and constructed. The source with its extraction system, the solenoid lens and the first diagnostic chamber are placed on it. The 90º bending magnet is mounted on a separate stand. The connection to the existing Q-beam line is done with the second diagnostic chamber and an Einzel lens which is positioned in the entrance of the bending magnet B1Q, shown in Fig. 2. The diagnostic chambers each contain horizontal and vertical pairs of slits and a Faraday cup. The ion source and all beam transport components are aligned, using an optical telescope system. The installation of the necessary infrastructure like water cooling, compressed air, and electrical connection is completed and the equipment is under vacuum. The additional AC power required to feed the power supplies is provided from a new transformer. First beam experiments are expected to take place in the beginning of 2009.

THE GTS ECRIS

The existing Minimafios will be replaced by this new modern room temperature source which is a replica of the CERN ion source that was built by the CEA in Grenoble [8, 9]. Various companies in Europe were involved in the construction of parts for the source. The source will be coupled to 14 GHz and 18 GHz microwave generators. Provision is made for two ovens. The axial field can be varied between 0.5 T and 1.2 T by means of three solenoid coils and the radial field has a value of 1.3 T using FeNdB permanent magnets. The source is expected to deliver a beam current of 60 eμA for Xe^{30+} ions. The coils, permanent magnets, all mechanical parts and the RF generators have been delivered.

The expected improvements in beam performance by means of the HMI [10] and GTS [11] sources in beam intensity, charge states and final particle energy (after acceleration with SPC2 and SSC) are listed in table 2 and compared with the experimental results obtained with the existing Minimafios for the examples of ^{40}Ar and ^{129}Xe.

Table 2: Expected beam currents, charge states and final particle energies for the HMI, GTS and Minimafios sources.

Ion Source	Element	Charge State	Beam Current eμA	Final Energy MeV
Minimafios	Ar	11	1	665
HMI	Ar	14	1.5	1078
GTS	Ar	17	4.2	1590
Minimafios	Xe	22	3.4	825
HMI	Xe	26	5	1153
GTS	Xe	37	5.4	2335

It is clear from the table that with the new sources, especially with respect to the achievable final energies, a new area of nuclear physics experiments at iThemba LABS will be possible.

NEW BEAM LINE LAYOUT

The two new sources are part of the infrastructure upgrade process at iThemba LABS. A schematic layout of how these sources will be connected to the injector cyclotron SPC2 via the existing Q-beam line is shown in Fig. 4. The beam extracted from the HMI ECRIS4 is focused with a solenoid of 0.2 m length and a maximum magnetic induction of 0.75 T into the position of a horizontal and vertical slit system in the front of the double focusing 90º bending magnet which has a rigidity of 0.1 Tm. The magnet focuses the beam at the second pair of slits in the second diagnostic chamber. The beam current can be measured before and behind the bending magnet. The beam then drifts to the entrance of the existing Q-line where it is focused by means of an

electrostatic Einzel lens. This reduces the beam envelope during the drift to the first solenoid of the Q line.

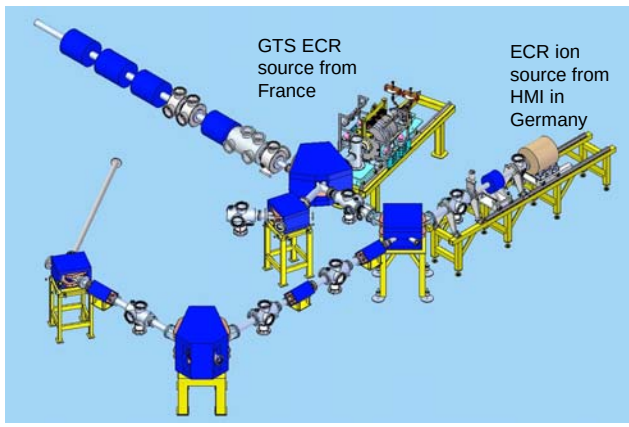

Figure 4: Low-energy beam lines connecting the two new ECR ion sources to SPC2.

The beam of the GTS ECRIS is focused by an Einzel lens and injected into the existing Q-line by a double focusing 104º bending magnet. This setup allows for simultaneous operation of both sources which is important for developing new ion beams from elements like lithium, vanadium, or calcium. When the GTS source is used to inject beam into SPC2 for nuclear physics experiments, the beam of the HMI source is stopped at the second Faraday cup before the 104º magnet. Alternatively, when the HMI source delivers beam the 104º magnet is switched off and the beam from the GTS source can be diagnosed in a diagnostic chamber after an additional 60º-bending magnet as shown in Fig. 4.

The beam line of the HMI source is insulated from ground potential and can be biased to a potential of -20 kV. This allows for experiments with very low energy ions as was demonstrated at the HMI for many years [12]. At a later date a similar beam line will be constructed. As shown in Fig. 4 this line will consist of two quadrupole magnets transporting the beam to a 90º-bending magnet, followed by another quadrupole magnet and a 60º bending magnet to focus the beam on the target. All components needed to build up this beam line are available.

ACKNOWLEDGEMENTS

We are deeply indebted to the management of the Hahn Meitner Institute, Berlin for transferring their ECR ion source, including the power supplies and other peripheral equipment, free of charge, to iThemba LABS, and are grateful to Dr A. Denker, Mr J. Bundesmann and Dr J. Röhrich of this institute, for their assistance in dismantling, packing and forwarding the equipment to South Africa.

REFERENCES

[1] J.L. Conradie, et al., “Cyclotrons at iThemba LABS”, Cyclotrons’04, Tokyo, October 2004, p. 105.

[2] J.L. Conradie et al., “Improvements to the iThemba LABS Cyclotron Facilities”, Cyclotrons’07, Catania, October 2007, p. 140.

[3] J. Cornell, et al., “Beam Lines for a 2nd Injector Cyclotron at NAC, Cyclotrons’92, Vancouver, July 1992, p. 621.

[4] Technical Report of the Accelerator Task Group, National Accelerator Centre, 1976, unpublished.

[5] R. Geller and B. Jacquot, Phys. Scr., T3, 1984, p. 19.

[6] P. Sortais, Nucl. Instr. and Meth. B98, 1995, p. 508.

[7] H. Waldmann and B. Martin, Nucl. Instr. and Meth. B98, 1995, p. 532.

[8] D. Hitz, et al., Nucl. Instr. and Meth. B205, 2003, p. 168.

[9] D. Hitz, et al., “A New Room Temperature ECR Ion Source for Accelerator facilities”, EPAC’02, Paris, June 2002, p. 1781.

[10] GANIL Report 88 07.

[11] D. Hitz et al., Production of Highly Charged Ions with the Grenoble Test ECR Ion Source, Proc. 10th Int. Conf. on Ion Sources, Dubna, September 2003, Rev. Sci. Inst., 75, 1403, 2004.

[12] 2005 Annual Report of the Hahn-Meitner-Institute, HMI-Report B 609, Berlin, 2006, p. 85.

PAPER NOT RECEIVED

MEASUREMENTS OF X-RAY SPECTRA ON ECR-II*

B. P. Cluggish#, I. N. Bogatu, L. Zhao, J.S. Kim, FAR-TECH, Inc., San Diego, CA 92121 USA.
R. C. Vondrasek, R.C. Pardo, R. H. Scott, ANL, Argonne, IL 60439

Abstract

FAR-TECH, Inc. has been developing an inexpensive and robust X-ray spectral diagnostic for monitoring electron cyclotron resonance ion sources (ECRIS). To this end, FAR-TECH, Inc. has recently performed extensive measurements of X-ray emission from the ECR-II device in the ATLAS facility at Argonne National Laboratory. We find that both the intensity and the shape of the observed spectra are highly correlated with the charge state distribution (CSD) of ions extracted from the ECR-II plasma as measured by a Faraday cup (FC).

INTRODUCTION

X-ray measurements provide much useful information about ECRIS plasmas. The intensity, width, and energy shift of the *K* and *L* lines provide information about the species present in the plasma and their charge states. The bremsstrahlung continuum provides information about the electron distribution function (EDF). The EDF determines both the ionization rates as well as the particle confinement time, thus determining the CSD. This information can be of great use in improving ECRIS modeling codes. In addition, X-ray measurements are non-invasive and can be made without taking the beam offline. However, many X-ray detectors, such as crystal spectrometers [1] or CCD cameras [2] are expensive (~$100K) and/or difficult to use and maintain. In addition, many detectors have limited energy range (< 20 keV) [2], which is insufficient for measuring the bremsstrahlung spectra, where photon energies can be over 100 keV. Therefore, FAR-TECH, Inc. has been developing an inexpensive, robust X-ray diagnostic tool for ECRIS plasmas.

EXPERIMENTAL SETUP

The X-ray measurements described here were performed using an Amptek XR-100T-CdTe detector [3]. The CdTe diode has a detection efficiency of over 20% from 2 to 200 keV and an energy resolution of 600 eV at 60 keV. The detector was controlled using an Amptek PX4 digital pulse processor. The detector and controller together cost only $10K.

The detector was installed on the ECR-II device [4] at the ATLAS facility at Argonne National Laboratory. The detector was installed inside the vacuum chamber through a side port so as to have a view across the plasma transverse to the axis of the device, as shown in Figure 1. The port is located at the midplane of the plasma, where the X-ray detector can view the plasma through apertures between the hexapole magnets. Considerable care was taken ensure that only X-rays generated by collisions in the plasma would be detected, and not X-rays generated by electron collisions with the walls of the device. Lead shielding and two, 2 mm thick, tungsten collimator plates separated by a tungsten spacer blocked all line-of-sight X-rays except those passing through the collimator holes. The holes in the collimator plates (100 μm and 200 μm) are small enough that the solid angle viewed by the detector passes through apertures on either side of the plasma chamber without intersecting it. Thus, only X-rays generated in the plasma pass through the collimator holes.

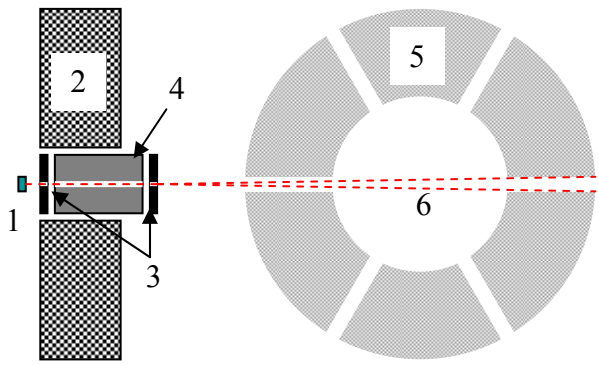

Figure 1: Experimental setup of the X-ray diagnostic. (Not to scale.) Device axis is perpendicular to the page. All components shown are in vacuum. (1) CdTe detector (2) Lead shielding (3) Collimator plates (4) Tungsten spacer (5) Plasma chamber (6) Viewing solid angle

The X-ray measurements presented here were performed on argon plasmas. Unless otherwise stated, the operating parameters were RF frequency ω_{RF} = 14 GHz, minimum magnetic field B_{min} = 3080 G, argon pressure p = 8 x 10^{-8} torr, and RF power P_{RF} = 300 W. The charge state distribution (CSD) of extracted ions was measured with an analyzing magnet and Faraday cup. The RF frequency at 14 GHz is resonant with the electron cyclotron motion at a magnetic field of B_{ECR} = 5000 G, so B_{min}/B_{ECR} = 0.62.

Typical acquisition times for X-ray spectra were 20 minutes for ~10^6 counts. Figure 2 shows a typical raw spectrum acquired on ECR-II. Characteristic K_α and K_β ($K_{\alpha/\beta}$) lines for different species visible to the detector are easily seen. Lead is in the shielding, tungsten is in the collimator, and CdTe is in the detector itself. The argon $K_{\alpha/\beta}$ line disappears if a different working gas is used, which shows that it comes from the plasma and is not an artifact of the detector.

Most of the X-ray counts come from the bremsstrahlung continuum. Our measurements showed a broad peak in the continuum around 120 keV, similar to

*This research was performed under a U.S. DOE SBIR grant and the Office of Nuclear Physics under contract # DE-AC02-06CH11357.
#cluggish@far-tech.com

that observed by other researchers [5,6]. It is unlikely that this broad peak is due to bremsstrahlung alone, since theory predicts that the bremsstrahlung spectrum should monotonically decrease with energy. Instead, we attribute this peak to X-rays that circumvent the lead and tungsten shielding by diffusing through the copper magnets and steel vacuum chamber by Compton scattering. Only X-rays with energies above 100 keV or so can do this; lower energy X-rays are absorbed, resulting in the observed broad peak.

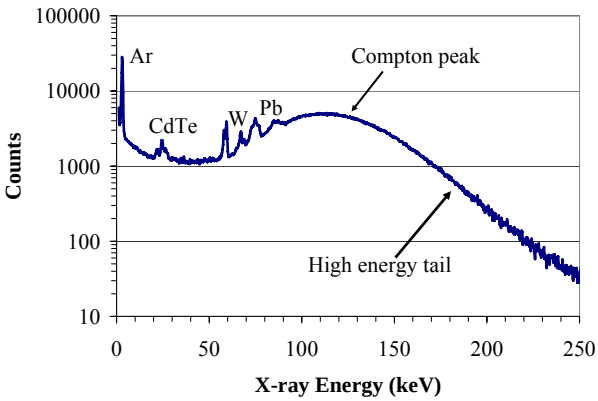

Figure 2: Typical X-ray spectrum, with $K_{\alpha/\beta}$ lines of lead (Pb), tungsten (W), argon (Ar) and CdTe labeled.

Multiplying the raw counts, $C(E)$, by X-ray energy E and dividing by the detection efficiency, $\eta(E)$ [7], and the acquisition time τ gives the X-ray power spectrum:

$$\frac{dP_{XR}}{dE} = \frac{C(E)}{\tau\eta(E)}E$$

The contamination of the spectra by the Compton scattering peak prevented us from determining the EDF from the bremsstrahlung spectrum. However, we can determine an effective temperature of the tail of the EDF, T_{eff}, by fitting a line to logarithm of the exponentially decreasing high energy tail of the power spectrum:

$$\frac{dP_{XR}}{dE} \sim \exp\left(-\frac{E}{T_{eff}}\right)$$

This effective temperature is a relative measurement of the distribution of high energy electrons, but not a direct measurement of the EDF. Another useful quantity is the total measured X-ray power, obtained by integrating the power spectrum over energy:

$$P_{XR} = \int \frac{dP_{XR}}{dE}dE$$

The range of integration can be the whole spectrum to give the total X-ray power or just over the width of a $K_{\alpha/\beta}$ line to give the power in that line.

EXPERIMENTAL RESULTS

The X-ray signal from the plasma was found to depend strongly on the plasma parameters, often more strongly than the CSD. In general, an increase in intensity or effective temperature was accompanied by a shift in the CSD towards higher charge states.

The dependence of X-ray intensity on the pressure of the argon working gas is shown in Figure 3. The plot shows that the intensity of the bremsstrahlung decreases with increasing argon pressure even as the intensity of the argon $K_{\alpha/\beta}$ line increases. This is probably because while increasing the argon pressure reduces the number of high energy electrons, there are still plenty of electrons left with sufficient energy (~3 keV) to ionize the K shell of argon.

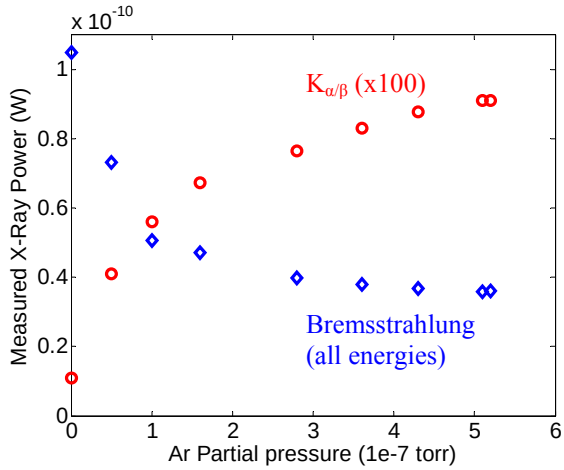

Figure 3: The measured X-ray power, P_{XR}, over all energies (diamonds) and in the argon $K_{\alpha/\beta}$ line (circles) vs. the argon pressure. The $K_{\alpha/\beta}$ data has been multiplied by 100. Note that at "zero" pressure there was still a small but non-zero argon flow.

We have also studied the effect of two-frequency heating on X-ray emission. In these experiments, RF power was supplied to ECR-II with two power supplies operating at two different frequencies, 14 GHz and 11.1 GHz, while maintaining a constant total power of 300 W. Figure 4 shows the measured total X-ray power and the effective temperature as a function of the fraction of 11.1 GHz power.

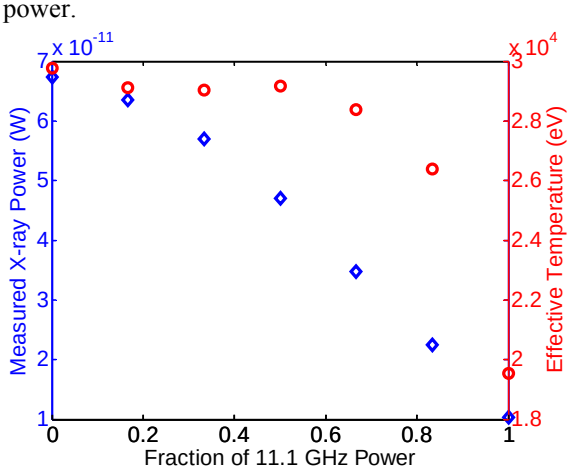

Figure 4: The measured X-ray power over all energies (diamonds) and the effective temperature (circles) vs. the fraction of 11.1 GHz power used.

The total X-ray power decreases by a factor of 7 as the fraction of 11.1 GHz power increases from 0% to 100%. The effective temperature also drops, but only after the 11.1 GHz fraction increases to more than 50%, and only from 30 keV to 20 keV. The corresponding CSDs are shown in Figure 5. A small amount (17%) of 11.1 GHz power pushes the CSD to higher charge states, but further increasing the fraction of lower frequency power causes the CSD to move towards lower charge states. For instance, the current of Ar^{14+} increases by factor of 1.6 as the fraction of 11.1 GHz power increases from 0% to 17%, but then drops by more than an order of magnitude as the fraction increases to 100%.

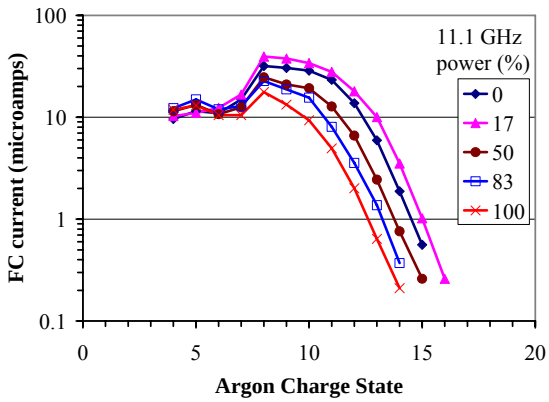

Figure 5: Current to Faraday cup as a function of charge state for different fractions of 11.1 GHz power in the two-frequency heating experiments.

The X-ray signal is also a strong function of the magnetic field strength. Figure 6 shows that both the effective temperature and the total X-ray power increase as the ratio of B_{min} to B_{ECR} increases.

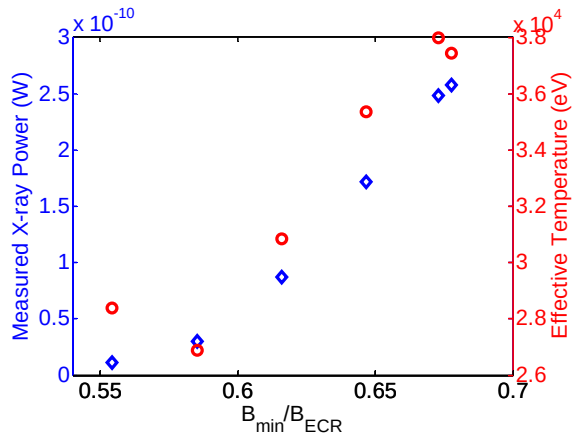

Figure 6: Measured total X-ray power and effective temperature vs. ratio of minimum field to resonance field.

In this experiment, the magnitude of the mirror field was changed while the profile was kept constant by changing the current in the injection and extraction solenoids while keeping the ratio of their currents constant. Since ECR-II has only two solenoid magnets, the ratio of the injection field, B_{inj}, to the extraction field, B_{ext}, and the minimum field, B_{min}, is kept constant. Only one RF power supply was used, at a constant RF frequency of 14 GHz, so that the ratio B_{min}/B_{ECR} is proportional to the strength of the mirror field.

Note the very strong dependence of the measured X-ray power on the strength of the mirror field – a factor of 20 increase for a 20% increase in field strength. The increase in X-ray emission is accompanied by a higher charge states in the CSD, as shown in Figure 7. A 20% increase in magnetic field strength increases the peak of the CSD from Ar^{+8} to Ar^{+10} and gives a factor of 10 increase in the current of Ar^{+14}.

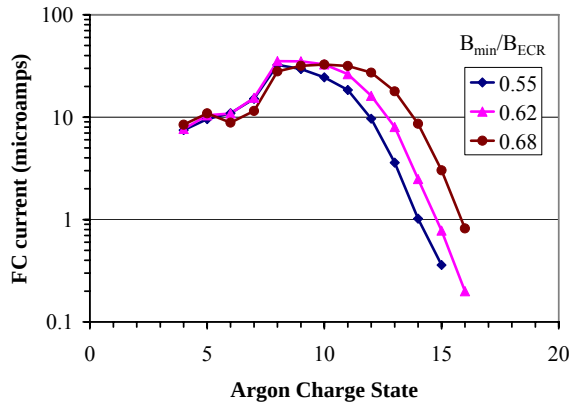

Figure 7: Current to Faraday cup as a function of charge state for different magnetic field strengths.

DISCUSSION

It is clear from the data presented here that much useful information can be obtained by measuring X-ray emission using an inexpensive and robust diode detector. In general, increases in both the intensity and the effective temperature of the X-ray signal tend to be correlated with higher charge states in the CSD. This makes sense, as the same factors that increase X-ray emission (increases in electron density and energy) also lead to higher ionization rates and confinement times.

Many of the experiments presented here have been performed by other researchers, but under different conditions. For instance, previous researchers [8] observed that the intensity of the krypton K_α line decreased with increasing krypton pressure, in apparent contradiction with our results. However, in that experiment the RF power (13 W) was much lower than ours and the gas pressure (>3.8 x 10^{-5} torr) was ~100 times higher. Certainly, the argon $K_{\alpha/\beta}$ line must disappear when the argon pressure goes to zero, as we observed in our experiments. However, we also observed that the intensity of the $K_{\alpha/\beta}$ line started to saturate at higher pressure, and it would not be inconsistent if further increases in the pressure resulted in a drop in the $K_{\alpha/\beta}$ intensity due to a decrease in the electron density and energy.

Increases in X-ray intensity, effective temperature, and charge state with changes in frequency and magnetic field have also been observed by other researchers [9,10], but

the effects are not as dramatic as those we observe. For instance, Figure 4 shows that when using 100% of 11.1 GHz heating then the measured total X-ray power was 1 x 10^{-11} W. At 11.1 GHz, the field strength ratio is B_{min}/B_{ECR} = 0.78. Extrapolating the data in Figure 6 indicates that for 14 GHz heating we would expect to measure around 5 x 10^{-10} W of X-ray power for 14 GHz heating at the same value of B_{min}/B_{ECR}. That is, our results indicate a factor of 50 increase in X-ray power for a factor of 1.26 increase in RF frequency at B_{min}/B_{ECR} = 0.78. This is a remarkable jump in X-ray power, given that theory [11] predicts only a factor of $(1.26)^2$ = 1.59 increase in the electron energy density for this change in RF frequency. In contrast, only a factor of 3 increase in X-ray power for a factor of 1.56 increase in RF frequency at B_{min}/B_{ECR} = 0.70 was reported in [10]. This may be related to the fact that ECR-II uses permanent hexapole magnets, while the data in [10] was obtained from an all superconducting device in which the mirror field and the hexapole field could be scaled together.

Finally, it is interesting to note that while we do observe some increase in the higher charge states, similar to other researchers [12], when employing two-frequency heating with a small amount (17%) of 11.1 GHZ heating, it is not accompanied by an increase in the X-ray power or effective temperature. To our knowledge, the effect of two-frequency heating on the X-ray spectrum has not been systematically investigated by other researchers.

REFERENCES

[1] G. Douysset, H. Khodja, A. Girard, and J. P. Briand, "Highly charged ion densities and ion confinement properties in an electron-cyclotron-resonance ion source," Physical Review E **61**, 3015 (2000)

[2] S. Biri, A. Valek, T. Suta, E. Takacs and Cs. Szabo, L. T. Hudson, B. Radics, J. Imrek, B. Juhasz, and J. Palinkas, "Imaging of ECR plasmas with a pinhole x-ray camera," Rev. Sci. Instrum. **75**, 1420 (2004)

[3] http://www.amptek.com/xr100cdt.html

[4] Schlapp, M. Vondrasek, R.C. Szczech, J. Billquist, P.J. Xie, Z.Q. Harkewicz, R. Pardo, R.C., "A new 14 GHz electron-cyclotron-resonance ion source (ECRIS) for the heavy ion accelerator facility ATLAS," Proc. 1997 Particle Accelerator Conf., 2702 (1997)

[5] L. Schachtera, S. Dobrescu, K. E. Stiebing and J. D. Meyer, "On the physics of metal–dielectric structures in ECR ion sources," Rev. Sci. Instrum. **75**, 1511 (2004)

[6] R. Baskaranb, T. S. Selvakumaran, G. Rodrigues, D. Kanjilal, and A. Roy, "Measurements and analysis of bremsstrahlung x-ray spectrum obtained in NANOGAN electron cyclotron resonance ion source," Rev. Sci. Instrum. **79**, 02A324 (2008)

[7] http://www.amptek.com/anczt1.html

[8] P. Grubling, J. Hollandt, and G. Ulm, "Performance of the new monomode 10 GHz ECR radiation source ELISA," Nuclear Instruments and Methods in Physics Research A **437**, 152 (1999)

[9] T. Nakagawa, Y. Higurashi, M. Kidera, T. Aihara, M. Kase et al., "Effect of magnetic field configuration on the beam intensity from electron cyclotron resonance ion source and RIKEN superconducting electron cyclotron resonance ion source," Rev. Sci. Instrum. **77**, 03A304 (2006)

[10] D. Leitner, J. Y. Benitez, C. M. Lyneis, D. S. Todd, T. Ropponen, J. Ropponen, H. Koivisto, and S. Gammino, "Measurement of the high energy component of the x-ray spectra in the VENUS electron cyclotron resonance ion source," Rev. Sci. Instrum. 79, 033302 (2008)

[11] A Girard, D Hitz, G Melin, and K Serebrennikov, "Electron cyclotron resonance plasmas and electron cyclotron resonance ion sources: Physics and technology," Rev. Sci. Instrum. **75**, 1381 (2004)

[12] R. C. Vondrasek, R. Scott, R. C. Pardo, "ECRIS Operation With Multiple Frequencies," Rev. Sci. Instrum. **77**, 03A337 (2006)

HIGH ENERGY COMPONENT OF X-RAY SPECTRA IN ECR ION SOURCES

J.Y. Benitez[1*], J.D. Noland[1], D. Leitner[1], C. Lyneis[1], D.S. Todd[1], and J. Verboncoeur[2]
[1]One Cyclotron Road, LBNL, Berkeley, CA 94720, U.S.A.

[2]Department of Nuclear Engineering, UCB, 4155 Etcheverry Hall, Berkeley, CA 94720, U.S.A.

[*] Corresponding author: jybenitez@lbl.gov

Abstract

The 88-Inch Cyclotron at LBNL is home to three powerful ECR ion sources, which operate at a range of heating frequencies from 6.4 GHz for the ECR to a combination of 18GHz and 28GHz for the VENUS superconducting ECR. Over the last few years we have investigated the production of x-rays from ECR ion sources with the goal of improving the understanding of the electron energy distribution within these sources. By measuring the spectral temperatures (defined as the reciprocal of the slope of the semi-logarithmic plot of the x-ray energy spectra) and using them as relative indicators of the electron temperatures, different plasma conditions and tuning parameters can be evaluated. A comparison of the axial x-ray spectra measured with the 6.4GHz ECR ion source to spectra obtained using the 18 and 28GHz VENUS source at equivalent power densities is presented. In addition, the paper discusses the experimental setup and analysis of the x-ray measurements. In particular, we discuss how to remove artifacts from the energy spectra resulting from the interaction of x-rays with the detector in order to accurately represent the x-rays emitted from the source.

INTRODUCTION

Lawrence Berkeley National Lab (LBNL) has three electron cyclotron resonance ion sources (ECRIS): LBNL-ECR, AECR-U, and VENUS, which operate at frequencies of 6.4GHz, 10 & 14GHz, and 18 & 28 GHz, respectively. This wide range of operating frequencies presents a unique opportunity to examine how various plasma parameters scale with frequency.

Several interactions lead to the emission of bremsstrahlung by electrons, in the form of x-rays. For example, electrons colliding with ions and electrons which are lost from the plasma and collide with the plasma chamber wall radiate x-rays due to their sudden deceleration. Studying the radiated x-ray spectra is a step towards our ultimate goal of determining the electron energy distribution function (EEDF).

The difficulty preventing one from making direct conclusions of the EEDF from an x-ray spectrum is that the detected spectrum does not directly reflect the energy of the electrons in the plasma and the spectra emitted by such a distribution. The detected spectrum is a result of many parameters. For example, the detector, a thallium-activated sodium iodine (Na(Tl)) scintillator, reacts differently to photons depending on their energy and the dimensions of the scintillator itself. Correcting the detected spectra so that they more accurately represent the emitted spectra is crucial in our attempt to characterize the plasma electrons. In addition the bremsstrahlung coming from the walls must be separated from the bremsstrahlung coming from the electron-ion collisions inside the plasma, since we want to measure the EEDF of the confined plasma and not the EEDF of the electrons lost to the walls. Therefore, specific collimation of the emitted x-rays is necessary in order to minimize the amount of wall bremsstrahlung visible to the detector.

The data presented in this paper include bremsstrahlung measurements from the VENUS ion source when using 18GHz and 28GHz heating and bremsstrahlung measurements from the LBNL-ECR ion source using 6.4GHz heating, both emitted axially and observed through the extraction aperture. The emitted x-rays are collimated and then detected with a NaI(Tl) scintillator. The specific collimation, which controls the region visible to the detector, and its significance, is discussed as well as the response of the NaI(Tl) detector to the x-rays and the correction applied. Finally, a preliminary comparison is made between the LBNL-ECR and VENUS bremsstrahlung emitted at equivalent plasma power densities and similar collimation geometries.

EXPERIMENTAL SETUP

Collimation and Detector

The experimental setup and collimation geometry for both VENUS and LBNL-ECR spectra were designed to minimize background radiation from other sources such as the nearby AECR-U. Despite the effort to shield the detector from the AECR-U's x-rays, background measurements showed that the background was minimized but not completely eliminated. Figure 1 shows the significance of the background for LBNL-ECR spectra at low power, at which the x-ray intensity is relatively low in comparison. Note, in particular, for a spectrum taken at a low power of 115W, as shown, the counts are only a factor of ~2 greater than the background.

ECR

The experimental setup of the LBNL-ECR and NaI detector is shown in Figure 2. The collimation consists of

two copper blocks and one Heavymet (95% W and 5% Cu) block. Copper was chosen despite lower density than lead because the 0.100 m copper block effectively absorbs x-rays below 1 MeV.

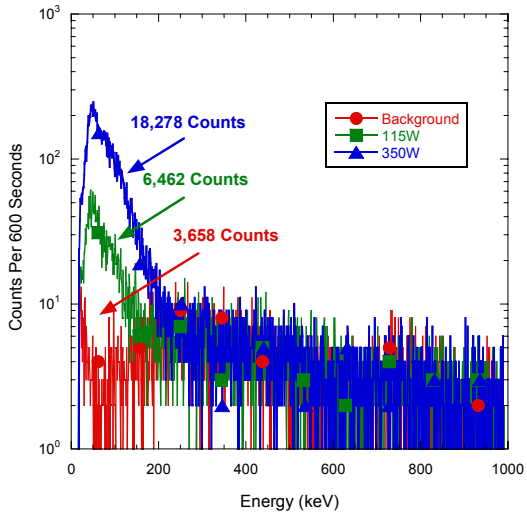

Figure 1. The background x-ray spectrum is high compared to the ECR spectra at low power.

Furthermore copper does not have absorption edges in the range of energies we are interested in. This decreases the probability of characteristic x-rays, produced by photoelectric absorption in the copper, from entering the detector. The first collimator, a copper block, is located inside of the bending magnet vacuum chamber, 2.75m after the extraction aperture. It is 100mm long and has a 10mm square aperture. The purpose of this first collimator is to lower the number of x-rays that can enter the remaining three collimators at large angles with respect to the collimation axis, and thus reduce the number of scattered x-rays that reach the detector. The second collimator, Heavymet (95% W and 5% Cu), located 35mm behind the first collimator, is 127mm long and has a 1mm square aperture. The third collimator, copper, located 2.7 m after the second collimator, is 100 mm long and has a 3 mm square aperture. A fourth collimator, 51mm long with a 13mm circular aperture and made of lead, is located directly before the detector. The geometric acceptance angle of this collimator system is approximately 0.04 deg. This corresponds to a 5mm square area at the 8mm diameter extraction aperture. By ensuring that the detector does not see any solid walls at the extraction end of the plasma chamber, we minimize the chances of detecting wall bremsstrahlung, or x-rays produced by thick-target interactions.

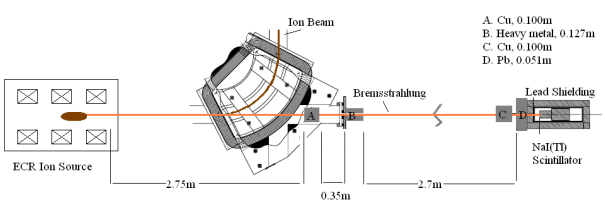

Figure 2. ECR x-ray collimation and detection setup.

VENUS

The experimental setup of the VENUS ion source and NaI detector is shown in Figure 3. The first collimator, 2.37m after the extraction aperture, is a 127mm long Heavymet collimator with a 1mm square aperture. The NaI(Tl) and photomultiplier (PMT) detector system follows the first collimator by 2.16m. In addition a second collimator is placed directly before the detector. The second collimator, made of lead, is 51mm long with a 13mm diameter aperture. The experimental setup results in a 14mm square area visible to the detector at the extraction aperture. Since VENUS' extraction aperture is only 8mm in diameter, all of the VENUS spectra shown in this paper contain wall bremsstrahlung.

In order to compare VENUS spectra with the LBNL-ECR spectra, the second copper collimator is removed from the LBNL-ECR setup. With this removal, the LBNL-ECR and VENUS detection setups both see a 14 mm square area at their 8 mm diameter extraction apertures. Differences in x-ray spectra for the two LBNL-ECR collimator setups are discussed in the next section.

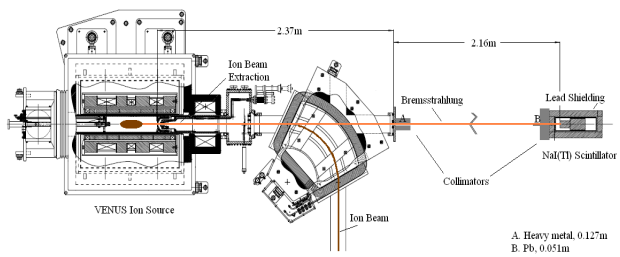

Figure 3. VENUS x-ray collimation and detection setup.

Influence of Wall Bremsstrahlung on X-Ray Spectra

A study was undertaken to compare x-ray spectra for which the area visible to the detector includes the extraction wall of the plasma chamber to ones for which only the bulk plasma is visible. First we note that the extraction aperture of the LBNL-ECR has a diameter of 8 mm. As discussed in the previous section, two collimation setups were used for LBNL-ECR spectra. One setup, with collimator "C" in Figure 2 removed, allows the detector to see a 14 mm square area at the extraction aperture, ensuring that extraction-end wall is visible to the detector. The second setup provides a 5mm square area visible to the detector, ensuring that no extraction-end wall is visible. In Figure 4 one compares the two setups and it can be seen that the number of recorded counts and the shape of the spectra change when the extraction plate is visible.

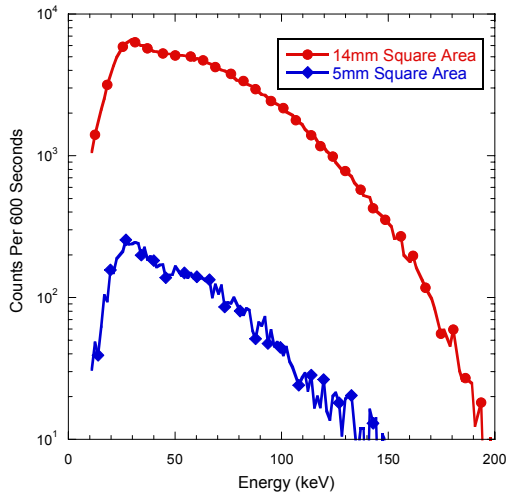

Figure 4. LBNL-ECR X-ray spectra at 300W of 6.4GHz power recorded with a 5mm square area versus a 14mm square area visible to the detector at the 8mm circ3ular diameter extraction aperture.

A possible explanation for these results is that unconfined electrons stream towards and hit the extraction plate emitting thick-target bremsstrahlung. The presence of thick-target bremsstrahlung overwhelms bremsstrahlung produced in the plasma [1]. As shown in [1], the electron bremsstrahlung emissivity can be written as:

$$J(h\upsilon) = \int_{h\upsilon}^{\infty} j(E,h\upsilon) v g(E) dE \qquad (1)$$

where v is the electron velocity, g(E) is the EEDF, E is the electron energy, hυ is the energy radiated, and where $j(E,h\upsilon)$, the energy radiated per electron, is given by

$$j_{at}(E,h\upsilon) = 1.43\times10^{-28} N_{at} \frac{Z^2}{E} \Delta z \qquad (2)$$

for thin-target bremsstrahlung, and by

$$j_{sol}(E,h\upsilon) = 1.10\times10^{-5} \frac{Z_{sol}}{l} (E - h\upsilon) \qquad (3)$$

for thick-target bremsstrahlung, where N_{at} is atomic density, Z_{sol} is the atomic number, E is the electron energy, and l is a constant on the order of one. Equation (1) is applicable to plasma bremsstrahlung as well. One detail to notice about the equations for $j_{at}(E,h\upsilon)$ and $j_{sol}(E,h\upsilon)$ is the size of the constant coefficient. Because the size of the coefficient is so much larger for thick-target bremsstrahlung its contribution to the recorded x-ray spectra is significant, as is apparent in Figure 4. For this reason, proper collimation is important.

NaI(Tl) Detector Efficiency

For our measurements, a 3-in. diameter by 3-in. long NaI(Tl) scintillator was utilized. To correct the x-ray spectra for detection efficiency, the detector was characterized in terms of scintillator material, scintillator size, and photon energy.

The scintillator produces pulses of light that are converted to an electric pulse by a photomultiplier tube (PMT) which is recorded by a multichannel analyzer (MCA). However, the recorded spectrum does not directly reflect the photon spectrum emitted by the electrons that reaches the detector. Several processes that can change the recorded spectrum take place before the photons are recorded in the data acquisition system.

First, the photons emitted by the electrons undergo attenuation and scattering in the media they traverse before reaching the detector. The media the photons pass through are a 3mm thick vacuum quartz window and approximately 2.7m of air (LBNL-ECR data) or 2.2m of air (VENUS data), and a thin layer, ~0.5mm, of aluminum that surrounds the NaI(Tl) scintillator. In addition, there is a finite probability that the photons will be detected at all by the 3-in.thick NaI(Tl) scintillator. The detection probability is slightly reduced for higher x-ray energies. The absorption efficiency of photons in these media is shown in Figure 5. The spectra in this paper are not corrected for this absorption resulting from media present between emission and detection. Nonetheless, it is important to note the poor representation of the low energy x-rays in the spectra. Future work will concentrate on detecting the low energy x-rays.

The second process the photons undergo has to do with the probability the detector will fully absorb them once they reach the detector and are detected. This probability arises from the interaction of the photons with the detector. A photon may be completely absorbed, resulting from photoelectric absorption. Also, a photon may be partially absorbed through Compton scattering with an absorbing recoil electron.

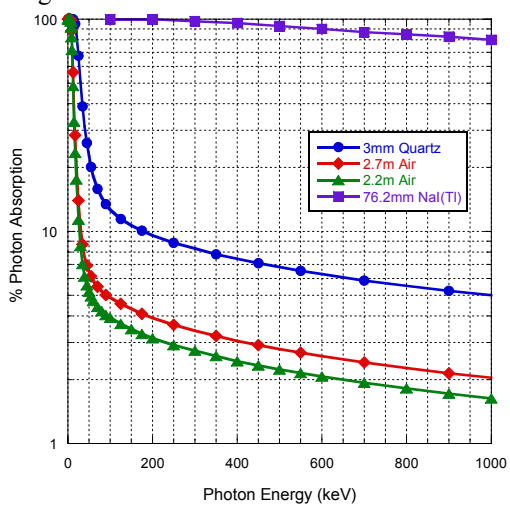

Figure 5. The absorption of photons in media decreases with increasing energy. See [2] for quartz and air attenuation coefficients. See [3] for a NaI(Tl) absorption curve.

The maximum energy that can be absorbed due to Compton scattering is called the Compton Edge, which

results from a 180° scattering angle between the photon and recoil electron, and is given by:

$$E_C = \frac{2E_\gamma^{\,2}}{m_e c^2 + 2E_\gamma} \quad (4)$$

where m_e is the electron mass and E_γ is the photon energy. Scattering at angles less then 180° gives rise to a Compton Plateau extending from zero to the Compton Edge. Backscatter peaks and pair production are not accounted for.

In other words, a photon emitted with energy K' has a certain probability of being fully detected, as energy K=K', or partially detected as an energy less than K', K<K'. The probability that a photon of energy K' is detected with energy K is given by the response matrix R(K',K) (See Figure 7).

In order to obtain the response matrix, R(K',K), one first needs the 3-in. x 3-in. NaI(Tl) scintillator's peak-to-total (P/T) curve from [6], shown in Figure 6, which gives the diagonal of the response matrix, shown in Table 1. The P/T curve describes the probability a photon's energy, K', when detected, is completely absorbed. Specifically, for a monoenergetic source of photons of energy K', the P/T is the ratio of counts detected in the full-energy peak, at K', to the total counts. Ideally, the monoenergetic source of photons would all be completely absorbed and a spectrum would show only a single line at energy K'. Data analysis was done using the published P/T 's from [6].

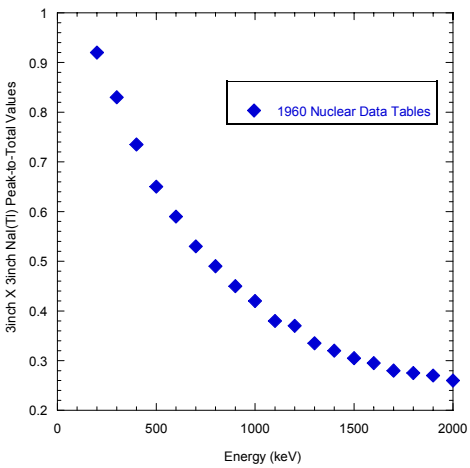

Figure 6. NaI(Tl) peak-to-total, P/T, curve from [6] compared with experimental findings. The values from [6] are approximate.

As previously stated, the P/T's are the diagonal of the response matrix R(K',K). In order to fill in the remainder of R(K',K), the P/T for each photon energy K' is subtracted from unity and the remainder is distributed equally amongst the Compton Plateau beginning with the Compton Edge, Equation 4, for the respective photon energy K'. As such, one approximation made is that the plateau is flat. A response matrix example is shown in Table 1 and Figure 7. For simplification, the response matrix used does not take into account the energy resolution of the detector in that the P/T is only assigned to one matrix element, corresponding to one energy value. This allows us to use a 100 element square response matrix.

K / K'	…	60 keV	100 keV	…	200 keV	300 keV	400 keV	…
100keV	…	0	**0.97**	…	0	0	0	…
200keV	…	0.012	0	…	**0.87**	0	0	…
300keV	…	0.013	0.013	…	0	**0.80**		…
400keV	…	0.014	0.014	…	0.014	0	**0.72**	…
⋮	⋮	⋮	⋮	⋮	⋮	⋮	⋮	⋮

Table 1. Response matrix elements. The matrix describes the probability a photon pf energy K' that reached the detector is detected as having an energy K. The diagonal, in bold, are the peak-to-total values for the scintillator.

As shown in [4], the relationship between the true photon spectrum I(K') and the detected spectrum P(K) is:

$$P(K) = \int_0^{K'_{max}} I(K') \cdot R(K', K) dK' \quad (5)$$

Discretely, the recorded spectra can be written as a series of linear equations:

$$P(K) = \sum_0^{K'_{max}} I(K') \cdot R(K', K) \quad (6)$$

This method of solving for the physical spectrum, free of detector influence, I(K'), is called direct matrix inversion [4,5]. The desired photon spectrum I(K') is obtained as follows:

$$I = PR^{-1} \quad (7)$$

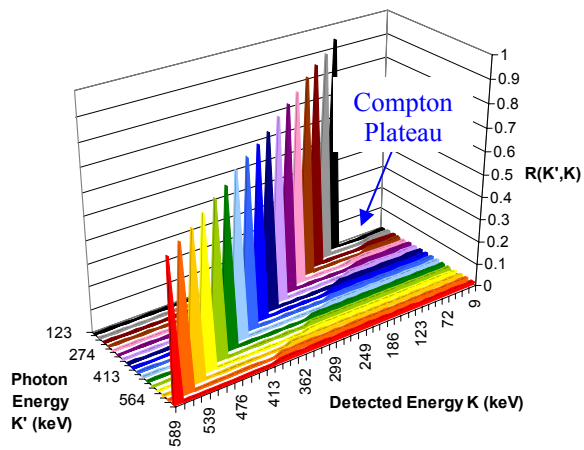

Figure 7. Example of a NaI(Tl) Response Matrix R(K',K) for photons of various energies.

Figure 8 shows an example of the results obtained when the direct matrix inversion method is applied. The amount of counts at the high energy end of the spectrum increase as counts are removed from the low energy end and placed into the high energy end.

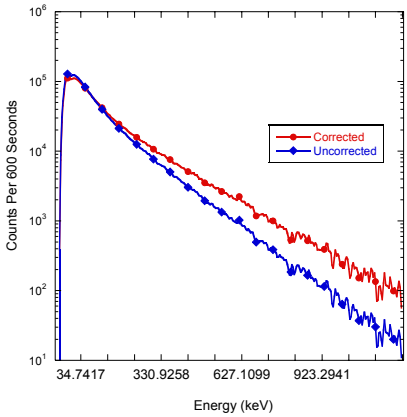

Figure 8. Applying the direct matrix inversion method corrects the detected spectra. The spectrum shown is from VENUS when operating at 1.5kW of 28GHz.

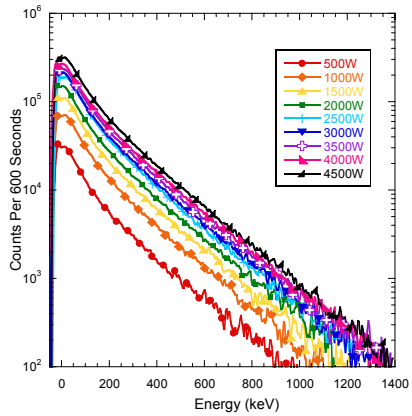

Figure 9. VENUS x-ray spectra for varying powers using 28GHz heating.

ANALYSIS

Our data analysis of the recorded spectra, using a code written in Python [7], is done in a number of steps. First, a background spectrum, such as shown in Figure 1, is subtracted from the x-ray spectra. The code then calibrates the x-ray spectra using a radioactive source spectrum that is recorded after each data set. The VENUS spectra, which often extend up to energies of 1MeV, are calibrated using a ^{207}Bi source with gamma-ray line energies of 569keV and 1063keV. The LBNL-ECR spectra, whose energies barely exceed 300keV, are calibrated using a ^{133}Ba source with a x-ray line energy of 31keV and gamma-ray line energies of 81keV, and 356keV. Once a spectrum has been calibrated it is corrected for detector efficiencies. Then its spectral temperature, T_S, is obtained using:

$$j(h\nu) \propto \exp\left(\frac{-h\nu}{kT_S}\right) \quad (8)$$

where hν is the energy of the radiated photon [8]. Using a semi-logarithmic representation of the data a least-squares fit is applied, from which the inverse of the slope is taken to represent the spectral temperature T_S. In addition to the T_S, the Python code also integrates the spectra for certain energy ranges to give the total amount of counts. The spectral temperatures and integrated count numbers are used as relative indicators of changes in the electron energy distribution as parameters such as power and frequency are varied.

RESULTS

X-Ray Spectra at Varying Powers

In Figure 9 VENUS x-ray spectra for a series of microwave powers at 28 GHz are shown.

One trend that is immediately noticeable is that the slope remains relatively constant as microwave power is increased. Note, this can also be seen in Figure 10, which shows that the spectral temperature remains essentially constant with power. While we do not observe a strong increase in spectral temperature when increasing power, especially at higher microwave powers, there is a slight increase observable at very low powers.

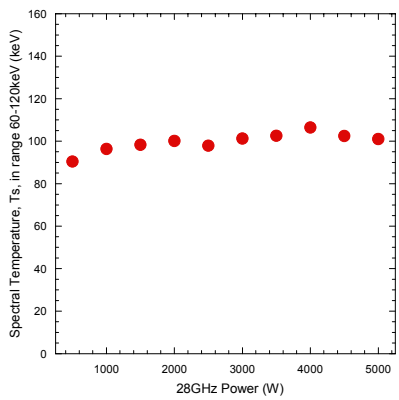

Figure 10. Spectral temperature for the 28GHz VENUS spectra, at various powers, in Figure 9.

The power radiated by the plasma per unit time in volume ΔV is [1]:

$$J_{pl}(h\nu) = (3.0\times10^{-21}) N_i N_e Z_i^2 \frac{1}{\sqrt{kT}} \exp\left(-\frac{h\nu}{kT}\right)\Delta V \quad (9)$$

where N_i is ion density, N_e is electron density, Z_i is ion atomic number, k is Boltzmann's constant, T is the electron temperature, and hυ is the energy of the radiated photon. From this equation it is obvious that the power radiated is linearly related to the electron density. A trend that can be deduced from Figure 11 is that the increase in x-ray counts is essentially linear with increased power. This result is consistent with results presented previously in references [9] and [10].

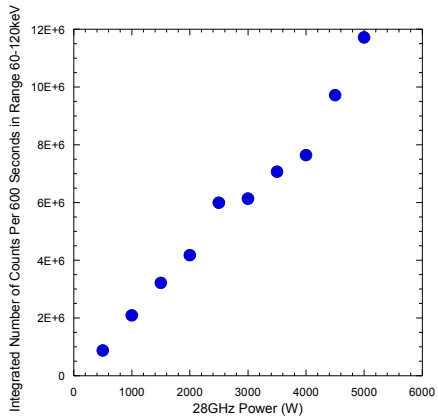

Figure 11. Integrated number of counts for 600 seconds over the energy range 60-120keV corresponding to the VENUS spectra in Figure 9.

Because the x-ray count is linearly dependent on density, and it is observed to increase linearly with power, it can be assumed that the primary effect of increasing power is to increase plasma density.

To show that increasing power does indeed cause density to rise, we can examine the behavior of the total particle current as power changes. To calculate the total particle current we use the recorded faraday cup (FC) current spectrum. The particle current is simply the FC current divided by the charge state of the particle. The total particle current, then, is the sum of particle currents for all species (Argon and Oxygen, in this case) and charge states present at a given power level. As shown in Figure 12, the particle current increases as power increases. This data corresponds to the data used to produce Figures 9-11, above. For similar confinement parameters, then, larger particle currents will principally be caused by larger plasma densities. Thus, plasma density increases with power.

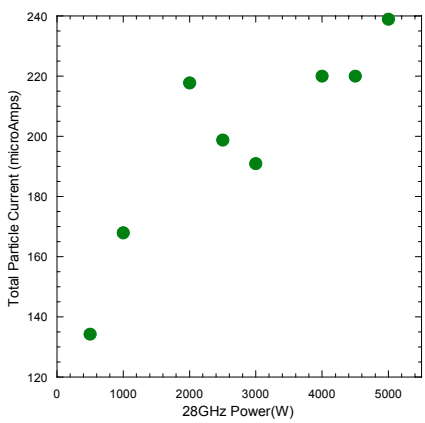

Figure 12. Total particle current corresponding to the VENUS spectra in Figure 9.

X-Ray Spectra at Varying Frequencies

Figure 13 shows calibrated x-ray spectra for 6.4GHz, 18GHz, and 28GHz at a roughly equivalent power density of ~2.3W/L. Note that for this comparison, using power per volume, the volume refers to the ECR zone and not the plasma chamber. We see an increase in the total recorded counts as well as the maximum recorded photon energy.

According to theory outlined in [11], increased microwave frequency causes both the electron density and mean energy of electrons to increase. Similarly, a larger mirror ratio, B_{max}/B_{min}, is predicted to lead to increases in both electron density and mean electron energy. For the data presented in Figure 13, the LBNL-ECR B_{max}/B_{min} ~2.3 while for VENUS B_{max}/B_{min} ~5. As such, when going from 6.4GHz (LBNL-ECR) to 18GHz (VENUS) the change in spectra is likely attributed to both increasing frequency and mirror ratio. On the other hand, for the VENUS data for 18GHz and 28GHz, the magnetic field ratios are identical and the only change is the frequency which causes the change in spectra shape.

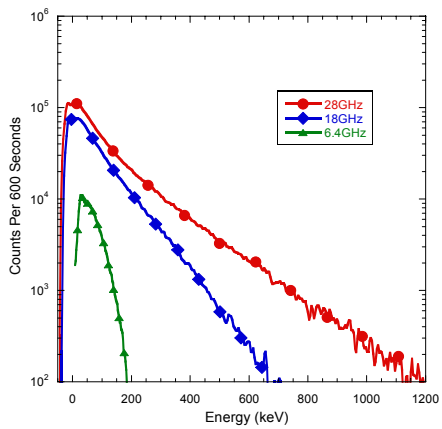

Figure 13. 6.4GHz (LBNL-ECR), 18GHz (VENUS), and 28GHz (VENUS) x-ray spectra at an equivalent power density of ~2.3kW/L.

Figure 14 shows a comparison of spectral temperatures for the three frequencies at equivalent power densities. There is an increase in spectral temperature when going from 6.4GHz to 18GHz of 40%. The increase from 18GHz to 28GHz is only 10%. The change in spectral temperature is a result of a change in the slope of the spectrum. The change in slope, or spectral temperature, indicates a change in the average electron energy in the plasma. Models [11] have shown that microwave heating frequency and the mirror ratio both change the mean energy of the electrons. Figure 14 reflects the change in mean energy as microwave heating frequency is changed.

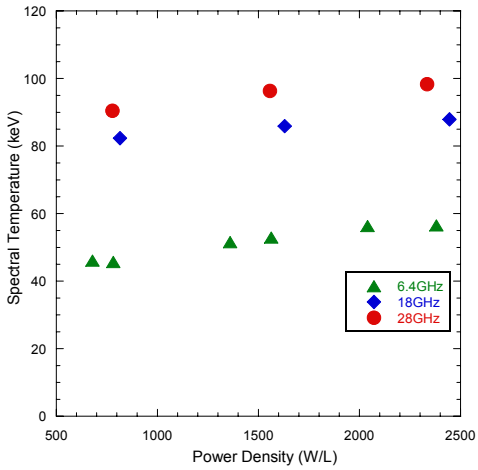

Figure 14. 6.4GHz (ECR, 50-100keV), 18GHz (VENUS, 60-120keV), and 28GHz (VENUS, 60-120keV) spectral temperatures as a function of power density.

X-Ray Spectra at Varying Mirror Ratios

Most electron cyclotron resonance ion sources, including LBNL's three sources, rely on the superposition of solenoid and sextupole magnetic fields for plasma confinement. The effect of magnetic field configuration on x-ray spectra has been shown recently [9, 12]. One study carried out in [12] showed that increasing the magnitude of the minimum magnetic field caused the spectral temperature to increase, as well as the maximum energy of the recorded photons. The magnitude of the maximum magnetic field at both injection and extraction were kept approximately constant. Increasing the minimum magnetic field has two effects: a decreased mirror ratio and a smaller magnetic field gradient at the resonance point. Models show (see, for example, [13]) that a lower gradient in the resonance zone should increase the heating efficiency of the electrons. This, in turn, should increase the number of higher energy electrons, and thus the number of recorded photons at larger energies.

The second effect of increasing the minimum magnetic field is a lower mirror ratio which might also lead to an increase in recorded x-ray counts, although not necessarily to an increase in the maximum energy of recorded x-rays. Lowering the mirror ratio increases the size of the loss cone according to

$$\alpha = \arcsin\left[\left(\frac{B_{\min}}{B_{\max}}\right)^{1/2}\right] = \arcsin\left[\left(\frac{1}{R}\right)^{1/2}\right] \quad (9)$$

Where, $R=B_{max}/B_{min}$ is the mirror ratio. In theory, then, a larger number of particles, both electrons and ions, should escape confinement in the mirror field. If the collimation system is designed such that some of the extraction plate is visible to the detector, we would expect an increase in x-ray counts due to the increased number of lost electrons impacting the extraction plate and creating bremsstrahlung. A recorded x-ray spectrum that is made using a collimation system that allows the detector to see the extraction plate will have contributions from both the decreased resonance zone magnetic gradient, and the decreased mirror ratio. Because the detector in [9] could see the extraction plate, the x-ray spectra most likely included both effects. A question that might be asked is: what is the relative importance of these effects?

To answer this we recorded two sets of spectra. Both sets of spectra are taken at the same power level, but at varying extraction mirror ratios. Table 2 summarizes the changes in magnetic field configuration at the extraction plane.

Mirror Ratio (B_{max}/B_{min})	**1.39**	**1.41**	**1.43**	**1.45**
Gradient (Gauss/cm)	69	72	75	78
Bmax (Gauss)	2859	2849	2839	2829
Bmin(Guass)	2056	2021	1986	1950

Table 2. Summary of magnetic field parameters at extraction for the LBNL-ECR ion source.

One set of spectra is taken using the complete collimation system (only plasma visible to the detector), and the other is taken with the last copper collimator, collimator "C" in Figure 2, removed (both plasma and extraction plate visible to detector). The results are shown in Figure 15. With partial collimation there is a definite increase in x-ray counts at higher energies as the mirror ratio is decreased. This increase is most likely due to lost electrons striking the extraction plate and creating bremsstrahlung, though, some portion may be due to the increased heating efficiency at lower magnetic field gradients. With full collimation, however, there is very little change in the spectra as the mirror ratio is changed. Further studies will be undertaken to determine whether the results shown in Figure 15 are real, physical results, or just poor statistics due to the low count rate with full collimation. A more significant change in mirror ratio might also be required to have a larger change in the x-ray spectra in the case of full collimation.

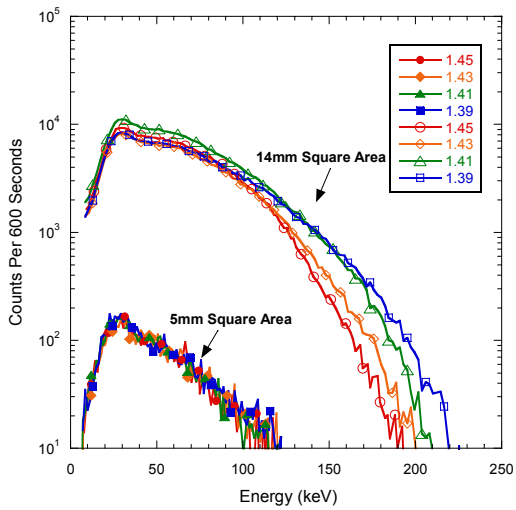

Figure 15. 6.4GHz (LBNL-ECR) spectra at varying mirror ratios. As the mirror ratio increases the amount of counts at the higher energy end increases only when a 14mm square area is visible to the detector at the 8mm diameter circular extraction aperture. This trend is not seen when a 5mm square area is visible.

SUMMARY

The bremsstrahlung spectra presented in this paper are emitted through the extraction end of the LBNL-ECR and VENUS ion sources, which operate at heating frequencies of 6.4GHz, and 18 and 28GHz, respectively. The spectral temperatures and integrated count numbers obtained from the x-ray spectra when varying parameters such as microwave frequency, microwave power, and mirror ratio give insight into the behavior of the electrons in the plasma. Our ultimate goal is to determine the distribution of electron energies in the plasma, and, for this reason, it is important that the recorded bremsstrahlung spectra reflect the spectra emitted by the electrons as accurately as possible. We have shown that a careful collimation geometry of the bremsstrahlung spectra is important. Specifically, the amount of wall bremsstrahlung visible to the detection system can significantly impact the energy and counts of the recorded spectrum.

We have observed trends in the spectra that agree with previous predictions. Increasing power leads to a linear increase in the amount of counts but does not change the spectral temperatures of the spectra. On the other hand, increasing the heating frequency increases the energy of the electrons which is observed in the spectra since they extend to higher energies. Lastly, decreasing the mirror ratio also appears to increase the energy of the observed spectra. We have noted that in this study this last trend was only seen in spectra for which the extraction wall was visible to the detector. An attempt to explain this is made by considering magnetic field gradient at the resonance zone as well as the size of the loss cone. More attention will be paid to this in future studies. In addition to this, future studies will include simultaneous axial and radial bremsstrahlung measurements. Bremsstrahlung measurements from the AECR-U, using 10GHz and 14GHz heating will also be collected.

ACKNOWLEDGEMENTS

The authors would like to thank Dr. David Ward for his invaluable suggestions and help.

This work was supported by the Director, Office of Energy Research, Office of High Energy and Nuclear Physics, Nuclear Physics Division of the U.S. Department of Energy under Contract DE AC03-76SF00098.

REFERENCES

[1] M. Lamoureux, P. Waller, P. Charles, and N.B. Avdonina, Physical Review E **62** (2000) 4091.

[2] M.J. Berger, J.H. Hubbell, S.M. Seltzer, J. Chang, J.S. Coursey, R. Sukumar, D.S. Zucker, " XCOM: Photon Cross Sections Database", [cited 2008 Oct 15], http://physics.nist.gov/PhysRefData/Xcom/Text/XCOM.html

[3] "Efficiency Calculations for Selected Scintillators", Saint-Gobain Crystals, [cited 2008 Oct 15], http://www.detectors.saint-gobain.com/media/documents/S000000000000001004/SGC_Efficiency_Calculations.pdf

[4] P.C. Fisher and L.B. Engle, Physical Review **134** (1964) B796-B816.

[5] D. Ward, H.R. Andrews, B. Haas, P. Taras, and N. Rud, Nuclear Physics **A397** (1983) 161-204.

[6] Nuclear Data Tables, 1960: 59.

[7] "Python Programming Language-Official Website," [cited 2008 Sep 10], http://www.python.org/.

[8] R. Geller, *Electron Cyclotron Resonance Ion Sources and ECR Plasmas*, Bristol: Institute of Physics Publishing, 1998: 252.

[9] D. Leitner, J.Y. Benitez, C.M. Lyneis, D.S. Todd, T. Ropponen, J. Ropponen, H. Koivisto, and S. Gammino, Rev. of Sci. Inst., **79** (2008) 033302.

[10] Z.Q. Xie, Rev. of Sci. Inst., **69** (1998) 625.

[11] A. Girard, C. Pernot, and G. Melin, Physical Review E **62** (2000) 1182.

[12] C.M. Lyneis, D. Leitner, D. Todd, S. Virostek, T. Loew, A. Heinen, O. Tarvainen, Rev. of Sci. Inst., **77** (2006) 03A342.

[13] Y. Jongen, C. Pirate, and G. Ryckewaert, Proceedings of the 6th International Workshop on ECR Ion Sources, Lawrence Berkeley National Laboratory, LBNL, (1985) 238-255.

PAPER NOT RECEIVED

EXPERIENCE AT THE ION BEAM THERAPY CENTER (HIT) WITH 2 YEARS OF CONTINUOUS ECR ION SOURCE OPERATION

T. Winkelmann, R. Cee, T. Haberer, B. Naas, A. Peters, S. Scheloske
Heidelberger Ionenstrahl-Therapie Centrum (HIT), D-69120 Heidelberg, Germany

Abstract

Radiotherapy with heavy ions is an upcoming cancer treatment method with to date unachieved precision. It associates higher control rates particularly for radiation resistant tumour species with reduced adverse effects compared to conventional photon therapy. This paper will provide an overview about the project, with special attention given to the two 14.5 GHz electron cyclotron resonance (ECR) ion sources. The HIT ECR ion sources are routinely used to produce a variety of ion beams from proton up to oxygen. The runtime of these two sources are 330 days per year, our experience with two years of continuous operation will be presented, with special emphasis on stability and breakdowns of components. In addition, an outlook of further planned developments at the HIT ECR ion sources will be given.

INTRODUCTION

The facility of the Heidelberg Ion Beam Therapy Center (HIT) [1] is the first dedicated proton and carbon therapy facility in Europe. HIT is located at the radiological university hospital in Heidelberg (Radiologische Universitätsklinik Heidelberg, Germany).

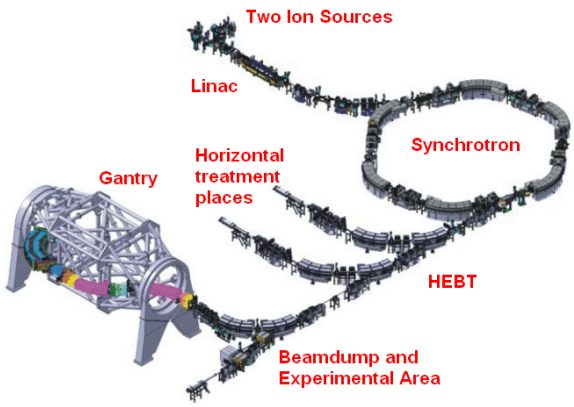

Figure 1: Overview of the HIT accelerator facility

Over the last two years the HIT accelerator [2,3] was commissioned by GSI Darmstadt [4,5,6], while the technical systems were operated under the responsibility of the HIT operating team. In parallel the implementation of the medical equipment took place.

The acceptance tests with beam started in 2006, when sources, low energy beam transport system (LEBT) and the linear accelerator (LINAC) were commissioned [4], followed by synchrotron [5] and high energy beam transport system (HEBT) in 2007 and 2008. The first turn in the synchrotron was achieved in February 2007, the first beam in the treatment place was seen in March 2007. Beam performance for protons and carbons had reached a level enabling patient treatment at the two fixed beam patient treatment places by December 2007, at the experimental area by April 2008. Gantry commissioning started at January 2008 [6].

The beam production at HIT consists of two 14.5 GHz permanent magnet ECR ion sources from PANTECHNIK [7]. The 7 MeV/u injector linac [3] (Figure 2) comprises of the LEBT, a 400 keV/u radio frequency quadrupole accelerator (RFQ) [8,9], and a 7 MeV/u IH-type drift tube linac (IH-DTL) [3,8,9].

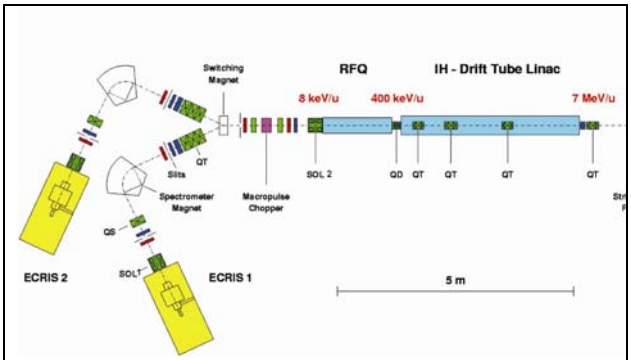

Figure 2: Layout of the Injector Linac [2]. SOL = solenoid magnet, QS = quadrupole singulet, QT = quadrupole triplet. Green: focusing and steering magnets, red: profile grids and tantalum screen, blue: beam current monitors (Faraday cups and beam transformers).

The linac beam is injected in a compact 6.5 Tm synchrotron [10] with a circumference of about 65m to accelerate the ions to final energies of 50 – 430 MeV/u, which is the key to the enormous variety of beam parameters provided by the HIT accelerator. The beam is distributed by the high energy beam transport line (HEBT) to the four beam stations. There are two horizontal fixed beam stations for patient treatment. In station three the beam is guided along an isocentric gantry. The fixed beam station for quality assurance is dedicated to development and research activities. All places are fully equipped for a 3D rasterscan volume conformal irradiation.

The maximum available beam intensity at the patient treatment place are $8 \cdot 10^7$ ions/s for carbon and $3.2 \cdot 10^9$ ions/s for protons. With respect to the patient treatment, these intensities are sufficient, but for an effective quality assurance it will be important to reach the design

parameters (C: $5 \cdot 10^8$ ions/s, p: $2 \cdot 10^{10}$ ions/s). Taking into account the variable spill-length, the intensity has to be increased by a factor of 2.5 for carbon and by a factor of 4 for protons.

The main contribution of particle losses is caused by the poor transmission of the beam through the RFQ. Therefore the upgrade programme concentrates on a redesign of the RFQ [11]. In parallel we start to optimise the ion source performance.

ION SOURCE

We are operating two ECR Supernanoguns. During the commissioning of the LEBT the design values for the beam emittance could not be fully reached, especially for the proton beam [12].

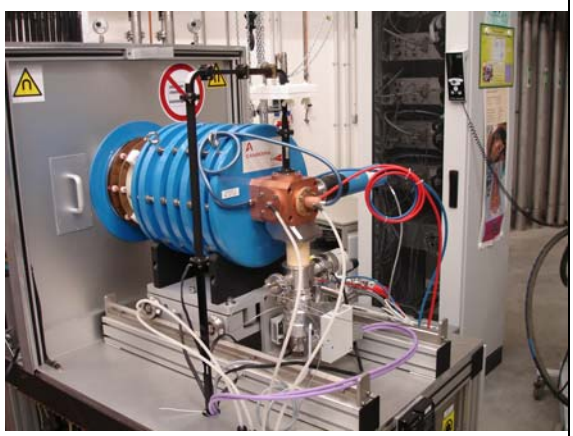

Figure 3: The 14.5 GHz high-performance permanent magnet ECRIS SUPERNANOGAN. This source was developed at GANIL, and is commercially available from PANTECHNIK S.A., Caen, France [7,13].

We are hence planning to adopt modifications resulting from recent experiments with ECR ion sources to reach a better emittance [14]. They have shown that a remarkable intensity gain can be obtained by varying the microwave frequency within a narrow range around the centre frequency. Furthermore we intend to investigate the performance of an extended extraction system. In Fig.4 you can see the extraction system that we bought two years ago with the ECR- Source from Pantechnik.

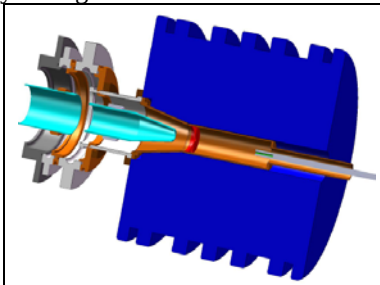

Figure 4: 3D-Model of the first extraction system design by PANTECHNIK S.A., Caen, France [7,13].

After 2 years of permanent operation the ceramic isolator showed relevant evaporation.

Figure 5: Isolator after 3 weeks of CO_2 operation of the first extraction system that HIT bought with the source (e.g. Figure 4).

Pantechnik supplied us with a longer first electrode (puller electrode) to make an overlap of 3mm to minimize the evaporation, see Figure 6.

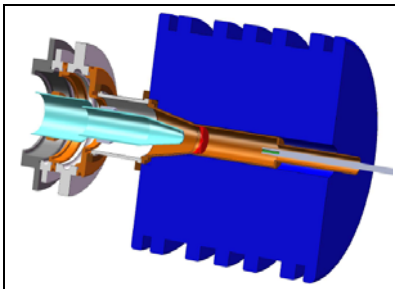

Figure 6: The new design of the extraction system by PANTECHNIK S.A., Caen, France [7,13]. The puller electrode got an overlap with the focus electrode.

Based on particle optics simulations performed by HIT a new extraction system was designed. As a next step COBRA simulations will be performed jointly with GSI to study the properties of the new design.

The goal for this new design is a better long time stability in combination with extended maintenance intervals. The beam transport with a smaller emittance and better isolator shielding could be achieved by simulations. This new design will also allow an optimized vertical plane position of the pumps.

OPERATION OF THE ION SOURCE IN THE LAST TWO YEARS

During the first two years of operation mainly carbon ions were used by 60 %, followed by hydrogen (38 %), helium (1 %) and oxygen (1 %). The continuous operation runtime of the two sources are 330 days per year 24h-operation! During the commissioning, the required intensities given in table 1 were very stable achieved for hydrogen, helium and oxygen. For carbon we cannot achieve the specified intensity at the moment, we are looking forward to reach the specified intensity after the next general cleaning of the plasma chamber.

Ion	I / eμA Reachable current	I / eμA Specified current	U_{source} / kV
H_2^+	1000	1000	16
$^3He^{1+}$	500	500	24
$^{12}C^{4+}$	150	200	24
$^{16}O^{6+}$	150	150	21.3

Table 1: Specified ion species and intensities behind the 90° analysing magnet.

At the tip of the extraction we changed the puller electrode material (Figure 7), we also changed the material of the bias cap (Figure 8), with these modifications we reach long-therm stable operating conditions with extended maintenance intervals.

Figure 7: Left the new design of the titanium puller cap after 6 months of operation, right the old design made of steel after the same time of operation (broken).

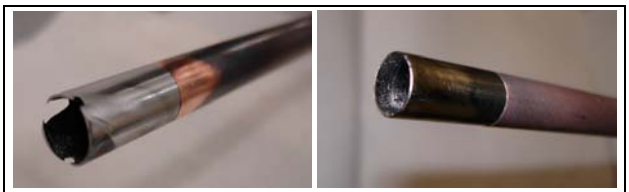

Figure 8: Left the new design of the titanium bias cap after 6 months of operation (still o.k.), right the old design made of molybdenum after 3 months of operation (broken).

The main problem during the two years of continuous operation were due to the RF-amplifier breakdown which occurred 11 times within the last 2 years. The time to exchange the defect amplifier by a spare part and to restart the source for operation took mostly just some hours.

We spent a lot of time to investigate this insufficient durability of the RF-amplifiers. We tried a better magnetic shielding and a better grounding system, but it seems that the problem is still not solved.

OUTLOOK

To summarize, the following developments are planned:

- A new extraction system for a stable beam and better focusing will be build.
- Intensity gain can be obtained by varying the microwave frequency within a narrow range around the centre frequency.
- Problems with the short life time of the RF-Amplifiers have to be solved

ACKNOWLEDGEMENTS

We would like to thank all colleagues from GSI Darmstadt who have participated in the successful commissioning. Particularly we would like to mention the ion source group of P. Spädtke who will help us to simulate the new extraction system.

REFERENCES

[1] T. Haberer et al., "The Heidelberg Ion Therapy Center", Radiotherapy and Oncology, Vol. 73 (Supplement2), P186-199,2004
[2] H. Eickhoff et al., Proc. EPAC 2004, p. 290.
[3] B. Schlitt et al., Proc. LINAC 2004, p. 51.
[4] M. Maier et al., Proc. PAC 2007, MOP046.
[5] D. Ondreka et al. EPAC 2008 TUOCG01
[6] U. Weinrich et al.,"Commissioning of the Carbon Beam Gantry at the HIT Accelerator", TUPP134, EPAC08
[7] PANTECHNIK S.A., 12 Rue Alfred Kastler, F-14000 CAEN, FRANCE.
[8] A. Bechtold, PhD Thesis, J.-W.-Goethe University Frankfurt am Main, 2003. http://iaprfq.physik.uni-frankfurt.de/
[9] C. Kleffner et al., LINAC 2006, THP 089.
[10] A. Dolinskii, "The Synchrotron of the Dedicated Ion Beam Facility for Cancer Therapy, proposed fort he clinic in Heidelberg" EPAC 2000, Vienna
[11] R.Cee et al.,"Intensity Upgrade Programme for the HIT Injector Linac", EPAC08, Genoa, Italy, TUPP113
[12] T. Winkelmann et al., "ECR Ion Source Experience at the Heidelberg Ion Beam Therapy Center (HIT)", Rev. Sci. Instr. 79, 02A331 (2008).
[13] P. Sortais, L. Bex, L. Maunoury, T. Lamy and A.C.C. Villari, General purpose highperformance electron cyclotron resonance ion source for production of multicharged ions, Rev. Sci. Instrum. 69, 656 (1998)
[14] L. Celona, G. Ciavola, F. Consoli, S. Gammino, F. Maimone,D. Mascali, P. Spaedtke, K. Tinschert, R. Lang, J. Maeder,J. Roßbach, S. Barbarino, and R.S. Catalano, "Observationsof the frequency tuning effect in ECR ion sources", Rev. Sci.Instr. 79, 023305 (2008).

First experience with the operation of the GTS-LHC ion source at 18 GHz

D. Küchler*, M. O'Neil, R. Scrivens
CERN, Geneva, Switzerland

Abstract

The GTS-LHC ion source delivers the heavy ion beam, in preparation for the ion collision experiments at CERN. The source was operating up to now with a microwave frequency of 14.5 GHz, in the afterglow mode, for the commissioning of the injector chain of the LHC. Tests have been made with injection of microwaves at 18 GHz, and the first results and experience are presented in this paper.

INTRODUCTION

Within the last years the ion injector chain for the Large Hadron Collider (LHC) was successful commissioned [1] with the so called "early" beam. This beam is ready to be used for the first heavy ion experiments at the LHC.

The goal of the frequency change was to ease the operation and have some margin for the "nominal" beam.

The main difference from the source and linac point of view between the "early" and the "nominal" beam is the number of shots need to be stacked in the following machine (Low Energy Ion Ring - LEIR). An increased intensity from the source reduces the number of shots necessary and simplifies the operation of LEIR.

OPERATION AT 14.5 GHz

For standard operation the source has used a microwave frequency of 14.5 GHz up to now[2]. All the commissioning of the ion injector chain for the LHC was done in this operation mode.

For the injection of the beam into the next synchotron (LEIR) a flat top of approximately 200 µs is needed. The source pulses at 10 Hz with 50% duty factor for the microwave heating and is tuned in an afterglow-mode of operation.

Beam intensity in an individual charge state is measured from the source using Faraday Cup 2 (see Fig. 1). For operational optimization of the source for the linac, it is critical to optimize firstly in Faraday Cup 3, after the RFQ. It is often the case that the optimization of beam on Faraday Cup 2 can be far from the best optimization on Faraday Cup 3 (even after thorough tuning of the intermediate elements). Finally the real figure of merit is the beam intensity from the full Linac, into the final stripped ion (see also [3]).

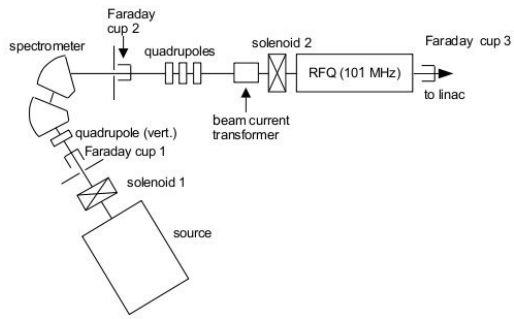

Figure 1: Sketch of the Low Energy Beam Transport (LEBT) of Linac3.

At the end of the linac, after a stripper and a spectrometer, the current is measured with a beam transformer.

Due to a better understanding and a careful tuning the source performance could be increased over the last years from around 100 eµA of Pb^{29+} to presently $\sim$ 131 eµA measured after the RFQ. This results at the end of Linac3 in a maximum current of $\sim$ 31 eµA of Pb^{54+}.

Figure 2 shows a charge state distribution when the beam was optimised into Faraday Cup 2. This was a peak performance, and did not deliver the maximum performance from the linac.

Typical conditions for operation at 14.5 GHz are: RF power of 540 W, bias disk voltage of −390 V (pulsed during the afterglow), extraction voltage of 18.52 kV, average drain current of 1.7 mA and solenoid settings of 1260 A/370 A/1200 A (injection/central/extraction coil) leading to a $B_{max} = 1.3$ T at extraction.

Under this conditions a stable beam can be delivered for a period of up to two weeks. Then the oven has to be refilled. The overall intensity variation is in the range of 10%. The source has to be fine tuned several times per day to keep this level.

OPERATION AT 18 GHz

For the ECR ion sources several scaling laws are known and well tested [4]. One of them predicts that the extracted current for a certain charge state is proportional to the square of the frequency ($I_q \propto \omega^2$). If

* detlef.kuchler@cern.ch

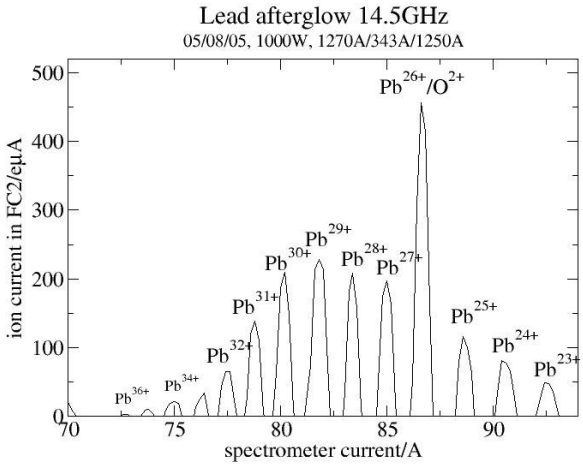

Figure 2: Lead charge state distribution from the source at 14.5 GHz operation (extraction voltage 20.07 kV).

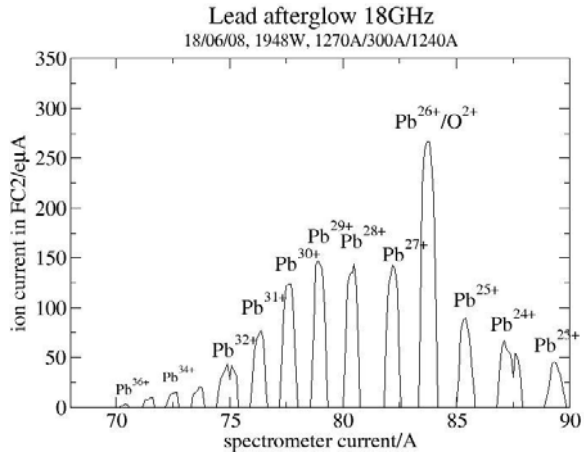

Figure 3: Lead charge state distribution from the source at 18 GHz operation (extraction voltage 18.52 kV).

one takes this into account the change from 14.5 GHz to 18 GHz should give than an increase of around 50%.

The magnetic structure of the GTS-LHC source was designed in a way that the source can run also with a microwave frequency of 18 GHz. In the first half of 2008 a short period was dedicated to test the source with 18 GHz. The results of this test are preliminary because they are the result of only one week of source operation.

In the start-up phase it was found that the HT break of the waveguide had to be modified for 18 GHz (see [5] for the theoretical background).

For the 14.5 GHz case the waveguide flanges are flat at both sides of the HT break and at this frequency the leakage of radiation is neglectable.

At 18 GHz the leakage was very high. One of the flat waveguide flanges was replaced with a grooved one, reducing the leakage to a acceptable level. But due to this modification now $\sim 10\%$ of the power is directly reflected at the HT break back to the generator. The addition of a tuner in this section of the waveguide could reduce this reflected power to nearly zero. This modification will be done in the future.

Figure 3 shows the resulting charge state distribution.Typical conditions for operation at 18 GHz are: RF power of 1994 W, bias disk voltage of -445 V, extraction voltage of 18.52 kV, drain current of 1.7 mA and solenoid settings of 1270 A/330 A/1260 A (injection/central/extraction coil). Compared to the 14.5 GHz case this is around 4-times the RF power, a higher bias disk voltage and a higher field in the extraction coil. Otherwise only minor changes.

With 18 GHz the source is a bit more difficult to tune to a stable mode of operation. Sometimes it jumps into a mode where the intensity varies very regularly between 0 and 100% with a period of several seconds. The reason for this mode is not understood and it is very difficult to come back to a stable mode.

The maximum Pb^{29+} current measured after the RFQ up to now is 136 eμA, only a small increase of the current compared to the 14.5 GHz case.

Quadrupole scan measurements of the emittance (the last quadrupole in the triplet before the RFQ was used for this, see Fig. 1) showed no appreciable difference of the emittance between the 14.5 GHz and 18 GHz case. But a scraping of the beam in the beam line cannot be excluded.

On the other hand not all source parameters could be optimised. One of the critical parameters is the position of the oven, relative to the plasma. The frequency change moves the plasma, causing additional heating of the oven, which changes the lead vapour pressure[6].

For a period of 8 hours the source showed a similar beam stability as for the 14.5 GHz case.

FREQUENCY MIXING

The use of two frequencies has increased the beam intensity of other sources[4].

The injection system of the GTS-LHC source includes two waveguides, in addition to a fixed power at 18 GHz a variable power at 14.5 GHz could be injected into the source.

Figure 4 shows the result of an small additional power at 14.5 GHz added to a fixed high power at 18 GHz. Already a small fraction of microwave power at 14.5 GHz reduced the intensity of the Pb^{29+} ion beam. No setting with improvements could be found.

CONCLUSIONS

The GTS-LHC source can operate at 18 GHz. The expected improvements could not be found yet, but not all parameters could be checked in the limited

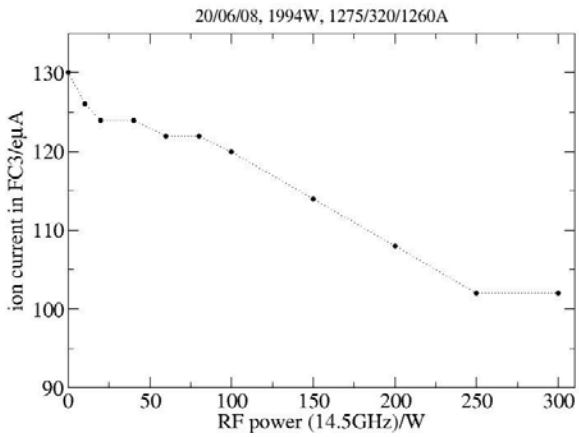

Figure 4: Mixing of a fixed power of 18 GHz (1994 W) with a variable power of 14.5 GHz.

time. In parallel with the setting up of the ion injector chain next year further source studies are planned to improve the present situation.

REFERENCES

[1] D. Manglunki et al. "Ions for LHC: Towards Completion of the Injector Chain'", Proceedings of EPAC08, Genoa, 2008, http://cape.elettra.eu/E08Papers/MOPC131.PDF.

[2] C.E. Hill, D. Küchler, C. Mastrostefano et al., "Experience with the GTS-LHC ion Source", Proceedings of the 3rd LHC Project Workshop Chamonix XV (2006) 239–241.

[3] L. Dumas, C. Hill, D. Hitz, D. Küchler, C. Mastrostefano, M. O'Neil, R. Scrivens, "Operation of the GTS-LHC Source for the Hadron Injector at CERN", Proceedings of ECRIS06, Lanzhou, 2006, in HEP & NP, Vol. 31, Suppl. 1 (2007) 51–54.

[4] D. Hitz, "Recent Progress in High Frequency Electron Cyclotron Resonance Ion Sources", Advances in Imaging and Electron Physics, Vol. 144 (2006) 1–164.

[5] M. Cavenago, C.T. Iatrou, "Studies on microwave coupling into the electron cyclotron resonance ion source Alice", Rev. Sci. Instrum. 65 (1994) 1122–1124.

[6] D. Hitz, private communication, 2008.

PRODUCTION OF MULTI-CHARGED IONS FOR EXPERIMENTAL USE AT HIMAC

A. Kitagawa, M. Muramatsu, T. Fujita
National Institute of Radiological Sciences (NIRS), 4-9-1 Anagawa,Inage,Chiba 263-8555, Japan
W. Takasugi, S. Wakaisami
Accelerator Engineering Corporation (AEC), 2-10-14 Konakadai, Inage, Chiba 263-0043, Japan
S. Biri, Institute of Nuclear Research (ATOMKI), H-4026 Debrecen, Bem ter 18/C, Hungary
A.G. Drentje, Kernfysisch Versneller Instituut (KVI), 9747AA Groningen, The Netherlands

Abstract

Since 1994, heavy-ion radiotherapy using carbon ions is successfully carried out with the Heavy Ion Medical Accelerator in Chiba (HIMAC) at the National Institute of Radiological Sciences (NIRS). HIMAC is dedicated to radiotherapy, but it has as a second essential task to operate as a users facility. In that scope it accelerates many ion species for basic experiments in e.g. biomedical and material science, physics and chemistry. In order to serve all HIMAC users at best, the extension of the range of ion species is an important subject in ion source development at HIMAC. Several developments on the 18GHz ECR ion source (called NIRS-HEC) are now in progress. In order to increase the beam intensity for heavier ions, additional microwave power is applied at a different frequency by a traveling wave tube amplifier. Various compounds are employed for the production of metallic ions by the metal ion volatile compound (MIVOC) technique. Results of recent developments are reported.

INTRODUCTION

Status of heavy-ion radiotherapy

Heavy-ion radiotherapy has physical and biological advantages over other types of radiation therapies. The physical advantage is a localized dose distribution just on a tumor in a human body. The biological advantages are a large relative biological effectiveness (RBE) due to the high linear energy transfer (LET), a small oxygen enhancement ratio (OER), and a small dependence on the cell cycle. Although LBL carried out pioneering trials in the 1970's – 1980's[1], it was not completed clinically. In order to verify the effectiveness and safety of heavy-ion radiotherapy clinically, the first medical dedicated heavy-ion accelerator in the world, named HIMAC, started operation at the National Institute of Radiological Sciences (NIRS) in 1993[2]. Over 4000 cancer patients have already been treated since 1994. These clinical results have clearly verified the advantages of heavy-ion therapy. The detailed results, i.e. a 5-year survival ratio, a local control ratio, grading of any side effect, and so on, are given in reference [3].

Based on 10 years-experience at HIMAC, a hospital-specified facility optimized for carbon ions has been designed[4]. The prototype injector, which consists of an ECR ion source (called Kei2[5]), a RFQ linac, and an IH linac[6], has been successfully developed at NIRS. Thus, in co-operation with NIRS, Gunma University has been constructing the carbon-therapy facility since April 2006. The first clinical trial is scheduled for FY2009.

Motivation of developments for ion sources

HIMAC is dedicated to radiotherapy, but - as mentioned above - it has as a second essential task to operate as a users facility. In that scope it accelerates - during evening, night and weekend- various ion species for basic experiments. Two ECR ion sources and one PIG ion source are installed in HIMAC at present. A 10 GHz ECR ion source, so called NIRS-ECR, has satisfied the medical requirements[7]. A PIG ion source[8] produces ion species from solid materials by the sputtering technique. Other ion species are supplied using the 18 GHz ECR ion source, so-called NIRS-HEC[9,10]. In order to serve all HIMAC users at best, the extension of the range of ion species is an important subject in ion source development at HIMAC. The requirement for ion sources is to produce ions with a charge-to-mass ratio over 1/7 and an injection energy of 8 keV/n. The present records of beam intensities are summarized in Table 1. However, more ion species and higher intensities for heavier ions are still required. Developments for ion sources are in progress.

Table 1: Records of beam intensities without afterglow

* E:NIRS-ECR, H:NIRS-HEC, P:NIRS-PIG

Ion	Output (eμA)	*	Ion	Output (eμA)	*	Ion	Output (eμA)	*
H_2^+	3000	P	Ne^{3+}	6000	P	Ti^{10+}	50	H
He^+	6000	P	Mg^{4+}	400	P	Fe^{9+}	400	H
B^{2+}	150	P	Si^{5+}	250	H	Co^{9+}	170	H
C^{2+}	470	E	Cl^{6+}	400	H	Ge^{14+}	50	H
N^{3+}	1050	H	Ar^{8+}	1100	H	Kr^{15+}	205	H
O^{3+}	930	H	Ca^{6+}	250	P	Xe^{20+}	95	H

Scope of the developments

In order to increase the NIRS-HEC beam intensity, the optimization of the extraction configuration was most

effective in our case. We optimized the position the movable electrode following the simulation study[11], increased the extraction voltage[9], and optimized the radial magnetic field[10]. These results for most gaseous ion species were generally satisfying.

In addition, several techniques (tricks) are very useful to shift toward the higher charge of the charge-state distribution (CSD). That is the afterglow mode[12], the gas mixing[13], the biased electrode[14, 15, 16], and so on. The gas mixing technique is very sufficient and convenient, because it can be utilized while maintaining the present ion source structure with proven good performance, i.e. reproducibility and stability.

For the metallic ions, the effort generally is to make gas vapour from a solid material. The metal ion volatile compound (MIVOC) technique is very easy and useful way to produce some elements[17]. Below we will report on recent experimental results. Toxic (or caustic) gasses like chloride gasses are also easy to ionize, but they should of course be handled with extreme care. We developed a special gas feeding system with a gas eliminator and utilized them[18].

Unfortunately, the intensities for most heavier ion species obtained in this way are not enough for an effective extension of the range of ion species. In particular, the plasma maintained by MIVOC contains many impurities like carbon, and it disturbs effectiveness of the gas mixing. It is necessary to develop a technique to improve of CSD for heavier ions and to supply various ions.

For such 'dirty' gasses, the development of biased electrodes stimulating an 'anti-wall coating' effect is planned[7]. The Bio-Nano ECRIS at Toyo Univ.[19] is assigned as a test bench under the cooperation. Two-frequency heating appears to be also a promising technique to handle such a dirty plasma. We will report recent experimental results in this paper.

It is, of course, important to develop new techniques for the production of pure plasmas in a more general way for every solid material. An electron bombardment evaporator and / or an induction heating oven for high temperature are being planned for that purpose.

EXPERIMENTAL RESULTS OF TWO-FREQUENCY HEATING

Summary of former experiences

Many reports pointed at the improvement of highly charged ion production by feeding multiple microwaves with different frequencies[20]. In an early stage of the development of two-frequency heating using two klystron amplifiers (KLY), we could confirm that the two different frequency microwaves were absorbed at different ECR zone by observing the shapes of visible radiations[21]. Although the beam intensity was improved, the tuning of operation parameters was difficult and not so reliable. We thought the reason was due to interference of one microwave with the plasma made by the other microwave.

The KLY had over 1 kW power, but its frequency was fixed. In order to investigate the frequency dependence precisely, we added an additional travelling wave tube amplifier (TWT) with a wide frequency range between 10 and 18 GHz. A hyperfine structure appeared in the frequency dependence of the additional microwave[22]. Three major parameters for operation of ECRIS, i.e., the vacuum pressure, the magnetic confinement, and the power of the microwave, are correlated to each other. Although the frequency of microwave changed the plasma condition, the optimizing of other two parameters usually recovered from the bad condition. On the other hand, since the magnetic confinement can not be optimized in the case of the permanent magnet ECRIS, it was very important to tune the frequency. In the case of two-frequency heating, it is also important to adjust one frequency to the fixed condition given by the other frequency. Our TWT had only a maximum power of 250 W at the former experiments. As a result, it was not enough to improve the performance. Therefore, the conclusion of our initial experiences is that a TWT with fine tuning of frequency and enough power is required.

Experimental setup

The experiments are being performed with NIRS-HEC. NIRS-HEC was designed to reach a high extraction voltage and a high magnetic field with normal conducting magnets. The maximum extraction voltage between the plasma slit and the extraction electrode is 60 kV. The maximum mirror fields at the injection and at the extraction side are 1.3 and 1.2 T, respectively. The microwave power is usually supplied by an 18.0 GHz KLY with a maximum power of 1.5kW.

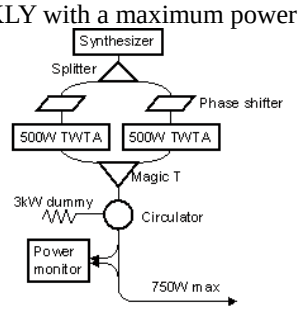

Figure 1: Circuit diagram of the additional microwave system.

Figure 2: Layout of waveguides.

In order to investigate the effects of two-frequency heating, an additional microwave-injection system was added to NIRS-HEC which has a frequency range of 17.75 to 18.25GHz. The system consists of a frequency synthesizer, two 500W TWT and a waveguide system. The waveguide system has a power combiner and a feedback monitor to stabilize the forward power in the full frequency range. The maximum input power is over 600W at the entrance into the ion source's chamber.

Figure 1 shows a circuit diagram of the additional microwave system. The microwaves from KLY and from TWT are injected into the plasma chamber by two rectangular waveguides at the RF shielding endplate shown in Figure 2.

Experimental result

Experimental data were obtained with ^{84}Kr gas (isotopic enrichment 80%). Initially, the frequency and microwave power from theTWT were set at 18.0 GHz and 600 W, respectively. The other parameters, i.e., amount of gas, magnetic field, extraction voltage, and so on, were optimized. Then, the frequency dependence of the output current of Kr^{15+} was measured as shown in Figure 3 (solid line). The phenomena of frequency dependence have been studied by many groups, and they were very complicated (for a recent example see ref.[23]). In our case the effect case was related to a shift in the CSD. Mass spectra which were measured at three different frequencies clearly show that the CSDs varied with frequency in Figure 4.

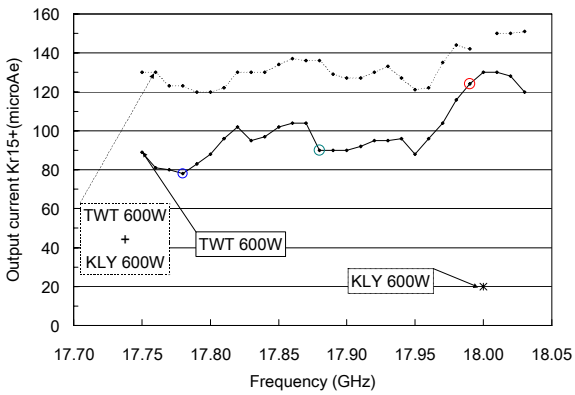

Figure 3: Frequency dependence of Kr15+ output current. The solid line and broken line are obtained by TWT only and TWT+KLY, respectively. The asterisk mark is obtained by KLY only.

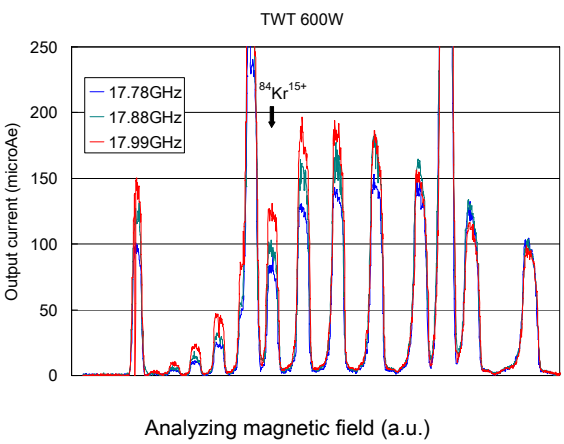

Figure 4: Mass spectra with 17.78 GHz, 17.88 GHz, and 17.99 GHz.

When TWT was stopped and only KLY supplied 600 W, the beam intensity was decreased as shown in Figure 3 (asterisk). When the microwave power from KLY was increasing, the output current was also increasing. However, the beam instability was appeared over 700 W. Figure 5 shows measured time structures of beams with different microwave powers, 600, 800 and 900 W. The plasma collapsed every several milliseconds and recovered in about 1 ms. When TWT turned on in this situation, the beam stability was improved and the large output current was obtained as shown in Figure 5. The frequency dependence with TWT+KLY was also appeared as shown in Figure 3 (broken line), but its fluctuation became more calmly. It is noted that each microwave power does not equal exactly due to loss in the waveguides.

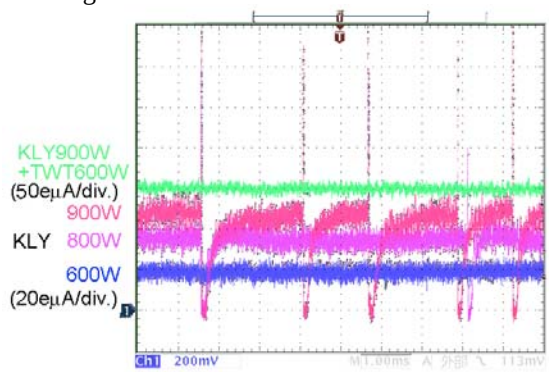

Figure 5: Time structures of beams.

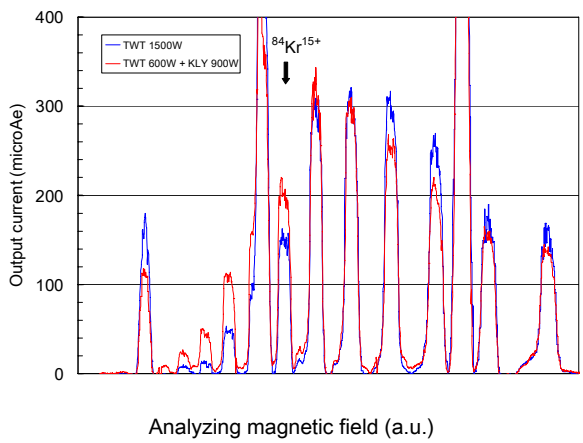

Figure 6: Comparison between the single frequency and two-frequency heating.

As a conclusion, the double frequency heating improved the beam intensity under the conditions of enough power and precise frequency tuning for the additional microwave. It seems it is mainly due to prevent the plasma instability in our cases. The maximum record of output current for $^{84}Kr^{15+}$ was 205 eμA (80% enrichment). This record was about 30 % larger than the

record with the single frequency heating, and its beam stability was more stable. The optimized microwave power is not saturated. Applying a more powerful TWT would be promising. For higher charge state ions, it is more effective as shown in Figure 6.

EXPERIMENTAL RESULTS OF MIVOC

The MIVOC - method is used for the production of various ion species in Table 2. In order to obtain the desired evaporation and consumption rates in each case, the temperatures of the MIVOC oven and of the gas-feeding line are controlled independently. A thermal-control system has been developed for utilizing metal ion volatile compounds with various vapour pressures.

For low vapour pressure like $(C_2H_5)_2Mg$, a thermostat is heating a container with the compound up to a suitable temperature. The gas feeding tube must be kept higher temperature than the container to prevent condensation or adsorption to the tube's wall. On the other hand, for high vapour pressure like $(CH_3C_5H_4)_2Co$, the compound must be cooled lower than the room temperature. A cryostat with Peltier elements is utilized here.

Table 2: Ion species produced by MIVOC

Ion	Compound	Output (eμA)	Remarks
$^{24}Mg^{5+}$	$(C_2H_5)_2Mg$	150	Necessary to heat
$^{28}Si^{5+}$	$Si(CH_3)_4$	250	
$^{56}Fe^{9+}$	$(C_5H_5)_2Fe$	400	Better with heating
$^{59}Co^{9+}$	$(CH_3C_5H_4)_2Co$	170	Necessary to cool
$^{74}Ge^{12+}$	$GeH(CH_3)_3$	50	

FUTURE PLANS FOR PURE METALLIC IONS

Induction heating oven

MIVOC is a useful technique for several metallic ions. However, it is necessary to make efforts for developments of each new ion species, and there is the well known disadvantage that inherently many contaminations are included in the production. Carbon ions from many compounds (See Table 2.), due to their deposition on the wall or an insulator, especially disturb application of other useful tricks like wall coating or biasing electrodes. Also, it is difficult to optimize the amount of support gas for gas mixing. In order to prevent such disadvantages and to produce a "more pure metallic gas" from various materials, an induction heating oven is under considered.

The Osaka University group has developed such an oven system[24] that could be tested at Kei2[25]. We have a plan to use this type of oven to NIRS-HEC.

Electron bombarder

In order to produce more pure metallic gas from especially high melting point materials, a gas supply or feed method by electron bombardment is under development. A metallic target rod or crucible at a high positive potential is heated by the electron bombardment technique. The temperature of materials easily reaches more than 2000 °C. Although we obtained an output current of 25 eμA for Fe^{6+}[26], the evaporation rate and the lifetime are still not stable and have to be controlled better.

REFERENCES

[1] Biological and Medical Research with Accelerated Heavy Ions at the Bevalac, LBL-11220, UC-48 (1980).
[2] Y. Hirao *et al.*, Nucl. Phys. A 538, 541c (1992).
[3] D. Schulz-Ertner, H. Tsujii, Journal of Clinical Oncology, **2** , 953 (2007).
[4] K. Noda *et al.*, J. Radiat. Res. **48**:Suppl.A A43 (2007).
[5] M. Muramatsu *et al.*, Rev. Sci. Instrum. **76**, 113304 (2005).
[6] Y. Iwata *et al.*, Nucl. Instrum. Meth. **A572**, 1007 (2007).
[7] A. Kitagawa *et al.*, Rev. Sci. Instrum. **79**, 02C303 (2008).
[8] T. Miyata *et al.*, Rev. Sci. Instrum. **75**, 1863 (2004).
[9] A. Kitagawa *et al.*, Rev.Sci.Instrum. **69**, 674 (1998).
[10] A. Kitagawa *et al.*, Rev.Sci.Instrum. **73**, 604 (2002).
[11] S. Fu *et al.*, Rev.Sci.Instrum.**65**,1437(1994).
[12] P. Sortais *et al.*, Rev. Sci. Instrum. **63(4)**, 2801 (1992)
[13] A. G. Drentje, Rev. Sci. Instrum. **74**, 2631 (2003), and references therein.
[14] G. Melin *et al.*, Proc. of 10th International Workshop on ECRIS, Knoxville, TN, 1990, p.1.
[15] S. Gammino *et al.*, Rev. Sci. Instrum. **63**, 2872 (1992).
[16] A. G. Drentje *et al.*, IEEE Transactions on Plasma Science, **36(4)**, 1502 (2008).
[17] J. Ärje *et al.*, Proc. of the 12th International Workshop on ECRIS, Wako, INS-J-182 (1995), p.136.
[18] A. Kitagawa *et al.*, Proc. of the 15th International Workshop on ECRIS, Jyväskylä, 2002, p..
[19] T. Uchida *et al.*, in these proceedings.
[20] Z. Q. Xie and C. M. Lyneis *et al.*, Proc. of the 12th International Workshop on ECRIS, Wako, INS-J-182 (1995), p.24.
[21] A. Kitagawa *et al.*, Rev.Sci.Instrum. **71**, 1061 (2000).
[22] A. Kitagawa *et al.*, Proc. of European Particle Accelerator Conf., Wien, 2000, p. 1607.
[23] L. Celona *et al.*, Rev. Sci. Instrum. **79**, 023305 (2008).
[24] Y. Kato *et al.*, Rev. Sci. Instrum. **77**, 03A335 (2006).
[25] M. Muramatsu *et al.*, Rev. Sci. Instrum. **79**, 02A328 (2008).
[26] M. Sasaki *et al.*, Rev. Sci. Instrum. **73**, 545 (2002).

PAPER NOT RECEIVED

Ion beam production from rare isotopes with GSI ECR Ion Sources

K. Tinschert*, R. Lang, J. Mäder, J. Roßbach, P. Spädtke, A. Yakushev+

Gesellschaft für Schwerionenforschung (GSI), Planckstraße 1, D-64291 Darmstadt, Germany
+ Technische Universität München, Walther-Meissner-Str. 3, D-85748 Garching, Germany

Abstract

ECR ion sources (ECRIS) of CAPRICE-type, working at 14.5 GHz, are in use at the High Charge State Injector (HLI) of the accelerator facility at GSI for beam production and at a test bench for development work. The ECRIS is mostly used to produce ion beams from rare isotopes because of its high efficiency and low material consumption. Depending on their material properties beams of rare isotopes are produced from gases, gaseous compounds, solid materials or solid compounds. Gases can be used directly, while solids have to be transformed into the gaseous state for the ECR plasma which is achieved by using resistively heated ovens. As enriched materials are produced by isotopic separation processes their composition including contamination by impurities can be of importance for the handling in the evaporation process and can be detrimental for the beam user if the ion beam contains additional ion species. Characteristics and suitable treatment of materials and production processes are described. Experimental investigations with different sample materials and operational experiences are reported.

INTRODUCTION

Two preaccelerators are providing ion beams for the heavy ion Universal Linear Accelerator (UNILAC) at GSI which in turn delivers the ion beam to an experimental area with high duty cycle (pulses of typ. 5 ms length, $50\,s^{-1}$ repetition frequency) and to the Heavy Ion Synchrotron (SIS) with low duty cycle (pulses of typically 300 μs length, $1\,s^{-1}$ repetition frequency). The High Charge State Injector (HLI) is mainly used for the high duty cycle operation. In this mode the CAPRICE type ECR ion source (ECRIS) at the HLI is working in DC mode [1]. The appropriate input velocity for injection into the preaccelerator and the maximum mass/charge ratio of 8.5 determines the choice of ion charge state and extraction voltage, respectively . Typical ion charge states are Mg^{5+}, Ni^{9+}, and Xe^{18+}. The respective extraction voltages are between 5 kV and 22 kV. The basic demand to the operation of the ECRIS at the accelerator is to provide a great variety of ion species in stable and reproducible long time operation. These requirements are well fulfilled for the operation with gases. For non gaseous elements which are more than 85% of all elements sometimes gaseous compounds of the desired element can be used. In all other cases the solids must be transformed into the gaseous state at a suitable vapor pressure in the order of 10^{-3} mbar.

At GSI the oven technique has been preferred because it resembles closely the operation with gases. So it provides higher intensities in comparison with sputtering and lower contaminations compared to the MIVOC method (Metal Ions from Volatile Organic Compounds).

Many experiments at GSI request beams of specific isotopes which require highly enriched isotope materials. For rare isotopes the ECRIS is favorable due to its low material consumption and its high efficiency of conversion of sample material into the ion beam. Fig. 1 shows a statistical overview of the ion species produced for accelerator beam times from 2002 until August 2008. Without taking into account the C^{2+} beam time for cancer therapy the proportion of isotopically enriched sample material is exceeding 80 %.

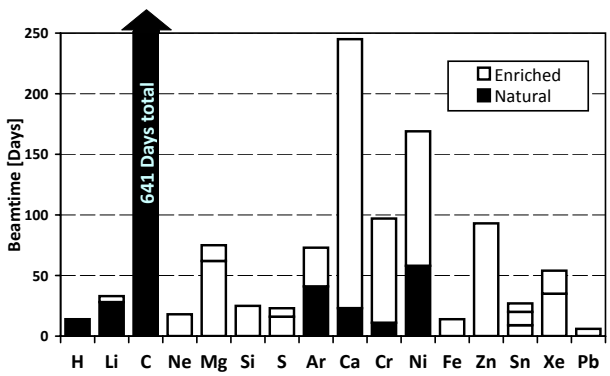

Figure 1: Ion beams produced for accelerator beam times from 2002 to August 2008.

ENRICHED MATERIALS

Natural sample material can be easily obtained in the desired forms and with high chemical purity. For isotopically enriched materials the enrichment processes as well as additional chemical treatments can result in different material properties compared to natural materials. These can be chemical composition including impurities, mechanical and structural characteristics. E. g. metal powders have a huge internal surface facilitating oxidation or hydration processes which are detrimental for the evaporation.

* K.Tinschert@gsi.de

Table 1: Ion species of rare isotopes produced from the CAPRICE ECRIS for accelerator injection, * designates values including material recycling.

ion species of accelerated charge state q	natural abundance (%)	isotope enrichment (%)	sample material	material consumption (μg/h)	average particle intensity (pμA)	efficiency all charge states (%/qi...qf)	efficiency charge state q (%)
$^{3}He^{1+}$	0.00014	99.9	He				
$^{6}Li^{1+}$	7.5	95	LiF	1120			
$^{22}Ne^{4+}$	9.25	99.9	Ne				
$^{25}Mg^{4+}$	10	99	Mg	620	38	26/2...8	5.7
$^{26}Mg^{5+}$	11	99	Mg	310/170*	20	26/47*/2...9	6.4/11.5*
$^{30}Si^{6+}$	3.1	99.5	SiO	1090/580*	13.3	5/10*/3...9	1.3/2.6*
$^{34}S^{5+}$	4.2	80	SO_2	660	12.4	14/2...9	2.5
$^{36}S^{5+}$	0.02	79	SO_2	420	12.4	23/2...8	4
$^{36}Ar^{7+}$	0.34	99.5	Ar				
$^{48}Ca^{7+}$	0.19	96	Ca	210	6.6	40/3...12	5.7
$^{48}Ca^{10+}$	0.19	96	Ca	200	14.0	43/3...11	12.6
$^{50}Cr^{7+}$	4.35	96.5	Cr	2300			
$^{54}Cr^{7+}$	2.37	99	Cr	2300			
$^{58}Fe^{8+}$	0.28	>90	Fe	3100/1440*			
$^{64}Ni^{9+}$	0.93	93	Ni	1300	4.5	4.5/4...13	0.8
$^{70}Zn^{10+}$	0.6	95	ZnO	3170	7.8	3.3/5...14	0.5
$^{112}Sn^{15+}$	0.97	99	Sn	890			
$^{114}Sn^{17+}$	0.65	87	Sn	1000			
$^{124}Sn^{16+}$	5.8	96	Sn	1200			
$^{124}Xe^{17+}$	0.1	99.9	Xe				
$^{136}Xe^{18+}$	8.9	99.9	Xe	550	2.2	50/6...25	2

As the range of usable charge states is strongly limited it may be a problem if the beam is contaminated by another ionic component from the ion source plasma. This can originate from residual gas components but also from the sample material itself.

One lot of ^{54}Cr sample material used for delivering a requested $^{54}Cr^{8+}$ beam contained several hundred ppm of Al. Due to the different vapor pressures of Cr and Al this was sufficient to generate a considerable superposition of Al^{4+} on top of $^{54}Cr^{8+}$ as shown in Fig. 2. As the Al impurities did not vanish within an tolerable time the only solution was to change the charge state from $^{54}Cr^{8+}$ to $^{54}Cr^{7+}$ in order to obtain a pure ^{54}Cr ion beam on target.

Contaminations can hinder the evaporation process if they reach high vapor pressure at lower temperatures than the bulk material. Thus they may cause an excessive drain current at the extraction. So these contaminations have to be heated off before evaporation of the bulk material can start. This can take a considerable time like for one kind of ^{70}ZnO sample material which started to evaporate at first S then followed by Cd (which was present in the sample material as a fraction of 800 ppm). It took 40 hours until regular evaporation of ^{70}ZnO was achieved. In some cases an additional treatment of the material like preheating in a separate vacuum vessel or under inert gas atmosphere before use in the ECRIS can help to get rid of impurities.

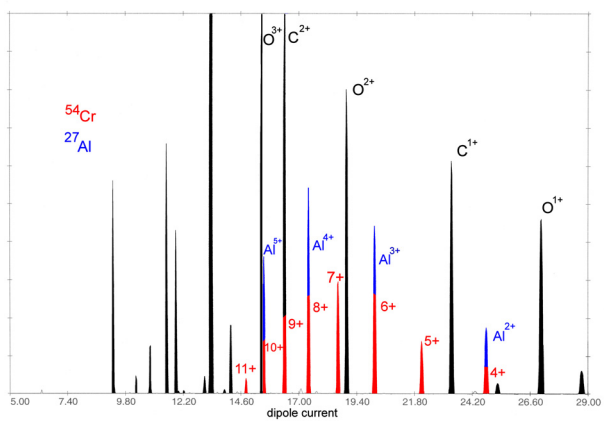

Figure 2: Charge state spectrum of $^{54}Cr + He$ with superposition of Al; 100 eμA full scale.

Another example is a ^{54}Cr sample which was pressed into pellets with the aid of paraffin by the provider. It caused such a high evaporation rate that it was not usable in the ion source. A complete heat treatment prior to the beamtime was necessary to get suitable operating conditions.

EFFICIENCY

Table 1 gives an overview of most of the rare isotopes produced from the CAPRICE ECRIS for accelerator injection. The values of efficiency given in the table are not corrected and include the beam losses in the low energy beam transport line to the RF accelerator.

The lowest material consumption rates and the highest efficiencies are obtained for the alkaline earth metals Mg and Ca because one can take advantage of immediate re–evaporation from a hot surface by using a cylindrical insert ("hot screen") [2] in the plasma chamber which is passively heated by microwave and plasma. Much lower efficiencies are observed for materials like Ni and ZnO which suffer from condensation on cold surfaces which cannot be completely avoided.

With increasing atomic number Z of the ions the number of electrons in the atomic shell increase. Hence the charge state distribution covers an increasing number of charge states, because in a steady state plasma the population of charge states is subject to an equilibrium between electron loss and electron capture processes. Thus in a complex atomic shell more electrons are participating in these processes. So the efficiency for ^{136}Xe can be as high as 50 % for all ionic charge states present in the extracted ion beam, but its charge state distribution covers charge states between 5+ and 25+ while the charge state of interest (18+) contains only a small fraction of 2 %.

A low material consumption rate of 210 μg/h was observed for ^{48}Ca when optimized on 7+. Up to 40 % of the evaporated ^{48}Ca could be analyzed behind the dipole magnet spectrometer as ions of the charge states 3+...12+ while 5.7 % of the material could be provided as ion beam of the requested charge state 7+. For $^{48}Ca^{10+}$ a long run of 67 days was characterized by exceptional stability at high intensity level. The lifetime of the oven exceeded 1500 hours while 3 fillings of the crucible were consumed. Taking into account the amount of material recovered from condensates a consumption of only 200 μg/h has been achieved which corresponds to a further improved efficiency with respect to $^{48}Ca^{7+}$ (see table 1).

For ^{26}Mg operation up to 26 % of the sample material is transformed into the ion beam distributed in the charge states 2+...9+. 6.4 % of the material are then analyzed as ions of the requested charge state 5+. The net efficiency increases to 11.5 % if the recovery of material from the plasma chamber and hot screen is taken into account. Fig. 3 shows a charge state spectrum of an analyzed ^{25}Mg beam which is already optimized on $^{25}Mg^{4+}$ and $^{25}Mg^{5+}$, respectively. The high intensity of almost 40 μA particles at moderate material consumption results in an even better efficiency of 5.7 % for the charge state 4+.

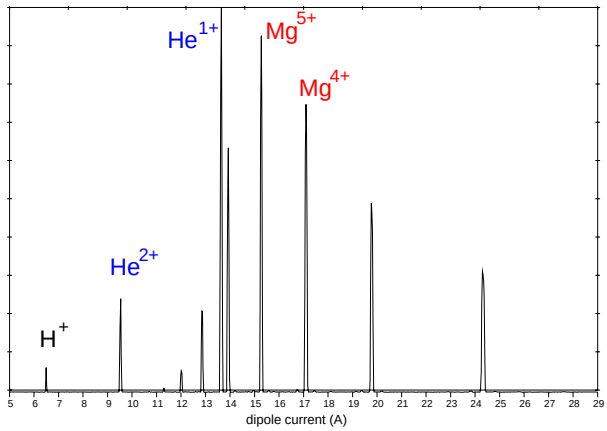

Figure 3: Charge state spectrum of ^{25}Mg + He; 200 eμA full scale

EVAPORATION OF SOLID MATERIALS

The basic characteristics of the GSI standard oven (STO) have been described in detail before [3]. Several additional features have been applied to improve stability of evaporation, reduction of condensates and increase of efficiency. It is used for temperatures between 600 °C and 1500 °C.

For high temperature operation of the STO for materials of low vapor pressure like e. g. Ni, Fe or Cr, an additional heat shield was developed to get a more homogeneous temperature distribution in axial direction of the oven and to reduce the material condensation in its orifice. The heat shield consists of several layers of corrugated tantalum foil with the same aperture as the oven housing. Reliable long time operation of the modified STO could be approved showing the expected reduction of condensates. Thus the material consumption can be reduced and maintenance periods for the oven can be extended.

For low temperature operation of the STO for materials of high vapor pressure a parasitic heating of the oven has to be avoided. Generally, a complete decoupling of ion beam extraction and plasma generation would be desired. Additional aperture rings and enclosure of the complete oven in the injector tube are mechanical measures while the use of an accel–decel extraction system avoids parasitic heating of the oven front by electrons accelerated on axis from the ground electrode of the extraction system into the plasma towards the injection side [4].

COMPOUNDS

The use of gaseous or solid compounds is recommended if elements are not usable due to their physical properties. The use of chemical metal compounds as evaporation source can be an alternative if the vapor pressure of the pure metal is not matching the capabilities of the oven.

Initiated by a request of the Super Heavy Element pro-

gramme for a ^{30}Si beam tests were performed at the ECR injector test setup (EIS) using natural SiO to produce a $^{28}Si^{5+}$ beam by evaporation from the oven. As the use of ZnO has become a standard procedure for producing Zn ion beams SiO appeared to be the only choice, because the vapor pressure of elementary Si and SiO_2 are by far to low. After the successful test a beam of $^{30}Si^{6+}$ could be provided from the ECRIS to the accelerator. Highly enriched ^{30}SiO has been used to provide a beam of high stability and intensity for nearly 4 weeks.

PREPARATION OF SAMPLE MATERIALS

Some of the required enriched materials can be procured in suitable form while others have to be transformed prior to be used with the ECRIS. Metallic ^{48}Ca is obtained as $^{48}CaCO_3$ and is transformed into metallic ^{48}Ca by chemical reduction [5].

A $^{32}S^{5+}$–beam has been produced from natural SO_2 gas at GSI several years ago while at GANIL enriched (63 %) $^{36}SF_6$ has been used for ion beam production [6]. At GSI SF_6 was not chosen as sample material because of the high number of F–atoms in the molecule and because of the high chemical reactivity of F. Following the good experiences with CO_2 gas and with SO_2 gas for producing C ion beams and S ion beams, respectively, SO_2 was also chosen for the rare isotopes.

As the isotope material could only be obtained as elementary material it was necessary to do a conversion to SO_2 gas. A special procedure could be developed to convert at first 2500 mg of highly enriched elementary ^{34}S and then to convert 1950 mg of highly enriched elementary ^{36}S, respectively.

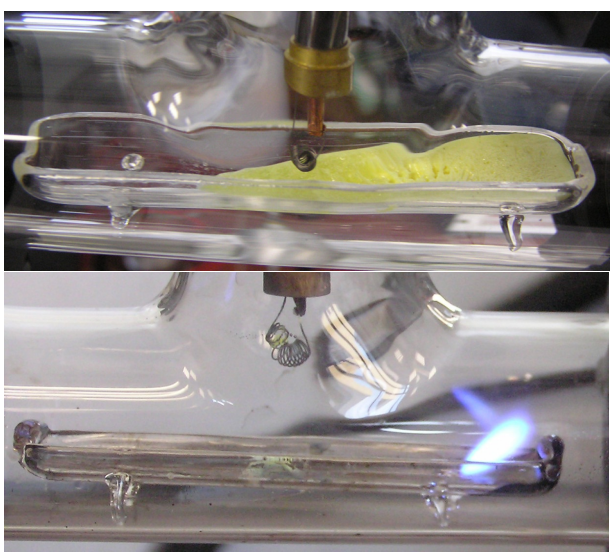

Figure 4: Quartz boat with elementary ^{36}S before and during the combustion process

The sulfur material (powder in elementary form, ≈ 80% enrichment) was melted in a boat of quartz glass at a temperature of 160 °C and then placed inside a glass "T" part with KF flanges DN 25 as vacuum recipient. Through the top flange a sparking plug was introduced, and the other flanges were used as gas inlet and outlet. Three flasks made from stainless steel were connected in series with cooling mantles made from copper tubes. The flasks were covered inside with PTFE; each of them had two valves at both sides. The whole vacuum–tight system was first pumped to 10^{-3} mbar and then flushed with helium. The flasks were cooled down to −140°C by liquid nitrogen vapor flowing through the copper cooling tubes. Then helium flow was switched to oxygen gas flow of ≈ 50 ml/min. The oxygen gas was purified from water content by molecular sieves. The sparking plug was used to ignite a self supporting combustion of the sulfur material. The complete oxidation was finished after ≈ 10 min (see Fig. 4). At the exit from the third flask, the outgoing gas was bubbled through a SO_2 trap - a glass flask filled with NaOH solution. No sulfur has been found in the trap. The content of condensed $^{36}SO_2$ has been measured in all three flasks after the oxidation process. More than 80% of produced $^{36}SO_2$ have been found in the first flask, while 16% have been condensed in the second flask and 2–3% in the last one, respectively. The total conversion yield was ≈ 99%. Afterwards the flasks were heated up to equilibrate the gas pressure. Then each flask was closed from both sides and disconnected separately.

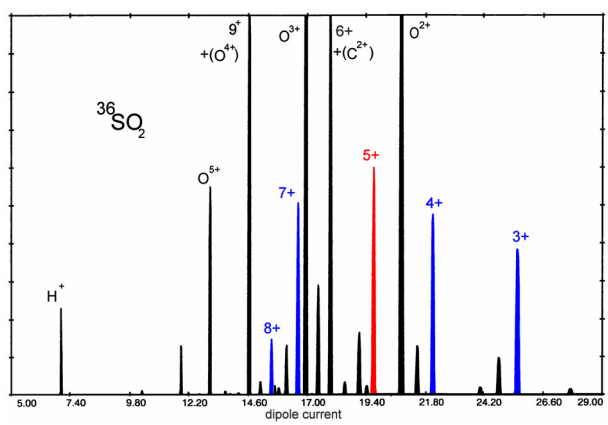

Figure 5: Charge state spectrum of ^{36}S + O; 100 eμA full scale

A test run with $^{34}SO_2$ showed that the sample material is well suited for ECRIS operation. The long time stability of about ±3% with only a few deviations was demonstrated in a continuous run of 8 days. $^{36}SO_2$ was then used for an accelerator beam time delivering $^{36}S^{5+}$ under same conditions. As Fig. 5 shows 60 eμA of $^{36}S^{5+}$ could be obtained, which is the required charge state for acceleration. The average material consumption could be determined to be 420 μg of ^{36}S per hour.

REFERENCES

[1] K. Tinschert, J. Boßler, S. Schennach, H. Schulte, Rev. Sci. Instrum. 69, 709 (1998).

[2] V. B. Kutner S. L. Bogomolov, A. A. Efremov, A. N. Lebedev, V. Ya. Lebedev, V. N. Loginov, A. B. Yakushev, N. Yu. Yazvitsky, Rev. Sci. Instrum. 71, 860 (2000);

[3] R. Lang, J. Boßler, H. Schulte, K. Tinschert, Rev. Sci. Instrum. 71, 651 (2000); R. Lang, J. Boßler, R. Iannucci, K. Tinschert,, Proc. 15^{th} Int. Workshop on ECRIS, University of Jyväskylä, Finland, 180 (2002).

[4] K. Tinschert, P. Spädtke, J. Boßler, R. Iannucci, R. Lang, Proc. 16^{th} Int. Workshop on ECRIS, Berkeley, California, AIP Conference Proceedings 749, 241 (2005).

[5] B. Lommel, W. Hartmann, S. Hofmann, B. Kindler, J. Klemm, J. Steiner, K. Tinschert, J. Radioanalytical Nucl. Chem. 257, 161 (2003); B. Lommel, W. Hartmann, B. Kindler, J. Steiner, Nucl. Instrum. Meth in Phys. Res. A561, 100 (2006).

[6] G. Gaubert et al., Rev. Sci. Instrum. 79, 02A309 (2008).

PERMANENT MAGNETS UNDER IRRADIATION AND RADIOACTIVE ALKALI ION BEAM DEVELOPMENT FOR SPIRAL 1

M. Dubois, J. Alcántara-Núñez, R. Alves-Condé, C. Barué, C. Canet, M. Dupuis, J.L. Flambard, R. Frigot, P. Jardin, C. Leboucher, N. Lecesne, P. Lecomte, P. Leherissier, F. Lemagnen, J.Y. Pacquet, A. Pichard, M.G. Saint-Laurent, GANIL, CEA/DSM-CNRS/IN2P3, F-14076 Caen, France

Abstract

Up to now, eighteen Target Ion Source Systems (TISSs) have been built and used for the production of radioactive ion beams on SPIRAL 1 facility, based on the Isotope-Separator-On-Line (ISOL) method. The TISSs are composed of thick carbon targets and of fully permanent-magnet Electron Cyclotron Resonance Ion Sources (ECRISs) of the Nanogan III type. After irradiation and a decay period of two years, the irradiated TISSs are dismounted and if their magnetic fields are still suitable, the ECRIS are used with a new target. Thereby thirty-two runs have been performed using new or renewed TISSs. , After irradiation, the measured magnetic field sometimes reveals magnet damage. Our experience is reported here. In the second section, we present the progress on the NanoNaKE setup, which aims to extend the radioactive ion beams in SPIRAL 1 to the alkali elements, by connecting a surface-ionization source to the Nanogan III ECRIS via a compact 1+ ion beam line. The main issues and difficulties are discussed and the preliminary solutions are described.

INTRODUCTION

The use of high-energy fragmentation as well as the ISOL methods for exploring the structure of nuclei far from the stability has become one of the major activities at GANIL (*Grand Accelerateur National d'Ions Lourds*). The ISOL method, used in SPIRAL, provides radioactive ion beams, with subsequent acceleration by a K=265 cyclotron CIME, (*Cyclotron d' Ions à Moyenne Energie*).

Three cyclotrons are used to produce the primary beam which bombards the target of the TISS (Figure 1) placed in a heavily shielded cave. Exotic nuclei produced by nuclear reactions are released from the high temperature target (2000°C), effuse through a cold transfer tube up to a multi-charged ECR ion source. After extraction from the ECRIS at low energy ($\leq 34\ q$.keV), the beam of interest is selected by a magnetic spectrometer ($m/\Delta m = 250$) and injected into CIME. The exotic beams can be accelerated in an energy range of 1.7 to 25 MeV/u and, after extraction, the proper magnetic rigidity is selected by GANIL's modified alpha spectrometer and directed to one of the existing experimental areas.

Two kinds of carbon target are used for the radioactive ion beam production, one dedicated to the production of He isotopes, the other to heavier gaseous element up to Krypton. The restriction to gaseous elements is provided by a cold transfer tube, situated between the target cavity and the source chamber. Available intensities are given on the GANIL web site [1]

PERMANENT MAGNETS UNDER IRRADIATION

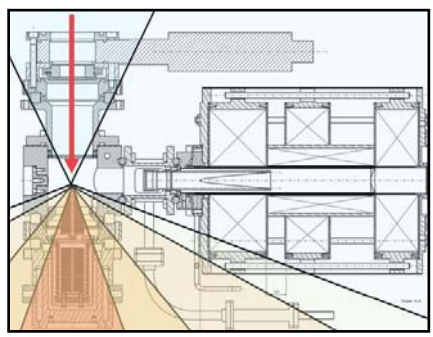

Figure 1: angular distribution of neutrons downstream from the target

The carbon target is placed close to the permanent magnets of the ion source (Nanogan III), which can then be damaged by neutron irradiation, leading to losses in axial and radial confinement of the source. For this reason, after a radioactive decay period of some years, the irradiated TISSs are placed in a glove box and dismounted. The target part is discarded as nuclear waste, and the magnetic field of the ion source is measured: if it is still acceptable, the ion source is reassembled with a new target.

During recent years, magnetic measurements have revealed more and more damage. Among the eighteen TISSs constructed since 2001, two types of degradation have been observed:

(a) Degradation of the injection magnet (close to the target):

Figure 2 shows an example of the decrease of the axial magnetic field on the injection side, with no modification at the opposite (or extraction) side.

Measurements all around the injection magnet (Figure 3) show an average loss of magnetic field of about 20%, with a maximum of 40% on the target side.

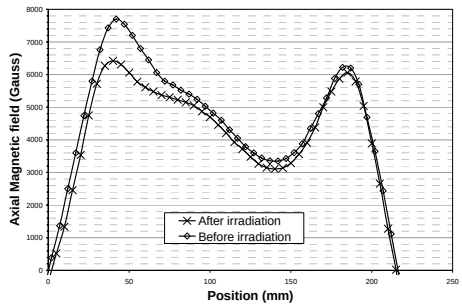

Figure 2: axial magnetic field before and after irradiation along the axis of the ECRIS.

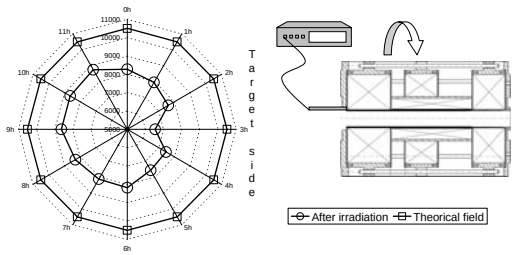

Figure 3: radial magnetic field measured on the injection magnet (left) and schematic of the measurement method (right).

(b) Damage to the hexapole:

A significant decrease of the radial magnetic field has also been measured on different TISSs (Figure 4).

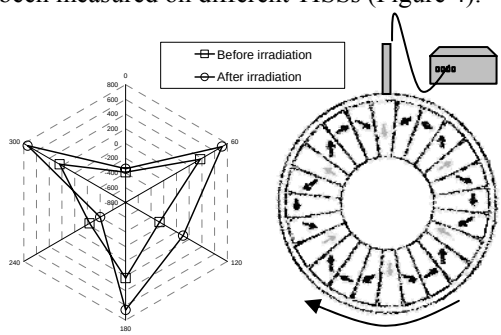

Figure 4: Radial magnetic field of the hexapole structure before and after irradiation (left side), and schematic of the measurement method (right).

This damage to the magnets can be explained by the coercivity of the magnets and by the intensity of the neutron flux

- Coercivity of the magnets

One important characteristic of the magnets is their coercivity, which corresponds to the maximum magnetic field they can withstand without magnetic changes. Moreover, this maximum strongly depends on the temperature (Figure 5). In the case of the NANOGAN III ECRIS, some magnets are subjected to fields close to the maximum.

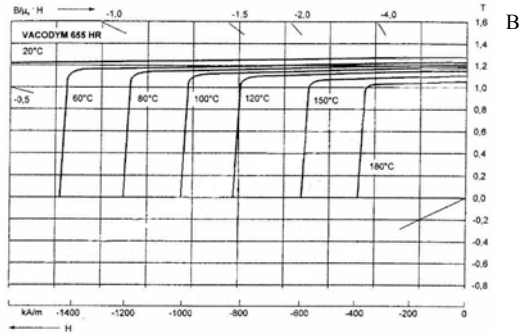

Figure 5: Coercivity of permanent FeNdB magnets (Vacodym 655HR) for different temperatures. *B* is the remanence field and *H* is the opposite magnetic fields.

- Particle effect on the permanent magnets

Neutrons, protons, gamma rays and light fragments produced by primary beams of energy ranging from 60 A.MeV to 95 A.MeV striking a carbon target can reach and damage the magnets [2]. Neutrons especially, with energies up to 95 MeV, have a high cross section for interaction with the boron contained in the magnets, and can thus damage them by microscopic structural modifications of the material.

The magnetic components of all the irradiated TISSs cannot be fully dismounted to do a fine diagnosis, particularly for the hexapole structure. Thus all the refurbished sources are tested on a dedicated test bench to ensure the same test conditions during the tests, allowing us to make a comparison of the performance of the respective sources. The charge state distribution of the argon spectrum (fig. 6) is taken as a reference to determine if a TISS is suitable for use in the SPIRAL ISOL process.

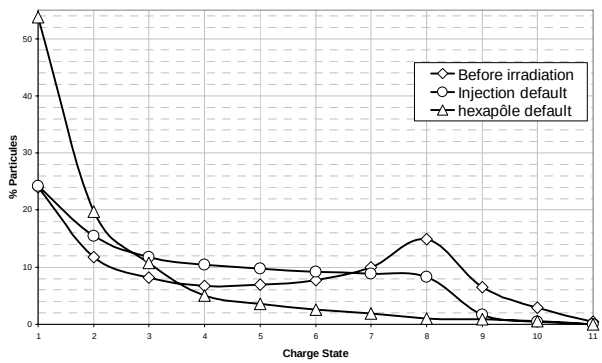

Figure 6: Influence of the state of the magnetic structure on the charge state distribution of argon.

Two types of target are used on SPIRAL, one for He production, and one for heavier gas production. Owing to the position of the He target, closer to the source axis than the other, and because the first degradation occurred with "He type" targets, we thought that the magnets were exposed to a more intense neutron flux.

This assumption was not confirmed, after we calculated the number of neutrons seen by each ion source.

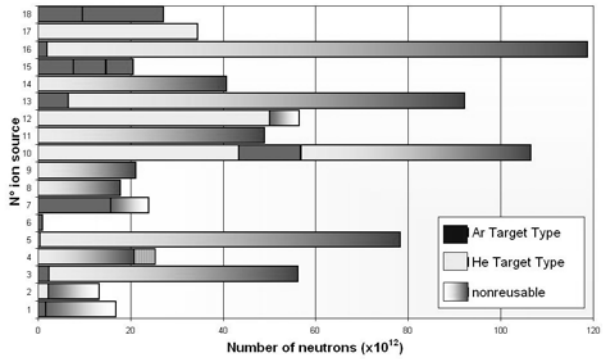

Figure 7: Reference number of each irradiated source versus total neutron number seen by the source. The different shading correspond to the type of target used for the run. A darker shade means the ion source cannot be reused.

CONCLUSION

We are not able to predict when the ion source will become unusable. The damage to the magnets depends on the neutron flux, but also on the primary beam features (energy, intensity, position on the target) and on the kind of target.

As on-line diagnosis is not possible while the beam is delivered to the physics experiments, we check the performance of each ion source at the end of a run, and check the magnetic field after the storage period and we also check the off-line performance of the source on a test bench before using the TISS in the production cave.

RADIOACTIVE ALKALI ION BEAM DEVELOPMENT FOR SPIRAL 1: ISSUES

In the framework of the production of multi-charged radioactive alkali ion beams in SPIRAL 1 at GANIL, a surface ionization source associated with the multi-charged ECR NANOGAN III [3] has been developed to produce singly-charged ions of Na and K. The system, called NanoNaKE, produces radioactive atoms in a carbon target, which diffuse and effuse into a surface ionizer. Once ionized, they are accelerated by an extraction electrode to form a beam, which is shaped by an electrostatic lens to go through a drift tube before entering the ECRIS chamber. This very compact system has demonstrated the possibility to convert $^{47}K^{+}$ ions into $^{47}K^{5+}$ ions, but with an efficiency somewhat lower than that expected [4].

These low efficiency results could have different origins:

- Losses during the 1+ beam transport by the spread in energy and angle induced by interaction of the 1+ ion beam with the residual gas coming from the hot parts of the system (i.e. the oven and ionizer) and from the ECRIS (feeding gas).
- Losses by interaction of the 1+ beam with the backward N+ ion beam extracted from the ECR ion source.

Since the target and 1+ ion source system has previously been characterized, it has been removed and replaced by an alkali ion gun, which is easier to use: the emerging ion current easily can be measured, and it can be chopped, which is important to determine if the multi-charged ions observed at the exit of the ECRIS come from a slow conversion process (migration of atoms from the 1+ to the ECRIS and ionization) or from a fast conversion process (transport as 1+ ions from the 1+ to the ECRIS, capture and charge breeding). The behavior of the ion gun and the transport in the beam line have been previously simulated using the CPO (Charged Particle Optics) program [5] and SIMION [6] codes

Experimental measurements

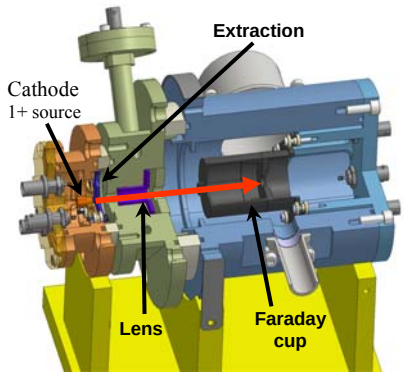

Figure 8: Setup for calibrating the alkali ion gun

The current and time calibration of the 1+ alkali ion gun was performed with a dedicated setup (Figure 8), for a maximum $^{39}K^{+}$ current of 15µA.

After calibrating the alkalis ion gun, the system was installed on the NanoNaKE setup.

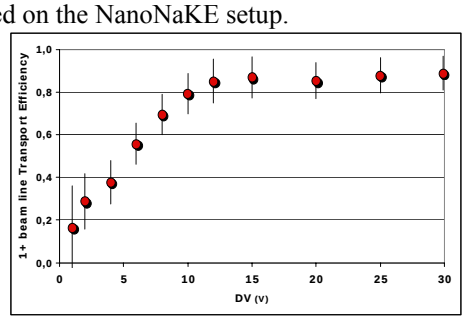

Figure 9: 1+ beam line transport efficiency versus voltage difference ΔV applied between the 1^{+} ion source and the ECR potential.

One of the main conclusions is that a voltage difference ΔV applied between the 1+ ion gun and the ECRIS potential must be higher than 12V to obtain a transport efficiency higher than 80%. But this value may be too high for ion capture by the ECR plasma, according to the "charge breeding" [7].

Owing to the design of the present beam line, several problems occur: at low ΔV, the current extracted from the alkali emitter decreases up to values difficult to observe, and the focus of the beam does not act as expected from simulations and the losses increase strongly. Moreover, the lack of physical separation between the different electrostatic electrodes induces a coupling of their effects. Finally, for a voltage of some hundreds of volts – which is a minimum to transport a 1+ beam while minimizing the losses – a Penning discharge appears on the beam line, inducing currents on the different electrodes much higher than the 1+ ion beam current, thus making it difficult to determine the transport efficiency.

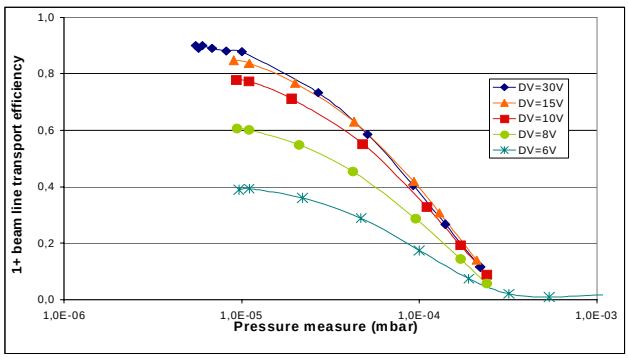

Figure 10: Gas pressure effect on the 1+ beam line efficiency.

As shown in Figure 10, one main origin of the losses during the 1+ beam line transport is probably the rest gas pressure. In our case, the order of magnitude of the pressure was estimated to some 10^{-4} mbar.

As the losses during the transport and the background of the ECRIS (when ON) are too large, it has until now not been possible to observe the charge breeding conversion.

CONCLUSION

A diagnostic study of the 1+ beam line has been made and several problems have been revealed:

- a gas pressure effect
- coupling of the electrodes
- limited value of extraction potential
- Penning discharge.
- a difficulty in simulating ion transport at low energy (□10V)

A new 1+ beam line (fig.11) is under construction, taking account all these problems. The next tests should be performed by the end of 2008.

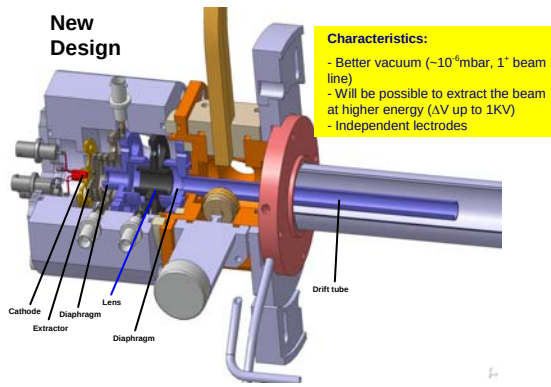

Figure 11: New 1+ beam line design

References:

[1] GANIL web site : http://www.ganil.fr
[2] N. Lecesne. These "Study of multicharged radioactive ions production on line". (1997) p 112.
[3] C. Eléon et al., Proceedings of EMIS 2007, to be published by Nucl. Instrum. and Methods in Physics Research, Section B (NIMB).
[4] C. Eléon et al., Proceedings of ICIS07, to be published in Rev. Sci. Instrum.
[5] CPO Programs, available on the web site http:// electronoptics.com
[6] SIMION Program.
[7] N. Chauvin, PhD Thesis, Grenoble (2000)

PAPER NOT RECEIVED

OPERATIONAL EXPERIENCE WITH THE 18 GHz HTS-ECRIS, PKDELIS*

G.Rodrigues*, P. S. Lakshmy, Y. Mathur, U. K. Rao, R. N. Dutt, P. Kumar, A. Mandal, D. Kanjilal & A. Roy
Inter University Accelerator Centre, Aruna Asaf Ali Marg, New Delhi -110067, India

Abstract

The high temperature superconducting electron cyclotron resonance ion source (HTS-ECRIS), PKDELIS was installed at IUAC in the beginning of 2005. There were some initial problems with one of the two cryo-coolers for the axial HTS coils and vacuum related problems at the intermediate location for test run. These were rectified subsequently. X-ray Bremsstrahlung measurements are carried out systematically to develop deeper understanding of the ECR plasma production processes. The source and low energy beam transport (LEBT) system are planned to be re-installed on a high voltage platform in the new beam hall III to prepare for injection into high current injector of the superconducting linear accelerator. Recent results of the PKDELIS and operational experience will be reported.

INTRODUCTION

At the Inter University Accelerator Centre, New Delhi, the accelerator augmentation programme involves the development of new accelerators for further boosting the beam energies to above 5 MeV/u (above Coulomb barrier) around mass 100 a.m.u. With the existing tandem accelerator, it was realised that the beam currents and mass range available were not sufficient for most of the experiments in nuclear physics and related areas The tandem-LINAC combination in parallel with a high current injector was proposed to meet the above design goal [1]. An alternate high current injector was proposed based on a reasonable high performing electron cyclotron resonance ion source capable of delivering higher beam currents and covering a wide mass range [2]. In this paper, the operational experiences of the HTS-ECRIS PKDELIS at ground potential (presently) is described. This kind of source was designed for operation on a 400 kV high voltage platform to inject beams with initial velocities at 1 % of the velocity of light and further accelerate to ~ 8 % of the velocity of light before injection into the superconducting linear accelerator. In the near future, the source and low energy beam transport section will be finally shifted for installation on a high voltage platform to prepare for injection into the superconducting linear accelerator. The new beam hall III construction is complete and various beam hall utilities are nearing completion.

#gerosro@gmail.com

HTS-ECRIS PKDELIS

The HTS-ECRIS PKDELIS is designed for operation at two frequencies, viz. 14.5 and 18 GHz. Further description of the source can be found in earlier publications [3]. The test bench results of the source at Pantechnik, France during the end of 2003 gives more information about the beam currents of various ions extracted which are required for the high current injector [4]. Later, the source was initially installed at our centre at a test set-up position in the beginning of 2005. The source commissioning was delayed due to various problems that are described below.

Cryo-cooler cool down issues

During initial start-up, we had problems with the extraction cryo-cooler which eventually could not cool down the coil to ~ 20 K. This limited the source start-up and delayed the source commissioning. Initially it was thought that that due to the leak in the helium line, the cooling efficiency reduced. After re-charging the line (adding more helium), the cooling did not improve. It was further thought that the helium was contaminated. The helium was completely removed and re-charged again which still did not improve the situation. Since the extraction cryocooler was generating a much feebler sound when compared to the normal operating injection cryocooler which had a loud tapping sound, it was decided to open up the cold head section to investigate further. It was found that the bottom flange was not properly fastened to the piston and this impeded the motion and resulted in poor performance. This was rectified and the efficiency of the cooling improved. The vacuum on the injection side of the source was also poor leading to lower charge states. After these problems were rectified in the beginning of 2007, a wireless control system for operating the source in the middle of 2007 was implemented. The source was finally commissioned during the end of 2007.

Wireless control system

After experiences with other accelerators using fibre optic cables for source control especially in high voltage environments, using a wireless communication would appear to be better in terms of minimising the source downtime especially for running round-the-clock experiments. A wireless control system was developed based on MODBUS RTU on RS 485. Using 2.45 GHz radio modems, and PLC's for interlocking purposes, a

client-server based remote control was established and proved economical and highly reliable. The software uses LABVIEW based HMI software.

Source performance

A schematic view of the source together with the low energy beam transport system coupled to a large acceptance analysing magnet [5] is shown in figure 1. below. Typical base pressures at the injection side and post analyser section are 3 x 10^{-7} mbar and 1 x 10^{-8} mbar. A typical spectrum optimised on Ar^{8+} at an absorbed power of 300 W is shown in figure 2.

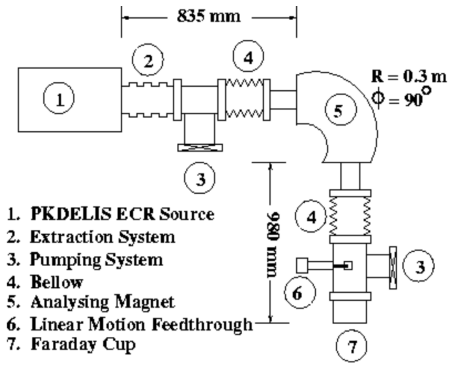

Figure 1: Schematic of the low energy beam transport system

The optimised parameters were RF power, gas pressure, bias voltage, axial field and position of the RF tuner. These were the main determining parameters besides the extraction voltage (for improving the transmission) for obtaining 300 µA of Ar^{8+} at 300 W absorbed power

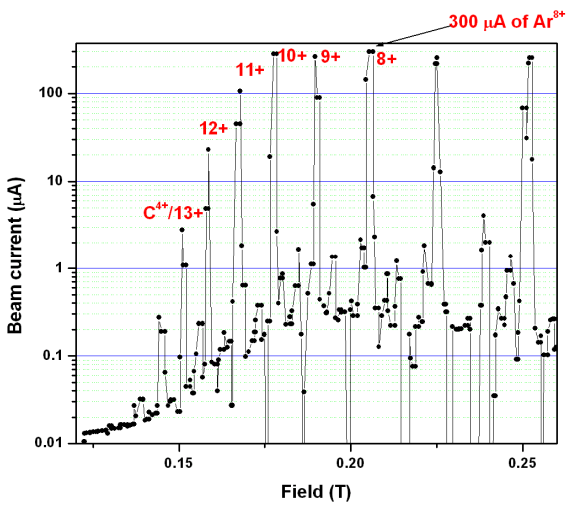

Figure 2: CSD optimised on Ar^{8+}

without using mixing gases. A table showing the optimised parameters is shown below (Table 1.).

Table 1: parameters optimised on Ar^{8+}

parameter	**value**
RF absorbed power	300 W (330 W/30 W)
Extraction voltage	25 kV
Injection vacuum	1.4 x 10^{-4} mbar
Post analyser vacuum	8.6x 10^{-7} mbar
Bias voltage	–134 V
Bias current	0.22 mA
B_{min}/B_{ecr}	0.58
Total source current	4 mA
Injection / extraction field	1.4 T / 0.95 T

Use of mixing gas with argon, the beam current of Ar^{8+} is expected to improve further. Due to a leak in the mixing gas line, it was not possible to further improve the beam currents at present. Further optimisation on Ar^{11+} at higher levels of power showed that it was possible to extract 150 µA of Ar^{11+} at 425 W of totally absorbed power. Figure 3. shows a charge state distribution optimised on Ar^{11+}.

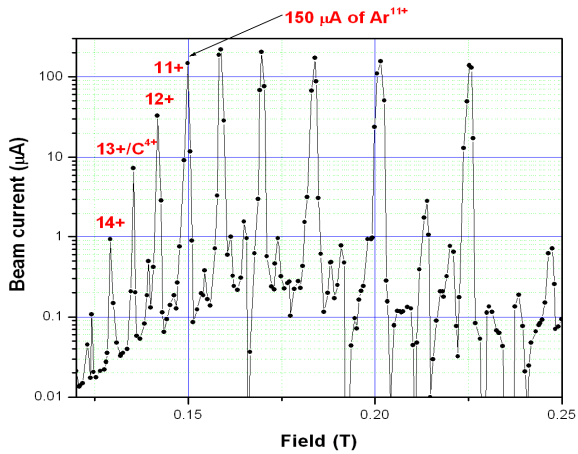

Figure 3: CSD optimised on Ar^{11+}

Table 2: parameters optimised on Ar^{11+}

parameter	**value**
RF absorbed power	425 W (473 W/48 W)
Extraction voltage	20 kV
Injection vacuum	1.1 x 10^{-4} mbar
Post analyser vacuum	6.4 x 10^{-7} mbar
Bias voltage	–110 V
Bias current	0.05 mA
B_{min}/B_{ecr}	0.58
Total source current	3.4 mA
Injection / extraction field	1.4 T / 0.96 T

During the tuning and optimisation of Ar^{8+} and Ar^{11+} beams, it was observed that the best axial field distribution (shown in figure 4.) corresponding to B_{min}/B_{ecr} was best at the value of 0.58 which was the calculated value from the observed injection and extraction fields. This value does not change for medium (8+) and high charge state (11+) of argon although the value of the extraction field changes slightly. From the measurements, it was also observed that the injection vacuum deteriorates when sufficient gas is bled into the source. This may be limiting the build up of higher charge states. Further improvements in the gas injection line/pumping system are being pursued.

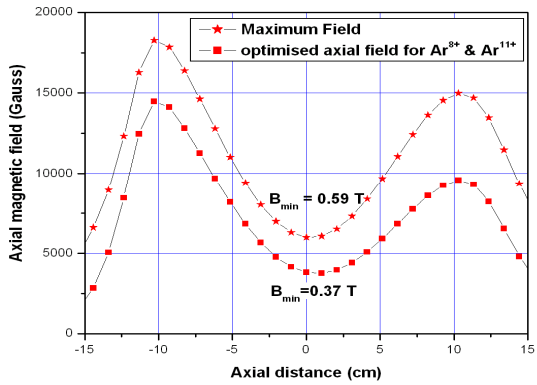

Figure 4: Optimised axial field for Ar^{8+} and Ar^{11+}

X-ray Bremsstrahlung measurements

Besides the beam optimisation experiments of argon for medium and high charge state, it was necesssary to measure the x-ray Bremsstrahlung and if possible to correlate with the beam optimisation experiments for argon. Alternatively these measurements could give further information on the source performance. Therefore, it was decided to measure the x-ray Bremsstrahlung using NaI detector due to the higher efficiency as compared to a germanium detector. X-ray Bremsstrahlung was measured using a 3 inch NaI detector from the ECR plasma along the extraction side through the 0^o port of the analysing magnet.

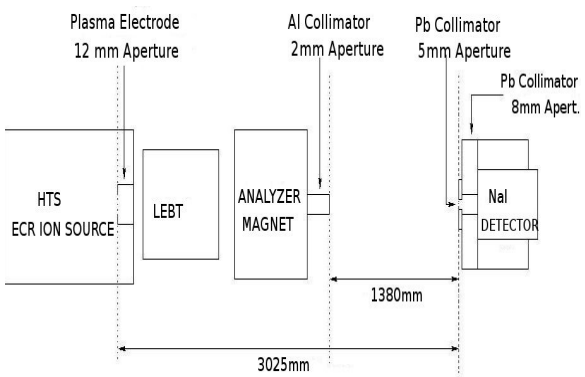

Figure 5: Schematic of X-ray Bremsstrahlung measurement set-up

A schematic of the set-up to measure the x-ray Bremsstrahlung is shown in figure 5. Special care was taken to shield the detector using Pb bricks and to collimate the x-ray Bremsstrahlung from the plasma only. Besides the plasma electrode having an aperture of 6 mm, three additional collimator's are used for proper collimation as shown in the figure. One collimator of diameter 2 mm, length ~ 50 mm and made of aluminium was positioned on the analysing magnet 0^o exit port at a distance of 1645 mm from the plasma electrode. An additional collimator made of lead and having a diameter of 5 mm and length 2 mm (positioned at a distance of 1380 mm from the first collimator) was sandwiched on to another collimator of diameter 8 mm and length 50 mm. The detector was positioned behind the last collimator with proper lead shielding around it using 50 mm thick lead bricks. Due to the high count rate, the distance between the detector and the source had to be increased. The x-ray spectra were measured as a function of negative bias voltage keeping the extraction voltage OFF with each measurement taken for 900 seconds (shown in figure 6.). The other parameters relevant for this measurement are shown in table 3 below.

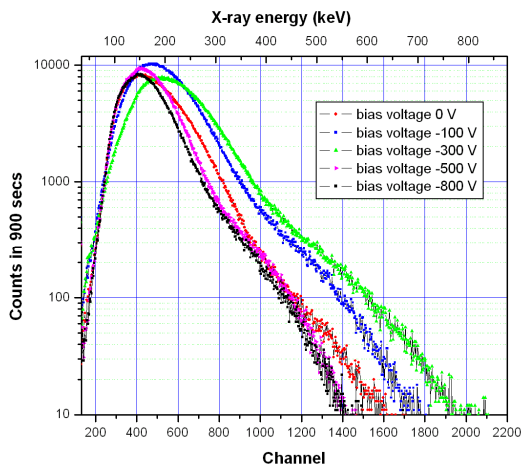

Figure 6: X-ray Bremsstrahlung spectra as a function of negative bias voltage

Table 3: parameters set for X-ray Bremsstrahlung measurements

parameter	**value**
RF absorbed power	400 W
Extraction voltage	OFF
Injection vacuum	1.0 x 10^{-4} mbar
Post analyser vacuum	3.2 x 10^{-7} mbar
B_{min}/B_{ecr}	0.58
Injection / extraction field	1.4 T / 0.95 T

From these measurements, it can be observed that as the bias voltage was increased up to -300 V, the bias voltage

had a maximum effect on the x-ray Bremsstrahlung at a value of -300 V in terms of increased x-ray energy (data plotted in green colour) and shift of the peak of the distribution. From the value of -500 V and that at -800 V, the effect was of reducing the x-ray Bremsstrahlung. So it can be inferred that the negative bias effect was best at the value of -300 V. However, in the beam optimisation experiments for argon (Ar^{8+} and Ar^{11+}), the best beam currents at this value assuming similar vacuum conditions, Rf power and magnetic fields were not observed. The best value was -134 V for optimising on Ar^{8+} and -110 V for Ar^{11+}. The explanation for this behaviour is not available at the moment. The errors involved in these measurements are quite small and do not significantly influence this behaviour. It should be pointed out that when the extraction voltage was raised to 20 kV, the slope of the distribution had a bump from 150 keV onwards. Most probably the emission of this additional Bremsstrahlung is due to change of the electron trajectories inside the source. This is shown in figure 7.

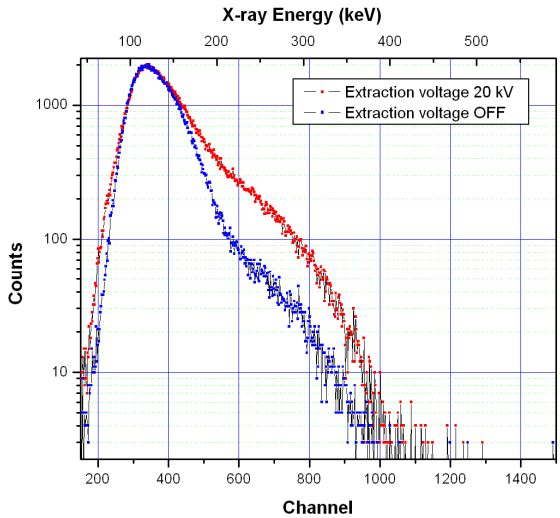

Figure 7: X-ray Bremsstrahlung spectra as a function of negative bias voltage

CONCLUSIONS

From the time the source was commissioned at the test set-up at ground potential, the operational experiences of the source have been satisfactory so far. Much higher beam currents are expected by using mixing gas which was not possible at present due to a leak in the injection line. The source stability has been good. The x-ray Bremsstrahlung shows that there exists high energy electrons measured up to 800 keV at the optimum field corresponding to $B_{min}/B_{ecr} = 0.58$.

REFERENCES

[1]A. Roy, Curr. Sci. **76** (1999) 149.
[2]D. Kanjilal, G. Rodrigues, C. Bieth, S. Kantas, P. Sortais, C. P. Safvan,P. Kumar, U. K. Rao, A. Mandal, and A. Roy, ***Proceedings of Indian Particle Accelerator Conference*****,** Indore, India, 3–6 February 2003,p. 144 unpublished ;D. Kanjilal ***et al.*****,** ***16th International Workshop on ECR Ion Sources*****, AIP** Conf. Proc. Vol. 749, Berkeley, 26–30 September 2004, p. 19.
[3]C. Bieth, S. Kantas, P. Sortais, D. Kanjilal, G. Rodrigues, S.Milward, S. Harrison, and R. McMahon, Nucl. Instr. Meth. B **235** (2005) 498
[4]D.Kanjilal, G.Rodrigues, P.Kumar, A.Mandal, A.Roy, C.Bieth, S.Kantas, P.Sortais, Rev.Sci.Instrum.,**77** (2006) 03A317
[5]A. Mandal, G. Rodrigues, D. Kanjilal, Peter Brodt, Franz Bødker, Nucl. Instr. and Meth. A 583 (2007) 219

MICROWAVE POWER SAVING AND REDUCED BREEMSTRAHLUNG EMISSION FOR A HIGH CHARGE STATE ION PRODUCTION IN AN ECRIS EQUIPPED WITH MD STRUCTURES*

L. Schachter,[1] K. E. Stiebing[2], S. Dobrescu[1]

[1)]National Institute for Physics and Nuclear Engineering, Bucharest, Romania
[2)]Institut für Kernphysik der J. W. Goethe Universität, Frankfurt / Main, Germany

Abstract

Metal dielectric structures (MD), installed in the plasma chamber of the Frankfurt 14GHz electron cyclotron resonance ion source (ECRIS), have been used to significantly reduce the level of microwave power, necessary to create comparable ion intensities as for the standard operation of the Frankfurt ECRIS. The measurements indicate that the RF-power may be reduced by a factor of 2-3 to obtain the same output of high argon charge states as in the standard source with stainless steel plasma chamber. This reduced level of microwave power also leads to a much lower level of X-ray emission from the source.

INTRODUCTION

The performance of an electron cyclotron resonance ion source (ECRIS) may be expressed in terms of the „quality factor" QF= $n_e \bullet \tau_{i,}$, where n_e is the density of the plasma electrons and $\tau_{i,}$ the ion dwell time in the plasma. Basically all methods and scaling prescriptions for the optimization of an ECRIS act on one or both of the above factors. One consequent approach is the continuous increase of the microwave power and frequency to enhance the density and energy of the plasma electrons. In modern constructions (e.g. 4th generation ECRIS) this usually goes along with a continuous increase of the plasma volumes, which now have several times the volumes used e.g. in the 14GHz sources of the second generation. Special effects like gas mixing, isotope effect or wall coating also base on the optimization of the above two factors. Approaching the 4th generation of ECRIS's now with microwave powers of tens of kW at frequencies as high as 28-30GHz, reveals unexpected technical problems which set serious constraints to the continually scaling of e.g. the frequency as suggested by the above formula. Only one of these limits is the massive heat load transferred by the Bremsstrahlung radiation into the plasma chamber walls and into the superconducting structure of the magnetic trap. Superconducting technology has become necessary to fulfill both, the resonance condition but also the need for very high mirror ratios for the effective electron confinement.

In this article we report on a method to significantly reduce this production of Bremsstrahlung radiation or alternatively to substantially improve the performance of existing sources of the 2nd and 3 rd generation. This method is based on a development made at the Institute of Physics and Nuclear Engineering, Bucharest, Romania, and consists in the production of metal- dielectric (MD) structures (Al-Al_2O_3 transitions) by a special electrochemical treatment of pure aluminum plates. The structures are characterized by high yields of secondary electron emission under bombardment by charged particles (electrons and ions from the plasma), which serves to significantly enhance n_e by sending cold electrons to the plasma, when MD-layers are introduced as wall coating into the plasma chamber [(2)]. Additionally, facing the plasma as insulators , the MD structures substantially increase the ion dwell times (ion confinement) by blocking compensating wall currents, hence restoring the plasma ambipolarity. The degree of this restoration depends on the actual configuration of MD-coverage of the plasma chamber walls and can be almost complete even if only part of the chamber is covered by the MD structure [(1)].

In this way, MD structures allow operation of the source at lower working pressure and RF powers. The reduction of the working pressure is very important to minimize charge exchange and electron recombination in the plasma and in the extraction region. The MD-ECRIS gives much better results than using gas mixing [(4)] . It is an additional advantage of the use of MD structures that the extraction of distinctly different charge states (e.g. Ar^{5+}, Ar^{10+}, and Ar^{15+}) from one source tuning is not excluded like in the case of gas mixing.

In the present experiment we focus on the possibility to utilize MD structures to extract essentially the same ion-beam intensities like in the standard ECRIS, however, at a strongly reduced level of RF power. This, of course, means also a significantly reduced level of emission of X-rays with important consequences for the lifetime of ECRIS components, for safety considerations and, quite generally, for the feasibility of improvements.

EXPERIMENTAL PROCEDURE

The experiment was performed at the 14 GHz IKF ECRIS of the Institut für Kernphysik, Frankfurt/Main, Germany (IKF). The plasma chamber of the source was equipped with two MD-structures of 1mm thickness. One structure (MD-liner) was installed in the stainless steel plasma chamber symmetrically with respect to the hexapole magnet for the radial plasma confinement. It covered the radial walls at a length of 150 mm (i.e. roughly 3/4 of the whole radial plasma chamber walls). The other structure (MD-electrode) covered the entire

stainless steel extraction electrode of the source. The emissive layers of both structures faced towards plasma.

The source geometries and the main electrical parameters were kept unchanged during all measurements. The extraction voltage was 15 kV and measurements were performed at RF power levels of 200-1000 W. Tests were also performed up to 1500 W. Two types of working gas were used, pure argon and argon-oxygen mixing gas(20% Ar + 80%O_2). The beam optical elements were optimized for the transport of Ar^{8+}, Ar^{12+} and Ar^{14+} ions.

During the experiment the CSD for different levels of the microwave power at different optimizations were registered and studied for the source operated in "reference" mode (i.e. standard stainless steel source) and for the "MD-ECRIS" (i.e. with the above described insertions.

The X-ray emission form the source was measured using a Ge(Li) detector positioned ~4 m downstream from the source. Its solid angle was limited to the size of the extraction electrode by means of a special multilayer-collimator (Pb-Cu-Al) with a bore of 50mm in length and 1mm in diameter. Typical values of the vacuum during operation of the source were at the injection (1.0 - 5.0) x 10^{-7}mbar and (7.0 - 8.0) x 10^{-8} mbar at the extraction. A biased stainless steel electrode was located at the injection side of the plasma chamber. Axial position and voltage of this electrode were adjusted by optimizing the extracted ion currents measured in a Faraday cup after the 90^0 analyzing magnet.

RESULTS AND COMMENTS

In a previous publication we have demonstrated the gain of performance of an ECRIS equipped with MD structures (MD-electrode and MD-liner) [1]. In figure 1 this is shown again for the new series of experiments. The spectra shown in figure 1 are for a source tuning for the production of intermediate charge states of argon.

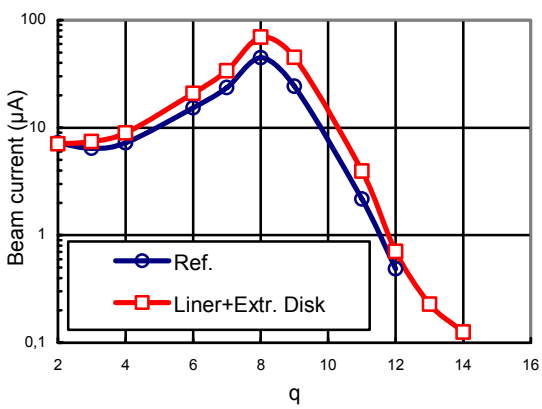

Figure 1

The beam transport system was tuned for the transport of Ar^{8+}. Indeed, as expected from a partial restoration of the plasma ambipolarity[3], all currents of the extracted charge states are enhanced compared to those, obtained from the reference mode (denoted as Ref. in the figure). Up to q ≤ 11+ this enhancement varies from 30% to 90%. The apparent decrease for the charge states higher than q = 11 is readily understood from the source tuning at intermediate charge states, where the comparatively high source pressure leads to increased charge transfer. Hence recombination rates are higher as compared to a typical tuning for highest charge states. The measurements were performed at 800 W RF power.

As demonstrated in a large number of experiments [4,5], MD structures (in particular MD liners covering the radial plasma chamber walls) are capable of enhancing the high-charge -state ion production from an ECRIS by orders of magnitude. Therefore, the most interesting situation is represented by the gain for the production of high charge states. It was the purpose of this experiment to take advantage of this performance and to introduce a facile possibility to strongly reduce the level of microwave power and still obtain the same high beam intensities for highly charged ions as in the reference mode at high microwave powers.

The results from this series of measurements are summed up in the nomograph in figure 2. It is evident that the necessary RF power is reduced by a factor 2-3 for obtaining the same intensity of Ar 12+ / Ar 14+ if MD-structures are installed. For example, to obtain 100nA of Ar 14+ a RF-output level of 800 W was needed in reference mode, whereas only 380 W were necessary with the MD-structures installed at otherwise very similar conditions of tuning of the source and the beam optics.

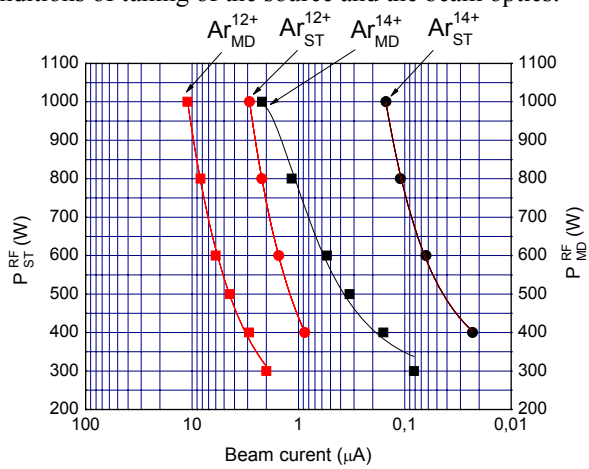

Figure 2

A series of dedicated experiments[6] demonstrate that the MD structures in the plasma chamber of an ECRIS generally serve to drastically reduce the level od electron Bremsstrahlung radiation compared to the standard(stainless steel) source. This very important consequence is illustrated in figure 3, where the Bremsstrahlung radiation spectra for Ar^{12+} (with MD at 300 Watt) and Ar^{12+} (reference at 800 Watt) are compared. The use of MD structures allows a reduction

in X-ray load by a factor of 10 for obtaining the same output of highly charged ions as in reference mode. It is obvious that any reduction of the level of microwave power and hence of X-ray load to the source components is transferred into longer source lifetime, into relaxed safety problems and, last but not least, into considerably reduced energy consumption.

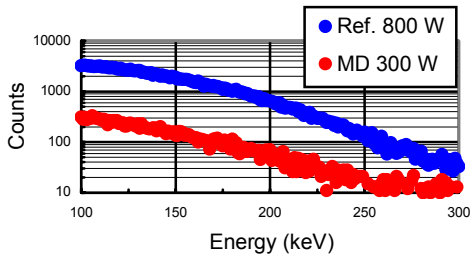

Figure 3

This gain in source performance is entirely due to the intrinsic properties of the specially produced MD layers. It cannot be achieved by any other of the established methods to increase beam intensities extracted from an ECRIS. In particular, despite of contrary experimental evidence [5] "gas mixing" is still sometimes misunderstood as the working mechanism of the MD effect. We therefore have carried out one series of measurements with Ar/O_2 mixing gas. An optimized mixture of 20% argon and 80% Oxygen has been used.

The results are displayed in figure 4 It is obvious, that gas mixing in the presence of the MD structures in the plasma chamber changes the shape of CSD. While the high charge states are increased by a factor of less than 2 compared to MD, lower charge states are strongly depleted if compare with the depletion due to the MD for the same plasma. The total amount of extracted ions is not drastically changed. This is in clear contrast to the MD-effect, which increasing the output from the source significantly for all charge states(fig 1) has a much lower effect on the low charge state depletion as the gaz mixing.

This relative gain is stronger for very high charge states, as one would expect from a more ambipolar source. This fundamental difference is enhanced by the fact, that for the case of MD, after some period of conditioning, the amount of gas admixtures (representing an unwanted background here) becomes more and more negligible (less than 1‰ at effective MD-layers) at otherwise unchanged or even still improving performance. In contrast to this, with mixing gas the dominant content of ions in the plasma consists of supporting gas ions. The result displayed in figure 4 is is in perfect agreement with earlier dedicated experiments,where we have shown that the intrinsic MD effect is 3 times stronger than the gas mixing effect.[4]

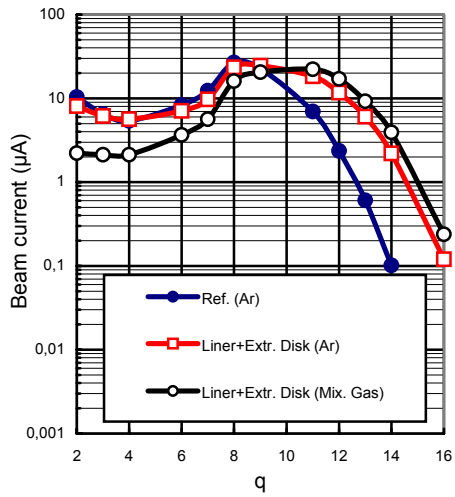

Figure 4

REFERENCES

[1] L. Schachter, K. E. Stiebing, S. Dobrescu, T. Thuiller, T. Lamy, Rev. Sci. Instrum. 79,2, 02A 329, 2008

[2] L. Schachter, S. Dobrescu, K.E. Stiebing, J.D. Meyer, Rev. Sci. Instrum. 75,5,1511, 2004

[3] A. G. Drentje, U. Wolters, A. Nadzeyka, D. Meyer, and K. Wiesemann, Rev. Sci. Instrum. 73, 516, 2002

[4] L. Schachter, K.E. Stiebing, S. Dobrescu, Al. I. Badescu- Singureanu, S. Runkel, l. Schmidt, and H. Schmidt-Bocking, Rev. Sci. Instrum. 71,2 .918, 2000

[5] L. Schachter, S. Dobrescu, G. Rodrigues and A. G. Drentje, Rev. Sci. Instrum. 73, 2, 570, 2002

[6] L. Schachter, K. E. Stiebing, S. Dobrescu. "Influence of the ECR plasma confinement on reducing the Bremsstrahlung production of an ECRIS with MD configuration" (to be submitted for publication)

PAPER NOT RECEIVED

PAPER NOT RECEIVED

MODELING ECRIS PLASMA USING 2D GEM* (GENERAL ECRIS MODEL)

L. Zhao#, J. S. Kim, B. Cluggish,
FAR-TECH, Inc., San Diego, CA 92121, U.S.A.

Abstract

The GEM 1D code [1] is developed by FAR-TECH, Inc. to model the plasmas in ECRIS devices using experimental knobs such as the magnetic field, rf power and frequency, and the geometry of the device. The code models EDF (electron distribution function) by solving Fokker-Planck equation, ions as fluid and neutrals by particle balancing. It has been extended to include 2D (axial and radial) spatial features such as 2D ECR heating and ion radial diffusion. The convergence and consistency of the code have been studied. It is parallelized using the MPI technique to boost the calculation speed. Results of the GEM 2D simulation and comparisons of GEM 2D with GEM 1D results and experimental measurements will be presented. The predicted hollow profile of ECRIS plasma is consistent with experimental observations.

INTRODUCTION

GEM 2D is extended from an advanced ECRIS modeling code, GEM 1D, which has been developed by FAR-TECH to predict axial steady-state ECRIS plasma profiles and charge state distribution (CSD) of output beam self-consistently using experimental knobs as input, such as rf power, rf frequency, gas pressure, and device configurations. GEM 1D calculates non-Maxwellian EDF (electron distribution function) of hot electrons using a bounce-averaged Fokker-Planck code [2] and solves the flow of the cold ions using 1D ion fluid code. It has obtained some numerical results consistent with experiments. However, the further applications of GEM to beam capture [3] and beam extraction simulation require GEM to be extended to 2D to acquire both axial and radial profiles of the plasma parameters. Also, 2D models can simulate the complicate magnetic field in ECRIS and ECR heating zone more accurately. This paper presents the modeling theories of GEM 2D and the results of the simulation of a typical ECRIS device, ECR-I in ANL [4]. The comparisons with GEM 1D results and experimental data will also be presented and discussed.

DESCRIPTION OF GEM 2D MODELS

GEM-1D simulates the dynamics of an ECRIS plasma along the field lines but assumes the plasma is uniform in the radial direction. GEM 2D is extended from GEM 1D by adding a radial dimension to GEM 1D's numerical models. It can predict ECRIS plasma in both radial and axial directions by a combination of 2D physical models including 2D magnetic field and ECR heating modeling, bounce-averaged Fokker-Planck EDF modeling and 2D ion fluid modeling. In the following discussion, we will use ECR-I at ANL as the standard device for the simulation. The typical operation parameters are listed in table 1.

Table 1: Operating parameters for ECR-I

Parameters	Typical Values
Plasma	Oxygen
Length	29 cm
Radius	4 cm
Gas pressure	1.2e-7 Torr
rf power	323W
rf frequency	10 GHz
B field ratio	4.5 and 3

2D modeling of the Magnetic field and ECR resonance surface

The magnetic field on ECR-I is a typical minimum-B structure which is composed by a mirror field and a hexapole field. The full 3D ECR resonance surface is a football shape structure [5] which depends on z, r, θ in cylindrical coordinate. For 2D simulations, the magnetic field is azimuthally averaged to eliminate θ dependence. The radial grids are tied onto the flux surfaces that are evenly distributed on the mid-plane and then extended to the whole chamber along the field lines (Fig 1a). The axial profiles of the field strength on the field flux surfaces are plotted in Fig. 1b. Note that the field strength increases with radius. This is because while we average over the hexapole variation in the direction of magnetic field, the magnitude of the hexapole field strength is still included in GEM-2D. This allows a proper calculation of the ECR resonance zone.

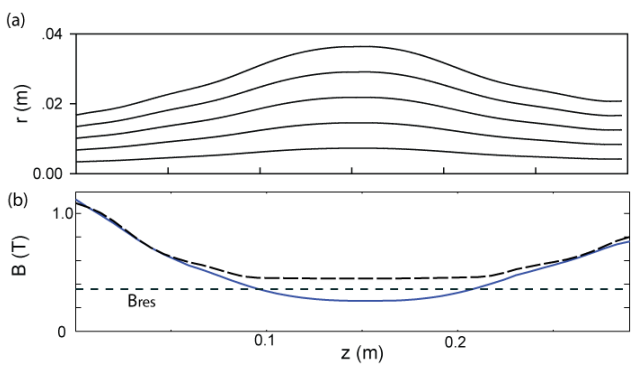

Figure 1: a) Radial grids that are tied onto the magnetic

field lines. b) Magnetic field strengths along the field lines. The short dashed line is the resonance field, B_{res} =0.357 T. The solid line is the field along the field line that is at r=0, the long dashed line is the field along the field line outside of the resonance zone at r=0.03m.

The 2D azimuthally averaged ECR resonance surface is shown in Fig. 2. The ECR resonance surface is a closed surface which is distributed on both radial and axial directions. GEM 2D can model the ECR heating surface with fairly good accuracy compared with the full 3D ECR resonance surface while GEM 1D has to ignore the radial dependence of ECR heating. The radial dependence of the later GEM 2D results is mainly from this 2D feature of the ECR heating.

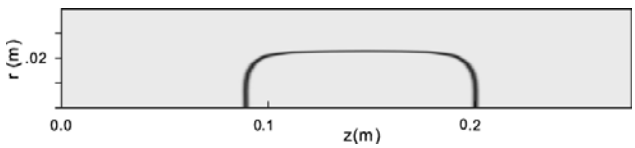

Figure 2: Azimuthally averaged ECR resonance surface modeled by GEM 2D.

Fokker-Planck Electron modeling

In a typical ECR plasma, electrons are hot (temperature >1 keV) due to ECR heating and the electron collision frequency is much less than the bounce frequency in the mirror field. As a result, the electron distribution function (EDF) is usually highly non-Maxwellian (Fig 3).

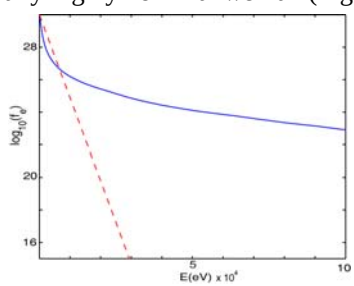

Figure 3: An example of non-Maxwellian EDF of ECRIS plasma modeled by GEM (solid line) and a Maxwellian EDF (dashed line), which drops exponentially with electron energy.

A bounce-averaged Fokker-Planck code [4] is feasible for predicting EDF on the midplane, $f(\upsilon,\theta_\upsilon;z_{mid})$, for mirror confined plasmas. The plasma parameters are averaged over the bouncing orbits in the mirror field under the assumption that the bouncing frequency is much greater than the collision frequency. EDF is then mapped axially along the magnetic flux surface through electron energy conservation and magnetic momentum conservation. Since the radial transport of electrons is negligible, EDF on each radial grid can be calculated independently using the same technique. The obtained full EDF $f(\upsilon,\theta_\upsilon;z,r)$ is then used in the ionization calculations and ion fluid modeling.

The ECR heating term is treated using the same bounce-averaging technique as the collision term in the Fokker-Planck code. The ECR power deposited in the plasma is described by four velocity space diffusion coefficients which are proportional to the rf power and have the 2D spatial profile shown in Fig 2.

2D fluid ion modeling

Since the ions in ECRIS plasma are highly collisional and cold (only ~1eV), the ions are treated as fluid. The 2D ion continuity equation for ions of species *j* and charge state *q* is

$$\frac{\partial n_{j,q}}{\partial t}+\frac{1}{A_z}\frac{\partial}{\partial z}\left[A_z n_{j,q}u_z\right]+\frac{1}{r}\frac{\partial}{\partial r}\left[r n_{j,q}u_{r\,j,q}\right]=S_{j,q} \quad , \quad (1)$$

where A_z is grid cross-section, u_z and u_r are ion velocity in axial and radial direction, S is a source/sink term that includes gains and/or losses due to ionization and charge-exchange. The axial velocity u_z is assuming to be the same for different ion species, but the radial velocity u_r is different due to the difference in Coulomb collision rates. The radial velocity u_r in Eq. 1 can be calculated by radial and azimuthal momentum equations,

$$m_j n_{j,q}\frac{\partial u_{j,qr}}{\partial t}=qn_{j,q}e(E_r+u_{j,q\theta}B)-k_B T_{j,q}\frac{\partial n_{j,q}}{\partial r}-F_r^{jk}$$

$$F_r^{jk}=n_{j,q}\sum_{k,p}\mu_{jk}n_{k,p}K_{j,q\to k,p}(u_{j,qr}-u_{k,pr})$$

$$m_j n_{j,q}\frac{\partial u_{j,q\theta}}{\partial t}=-qn_{j,q}eu_{j,qr}B-F_\theta^{jk}$$

$$F_\theta^{jk}=n_{j,q}\sum_{k,p}\mu_{jk}n_{k,p}K_{j,q\to k,p}(u_{j,q\theta}-u_{k,p\theta}) \quad (2)$$

E and B are electrical and magnetic field in the plasma, F is the friction force due to ion-ion Coulomb collisions, μ is the collision rate. The convection term is ignored since the velocities are slow.

The ion momentum equation in axial direction is

$$n_e\frac{\partial u_i}{\partial t}=-\frac{J_r}{e}\frac{\partial u_i}{\partial r}-n_e u_i\frac{\partial u_i}{\partial z}-\sum_{j,q}\frac{qk_B T_{j,q}}{m_j}\frac{\partial n_{j,q}}{\partial z}+$$

$$\sum_{j,q}qS_{j,q}^{in}\left(\langle u\rangle^{in}-u_i\right)+E_z\sum_{j,q}\frac{qn_{j,q}e}{m_j} \quad (3)$$

The axial electrical field E_z and plasma potential (the integral of E) can be solved from this equation together with the electron continuity equation.

RESULTS AND DISCUSSION

The GEM 2D has successfully simulated the plasma in ECR-I with typical parameters listed in Table 1. For this particular run, the radial grid number was set as 12. The calculation was parallelized on 6 processors using MPI technique.

Figure 4 shows the 2D potential profile in the plasma. The potential profile shows a “dip” in the center of the plasma, as has been previously predicted. This dip confines the ions in both the axial and radial directions.

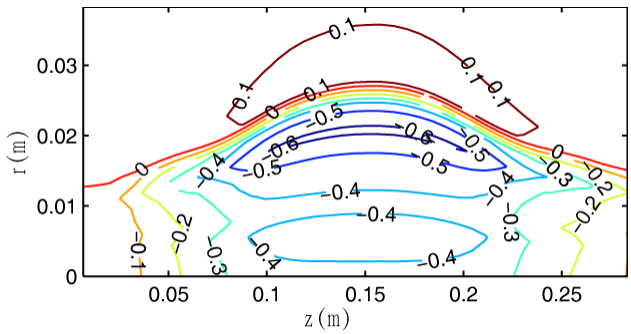

Figure 4: The contour plot of the plasma potential modeled by GEM 2D. Potential is in volts.

The profiles of electron density, temperature, ion density and ion fluxes that are predicted by GEM 2D modeling are showing clear radial dependence due to the spatial distribution of ECR heating in Fig. 2. For example, the predicted electron density profile shown in Fig 5 is a hollow profile with the density peaked at the ECR resonance surface which is 2 cm away from the device center. The hollow profile of ECRIS plasma has also been observed in the experiments [6,7]. GEM simulation results and the experimental results are showing that the plasma density peaks around the ECR heating surface. Also, the GEM 2D result is matched well with the profile predicted by GEM 1D (Fig. 5b), which predicts the radially averaged ECR plasma by assuming that the ECR heating profile has no radial dependence.

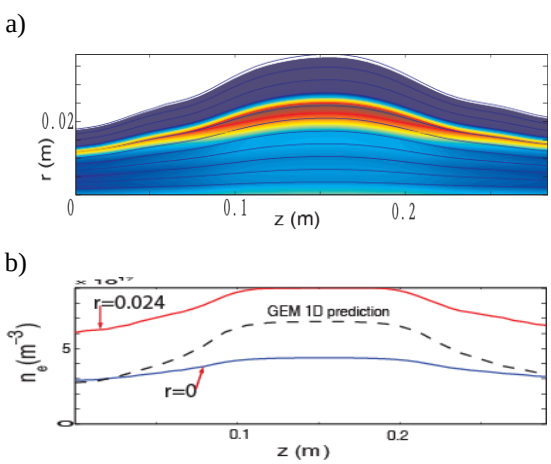

Figure 5: a) The contour plot of the plasma density modeled by GEM 2D. b) The axial profiles of the plasma density at different radial positions and the comparison with GEM 1D prediction (dashed line).

The extracted ion charge state distribution (CSD) has shown similar radial dependence as the plasma density profile. To compare with GEM 1D result and the experimental data discussed in [1], CSD calculated by GEM 2D is obtained by integrating the ion extraction current density over the cross-sections along the radial direction (Fig. 6). The CSD predicted by GEM 2D is more consistent with the experimental data than GEM 1D predictions.

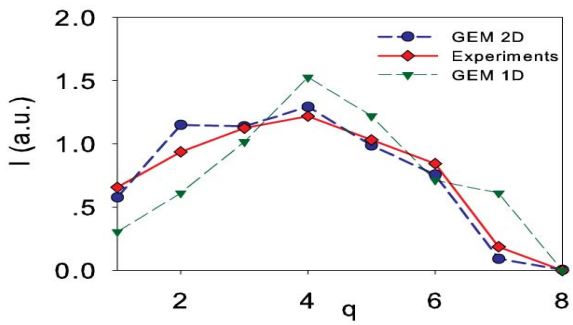

Figure 6: CSD predicted by GEM 2D (dots), GEM 1D (triangles) and experimental measurements (diamonds).

CONCLUSIONS

Extended from GEM 1D, GEM 2D is an advanced ECRIS plasma modeling tool which can simulate ECRIS plasma in both radial and axial directions. GEM 2D calculates 2d2v non-Maxwellian EDF $f(\upsilon,\theta;z,r)$ of the electrons by solving Fokker-Planck equation using bounce-averaging method and the spatial transport of cold ions by solving 2D fluid equations. The results of GEM 2D simulation of ANL ECR-I are consistent with the experimental data and observations.

Future work of GEM 2D will be focused on the validation of GEM 2D using available experimental data and the application of the GEM 2D on charge-breeder optimizations and ion extraction studies.

REFERENCES

[1] D.H. Edgell, J.S. Kim, and I.N. Bogatu, R.C. Pardo and R.C. Vondrasek, Rev. Sci. Instrum., **73**, 641 (2002).

[2] A. Mirin, M. McCoy, G. Tomaschke and J. Killeen, *Comput. Phys. Commun.* **81**, 403 (1994)

[3] J.S. Kim, C. Liu, D.H. Edgell, and R. Pardo, *Rev. Sci. Instrum.*, **77**, 03B106 (2006).

[4] F. Ames, R. Baartman, P. Bricault, K. Jayamanna, M. McDonald, M. Olivo, P. Schmor, D.H.L. Yuan, and T. Lamy, *Rev. Sci. Instrum.*, **77**, 3B103 (2006).

[5] L. Zhao, J. S. Kim, B. Cluggish, "2D Extension of GEM", Proceedings PAC07, Albuquerque NM (2007) .

[6] S. Biri, A. Valek,, and T. Suta, *Rev. Sci. Instrum.*, **75**, 1420 (2004).
[7] P. Grübling, J. Hollandt, and G. Ulm, *Rev. Sci. Instrum.*, **73**, 614 (2002).

WALL DISTRIBUTION OF IONS EXTERNALLY INJECTED FOR CHARGE –BREEDING IN ECRIS

M. Oyaizu, S. C. Jeong, N. Imai, Y. Fuchi, Y. Hirayama, H. Ishiyama, H. Miyatake, M. Okada, Y. X. Watanabe,
S. Ichikawa*, H. Kabumoto*, M. Matsuda*, A. Osa*, Y. Otokawa*
High Energy Accelerator Research Organization (KEK), Oho 1-1, Tsukuba, Ibaraki 305-0801, Japan
*Japan Atomic Energy Agency (JAEA), Shiragata Shirakane 2-4, Tokai, Ibaraki 319-1195, Japan

Abstract

We have investigated the ion loss distribution in an electron cyclotron resonance (ECR) ion source. The ions, radioactive and singly charged ^{111}In, were injected into the ECR ion source (ECRIS) for breeding their charge states at the Tokai Radioactive Ion Accelerator Complex (TRIAC). The residual radioactivity on the wall of the ECR plasma chamber of the source was measured, giving a two-dimensional distribution of the ions failed to be re-extracted during charge breeding. The distribution was decomposed, according to azimuthal symmetry, into three components, asymmetric, 120-degree symmetric, and isotropic ones, whose origins were quantitatively discussed for clarifying ion-losses in the course of charge breeding in ECRIS.

INTRODUCTION

The radioactive ion beam (RIB) facility TRIAC [1] has been jointly constructed under the collaboration between KEK and JAEA and operated for experiments since November, 2005. The facility is based on an isotope-separator on-line (ISOL) technique. The radioactive nuclei are produced by means of proton-induced fission of ^{238}U or heavy-ion reactions with the primary beams from the JAEA tandem accelerator. The produced radioactive nuclei are singly ionized and mass-separated by the JAEA-ISOL [2]. They are fed to the 18 GHz ECR ion source for charge breeding (KEKCB), where the singly charged ions are converted to multi-charged ions with the mass-to-charge ratio (A/q) of around 7. The charge-bred radioactive ions are extracted again and fed to the post-accelerator [3] for further acceleration.

Several RI beams as well as stable ion beams have been successfully charge-bred to A/q~7. Recently, we have accelerated to 178keV/A the medium-mass charge-bred radioisotopes of Kr and In. The acceleration of RI beams charge-bred by ECRIS was the first time over the world. Details on the charge breeding experiments for the KEKCB can be found elsewhere [4].

In charge breeding experiments using KEKCB at TRIAC, we observed large differences in charge breeding gaseous and non-gaseous ion species, i.e. in the injection optics and the resultant charge breeding efficiencies [5]. In order to understand the differences we investigated how the ions, which were externally injected to the ECR plasma of KEKCB for breeding their charge states but failed to be re-extracted, were distributed on the wall (surface) of the plasma chamber.

EXPERIMENT

For the measurement of ion distribution on the wall of the plasma chamber, we injected into KEKCB and charge-bred radioactive singly-charged ^{111}In ions with a half-life of 2.8 days. After charge breeding, we measured the distribution of the ^{111}In by detecting the residual activity on the wall of the chamber. We here just introduce the experiments for measuring the residual activity since detailed experimental procedures for charge breeding can be found elsewhere [5].

As shown in Figure 1, after charge breeding, we removed the inner tube (a 350mm-long cylindrical tube with a diameter of 76mm) from the plasma chamber and measured two γ-rays emitted from ^{111}In (after beta-decay to ^{111}Cd) deposited on the wall of the inner tube by a Ge(Li) detector. In front of the Ge(Li) detector, a 20mm-thick lead shield with a hole of 20 mm in diameter was placed as a collimator. In addition, we placed a cylindrical lead block inside the inner tube to prevent γ rays from the opposite side of the tube. By changing the azimuthal angle and longitudinal position on the inner tube, around and along the axis of injection and extraction in a cylindrical coordinate, the measurements were performed at several tens of points on the tube. (Lower part of Figure 1 and Figure 2)

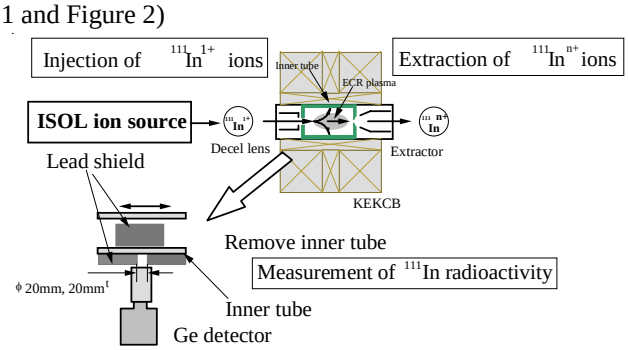

Figure 1: Experimental set-up for charge breeding and measuring the residual radioactivity of ^{111}In on the surface of the inner tube.

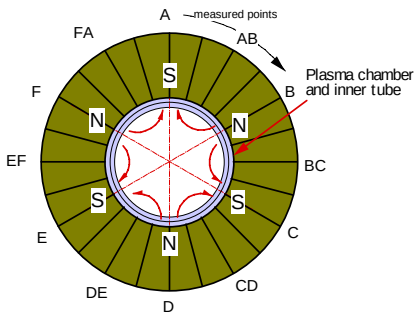

Figure 2: Hexapole radial magnetic field and definition of measured points around the chamber. Viewed along the ion beam direction.

EXPERIMENTAL RESULTS

Figure 3 shows a two-dimensional distribution of the radioactivity of ^{111}In ions deposited on the surface of the inner tube, which is efficient to overview the distribution although the interpolation, not rigorous, can cause a misunderstanding because of the limited number of data points. From the overview, we could identify azimuthally asymmetric distributions around the longitudinal position with B_{min} of axial field, i.e. around z~200mm in the configuration shown in the lower part of Figure 3, and rather symmetric and isotropic distribution at the extraction side close to the position with B_{max}.

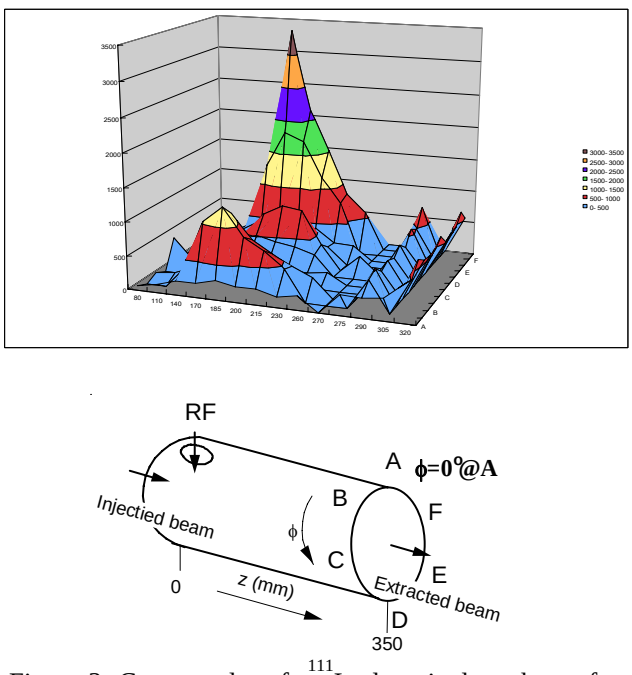

Figure 3: Contour plot of ^{111}In deposited on the surface of the inner tube. The interpolation is not rigorous, just for eye-guiding.

A typical azimuthal distribution around the B_{min} is given in Figure 4. We assumed that the distribution consisted of three components, azimuthally isotropic, 120-degree symmetric and asymmetric ones. At each longitudinal position, as indicated in Figure 4, we decomposed the distribution according to the azimuthal symmetry; asymmetric and symmetric components. The symmetric includes isotropic and 120-degree symmetric components. Integrating over azimuthal angle, the longitudinal distributions were extracted and compared in Figure 5, where axial magnetic field configuration is also given. The asymmetric component is localized around B_{min}, while the symmetric component is concentrated around the B_{min} as well as at the extraction side.

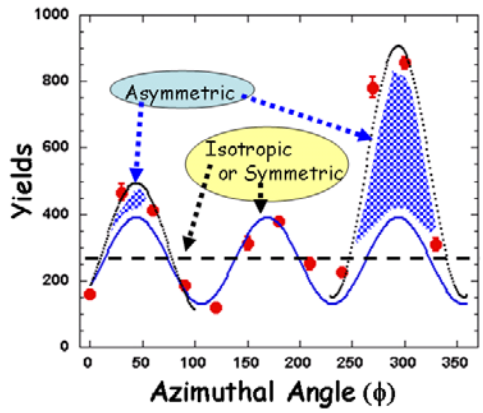

Figure 4: Azimuthal distribution of ^{111}In around B_{min}. Decomposed into 3 components; azimuthally isotropic, 120-degree symmetric, asymmetric ones.

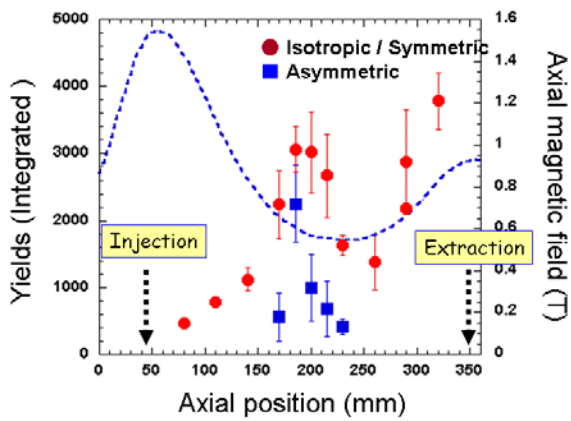

Figure 5: Longitudinal distribution of the symmetric and asymmetric components, as defined in Figure 4. The symmetric include both the isotropic and 120-degree symmetric components. Axial magnetic filed configuration is also given for comparison.

The asymmetric component representing 13.5 % of the total activity residual on the surface might be associated with ions injected in a rather asymmetric manner since the (axial and radial) magnetic field

configuration for the confinement of electrons in ECR plasma cannot produce such asymmetry. More careful optimization of the beam optics for the injection is necessary for the elimination of the asymmetric component in the ion-losses in the course of charge breeding.

The 120-degree symmetric distribution of ions reminds us of the electron losses due to the combined field configuration of the axial and the radial magnetic field for electron confinement[6]. Although the behavior of ions in ECR plasma has not yet been studied in detail both experimentally and theoretically, we can expect that both electrons and ions should show a quite similar behavior. Therefore, the 120-degree symmetric distribution can be considered as a characteristic behavior of ions in ECR plasma. When considering the charge-breeding process as two successive processes, i.e. stopping and ionizing processes [7], the ions with the 120-degree azimuthal symmetry would correspond to those lost during the second, ionizing process. In the ionization process, those ions, though successfully captured by ECR plasma in the stopping process, are supposed to be lost to the wall of plasma container along the hexagonal radial magnetic field. The fraction, i.e. how many ions are lost in the ionization process, is nothing but the ionization efficiency for the ions in ECRIS.

As shown in Figure 4, the 120-degree symmetric component is on the top of the isotropic one. The isotropic one is actually the main component of the symmetric distribution, which is observed all over the wall as shown in Figure 3. The 120-degree symmetric component was observed only around B_{min}, even where the isotropic component amounts to a large fraction (refer to Figure 4). Along the discussion given above for the 120-degree symmetry in the distribution, the isotropic component could be also associated with the incomplete confinement of ions, i.e. the losses simply by the ambipolar diffusion of plasma constituents.

The symmetric component, including isotropic and 120-degree asymmetric components, represent 86.5% of the total. The 38% of the symmetric component were observed at the extraction side. The large fraction of ion losses around the extraction side could be understood quantitatively by a weak confinement field. The weak radial field caused by the geometrical limit of permanent magnets at the extraction side, as well as the weak axial field for efficient ion extraction, could lead rather poor radial confinement of electrons and consequently large loss of ions along the radial direction.

SUMMERY AND OUTLOOK

We have injected radioactive ions of ^{111}In into the KEKCB and, after charge breeding, measured the residual activity to investigate how ions externally injected for charge breeding be lost in the course of charge breeding. By analyzing the distribution, we found three components, asymmetric around B_{min}, 120-degree symmetric, and isotropic ones. The asymmetric one could be removed by further tuning the injection optics. About 38% of the second and the third component were observed around the extraction side, implying that the ions were strongly influenced by the weak confinement field both for the radial and axial direction.

Further measurements using the gaseous element ^{140}Xe are scheduled. Comparison between the distribution of the ^{111}In distribution and the one of the ^{140}Xe will give a hint to understand the difference of charge-breeding efficiencies for gaseous and metallic elements, i.e. the element-dependent efficiencies observed so far in the charge breeding experiments using ECRIS.

REFERENCE

[1] http://triac.kek.jp/
[2] A. Osa, M. Matsuda, T.K. Sato, and S. Ichikawa, Nucl. Instrum. Methods B 266 (2008) 4373.
[3] S. Arai et al., Proc. Int. Linac Conf., Geneva, Switzerland, 1996, p.575.
[4] S.C. Jeong et al., Rev. Sci. Instrum. 75 (2004) 293.
[5] S.C. Jeong et al., Nucl. Instrum. Methds B 266 (2008) 4411.
[6] R. Geller, Electron Cyclotron Resonance Ion Sources and ECR plasmas, Institute of Physics Publishing, London, 1996, p122.
[7] S.C. Jeong et al, Rev. Sci. Instrum. 73 (2002) 803.

NEW SPINDLE CUSP ZERO-B FIELD FOR ECR ION AND PLASMA SOURCES

M.H. Rashid[#], C. Mallik and R.K. Bhandari, VECC, 1/AF- Salt Lake, Kolkata-700 064, India

Abstract

A traditional ECR ion source (ECRIS) or plasma source use magnetic min-B field for plasma containment and energizing electrons based on the principle of the ECR process. A cusp field produces modified min-B or zero-B field. A new cusp magnetic field (NCMF) configuration with symmetric field at the cusp positions, corresponding to a given RF frequency confirming the standard model of ECR Ion Source, is simulated to contain large volume high density plasma for producing beam for low or high charged ion. The magnetic field increases along and across the magnetic lines of force starting from zero at the centre and maximum value at the periphery. The cusp field with convex lines of force towards the plasma is ideal for confining it as drift of the particles take place either in the azimuth or towards the low field region at the centre. Non-adiabatic behaviour of electrons at the centre can be either tackled by gas-dynamic confinement at high density or exploited to generate more secondary electrons. Confinement feature of the field is assessed by electron simulation. A new technically viable cusp ECRIS has a bright prospect ahead as it is simple, stable, compact and cost-effective compared to the traditional ECRIS.

INTRODUCTION

Geller's group pioneered constructing ECRIS like MAFIOS and its variants [1-3] at Grenoble in 1970's and later. The ECR plasma and its property have been described well by him [4] in terms of confinement of plasma, ECR heating and techniques to improve working of an ECRIS. A minimum-B field was produced employing axial field and radial magnetic field for confining plasma quiescently. The cold electrons with some initial kinetic energy gyrate about a magnetic line of force, that is magnetic line of force (MLF) with f_G (gyro-frequency) $\propto$ B (magnetic field). At resonance condition, $f_G \approx f_{RF}$, electrons get energy from the RF wave.

The main motivating factors of the present study are i) to study the possibility of more confinement of electrons and ii) to construct a simple, compact and cost-effective ECRIS to alleviate some of the problems of traditional ECRIS like complicated magnet system, small plasma volume, limited injection and extraction regions etc.

Earlier the classical CMF was used to design an ECR ion source (ECRIS) [5] because of its inherent plasma confining nature. But it had a little success because of huge loss of plasma at the cusp (mainly ring cusp, RC) positions owing to insufficient and asymmetric magnetic field. The CMF has been reconfigured here adopting a simple, novel and cost-effective technique to shrink the loss area [6]. It helps to achieve high value of $n_e\tau_i$ for generating intense HCI beam. The variation of plasma pressure, $P_{par} = n_e k_B T_e$, along the MLF depends on the magnetic pressure, $P_B = B^2/(2\mu_0)$. The gravitation-like inward force because of the curvature of MLF's produces a MHD-stable configuration.

DESIGN SCHEME TO PRODUCE NCMF

A classical CMF can be produced using either a pair of coaxial coils carrying opposite current or a single ring of radially magnetized permament magnet. The field does not rise along the radius at the mid-plane as rapidly as along the central axis. But rise in field in both the direction in new improved CMF (NCMF), on the average, is equal. The field is zero at the centre and is weak in a small region around it. The deduced vector potential in eq. (1) represents the NCMF and can be used to visualize the field line distribution and calculate the field components in the cylindrical co-ordinates.

$$A_\theta(r,z) = g\, rz + b\, rz^3 + c\, r^3 z + C \quad (1)$$

$$B_r(r,z) = -g\, r - 3b\, rz^2 - c\, r^3 \quad (2)$$

$$B_z(r,z) = 2g\, z + 2b\, z^3 + 4c\, r^2 z \quad (3)$$

Where constants $g = (11B_0)/(14L)$, $b = (-2B_0)/(7L3)$, $c = -(3/4)b$ and $C=0$ (say). A NCMF of any dimension, L and maximum field, B_0 can be evaluated. The absolute NCMF for B_0=40 kG and L=16cm is plotted in Fig. 1 using eqs. (2) and (3).

The magnet geometry consists of yoke, end-plugs and centre disk of highly permeable material in addition to coil pair or PM ring to generate NCMF. There is no limitation to magnet size and field strength in case of using coils to produce NCMF. Application of PM discards the power supplies, major cooling system etc. It can be used to produce NCMF for high-B mode cusp ECRIS of as high as 18 GHz RF frequency [7]. The calculated field can be realized feeding proper geometry similar to Fig. 2 in a field computing code [8, 9].

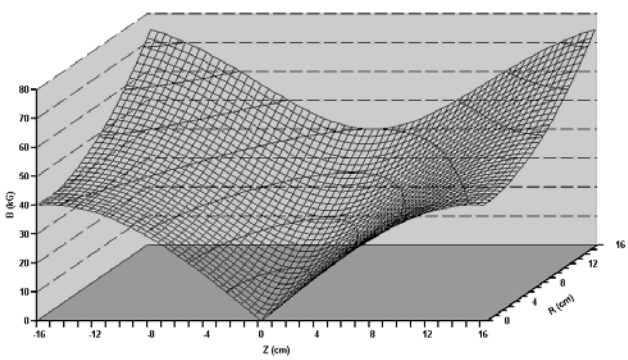

Figure 1: Plot of absolute field due to NCMF

[#]E-mail for more information to: haroon@veccal.ernet.in

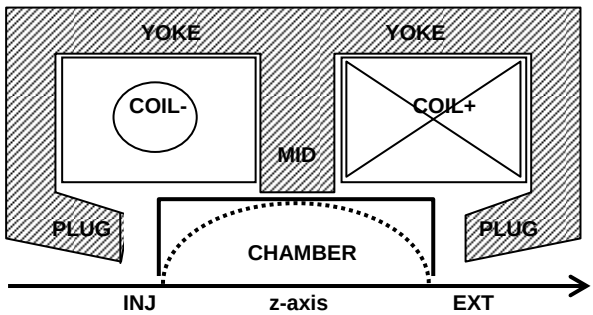

Figure 2: Scheme of magnet system to produce a NCMF

CHARACTERISTICS OF NCMF

Some initial results of NCMF computation were reported in the InPAC [10] showing that a traditional ECRIS of 14.4 GHz [11] can, on paper, be split into two NCMF ECRIS'es; one using the same coils and the other using the same PM after rearrangement to generate the required improved CMF.

Bent mirror ratio in the calculated NCMF

It is seen that the magnitude of the field at the cusp positions is sufficiently high to achieve the high-B mode condition as well as $\pi/2$ angle rotated point cusp-ring cusp (PC-RC) mirror [12]. The TrapCAD code [13] is capable of calculating the magnetic mirror ratio, M_R on a MLF. The M_R on a MLF passing through (r, z) points on r = z line starting from r=0.1cm to 10.0 cm is shown in Fig. 3 in the calculated field. The M_R, with respect to the B_{min} on $|z|\approx|r|$ conical plane, increases as one goes towards the centre of the field, so the loss cone angle (α_{apex}= $\arcsin(1/\sqrt{M_R})$) narrows down too.

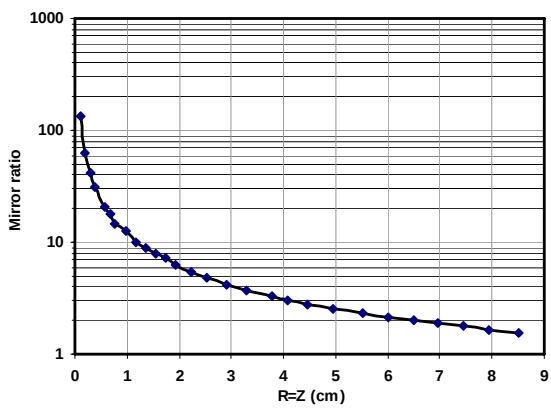

Figure 3: Mirror ratio with distance r=z from the centre

Electron simulation in the calculated NCMF

The calculated field was fed into the TrapCAD code to visualize the electron motion when launched at various positions around the magnetic centre in the plasma chamber with different energy and energy partition along the direction of the magnetic field ($W_{\parallel}$) and perpendicular ($W_{\perp}$) to it. It is seen that there are three types of motion, electrons undergo.

A little far away from the low field region the electrons always execute a stable adiabatic motion The guiding centre of the electrons oscillates between mirror points placed at PC and RC positions on the chamber surface. There are MLF's towards which electron moves on the average, so they gradually but constantly shift on the adjacent flux tube. This fact signifies that the flux enclosed by the tube, on which the electron moves, is not conserved as the enclosed flux slowly varies with its longitudinal position of the electron between the bouncing points [14]. So, electrons perform stable adiabatic motion drifting slightly towards the higher field direction at higher radius after successive bounce from PC and RC. The region beyond a small so called black region of approximate diameter ~2.14 cm is stable for electron energy upto ~35.0 keV with the energy partition confirming $\alpha_{loss} \geq \alpha_{apex}$, where α represents the loss-cone angle. As a matter of fact, the value of α_{apex} decreases as one moves inward on the r=|z| cone surface.

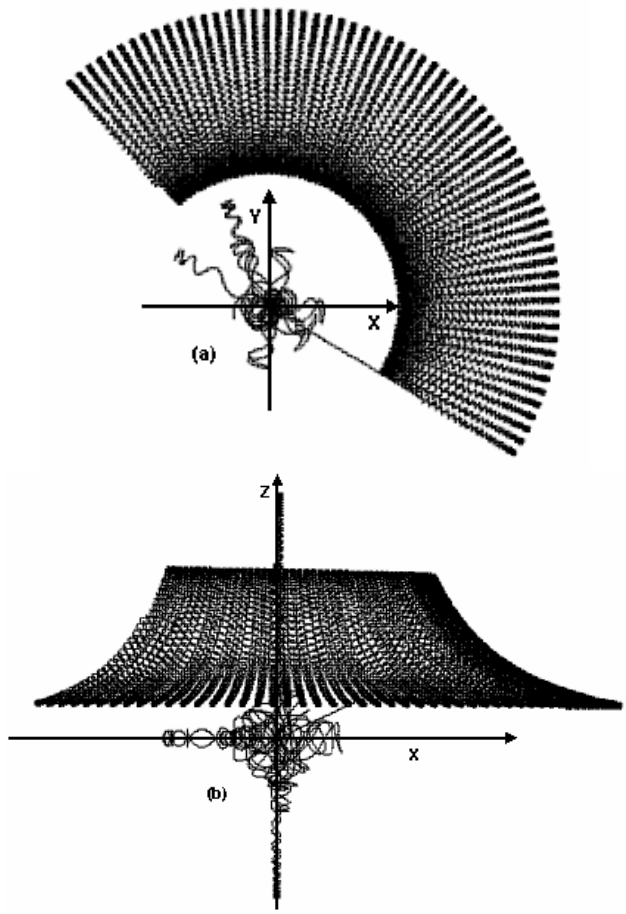

Figure 4: Electron motion when launched near the centre.

When the total launching energy of an electron is increased, it mostly executes unstable or non-adiabatic motion while passing through r=|z| points because of either approaching the apex angle of the loss cone due to high $W_{\parallel}$ or enclosing a thick flux tube having large gyration radius due to very high $W_{\perp}$. An electron having lower energy and low $W_{\perp}$ tends to be unstable as the

launching point approaches the magnetic centre where the $(r/B)\nabla B$ approaches 1.0 for the MLF, which signifies that the local curvature of the MLF becomes comparable with the curvature of electron trajectory. The electron may ultimately be lost at the PC or RC positions (at 16 cm away from the centre) in a short time because of instability. Or it may execute stable motion for long time. This region may be termed as the transition region from adiabatic to non-adiabatic motion of electrons for the caculated magnetic field and chamber geometry.

If electrons are launched further near the magnetic centre, they execute random motion due to Coulomb like scattering as little flux is defined by $\boldsymbol{\mu}\cdot\mathbf{B}$. In this case the invariance principle of electron magnetic moment is not applicable. The average length of the electron excursion in this region does not depend on the history of an orbit. Yet, the electrons are bounced several times towards the low field region performing spiral or banana motion before being lost in little time, which is, dependent on the launching energy W as well as on $W_{\parallel}$ and $W_{\perp}$.

It is worth mentioning the observation during the simulation that a non-adiabatic motion of electron near the centre may turn into an adiabatic motion while travelling far away from the centre (Figs. 4) or vice versa due to scattering of electrons towards the centre as a result of binary collision among the particles. The simulation also establishes that the electrons get lost innately at the RC or PC positions on the chamber surface.

Mitigating effect of non-adiabatic motion

The magnetic field at the central region of the CMF is weak and the invariance principle of adiabatic magnetic moment of electron is not perfectly valid. The plasma density at 18 GHz or higher frequencies exceeds $1x10^{12}$ /cm^3, so the plasma enters into a collisional regime. Then, quasi-gas-dynamic confinement of plasma takes place [15] because of the collisions of the electrons with slow ions on their course of being lost. The quasi-gas-dynamic regime is characterized by very small mean free path of electrons under electron-ion collisions compared to the extent of the excursion of the electrons between the magnetic mirror plugs. The rate of filling the loss cone by electrons due to high collision frequency is more than the rate of electron-loss within. The average electron velocity distribution function remains isotropic in the filled loss cone. Then the non-adiabatic motion of electrons at the magnetic centre is insignificant [16, 17] for generation of multi-charged ions of heavy elements.

CONCLUSION

A CMF has inherent property of MHD stability, so quiescent plasma is contained in such field. The designed NCMF can be used to construct very cost-effective and simple cusp ECRIS. Since it does not need any sextupole for radial confinement of plasma, the volume of the plasma chamber increases, which helps in extraction of an intense beam of HCI's. The EM energy can be injected to boost the source operation at several lower RF frequencies simultaneously.

The plasma loss is reduced because of high mirror field, shorter cusp line ($2\pi L$, where 2L is the chamber diameter), convexity of lines of forces, further electrostatic mirror action, secondary electron emission and gas-dynamic confinement effect due to collision dominated plasma. A cusp ECRIS with further high microwave frequency will need more upgraded NCMF, which is possible to be generated using superconductors [18]. The cusp ECRIS is capable of accepting radioactive fragments or particles also from targets to produce and deliver intense radioactive ion beam. It can work in continuous or pulsed modes. The loss of electron at the cusp positions can be utilized to produce secondary electrons to further boost the plasma density.

REFERENCES

[1] R. Geller et al, IEEE Tran. Nucl. Sci NS-23 (1978) 904; NIM A 243 (1986) 244.
[2] R. Geller, IEEE Tran. Nucl. Sci. NS-26 (1979) 2120.
[3] R. Geller and B. Jacquot, NIM, A 184 (1981) 293.
[4] R. Geller, 'Electron Cyclotron Resonance Ion Sources and ECR Plasmas', IOP, Bristol, UK, 1996.
[5] K. Sudlitz et al. Proc. 12th Intl. Workshop on ECRIS, RIKEN, 1995 p. 217.
[6] M.H. Rashid, Thesis "*Studies on Electric … in Electron Cyclotron Resonance Ion Devices*," Jadavpur Univ., Kolkata, India , 2003.
[7] M.H. Rashid et al., Proc. Inter. Conf. Cyclotron Their Applications, Cyclotrons-2007, Italy, 2007 p. 286.
[8] M.T. Menzel et al., POISSON/SUPERFISH Group of Codes, LANL Internal Report LA-UR-87-115, 1987.
[9] D.C. Meeker, User's Manual for Finite Element Method Magnetics (FEMM), Ver. 4.0, 2006.
[10] M.H. Rashid et al, 2nd. Ind. Part. Accel. Conf., VECC, Kolkata, India, InPAC 05, 2005 p. 312.
[11] M.H. Rashid et al, Indian J. Phys. 76A (2002) 193.
[12] M.H. Rashid et al, NIM B 262 (2007) 95.
[13] S. Biri et al., High Energy Phys. & Nucl. Phys.; Chinese Phys. Soc. Supp I, 31 (2007) 165.
[14] G.N. Theodore, Plasma Physics in Theory and Application, Ed. Wulf B. Kunkel, Mc Graw Hill Book Company, New York, 1966 p. 39.
[15] D.D. Ryutov et al, Plas. Phys. Control. Fusion 28 (1986) 191.
[16] V. Skalyga et al, AIP Conf. Proc. Inter. Workshop on ECRIS Ed. M. Leitner, LBNL CP749, 2004 p. 112.
[17] S.V. Golubev et al, Trans. Fusion Sci. Tech. 47 (2005) 345.
[18] D. Leitner et al., Proc. Inter. Conf. Cyclotron Their Applications, Cyclotrons-2007, Italy, 2007, p. 265.

PAPER NOT RECEIVED

PAPER NOT RECEIVED

GASDYNAMIC ECR SOURCES OF MULTICHARGED IONS

V.G. Zorin, A.F. Bokhanov, S.V. Golubev, I.V. Izotov, D.A. Mansfeld, S.V. Razin, A.V. Sidorov, V.A. Skalyga, and A.V. Vodopyanov, Institute of Applied Physics RAS, 46 Ulyanov St., Nizhny Novgorod, Russia.

Abstract

A new type of pulsed sources of multicharged ions(MCI), namely, a gasdynamic ECR source is proposed. Its main difference from the classical ECR ion sources is a different, quasi-gasdynamic regime of plasma confinement in a magnetic trap. Plasma was produced and heated by radiation of a pulsed gyrotrons with the frequencies of 37.5 and 75 GHz in magnetic traps of various configurations. Plasma confinement in quasi-gasdynamic regime under such conditions was studied. It was demonstrated that with such a confinement regime it is possible to generate multicharged ions and create intense (more than 1 A/cm^2) ion fluxes through the trap plugs. Creation of intense plasma fluxes allows one to extract high-current MCI beams of high brightness. Transverse homogeneity of a plasma flux makes it possible to use a multi-aperture extraction system for the formation of broad intense MCI beams. MCI beams with current up to 150mA and normalized emittance lower than 1 π·mm·mrad were produced. Comparison of results of calculations and data of experiments shows that they are in a good agreement, which allows us to predict creation of a new type of ECR source.

INTRODUCTION

The recent experimental and theoretical research carried out at the Institute of Applied Physics (IAP RAS, Nizhniy Novgorod, Russia) resulted in development of a new type of pulsed ECR sources of multicharged ions – gasdynamic ECR ion sources (ReGIS). It will be demonstrated that such sources are capable of generating high-current and high-brightness ion beams with a moderate ion charge.

The ideas underlying development of such sources were borrowed from the field of classical ECR sources of multicharged ions (we will refer to them as to the Geller ECR ion sources (GECRIS)) [1], as well as from investigations of fusion mirror traps (FMT) [2]. The ReGISs differ from the Geller sources by the mechanism of plasma confinement in a magnetic trap. It is the quasi-gasdynamic mechanism [3] similar to that used in FMT. The principal distinction from FMT is strong nonequilibrium of confined plasma (the temperature of the electrons is much higher than the temperature of the ions), which is typical of GECRIS.

REGIS PRINCIPALS

A possibility of realizing two different (classical and quasi-gasdynamic) regimes of confinement of nonequilibrium plasma in open magnetic traps at powerful ECR heating by millimeter wave radiation was demonstrated in [3]. The great majority of modern ECR sources of MCI operates in the regime of classical plasma confinement in a trap. Ion confinement in this case is determined by ambipolar potential distribution in the trap [4]. In a mirror trap, electrons get into a loss cone either as a result of collisions with ions or with each other, or due to quasi-linear diffusion in velocity space due to intense ECR heating [5]. With increasing plasma density the transition from the classical to the quasi-gasdynamic regime of plasma confinement was observed in experiments [3]. The mechanism of plasma confinement in a trap changes for the values of the plasma such that the velocity at which the loss cone is filled in by electrons in velocity space is higher than the velocity of plasma escape from the trap. The loss cone is filled in, the electrons are confined in the trap by ambipolar potential, and plasma losses are determined by gasdynamic ejection of ions. This regime of confinement of nonequilibrium plasma with filled loss cone is called a quasi-gasdynamic regime. The transition to this regime of plasma confinement is inevitable when its density is increased [6]. The plane of plasma parameters divided into characteristic regions for the two regimes of plasma confinement with characteristic regions for classical and gasdynamic ECR ion sources is presented in fig.1.

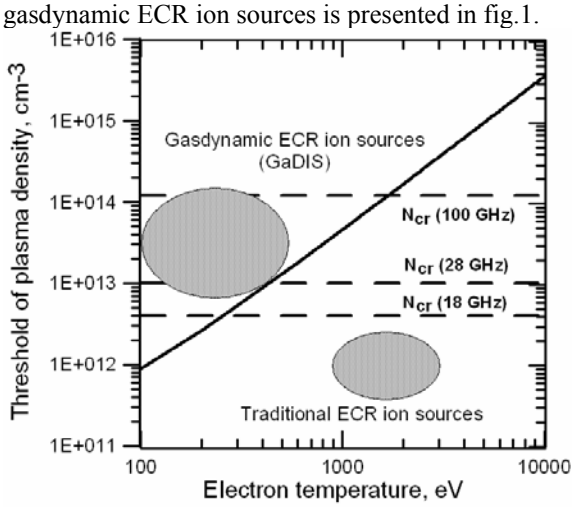

Fig. 1. The border between the two regimes of plasma confinement.

In quasi-gasdynamic regime plasma life time can be roughly determined as $\tau = \frac{R \cdot L}{2 \cdot V_s}$, where R is the mirror ratio and L is the length of the trap and V_s is the ion-sound velocity. Thus, in the quasi-gasdynamic regime plasma lifetime is determined only by ion-sound velocity and

geometry of the trap and does not depend on plasma density. Due to this plasma confinement parameter (N_e τ) can be increased by enlargement of the trap size (trap length) and creation of plasma with higher density. For increasing of plasma density it is necessary to apply MW radiation with higher frequency. Effectiveness of both approaches was demonstrated in our experiments.
Deformation of ion charge state distribution due to modifying of the trap length, which lead in accord with (5) to a change in the confinement time, shown in fig.2.

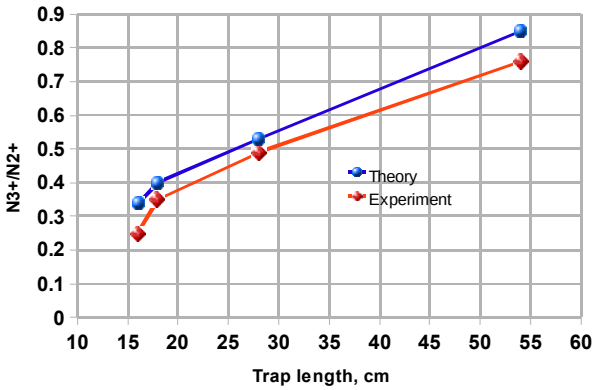

Fig. 2. The ratio of N ions with charge +3 and +2 *versus* the effective trap length (calculation and experiment).

In fig.3 the results of experiments for two frequencies of heating MW radiation (37.5 and 75 GHz) in helium are shown.

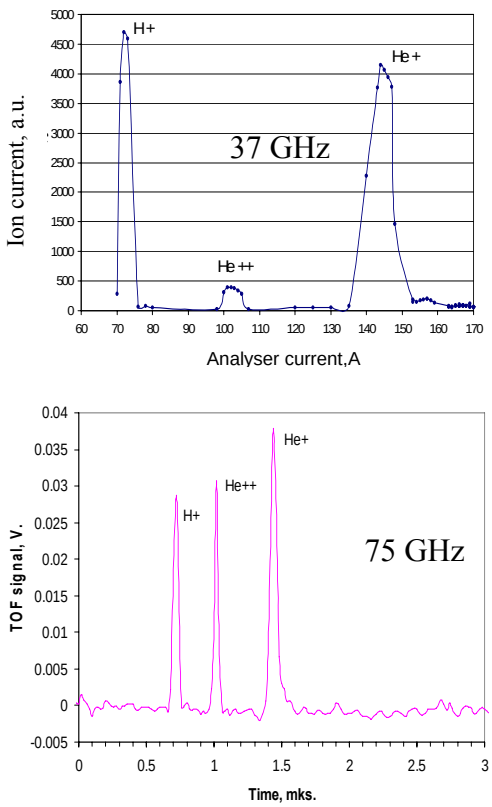

Figure 3. Helium charge state distributions for 37.5 GHz (upper one) and 75 GHz.

ION BEAM CURRENT AND EMITTANCE

The latest experiments were performed with multi-aperture extraction system, which is shown in fig.4.

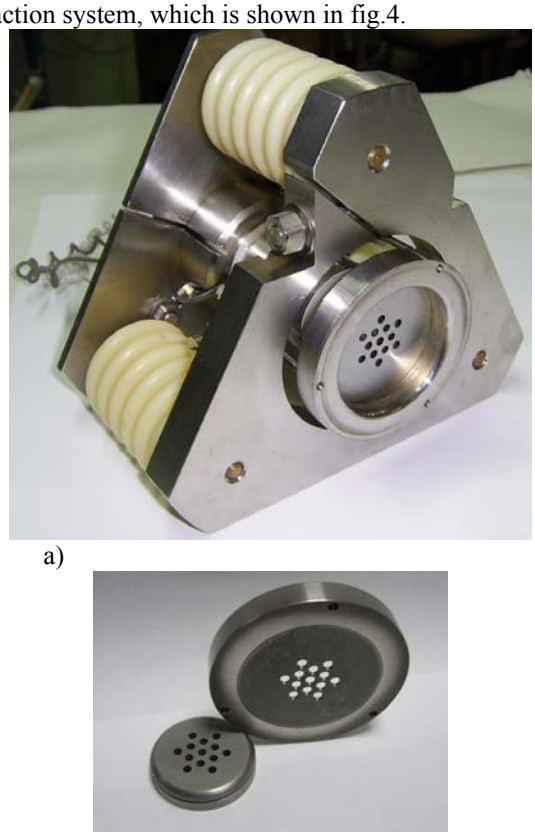

a)

b)

Fig. 4. 13-aperture extractor (photo). a) General view; the holes in plasma electrode can be seen at foreground. b) Electrodes of the extractor.

The 13-aperture extractor has been optimized; the beam current at the extraction system exit (Faraday cup current) and puller current have been measured as a function of the extraction voltage. The ion beam emittance has been measured at the extracting voltage equal to 30 kV.
The ion beam current (Faraday cup current) of 160 mA has been obtained at 30 kV extracting voltage (fig. 5), 85 kW gyrotron microwave power and 1.6 T magnetic field in trap plugs (with cusp magnetic configuration), puller current being near 100 mA. In these experiments the extractor was placed 21 cm off the magnetic trap plug, distance between electrodes being 9 mm.
The emittance of the obtained ion beam was measured with use of 'pepper-pot' screen and scintillator. Analysis of experimental data has demonstrated that normalized emittance of the beam is equal to 0.9 π·mm·mrad (for 30 kV extracting voltage).

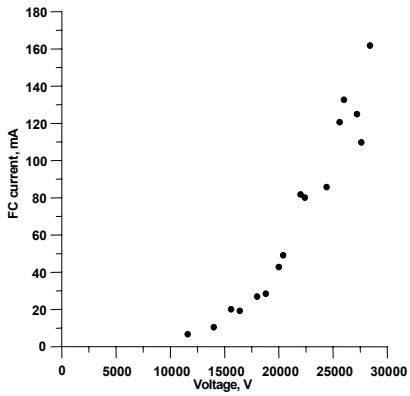

Fig. 5. Ion beam current (Faraday cup current) versus extracting voltage in 13-aperture extractor. Nitrogen is used as working gas.

CHARGE STATE DISTRIBUTION

The primary experiments have been carried out on generation of multi-charged ions of nitrogen with use of modified cusp magnetic trap.

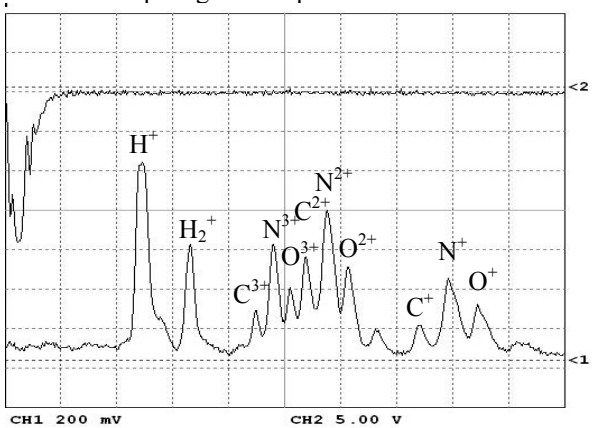

Fig. 6. Mass-charge ion spectrum of nitrogen plasma.

Fig. 6 present mass-charge ion spectra obtained in ECR plasma of nitrogen (the time-of-flight ion analyzer was used in these experiments). Plasma was created in modified cusp magnetic trap with effective length equal to 54 cm, magnetic field in plugs reached 2.3 T, and pulsed power of gyrotron radiation was 85 kW. It can be seen from this figure that nitrogen ion charge state distribution has maximum at + 2 charge (peak corresponding to N^{3+} ions being only 25% less). This indicates more effective generation of multi-charged ions under conditions of the described experiments compared with earlier ones with shorter (L_{eff} = 28 cm) cusp trap[7]. Unfortunately we couldn't avoid large amount of admixtures polluting plasma on this stage due to low repetition rate.

ACKNOWLEDGMENTS

The authors thank Dr. P. Spaedtke and the LPSC Grenoble team: Dr. T. Lamy, Dr. T. Thuillier for fruitful discussions and attention to the experiments.

The authors are grateful to M. Kazakov (IAP RAS) for his help with the experiments and technical assistance.

This work was supported by the RFBR grant # 08-02-00531-a, 02-08-00140-a, 06-02-22002-PICS_a, ISTC grant # 2753 . The work of Skalyga V.A. was supported by grant of the President of Russian Federation # МК-4866.2008.2 and by Dynasty Foundation. The work of D. Mansfeld was also supported by Dynasty Foundation.

REFERENCES

[1] R. Geller, Electron Cyclotron Resonance Ion Sources and ECR Plasmas (UK, London, Institute of Physics Publishing, 1996).

[2] G.I. Dimov, A.A. Ivanov, V.S. Koidan, E.P. Kruglyakov, (28th EPS Conference on Controlled Fusion and Plasma Physics, 18-22 June 2001, Funchal, Madeira, Portugal) Contributions ECA, 25A, 461-464 (2001).

[3] A. Vodopyanov, S. Golubev, V. Zorin, S. Razin, M. Shilov. Tech. Phys. Let., vol.25, no. 7, 588-589 (1999).

[4] V. P. Pastukhov, Nucl. Fusion, 14 (3), 68 (1974).

[5] E.V. Suvorov and M.D. Tokman, Sov. J. Plasma Phys. 15, 540, (1989).

[6] V. Semenov, V. Skalyga, A. Smirnov, V. Zorin. Rev. of Sci. Instr., vol.73, no. 2, 635-637 (2002).

[7] S.V. Golubev, I.V. Izotov, S.V. Razin, V.A. Skalyga, A.V. Vodopyanov, S.V. Razin, V.G. Zorin. Trans. of Fus. Sci. and Tech., vol. 47, no. 1T, 345-347 (2005).

A 60 GHZ ELECTRON CYCLOTRON RESONANCE ION SOURCE FOR PULSED RADIOACTIVE ION BEAM PRODUCTION

T. Thuillier, L. Latrasse, T. Lamy, C. Fourel, J. Giraud,
Laboratoire de Physique Subatomique et de Cosmologie, CNRS/IN2P3-UJF-INP Grenoble,
53 rue des Martyrs, 38026 Grenoble CEDEX, France

C. Trophime, P. Sala, J. Dumas, F. Debray,
Laboratoire des Champs Magnétiques Intenses, CNRS
25 rue des Martyrs, B.P. 166, 38042 Grenoble CEDEX 9 France

Abstract

The efficient production of short pulses of radioactive ion beams is a key point of the long term CERN beta-beam project. A strong R&D effort in the field of ion sources is required to reach this challenging objective. A summary of the pulsed beta-beam ion source specification is proposed. A discussion follows on the ion source technologies suitable for this demanding project. The proposed solution foreseen (a 60 GHz ECRIS), uses a cusp magnetic configuration based on water cooled copper coils. The 3D magnetic field structure, along with the mechanical design status is presented. An experimental test with an aluminium prototype shows a good agreement with simulation and validates the design.

THE BETA-BEAM PROJECT

The neutrino physicist community is currently discussing the next generation neutrino beam factory. Nowadays, several projects are still under competition. The Beta-Beam is a project studied by the CERN [1]. The baseline scenario is to generate, ionize, and then accelerate Radioactive Ion Beams (RIB) ~5×10^{13}/s ^{18}Ne or ^{6}He to high energies (with a Lorentz factor γ>100). These nuclei which undergo a β decay are stored in a long race track decay ring to produce intense neutrino beams (see Figure1, blue arrows). The goal of these beams is to study the neutrino oscillations properties and give constraints on the mixing angle θ_{13}.

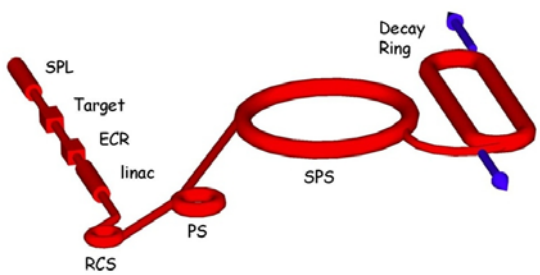

Figure 1: Baseline scenario of the beta-beam accelerator.

The radioactive elements are expected to be produced in the future EURISOL facility. The primary beam, delivered by a proton LINAC, induces nuclear reactions in a set of target stations. Radioactive Gases effuse from the target to the ion source through a high conductance cooled pipe to filter gas and condensable contaminants. The ion source should bunch the beam in order to inject ions as efficiently as possible in the 3 synchrotrons rings included in the project.

SPECIFICATIONS FOR THE PULSED ION SOURCE

Pulsed Ion beam Current specifications

Consider an ideal source able to ionize the RIB of interest with 100% efficiency. If the ion extraction is performed in continuous working (CW) operation, the 5×10^{13} /s ^{18}Ne flux would result in a 8 pμA extracted CW beam. Such ionic intensity is very easy to extract from a classical Electron Cyclotron Resonance Ion Source (ECRIS). The Beta-Beams pulse width at the source extraction is expected to be <50 μs, with a frequency repetition rate f=1/T ranging within the 10 to 25 Hz range. The highest peak current, derived from these values is ~16 pmA. Moreover, other gases will be extracted from the target and ionized in the source. Thus, an unknown number of contaminants will be added to the peak current.

High radioactivity environment constraints

The ^{18}Ne and ^{6}He half lives $T_{1/2}$ are respectively 1.67s and 0.807s. The time for a radioactive atom to exit the target and reach a classical ion source located several meters away already approximately reduces the initial atoms flux by a factor 0.4. A key parameter for the project is to design an efficient ion source located as close as possible to the target in order to minimize the radioactive decay losses. Moreover, the source should hold radiation damages for a long time (~1 month). Consequently, the ion source mechanical parts shall not contain permanent magnets, plastic gaskets; even radiation damage on glass fibre may cause problems. Due to the high radiation level, the maintenance of the ion source will not be possible and its cost per unit will have to be moderate, since it may be necessary to change it periodically.

DISCUSSION ON THE ION SOURCE REQUIRED

Charge state distribution and RIB efficiency

A physical limit of a RIB ion source efficiency comes from the natural charge state distribution (CSD) generated by the plasma. In an ECRIS dedicated to the production of afterglow pulses, the hot electrons of the plasma along with a high magnetic confinement (τ_c) will favour high charge states ions extraction. The RIB of interest will then be extracted into several beams of different charge states. At best one of these charge states could reach 20% of the total ion CSD. Nevertheless, it is still possible to design a special LINAC or a Fixed-field alternating-gradient accelerator (FFAG) to accelerate several charge states, say 2 or 3, at the same time [2]. In this case, one can expect an increase of the overall maximum efficiency of the RIB ionization to reach ~30-50%. A second possible scenario is based on the studies initiated at IAP Nijni Novgorod. There, a simple ECR magnetic trap (either axial mirror or axial CUSP) is used. Very powerful RF pulses (>100 kW) are used to build fast intense ions pulses. Recent promising results have shown the feasibility to produce very high currents up to 150 mA [3], [4] and very short ions pulses (<100 μs) of low to medium charge states [5]. The ionization efficiency of the method needs to be experimentally investigated. Another third possible scenario is to use a compact source with a low magnetic field to preferably produce low charge state ions. There, the ion charge state distribution follows naturally the Poisson statistics and the 1+ beam can be optimized to reach ~90% of the RIB of interest. Of course a special care must be taken to insure a high level of radioactive atoms ionization efficiency in the plasma.

Source of losses and RIB source foreseen

Let's define the residence time (τ_r) as the duration between the atom injection in the plasma chamber and its extraction through the plasma electrode hole. A necessary condition to insure a negligible radioactive decay of the atoms in the source is to have $\tau_r << T_{1/2}$. If the plasma density is high, the ionization time will be low and $\tau_r \sim \tau_c$. Experimental confinement times in ECRIS are roughly in the range τ_c~1-100 ms, so $\tau_r << T_{1/2}$ is satisfied, provided the plasma to be dense. In pulsed mode, the radioactive atom of interest can either be extracted as an ion beam, or as neutral gas. This last case will occur in case of too low plasma density. The plasma density of the ion source should definitely be as high as possible. Another cause of loss occurs if $\tau_c << T$ (T=1/f). In this case, the pulsed plasma disappears totally before the next pulse, letting room to natural gas diffusion through the electrode hole. When $\tau_c \sim T$, another source of loss comes from the low charge state afterglow extraction that will continue until the next RF pulse. These losses can be reduced by installing a pulsed valve at gas injection, or by designing an iris able to close the electrode hole on trigger.

The plasma volume is also a critical parameter. We have seen that the foreseen pulsed RIB intensity to be extracted is high (>16 pmA). Assuming the use of an innovative 60 GHz ECRIS, with a plasma density near the cut-off ~4×10^{13} /cm3, the amount of gas required per pulse (for a mean charge <Z> plasma) is ~$4/<Z>\times10^{16}$ atoms/liter, to be compared with the ~5×10^{13} /s RIB flux. If the plasma volume is large, the radioactive flux could not be sufficient to reach the high density plasma condition and a buffer gas flow will have to be added. The more the buffer gas flow, the higher the extracted pulsed beam intensity, and the higher the difficulties for the ion extraction. So the ion source should have a volume as small as possible in order to minimize the total extracted pulsed ionic current. A small volume is a challenging constraint for a 'standard model' complying ECRIS, since the use of superconducting technology requires a large volume to relax superconductor wire constraints.

The use of a pulsed duo-plasmatron is questionable. This kind of ion source produces naturally 1+ beam with very high intensities and pulse duration can be easily adapted to the requirement. The drawback is the high pressure (~1 mbar) required inside the plasma chamber of the duo-plasmatron that will make RIB filling rather complicated, since they are produced in secondary vacuum. The global ionization efficiency is expected to be in the range of some 1%, but this order of magnitude has to be confirmed experimentally. A duo plasmatron available at LPSC will be tested in the next months to measure properly the ionization efficiency as a function of the duo-plasmatron parameters.

Summary and strategy

We have seen that the Beta Beam pulsed Ion Source high plasma density which implies high current extraction. A 4th generation ECRIS is the best option. The volume should be as small as possible in order to limit the total extracted current. The extracted RIB charge state is of secondary importance for the moment: in order to investigate the topic, LPSC team decided to start an ambitious 60 GHz R&D program. The goal is to build several prototypes of 60 GHz innovative magnetic structures and test them in pulsed mode. The structures foreseen may be as simple as a single field gradient or as complex as a minimum-|B| structure. The development of several operational superconducting technologies at 60 GHz is not realistic since it takes a lot of time and requires a lot of money. The collaboration with the Grenoble High Magnetic Field Laboratory (GHMFL) provides an opportunity to make 60 GHz ECRIS R&D for an affordable price and short design time. GHMFL is equipped with a set of 20 MW/20-35 Tesla resistive coils available for fundamental physics studies. The original idea consists in developing different sets of magnetic coils using the helix coil resistive technology [6] invented at GHMFL and test them on site with a new dedicated ECRIS test bench. The 60 GHz prototypes will be dimensioned to comply with the GHMFL electrical power and water cooling systems. Moreover, this technology is

usable in a highly radioactive environment, since the magnetic structure is mainly composed of copper, steel and water.

DESIGN OF A 60 GHZ ION SOURCE IN CUSP CONFIGURATION

As a first step, LPSC and GHMFL decided to design an axi-symmetric MHD stable magnetic structure: a cusp. The initial design specifications include the following magnetic properties, illustrated in figure 2:

- a closed 2.1 Tesla 60 GHz ECR zone;
- a 4 Tesla radial mirror;
- 6 Tesla at the injection;
- 3 Tesla at the extraction;
- field lines going through the ECR zone must be connected to the above magnetic mirrors without intercepting the plasma chamber wall;
- a 10 cm mirror length.

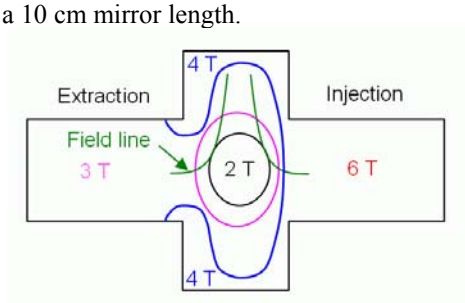

Figure 2: Magnetic field expected in the plasma chamber.

The coil helices are made of copper alloy cylinders into which a helical slit is cut by electro erosion. It is possible to adapt locally the coil current density by changing the helix pitch along the copper coil.

Magnetic simulation

A 2D simulation was performed using both RADIA [7] and Getdp (software developed at Liege University), specially adapted to the helix technique [8]. A flexible solution has been found with a set of 4 radially cooled helices coils, named H1, H2, H3 and H4, presented on figure 3:

- H1, the longest helix, mainly generates the magnetic field at injection. H1 is composed of 3 successive pitch areas (visible on figure 3). The shortest pitch is located on the inner side of the source, close to the largest diameter of the plasma chamber (shoulder), to concentrate the closed ECR zone and generate radial mirror;
- H2 is very short and permits to keep the ECR zone close to the centre of the source and to generate the radial mirror;
- H3 and H4 help to generate the radial mirror in the shoulder;
- H4 mainly produces the extraction magnetic field.

The concentration of a high magnetic field gradient in a 100 mm peak to peak axial cusp rendered the optimization difficult. When the distance between the injection and extraction coils is small, the radial magnetic mirror value is high (sum of radial magnetic components), but consequently the axial magnetic peaks at injection and extraction are reduced (subtraction of the axial magnetic component). A compromise was found when the smaller inner radius of the coils was close to the distance between them. The inner plasma chamber diameter was set to the minimum value possible (60 mm). The corresponding inner coils diameter was set to 80 mm. Below this diameter, the condition concerning the field lines (bullet 5) could not be fulfilled.

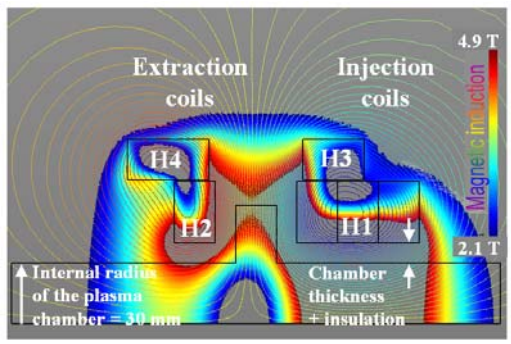

Figure 3: 2D simulation with pitch change configuration of H1. Half of the plasma chamber is represented.

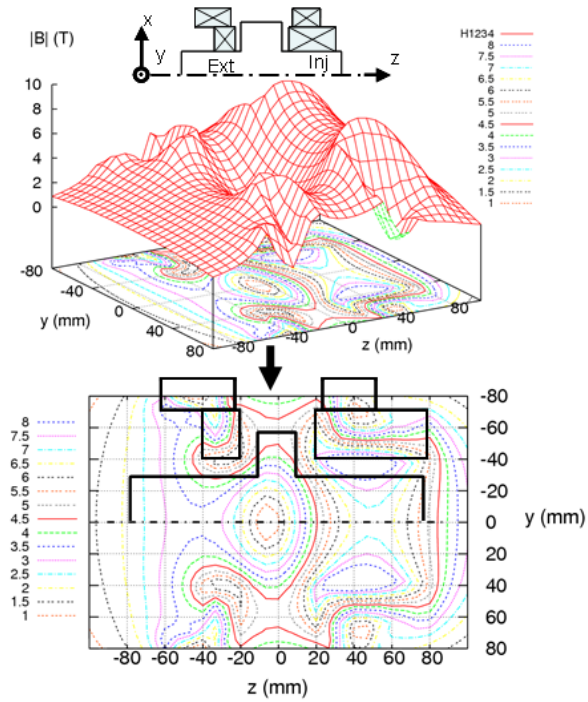

Figure 4. 3D simulation. Magnetic field |B| in the Oy-Oz plane.

A 3D simulation has been performed with another code based on Getdp [9]. It includes thermal analysis (helices water cooling) and exact helices geometry (width of the electro erosion slit) which was not the case in the 2D calculation. The helices were designed with CATIA and then meshed by Samcef Field. The current injected in the

coils is 30000 A. The conductivity of the helices is 90 % of the International Annealed Copper Standard (IACS). 3D simulation gave results in good agreements with the 2D ones. Figure 4, represents the magnetic field norm |B| in the Oy-Oz plane as calculated with the 3D simulation. The magnetic field intensity reaches 6.9 T at the injection on the z axis and 3.4 T at the extraction. The radial mirror intensity varies between 4.8 and 4.9 T, due to the imperfect helices symmetry. These results are above the initial specifications, so more flexibility will be available for the injected currents. The magnetic structure can be seen in 3 dimensions using the EnSight 8 software. Thus, in figure 5, the temperature in the helices, the iso-B surface of 7 T at the injection, the iso-B surface of 3.5 T at the extraction and the iso-B of 2.1 T (ECR zone) are represented in the plasma chamber. For more visibility, the mirror surface in the shoulder is not represented.

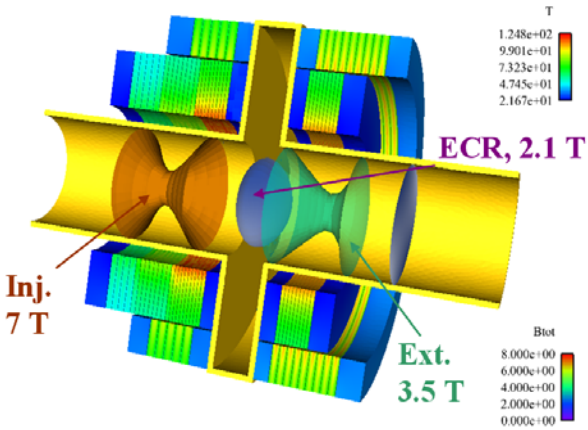

Figure 5. Temperature in the helices and iso-B surfaces of 7 T, 3.5 T and 2.1 T in the plasma chamber.

Validation with an aluminium prototype

Since the design includes an innovative small pitch of 2 mm never used before, an H1 aluminum helix prototype has been machined to experimentally test the accuracy of the calculations (see figure 6(a)). Figure 6(b) represents a comparison between the calculated axial magnetic field and the measured axial magnetic field along the coil axis at low current density (144 A injected). z = 0 mm is the beginning of the helix on the thin pitch side. The difference is only of 3 % at the maximum peak value and both curves have the same magnetic center.

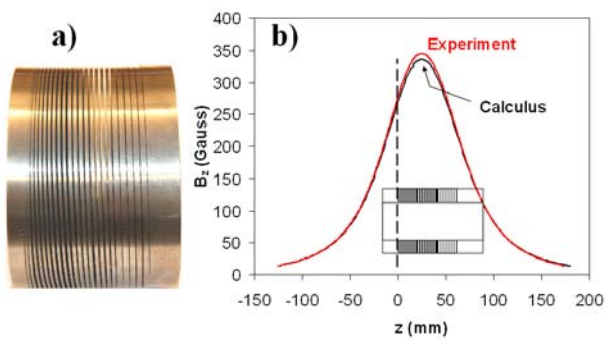

Figure 6. (a) H1 aluminum prototype, (b) Axial magnetic profile of H1.

Engineering design

The current intensity in the cusp has been chosen to be 30000 A Thus, the maximum current density reaches 640 A/mm^2 on the internal radius of H1 and H2, where the pitch is only of 2 mm. The maximum electrical power needed is about 5 MW, depending on the final coils resistivity, so the structure is actively de-ionized water cooled. The inlet water pressure is 2.7 MPa (27 bars), while the outlet one is 0.4 MPa (4 bars). The average water temperature increase is 20°C. The water flow rate is ~20 l/s in the two set of coils. The water speed in the radial helices slit ranges within 30 to 35 m/s, providing a convection heat transfer coefficient h~150 kW/m^2/°C. The average coils temperature varies from 70 to 95 °C while the peak temperature locally reaches 125°C. Pessimist calculations have been performed using a conductivity of 80 % IACS and h~120 kW/m^2/°C for each coil. In this case the mean coils temperature varies between 80 and 115 °C, the peak temperature is 150 °C and the power needed is 6.5 MW. In these conditions, the maximum hoop stress in the coils is σ~280 MPa, far below the copper alloy limit of elasticity (360 MPa). At full current, the two sets of coils repel each other with a force of 600 kN.

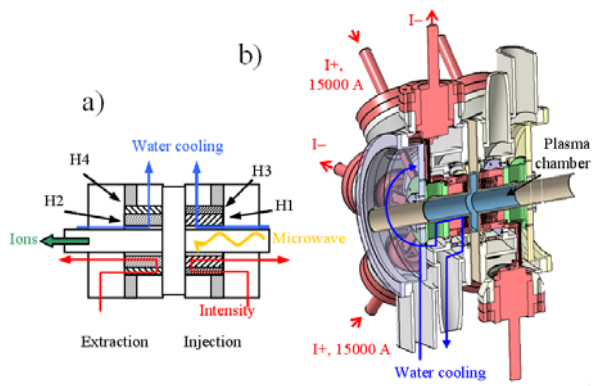

Figure 7. (a) Principle of the source, (b) details of the source.

In case of an extraction coils supply failure (H2+H4), a 50 kN force will arise between H1 and H3 since these two coils have a different magnetic center. The CAD mechanical design of the magnetic structure, taking in account all these data is under progress at LPSC. Figure 7(a) shows the principle of the source and figure 7(b) represents details of the source.

Planning

This first 60 GHz magnetic structure (helices coils in their tanks, electrical and water cooling environment) should be available at the beginning of 2009. The 60 GHz Gyrotron is expected at best for the end of 2009. First experiments of the prototype at a 28 GHz ECR frequency should be done in 2009. The first pulsed beam at 60 GHz is expected in 2010.

REFERENCES

[1] http://cern.ch/beta-beam/

[2] P.N.Ostroumov, K.W.Shepard, V.N.Aseev; A.A.Kolomiets, "Heavy ion beam acceleration of two charge states from an ECR ion source", XX International Linac Conference; Monterey, California.

[3] A. Sidorov, M. Dorf, A. Bokhanov, I. Izotov, S. Razin, V. Skalyga, V. Zorin, A. Balabaev, P Spedtke, J. RoЯbach. Multi-aperture ion beam extraction from gas-dynamic electron cyclotron resonance source of multicharged ions, Rev. Sci. Instrum., 79, 02A317 (2008).

[4] V. Skalyga, proc. of the 8th international workshop on ECR Ions Sources, Chicago, Illinois USA-September 15-18, 2008.

[5] A.V. Vodopyanov, S.V. Golubev, I.V. Izotov, V.I. Khizhnyak. D.A. Mansfeld, V.A. Skalyga and V.G. Zorin. ECR Plasma With 75 GHz Pumping. High Energy Physics and Nuclear Physics. 2007, **31**(S1): 152—155.

[6] P. Rub and W. Joss 1996 A new type of radially cooled helices designed for a 25 T magnet *IEEE Transactions on Magnetics* **32** 2570 – 3

[7] O. Chubar, P. Elleaume and J. Chavanne 1998 A three-dimensional magnetostatics computer code for insertion devices *J. Synchrotron Rad.* **5** 481 – 4

[8] C. Trophime, K. Egorov, F. Debray, W. Joss and G. Aubert 2002 Magnet Calculations at the Grenoble High Magnetic Field Laboratory *IEEE Trans. Appl. Superconduct.* **12** 1483 – 7

[9] C. Trophime, S. Krämer and G. Aubert 2006 Magnetic Field Homogeneity Optimization of the Giga-NMR Resistive Insert *IEEE Trans. Appl. Superconduct.* **16** 1509 – 12

MICROWAVE SOURCES FOR 3-rd AND 4-th GENERATIONS OF ECRIS

Yu. Bykov#, G. Denisov, A. Eremeev, S. Samsonov, IAP RAS, Nizhny Novgorod, Russia

Abstract

Recent results in the development of the electron cyclotron resonance ion sources (ECRIS) have proven the potential of the operating frequency for the production of high-intensity multicharge ion beams. The next ambitious steps are discussed today which include further increase in frequency up to 60 GHz, use of broadband microwave sources, and two- or three-frequency heating. Microwave sources capable of meeting the needs of the next generation of ECRIS are considered here based on many-year experience of the Institute of Applied Physics in the design and fabrication of high-power millimeter-wave equipment and achievements of other research groups. Different varieties of gyro-devices producing broadband radiation (multi-frequency or fast-swept in time) with CW or average power of order of 10-15 kW and the center frequency within the range 24-60 GHz are discussed.

INTRODUCTION

The progress in the development as well as the domain of operating parameters for any microwave power source are strongly stimulated and dictated by the applications. For example, gyrotrons with frequencies of 140 GHz and 170 GHz, and CW power of megawatt level have been developed for thermonuclear fusion installations (tokamaks, stellarators); amplifiers having broad frequency band, pulsed power of order of 100 kW and center frequencies lying in the transparency windows of the atmosphere (e.g. 35 GHz and 94 GHz) were worked out for radars. The electron cyclotron resonance ion sources are a relatively new line of application based on the use of moderate microwave power (on the order 10 kW) at frequencies of tens GHz. A significant improvement of ECRIS performance parameters upon a transition to the frequency of 28 GHz has been prove recently by experimental results obtained at several facilities. According to current concepts, further progress in ECRIS operating characteristics can be achieved using microwave sources of higher frequency and such additional options as fast frequency sweeping (with a sweep time less than 10^{-4} s within a frequency band of few percents) or multi-frequency generation or generation of CW signal with a broadband spectrum [1, 2].

It is generally recognized that the only microwave sources capable of delivering CW or average power on the order of 10 kW in the frequency range of tens GHz are vacuum electron devices based on the cyclotron resonance maser (CRM) instability and using low-relativistic electron beams (particle energy of about tens keV), often called gyro-devices. The operation of these high-power coherent radiation sources (gyro-devices) is based on the interaction of the electrons gyrating in the external magnetic field with a fast electromagnetic wave under the cyclotron resonance condition: $\omega - hv_{\parallel} \approx n\omega_H$, where ω and h are the frequency and the axial wavenumber of the wave, $v_{\parallel}$ and ω_H are the axial velocity and the cyclotron frequency of the electrons, n is the cyclotron harmonic number. The interaction of electrons with fast electromagnetic waves propagating in the cavities and waveguides with smooth metal walls is the distinguishing feature of gyro-devices as opposed to conventional slow-wave electron devices. Since no periodic structure is employed, enhanced power handling capability exists in gyro-devices.

Formally, the orbital bunching of gyrating relativistic electrons has much in common with bunching of linear electron beams being used in ordinary ("O" type) devices. Therefore each CRM has its "O" type analog: monotron, klystron, travelling-wave-tube (TWT), backward-wave oscillator (BWO). The differences in operation principles of these gyro-devices can be seen from the dispersion diagram shown in Fig.°1. This diagram will be discussed later in more detail as applied to each type of gyro-device.

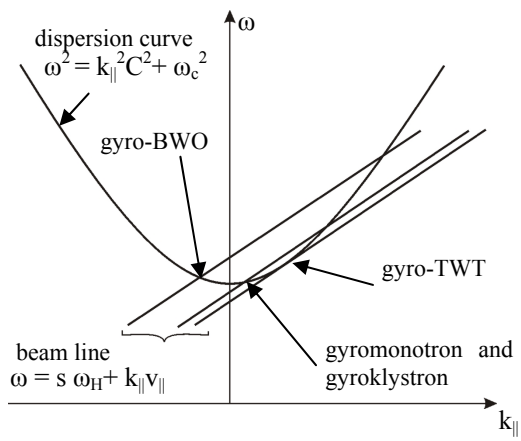

Figure 1: Dispersion diagram showing the operating point for gyro-devices: ω_H – electron cyclotron frequency, ω_c – the cutoff frequency of the waveguide mode, $k_{\parallel}$ – axial wave number, $v_{\parallel}$ – axial velocity of electron beam.

A review of the experimental results obtained during last two decades shows that gyro-devices are capable of meeting the requirements imposed by the next generation of ECRIS. Here, the general concepts of various gyro-devices are briefly introduced. Examples of last experimental achievements obtained in application-driven developments are presented to illustrate the feasibility of custom-made gyro-device based systems for ECRIS.

GYROTRON (gyro-MONOTRON)

The feasibility of implementing fixed-frequency gyrotrons for a customer-ordered frequency and power of 10-15 kW in both CW and pulse regimes is beyond question today and gyrotrons operating at frequencies of 28, 37 and 75 GHz are already used in some ECRIS

experiments. In the conventional gyrotron the resonant cavity has a fixed structure, and fixed and discreet spectrum of the supported eigenmodes. The gyrotrons operate near the electron cyclotron frequency $\omega_c = eH_0/\gamma m_0$ or its harmonic $n\omega_c$ (e is the electric charge, m_0 is the mass of the electron, $\gamma = 1 + eU/m_0c^2$ is the relativistic mass factor), and the operating frequency can be controlled only by varying the electron beam energy eU (rapid electrical tuning) or the static magnetic field strength H_0 (slow magnetic tuning). Here we omit the case when a resonant cavity of special design has mechanically movable elements such as split walls or inner coaxial rod, since these methods can provide only very slow tuning and, moreover, offer problems with cooling at the CW operation.

As with any kind of oscillators the bandwidth of frequency tuning is inversely proportional to the quality factor of the resonator. For gyrotrons the frequency bandwidth is a function of many operating parameters: $\Delta\omega = (\omega/Q)\cdot F(I, U, H,...)$, where Q is the quality-factor of a resonator, I is the electron beam current, U is the acceleration voltage. The variation of any of the arguments of F leads to a shift of the operating frequency. The qualityfactor in the gyrotrons of moderate power is over 10^3 and the frequency tuning range is typically less than 0.1%. For example, in [3] it was shown experimentally that in the 75 GHz gyrotron with the Q-factor of 10^3 the relative frequency shift at half-power level equaled to 0.1, 0.05, and 0.01% at variation of the magnetic field, anode voltage and beam voltage, respectively. It is necessary to note that any change of the operation parameters changes not only the frequency but also the efficiency of interaction of the electron beam with the electromagnetic wave and eventually the output power of gyrotrons.

Among many research efforts undertaken in an attempt to increase the frequency bandwidth of gyrotrons it is worth noting [4] where a 0.96% tuning range was achieved in an X-band gyrotron with coupled cavities. The RF circuit of the gyrotron consisted of two circular cavities separated by a thin iris. A tenfold increase in the tuning range over that of an ordinary gyrotron resulted from the effective interaction of the electron beam with two modes having the same azimuthal and radial but different axial structures. The frequency tuning was performed by a variation of the magnetic field strength. The efficiency of oscillation was about 18% and remained constant within a ± 1% limit over the whole frequency tuning range.

GYROKLYSTRON

The development of the millimeter-wave K_a-band (34-36 GHz) and W-band (93-95 GHz) gyroklystrons was primarily stimulated by radar applications within the ranges of the atmospheric RF "windows". Later, high-power pulse gyroklystrons attracted attention as sources of coherent radiation for compact, high-gradient linear accelerators. As the result of the radar application-driven efforts, quite impressive parameters were achieved in a K_a-band gyroklystron as early as in 1993 [5]. The two-cavity gyroklystron delivered 750 kW output power in up to 100 microsecond pulses. A maximum efficiency of 32% was obtained at the 300 kW output power level. At the 600 kW power level, the gain was 22 dB and the instantaneous bandwidth at the – 3 dB level was 0.61%. The bandwidth was limited by the Q-factor of the output cavity which was about 320.

The Q-factor of 200-300 is typical for the resonant cavities used in gyroklystrons. The bandwidth of gyroklystrons can be increased by the so-called stagger tuning when the resonant eigenfrequencies of cavities are slightly detuned around the output cavity frequency [6]. This method is widely used in conventional klystrons. In general, the larger is the stagger tuning, the larger both the increase in bandwidth and decrease in gain. However, some reduction of gain is seemingly not very critical for gyroklystrons of moderate power. A high-signal gain of 30 dB is achievable in a multicavity gyroklystron, and a 10 kW output power can be obtained using a solid state driver since an input power of 1 W is sufficient to saturate the device.

Regarding a CW or high average power operation of gyroklystrons, it is necessary to mention the serious technical problem arising from high thermal loads on some components. High-loss ceramic loads are typically introduced between cavities to suppress instabilities and spurious oscillations. Even heavier can be the thermal load in the penultimate cavity of multicavity gyroklystrons.

An example of a successful solution of these problems can be found in [7], where authors reported on the development of a four-cavity W-band gyroklystron delivering over 10 kW average power with 11% duty cycle (100 μs pulse, 1.1 kHz repetition rate). The instantaneous bandwidth of this device at the – 3 dB level was 420 MHz (0,5%), the gain was 35 dB, and the efficiency was 33%.

GYRO–BACKWARD WAVE OSCILLATOR (gyro-BWO)

The gyro-BWO is based on the resonant cyclotron interaction of the electrons gyrating in the external magnetic field with the electromagnetic wave travelling in the direction opposite to the longitudinal velocity of electrons. A gyro-BWO operating with a travelling wave of non-resonant microwave structure can provide broad-band smooth frequency tuning by variation of the magnetic field strength or the electron beam energy.

The gyro-BWO operation has been successfully tested in the early 1990's in a number of experiments. In [8], a short-pulse K_a-band gyro-BWO operating at the fundamental cyclotron harmonic and fundamental TE_{10} mode of a smooth cylindrical waveguide was described. The continuous magnetic field tuning bandwidth was 13% (from 27.5 to 31.5 GHz) and the voltage tuning bandwidth was 3% at the half-power level, while the power approached 7 kW with nearly 20% efficiency. The

3 dB 5% voltage tuning range was achieved in a pulse K_a-band gyro BWO reported in [9].

The relatively low efficiency of backward-wave oscillators is explained by an unfavorable axial structure of the RF field. Electrons are modulated near the entrance to the waveguide structure by a high-amplitude RF field while electron bunches lose the energy near the exit where the field amplitude is low. However, the efficiency can be drastically increased up to 30 and even to 50% by the tapering of the external magnetic field or the waveguide radius, as it was shown in [10, 11].

The use of a novel microwave structure in the form of a helically grooved waveguide was suggested in [12]. A properly chosen helical corrugation of the surface of an oversized circular waveguide provides dispersion of a circularly polarized eigenmode that is favorable for the traveling-wave based gyro-devices, such as gyro-BWO and gyro-TWT. The main advantage of the so produced eigenwave dispersion is in its sufficiently large group velocity at zero axial wavenumber, which ensures broadband operation with minimum negative impact of the electron velocity spread. In the experiments on the helical-waveguide gyro-TWT performed at IAP, the gyro-BWO operation was also studied [13], which was simplified by the fact that switching between TWT and BWO operation required just the change of polarity of the external magnetic field. In these proof-of-principle experiments, stable and reliable K_a-band pulse gyro-BWO operation at the second cyclotron harmonic was obtained. Later, a CW gyro-BWO with a helically grooved waveguide was designed for a number of technological applications [14]. The device operated with a weakly relativistic (20 keV) electron beam. A maximum power of 7 kW with the efficiency of 15% at a frequency of 24.7 GHz was achieved. The frequency tuning range at the half-power level was about 5% when varying the magnetic field (Fig. 2) and 0.8% when varying the beam voltage. The variations in the output power can be explained by reflection from unmatched output window.

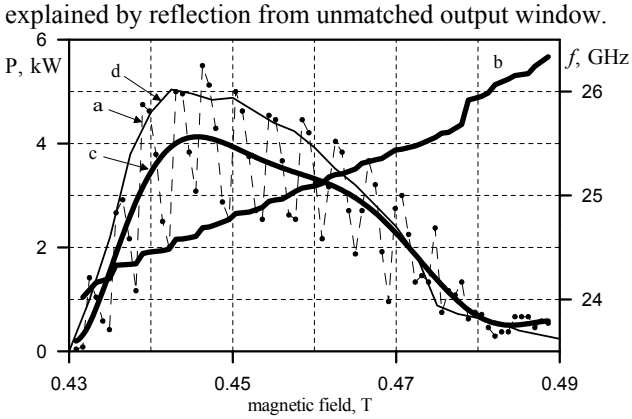

Figure 2: The output microwave power (a) and frequency (b) of the gyro-BWO as functions of magnetic field for the beam voltage of 20 kV and beam current of 2 A; curves (c) and (d) are the averaged experimental output power and the power obtained as the result of the performance simulation, respectively.

A 2.5 kW CW 24 GHz gyro-BWO of a similar design has been incorporated in a two-frequency gyro-device based system for microwave processing of materials, produced by IAP for the Far Infrared Center, Fukui University, Japan (Fig. 3). Another microwave source in this system was a 15 kW CW 28 GHz gyrotron.

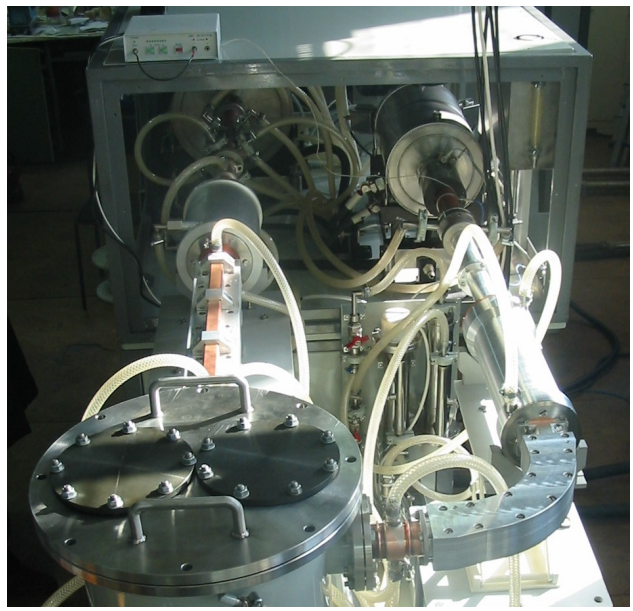

Figure 3: Two-frequency gyro-device based system combined of a 2.5 kW CW 24 GHz gyro-BWO and 15 kW CW 28 GHz gyrotron.

GYRO–TRAWELLING WAVE TUBE (gyro-TWT)

Despite a long history of the development of gyro-TWTs and impressive results achieved by many groups, at present there are no systems in which these devices are used. As is often the case, there is a trade-off between the performance characteristics of a gyro-TWT such as a gain and a frequency bandwidth. This trade-off can be resolved in favor of one or other parameters depending on a given application. Since the next generation of ECRISs needs a rather moderate, for gyro-devices, level of millimeter-wave power it appears that an increased bandwidth is a more critical parameter than a large gain in this application.

At the early stage of research most experiments were performed on pulse gyro-TWTs. The bandwidth exceeding 10% even in the large-signal regime of a K_a-band gyro-TWT was obtained in one of the first experimental works reported in 1990 [15]. Later on, a significant increase in the instantaneous bandwidth up to 33%, the largest for a gyro-TWT, was achieved in a gyro-TWT with the tapered magnetic field [16]. This device operated with the efficiency of about 10% and a small-signal gain in excess of 20 dB.

The implementation of an amplifier operating with high average or CW power is impeded by serious difficulties. The most severe of them is spurious oscillations which arise partly due to the electron velocity spread. The

common method for suppression of spurious oscillation is the use of a distributed loss. Most distributed loss stabilized gyro-TWTs to date employ a thin lossy coating that is not compatible with high-average power operation. An elaborate suppression technique was developed at the Naval Research Laboratory, based on loading the most part of the interaction space of a 35 GHz TE_{01} mode gyro-TWT with a lining of lossy ceramic cylindrical shells periodically interspaced with narrow metal rings. A high gain of 60 dB and a 3 dB bandwidth of 4.2 GHz (12%) were achieved but the device was tested in the pulse regime only with a pulse length of 11 μs and repetition rate of 3 Hz [17].

The above mentioned idea about the use of a helically grooved waveguide works advantageously for a high average power gyro-TWT. Low sensitivity of the operation mode to the electron velocity spread allows good stability against oscillations and significant increase in efficiency. In addition, the danger of overheating of the elements of the device is reduced, and proper cooling becomes much easier when a completely metal waveguide structure is used.

The bandwidth capabilities of such a gyro-TWT with a helically grooved waveguide were tested firstly in the X-band (9.4 GHz) [18]. A saturated gain of 37 dB with the efficiency close to 30% was obtained over 21% bandwidth in a short pulse device. Later on, operation of a second-harmonic K_a–band gyro-TWT was demonstrated [19]. A maximum efficiency of 27%, power of 180 kW, saturated gain of 25 dB and instantaneous -3 dB bandwidth of nearly 10% were obtained at pulse operation with a 10 μs pulse duration and a 1 Hz repetition rate.

These results clearly demonstrate the potential of this new concept of the waveguide structure for high average power gyro-TWTs operating in the millimeter-wave range.

CONCLUSION

The experimental results achieved to date demonstrate that gyro-devices of all types considered here can meet the requirements of the next generation of ECRIS in terms of power and frequency. As for the requirements for a frequency bandwidth and frequency sweeping, they can also be met but the detailed specification should be elaborated for each particular facility in order to develop a gyro-device most precisely fitting the user's needs. There is a trade-off between performance characteristics, and the priorities are dictated by a given application.

It is clear that an increase in both the power and frequency of the millimeter wave sources that feed the ECRIS requires a new type of microwave transmission lines. The lines should be composed of the oversized multimode and/or quasioptical components. A large experience in designing such components and transmission lines as a whole has been acquired to date as the result of the development of millimeter wave power facilities for high power applications.

REFERENCES

[1] S. Gammino, High Energy Physics and Nuclear Physics, 31, Supp. I, (2007) 137.

[2[D. Hitz, High Energy Physics and Nuclear Physics, 31, Supp. I, (2007) 123.

[3] I.I. Antakov, E.V. Zasypkin and E.V. Sokolov, Int. J. Infrared and Millimeter Waves 14 (1993) 1001.

[4] E. Zasypkin, M. Moiseev and L. Nemirovskaya, Int. J. Electronics 85 (1998) 207.

[5] I.I. Antakov, A.V. Gaponov, E.V. Zasypkin, et al., "Gyroklystrons – millimetre wave amplifiers of the highest power", Proc. 3rd Int. Workshop Strong microwaves in plasmas, Nizhny Novgorod, August 1993, 2, p. 587 (1994).

[6] G.S. Nusinovich, B.G. Danly and B. Levush, Phys. Plasmas, 4 (1997) 469.

[7] M. Blank, B.G. Danly, B. Levush et al., Phys. Plasmas 6 (1999) 4405.

[8] S.Y. Park, R.H. Kyser, C.M. Armstrong et al., IEEE Trans. Plasma Sci. 18 (1990) 321.

[9] C.S. Kou, S.G. Chen, L.R. Barnett et al,. Phys. Rev. Lett. 70 (1993) 924.

[10] A.K. Ganguly and S. Ahn, Int. J. Electronics 67 (1989) 261.

[11] G.S. Nusinovich and O. Dumbrais, IEEE Trans. Plasma Sci., 24 (1996) 620

[12] G.G. Denisov, V.L. Bratman, A.D.R. Phelps and S.V. Samsonov, IEEE Trans. Plasma Sci. 26 (1998) 508.

[13] V.L. Bratman, A.W. Cross, G.G. Denisov et al., "Broadband gyro-TWT's and gyro-BWO's with helically rippled waveguides", Proc. 5th Int. Workshop Strong microwaves in plasmas, Nizhny Novgorod, August 2002, p. 46 (2002).

[14] S.V. Samsonov, G.G. Denisov, V.L. Bratman et al., IEEE Trans. Plasma. Sci., 32 (2004) 884.

[15] K.R. Chu, L. R. Barnet, H.Y. Chen et al, IEEE Trans. Electron Devices, 37 (1990) 1557.

[16] G.S. Park, S.Y. Park, R.H. Kyser et al, IEEE Trans. Plasma Sci., 22 (1994) 536.

[17] D.E. Pershing, K.T. Nguen, J.P. Calame et al, IEEE Trans. Plasma Sci., 32 (2004) 947.

[18] V.L. Bratman, A.W. Cross, G.G. Denisov et al, Phys. Rev. Lett. 84 (2000) 2746.

[19] V.L. Bratman, A.W. Cross, G.G. Denisov et al, "Broadband gyro-TWTs and gyro-BWOs with helically rippled waveguides", Proc. 5th Int. Workshop Strong microwaves in plasmas, Nizhny Novgorod, August 2002, 2, p. 46 (2003).

ON THE OBSERVATION OF STANDING WAVES IN CYLINDRICAL CAVITIES FILLED BY MICROWAVE DISCHARGE PLASMAS*

L. Celona#, G. Ciavola, S. Gammino, N. Gambino, F. Maimone, D. Mascali, R. Miracoli
INFN-LNS, Via S. Sofia 62, 95123 Catania, Italy

Abstract

A set of measurements has been carried out at INFN-LNS on a plasma reactor used for environmental applications with the aim to characterize it in terms of possible excited resonant modes inside the cavity with and without plasma.

The results have put in evidence that resonant modes are excited inside the cavity and standing waves are formed even in presence of a dense plasma. The measurement of the eigen-frequency shift, which occurs after the plasma ignition, has been carried out, for several values of pressure and power.

The changes in plasma shape, density and electron temperature have been also monitored for different operating conditions by means of a Langmuir Probe.

Such measurements are also relevant for the ECR Ion Sources, as they confirm that the variation of their performances with the frequency can be explained by considering that resonant modes are excited inside the plasma chamber even in presence of a dense plasma.

INTRODUCTION

Many experiments in the last years have shown that significant improvements of ECRIS performances are obtainable by means of a multi-frequency heating of ECR plasmas. On the other hand, it has been demonstrated that a substantial increase of the extracted currents is achieved also by slightly varying the microwave frequency even in the case of single frequency heating [1,2]. This "frequency tuning effect" has been verified experimentally for different ion sources, and in particular some tests carried out on a CAPRICE source at the GSI testbench by sweeping the microwaves in a range of ±40 MHz around 14.5 GHz, have also shown a dependence of the beam intensity distribution from the microwave frequency feeding the plasma chamber [2].

This means that an improvement of the coupling and of the heating phenomena is achieved by properly tuning the frequency of the microwaves. At the same time, from the observations in [2] we can also state that the beam formation process and the beam shape are strongly affected from the frequency variations.

The explanation of these results is strictly linked to the electromagnetic field pattern inside the chamber: in particular, the ECRH and the ionization process change with the electromagnetic field distribution and with its value over the resonance surface. Such distribution cannot be simply determined even supposing the plasma chamber as a cylindrical cavity air filled. In fact, the microwave feeding wavelength is usually much lower with respect to the plasma chamber dimensions; therefore the first resonant frequency of the plasma chamber in vacuum conditions is very far from the operating one (e.g.: for the SERSE source the first resonant frequency is at 1.39 GHz, while the operating frequency is within the 14-18 GHz range). Consequently, the electromagnetic field pattern at the operating frequency is the result of the superposition of the different modes excited in the chamber, each one weighted by its coupling factor.

When the plasma is triggered its presence changes the electromagnetic properties of the whole structure; the previous observations suggest that an electromagnetic modal structure is present in the source even in presence of plasma. In this case, a different electromagnetic field pattern can be produced if the frequency is slightly changed, determining a different efficiency of the plasma heating and of the ionization process [3].

In order to study the evolution of the modes in the plasma chamber when the plasma is created, we exploited a plasma reactor in use at LNS for environmental purposes. This choice has the great advantage with respect to an ECR ion source to have different ports for diagnostics and also to have the possibility to monitor the plasma properties by means of a Langmuir probe (LP).

PLASMA REACTOR DESCRIPTION

The plasma reactor operating at LNS is based on the same physics principles of the Microwave Discharge Ion Sources, that generally are used for industrial applications or as proton sources in nuclear physics. The plasma chamber is a stainless steel cylinder 268.2 mm long, with a radius of 68.5 mm. A magnetic system which consists of three NdFeB permanent magnets rings generates an off-resonance magnetic field along the plasma chamber axis. In the injection side the flanges for the pumping and for the gas injection are located together with a WR284 rectangular waveguide operating in the TE_{10} dominant mode and placed on the cavity axis. In the opposite side DN 40 and DN 25 flanges are used to connect the plasma diagnostics devices such as: mass spectrometer, optical window (to be used for plasma observation and for optical spectroscopy), microwave probes and the Langmuir probe (see figure 1). The microwaves are generated by a Magnetron operating at 2.45 GHz with a 300 W cw of maximum power. A rotative pump is used for vacuum (pressures in the order of a few 10^{-2} mbar are usually obtained).

*Work supported by INFN through the NTA-HPPA strategic project.
#celona@lns.infn.it

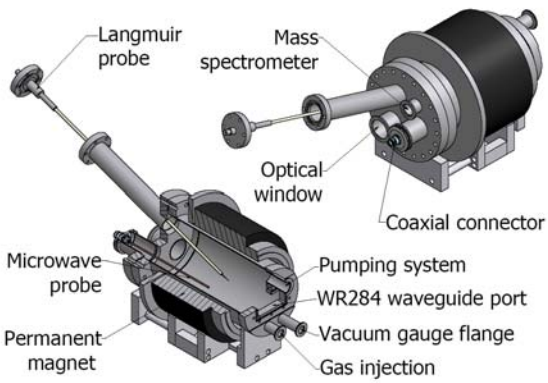

Figure 1: The plasma reactor

The first experiments carried out in the 2007 has permitted a complete characterization of the reactor, in terms of electron density and electron temperature [4]. Optimum operating conditions of microwave power and gas pressure have permitted the n-hexane (C6H14) and cyclo-hexane (C6H16) dissociation [5].

This testbench has been used to investigate the standing wave formation inside the resonant cavity in presence of plasma. Preliminary studies about the coupling between microwave generators and ECRIS have been carried out at INFN-LNS for the SERSE superconducting ion source. Several measurements were performed by means of a Vector Network Analyzer (VNA) able to operate up to 50 GHz, in order to characterize the system including the plasma chamber (in vacuum) and the microwaves line in terms of S matrix [6]. The same VNA has been used for the plasma reactor and the S matrix has been characterized with and without plasma. In our experiment we fixed the microwave frequency feeding the plasma at 2.45 GHz and analysed the plasma properties in terms of the reflection coefficient in the 1-3 GHz frequency range. The experimental set-up is shown in figure 2. A coaxial connector permitted to determine the scattering parameters in presence of the plasma (a series of attenuators were used to reduce the coupled power) and to investigate the best condition of wave-plasma coupling by varying its length.

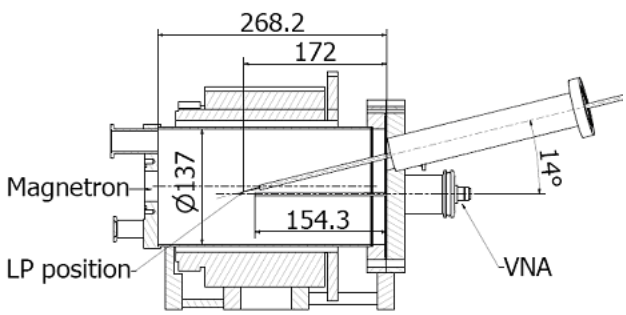

Figure 2: The experimental setup

In order to measure the S_{11} parameters in the different operating conditions the VNA was connected to the coaxial connector while the plasma was ignited through the waveguide. Such not perturbative method allowed to characterize the plasma effect on the resonating modes that exist inside the resonating cavity and also to obtain a reasonable method to evaluate the plasma parameters in terms of electron density. Such calculations are in a reasonable agreement with the plasma parameters measurements carried out with a Langmuir Probe inserted inside the plasma chamber off axis with a slope of 14° as shown in figure 2. Measurements at different positions of the Langmuir probe have been carried out and is was observed that the electron density and temperature increased as the probe penetrated inside the plasma chamber [4]. All the measurements here reported have been carried out by positioning the Langmuir probe tip at z= 17.2 cm inside the cavity, as shown in figure 2, being more stable the plasma and more reliable the data acquired in this position.

EXPERIMENTAL RESULTS

At the beginning we investigated the modes of the cavity in vacuum by measuring the S_{11} seen from the microwave probe and from the WR284 waveguide. The results of the measurement carried out in the 1÷3 GHz frequency range are shown in figure 3: a good agreement has been found with the numerical calculation, as shown in table 1.

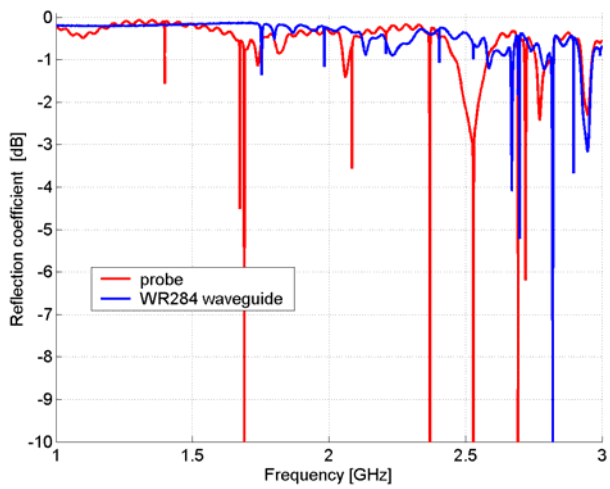

Figure 3: Reflection coefficient measured at the two microwave inputs

By analyzing the reflection coefficient it is possible to characterize the modes that exist inside the plasma chamber. In fact the frequencies for which the minimum values of the S_{11} occur represent the excited modes.

The theoretical calculation of the resonant modes in vacuum has been carried out by solving the eigenvalue equations for the electromagnetic field inside the cylindrical plasma chamber and by using a simplified model of the cavity (it has been considered empty and completely closed).

Table 1: Modes inside the plasma reactor chamber in the 1÷3 GHz frequency range

	Mode	Calculated resonance frequency [GHz]	Measured resonance frequency probe [GHz]	Measured resonance frequency WR284 [GHz]
1	TE_{111}	1.39896	1.3978	
2	TM_{010}	1.67507	1.6731	
3	TE_{112}	1.70123	1.6897	
4	TM_{011}	1.76585		1.7534
5	TM_{012}	2.01378		1.9822
6	TE_{113}	2.11092	2.0838	
7	TE_{211}	2.19960	2.2091	2.2089
8	TM_{013}	2.37005	2.3687	
9	TE_{212}	2.40320		2.4033
10	TE_{114}	2.57732	2.5288	2.5287
11	TM_{110}	2.66896	2.6925	2.6925
12	TE_{213}	2.70872	2.6975	2.6975
13	TE_{011}	2.72685	2.7198	
14	TM_{111}			
15	TM_{014}	2.79351	2.8191	2.8191
16	TE_{012}	2.89358	2.8956	2.8956
17	TM_{112}			

The equations that determine the allowed frequencies for TM and TE modes are respectively [7]:

$$f_{nml}^{TM\,\mathrm{mode}} = \frac{c}{2\pi\sqrt{\mu_r\varepsilon_r}}\sqrt{\left(\frac{p_{nm}}{a}\right)^2+\left(\frac{l\pi}{d}\right)^2} \quad (1)$$

$$f_{nml}^{TE\,\mathrm{mode}} = \frac{c}{2\pi\sqrt{\mu_r\varepsilon_r}}\sqrt{\left(\frac{p'_{nm}}{a}\right)^2+\left(\frac{l\pi}{d}\right)^2} \quad (2)$$

where: c is the speed of light, ε_r and μ_r are respectively the electrical and magnetic permittivity of the medium filling the cavity (for the air $\varepsilon_r=\mu_r=1$), a and d are the radius and length of the plasma chamber (in our case a=68.5 mm and d=268.2 mm) and finally p_{nm} and p'_{nm} are respectively the zeros of order m of the Bessel functions of order n and its first derivative. Then the three indices n, m, l identify the electromagnetic field pattern of each mode.

The introduction of the LP at z= 17.2 cm, significantly changed the scenario introducing some perturbations which are evident from the measure of the S_{11} parameters at the coaxial probe as shown in fig. 4. Some of the observed modes have resonant frequencies close to ones calculated and measured in vacuum conditions. However, due to the perturbations introduced by the LP we cannot argue if they are TE or TM modes.

When the microwaves are switched on and the plasma is created, for the different operating conditions which have been explored during these measurements, it can be stated that in the 1-3 GHz range a clear electromagnetic modal structure with at least 7 points of minima can be recognized as shown in fig.5.

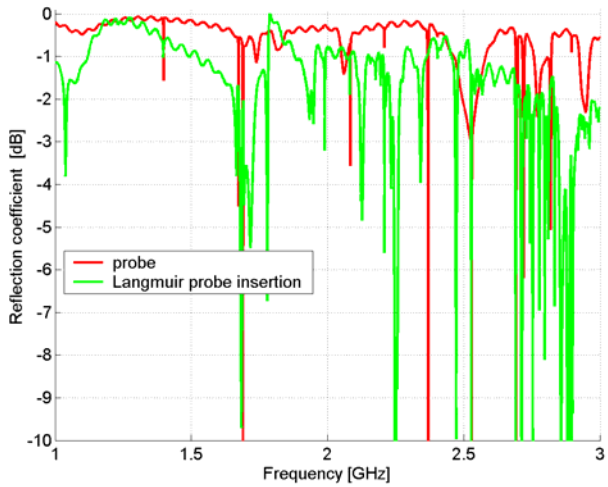

Figure 4: The effect of LP insertion

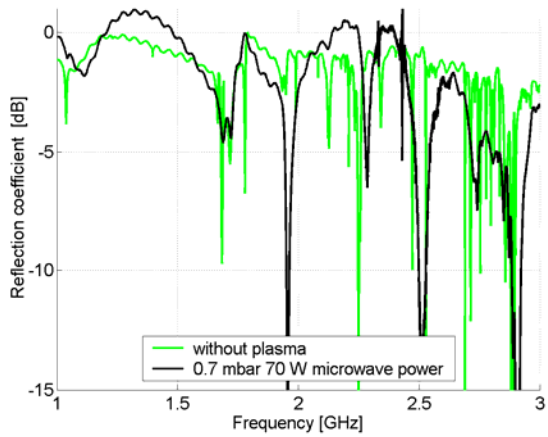

Figure 5: The S_{11} before and after that the plasma is created for a gas pressure of 0.7 mbar and 70 W of microwave power.

It must be pointed out that this analysis do not permit to affirm which modes are really excited inside the plasma chamber, but only that a electromagnetic modal structure is preserved even in presence of plasma.

The excitation of the modes will depend from other parameters such as the chamber dimensions, the location of the waveguide in the injection flange and the waveguide operating mode.

The S_{11} measurements have been carried out with the LP in the position z=17.2 cm at the coaxial input in vacuum conditions; the plasma was created inside the cavity for different operating conditions of gas pressure and microwave power (gas pressure in the range of 0.1-0.9 mbar and microwave power in the range of 40-70 W). It must be remarked that the performed measurements are well reproducible for a given conditions of gas pressure and microwave power.

Figure 6 and 7 report a zoom around the mode at 2.2 GHz. In figure 6 the microwave power was fixed at 70 W and the gas pressure ranged from 0.1 mbar to 0.9 mbar; in figure 7 the gas pressure was fixed at 0.7 mbar and the

microwave power was varied from 40 to 70 W. An evident resonating structure can be noticed inside the plasma chamber even in presence of the plasma. The resonances that exist inside the plasma chamber in vacuum shift to higher frequencies decreasing the gas pressure or increasing the microwave power. The origin of the observed effect is the change of plasma density for the different operating conditions.

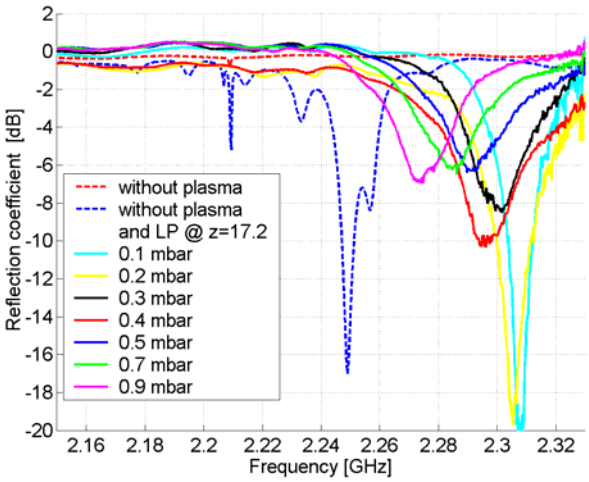

Figure 6: Reflection coefficient without plasma and with plasma vs frequency at different gas pressures and 70 W microwave power

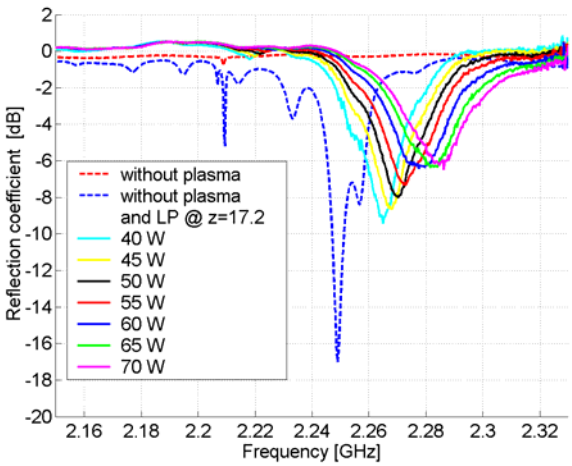

Figure 7: Reflection coefficient without plasma and with plasma vs frequency at different microwave powers and 0.7 mbar gas pressure

In fact, by supposing that the resonance cavity is filled with a homogeneous and un-magnetized plasma, the electrical permittivity in the (1) and (2) is lower than one according to:

$$\varepsilon_r = \left(1 - \frac{\omega_p^2}{\omega^2}\right) \tag{3}$$

where ω is the pulsation generating the plasma (2.45 GHz) and ω_p is the plasma pulsation:

$$\omega_p = \sqrt{\frac{n_e e^2}{m_e \varepsilon_0}} \tag{4}$$

where m_e and e and respectively the electron mass and electron charge, ε_0 is the electrical permittivity in vacuum and n_e is the electron density. Then , under the previous hypothesis, the effect of the plasma on the resonances is a frequency shift due to a decreasing value of the electrical permittivity in (1) and (2). This method can be also used to determine the electron density from the frequency shift. In our case the perturbations due to the LP insertions make difficult to reveal which is the mode that it is shifting to higher frequency when the plasma is ignited. However the LP measurement can be used to identify the mode in vacuum conditions. In particular for 70 W of microwave power and 0.7 mbar of gas pressure an electron density value of $6 \cdot 10^{15}$ m^{-3} is measured with the LP. Inserting such value in (4) and calculating the corresponding electrical permittivity, it is possible to reconstruct that the mode in vacuum conditions should be around 2.21 GHz. At this value in fig. 6 a mode which is present before and after the LP insertion can be observed.
By using the same value of permittivity to the mode at 2.9130 GHz in fig. 5, we obtain that this mode in vacuum conditions should be around 2.8 GHz. In this region of frequency the perturbations due to the LP are stronger with respect to the previous case and different points of minima can be recognized. For our calculations we assumed that the shifting mode is the closer one with frequency of 2.8191 GHz.
If we suppose that the modes which are shifting to higher frequency are the ones above reported we obtain two electron densities curves close one each other and with a reasonable agreement with the values measured with the Langmuir Probe (figure 8).
By applying the same considerations to the measurements performed in fig. 7, the evaluation of electron density has been carried for a gas pressure of 0.7 mbar and for different value of microwave power. Electron density slightly higher than the measured one with the LP have been calculated as shown in fig.9.

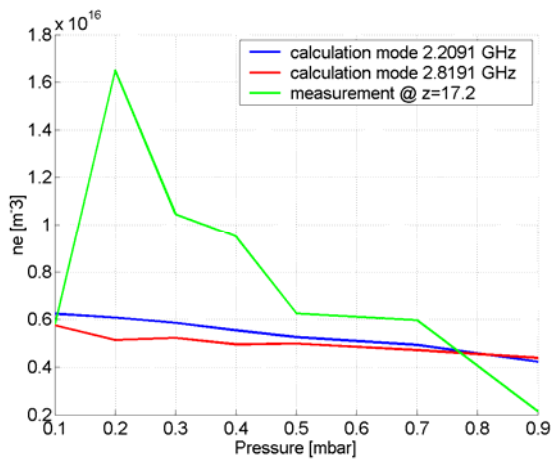

Figure 8: Electron density vs gas pressure for 70 W of microwave power.

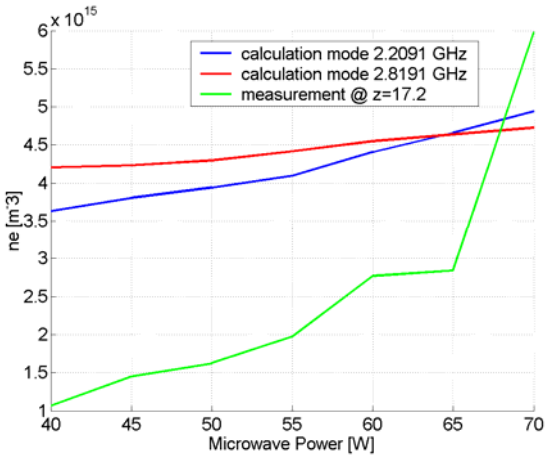

Figure 9: Electron density vs. microwave power for 0.7 mbar of gas pressure.

CONCLUSIONS

The observations above described have permitted to be more confident with the description of the tuning effect given in [2,3,8]. An evident resonating structure have been observed inside the plasma chamber even in presence of the plasma. The resonances present in vacuum conditions shift to higher frequencies when the plasma density increases. The measurement of such shift can be also used to have a rough evaluation of the plasma density. It is evident that the procedure is still not so precise but it is promising as non-perturbing diagnostics. For this reason additional measurements are scheduled for December 2008, with and without the LP in order to have less perturbation on the signals acquired on the VNA. Moreover, theoretical studies will be continued in order to prepare a similar experiment with ECR ion sources.

ACKNOWLEDGEMENTS

The contribution of L. Allegra to the preparation of the plasma reactor is warmly acknowledged.

REFERENCES

[1] S. Gammino, High Energy Physics &Nuclear Physics 2007, 31 (S1), 137.
[2] L. Celona et al., Rev. Sci. Instrum., 79, 023305 (2008)
[3] F. Consoli et al., Rev. Sci. Instrum., 79, 02A308 (2008)
[4] D. Mascali et al., Radiation Effects & Defects in Solids, Vol. 163, Nos. 4-6, April-June 2008, 471.
[5] S. Gammino et al., Proceedings of the 35th e EPS Plasma Physics Conference, 9-13 June 2008, Hersonissos, Crete, Greece.
[6] L. Celona et al., High Energy Physics &Nuclear Physics 2007, 31 (S1), 147.
[7] D.M. Pozar, Microwave Engineering, Wiley
[8] S. Gammino et al., IEEE Transaction on Plasma Science, Vol.36, No.4, 2008, 1522.

Broadband Excitation of ECR Plasmas*

Wayne D. Cornelius, Scientific Solutions, San Diego CA USA†
D. Leitner, M. Galloway, Lawrence Berkeley National Laboratory, Berkeley CA, USA
D. P. May, Cyclotron Institute, Texas A&M University, College Station, Texas USA
R. D. Penny, SAIC, San Diego CA USA

Abstract

Scientific Solutions developed an rf source capable of producing a variety of rf spectra for excitation of ECR plasmas at 2.45, 6.5, 14.5, 18.0 and 28.0 GHz. This device replaces the crystal oscillator in the rf chain and is essentially a software-defined radio transmitter that allows the user to select from a variety of different rf spectral patterns via an Ethernet link. Two specific patterns were chosen for our initial series of tests: 1) a simultaneous multimode pattern comprised of n rf-modes within a specified bandwidth and 2) a "chirp" spectral pattern comprised of n discrete frequencies where the chirp bandwidth, slew direction, and slew rate are user-selectable. In either case "n" is a user-defined value between 1 and 1024. This paper describes the design of the rf circuit and its theory of operation. Initial results of our tests with the 6.4 and 14.5 GHz ECR sources at Texas A&M University and with the AECR-U at the Lawerence Berkeley National Laboratory are also presented.

BACKGROUND

ECR sources depend on coupling energy into plasma electrons via the electron-cyclotron resonance. Plasma electrons transiting the resonance region inside the source absorb energy from the radio-frequency field. The change in electron energy is determined by the magnitude of the rf field in the resonance zone integrated over the time required to transit the zone. The effective width of the resonance zone is derived from the gradient of the magnetic field (dB/dz) and the bandwidth of the rf energy. Therefore to increase the volume of the resonance zone, we need to decrease the field gradient or increase the rf bandwidth. The question addressed here is: given a constant field gradient, which is more efficient in transferring rf energy to plasma electrons: 1) high peak rf power with a narrow resonance zone, or 2) lower peak power with a wider zone?

Kawai et. al. reported on experiments using an rf noise source to increase the rf bandwidth.[1] These experiments showed marginal improvement of ion current in a "plateau" style ECR source, but did show enhanced operational stability compared with single-frequency excitation. More recent experiments with a minimum-B configuration ECR source [2] demonstrated significant benefits of broadband excitation in producing Ar^{11+} ions with 400 W of rf power.

A possible reason for the lack of improved ion current in the first case is that noise sources have no coherence between adjacent frequency "bins." Therefore an electron transiting one frequency bin has a 50% probability of encountering the opposite phase in the adjacent bin, thereby decelerating the electron instead of continuing to accelerate it. Generating an rf spectrum in a coherent manner populates adjacent frequency bins with phase-related rf energy. Hence a modulated rf source may provide just the coherence needed to improve the rf coupling efficiency. The trick lies in discovering the optimal modulation scheme(s).

RF MODULATOR AND KLYSTRON DRIVER CIRCUIT

To investigate broadband radio frequency (rf) excitation of ECR plasmas, we utilized a software-defined radio transmitter (RF Injection Device or RID) originally developed for another application. This device, created to automatically analyze resonant frequency spectra between 100 MHz and 1 GHz, was modified to produce a variety of user-selectable spectra in the 1-2 GHz band. The baseband rf signal from the modified RID is passed through an Analog Devices AD8349 quadrature modulator that provides complete control of the rf waveform within a 20 MHz bandwidth centered around the operating frequency. The output waveform of the AD8349 is frequency multiplied into the range of interest using a variety of multiplier chains and amplifier circuits as illustrated in figure 1. The exact configuration of the multiplier chain depends on the target frequency range. The AD8349 actually supports much wider bandwidth. However we restricted the baseband frequency range to 20 MHz in order to keep the frequency-multiplied bandwidth within a reasonable range so as not to stress the klystron amplifiers typically used for ECR heating.

The operation of the RID is controlled by an embedded Xilinx processor connected via Ethernet to the user's computer running the interface control panel. Because the frequency synthesis is under complete software control, we can easily adjust the operating frequency, the bandwidth, and fill factor (i.e. the mode spacing) up to the limits of the AD8349.

As shown in figure 1, the output spectrum of the RID is frequency multiplied in a variety of circuits whose configuration depends on the desired operating frequency (figure 1). Note that the operating bandwidth of the

*This material is based upon work supported by the U.S. Department of Energy under Award Number DE-FG02-04ER84166. The views and opinions of authors expressed herein do not necessarily state or reflect those of the United States Government or any agency thereof.
†Current address: SAIC, 10740 Thornmint Road, San Diego CA 92127

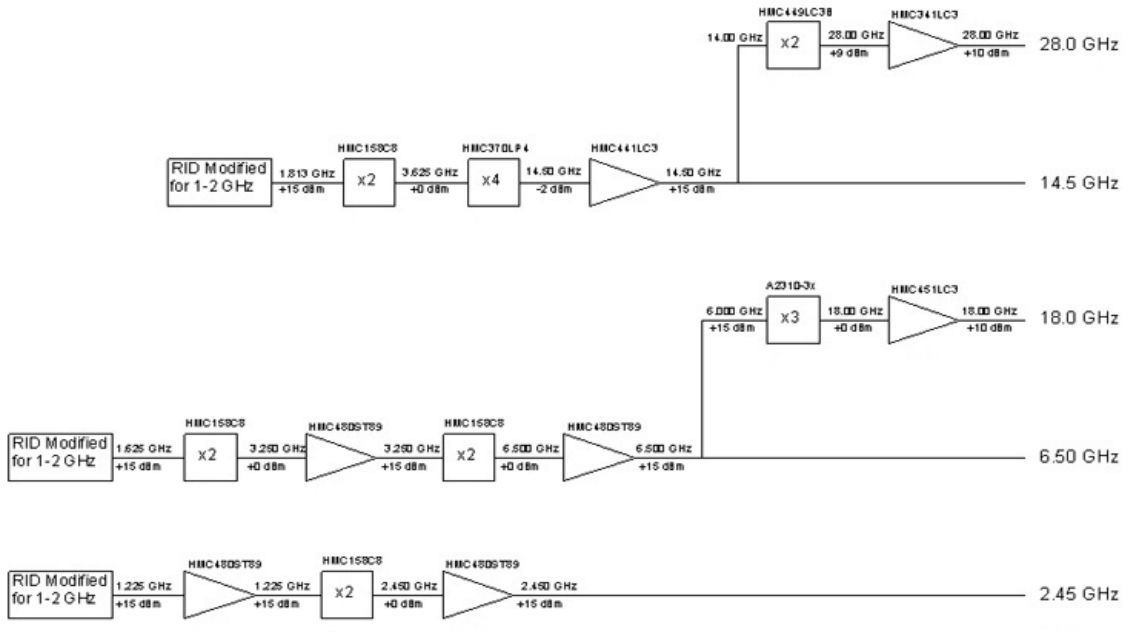

Figure 1. Detail of the frequency multiplier chains for common ECR frequency bands.

overall chain is multiplied by the same factor--multiplying the frequency by a factor of four increases the bandwidth by a factor of four. A complication of this approach is that the anti-aliasing filters used to eliminate spurious frequencies (spurs) in the baseband cannot eliminate spurs resulting from the multiplication process. The effect of these spurs is to produce "mirror" images of the mode structure around the center frequency. In general these additional spurs are mostly annoying. The primary effect is a larger number of frequencies in the rf spectrum than the software setpoint. These spurs would be a major problem in rf communications systems, but are not a significant problem in rf heating applications.

Figure 2 shows how two frequency-doubling processes transform a single-frequency spectrum at 1.60 GHz into a 9-mode structure at 6.40 GHz. Although the mode structure of figure 2 looks daunting on the semi-log scale, the power in these spurious modes is less than 1% of the total. These spurious frequencies would pose significant problems in rf communications systems, but are not a significant problem in the plasma-heating process.

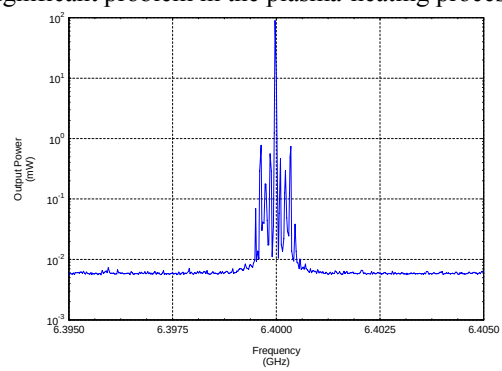

Figure 2. Single-mode power spectrum following frequency quadrupling from 1.6 to 6.4 GHz.

RF Comb Spectrum

The embedded Xilinx code utilizes a phase-hopping scheme and/or a frequency "chirp" to generate the frequency spectra. The series of phase changes in a single-frequency rf transmission are Fourier transformed into a frequency comb spectrum. The relative power in each "tooth" of the comb is a function of the phase-hopping pattern. A power spectrum with relatively uniform power in each mode is produced by visiting each possible phase change once during the transmit cycle. In other words, the phase diagram is divided into n segments (n is the number of modes in the spectrum so the 2π phase sheet is divided into n segments of $\Delta\phi$ phase width). The phase of the transmitted rf is sequentially stepped by values that visits all possible phase differences (i.e. 1x, 2x, 3x,…,$n\cdot\Delta\phi$). The number of modes (up to 1024) and the initial phase offset are under user-control. The relative power in each mode depends on the particular sequence of phase changes in the algorithm. Figure 3 compares the mode structure for a variety of different mode-hopping settings (1, 3, 4, 8, 16, 32, and 64 modes). The red curves denote the power in dB and the blue curves show the power on a linear scale.

RF Chirp Spectrum

Alternatively we can generate a "chirp" spectrum by slewing the frequency either up or down using n-steps within a specified bandwidth ($n \leq 1024$). The bandwidth and the dwell-time on each frequency step are under user control.

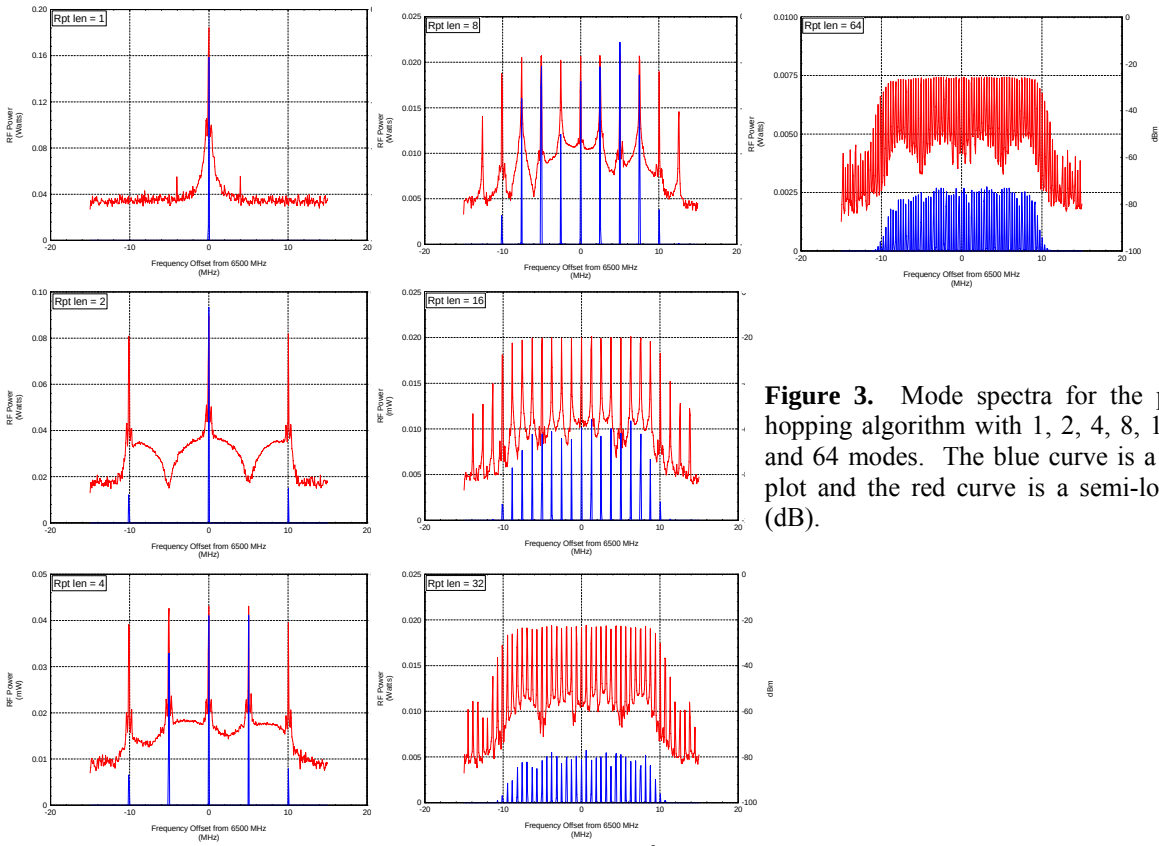

Figure 3. Mode spectra for the phase-hopping algorithm with 1, 2, 4, 8, 16, 32, and 64 modes. The blue curve is a linear plot and the red curve is a semi-log plot (dB).

Displays of chirp-mode spectra can be less revealing than comb-spectrum displays because an accurate representation of the spectrum is produced only when the scan rate is very slow compared with the slew rate of the chirp. Figure 4 (figure 5) compares rf excitation spectra (semi-log plots) for 1-, 2-, and 3-mode excitation at 6.4 GHz with TSRPT = 1(10). The Time-Slice Repeat (TSRPT) value sets the number of clock cycles the chirp remains in each frequency bin before moving on to the next bin. Note how increasing TSRPT reduces the power-weighted bandwidth of the excitation spectrum because the frequency remains for a longer duration at each frequency step. As we noted above, phase changes generate the frequency sidebands. Therefore dwelling for a longer period of time on each frequency reduces the number of phase changes per unit time and hence the number of spurious frequencies in the sidebands.

Figure 6 compares chirp spectra with 1, 2, 3, and 16 modes in a 4.3 MHz bandwidth centered around 6.40 GHz (semilog plot). Note how the number of modes and their separation within the peak of the spectrum coalesces into a solid bandwidth of frequencies. Figure 7 shows how the spurious frequencies disappear as the dwell time on each frequency increases.

RF COMBINATION MODE SPECTRUM

The user can also choose to chirp a comb spectrum. The frequency agility and flexibility allowed by these two modulation schemes provides a means for testing the efficacy of broadband excitation of the ECR plasmas under a wide variety of circumstances.

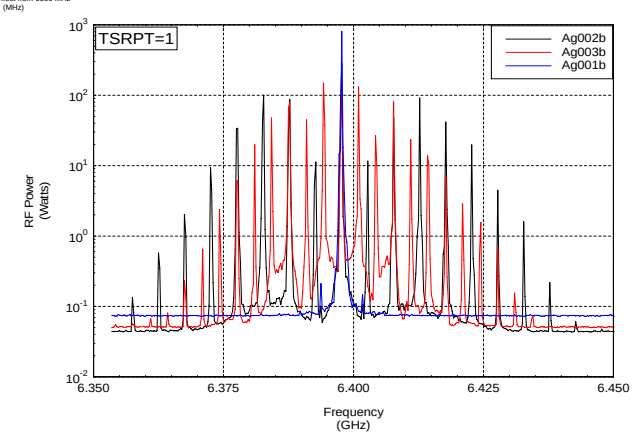

Figure 4. Comparison of rf excitation spectra with TSPRT=1 (1 mode=blue, 2 modes=black, 3 modes=red).

TEST RESULTS

A series of experiments were performed with the 6.4 GHz and 14.5 GHz ECR sources at Texas A&M University and with the 14.5 GHz AECR-U source at LBNL. Results of these tests are described below. Although the results of these tests did not show a dramatic improvement in ion current, some very interesting features were discovered that warrant further experimentation. These features include 1) improved plasma stability when operating with a multimode rf spectrum, 2) significantly improved operation for oxygen beams when operating at lower rf power levels, 3) slight improvement in ion currents for the highest measurable charge states, and 4) the opportunity to tune the frequency to better couple the rf power into the ion source.

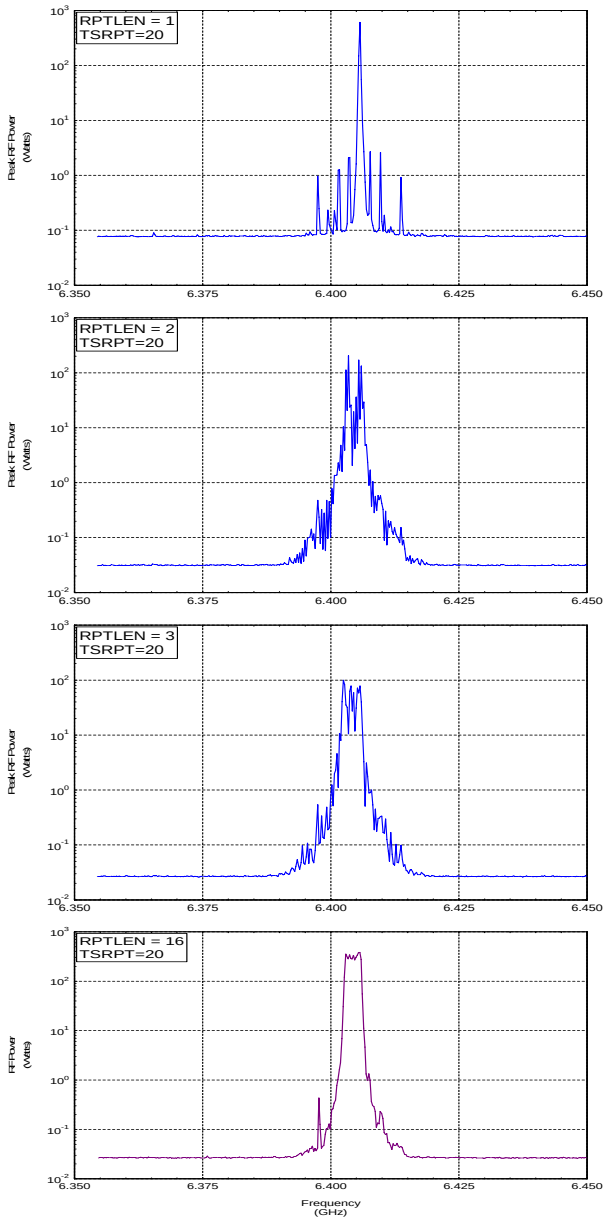

Figure 5. Comparison of rf excitation spectra with TSPRT=10 (1 mode=blue, 2 modes=red, 3 modes=black).

RESULTS FROM TAMU: COMB SPECTRUM EXCITATION

Figure 8 compares the O^{7+} ion current extracted from the TAMU 14.5 GHz ECR source as a function of rf power. The blue curve shows the ion current produced with a single mode in the rf spectrum whereas the red curve shows the ion current produced with two rf modes in the excitation spectrum. Although the two curves in figure 4 converge at higher power levels, at a power level of 500 Watts, multimode operation produced nearly 40% more ion current than single-mode excitation. This result correlates well with the results of Kawai et. al. [2] and Celona, et. al. [3]

Figure 9 summarizes results with 1-, 2-, and 3-mode excitation of the plasma in producing a Au^{23+} beam with the 6.4 GHz source. This particular ion is highly charged and requires high rf power levels. Unlike the O^{7+} results, we observed no benefit with multimode excitation at the lower rf power levels. However some slight benefit can be seen for 2- and 3-mode excitation at the highest power levels. Note also that rf spectra with an odd-number of modes seemed to have slightly greater efficiency than spectra with even numbers of modes. Perhaps this effect is because the odd-number excitation always has a mode in the center of the band whereas the even number has a gap between rf modes in the center of the band. This odd-even effect is only evident with relatively few rf modes in the spectrum (e.g. 7-mode excitation has a performance equivalent to 8-modes whereas 3-modes seem to have an advantage over 2-mode excitation).

Figure 10 compares 1-mode and 3-mode rf excitation in producing an Ar^{12+} beam with the 14.5 GHz source at TAMU. Note how the ion source changed plasma modes around 900 watts of excitation. As was the case for the oxygen beam, multimode excitation appears to improve the ion current at intermediate power levels, but this difference disappears at the highest power levels. The two 3-mode data points surrounding the 1-mode value at 1050 watts suggests that fine-tuning the ion source could recover the missing 3-mode ion current compared with the 1-mode value.

Figure 11 shows the Kr^{19+} ion current as a function of rf power and the number of excitation modes. This figure shows a clear benefit of multimode excitation compared with single-mode excitation. The 2-mode and 3-mode spectra produced a 6% increase in Kr^{19+}current and an 11% increase in Kr^{20+} current with 1.28 kW of rf power.

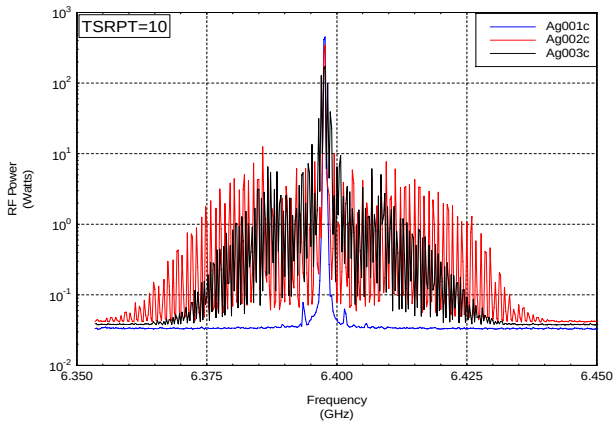

Figure 6. Chirp spectra with 1-, 2-, 3-, and 16-modes in a 4.3 MHz bandwidth (semi-log plots).

RESULTS FROM TAMU: CHIRP SPECTRUM EXCITATION

Figure 6 showed chirp spectra with 1-, 2-, 3-, and 16-modes in a 4.3 MHz bandwidth at 6.40 GHz. These spectra resulted in 1.36, 1.45, 1.49, and 1.50 uA respectively of Ag^{25+} beam ions with 0.9 kW of rf power and a 1 usec dwell time at each frequency. Figure 12 compares the performance of a 1-mode chirp with a 16-mode chirp with a Ag^{25+} beam as a funcion of rf power.

This figure shows some improvement in performancefor a 16-mode chirp at nearly all rf power levels.

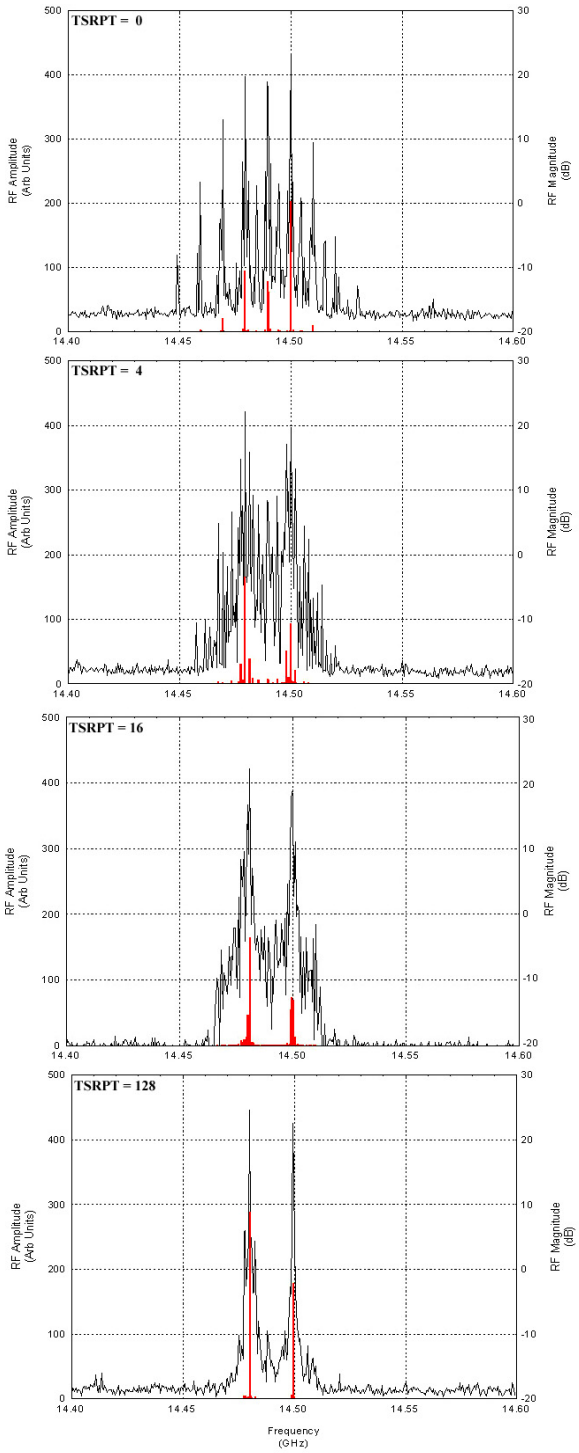

Figure 7. Chirp spectra with TSRPT = 0, 4, 16, and 128 (black: linear scale, red: semi-log scale).

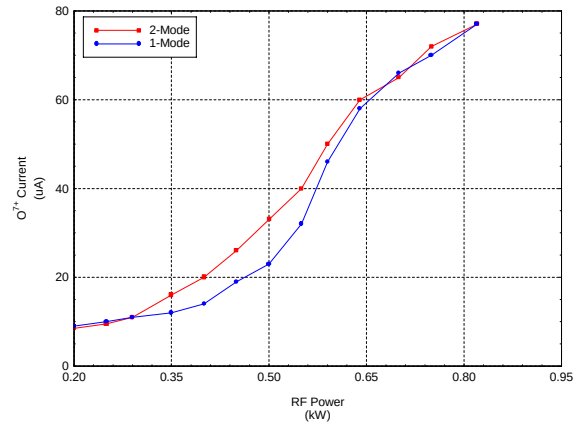

Figure 8. Oxygen 7+ current extracted from the TAMU 14.5 GHz ECR source as a function of rf power level for single-mode (blue curve) and two-modes (red curve) in the rf spectrum.

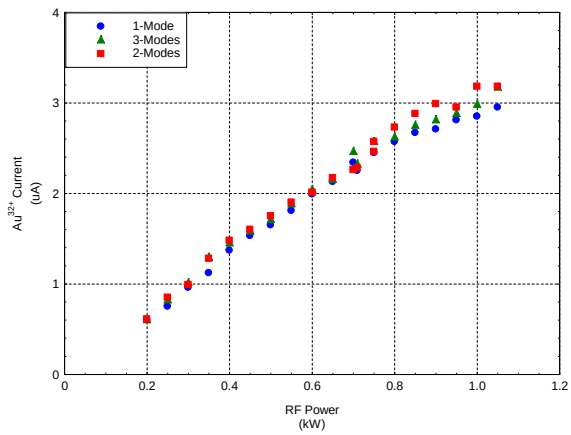

Figure 9. Plot of Au^{32+} current as a function of rf power and the number of rf excitation modes.

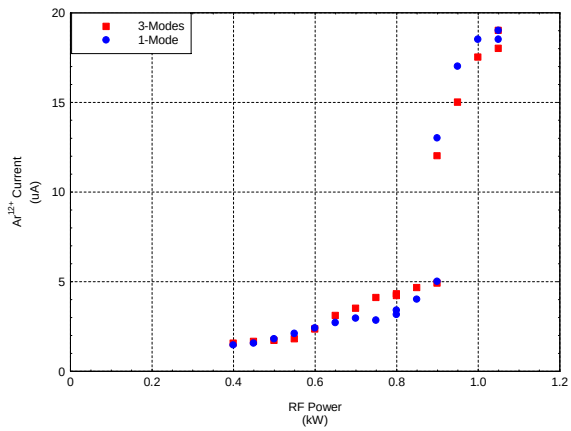

Figure 10. Plot of Ar^{12+} current as a function of rf power and the number of rf excitation modes at 6.4 GHz.

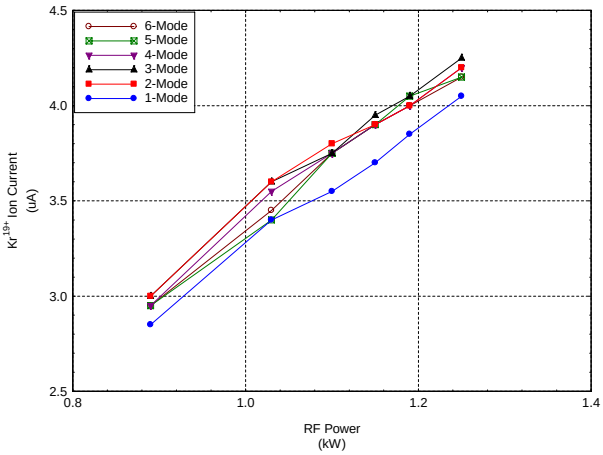

Figure 11. Plot of Kr^{19+} current as a function of rf power and the number of excitation modes at 14.5 GHz.

In summary, the data obtained with the TAMU 6.4 and 14.5 GHz ECR sources are encouraging in that some performance improvement was obtained for broadband excitation compared with single-mode excitation of the plasma. However the magnitude of this improvement is relatively modest, generally being less than 10% for the higher charge states and heavier ion species. This noted however, we observed substantial improvement in broadband performance at the lower power levels for O^{7+} in figure 4. We also noted significant improvement in the Ag^{25+} current in figure 12, particularly at the lower rf power levels. These observations correlate well with results reported in reference 3.

During experiments at LBNL (discussed in the next section), we discovered that some of the ion current lost in switching to broadband excitation could be recovered by retuning the ion source. The experimental procedure at TAMU was to optimally tune the ion source with single-mode excitation and then change the rf spectrum using software commands. In most, if not all, cases, multimode rf excitation improved the performance, but no significant retuning of the ion source was attempted. It is also important to note that the base vacuum pressure of the TAMU 6.4 GHz source was approximately a factor of two higher than the optimal pressure. How much of an effect this higher pressure had on these experiments is unclear. This increased base pressure may have masked performance changes that might have been obtained by retuning the TAMU source (as was observed with the AECR-U source). The excellent base vacuum pressure in the AECR-U source may have reduced the sensitivity to differences in single- versus multi-mode rf excitation.

RESULTS FROM LBNL: COMB SPECTRUM EXCITATION

Figure 13 compares the O^{5+}, O^{6+}, and O^{7+} ion currents extracted from the LBNL AECR-U source operating at 14.30 GHz. Unlike the data in Figure 4, each data point in this figure represents the optimal tuning of the ion source at each rf setting. The ion currents obtained with single-mode rf excitation are denoted by the solid-curves and the currents obtained with two-mode rf excitation are denoted by the dashed curves. In both figure 13 and in figure 8, the ionization appears to "saturate" at higher rf power levels so that no difference is observed between single- and multi-mode rf excitation patterns at the highest power levels. Note however that multi-mode excitation significantly increases the ion current for rf power levels between 500 and 600 Watts—particularly for the 6^+ and 7^+ charge states.

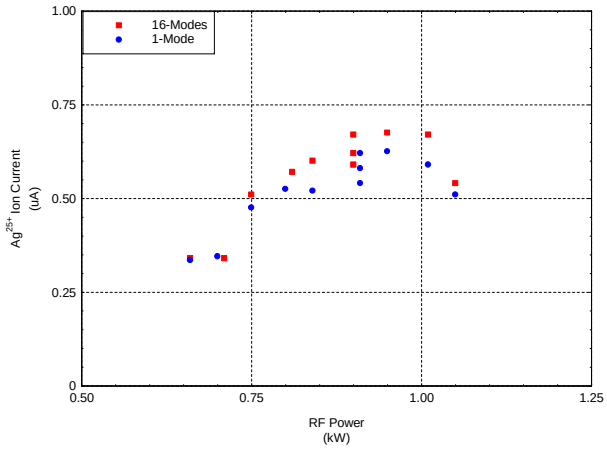

Figure 12. Comparison of Ag^{25+} ion current produced with the 1- and 16-mode chirp spectra from figure 8 as a function of rf power.

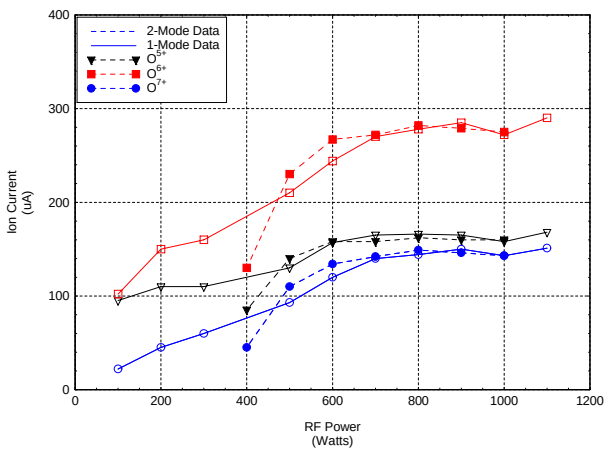

Figure 13. Oxygen 5^+ (black), 6^+ (red), and 7^+ (blue) ion currents extracted from the LBNL AECR-U ECR source as a function of rf power level for single-mode (solid curves, open symbols) and two-modes (dashed curves, closed symbols) in the rf spectrum. Each data point represents the "optimized" ion current for each rf setting.

Figure 14 shows the rf power spectrum of the AECR-U klystron amplifier for single-mode excitation. Unfortunately the GPIB cable was not available during the test program at LBNL so the rf spectra were captured from the spectrum analyzer display with a digital camera. As a result, these spectral data can be displayed, but cannot be analyzed (as was possible with the TAMU data). Figure 15 (16) shows a linear (semi-log) plot of the rf power spectrum for multimode rf excitation.

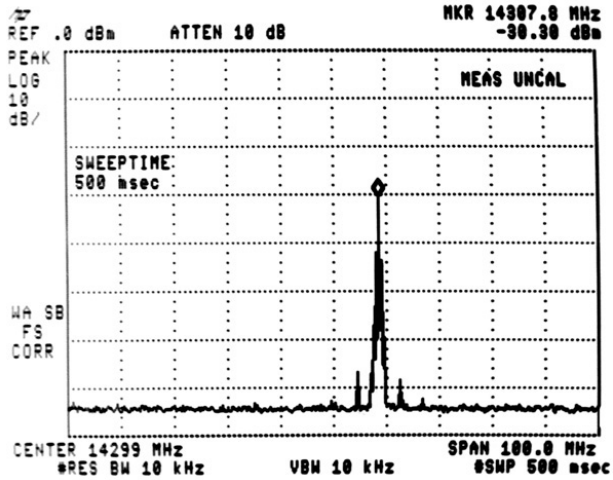

Figure 14. Single-mode rf spectrum at the output of the AECR-U klystron amplifier (dB scale).

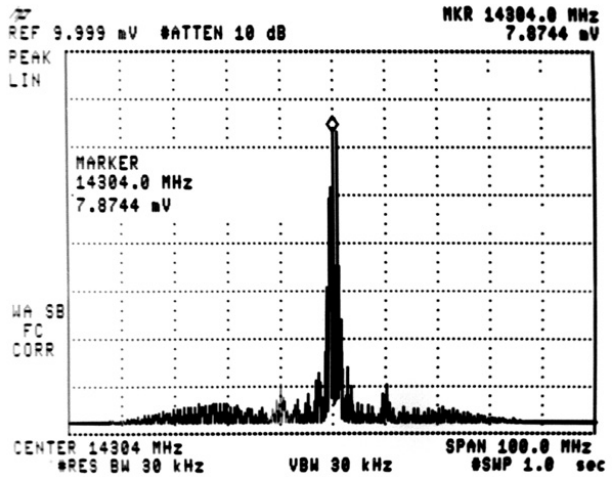

Figure 15. Multi-mode rf spectrum of the AECR-U klystron (linear scale). Note the significant satellite frequency bands on both sides of the central peaks.

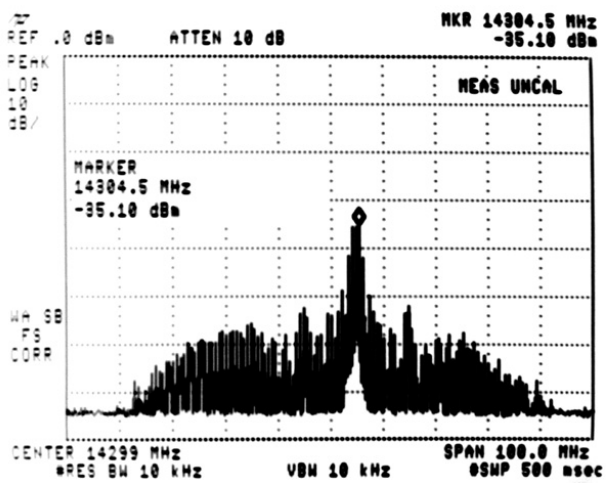

Figure 16. Multi-mode rf spectrum of the AECR-U klystron (semi-log plot).

Figure 17 shows the reflected power spectrum from the AECR-U source. Note how the lower sideband has significantly lower reflected power than the upper sideband. This effect was a clue that the operating frequency of the AECR-U source was set too high for optimal operation.

Figures 18 and 19 compare the forward and reflected power spectra for the AECR-U source operating with Xenon gas and 1024 modes in a 100 MHz chirp spectrum. The forward power is relatively uniform with frequency whereas the reflected power shows power absorption only from the center 30 MHz. At the conclusion of these experiments, the crystal oscillator rf source for the AECR-U was retuned approximately 30 MHz lower in frequency so that the operating frequency was closer to the frequency with minimum reflected power.

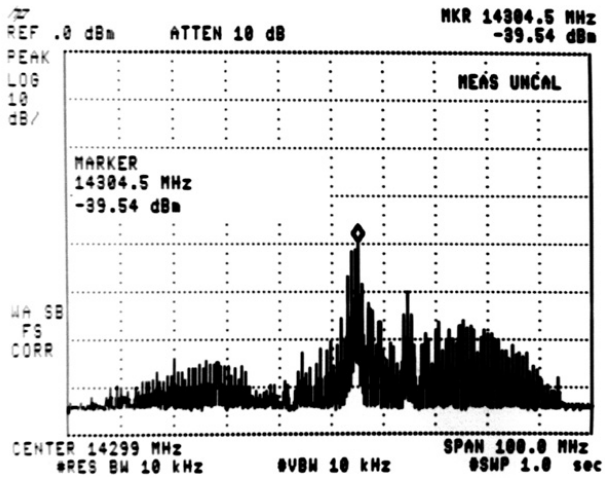

Figure 17. Reflected rf power spectrum corresponding to the multi-mode transmitted rf spectrum of figure 15 (semi-log plot). Note how the plasma absorbed more power from the lower frequency satellite band than from the upper satellite band.

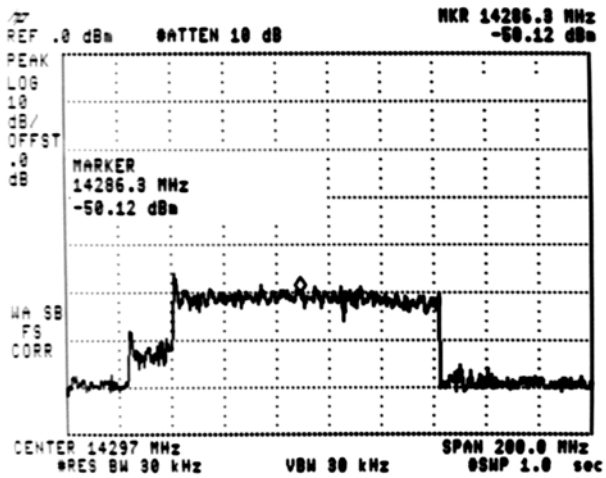

Figure 18. Forward power spectrum from the AECR-U source operating with Xe gas (linear scale). The klystron was producing a "flat" power spectrum with 1024 modes in a 100 MHz bandwidth.

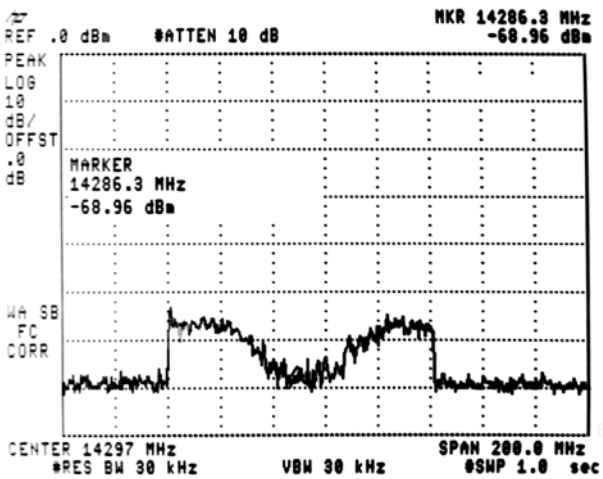

Figure 19. Reflected power spectrum from the AECR-U source operating with Xe gas (linear scale). The plasma was absorbing power from only the central 30 MHz of the spectrum shown in figure 18.

Figure 20 shows a ^{209}Bi spectrum for two-frequency rf heating. LBNL pioneered the techniques for two-frequency excitation of ECR plasmas. They employed rf power at 14.3 and 10 GHz to form two ECR regions in the plasma. This approach demonstrated significant improvement over single-frequency sources. One of the goals of our research project was to determine if multiple frequency heating would prove advantageous when the separation between the two frequencies was relatively small. As noted in the TAMU experiments, in-band 2-mode heating showed some improvement, but not as much as the K- and X-band heating approach used by LBNL. Note however that the 32-mode chirp spectrum improved the charge-state distribution as evidenced by a reduction of ion current at the lower charge-states (21^+, 22^+, and 25^+) with an accompanying increase in ion current at the highest charge-states (31^+ through 37^+). While relatively modest gains in charge-state distributions were observed, the 32-mode chirp resulted in more stable operation of the AECR-U.

Figure 21 is a comparison of various multi-mode chirp spectra along with single-mode heating for ^{209}Bi using two-frequency heating (14.3 and 10 GHz). Each of the traces in this figure represents the optimal performance achieved by fine-tuning the source parameters. Figure 22 is a close-up of the region detailing the highest charge states. The slight advantage of multimode heating is shown by the general shift of the red curve to higher values at higher charge states and lower values at lower charge states. Note that multi-mode excitation was always equal to or better than single-mode excitation.

Figure 23 details the charge-state distribution for the highest measurable charge states in ^{209}Bi with dual-frequency heating (multi-mode at 14.3 GHz and single mode at 10 GHz). This figure shows the slight improvement in current for all charge states with multi-mode rf at 14.3 GHz. Figure 24 details the ^{129}Xe charge-state distributions for a variety of chirp spectra at 14.3 GHz. Note that the 32-mode chirp spectrum shows significant improvement compared with single-mode excitation.

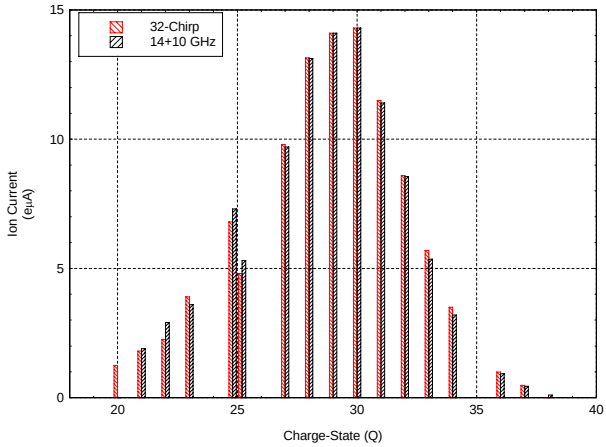

Figure 20. Charge-state distribution of ^{209}Bi Beam with 2-frequency heating. The values from normal AECR two-frequency heating (single-mode 10 and 14.3 GHz) is given by the black bars whereas the red bars indicate the current obtained with a 32-mode, 13.3 MHz chirp at 14.3 GHz in combination with the 10 GHz single-mode rf power.

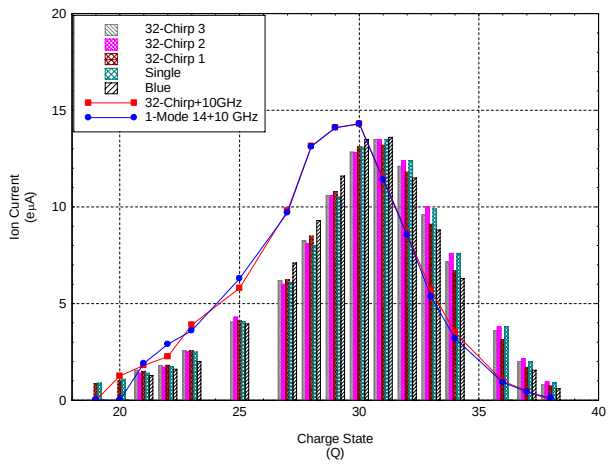

Figure 21. Charge-state distribution of ^{209}Bi Beam with multi-mode chirp at 14.3 GHz and 2-frequency heating (14.3 and 10 GHz).

CONCLUSION

The test results described above are interesting but not conclusive. Multi-mode rf heating showed some improvement compared with single-mode heating under most circumstances. However the improvement was generally modest (*5-10%) at the highest power levels and for the highest measurable charge states. Significant improvement was noted at lower rf power levels in some of the experiments, but this difference decreased with increasing rf power. The test program at LBNL demonstrated significant improvement in operational stability with multimode excitation. While it was usually possible to retune the AECR-U to achieve an equivalent

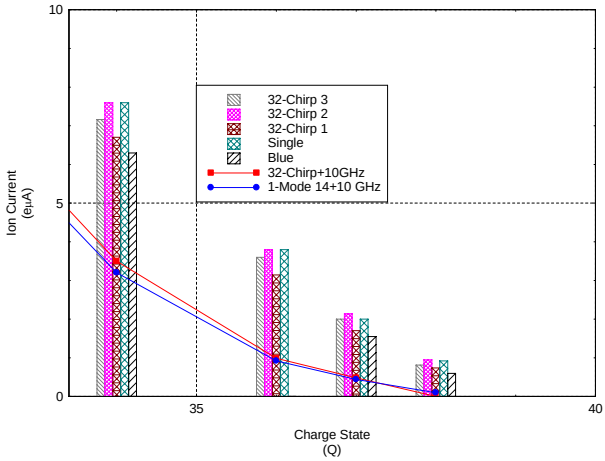

Figure 22. Close-up of the results at the highest charge-states shown in figure 21.

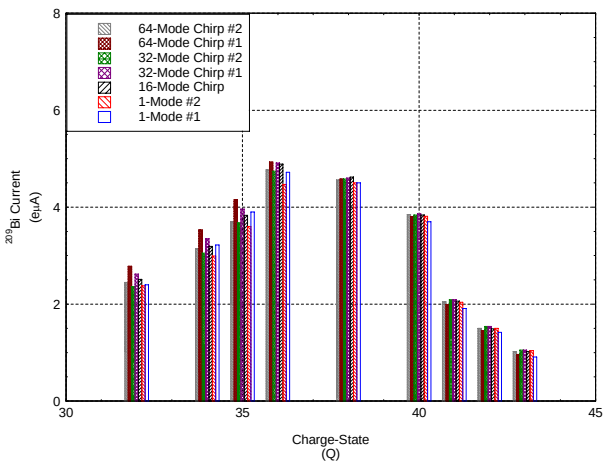

Figure 23. Charge-state distribution of ^{209}Bi Beam with multi-mode chirp at 14.3 GHz and 2-frequency heating. This figure details the region containing the highest measurable charge-states. Note the slight improvement obtained with a multi-mode chirp.

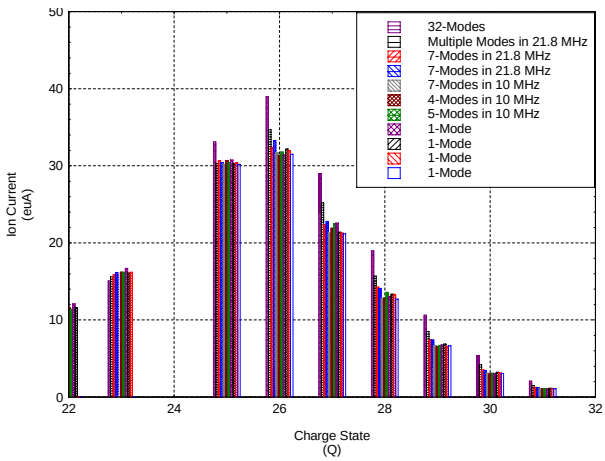

Figure 24. Charge-state distributions for Xe ions for a variety of rf excitation spectra. Note the significant improvement in performance provided by the 32-mode chirp compared with the single-mode results.

level of performance with single-mode excitation, the plasma was less stable with single-mode heating, often for periods exceeding several hours. Several times the AECR-U source was left operating with multi-mode rf for some period of time before it could be reliably switched over to single-mode rf heating. It is important to note that the AECR-U has a larger number of tuning "knobs" than are typical of ECR sources. It may not always be possible to achieve equivalent multi-mode and single-mode performance in ECR sources with fewer available tuning parameters.

The conclusion of these tests is that we do not yet have enough information on the efficacy of multi-mode heating. We observed modest improvement in charge-state distributions under some circumstances, but saw little effect under other conditions. The most significant observations are 1) the significant improvement in ion current when operating at less than optimal power levels, 2) the slight improvement in the ion currents of the highest charge-states, and 3) the improved operational stability. The improved stability might be significant enough to warrant switching to multi-mode heating under some conditions. The improvement in ion currents for the highest charge-states, while generally modest, might be enough to enable experimentation using those beams. Clearly more testing is needed.

REFERENCES

[1] Y. Kawai, G.D. Alton, and Y. Lui, Proceedings of the 2005 Particle Accelerator Conference, Knoxville TN, p 1529

[2] Y. Kawai, G. D. Alton, O. Tarmainen, P. Suominen, and H. Koivisto, Physics Letters A371(2007), p 307

[3] L. Celona, S. Gammino, G. Ciavola, F. Consoli, and A. Galata, in Proc. 16th International Workshop on ECR Ion Sources, Berkely CA, AIP Conference Proceedings V749(2005) p.99

PAPER NOT RECEIVED

PAPER NOT RECEIVED

STATUS OF FAR-TECH'S ELECTRON-CYCLOTRON-RESONANCE CHARGE-BREEDER SIMULATION TOOLSET; MCBC GEM AND IONEX *

J.S. Kim#, L. Zhao, B. P. Cluggish, I. N. Bogatu, S. Galkin, and L. Grubert,

FAR-TECH, Inc., San Diego, CA 92121 USA.

Abstract

The status of FAR-TECH's electron-cyclotron-resonance charge-breeder simulation toolset (MCBC, GEM and IonEx) is described. FAR-TECH, Inc. has been building a suite of comprehensive numerical tools for end-to-end Electron Cyclotron Resonance (ECR) charge breeding (CB) modeling [1]. They consist of the Monte Carlo Beam Capture (MCBC) code [2,3], the Generalized ECRIS Modeling (GEM) code [3,4], and the Ion Extraction (IonEx) code [6,7]. We present the main progresses since our last status presentation [1]. This progress includes upgrades in GEM to 2D and IonEx to 3D.

INTRODUCTION

In ECR "charge breeders" a beam of low (+1 or +2) charged ions is injected into an ECRIS plasma and charge bred to produce higher charge-state ions. The charge breeders are particularly useful for radioactive ion beam (RIB) production. Future large, expensive ion sources will require modeling and diagnostics for optimal and efficient design.

FAR-TECH, Inc. has been building a suite of comprehensive numerical tools for end-to-end Electron Cyclotron Resonance (ECR) Charge Breeder (CB) Ion Source (IS) modeling [1]. The tool consists of three modules, each representing distinctive physical processes. First, the Monte Carlo Beam Capture (MCBC) code [2,3] traces injected ions until they are captured by being slowed down to a speed less than the background ion thermal speed, lost to the walls, or pass through the extraction holes. Second, the Generalized ECRIS Modeling (GEM) code [4,5] calculates the charge state distribution (CSD) of an ECR ion source plasma including the captured injected beam ions. Finally, the Ion Extraction (IonEx) code [6,7] calculates extracted ion trajectories utilizing the phase space ion distributions obtained from GEM. The link between MCBC and GEM are in place, and the link between GEM and IonEx will be carried out in the near future.

Since our last status report [1], our main progress has been with GEM2D and IonEx upgrades. The 2D (r,z) spatial extension of GEM from 1D (z) allows more realistic modeling of the rf resonance, which is a key ingredient for ECRIS performance. Through GEM2D, the ellipsoidal shaped rf resonance surface can be modeled. For typical ECR plasmas GEM2D simulations indicate hollow profiles of electron density and temperature, consistent with experimental observations at ATOMKI [8], resulting in hollow profiles of extracted ion sources [9]. As for IonEx, while a user-friendly GUI is being built, a 3D spatial extension is being made. IonEx utilizes a meshfree technique, which uses points or nodes not cells, and an innovative meshfree technique called PICOP (particle-in-clouds-of-points) [6], not PIC (particle-in-cell). Generation and adaptation of points are easier than those of meshes and particularly for handling a complicated geometry and highly non-uniform problems (e.g., multi-scale problems like a plasma meniscus).

Next, we present a summary of these three modules.

SUMMARY OF MCBC, GEM, IONEX MODULES

As presented previously, GEM models ECR ion source plasmas by fluid ions and bounce averaged Fokker Planck electrons [5,10]. The MCBC code simulates beam slowing down dynamics in a plasma due to Coulomb collisions, and atomic processes which includes ionization due to hot electrons and charge exchange. MCBC provides ion source profiles to GEM, which in turn provides ion flux profiles to IonEx. Next we briefly describe the status of each of these modules.

MCBC

The full 3D3V Monte Carlo particle tracking code models Coulomb collisions, and atomic processes in a plasma. The Coulomb collisions are implemented by the Boozer model [11], after modifying the collision formula to ECR plasmas. The modified Boozer model and atomic processes modeled in the code can be found in our previous paper [1].

GEM

We made improvements in two main areas with GEM. The first area is in the convergence of the GEM1D code using the up-wind scheme for the ion contintuity equations. The second area is the extension of GEM to 2D. The 2D modeling allows for the resonant layer to be at finite radius as well as at finite axial locations. As rf heating is a main ingredient for producing ECR plasmas,

* Contributed paper, the **18**th ECRIS Conference, Chicago, IL, September 2008. This research was performed under a U.S. DOE SBIR grants.
#kim@far-tech.com

accurate modeling of the resonance region is important. The 2D grids of GEM represent the ECR plasma by a uniform axial grid and radially nested flux tubes. The radially nested flux tubes are obtained by averaging the magnetic fields azimuthally. The main GEM modeling remains the same; fluid ions with the same axial velocity due to strong collisions between them but with independent radial velocities, Fokker-Plank bounce averaged electrons at each flux tube, and particle balance neutrals. The detailed model of GEM2D is given by Zhao [12,13].

IonEx

Although there are several ion extraction codes commercially available [14,15], we have been developing our own extraction module for the following reasons: (1) An ion extraction code requires initial particle conditions, which should be obtained from plasma simulations such as GEM more realistically. (2) The plasma meniscus should be resolved, where the plasma meniscus region is many orders of magnitude smaller than the device size.

IonEx is being developed using our innovative numerical technique, Particle-In-Cloud-Of-Points (PICOP) [6]. It uses a meshless technique. Meshless computation does not require cells or meshes, rather it uses points. This feature allows easier handling of complex boundaries and easier adaptation where required, thus is suitable for multiple scale problems. As our technique is based on computational points rather than meshes or cells, we developed a new algorithm which we call Particle-In-Cloud-Of-Points (PICOP) as appose to Particle-In-Cell (PIC). The PICOP algorithm is a key element in IonEx. The 2D version is benchmarked, and the 3D version is close to being ready. The 3D computational point generation, adaptation, refinement and de-refinement of points, and the 3D PICOP algorithm, are all individually tested. The 3D IonEx is close to completion. Next we describe the basic modeling of IonEx.

THE IONEX MODEL AND BENCHMARKING

The IonEx module simulates steady state solutions of extracted ion trajectories from plasmas. The ions are treated kinetically and electrons as Boltzmann massless fluid. Steady state solutions are obtained by iterating solutions for field and particles alternately until a converged solution is found.

The fields are governed by the nonlinear Poisson's equation; $\varepsilon_0 \nabla^2 \phi = -\rho_i + \rho_e$ where ε_0 is permittivity of free space, and ρ_e and ρ_i are electron and ion charge densities respectively. IonEx solves the equation after normalization,

$$\lambda_D^2 \nabla^2 \Phi = -\rho + \exp(\Phi)$$

where λ_D is the Debye length, the normalized potential is $\Phi = -e(\phi_P - \phi)/T_e$ with ϕ_P being the plasma potential, and the normalize ion charge density is $\rho = \rho_i / e n_{e0}$ with $n_e = n_{e0} \exp\left[\frac{e(\phi - \phi_0)}{T_e}\right]$.

This nonlinear equation for the potential is solved by the Newton's iteration method except for the first couple of iterations using the Gauss-Seidel method. The Newton's iteration scheme is $F\Phi^{n+1} = -\rho + (1-u^n)\exp(\Phi^n)$, with $A\Phi^{n+1} = -\rho + \exp(\Phi^n)$, and $F = A - \exp(\Phi^n)$. Here, the matrix **A** is a discrete (meshless) analog of the Laplacian. The solution to this equation typically converges within a few iterations.

Once the field is solved, macro ions are tracked in the electric fields calculated from potentials at neighborhood points of the field solutions, and in the given static magnetic fields. Once ion trajectories are obtained, charge densities are distributed over "neighborhood" of points. The charge deposited to computational points is used to update the field solutions. By iteration between field solutions and particle traces, steady state macro ion trajectories are obtained in self-consistent electrostatic fields and static magnetic fields.

As the simulation evolves the trajectories are updated. Computational point locations and the number of points are adapted based on density and potential gradients to obtain self-consistent, steady state solution, accurately and fast. Some of the 2D IonEx results in the absence of magnetic fields were presented before [7], including a benchmark with IGUN [14]. Since then, we implemented magnetic field effects in IonEx. IonEx conserves total energy and the canonical momentum. A benchmark simulation is obtained for the parameters given in the parameters given in Eq.(1) and the magnetic field in Eq.(2), where $z_0 = 0$. The results are shown in Fig. 1 on the left for IonEx and on the right for IGUN.

$$\begin{aligned} &n_0 = 2.24\times10^{17}\, m^{-3}, \quad T_e = 20\, eV, \quad m_i = 1\, amu \\ &Z_i = 1, \quad U_i = 20\ eV \\ &\phi_0 = 60063\, V, \quad \phi_1 = 65000\, V, \quad \phi_2 = 0\, V \end{aligned} \tag{1}$$

$$\vec{B}(T) = 140 r(z - z_0)\hat{r} + (1 - 140((z - z_0)^2 - r^2/2))\hat{z} \tag{2}$$

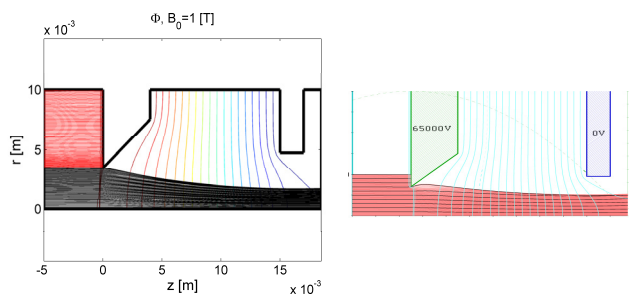

Figure 1. A benchmark run showing the results of IonEx on the left with IGUN on the right.

INTEGRATION OF THE MODULES AND GUI

The strength of our toolset is that it could provide end-to-end simulation to assist ECR CB optimization. If the current of injected beam ions is small enough so that they do not affect the background plasma, MCBC and GEM can be run in series only once to obtain CSD. From MCBC we obtain the steady state ion sources by the beam ions, and then GEM can use that information to obtain CSD. If the current of input beam ions is significant enough to affect background plasma, the two modules need to be run one after the other, and iterated until convergence. This iteration process is implemented. From MCBC and GEM simulations, we obtain density and velocity profiles of each ion species at the extraction aperture. This phase space information distribution of each ion species at the extraction aperture will be the input to IonEx. This link is being implemented. Since GEM is a 2D2V code, the phase space information at the extraction has only r, z, υ_r, and υ_z information. GEM2D can provide much information we need to understand and optimize ECR CB plasmas. If necessary, 3D effects that includes the dependence in azimuthal direction could be examined within our model in a parametric manner.

We have started a GUI implementation for the IonEx module to ease the use of the code as shown in Fig. 2x. Ultimately the GUI will be extended to other modules and to integrate them.

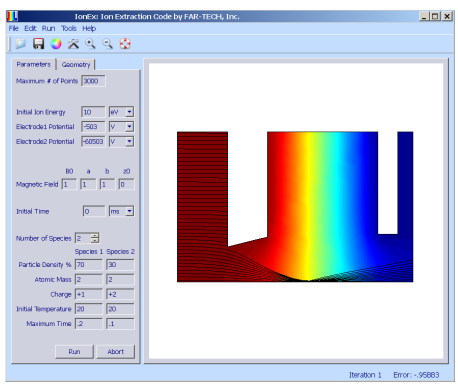

Figure 2. A screen capture of an initial GUI panel for IonEx.

DISCUSSION

Our ECR charge breeder simulation toolset has begun to produce results and some understanding of ECR plasma performance. However, more upgrades are needed before the toolset can fully provide a robust performance.

In addition to code performance such as speed and convergence, some model upgrades can be made in the future. As plasma is a complex system, much aspect of the GEM code is based on physics models. Therefore, it is important to understand the validity of the module and the assumptions used the model. One particular area that needs special attention is the rf heating. GEM uses the quasi-linear diffusion model [16] for rf heating.

Typical ECRIS plasmas operate at densities so that their ECR frequencies are below the cutoff frequency. Thus, rf waves penetrate as far as they can until absorbed by electrons, which occur at the resonance region where near rf frequency = eB/mc. However, an ECR plasma device is a cavity and has cavity modes. The cavity modes may alter the rf-absorption characteristics. The experimental evidence of sensitivity with respect to rf frequency is an indication of the cavity mode effect [17]. The effects of cavity mode to ECR heating has not been implemented in GEM.

A few other areas of needed implementations are as follows. First, when ions hit the walls, they either stick to the wall or a neutral may be coming out of the wall. The latter recycling effect is not implemented in MCBC. Second, while recombination is negligible compared to ionization in the plasma with hot electrons, it could play a role at the injection side as low charged ions have to traverse cold region before they reach the central hot electron zone. In fact, we plan to simulate beam ions starting at a little distance before they enter the ECR device. This way a more complete simulation of injected beam dynamics and beam capture will be simulated. It would also provide the possibility of simulating the effect of backstreaming ions on the injected ion beams before they enter the plasma, which has not been investigated.

REFERENCES

[1] J.S. Kim, L. Zhao, B.P. Cluggish, I.N. Bogatu, and R. Pardo, Rev. Sci. Instrum. 79, 02B906 (2008)

[2] J.S. Kim, C. Liu, D.H. Edgell, and R. Pardo, Rev. Sci. Instrum., 77, 03B106 (2006).

[3] J.S. Kim, L. Zhao, B.P. Cluggish, and R. Pardo, Rev. Sci. Instrum. **78**, 103503 (2007)

[4] D.H. Edgell, J.S. Kim, and I.N. Bogatu, R.C. Pardo and R.C. Vondrasek, Rev. Sci. Instrum., 73, 641 (2002).

[5] D.H. Edgell, J.S. Kim, S.K. Wong, R.C. Pardo, and R. Vondrasek, Phys. Rev. ST Accel. Beams, 2, 123 502 (1999).

[6] S. A. Galkin, B. P. Cluggish, J. S. Kim, and S. Y. Medvedev, Proc. of the Pulsed Power and Plasma Science Conference 2007. Section 8B6, Albuquerque, NM, 17-22 June, 2007.

[7] B.P. Cluggish, S.A. Galkin, J.S. Kim, TUPAS077, Proc. of the Particle Accelerator Conference, Albuquerque, NM, June 25-29, 2007

[8] S. Biri, A. Valek, and T. Suta, E. Takacs and Cs. Szabo, L. T. Hudson, B. Radics, J. Imrek, B. Juhasz, and J. Pa linkas, Rev. Sci. Instrum., Vol. 75, (2004)

[9] J.W. Stetson and P. Spadtke, Proceedings of PAC07, Albuquerque, NM, FROBAB02, (2008)

[10] Girard, K. Serebrennikov, C. Lécot, G. Melin, D. Hitz, L. Sun, 15th International Workshop on ECR

Ion Sources, June 12-14, 2002, University of Jyväskylâ, Finland
[11] A. H. Boozer, Phys. Plasmas 9, 4389 (2002)
[12] L. Zhao, J.S. Kim, B.P. Cluggish, TUPAS079, Particle Accelerator Conference, Albuquerque, NM, June, 2007
[13] L. Zhao, J.S. Kim, B.P. Cluggish, Presented to this conference, at the 18th ECR Ion Source workshop, Chicago, IL September 15-18, 2008
[14] http://www.egun-igun.com/
[15] P. Spadtke, Rev. Sci. Instrum., 75, 1643 (2004)
[16] T.H. Stix, Waves in plasmas, AIP press, (1992)
[17] L. Celona, G. Ciavola, F. Consoli, S. Gammino, F. Maimone, D. Mascali, P. Spädtke, K. Tinschert, R. Lang, J. Mäder, J. Roßbach, S. Barbarino, and R. S. Catalano, Rev. Sci. Instrum, 79, 023305 (2008)

Time Evolution of Endpoint Energy of Bremsstrahlung Spectra and Ion Production from an Electron Cyclotron Resonance Ion Source

T. Ropponen*, P. Jones, T. Kalvas, H. Koivisto, P. Peura, JYFL
O. Tarvainen, Los Alamos National Laboratory
P. Suominen, Prizztech Ltd / Magnet technology centre

Abstract

Electron cyclotron resonance ion sources (ECRIS) [1] are used to produce high charge state heavy ion beams for the use of nuclear and materials science, for instance. The most powerful ECR ion sources today are superconducting. One of the problems with superconducting ECR ion sources is the use of high radio frequency (RF) power which results in bremsstrahlung radiation adding an extra heat load to the cryostat. In order to understand the electron heating process and timescales in the ECR plasma, time evolution measurement of ECR bremsstrahlung was carried out. In the measurements JYFL 14 GHz ECRIS was operated in a pulsed mode and bremsstrahlung data from several hundred RF pulses was recorded. Time evolution of ion production was also studied and compared to one of the electron heating theories. To analyse the measurement data a C++ program was developed. Endpoint energies of the bremsstrahlung spectra as a function of axial magnetic field strength, pressure and RF power are presented and ion production timescales obtained from the measurements are compared to bremsstrahlung emission timescales and one of the stochastic heating theories.

DATA ACQUISITION SYSTEM AND DATA ANALYSIS

In order to study the time evolution of bremsstrahlung radiation JYFL 14 GHz ECRIS was operated in pulsed mode. The trigger signal for the RF pulse (leading edge) was synchronized with the data acquisition system. The duration of RF pulses launched into the plasma chamber was set to 1.76 seconds with 5.92 seconds off-time between consecutive pulses. The TTL type reference signal controls the RF switch which has a switching time of 40 ns (0–100 %) and provides timing signal for both the digital oscilloscope (used to record ion beam currents) and the digital signal processing unit (TNT2) [2]. The RF switch controls the 14 GHz oscillator signal to the klystron and a germanium detector was used to measure the radial bremsstrahlung spectra. TNT2 unit generates the data in binary format and a computer is used to store the data. Energy resolution of the germanium detector was 4.2 keV at peak energy of 444 keV and 7.4 keV at 1048 keV of ^{152}Eu (shaping time was set to 2.0 μs).

The effect of the lead shielding around the collimator was also studied. It was noticed [3] that while adding shielding around the lead collimator changed the count rates and also the shape of the bremsstrahlung spectra the timescales remained the same. The size of the collimator hole (from 0.5 mm^2 to 4 mm^2) was not affecting the spectra and had a insignificant effect on the count rate which means that most of the bremsstrahlung events do not come through the collimator but around it.

Data analysis was done with a self-written C++ program. While the TNT2 unit discarded ADC overflows on-the-fly everything else was left untouched in the raw data. Pile-up events are rejected during the data sorting. Typical measurement time per one set of ECR parameters was 90 minutes resulting in data from over 700 RF pulses. To analyze the data 680 RF pulses are used in every data set i.e. bremsstrahlung data of 680 different RF pulses are combined in order to obtain enough statistics. Data from a background measurement is used during the data processing and the background spectrum is subtracted from the measurement data. The data sorting code produces a significant amount of data files. Both "RF on" and "RF off" phases are analysed and, for example, spectrum data is written with 2 ms time step (if the first 1500 ms of the RF pulse is used 750 spectra are produced for both "RF on" and "RF off" phases) and total count rate data integrated over the whole energy spectrum (from 15 keV to 600 keV) is generated throughout the whole length of the RF pulse. Typically a 1 GB of ASCII data is sorted in about 30 seconds. However, because the code also generates figures of all the sorted data as well as gif animations (time evolution of the bremsstrahlung spectrum in 2 ms steps) the sorting time per one data set can be significantly increased. A typical time to sort all the 21 data sets that were recorded during the measurements is between 9 and 10 h (Intel C2D E6600, 3 GB RAM). Using parallel computing to analyze the data would be relatively easy, however, the creation of animations can take 3 GB of memory, or even more, depending on the settings of the analysing program meaning that a normal desktop computer does not have enough memory to run parallel data analysing. Rejection of "bad" RF pulses has also been coded into the analyse program. This ensures that possible incomplete or erroneous RF pulses are discarded from the final analyse. The code has been written for *Unix/Linux* environments and requires *Gnu Scientific Library (GSL)*, *Gnuplot* and *Convert* in order to generate the graphs and animations.

* tommi.ropponen@phys.jyu.fi

KEY ISSUES IN THE RADIAL BREMSSTRAHLUNG TIME EVOLUTION MEASUREMENTS

The radial bremsstrahlung measurement from a magnetic pole was chosen because information about the electron energies was wanted and the charged particle flux at the pole is much greater than between the poles (radial port to the chamber). If the detector would have been located between the radial magnetic field poles (or in axial direction) it is believed that the bremsstrahlung events would originate partially from the plasma (movement of the charged particles in the plasma chamber) due to the fact that there is only about 1.5 mm of aluminium between the plasma chamber and surrounding air. Additional measurements with better collimation, measurements between the poles and axial measurements are planned to take place in the future with JYFL 14 GHz ECRIS.

In the radial bremsstrahlung measurements there are quite a few issues that need to be addressed in order to obtain good results. Firstly, the angular distribution of bremsstrahlung events must be understood. In the non-relativistic energies the angular distribution of bremsstrahlung radiation is "double cone like" meaning that bremsstrahlung radiation is produced in both the direction of movement of the incident electron as well as in the opposite direction [4]. The intensity of the bremsstrahlung emission is larger in the direction of propagation of the incident electron than in the opposite direction. However, the bremsstrahlung cone in the opposite direction becomes meaningful when a vast amount of electrons collide with the plasma chamber walls. The angle of incidence between the electrons and the plasma chamber walls affects the spatial distribution of the bremsstrahlung radiation. In ECRIS plasmas the velocity vectors of high energy electrons are typically oriented almost perpendicularly with respect to the magnetic field. This causes the solid angle, into which bremsstrahlung is emitted, to be large on each magnetic pole. Secondly, the bremsstrahlung photons interact with the matter over a long distance (usually several tens of millimeters) and the scattering processes play an important role before the photon can be detected in the detector crystal. It is possible that a photon changes its path significantly in the media and loses therefore its energy. Because a typical ECRIS uses a sextupole structure for the radial magnetic field, it is understood that the bremsstrahlung radiation originating from all of the six magnetic poles contributes to the measurement that is done in the proximity of one of the six poles. Thirdly, the collimator in radial measurements should be located as close to the detector as possible or if the collimator is located close to the plasma chamber of an ECRIS it should cover basically the whole ECRIS surface which is in the solid angle of the detector.

In the measurements presented in this article a collimator close to the ECRIS was used. Lead plates were used to improve the shielding around the collimator. The amount of the shielding as well as the collimator opening was studied along with the time evolution of bremsstrahlung emission and ion production time measurements. The collimator aperture had an insignificant effect on the spectra: the count rate at the germanium detector was basically the same with open and closed collimator. The shielding around the collimator, however, plays an important role in the shape of the spectra. This can be seen from Figure 1 a) where the steady state spectra of argon plasma is presented with two shielding geometries (the original shielding had less lead plates than the latter shielding). There is a clearly visible "hump" at the energies of 175–375 keV in the spectrum that is recorded with the original collimator/shielding geometry. Presumably, the curve with the "hump" is closer to the real shape of the spectra than the curve without any "hump" because the high energy part of the spectra is not attenuated so much. Adding lead plates around the collimator absorbs the higher energy electron population. However, the lower energy part of the spectra is not affected very much while adding shielding next to the collimator as can be seen from Figure 1 a). This could be a result from a situation where the lower energy part of the spectra is coming through a thinner part of the lead plate shielding (on the edges of the shielding) or partly through the ECR coil structure and therefore remains relatively unchanged. The size of the "hump" for different source parameters (argon plasma) is presented in the subfigures b), c) and d) of Figure 1. In subfigure a) the upper curve at 250 keV represents the original shielding and collimator aperture and the lower curve represents the situation after the changes. In b) and d) at 250 keV: the uppermost curve – coil currents of 550/550 A or 690 W, the middle curve – 500/500 A or 500 W and the lowest curve – 470/470 A or 300 W. Changing the neutral gas pressure does not affect the the steady state count rate very much and all the curves overlap (subfigure c). This means also that the "hump" remains unchanged while the pressure is varied from $1.5{\cdot}10^{-7}$ mbar to $3.5{\cdot}10^{-7}$ mbar. However changing the axial magnetic field strength (subfigure b) or RF power (subfigure d) affects the total count rate integrated over the energies from 15 keV to 600 keV. The height of the "hump" (in relative counts / 2 ms) can be compared to the maximum height of the spectra (lower characteristic lead peak). These values are presented in Table 1 from which it can be seen that increasing the axial magnetic field strength (lowering the gradient) increases the "hump"/max (H/M) relation by over 10 percent. While the RF power is increased the H/M relation increases again 10 percent. The "hump" is growing while magnetic field gradient is lowered or RF power is increased meaning that the amount of hot electrons is increased inside the ECRIS plasma chamber. It has been reported that the effect from increasing the magnetic field (decreasing the distance between the resonances) is comparable to increasing the RF power in terms of heating efficiency [5].

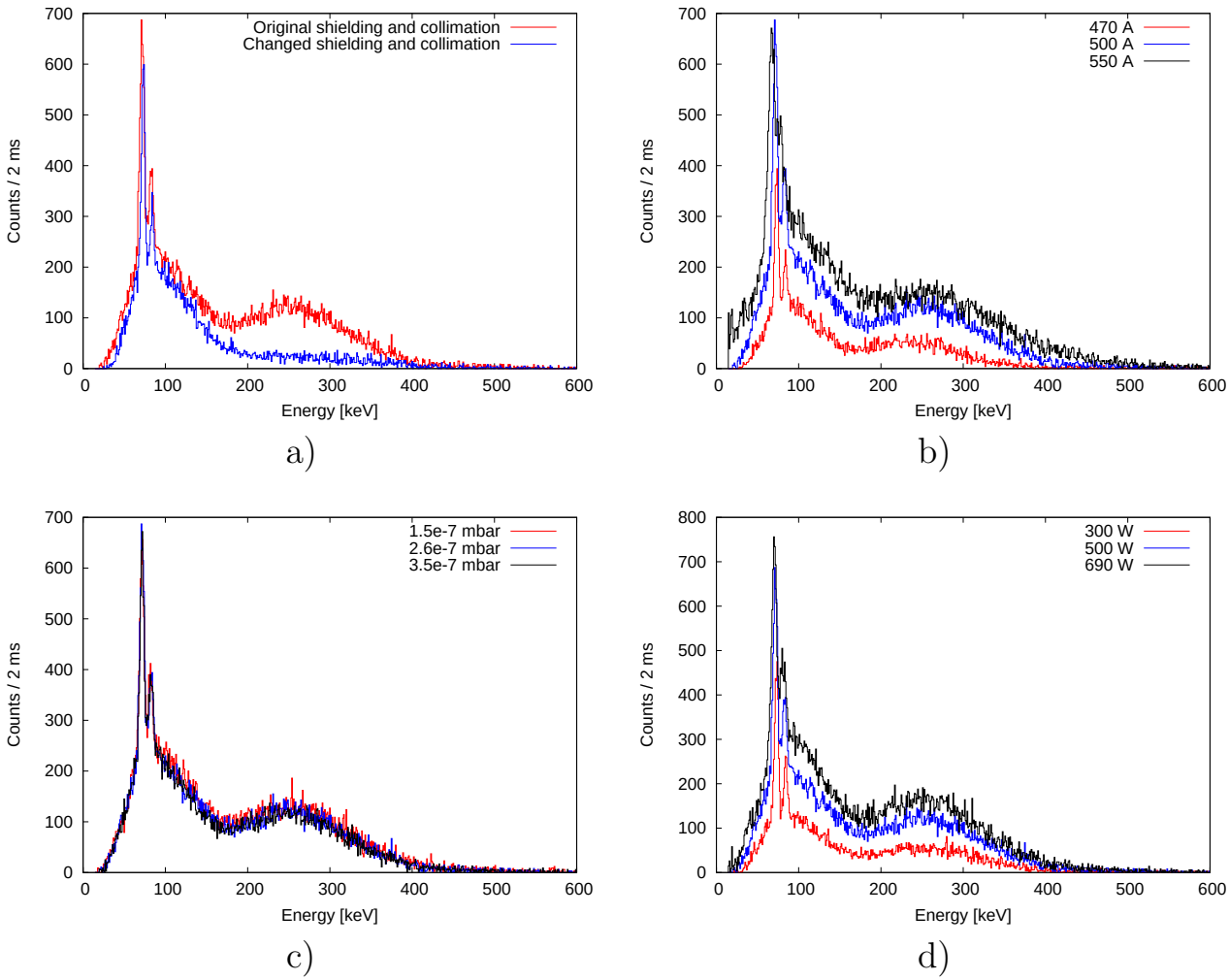

Figure 1: Steady state spectra of argon plasma in a time window of 1500–1502 ms from the leading edge of the RF pulse. a) different shielding and opening of the collimator, b) as a function of axial magnetic field strength, c) as a function of neutral gas pressure, d) as a function of RF power.

EXPERIMENTAL RESULTS

The time evolution of ECR bremsstrahlung emission has been presented as a function of the axial magnetic field, neutral gas pressure and RF power in the references [3] and [6]. The latter includes also the time evolution of argon ion production from the beginning of the RF pulse with some argon charge states. In this section the time evolution of the endpoint energy of the bremsstrahlung emission spectra is presented as a function of the axial magnetic field strength, neutral gas pressure and RF power. The time evolution of oxygen and argon ion production is also presented during the whole RF pulse and the timescales are compared to the bremsstrahlung emission timescales.

Endpoint energy of the bremsstrahlung spectra as a function of axial magnetic field strength, neutral gas pressure and RF power

Table 2 lists the endpoint energies with different ECRIS parameters for argon plasma. The endpoint energies in the steady state phase has been calculated using the following method: 5 % of the maximum count rate in the spectra (75 keV characteristic peak of lead) between times of 1500 and 1502 ms is used as a threshold value. When the average of nine consecutive count rates (each corresponding a single 1 keV energy window) in the aforementioned time window drops below the threshold the median energy corresponding to these nine count rates is defined as the endpoint energy of the spectrum. This is done in order to decrease the effect of statistical behaviour of the count rates.

With argon plasma the endpoint energy of the bremsstrahlung spectra is increasing rapidly when the axial magnetic field gradient is lowered. B_{min} of 0.321 T results

Table 1: Relative count rate at the middle of the "hump" divided by the maximum count rate of the spectra (lower characteristic lead peak) with different ECRIS parameters. Steady state spectra at time window 1500-1502 ms are used (see Figure 1).

	470 A	500 A	550 A	300 W	500 W	690 W
Max / "hump"	13.5 %	18.2 %	23.7 %	12.2 %	18.0 %	22.5 %

Table 2: Endpoint energies of argon bremsstrahlung spectra between 1500–1502 ms from the RF power triggering (see Figure 1) with different JYFL 14 GHz ECRIS settings.

Argon plasma			
B_{inj} / B_{ext}	1.945/0.901 T	2.011/0.946 T	2.111/1.019 T
Endpoint energy	311 keV	364 keV	417 keV
Pressure	$1.5{\cdot}10^{-7}$ mbar	$2.6{\cdot}10^{-7}$ mbar	$3.5{\cdot}10^{-7}$ mbar
Endpoint energy	372 keV	364 keV	363 keV
RF power	300 W	500 W	690 W
Endpoint energy	338 keV	364 keV	375 keV

in 311 keV and endpoint energies of 364 keV and 417 keV are measured for B_{min} of 0.346 and 0.388 T, respectively. The total increase of the endpoint energy is roughly 34 % while the B_{min} increases less than 20 %.

Increased pressure of neutral argon gas has almost no effect on the endpoint energy. Corresponding endpoint energies are: 372 keV ($1.5{\cdot}10^{-7}$ mbar), 364 keV ($2.6{\cdot}10^{-7}$ mbar) and 363 keV ($3.5{\cdot}10^{-7}$ mbar). The total decrease of the endpoint energy is about 2 % while the pressure is varied about 130 %.

Using an RF power of 300 W results in endpoint energy of 338 keV and energies of 364 and 375 keV are recorded with RF powers of 500 and 690 W, respectively. An increase of RF power by a factor of 2.3 results in an endpoint energy increase of about 11 %.

Timescales of oxygen and argon ion production

Timescales of ion production were measured along with the bremsstrahlung emission with JYFL 14 GHz ECRIS. In the ion production measurements both oxygen and argon plasma were used and the results are presented here (for detailed time evolution of argon ion production see [6]). Operation parameters for the ECR for both oxygen and argon plasmas are presented in Table 3. During the measurements the ion source was tuned to O^{7+}(110 μA) or to Ar^{9+} (117 μA) in CW mode. The sampling rate of the oscilloscope (250 ks/sec) was too low in order to use averaging over the noise period and therefore, the ion current data is averaged over 20 consecutive measurement points in order to decrease the amount of noise which was observed at a frequency of 5 MHz (the source for this remained unknown).

Figure 2 illustrates the ion currents during the whole RF pulse. The curves at 1500 ms are the following: the uppermost curve – total count rate of bremsstrahlung events, the second highest curve – O^{7+}, the middle curve – O^{5+}, second lowest curve – O^{3+} and the lowest curve – O^{2+}. With charge states of 2+ and 3+ a so called preglow effect is seen during the first 4–7 ms. Maximum ion current of O^{2+} during the preglow peak is about 200 μA while the steady state current is about 35 μA. This means that during the preglow there is a boost of about 470 %. With O^{3+} the boost at the preglow maximum is 275 % (225 μA) compared to the steady state current of 60 μA.

The steady state of bremsstrahlung emission is reached at around 600 ms (see the vertical line in Figure 2). If short RF pulses (around 4 to 7 ms) were used the production of lower charge states of oxygen (O^{2+}, O^{3+}) could be increased while the amount of bremsstrahlung radiation would still be lower than in steady state phase. From Figure 2 it is also seen that the lower charge states like O^{2+} and O^{3+} start to build up before O^{5+} and the highest charge state presented (O^{7+}) reaches the steady state current around 500 ms.

Figure 3 illustrates the ion currents of the whole RF pulse can be seen in the case of argon plasma. A vertical line is located at 275 ms to mark the time when steady state of the bremsstrahlung production is reached. The following curves can be distinguished at 1500 ms: the uppermost curve – total bremsstrahlung count rate, the second highest curve – Ar^{10+}, the second lowest curve – Ar^{11+} and the lowest curve – Ar^{6+}. The lowest charge state (Ar^{6+}) starts to rise at 5 ms and the maximum of the preglow peak is located around 8 ms (preglow peaks were also observed with argon charge states of 5+,7+ and 8+ and the data for these is presented in [6]). The maximum of the ion current in the preglow peak of Ar^{6+} is about 75 μA while the steady state ion current is 34 μA (factor of 2.2 difference). The higher charge states (10+, 11+) start to rise when roughly 10 ms has elapsed from the launching the RF power into the plasma chamber. Preglow peak is not observed with these higher charge states because the ion source was tuned to

Table 3: Magnetic field strengths of the JYFL 14 GHz ECRIS in ion production measurements, the corresponding resonance lengths in axial direction, neutral gas pressures and RF powers.

Plasma	B_{inj}	B_{min}	B_{ext}	∇B_{inj}^{res}	∇B_{ext}^{res}	d_{res}	Pressure	RF power
Oxygen	2.026 T	0.353 T	0.962 T	6.038 T/m	5.663 T/m	112.6 mm	$4.3{\cdot}10^{-7}$ mbar	745 W
Argon	1.992 T	0.338 T	0.932 T	6.271 T/m	5.815 T/m	118.8 mm	$4.2{\cdot}10^{-7}$ mbar	515 W

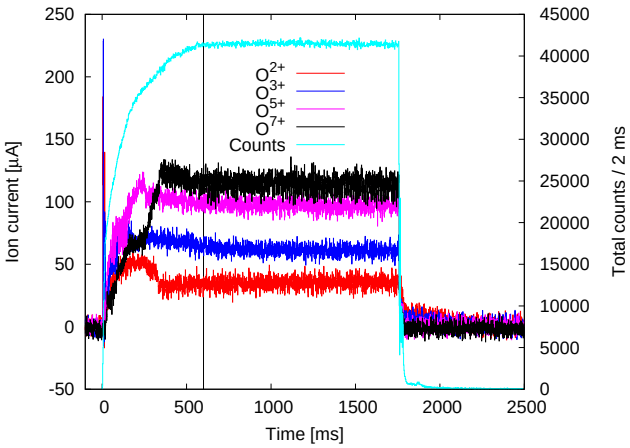

Figure 2: Time evolution of oxygen ions and bremsstrahlung count rate during the whole RF pulse. T=0 corresponds to the leading edge of the RF pulse. A vertical line at 600 ms marks the time when the steady state of bremsstrahlung count rate is reached.

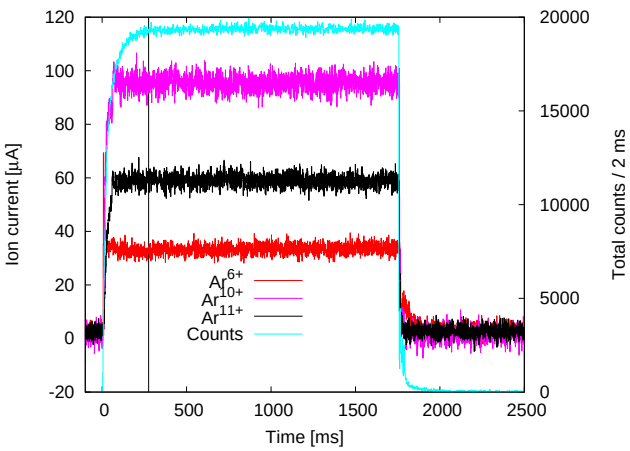

Figure 3: Time evolution of argon ions and bremsstrahlung count rate during the whole RF pulse. A vertical line at 275 ms marks the time when the steady state of bremsstrahlung count rate is reached.

Ar^{9+}. Similar behaviour has been observed in [9].

With argon the ion currents have saturated well before the bremsstrahlung emission saturates. Ion saturation times are roughly 50 ms for Ar^{6+} and about 65 ms for the two higher charge states. The times are significantly lower for argon than oxygen plasma (hundreds of milliseconds, see Figure 2). With oxygen plasma the oxygen atoms can be deposited on the plasma chamber walls and can be released during particle bombardment of the plasma and therefore the time to reach steady state with oxygen plasma could be longer than with argon plasma. However, this needs to be confirmed with additional measurements.

Ion production during the preglow pulse was also studied with argon plasma as a function of the RF power. In this measurement set JYFL 14 GHz ECRIS was tuned with same setting as in the previous measurement and the ion current of Ar^{6+} was observed while varying the RF power from 180 W to 690 W. The following steady state currents for different RF powers were measured: 34 μA (180 W), 33 μA (300 W), 27 μA (500 W), 26 μA (600 W) and 29 μA (690 W). The time evolution of Ar^{6+} ion current for the first 20 ms is presented in Figure 4. At the "peak" the curves are: the lowest curve – 180 W, the second lowest – 300 W, the middle – 600 W, the second highest – 500 W and the highest curve – 690 W. The ion current starts to rise a bit after 4 ms with the two lowest RF powers and with the three highest RF power the rise starts approximately one millisecond later. Reason for this remains unknown. With 180 W there are not a clear maximum in the ion current but with higher RF powers the maximum is well defined. The steady state ion currents are relatively close to each other (from 34 to 26 μA), but the maximum of the preglow peak rises as the RF power is increased. Lowest "peak" current of less than 45 μA is recorded with 180 W and the use of an RF power of 690 W results in the ion current of about 95 μA. Changing the RF power with a factor of 3.8 changes the ion current maximum with a factor of 2.1. After about 20 ms the ion currents are in a steady state phase.

TIMESCALE COMPARISON - MEASUREMENTS VERSUS STOCHASTIC HEATING THEORY

As shown, the steady state of bremsstrahlung count rates is reached in 275 ms with argon plasma and in 600 ms with oxygen plasma. A model by Sergeichev *et al.* [10] is used here to compare the observed timescales to the theory of stochastic electron heating. The model requires information about the magnetic field minimum ($B_{\min}$), microwave power (amplitude of electric field), microwave frequency and the bandwidth of the microwave. According to the heating model the transverse electron energy in the stochastic acceleration regime can be written as

$$W_{\perp}^{0}\,[eV] = DE_0^{\frac{8}{7}} t^{\frac{2}{7}}, \qquad (1)$$

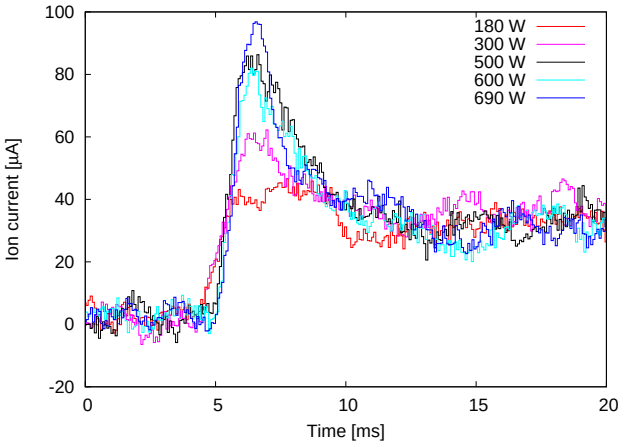

Figure 4: Time evolution of Ar^{6+} during the first 20 ms of the RF pulse with different RF powers.

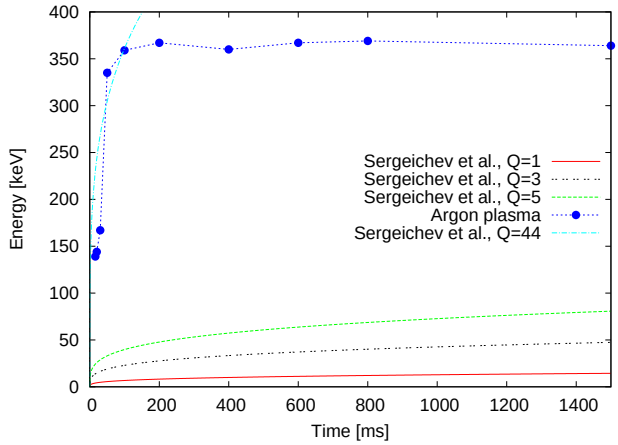

Figure 5: Comparison between the theory of stochastic heating and the endpoint energies measured with JYFL 14 GHz ECRIS. Theoretical curves plotted with different plasma chamber quality factors.

where D is defined as

$$D = \left(\frac{\Delta\omega}{\omega_0}\frac{B_c}{B_c - B_0}\right)^{\frac{4}{7}} \left(\frac{2e}{m}\right)^{\frac{1}{7}} k^{-\frac{3}{7}} \pi^{-\frac{2}{7}}. \qquad (2)$$

In these equations E_0 is the electric field amplitude at the resonance, t time, $\Delta\omega$ frequency bandwidth, ω_0 microwave frequency, B_c resonant magnetic field, B_0 B-minimum and k is derived from the second order axial magnetic field approximation. In the case where the coil currents in JYFL 14 GHz ECRIS are 500/500 A $B_0 = 0.35$ and k is about 147. The klystron of the 14 GHz ECRIS is tuned for a frequency of 14.1 GHz and the reported bandwidth according to the manual is at least 85 MHz. The RF power of 500 W is used thus, the amplitude of the electric field can be calculated approximately using Poynting vector to be about 9.1 kV/m in an empty chamber with plasma chamber quality factor of 1. The stochastic heating model of equation 2 does not explicitly take into account that the resonance field shifts to higher B field as the electrons gain energy (relativistic effect). This shortcome was treated by inserting the functional dependence of the resonance field on the electron energy i.e. $B_c = B_c(W)$ into equation 2 and solving it numerically with a time step of 0.5 ms.

If the value of k is changed from 147 to 139 (corresponding to coil currents of 550/550 A) the maximum energy in stochastic heating according to Sergeichev (Q=1) increases about 0.3 keV (from 14.4 to 14.7 keV). With Q=5 (the amplitude of the electric field is multiplied by 5) the lower value of k (139) produces 1.8 keV higher energy (82.5 keV versus 80.7 keV) than the higher k value after 1500 ms of heating time. Therefore it can be stated that the value of k does not have a major impact on the final maximum energy.

Comparison of timescales between the theory (after Sergeichev) and measurements is presented in Figure 5. Just before 200 ms the lowest curve is after Sergeichev's theory with plasma chamber quality factor of 1, the second lowest curve is theory with Q=3, the middle curve is theory with Q=5, the second highest curve is endpoint energy data from measurements with argon (at given time) and the uppermost curve is calculated from the theory using Q=44. With this very high quality factor the first 100 ms seem to fit relatively well to the measured data, however, after that the Q=44 curve overshoots the measurement values rapidly. This could be due to the fact that the theory does not take into account the limit of stochastic heating, which depends on the group velocity of the EM waves in the plasma. Therefore, the electron energy calculated from the theory does not exhibit saturation behaviour, clearly observed in the measurements, and quality factor Q=44 becomes obsolete after the saturation has been reached. It is suggested that in an empty chamber the quality factor can be in the order of tens or hundreds of thousands [11] and after the plasma has been ignited the quality factor drops down and is around 3 [5]. During the plasma breakdown the quality factor changes rapidly as a function of plasma density (permittivity) but the timescales for this time evolution of quality factor remains unknown. However, another explanation must also be considered. The maximum value of radial magnetic field in the chamber walls of JYFL 14 GHz ECRIS is 0.85 T which corresponds to resonance field for electrons which have energy around 360 keV. The reached steady state behaviour, observed for example in Figure 5, could be a result from a fact that the resonance region has moved into plasma chamber walls and higher energy electrons do not have a resonance zone anymore inside the chamber.

Timescales can be roughly extracted from Figure 5 which presents the time evolution of endpoint energy for the measurement data. The electron energy after 200 ms is about 8 keV according to the stochastic heating theory with plasma chamber quality factor of 1. With Q=3 the energy is 27 keV and with Q=5 the energy is 48 keV at 200 ms. The endpoint energy for argon plasma, using the same 5 % threshold as before, is 367 keV at 200 ms. It

is clear that there are discrepancies between the theory and the measurements. If the quality factor Q is changed the energies according to the theory will increase. However, the timescales from the theory do not match with the measurements: saturation of the endpoint energies is much faster in the measurements than according to the theory where the energies do not saturate at all. Sergeichev's theory does not include any electron energy losses caused by the friction between neutral particles and electrons [10]. These phenomena will, however, decrease the electron energies and some other explanation is needed to explain the measured behaviour.

Different theoretical model for phase regime heating (the electron remains in the accelerating phase all the time) is also presented in [10]. This theory, as expected, generates very high energies in very short time periods. Using the operation parameters from JYFL 14 GHz ECRIS this phase regime theory generates over 1 MeV electrons in 10 ms. These timescales and energies imply that the stochastic heating model needs some corrections (distance between the resonance points, stochastic heating limit) to be accurate and consistent with the measurements and on the other hand rules out the possibility of phase regime heating in an ECR ion source if several resonance crossings are taken into account. This is supported by simulation results reported in reference [12].

DISCUSSION

It is noticed that the steady states for endpoint energies are reached at around 200 ms with argon plasma (see Figure 5). Pressure of the neutral gas inside the ECRIS plasma chamber does not affect the endpoint energy very much. However, the highest endpoint energy (372 keV) is recorded with the lowest neutral gas pressure ($1.5{\cdot}10^{-7}$ mbar). This could be a result from the collision frequency: with the lowest pressures the collision frequency between the particles in the plasma is lowest resulting in longer heating times of electrons before they are collided with other particles or scattered into the radial loss cone of the magnetic field. Changing the RF power from 300 W to 690 W results in an increase of 11 % in endpoint energy. The magnetic field gradient plays, however, an important role in the evolution of endpoint energies. Increasing the axial magnetic field strength (lowering the magnetic field gradient) results into significant changes in the endpoint energy: from 311 keV to 417 keV. Therefore it is stated that the endpoint energy of a bremsstrahlung spectra is dependent on the magnetic field configuration ($B_{\min}$ and gradB) while the effect of the neutral gas pressure and RF power is very small. It is worth of note that the magnetic field generated by the permanent magnets of the JYFL 14 GHz ECRIS is 0.85 T on the magnetic poles. As the electrons gain energy their resonance field shifts towards higher values. Magnetic field value of 0.85 T corresponds to an energy of about 360 keV, which is close to observed endpoint energy of the bremsstrahlung spectra (see e.g. Figure 5). Therefore, it is plausible to claim that the magnetic field profile (and strength) in radial direction may limit the observed energies.

Production times of oxygen and argon ions were also studied and the time evolution of bremsstrahlung emission was compared to times to reach steady state ion currents. A so called preglow effect was observed with O^{2+} and O^{3+} ions. The maximum of the preglow peak ion current in the case of O^{2+} was about 5.7 times the steady state ion current, and with O^{3+} there was a difference by a factor of 3.75. With argon plasma the preglow was observed with Ar^{6+} (and with charge states 5+, 7+ and 8+, see reference [6]). Comparing the steady state of Ar^{6+} to the peak current there is a difference by a factor of 2.2. As expected, the higher charge states build up slower than the lower charge states with both oxygen and argon plasma. The differences in reaching the steady currents with oxygen and argon charge states might be due to more reactive oxygen which is deposited on the plasma chamber walls between the RF pulses and released by ion bombardment during the ignition of the plasma.

The preglow peaks appear several hundreds of milliseconds before the bremsstrahlung emission count rate reaches the steady state. This means that if short millisecond region RF pulses are used bremsstrahlung radiation levels could be decreased relatively more than the ion current, however this needs to be verified with measurements. Typical decay times for a bremsstrahlung spectra from JYFL 14 GHz ECRIS are around tens of milliseconds [3]. Therefore, using an ECR ion source to produce medium (or high, depending on the ECRIS tuning) charge states in a pulsed mode would require RF pulses with a duty factor around 20 % which is very low in terms of continuous ion beam. O^{2+} ion current saturates around 340 ms, O^{3+} and O^{5+} approximately at 700 ms and with O^{7+} it takes nearly 600 ms before the steady state current is reached. The bremsstrahlung count rate reaches the steady state around 600 ms meaning that the ion currents are reaching the steady state before or at same time as the bremsstrahlung emission saturates. With argon plasma the steady state time of the ion currents and the bremsstrahlung emission have a clear difference: Ar^{6+} saturates around 30 ms while Ar^{10+} and Ar^{11+} reaches the steady state ion current after about 70 ms has elapsed from the leading edge of the RF pulse and the bremsstrahlung emission saturates around 275 ms.

Similar behaviour for the ion current rise times with fast sputter sample and gas valve using neon, argon and gold ions have also been reported [13]. However, the ion rise times measured in [13] have been recorded while the ECRIS is in a steady state operation. Rise time for $^{20}Ne^{2+}$ was 1.6 ms and for $^{20}Ne^{8+}$ a rise time of 38.3 ms was measured at 407 W of RF power. In the ion production measurements presented in this article the rise time for O^{2+} is around 5 ms and for O^{7+} the rise time is roughly 20 ms. There are fundamental differences between the measurement setups used with JYFL 14 GHz ECRIS and with ATLAS ECR I (10 GHz). In the measurements presented in

this article, and in the references [3, 6], the ECR plasma was ignited during the RF pulse and turned off with the trailing edge of the RF pulse while the ATLAS ECR I was running in a steady state region with a buffer gas plasma and a fast gas valve or fast sputter sample was used.

When the argon ion production is studied as a function of the RF power it is observed that the maximum ion current of the preglow peak increases with the RF power while the steady state current of Ar^{6+} remained within a few microamperes. The preglow peak starts to rise after about 4 ms (180 W, 300 W) from the launching of the RF power and if higher RF powers (500 W, 600 W, 690 W) are used the rise point is moved to about 5 ms. No explanation for this behaviour has been found yet.

If the stochastic heating theory of Sergeichev *et al.* is compared to the time evolution of endpoint energies measured with JYFL 14 GHz ECRIS it is clear that the theory predicts (with Q=1) energies that are several times lower than the measured endpoint energies are. If the value of Q is increased the energies predicted by the theory will increase but with relatively small Q values the theoretical curves lie at significantly lower energies than the measured values. If Q=44 is used to calculate the electron energy from the theory the first 100 ms are in unison between the measured and theoretical values. After 100 ms the theoretical curve significantly overshoots the measured values. In addition, the timescales from the theory are significantly slower than the timescales obtained from the measurements when a reasonable value for Q is used. In a steady state region the endpoint energies extracted from argon plasma are about 360 keV. Because the timescales that the theory is predicting have a clear discrepancy to the measurement results, it seems that the theory needs some refinement like, for example, adding the stochastic heating limit into the theory.

ACKNOWLEDGMENTS

This work has been supported by the EU 6th Framework programme "Integrating Infrastructure Initiative - Transnational Access", Contract Number: 506065 (EURONS), by the Academy of Finland under the Finnish Centre of Excellence Programme 2006-2011 (Nuclear and Accelerator Based Physics Programme at JYFL) and US Department of Energy under the contract DE-AC52-06NA25396. T. Ropponen would also like to acknowledge financial support from the Graduate School in Particle and Nuclear Physics. The gamma spectroscopy group of JYFL and the use of germanium detector from GAMMAPOOL resource is gratefully acknowledged.

REFERENCES

[1] R. Geller. *Electron cyclotron resonance ion sources and ECR plasmas*. Taylor & Francis, 1996.

[2] L. Arnold, R. Baumann, E. Chambit, M. Filliger, C. Fuchs, C. Kieber, D. Klein, P. Medina, C. Parisel, M. Richer, C. Santos and C. Weber. TNT digital pulse processor. *IEEE Trans. Nucl. Sci.*, 53:723–728, 2006.

[3] T. Ropponen, O. Tarvainen, P. Jones, P. Peura, T. Kalvas, P. Suominen and H. Koivisto. The effect of magnetic field strength on the time evolution of bremsstrahlung radiation created by an electron cyclotron resonance ion source. Submitted to Nucl. Instr. and Meth. A, 2008.

[4] H. W. Koch and J. W. Motz. Bremsstrahlung cross-section formulas and related data. *National bureau of standards*, 31:920–956, 1959.

[5] Y. Jongen. E.C.R. electron acceleration. In *Workshop on the Sixth International ECR Ion Source*, pages 238–255, Berkeley, California, 1985. Lawrence Berkeley Laboratory.

[6] T. Ropponen, O. Tarvainen, P. Jones, P. Peura, T. Kalvas, P. Suominen and H. Koivisto. Time evolution of bremsstrahlung and ion production of an electron cyclotron resonance ion source. To be submitted.

[7] V. M. Povyshev, A. A. Sadovoy, V. P. Shevelko, G. D. Shirkov, E. G. Vasina and V. V. Vatulin. Electron-impact ionization cross sections of H, He, N, O, Ar, Xe, Au, Pb atoms and their ions in the electron energy range from the threshold up to 200 keV. Communication of the Joint Institute for Nuclear Research, Dubna, 2001.

[8] A. Li-Scholz *et al.*. *Atomic data and nuclear data tables.* 36, 1987.

[9] T. Thuillier, T. Lamy, L. Latrasse, I.V. Izotov, A. V. Sidorov, V. A. Skalyga, V. G. Zorin and M. Marie-Jeanne. Study of pulsed electron cyclotron resonance ion source plasma near breakdown: The preglow. In *Proceedings of the 12^{th} international conference on ion sources*, 79, 02A314. Rev. Sci. Instr., 2008.

[10] K. F. Sergeichev, D. M. Karfidov and N. A. Lukina. Electron cyclotron resonance acceleration of electrons to relativistic energies by a microwave field in a mirror trap. *Plasma Physics Reports*, 33:455–473, 2007.

[11] F. Consoli, S. Barbarino, L. Celona, G. Ciavola, S. Gammino and D. Mascali. Investigation about the modes in the cylindrical cavity of an ECR ion source *Radiation Effects and Defects in Solids*, 160:467–475, 2005.

[12] T. Ropponen, O. Tarvainen, P. Suominen, T. K. Koponen, T. Kalvas and H. Koivisto. Hybrid simulation of electron cyclotron resonance heating. *Nucl. Instr. and Meth. A*, 587:115–124, 2007.

[13] R. C. Vondrasek, R. H. Scott, R. C. Pardo and D. Edgell. Techniques for the measurement of ionization times in ECR ion sources using a fast sputter sample and fas gas valve. *Rev. Sci. Instr.*, 73:548–551, 2002.

PAPER NOT RECEIVED

STUDY OF THE DEPENDENCE OF ECR ION CURRENT ON PERIODIC PLASMA DISTURBANCE*

G.S. Taki[1], P.R. Sarma[1], D.K. Chakraborty[1], A.G. Drentje[2], T. Nakagawa[3], P.K. Ray[4] and R.K. Bhandari[1]

[1] Variable Energy Cyclotron Centre, Block-AF, Bidhannagar, Kolkata-700064, India
[2] Kernfysisch Versneller Instituut, Groningen, The Netherlands
[3] Institute of Physical and Chemical Research (RIKEN), Wakoshi-3510198, Japan
[4] Bengal Engineering and Science University, Shibpur, Howrah-711103, India

Abstract

In a recent work we observed the existence of periodic current bursts from an ECR ion source when a biased disc is used for enhancing the extracted beam current. It was concluded that the current per burst in the source remains essentially constant. When the disc bias voltage is increased, the burst frequency increases, and so does the total current. The increase in ion current has been found to be proportional to the charge state. However, in the case of protons a different trend is observed. In this work we have studied the periodic bursts in the proton current in order to understand the difference in the behaviour of current jump in protons and heavy ions.

INTRODUCTION

ECR ion sources are used in accelerators and various other laboratories for producing ion beams. In many applications it is needed to produce highly charged heavy ion beams. However, in general, the higher the charge state, the lower is the ion current. A number of techniques are employed to enhance the ion current. Often a lighter gas is added to the sample gas which reduces the ion temperature thereby increasing the retaining time. Ion current increases in this process [1]. Supply of low temperature electrons to the main stage plasma is another method. In this process the plasma becomes more stable, as a result of which the ion confinement time increases. Wall coating [2], use of an electron gun [3], and the insertion of a biased disc [4-6] are the methods of the electron supplying technique.

When a negative potential is applied to the disc, the electron density increases and thus increases the ion current [7]. Another explanation by D. Meyer [8] suggests that with the application of a negative potential on the disc, the plasma potential decreases and the plasma becomes more stable. With a stable plasma, production of high charge state ions increases.

*gstaki@veccal.ernet.in

In order to understand the aspects of the ion current enhancement by using a biased disc, we have tried to explore the time characteristics of the ion beams of various charge states. In an earlier work we measured the time spectra of neon ions, and observed the presence of periodic ion bursts [9]. The burst frequency varied with the disc bias voltage, and the ion current showed a good positive correlation with the burst frequency.

For investigating this feature further, we have measured and analyzed the time spectra of various ion species of high and low charge states. Spectra have been measured at a number of disc bias voltages and microwave power levels. Above a threshold mircowave power, there is a consistent presence of ion bursts.

EXPERIMENT

Experiments were performed with VEC-ECR source [10] for oxygen ECR plasma with helium as mixing gas. The source pressure was kept at 1.8×10^{-7} Torr. An aluminium biased disc of 3cm diameter was placed on the axis at the injection mirror point. Bias voltage was varied in steps from 0 to –55 Volt.

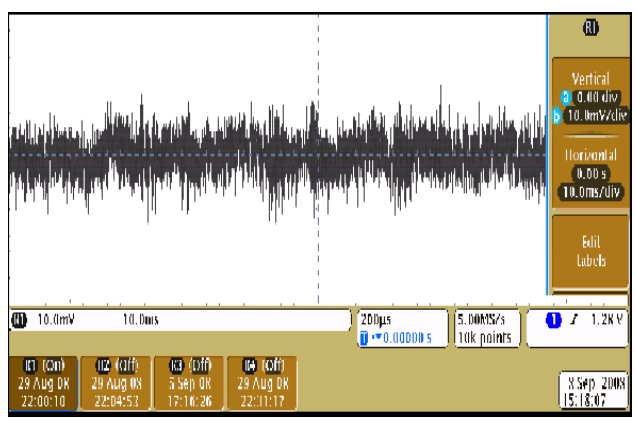

Figure 1: Time spectrum of O^{6+}

In the present experiment, a Faraday cup, located just beyond the image slit of the 90^0 analyzing magnet in the beam line, measured the ion current. Spectra for

individual analyzed ion species could be recorded in this way. The output of the Faraday cup was fed to a storage type 500 MHz Tektronix digital phosphor oscilloscope (DPO-4054).

We stored data at intervals of 0.04 ms. Duration of each measurement was 400 ms allowing us to collect 10000 data points in each time spectra. Fig.1 shows a typical spectrum. The time spectra were Fourier analyzed on-line with the spectrum analyzer available with the oscilloscope.

RESULTS

Spectra were measured for typical high and low charge state ions, viz. O^{6+}, O^{3+} and H^{+} at various disc bias voltages and microwave power levels. The ion current for all the species shows a DC component and a periodic contribution. For low microwave power, bursts are not observed. Above a threshold of about 90 watt bursts appear suddenly as shown in Fig.2. The burst frequency steadily increases as the power level is increased (Fig.3). Another interesting feature is that for high charge state (O^{6+}) there is a correlated increase in the ion current with the burst frequency.

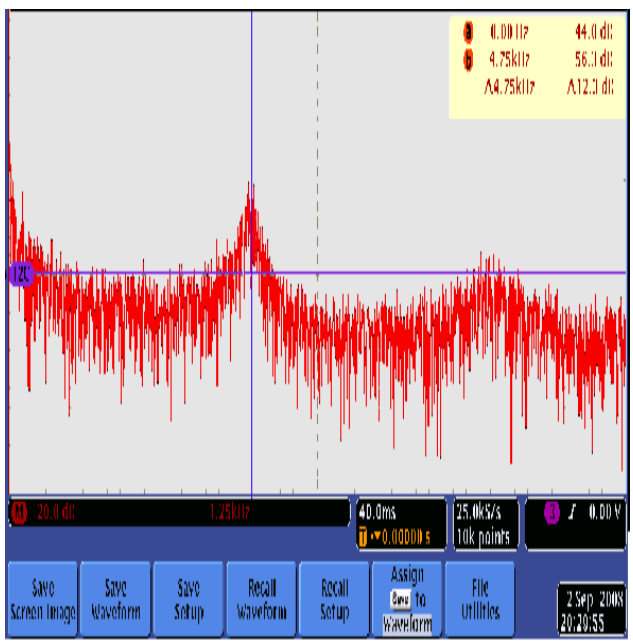

Figure 2: Typical Fourier spectrum

The correlation between the burst frequency and the increase in ion current suggests that the current per burst is a constant factor. The more the number of bursts, the higher is the contribution to the current.

For low charge states, e.g., protons, the trend is different. As the burst frequency increases the proton current decreases (Fig.4). One can understand this in the following manner. As the plasma absorbs more power, the higher charge states get populated at the sacrifice of lower charge states. This explains the increase in O^{6+} current and decrease of H^{+} current (Fig.5).

The burst frequency varies with the applied disc bias voltage also. As can be seen from Fig.5, for O^{6+} beyond a bias of –9 V the burst frequency increases with the bias voltage. The ion current also increases simultaneously.

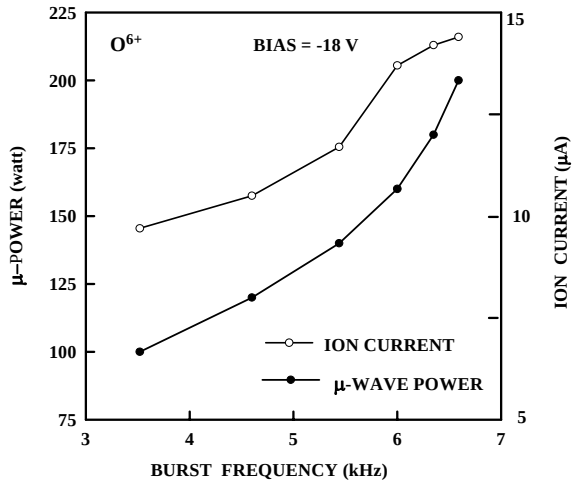

Figure 3: Ion current increases with burst frequency which, in turn, increases with absorbed μ-wave power.

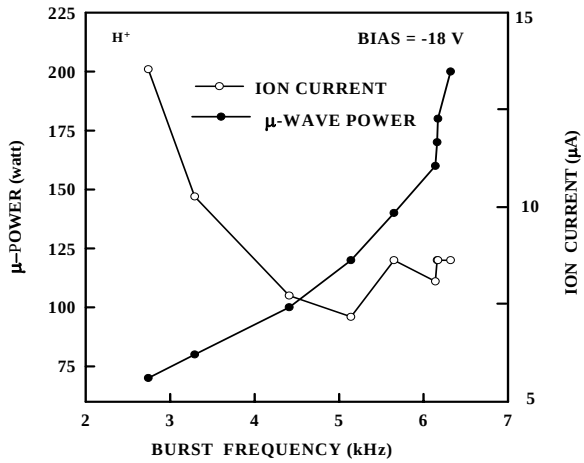

Figure 4: Ion current, in general, decreases with burst frequency in case of protons.

We have studied the effect of the disc bias potential on the observed appearance of burst frequency. Ion current and corresponding burst frequency for O6+, O3+ and proton were measured as a function of the disc voltage. It is clear from Fig.6 that as in the case of microwave power, the bust frequency and the ion current increase with the disc bias voltage in the case of O^{6+}.

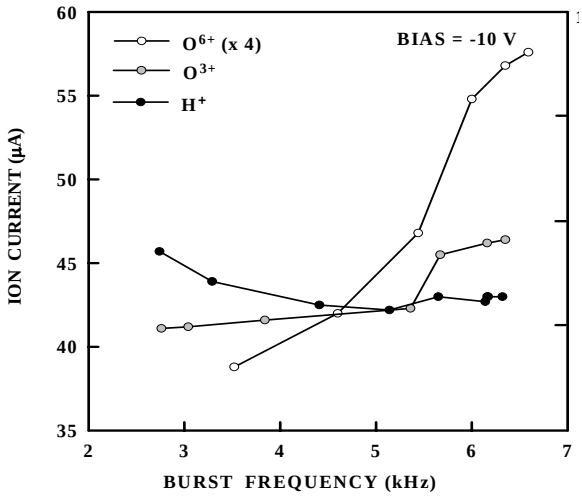

Figure 5: The nature of variation of ion current with burst frequency differs for high and low charge states.

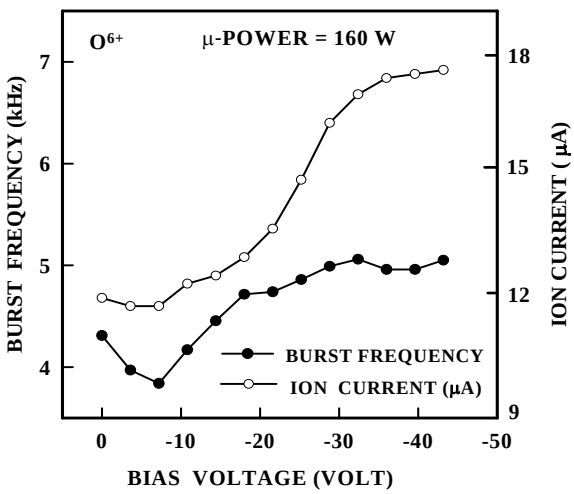

Figure 6: Burst frequency and ion current increases with bias voltage for O^{6+}

DISCUSSIONS

One is tempted to look at the phenomenon in terms of a periodic plasma disturbance and the electron and ion confinement time. Our recent work on ion and electron confinement showed [11] that ions inside an ECR chamber consists of two bunches (Fig.7). One bunch, which barely remains confined, are lost within an average confinement time of ~10^{-5} sec. These are the ions which escape quickly via straight radial or axial escape. Another bunch remains confined for a considerably longer time, and gain sufficient energy to take part in the ionization process. The average confinement time of such ions for a 6.4GHz source of our type is about 10^{-3} sec. The kilo-hertz oscillation observed by us is of similar time scale. The electrons inside the ECR chamber also show a similar behaviour (Fig.8). The average confinement time of the energetic electron component is 1.3×10^{-4} sec. If due to excess absorption of power by electrons, any plasma disturbance is created, the density of ionizing electrons are temporarily changed. Generation of another energetic electron bunch takes time to be confined. Thus ion production will show a temporal behaviour.

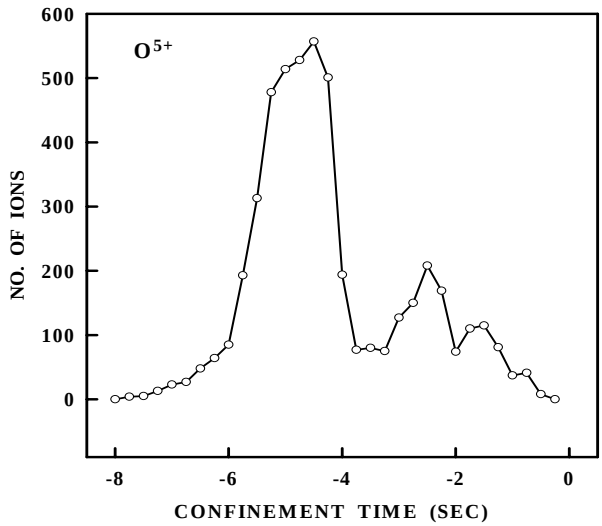

Figure 7: Two electron bunches of different confinement times.

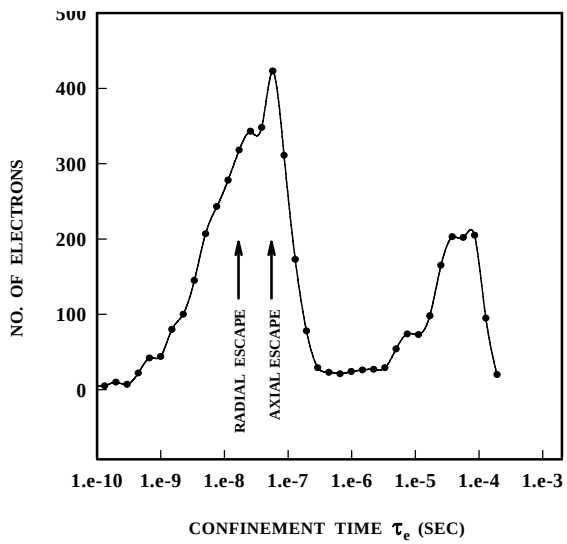

Figure 8: Electron confinement time

REFERENCES

[1] A.G. Drentje, Rev. Sci. Instr. **74** (2003) 2631.
[2] C.M. Lyneis, Proc. 8th Int. Workshop on ECR Ion Sources, 1987, Ed. J. Parker, NSCL Reports, MSUCP, p.42
[3] Z.Q. Xie and C.M. Lyneis, Proc. 11th Int. Workshop on ECR Ion Sources, Groningen, 1993, Ed. A.G. Drentje, KVI Report-996, p.106
[4] G. Melin et al. Proc. of the 10th Int. Workshop on ECR Ion Sources, Knoxville,1990, Ed. F.W. Meyer and M.I. Kirkpatrik, Oakridge report, Conf-9011136, p.1.
[5] S. Biri, T. Nakagawa, M. Kidera, L. Kenez, A. Valek, and Y. Yano, Proc. 14th Int. Workshop on ECR Ion Sources, CERN, Geneva,1999
[6] A.G. Drentje, A. Kitagawa, M. Muramatsu, H. Ogawa and Y. Sakamoto, Rev. Sci. Instr. 2004, **75**: 1399
[7] S. Gammino, J. Sijbring and A.G. Drentje , Rev. Sci. Instr. **63** (1992) 2872.
[8] D. Meyer, D.O. Bolshukhin, I.P. Vinogradov and K. Wiesemann, Proc. 12th Int. Workshop on ECR Ion Sources, 1995, (RIKEN, Japan), Ed. M. Sekiguchi and T. Nakagawa, INS, Tokyo, report INS-J-182, p.34
[9] G.S. Taki, P.R. Sarma, A.G. Drentje, T. Nakagawa, P.K. Ray and R.K. Bhandari, Chinese J. of High Energy Phys. and Nucl. Phys. **31**, (2007) 170.
[10] G.S. Taki, P.R. Sarma, D.K. Chakraborty, R.K. Bhandari, P.K. Ray and A.G. Drentje, Rev. Sci. Instrum. **77** (2006) 03A310.
[11] P.R. Sarma, G.S. Taki and R.K. Bhandari, Nucl. Instrum. and Meth. In Phys. Res. **B264**, (2007) 140.

PAPER NOT RECEIVED

GYROTRON INTRODUCTION FOR ECRIS 2008

H. Jory, S. Cauffman, M. Blank, and K. Felch,

Communications and Power Industries, Palo Alto, CA 94303, U.S.A

Abstract

Gyrotrons are proving to be very reliable sources of high power at frequencies in the range of 28 to 170 GHz, where other sources are very limited in power capability. As a specific example for ECRIS applications, a 10 kW, 28 GHz CW gyrotron has made possible significant increases in the ion currents generated by the Venus ion source at the Lawrence Berkeley Laboratory [1]. In this paper we briefly discuss the physics and engineering aspects of the gyrotron oscillator, point out some of the issues that require special treatment in the control system and power supplies for it, review related gyro-devices, and present important applications.

INTRODUCTION

The history of gyrotrons goes back to the 1950s. The basic idea of a cyclotron resonance interaction was recognized by a number of people. Particular recognition should be given to Russian scientists under the leadership of A. V. Gaponov [2]. A more recent detailed review of gyro-devices is given in [3].

Figure 1 shows specific CPI gyrotrons and other selected gyrotron sources in a plot of average power output versus wavelength. They occupy an empty region between lasers and conventional vacuum electron devices (VEDs) like klystrons, traveling-wave tubes, and magnetrons. The domain of solid-state devices is similar to conventional VEDs but at lower power level. A more detailed listing of gyrotrons worldwide can be found in [4].

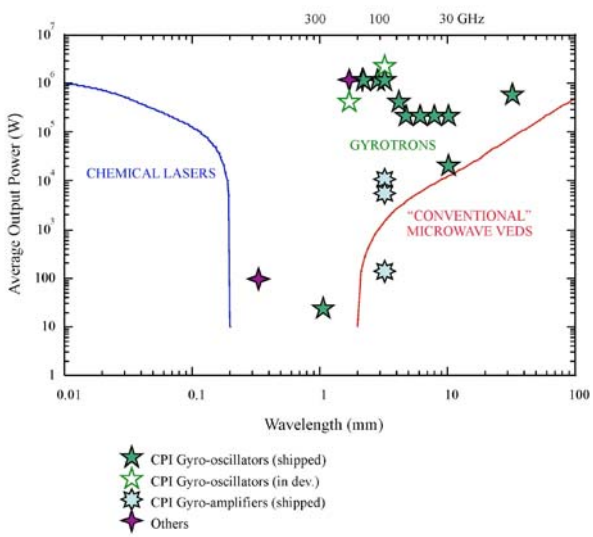

Figure 1: The role of gyrotrons in frequency-power parameter space

BASICS OF THE GYROTRON INTERACTION

Gyrotrons make use of the strong coupling that takes place between an electron moving in a circular orbit perpendicular to a dc magnetic field and an electromagnetic field in the plane of the orbit which has a frequency near the cyclotron resonance frequency of the electron.

The left side of Figure 2 shows 8 electrons at some initial time distributed equally around the orbit center. The electron in position 7 sees a maximum decelerating force, and the one at 3 sees maximum accelerating force. One half cycle later the field has reversed polarity and 7 has moved half way around the orbit and again is decelerated. Likewise 3 is again accelerated. At 1/4 and 3/4 cycle times the electric field is zero and only magnetic forces exist.

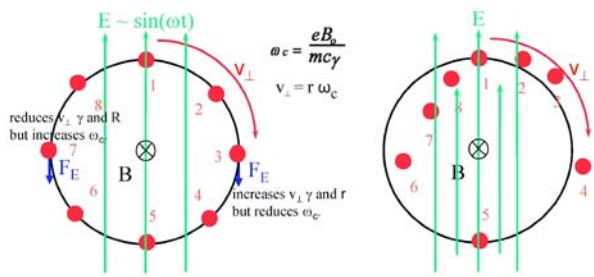

Figure 2: Electrons at cyclotron resonance with a time-varying electric field

The right side of Figure 2 shows the situation an integral number of cycles later, when the cumulative forces have produced a bunching in the rotational phases of the electrons. In this case there is no net energy loss of the electrons because equal numbers have been accelerated and decelerated. If, however, we have a slight difference between ω and ω_c, we can arrange for the bunch to form in a region of decelerating force, and the loss of electron energy will cause the electric field to grow.

To create a gyrotron we introduce a microwave resonator to define a volume for the fields and create an electron beam where all electrons have the same transverse component of velocity, $v_\perp$, and a small component of axial velocity so that the electrons are removed from the cavity before they slip further into a phase to gain energy back.

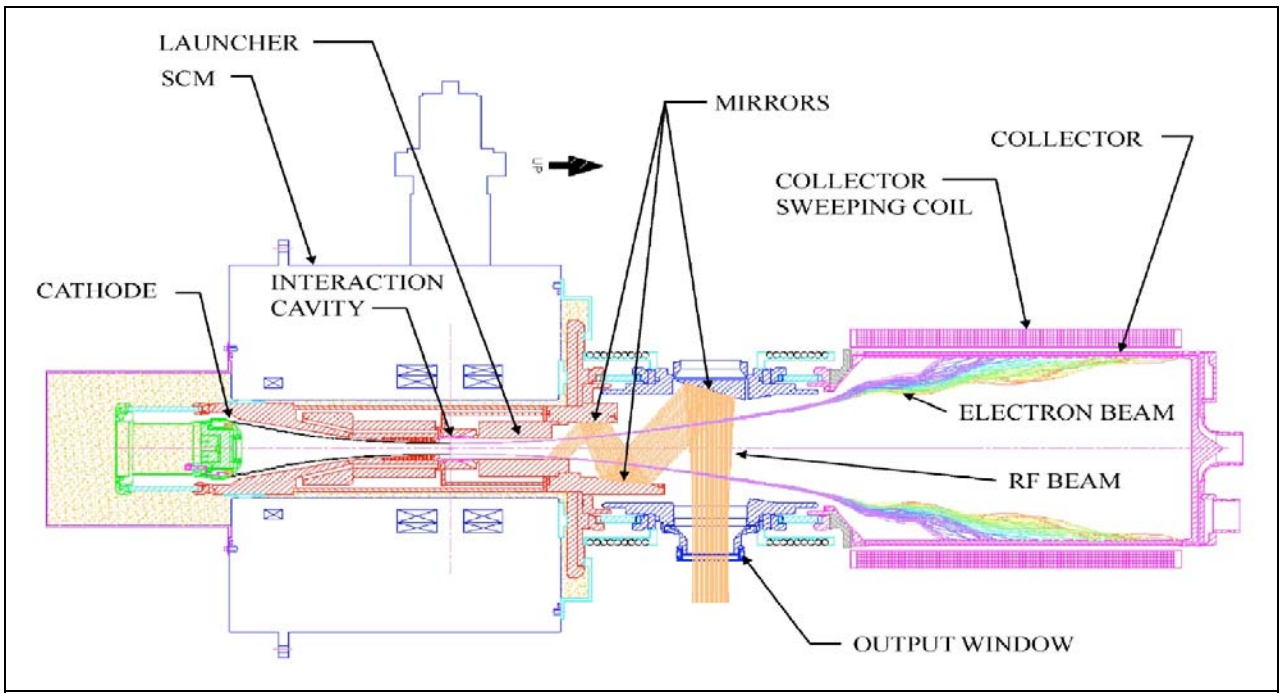

Figure 3: Layout of a 95 GHz, 2.5 MW gyrotron

Figure 3 shows the basic layout for a multi-megawatt gyrotron at 95 GHz. The required magnetic field is created by a superconducting magnet (SCM), which has two main coils to supply the field close to cyclotron resonance at the cavity, and a third coil near the cathode to help control the transverse energy of the electrons. The 95 GHz interaction cavity uses the $TE_{22,6,1}$ mode, and is formed by a slight diameter step on the left side and a slight up taper on the right. (Choice of operating mode is frequency and power dependent.)

The desired electron beam for interaction in the cavity is a thin hollow cylindrical beam having a ratio of transverse-to-axial velocity typically in the range of 1.3 to 2. For efficient operation, all electrons should have the same velocity components. At the cathode, the magnetic field is mainly axial and the electric field has both radial and axial components to launch the beam with a specific amount of transverse velocity. Space-charge forces are minimized to achieve good beam quality by operating the cathode in a regime where cathode temperature controls the amount of current emitted. In traveling from the cathode to the cavity the axial magnetic field amplitude increases to bring the transverse-to-axial velocity ratio to the desired value by adiabatic compression.

In the interaction cavity, the electrons lose 30 to 50% of their total energy, mostly by reduction of transverse velocity due to interaction with the transverse electric field of the resonant cavity mode. The cavity and beam parameters are chosen so that the electrons exit the high-field region of the cavity before they become re-accelerated by the resultant cavity fields.

The millimeter-wave power generated by the interaction passes out the right side of the cavity as a circularly polarized $TE_{22,6}$ mode. The launcher waveguide uses a pattern of small perturbations on its inner surface to convert the operating mode into a quasi-Gaussian mode, which is further shaped and optimized by the three mirrors.

The final mirror sends the beam through the output window. For very high power gyrotrons, a CVD diamond disc is used for the window. This material has the low dielectric loss, high strength, and high thermal conductivity properties that are needed to handle such high power at this frequency.

As the spent electron beam leaves the interaction cavity it enters a region where the dc axial magnetic field decreases in amplitude. This causes adiabatic reduction in the remaining transverse velocity with a corresponding increase in the axial velocity, average radius of the beam, and orbit radius of the electrons. This process reduces the power density of the beam to a point where it can be collected on a water-cooled copper collector.

For lower power gyrotrons, lower order cavity modes and smaller collectors can be used. If the collector power density is small enough, a launcher and mirrors are not required, since the collector can serve as an axially directed waveguide with an output window at the end.

ALTERNATIVE GYROTRON CONFIGURATIONS

The gyrotron oscillator described above is basically a single frequency device. It can be tuned slightly over a frequency range of the order of 1/Q, where Q is the loaded Q of the interaction cavity, typically in the range of 500 to 2000. This slight tuning is best accomplished by increasing the dc magnetic field beyond the optimum

value. The power output will drop approximately linearly to zero as the frequency is tuned.

Alternative gyro-device configurations are shown in Figure 4. On the left is a two-cavity gyro-klystron amplifier. An input signal is coupled into the first cavity through holes in the sidewall. The first cavity is only long enough to allow azimuthal bunching of the electron beam to begin. In the space between the two cavities, the drifting allows the bunching to become tighter. The second cavity is long enough to extract maximum energy from the beam. The gain and the bandwidth of the amplifier can be increased somewhat by adding additional cavities between the input and output cavities. A typical practical bandwith is 1 %.

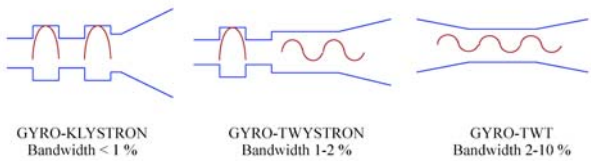

Figure 4: Alternative gyrotron configurations

The configuration on the right is a gyro-TWT (gyro-traveling-wave tube), where the interaction circuit is a waveguide rather than a cavity. For strong interaction the frequency must be close to the cutoff frequency of the mode of interest. Practical bandwidths are in the range of 2-10 %. A useful gyro-TWT must be stabilized by adding waveguide attenuation or loss to avoid oscillation with a waveguide mode traveling in the backward direction.

Another configuration called a gyro-twystron is shown in the center. It has a typical bandwith of 1-2 % by using a cavity for the input and a waveguide for the output. All of these amplifier configurations require a microwave input at a power level typically 30 or 40 db below the output power level.

Another variation (not shown) is called a gyro-BWO (gyro-backward wave oscillator). It uses the interaction that was avoided by introducing loss in the gyro-TWT. It can produce an output that can be tuned in frequency by changing beam voltage. Practical problems are that the output propagates to the left, opposite to the beam, and the efficiency is not as high as with the other configurations. It can produce an output over a 10-20 % frequency range.

GYROTRON POWER SUPPLY AND CONTROL ISSUES

Gyrotrons have power supply and control requirements similar to other microwave vacuum devices, with a few exceptions.

The temperature-limited cathode current has important implications for operating a gyrotron. Rapid changes in beam current are not possible because the thermal time constant for changing cathode temperature is of the order of 30 sec to 1 min.

Rapid changes in the gyrotron output power can be realized by rapid changes in beam voltage. The change in beam voltage directly changes the transverse energy of the electrons.

The axial magnetic field amplitude and axial profile are much more critical for the gyrotron than for linear beam microwave devices. For good performance the magnet current must typically be controlled to one part in 5000. A control system for the 28 GHz, 10 kW gyrotron is described in more detail in [5].

GYROTRON APPLICATIONS

A major application of gyrotrons has been for electron cyclotron resonance heating (ECRH) in fusion energy research. ECRH is one of the predominant methods for heating magnetically confined fusion plasmas. Frequencies have ranged from 28 to 170 GHz, with present state-of-the-art gyrotrons producing continuous wave (CW) power levels up to about 1 MW.

Industrial and scientific applications have included ceramic sintering, ion sources based on ECR, and surface treatment.

Figure 5 shows a 1 MW CW, 110 GHz, CPI gyrotron,

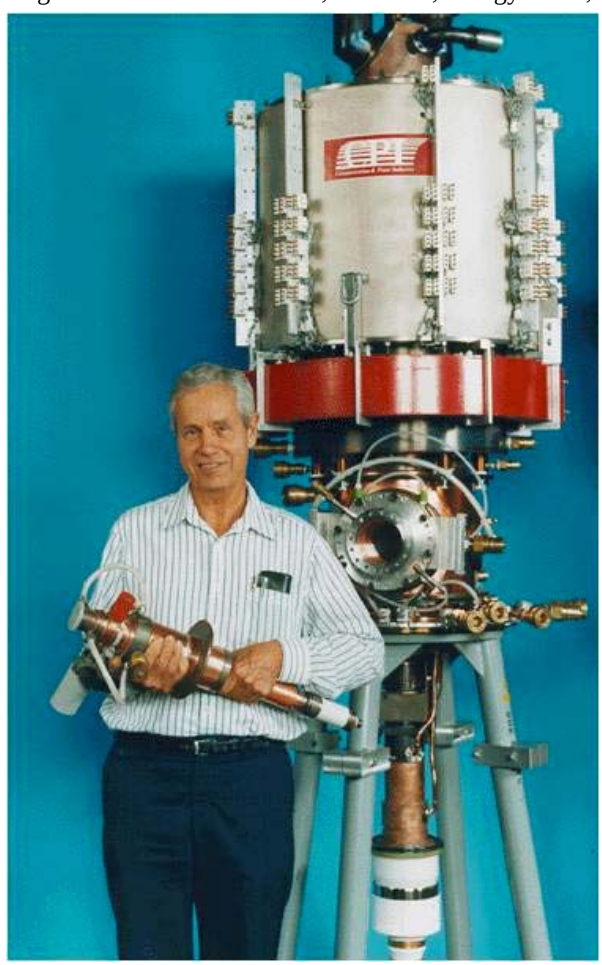

Figure 5: A 1 MW gyrotron and a 10 kW gyrotron

developed for the US Department of Energy for use at the DIII-D Tokamak at General Atomics. A total of six gyrotrons have operated simultaneously to heat the plasma in that system. This gyrotron operates in a superconducting magnet, which is not shown in the picture.

The smaller gyrotron in Figure 5 is a CPI 10 kW CW, 28 GHz gyrotron used in the Venus ion source and other industrial applications. It operates in a room temperature copper magnet (not shown) that requires 5.5 kW of power. In this case, the electron beam interacts with a mode at the second harmonic of the cyclotron frequency, so the required magnetic field is halved, and electrical power required for the magnet is greatly reduced.

Gyro-TWTs and gyro-klystrons have been delivered for use in radar systems. Figure 6 shows a 95 GHz gyro-twystron with a 1.5 GHz bandwidth, installed in its superconducting magnet for electrical testing. The magnet uses a closed-cycle helium refrigerator so the regular addition of liquid helium is not required. The cold head is shown at the bottom left of the picture. Three magnet coils are shown above the main magnet to control the spent beam distribution in the collector.

Another interesting application shown in Figure 7 is the Active Denial System (ADS). This is a military system being tested for use in dispersing hostile groups of people as an alternative to using lethal force. It uses a CPI 95 GHz, 100 kW gyrotron. At 95 GHz the depth of skin penetration is less than 1/64th of an inch, causing a very uncomfortable heating sensation without producing permanent damage.

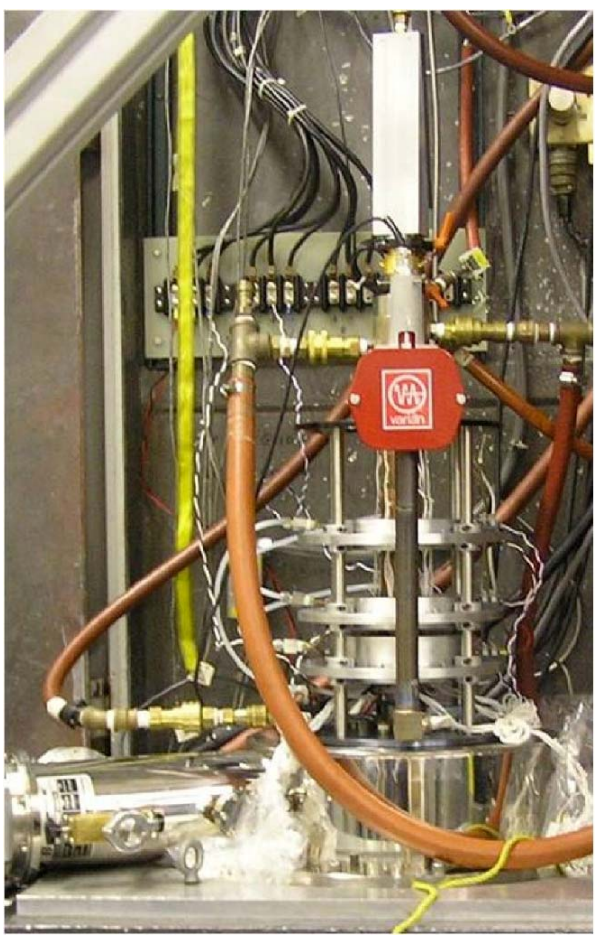

Figure 6: A 95 GHz gyro-twystron installed for testing

Figure 7: ADS system using a 100 kW, 95 GHz gyrotron

CONCLUSIONS

Gyrotrons have proven to be very useful to supply high power in a part of the electromagnetic spectrum where it has not been available from other sources. A number of interesting applications are emerging as a result.

REFERENCES

[1] D. Leitner, C. M. Lyneis, S. R. Abbott, R. D. Dwinell, D. Collins, and M. Leitner, "First Results of the Superconducting ECR Ion Source VENUS with 28 GHz", Proceedings of the 16th International Workshop on ECR Ion Sources, ECRIS'04, Berkeley, CA, September, 2004.

[2] A. V. Gaponov, "Interaction between electron fluxes and electromagnetic waves in waveguides," Izv. VUZ., Radiofizika, vol. 2, pp. 450-462, 1959, and "Addendum," Izv VUZ., Radiofizika, vol. 2, pp. 836-837, 1959.

[3] K. L. Felch, B. G. Danly, H. R. Jory, K. E. Kreischer, W Lawson, B Levush, and R. J. Temkin, "Characteristics and Applications of Fast-Wave Gyrodevices," Proc IEEE, Vol 87, No 5, pp. 752-781, May 1999.

[4] M. Thumm, "State-of-the-Art of High Power Gyro-Devices and Free Electron Masers Update 2007", Forschungszentrum Karlsruhe Technical Report FZKA 7392, March 2008.

[5] M. Marks, S. Evans, H. Jory, D. Holstein, R. Rizzo, P. Beck, B. Cisto, D. Leitner, C.M. Lyneis, D. Collins, R.D. Dwinell, "The 28 GHZ, 10 KW, CW Gyrotron Generator for the Venus ECR ION Source at LBNL", pp. 207–210, Proceedings of the 16th International Workshop on ECR Ion Sources, ECRIS'04, Berkeley, CA, September, 2004.

PAPER NOT RECEIVED

PAPER NOT RECEIVED

NEW CONFIGURATION AND RESULTS WITH THE LPSC CHARGE BREEDER

T. Lamy, J. Angot, C. Fourel, T. Thuillier, LPSC, UJF, CNRS/IN2P3, INPG, Grenoble, France

Abstract

A 1+ thermo ionization source has been used to produce Sodium and Rubidium beams in order to compare the PHOENIX charge breeder capture efficiency for different ion masses but with the same beam optics. Yields of 1.9% for $^{23}Na^{6+}$ and 3.5% for $^{85}Rb^{15+}$, with charge breeding times of 8,6 ms/charge and 4,7 ms/charge respectively, have been measured. 1+ and n+ emittance measurements are presented along with the capture sensitivity to different parameters (DeltaV plots). Technical modifications have been performed to the charge breeder: replacement of the plasma chamber to allow a double frequency operating (14 + 18 GHz), modification of the injection magnetic plug to reinforce the axial magnetic field and correct its dissymmetry in the 1+ beam deceleration zone, insulation improvement to allow 60 kV operation for the SPIRAL2 project. First charge breeding experimental results at 14 and 18 GHz in the new configuration are presented and discussed for Rb beams.

INTRODUCTION

Improvement of ECR charge breeding characteristics (efficiency yield, charge breeding time, emittance) will immediately benefit to the physics performed with accelerated Radioactive Ion Beams (RIB's) allowing higher intensities (and/or brilliance) available to the experiments. There are two ways to reach such improvements: either to increase the 1+ beam capture efficiency, either to use the known methods that improve the intensity and charge state distributions delivered by Electron Cyclotron Resonance Ion Sources (ECRIS). The work presented here is intended to act on both ways.

RUBIDIUM AND SODIUM RESULTS

The experimental setup has already been extensively described [1] and will not be detailed here. A 1+ beam is produced, characterized, and then multi ionized into the charge state breeder, the n+ beam extracted is then characterized too. The three characteristics measured are efficiency, charge breeding time and emittance.

Rubidium

A 20 keV - 80 nA beam is produced with a thermo ionization source and injected into the PHOENIX charge breeder. Figure 1 shows the emittance plots for the $^{85}Rb^{1+}$ (left) and $^{85}Rb^{15+}$ (right) ion beams, on the latter the emittance scan excursion allows to see peripheral beams of higher and lower Q/A beams (Q and A being the charge and the mass of the ions respectively). The emittance values are 2 π.mm.mrad and 13.5 π.mm.mrad for the 1+ and 15+ beams respectively. However, when measuring emittances of different n+ ion beams, we always measure the same value, we suspect wrong entrance and exit angles with the n+ spectrometer. This can be clearly seen on the n+ picture, the emittance of the beams is strongly decreasing for increasing exit angles (yellow lines). With the present exit angle, we think the n+ emittance is overestimated by a factor 2 at least. So, the n+ beam line has to be realigned in order to measure the real emittance of the source.

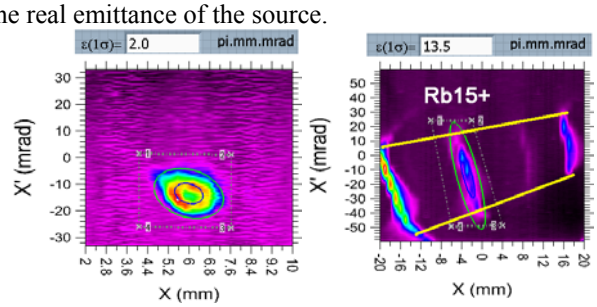

Figure 1: $^{85}Rb^{1+}$ and $^{85}Rb^{15+}$ emittances

Despite this problem, we have measured the transmission of the beam line to be 100% and we can then measure the charge breeding efficiency (1+⟶15+) which is η = 3.6% (result of the same order than in other laboratories, for example: [2], [3]).

The charge breeding time for this efficiency tuning was τ_{cbt} = 70 ms. Such a result has to be compared to ones which where obtained in previous experiments (η =5 %, τ_{cbt} = 225 ms). The charge breeder tuning (RF power, buffer gas flux and magnetic confinement) may give either low efficiency and fast process or higher efficiency but longer charge breeding time. In the context of radioactive ions the tuning will therefore be a compromise depending on the half life of the radioactive decay process.

Sodium

A 20 keV – 170 nA $^{23}Na^{1+}$ beam is produced with the same thermo ionization source as the one used for rubidium production, and injected. The emittance values for the $^{23}Na^{1+}$ injected and the $^{23}Na^{7+}$ produced are 1 π.mm.mrad and 15.6 π.mm.mrad respectively (Figure 2). The efficiency yield was 1.4 % and 1.9 % on the $^{23}Na^{7+}$ and $^{23}Na^{6+}$ respectively, with a charge breeding time of 52 ms for the 6+. In the case of light ions the tuning may be hard to find due to the capture sensitivity to the potential difference between the 1+ and the n+ sources (ΔV). However it seems that the ΔV width decreases for increasing charges, but not the potential value of the highest efficiency (Figure 3).

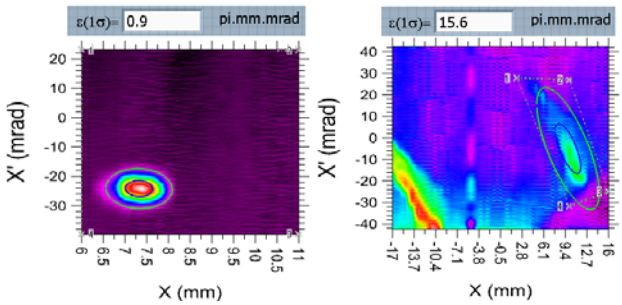

Figure 2: $^{23}Na^{1+}$ and $^{23}Na^{7+}$ emittances

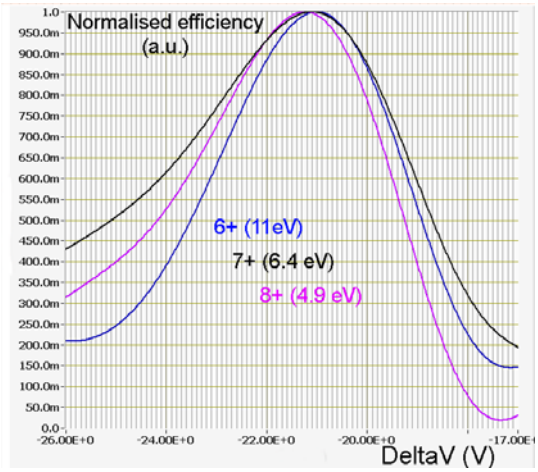

Figure 3: normalized deltaV plots for sodium 6+, 7+ and 8+.

IMPROVEMENT OF THE PHOENIX CHARGE BREEDER

High voltage insulation and rupture strength improvement

The central core (Figure 4) of the charge breeder is composed of a Fe-Nd-B hexapole H and two soft iron magnetic plugs (MPi and MPe) in which is inserted a plasma chamber.

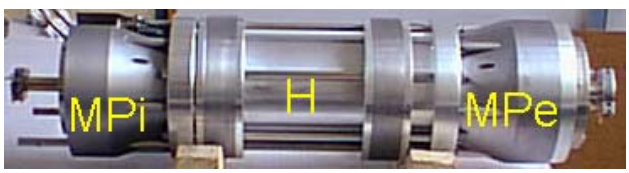

Figure 4: Photo of the central core of the PHOENIX charge breeder

This central core is inserted into a cylindrical insulator (Figure 5) and is maintained at the center of the charge breeder by the means of the blue part on the right and fixed by screws (in black).

For the SPIRAL2 project, this central core can be brought up to 60 kV with respect to the grounded body of the charge breeder (comporting 3 coils and soft iron to generate the axial magnetic field). On Figure 5, the lower part (under the axis) shows the original insulator shape (in green). On the right side the insulating cylinder was inserted into a slot machined in the blue part P. In case of a sudden breakdown of one of the 3 supplies of the coils, the central core undergoes a huge axial force (80 kN), the slot in the part P was inducing a mechanical weakness and the part P could brake. The insulator shape and the part P have been modified as shown on the upper part of the Figure 5, the slot has been suppressed in the part P and the recovering length of the insulator on the grounded body has been increased so the 60 kV insulation is insured and the resistance to tearing increased.

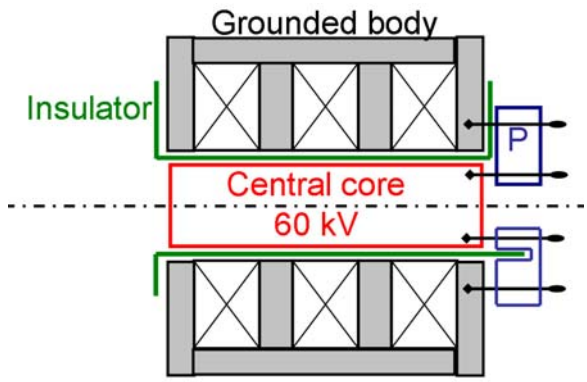

Figure 5: Charge breeder improvement scheme

Double frequency plasma chamber

Three modifications have been performed on the plasma chamber (Figure 6):

- An additional radial RF port has been soldered in order to permit the injection of 14 and 18 GHz microwave frequencies
- Two gas inlets have been added in order to directly inject the gas close to the plasma (in the previous version, it was flowing trough the grounded tube where the 1+ ions are injected)
- The inner diameter has been kept constant all along the chamber in order to be able to insert a liner where the ions will deposit. When working with radioactive ions it will facilitate the maintenance and limit the amount of radioactive wastes.

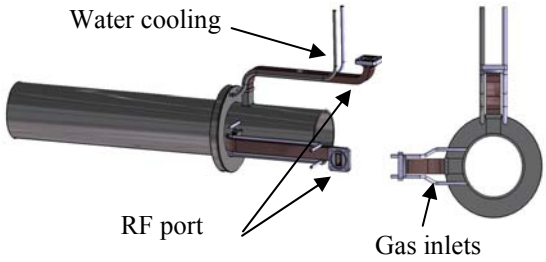

Figure 6: New 14 and 18 GHz plasma chamber

Magnetic field intensity and topology

The magnetic field intensity and topology at the injection side is of first importance for the efficient 1+ ions capture. The magnetic field characteristics are mainly due to a soft iron plug concentrating the flux lines of the injection coil and of the hexapole fringing field. The initial magnetic plug had a slot leaving a lot of spacefor the cooling tubes and the RF wave guide mounted on the plasma chamber. The redesign of this plug has been performed in order to increase the maximum axial induction and to correct the dissymmetry of the magnetic field lines due to the missing iron on the top of the plug. Additional parts have been added, to fill with iron as much empty space as possible (Figure 7).

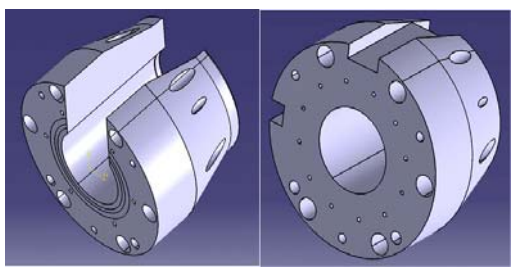

Figure 7: Initial and new magnetic plugs

Magnetic field calculations of the two configurations have been performed with RADIA [4] and Mathematica in 3D including the hexapole, the coils and the iron of the charge breeder. The current of the coils has been fixed to the typical experimental ones when tuned for charge breeding: 1100 A at the injection, 400 A at the middle and 600 A at the extraction side. The iso-B lines obtained for the old and new plugs, on a horizontal plane passing through the axis of the charge breeder, are shown Figure 8. For a better reading, only one half (injection side) of the charge breeder magnetic field calculation result in the plasma chamber is shown. The center of the charge breeder is at the coordinate 0, the grounded tube permitting the injection of the 1+ beam is the black line on the right. These calculations clearly show that the goals of the modifications have been fulfilled, the maximum induction at the injection side is 1.13 T after the modification (1.1 T before) and the dissymmetry of the magnetic flux is corrected. The pink and the red lines are the resonance zones for 14 and 18 GHz respectively.

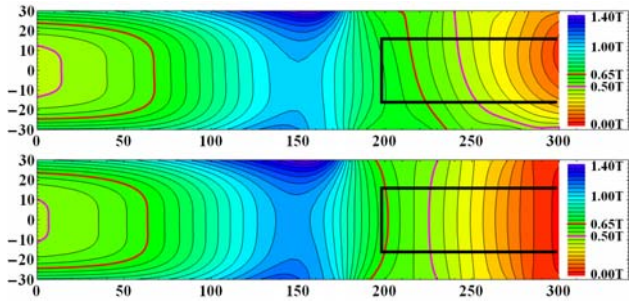

Figure 8: old and new magnetic configurations on the injection side of the charge breeder.

FREQUENCY MIXING EFFECT

In order to evaluate a frequency mixing effect, a first experiment has been performed. The relative variation of the $^{85}Rb^{13+}$ charge breeding efficiency has been measured for different total RF input powers varying the proportion of 14 and 18 Ghz powers. The results are presented Figure 9. The reference point has been chosen to be 400 W of pure 14 GHz injection because it is a rather usual tuning. One can see that the 18 GHz injection permits to improve the efficiency especially at higher powers and that the best effect is obtained for a mixing of 10 % of 14 GHz with 90% of 18 GHz . These preliminary results have to be confirmed, but we can conclude that frequency mixing can help to the charge breeding tuning process.

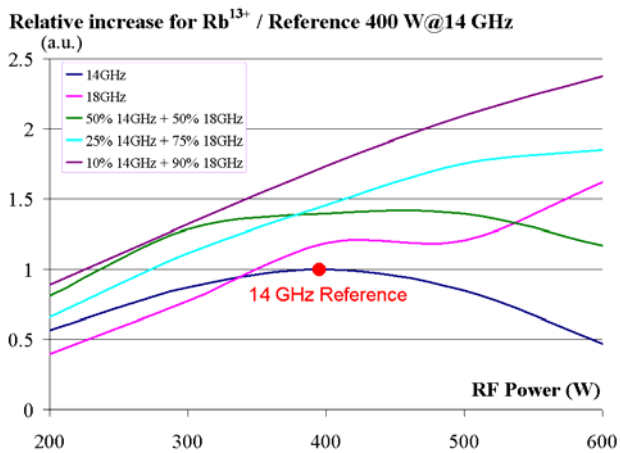

Figure 9: Frequency mixing effect on $^{85}Rb^{13+}$ production efficiency

REFERENCES

[1] T. Lamy, R. Geller, P. Sortais, and T. Thuillier Rev. Sci. Instrum. 77, 03B101 (2006).
[2] F. Ames et al., in these proceedings (WECO-A02)
[3] R. Vondrasek, J.R. Carr, R.C. Pardo, in these proceedings (WECO-A03)
[4] O. Chubar, P. Elleaume and J. Chavanne 1998 J. Synchrotron Rad. **5** 481 – 4 (1998)

PAPER NOT RECEIVED

PAPER NOT RECEIVED

Design of a Charge-Breeder Ion Source for Texas A&M University*

Wayne D. Cornelius, Scientific Solutions, San Diego CA USA†

Abstract

Scientific Solutions designed and fabricated a 14.5 GHz charge-breeder ECR source for the Texas A&M University Cyclotron facility. This charge-breeder source was designed as a charge-breeder from the start rather than as a conversion of an existing ECR system. In addition, the overall system was designed to be modular so that various components can be easily substituted to facilitate technology developments. This paper details the overall design, the design constraints, and reviews specific performance requirements that resulted in this particular system design.

BACKGROUND

The purpose of this project was to provide a test bed for developing technology and techniques specific to charge-breeder electron-cyclotron resonance (ECR) ion sources. Unlike "primary" ECR sources where the unionized elemental feedstock is introduced into the source as neutral atoms, a charge-breeder is designed for injection of short-lived radioactive ions. Because these exotic ions are produced in nuclear reactions, the number of ions is always severely limited. Therefore the overall efficiency of the charge-breeder source is extremely important. The source efficiency is the product of the injection efficiency, the ionization efficiency, the ion extraction efficiency, and the effective dwell time in the source. This project not only created a charge-breeder system for producing the highly charged ion species needed for nuclear physics experiments, but one that could be used as a test bed for testing and developing additional techniques and technologies.

DESIGN RULES

Once the choice of operating frequency is made, the design of the magnetic circuit is the next most important feature. The optimal magnetic field profile of a high charge-state ECR ionizer was determined primarily through trial-and-error over the last ten to fifteen years. [1-4] The preferred field profile has a peak magnetic field at the beam extraction point approximately equal to twice the ECR resonant field, B_{ECR}, (~2.79 GHz/kGauss). The minimum magnetic field should be in the range of $0.8 \cdot B_{ECR}$.[5] The peak magnetic field at the end opposite extraction has been the subject of more discussion.[6] Some argue that $2 \cdot B_{ECR}$ is adequate while others claim improved performance with fields up to $5 \cdot B_{ECR}$. Such high fields are generally obtained by inserting steel plugs into the bore of the solenoid magnet. However it is not possible to reach $3 \cdot B_{ECR}$ or higher without blocking a substantial part of the bore of a conventional copper-coil solenoid magnet. Blocking the bore blocks injection of ions. This conflict represents a major incompatibility between charge-breeders and primary ECR sources.

The bore of the solenoid is the next most important parameter in the overall system design (after the magnetic field profile). The bore should be as large as possible to maximize the diameter of the plasma chamber. However the sextupole magnet surrounding the plasma chamber pushes this critical dimension to values larger than can be excited by room-temperature copper coils when the ID of the plasma chamber exceeds 9 cm. As discussed below, 8" (20 cm) is the largest bore compatible with 14.5 GHz operation, a strong sextupole magnet, and copper coils.

The sextupole magnet plays an extremely important role in the confinement and stabilization of the plasma. To minimize electron loss to the interior walls of the plasma chamber, the sextupole should have a field magnitude of at least $2 \cdot B_{ECR}$ at the interior surface.

We chose a 24-block Halbach ring configuration [7] because this design makes the most efficient use of expensive permanent magnet material and provides the highest magnetic field strength available per unit mass of magnet block. The Halbach configuration rotates the magnetization vector at three times the rotation angle around the cylinder. This rotation effectively cancels the magnetic field outside the cylinder while doubling the interior field strength. The peak field at the inner wall of the plasma chamber of $2.2 \cdot B_{ECR}$. This radial field is significantly stronger than most primary ECR sources and is expected to significantly improve the performance.

Note that the cylindrical Halbach array completely surrounds the plasma chamber and permits no radial access. However a charge-breeder system should not require peripheral components, such as ovens or sample insertion ports. Therefore not having radial access should not be a disadvantage.

The ion injection system is comprised of a pair of electrostatic lenses and the beam extraction system is a relatively conventional "puller" assembly with an added electron trap to prevent electrons from backstreaming into the ion source.

DESIGN FEATURES

This charge-breeder design has a number of features that facilitate maintenance and repair, protect critical components, promote long operational lifetime, and enable technology development. These features include 1) no water-to-vacuum joints, 2) cooling channels between the plasma "cusps" and the sextupole magnet, 3) ample vacuum pumping of interior rf waveguides, 4) modular design with replaceable components, 5) mounting of solenoids and charge-breeder system on ball-bushing rails.

*This material is based upon work supported by the U.S. Department of Energy under Award Number DE-FG02-04ER84166. The views and opinions of authors expressed herein do not necessarily state or reflect those of the United States Government or any agency thereof.

†Current address: SAIC, 10740 Thornmint Road, San Diego CA 92127

SOLENOID MAGNETS

We used the design of the AECR-U solenoid magnets[1] as a starting point for our solenoid design study. These solenoids have demonstrated good performance and have operated reliably for a number of years. During this design study it became clear just how well matched the AECR-U solenoids are to the ECR requirements.

We were unable to increase the bore of these magnets without exceeding current density and steel saturation limits. The steel endwalls of the AECR-U shell are thick enough to keep most of the steel below saturation. However the steel plug is badly saturated with internal fields approaching 32 kGauss. This saturation contributes to a decrease in the efficiency of the excitation coils, requiring more excitation current. Increasing the solenoid bore increases the flux density in the steel plug and exacerbates the coil design problem. These effects resulted in our choice to limit the bore to 8" (20 cm).

A section view of the final solenoid configuration is shown in figure 1. The bore limits the maximum magnetic field to about $2.5 \cdot B_{ECR}$. However, as noted above, this system was designed to facilitate replacement of components. The steel plug could be replaced by one with a smaller bore if the electrostatic injector is replaced with a sextupole ion guide (SPIG).

Figures 2a and 2b compare the measured magnetic fields of the individual solenoids with the theoretical curves and 100 A excitation current. Figure 3 compares the measured field of both solenoids with 50 A excitation current in their final charge-breeder configuration. Although the solenoids were designed to operate with up to 500 Amps of excitation current, The facilities in San Diego limited the power to 2 kW of cooling. Hence the solenoids could be tested up to a maximum of 100 Amps in one solenoid or 50 Amps in two.

Solenoid #1 showed excellent agreement with the predicted magnetic field profile (figure 2a). Initially however, the magnetic field of solenoid #2 was somewhat weaker than expected (open red squares in figure 2b). Further investigation showed that one of the coils was shorted between the lead-in conductors outside the steel shell. Installation of a mylar sheet between the lead-in conductors removed the short and the field profile was exactly as predicted (blue dots in figure 2b). As a result of this discovery, mylar insulation was installed between all of the coil leads to eliminate the potential for shorted coils.

SEXTUPOLE MAGNET

The sextupole magnet is a Halbach array of keystone blocks arranged in a series of six rings with 24 blocks per ring (figure 4). The Halbach configuration results in near cancellation of the magnetic field outside the ring and a near doubling the field strength inside the ring. The magnetic field just inside the inner wall of the plasma chamber is 1.14 Tesla (e.g. $\sim 2.2 \cdot B_{ECR}$). This strong sextupole field provides much improved radial confinement of the plasma compared with the multiple bar arrays typical of primary ECR sources. Note however that the Halbach configuration precludes radial access to the plasma chamber. While this lack of radial access might be a problem with primary ECR sources, it is not expected to be a problem in a charge-breeder because the beam ions are axially injected.

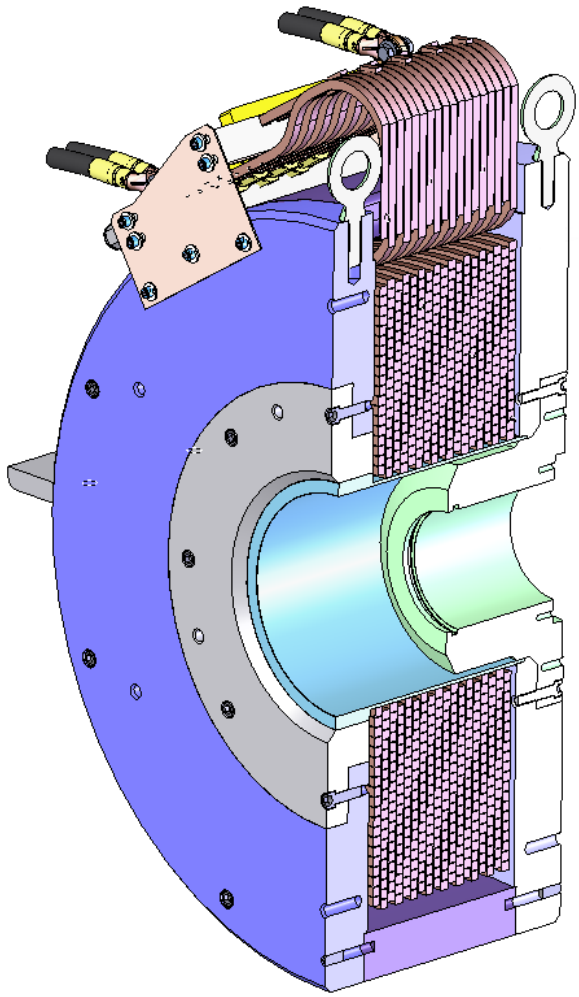

Figure 1. Section view of charge-breeder solenoid.

QA measurements were performed on the sextupole magnet to ensure that all magnet blocks in the assembly were of uniform strength and were oriented correctly so that the magnetic field profile had no significant weak areas that could reduce the plasma confinement efficiency. These measurements were made using a rotating wire loop. The rotation angle was derived from a shaft encoder with 540 steps per 360° rotation. Analysis of the resulting sine wave was used to derive the field components as a function of distance down the bore of the cylinder (figure 5).

The loop voltages showed a consistent pattern of 49 and 51 Hz signals that were coming from an uninterruptable power supply in the neighboring suite. We were unable to completely eliminate these spurious signals. However the

results of these measurements were not particularly sensitive to these relatively high frequency signals. The error bars shown in figure 5 include the effects of the spurious signals.

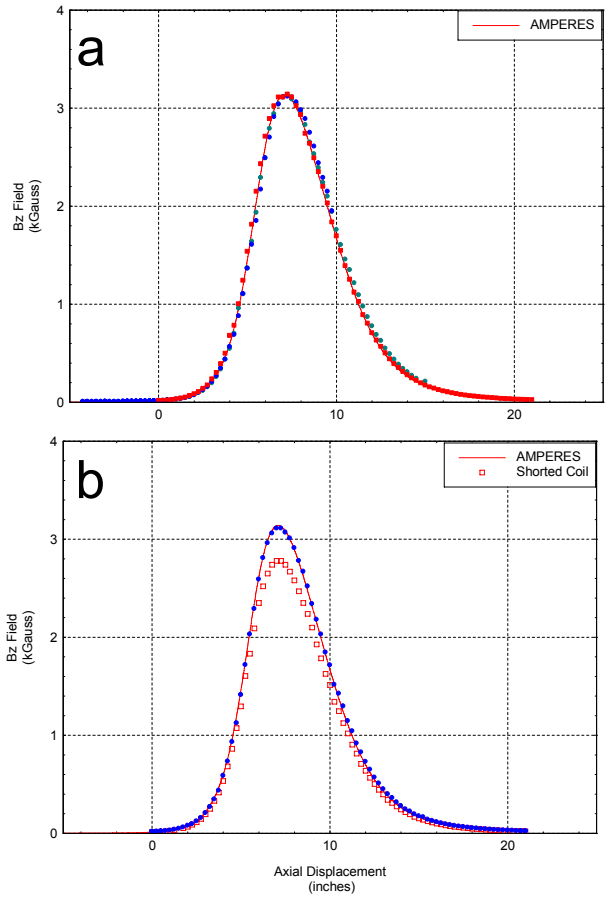

Figure 2. Comparison of the measured magnetic field profile of solenoid #1 (a) and solenoid #2 (b) with the theoretical field profile (red curve) for 100 A excitation current.

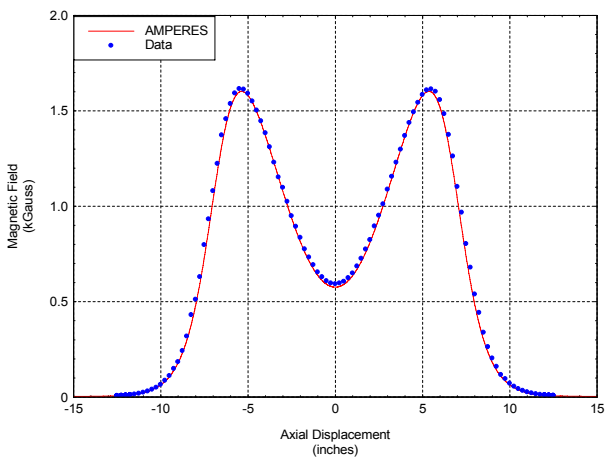

Figure 3. Comparison of the measured magnetic field profile of the charge-breeder solenoids (blue dots) with the theoretical profile (red line) for 50 A of excitation current.

Figure 4. View of partially assembled Halbach sextupole magnet showing the individual magnet blocks.

The data were analyzed using two different methods. The first method fit the waveform with a sine wave and the second computed the FFT of the waveform. The results of both analyses are shown in figure 5. The solid black rectangle indicates the outline of the sextupole magnet. The blue dots plot the magnitude of a sine-wave fit to the data (left-hand axis) and the red squares plot the FFT magnitude (right-hand axis). Note that, except for end effects, these data show relatively uniform field magnitude in the sextupole magnet. Typical accelerator beam applications require quantification of the non-sextupole components of the field. However the non-sextupole components have little effect on the confinement of the plasma and were not derived from the rotating-loop data.

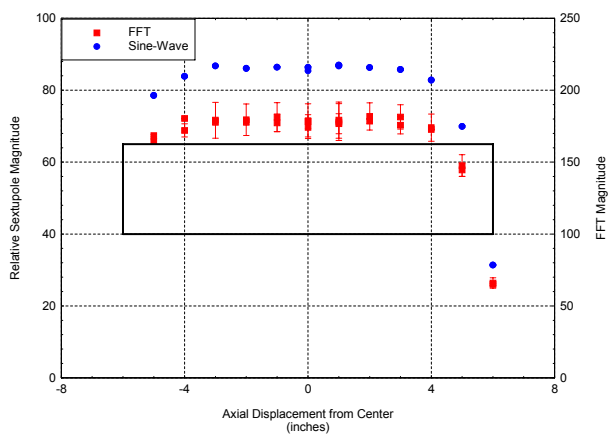

Figure 5. Results from the QA testing of the sextupole magnet. The blue dots plot results from fitting the

waveforms with a sine wave and the red squares plot the FFT magnitude of the waveforms.

The bore and both ends of the sextupole assembly are sealed with 0.025" thick stainless steel. Hence the sextupole is completely encapsulated in a corrosion-resistant shell. This approach allows cooling water to flow in the space between the plasma chamber and the inside of the sextupole shell without wetting the permanent magnet material. Getting cooling into this region is critical. Virtually all ECR sources have damaged their sextupole magnets at one time or another. Our design has "flats" onto the outside of the plasma chamber so that the cooling water can flow between the OD of the plasma chamber and the ID of the sextupole and intercept the heat between its source (the inside wall of the plasma chamber) and the magnet blocks (figure 6). This approach protects the expensive sextupole magnet from the plasma.

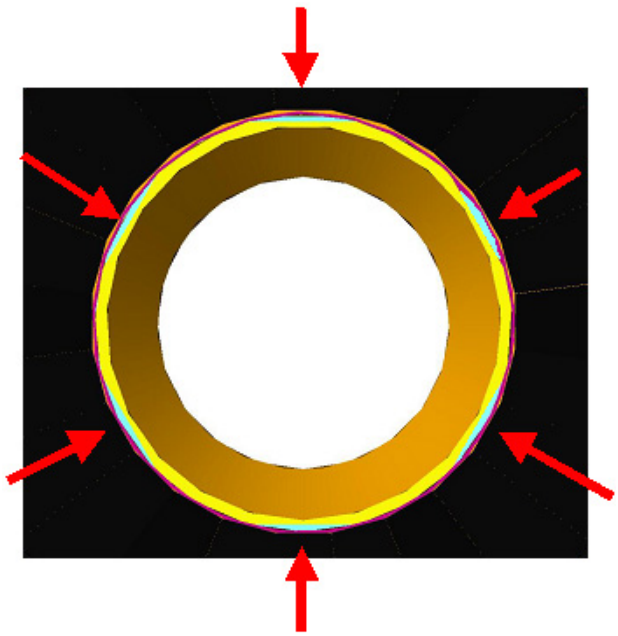

Figure 6. Sectioned view of the sextupole magnet assembly surrounding the plasma chamber. The cooling water (cyan) flows in the space between the "flats" on the OD of the plasma chamber and the ID of the sextupole assembly (red arrows).

PLASMA CHAMBER

A major design goal of this project was to provide flexibility so that the charge-breeder system could be used as a test bed to develop other techniques and technologies. Hence the plasma chamber was designed to be a very simple system that can be easily replaced.

The plasma chamber is made from thick-walled 6061 aluminum tube. The interior of this tube is bored out to produce a 9 cm ID chamber. Six "flats" were cut into the OD of the tube on the periphery of the plasma region (figure 6). As discussed above, cooling water flows in the region between these flats and the ID of the sextupole magnet. The minimum thickness of aluminum in the center of each flat is 1 mm. The pressure differential between the vacuum and the cooling water stresses this region. Stress analysis of the plasma chamber indicates a safety factor of 4.8 times the yield stress.

HIGH VOLTAGE ASSEMBLY

Figure 7 is a section view of the high voltage assembly including the plasma chamber (gold), high voltage insulators (white), and sextupole magnet (cyan shell surrounding the gray magnet blocks). The plasma electrode (also called extraction electrode or beam-formation electrode) is not shown, but mounts to the flange on the ID of the plasma chamber (right-hand end). The injection endwall seats against the ridge on the ID of the plasma tube (left-hand end). The vacuum is sealed by o-rings at each end of the plasma chamber. These circumferential o-rings help to align the plasma chamber with the axis of the solenoids and do not require fasteners to compress them. The cooling water pressure is sealed by a pair of o-rings on the outside surface of the plasma chamber in a separate location. Hence there are no water-to-vacuum o-ring joints in this assembly.

The plasma chamber and sextupole assembly are isolated from ground by a pair of Rexolite [8] insulators (red arrows in figure 7).

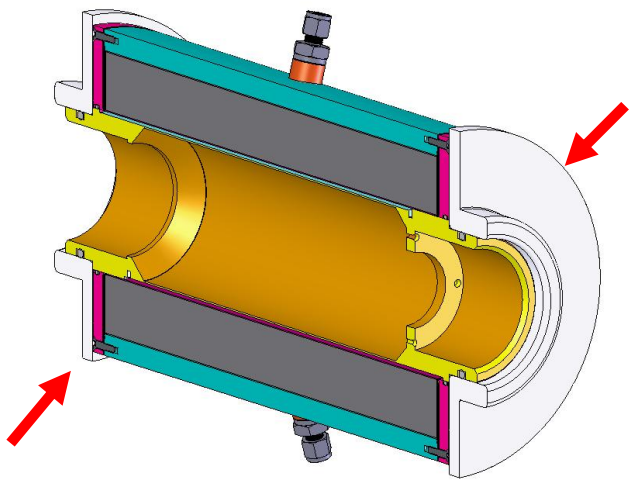

Figure 7. Section view of the high voltage assembly (plasma chamber, sextupole magnet, and high voltage insulators). The HV insulators are indicated by the red arrows.

Figure 8 shows the completed high voltage assembly ready for installation into the solenoid magnets. One of the Rexolite insulators is shown on the near end in the figure. The other is already mounted in the solenoid plug. The vacuum seal is made by o-rings on the ID of the steel solenoid plugs.

One of the solenoid magnets is mounted on rails to facilitate installation of the high voltage assembly. The solenoids are separated by turning a hand crank and the high voltage assembly is inserted between the two

magnets as shown in figure 10. The precision rails ensure that the alignment of the solenoids is preserved during the installation process. Once the high voltage assembly is installed, the separation of the solenoids is reduced by turning the crank. The hand crank provides the "feel" needed to ensure the o-rings are properly seating against the Rexolite. The final separation of the solenoids is locked with three turnbuckle assemblies connecting the inside steel endwalls of the solenoids.

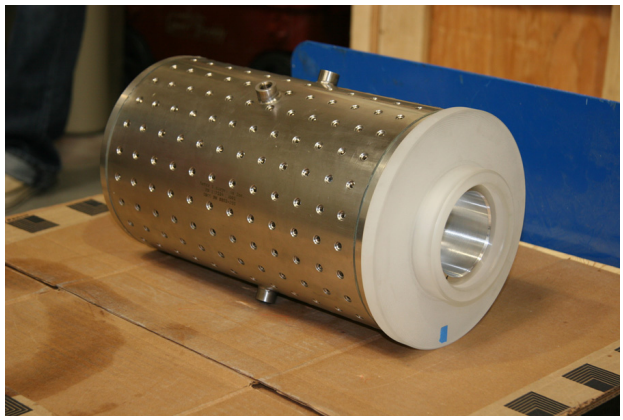

Figure 8. High voltage assembly ready for installation in the solenoid magnets.

Figure 9. Installation of the high voltage assembly in the charge-breeder solenoids.

BEAM EXTRACTOR

Figure 10 is an isometric section view of the extractor end of the charge-breeder. The extractor is a relatively conventional puller assembly with two electrodes attached to the cylindrical ground shield. The first electrode is biased negative with respect to ground to prevent electrons produced by ionization of the residual gas from being accelerated backwards into the ion source. These electrons can cause a variety of operational problems from overloading the high voltage power supply to burning through metal surfaces inside the source.

Note how the extractor assembly can be easily exchanged, substituted, or modified by attaching an alternative assembly to the mounting flange (blue) or by replacing the mounting flange. Additional space is available within the vacuum cross for mounting electrostatic lenses, steering magnets, or diagnostic devices.

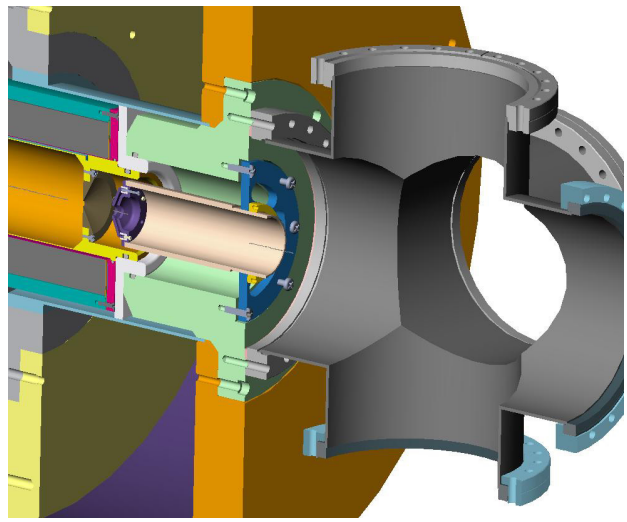

Figure 10. Isometric cross section of the extractor end of the charge-breeder showing the relative locations of the plasma chamber (gold), the plasma aperture (brown), the puller electrodes (violet), the puller mounting flange (blue), a Rexolite insulator (white), the steel solenoid end plug (blue-green), and the vacuum cross (gray). The solenoid coils are not shown.

Figure 11 details the area of the extraction gap. Note the two electrodes on the puller assembly (violet) and their location with respect to the plasma aperture (brown). Note also the vacuum o-rings on the ID and OD of the white Rexolite high voltage insulator and the smaller o-ring on the ID of the magenta sextupole flange. The small o-ring confines the cooling water to the ID of the sextupole magnet so that we have no water-to-vacuum o-ring joints. The extractor assembly is shown in figure 12.

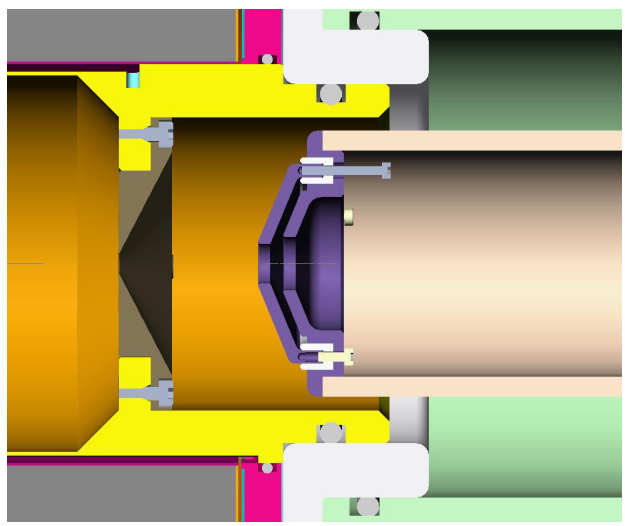

Figure 11. Detail cross section of the extractor end of the charge-breeder showing the relative locations of the plasma chamber (gold), the plasma aperture (brown), the puller electrodes (violet), the Rexolite insulator (white), and the steel solenoid end plug (blue-green)

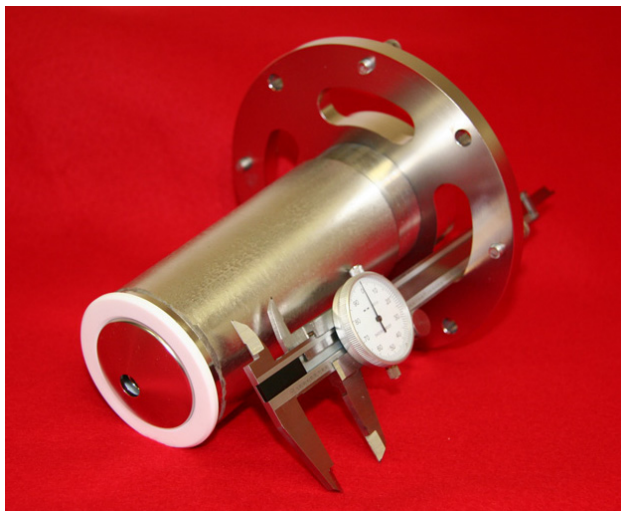

Figure 12. Extractor assembly of the charge-breeder source. The puller electrode is isolated from ground by the white Macor insulator and can be biased up to –2 kV with respect to ground.

BEAM INJECTOR

The injector is one of the more critical components of the charge-breeder system. The final energy of the injected ions needs to be no more than a few eV if these ions are to be effectively stripped of more electrons in the plasma. Too high an energy and the ions pass through the charge-breeder without interacting with the plasma. Too low an energy and the ions are repelled by the floating potential of the plasma chamber. Because the parameters of the effective source of ions (i.e. the helium gas cell) are not yet well characterized, we made the assumption that the emittance of the injected beam would be relatively poor. A design capable of injecting a poor emittance beam should be capable of transporting higher quality emittance beam.

Figure 13 shows results of simulated injection of 10 keV $^{84}Kr^{+}$ ions for a variety of Einzel lens voltages. Each grid square represents 1 cm in radial and longitudinal displacement. The ion trajectories are denoted by the lines originating at the left and continuing to the right. The Einzel lens electrode is denoted by the gray bar at the top of the frame approximately one-third of the way from the left-hand side. A grounded metallic shield is denoted by the horizontal, angled, and horizontal gray shape denoted with 0V. The plasma chamber endwall and bias disk are represented by the gray rectangles at the right-hand end.

Increasing the voltage on the Einzel lens focuses the ions towards the injection aperture. Note however that when the beam ions no longer intercept the ground shield (~7.0 kV), the ions still intercept the plasma endwall. This effect demonstrates that the distance between the Einzel lens and the endwall aperture is too large. Additional aberrations are due to the magnetic field.

These aberrations can be seen by noting how the increasing voltage on the Einzel lens "rolls over" the outside ion trajectories rather than smoothly focusing ions at all radii. These focusing aberrations result from the combination of electric and magnetic fields. Electrostatic focusing of the beam induces a velocity component transverse to the magnetic field. As a result, the beam ions begin to rotate around the flux lines. This rotation reduces the effectiveness of the electrostatic focusing and leads to the aberration evident in figure 13.

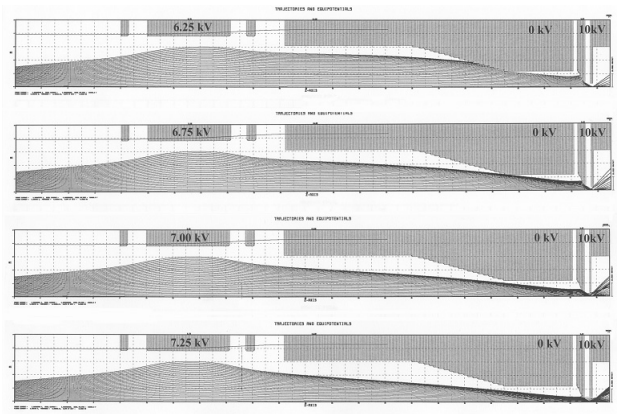

Figure 13. Injected ion trajectories for voltages of 6.25, 6.75, 7.00, and 7.25 kV on the Einzel lens.

Figure 13 demonstrates the need for a second Einzel lens near the injection aperture. An additional benefit of this approach is a reduction in the voltage difference between the injection endwall (at +10 kV) and the second Einzel lens (+2 to +6 kV). Reducing this voltage difference reduces the magnitude of the electric field at the plasma aperture and reduces the ion current extracted from the wrong end of the charge-breeder.

Figure 14 compares $^{84}Kr^{+}$ ion injection with 6.75 kV on the first Einzel lens and a variety of voltages on the second Einzel lens (top to bottom 0, 1, 2, 3, 4, and 5 kV). Note how increasing the voltage on the second Einzel lens improves the injection efficiency. In the last case (5 kV), magnetic focusing of the outside trajectories begins to dump beam ions on the injection aperture (similar to the bottom view in Figure 13). Figure 14 indicates a comfortable range of Einzel lens voltages that result in acceptable ion injection compared with the single lens design in figure 13. The charge-breeder injection scheme utilizes a pair of cylindrical electrostatic lenses to focus the ion beam into the plasma chamber.

Figure 15 shows the first Einzel lens and ground shield of the injector assembly. These components are attached directly to a mounting flange in a manner similar to the extractor electrodes. The ground shield protects the ion beam from the voltages on the components attached to the plasma chamber. Without this shield, the electric fields could disrupt the beam ions by steering and shearing the injected beam. The ground shield is electrically isolated from ground so that ion current impinging on the shield can be measured as a diagnostic tool. The mounting flange has the same pusher/puller alignment screws as the extractor assembly.

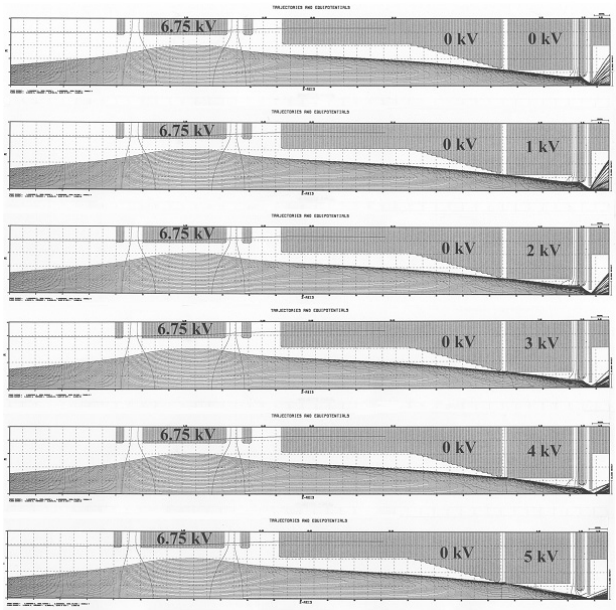

Figure 14. Comparison of $^{84}Kr^{+}$ ion trajectories for a variety of secondary Einzel lens voltages (from top to bottom: 0, 1, 2, 3, 4, and 5 kV).

Figure 15 details the charge-breeder injection system. The components include the WR-75 waveguide, ground shield, two Einzel lenses, plasma chamber endwall. Also shown are the sextupole magnet, Rexolite high voltage insulator, solenoid end plug, and the vacuum cross. The solenoid coils are not shown. Figure 16 details the region around the plasma chamber endwall.

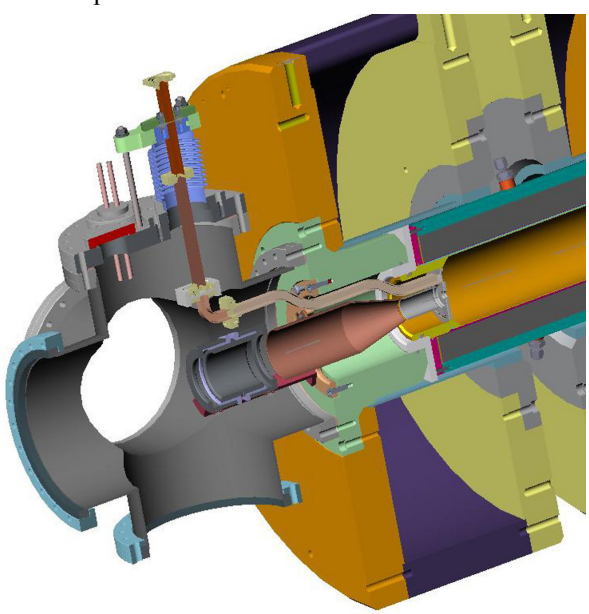

Figure 15. Section view detailing the injection end of the charge-breeder. The solenoid coils are not shown.

Figure 17 shows the plasma endwall sub-assembly. Included in this sub-assembly are the plasma chamber endwall, the WR-75 waveguide, the second Einzel lens, and the gas feed tube. Figure 18 is a close-up of the exterior of the endwall assembly. The second Einzel lens (cylinder) is isolated from the endwall by two ceramic insulators (white). The plasma endwall is water-cooled via the two copper cooling tubes attached to the waveguide and to the plasma endwall. These tubes pass through o-ring seals to the outside so that the system has no water-to-vacuum joints. The wire coming out of the near side in figure 18 (blue arrow) is for connecting the voltage to the bias disk on the inside of the endwall. The gas feed tube can be seen below the cylindrical Einzel lens. The rf spring-ring on the outside diameter of the endwall ensures good electrical contact with the interior surface of the plasma chamber. The slots in the waveguide allow gas atoms to escape from the interior and ensure good vacuum pressure inside the waveguide.

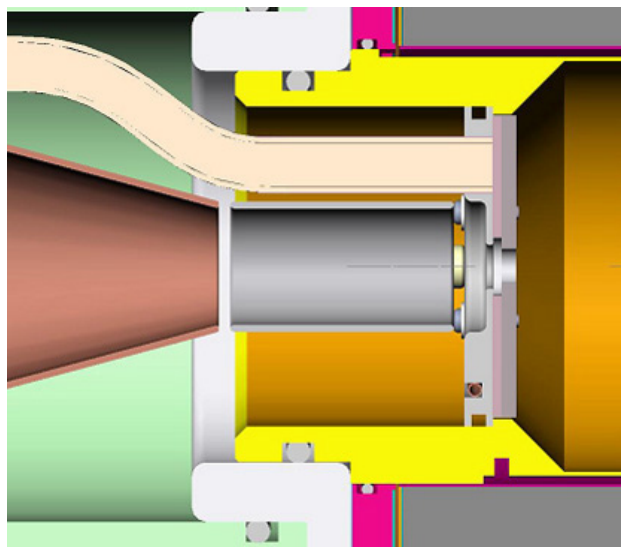

Figure 16. Detail cross section of the plasma endwall, second Einzel lens, ground shield, and WR-75 waveguide.

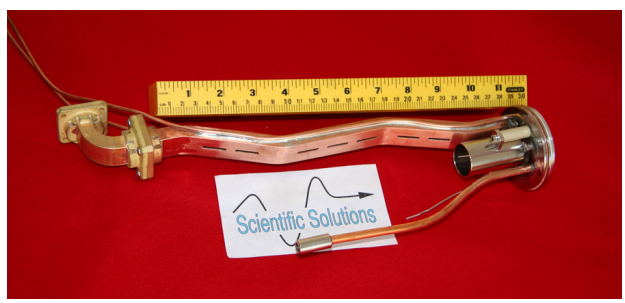

Figure 17. Plasma endwall assembly including the endwall, waveguide, gas feed tube, and second Einzel lens.

Figure 19 details the interior of the plasma endwall. The white ring is a boron-nitride disk that isolates the bias disk from the plasma chamber voltage. The rectangular cutout in the bias disk is for passing the rf energy from the waveguide into the plasma. The injected beam enters the plasma chamber through the hole in the center of the bias disk.

Figure 20 shows the first Einzel lens, mounting flange, and ground shield of the injector assembly. The ground shield protects the ion beam from the voltages on the components attached to the plasma chamber. Without this shield, the electric fields could disrupt the beam ions by steering and shearing the injected beam. The ground shield is electrically isolated from ground so that ion current impinging on the shield can be measured as a diagnostic tool. The mounting flange has the same pusher/puller alignment screws as the extractor assembly. Note that, like the extractor assembly, the injector system can be easily replaced.

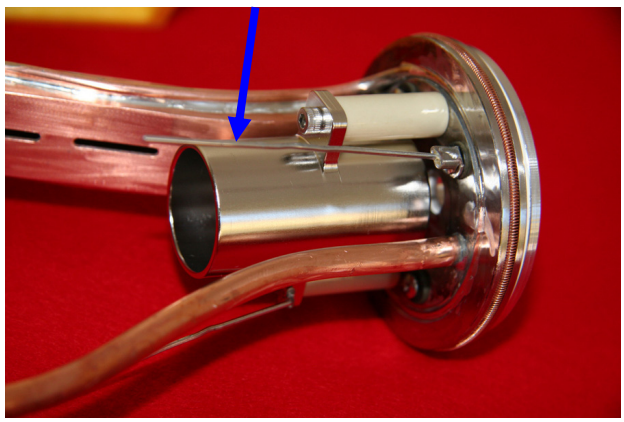

Figure 18. Detail of the plasma endwall assembly. The blue arrow denotes the voltage connection to the bias disk on the inside of the endwall.

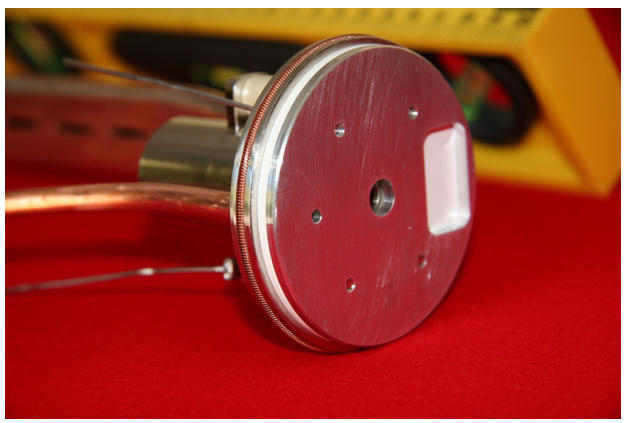

Figure 19. Close-up view of the inside of the plasma chamber endwall showing the bias disk and the white boron-nitride insulator.

Figure 21 shows the exterior of the injector vacuum cross. The white ring on top of the cross is a ceramic insulator that isolates the top flange from ground. All components attached to this top flange float at the voltage of the plasma chamber. The ion gauge is the blue box on the bottom flange. The turbomolecular vacuum pump is attached to the flange on the far side of the cross. The flange on the near side contains the high voltage feedthroughs for the Einzel lenses, a BNC connection to the ground shield, and a dial pressure gauge to indicate the status of the internal pressure when pumping down or venting the charge-breeder. The beam is injected through a hole (yet to be cut) in the blank flange on the near end of the cross.

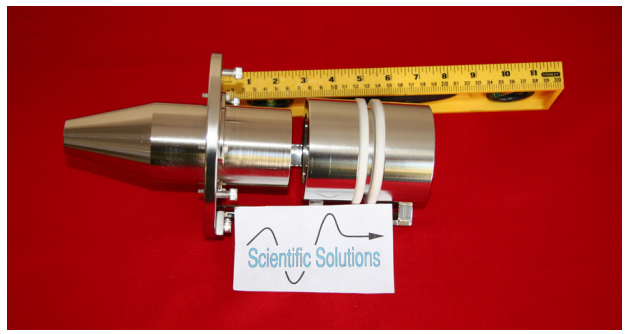

Figure 20. Ground shield (left) and first Einzel lens (right) in the injection line.

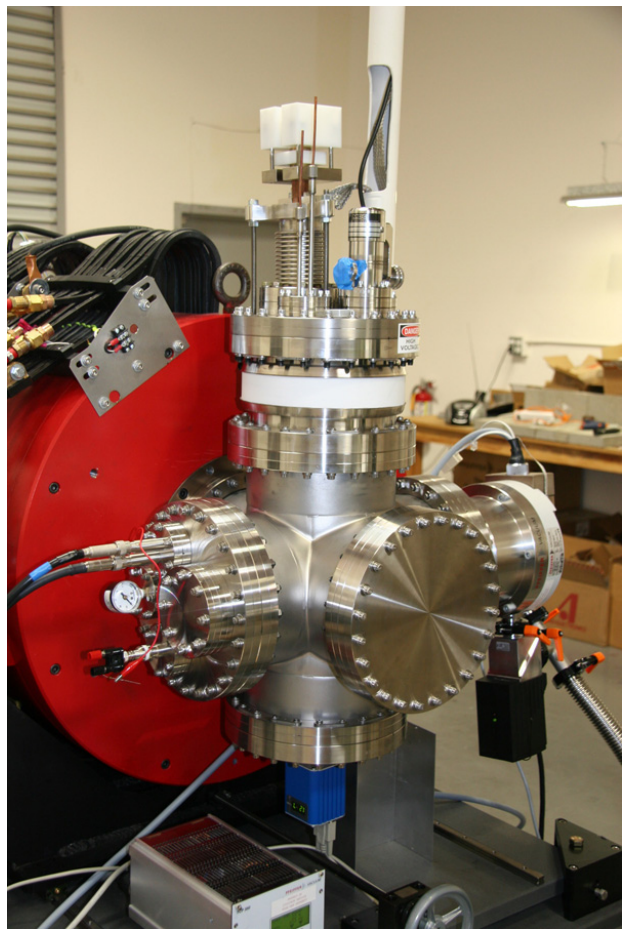

Figure 21. View of the injector vacuum cross.

SUPPORT STAND

The support stand was designed to facilitate maintenance of the charge-breeder. Longitudinal space in accelerator beamlines is precious and removing downstream (or upstream) components to align the charge-breeder by sighting down the bore is undesirable. The support stand was designed to move transverse to the beamline on precision ball-bushing rail assemblies. Hence the charge-breeder can be removed from the beamline for maintenance without affecting the alignment of the charge-breeder or any other component in the beamline. Additionally, the precision nature of the rails ensures that the charge-breeder returns to precisely the same location as before. Hence the charge-breeder can be aligned by bore-sighting along a line parallel to the main beamline and moved into position on the rails without having to realign the system.

The support and alignment structure of the support stand is divided into two sections. The charge-breeder components are aligned on an aluminum tooling plate that serves as a base plate for this assembly. This base plate is "floating" on a separate set of adjustments. The components of the charge-breeder are aligned relative to each other on the base plate and then, once moved into position, the base plate is aligned relative to the axis of the beamline.

SUMMARY

Figure 22 is an overhead view of the charge-breeder from the injector end prior to shipping to Texas A&M University. The large red cylinders are the solenoid magnets. The electronic equipment rack is on the left and is connected to the high voltage platform on the charge-breeder through the white PVC tube. The water chiller for cooling the plasma tube is located just behind the equipment rack. The vacuum control and interlock chassis and the turbopump controllers are located on the temporary table just to the left of the charge-breeder. The rotary vane vacuum pumps are located on the floor just to the right of the charge-breeder. The vacuum pressure stabilized in the high 10^{-8} Torr range prior to disassembly and shipping. The charge-breeder was shipped to Texas A&M University and installed in the target cave at the Cyclotron Institute in late October 2007. Since that time, the baseline vacuum pressure has dropped into the 10^{-9} Torr range.

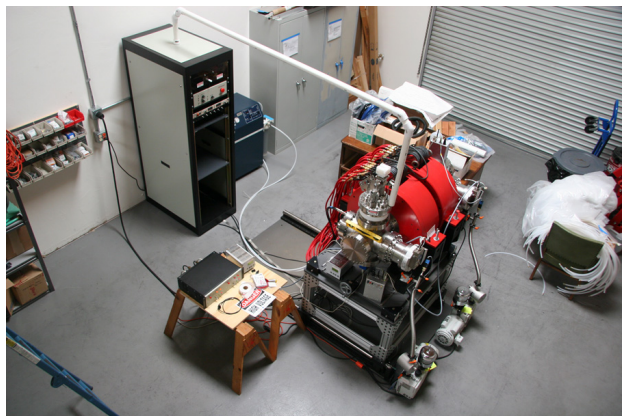

Figure 22. Overhead view of the charge-breeder prior to shipping to TAMU.

REFERENCES

[1] Z. Q. Xie and C. M. Lyneis, Rev. Sci. Instr. **66**(1995)4218

[2] M. Oyaizu, et. al., in Proc 15th International Workshop on ECR Ion Sources, ECRIS'02, June 12-14, 2002, University of Jyvaskyla, Finland

[3] M. Schlapp, et. al., in Proc. 1997 Particle Accelerator Conference, Vancouver BC, p. 2702

[4] J.-L. Bouly, et. al., in Proc. 16th Int. Conf. on Cyclotrons and Their Applications, Lansing MI, 2001, p. 228

[5] Recent data suggests that perhaps this minimum should be pushed even lower, perhaps as low as 0.5 B_{ECR}.

[6] While the relative magnitude of this peak field is subject to some discussion, there is universal agreement that the peak field at this end needs to be greater than the peak field at the extraction end.

[7] K. Halbach, Nucl. Instr. and Meth., **169** (1980), 1.

[8] Rexolite® is a thermoset, rigid, and translucent plastic produced by cross linking polystyrene with divinylbenzene. Rexolite has a combination of good physical and excellent electrical properties including low loss and stable dielectric constant and very low outgassing rate.

We wish to thank D. P. May of Texas A&M, C. M. Lyneis of LBNL, and R. Pardo of ANL for their many discussions, guidance, and reviews of this project.

THE LIGHT ION GUIDE CB-ECRIS PROJECT AT THE TEXAS A&M UNIVERSITY CYCLOTRON INSTITUTE

G. Tabacaru, D. P. May, Cyclotron Institute, Texas A&M University, College Station, 77843 TX, U.S.A.
J. Ärje, JYFL, Jyväskylä, Finland

Abstract

Texas A&M University is currently configuring a scheme for the production of radioactive-ion beams that incorporates a light-ion guide (LIG) coupled with an ECRIS constructed for charge-boosting (CB-ECRIS). This scheme is part of an upgrade to the Cyclotron Institute and is intended to produce radioactive beams suitable for injection into the K500 superconducting cyclotron. The principle of operation is the following: the primary beam interacts with a production target placed in the gas cell. A continuous flow of helium gas maintains a constant pressure of 500 mbar maximum in the cell. Recoils are thermalized in the helium buffer gas and ejected from the cell within the gas flow through a small exit hole. The positively charged recoil ions (1^+) are guided into a 2.43 m long rf-only hexapole and will be transported in this manner on-axis into the CB-ECRIS (Charge Breeding – ECRIS). The CB-ECRIS will operate at 14.5 GHz and has been specially constructed by Scientific Solutions of San Diego, California for charge-boosting [1]. An overall image of the entire project will be presented with details on different construction phases. Specific measurements and results will be presented as well as future developments.

PROJECT OVERVIEW

In 2005 the Cyclotron Institute at Texas A&M University initiated a facility upgrade project [2]. This project will extend the research capabilities as a stable beam facility with moderate rare beam capabilities. This will be achieved by re-activating the 88" Cyclotron to deliver high intensity light-particle and heavy-ion beams, to be used for production of rare isotopes for acceleration in the existing K500 Cyclotron. The plan is to produce radioactive species for re-acceleration by the existing K500 Cyclotron. The main items of the scientific program that drive this project are summarized as: nuclear astrophysics (the extension of the Asymptotic Normalization Coefficients method and study of the (^{3}He,d) reactions), nuclear structure (study of the Giant Monopole Resonances and the cluster structure of the nuclei using the radioactive beams), fundamental interactions and nuclear thermodynamics (multifragmentation). We are expecting also to gain valuable experience in the development of radioactive ion sources and different methods of diagnosis for weak beams.

The project is divided in three tasks: a) recommission of the existing 88" Cyclotron and install new beam lines; b) construct light-ion and heavy-ion guides and produce and transport 1^+ radioactive ions; c) charge boost radioactive ions, transport and accelerate in the K500 Cyclotron. Table 1 presents the new beams intended to be developed using the Light Ion Guide (LIG).

Table 1: Projected beam intensities from the LIG after K500 re-acceleration.

(p,n) reaction Product $T_{1/2}$	**Max Energy** [MeV/A]	**Intensity** [particles/sec]
^{27}Si (4.16s)	57	4×10^4
^{50}Mn (0.28s)	45	1×10^5
^{54}Co (0.19s)	45	4×10^4
^{64}Ga (2.63m)	45	2×10^5
^{92}Tc (4.25m)	35	2×10^5
^{106}In (6.20m)	28	4×10^5
^{108}In (58.0m)	28	2×10^5
^{110}In (4.9h)	26	4×10^5

PRODUCTION OF RADIOACTIVE IONS

The Light-Ion Guide (LIG) will produce radioactive species mainly from (p,n) reactions. The beam (a proton beam around 30 MeV) interacts with a production target (e.g. ^{27}Al) placed in a gas cell. In the gas cell helium gas is flowing continuously at constant pressure of 500 mbar maximum. The recoil ions (e.g. ^{27}Si from ^{27}Al(p,n)^{27}Si)) are trapped in the buffer gas and ejected at a 90° direction (with respect to the beam direction) through a small exit hole [3]. All ions created in the gas cell are collected and transported by a rf-only hexapole: a resonant structure similar to the RFQ in a residual gas analyzer. The large flow of helium gas is evacuated by a differential pumping system. The ions are then injected into a Charge Breeding ECRIS (CB-ECRIS) source which will ionize them to higher charge states. The radioactive species are injected into the K500 Cyclotron and re-accelerated. The primary beam (proton beam) will exit the gas cell and will be stopped in the beam dump. Figure 1 shows an engineering drawing of the LIG coupled with the CB-ECRIS. The main new feature of the device is the rf-only hexapole with a length of 2.43 m. Extensive calculations performed with SIMION [4] software confirm early theoretical approaches [5] where it was shown that all the particles entering the central region of the hexapole should have almost 100 % transport efficiency. The rf-only hexapole is non-selective device, meaning that all ions, singly and possibly doubly charged, as well

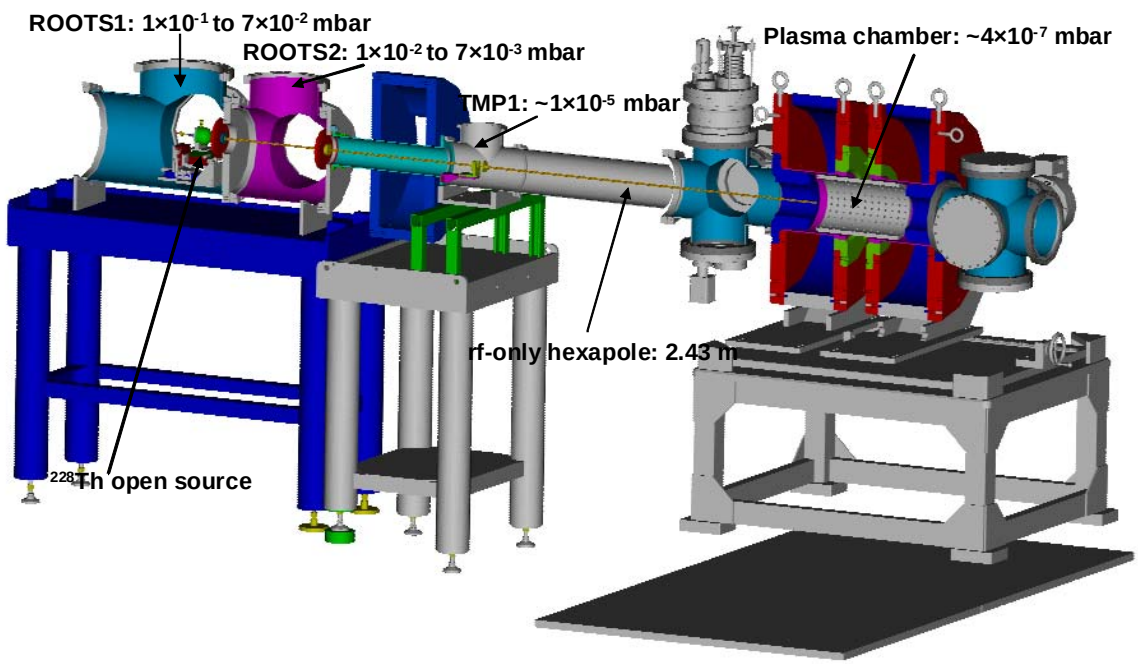

Figure 1: Engineering drawing of the Light Ion Guide coupled with the CB-ECRIS.

molecular ions, are transported with the same efficiency, independent of their mass-to-charge ratio.

DEVELOPMENT OF THE LIGHT ION GUIDE

At the Cyclotron Institute we developed, built and tested a prototype of the Light Ion Guide that will only suffer minor modifications for future operation. The vacuum system consists of two large chambers and a 2 m long beam tube for connection to the CB-ECRIS. The chambers are pumped with ROOTS blowers (2000 m^3/h and 1000 m^3/h pumping speed) and the beam tube is pumped with a turbo molecular pump (520 l/s pumping speed). Two similar turbo pumps are coupled also at the injection and extraction side of CB-ECRIS. Figure 1 indicates the helium pressures in the different sections of the device.

Inside the first vacuum chamber, stands a semispherical gas cell (volume of about 50 cm^3) with an exit orifice: 1 and 2 mm in diameters were used. Between the cell exit and the inlet of the CB-ECRIS plasma chamber is a 2.43 m long rf hexapole divided into three sections: two of 1 m and one of 0.43 m. The hexapole is made from 2 mm brass rods placed on a circle pattern with diameter of 6 mm (equivalent with an interior diameter of the hexapole of 4 mm).

The device was initially developed with ionized gas created by two high-voltage spark electrodes inside the gas cell. We were able to produce a few mA of current, mainly ionized helium and ionized impurities. The transported current (a few nA) was measured at the end of the rf hexapole on a Faraday cup. Figure 2 presents, as an example, a graph of the transported current at the end of the first 1 m long section rf hexapole as a function of the pressure inside the gas cell. The discharge voltage and current were 227 V and about 3.5 mA, respectively. The production of the ions via the spark method has drawbacks: the high voltage needed to ignite the spark accelerates the ions, and at the end of the rf hexapole the ions gain about 180 eV in energy. This energy is too high for the injection into the CB-ECRIS.

In order to eliminate the described feature, and reproduce more closely the future on-line operation, we decided to use an open radioactive source (^{228}Th) as the recoil-ion source. An effort to use a heated alkali source

was unsatisfactory due to the fact that the continuous flow of helium in the gas cell prevents attaining the temperature where the alkali source will start releasing the products.

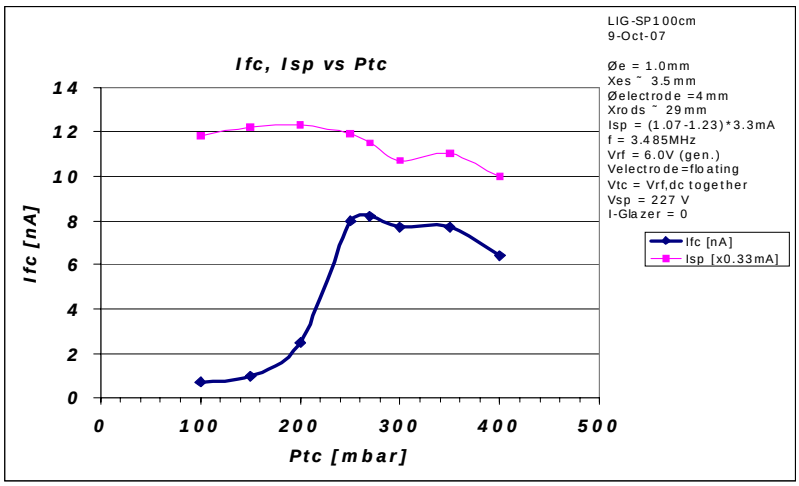

Figure 2: Faraday Cup current (Ifc) vs. the pressure in the gas cell (Ptc).

Inside the gas cell the daughters from ^{228}Th are released continuously and they are thermalized by the helium gas. In order to have maximum stopping efficiency of the radioactive products, a pressure of 30 mbar of helium was used. The daughters are injected into the rf-only hexapole within helium flow by applying a small (approx. 10 - 50 V) acceleration (guiding) voltage between the cell exit and the hexapole inlet. The same voltage will control the injection energy of the recoil ions into CB-ECRIS plasma chamber. In this preliminary experiment the recoil ions were transported to a collector plate (aluminized mylar), placed at the inlet of the CB-ECRIS plasma chamber. The collector plate is backed by a silicon detector. The alpha particles coming from the products pass through the collector plate and are detected with the Silicon detector. The decay series of ^{228}Th include ^{216}Po with a half life of 145 ms. This is an excellent candidate to test our device: the half-life is short enough to provide a reasonable counting rate and is long enough to be charged boosted in the CB-ECRIS. The first tests, without CB-ECRIS plasma, were successful: we were able to measure about 100 alphas/sec coming from the ^{216}Po. We measured also the energy of the ^{216}Po ions, and found that the energy spread is only around 1 eV (see Figure 3). This extra energy will have to be taken into account for stopping the products in the plasma of the CB-ECRIS. The extraction of radioactive highly charged ions will be attempted in future experiments when the CB-ECRIS will be operational.

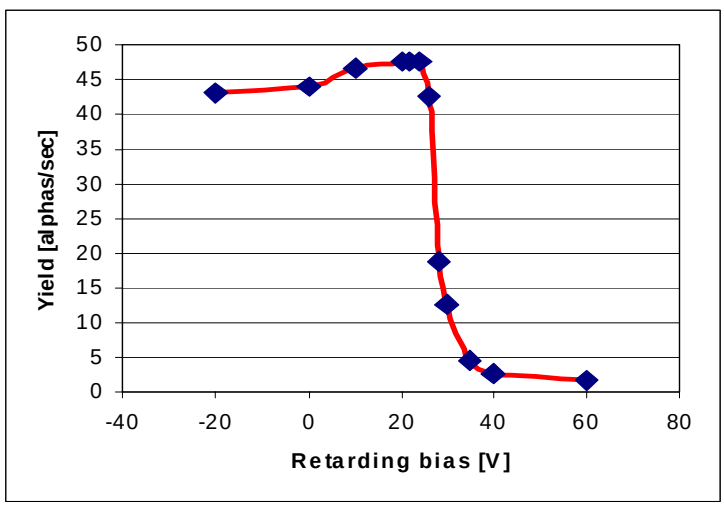

Figure 3: The retarding bias is a measure of the energy of the ions. The radioactive products exhibit an energy of 20-25 eV approximately. The acceleration voltage was 24 V.

FUTURE PLANS

Much further development of this system is necessary before it can produce a usable beam of highly charged radioactive ions with high efficiency for further re-acceleration in the K500 cyclotron. Two major directions should be followed to achieve the proposed efficiencies. The first is to find optimum parameters in the operation of the gas cell in conjunction with the rf-only hexapole. We need to determine the factors that will lead to high efficiency extraction of the radioactive products from the gas cell and high efficiency transport of the products to the CB-ECRIS. The second direction is to determine the ideal conditions for injection and extraction of the highly charged products from the CB-ECRIS with maximum efficiency. In pursuing these two directions the efficiencies of different sections of this system need to be measured along with finally the efficiency of the entire system.

Acknowledgments

The authors would like to thank the staff of the Cyclotron Institute Texas A&M University for the commitment to their work. This work is supported by the U.S. Department of Energy under Grant number DE-FG02-93ER40773.

REFERENCES

[1] W. D. Cornelius, Design of a Charge-Breeder Ion Source for Texas A&M University (these proceedings).
[2] “A proposed facility upgrade for the Texas A&M University Cyclotron Institute”, http://cyclotron.tamu.edu/facility_upgrade.pdf
[3] J. Ärje et al., Nucl. Instr. and Meth. A247, 431 (1986).
[4] SIMION: Industry standard charged particle optics simulation software. http://www.simion.com/
[5] C. Hagg and I. Szabo, Intl. Jour. of Mass Spectrometry and Ion Process, 73 (1986) 295-312.

PAPER NOT RECEIVED

EMITTANCE MEASUREMENTS OF ION BEAMS EXTRACTED FROM HIGH-INTENSITY PERMANENT MAGNET ECR ION SOURCE*

S. Kondrashev#, A. Barcikowski, B. Mustapha, P. N. Ostroumov, ANL, Argonne, IL 60439, U.S.A.
N. Vinogradov, Northern Illinois University, De Kalb, IL 60115, U.S.A.

Abstract

A pepper-pot – scintillator screen system has been developed and used to measure the emittance of DC ion beams extracted from a high-intensity permanent magnet ECR ion source. The system includes a fast beam shutter with a minimum dwell time of 18 ms to reduce the degradation of the CsI(Tl) scintillator by DC ion beam irradiation and a CCD camera with a variable shutter speed in the range of 1 μs to 65 s. On-line emittance measurements are performed by an application code developed on a LabVIEW platform. The sensitivity of the device is sufficient to measure the emittance of DC ion beams with current densities down to about 100 nA/cm^2. The emittance of all ion species extracted from the ECR ion source and post-accelerated to an energy of 75-90 keV/charge have been measured downstream of the LEBT. As the mass-to-charge ratio of ion species increases, the normalized RMS emittances in both transverse phase planes are reduced from 0.5-1.0 π mm·mrad for light ions to 0.05-0.09 π mm·mrad for highly charged ^{209}Bi ions. The dependence of the emittance on ion's mass-to-charge ratio follows very well the dependence expected from beam rotation induced by decreasing ECR axial magnetic field. The measured emittance values can not be explained by only ion beam rotation for all ion species and the contribution to emittance of ion temperature in plasma, non-linear electric fields and non-linear space charge is comparable or even higher than the contribution of ion beam rotation.

INTRODUCTION

During the last few years it became evident that ion beams extracted from ECR ion sources have complicated structure of both spatial and phase space distributions [1]. The ion motion in the horizontal and vertical planes is strongly coupled due to the magnetic field configuration inside the source and extraction region. Slits and Alison type emittance scanners, which were widely used previously, can not provide full information about such distributions. A pepper pot emittance probe is the most suitable device to study 4-D ion beam emittance. Another significant advantage of the pepper pot probe is the very short time of measurements. 4-D emittance data can be obtained in less than 1 s on-line, allowing ECR ion source tuning to minimize the emittance of extracted ion beams. Different scintillators were used previously to measure the emittance of intense ion beams extracted from pulsed ion sources [2, 3]. However, there are almost no data on emittance measurements of DC ion beams with moderate intensities typical for ECR ion sources using a pepper pot coupled to a scintillator probe. The main challenge is the choice of the viewing screen to provide high sensitivity, long life time, linearity and wide dynamic range of measurements. In most cases these parameters are un-known or not well known.

Our first tests of a pepper pot coupled to a CsI (Tl) crystal [4] show that the sensitivity of the probe is high enough to measure emittance of DC ion beams with energy 75 keV per charge state for a variety of ion species from protons to heavy ions with current densities even below 1 μA/cm^2. The simple COHU 2600 [www.cohu.com] monochrome CCD camera with shutter speed 60 frames per second has been used in these measurements. It is obvious that the sensitivity can be significantly enhanced using a CCD camera with longer integration time and higher gain. In this paper we describe recent developments of the pepper pot emittance probe based on a CsI (Tl) scintillator. A fast in-vacuum shutter with a minimum dwell time of 18 ms was employed to reduce the scintillator degradation by DC ion beam irradiation. A PC connected IMI TECH IMB-147FT 12-bit Firewire Monochrome [www.imi-tech.com] digital CCD camera with shutter speed variable in the range of 1 μs to 65 s and adjustable gain was used to acquire and save pepper pot images. On-line emittance measurements were performed by an application code developed on LabVIEW [www.ni.com] platform. The linearity of the emittance meter was studied. The emittance meter was used to measure the emittances of all ion species extracted from the high intensity permanent magnet ECR ion source.

EXPERIMENTAL SETUP

The structure of the pepper pot emittance meter is shown in Fig. 1.

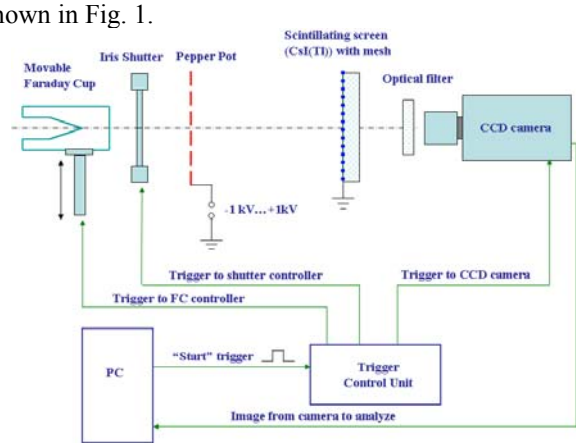

Figure 1: Emittance meter structure.

*This work was supported by the U.S. Department of Energy, Office of Nuclear Physics, under Contract No. DE-AC02-06CH11357.
#kondrashev@anl.gov

It includes a movable Faraday cup (FC) equipped with negative voltage suppression ring. The FC is shielded from secondary particles by outer grounded cylinder. The diameter of FC input aperture is 46 mm. The FC was driven by a compressed air cylinder. The time required to insert or remove the cup is about 1 s. The FC was used both as a detector of ion beam current at the input of the emittance meter and as a slow shutter to protect the normally closed iris-type fast shutter from long time irradiation by the DC ion beam with a maximum power of about 10 W. The normally closed iris-type UNIBLITZ-CS65S fast shutter with aperture 65 mm has an adjustable dwell time of a minimum of 18 ms and serves to protect the CsI (Tl) scintillator screen from possible degradation caused by DC ion beam irradiation. The tantalum pepper pot plate with diameter 70 mm and thickness 380 μm has an aperture array over the whole area with holes 100 μm diameter and 3 mm spacing. Optical certification has shown that diameters of all 415 holes were within 100 – 104 μm range. The pepper pot plate was isolated from ground and its potential can be varied in the range of ±1 kV to study the effect of secondary electrons on the emittance of ion beam. A CsI (Tl) scintillator screen with diameter of 80 mm and thickness of 3 mm is placed at a distance of 100 mm downstream of the pepper pot plate. A grounded fine Nickel mesh with transparency 88.6% and cell size of 200 μm was attached to the crystal surface irradiated by ions to prevent charge build-up caused by ion beam. The CCD camera connected to a PC was used to acquire and save pepper pot images. Fig. 2 shows the time diagram of the FC, fast shutter and CCD camera triggering. The time structure of the fast shutter opening and closing is shown in Fig. 2 as well. The scintillator screen pre-irradiation time (time between beginning of DC ion beam screen irradiation and pepper pot image acquiring) can be varied up to 1.4 s.

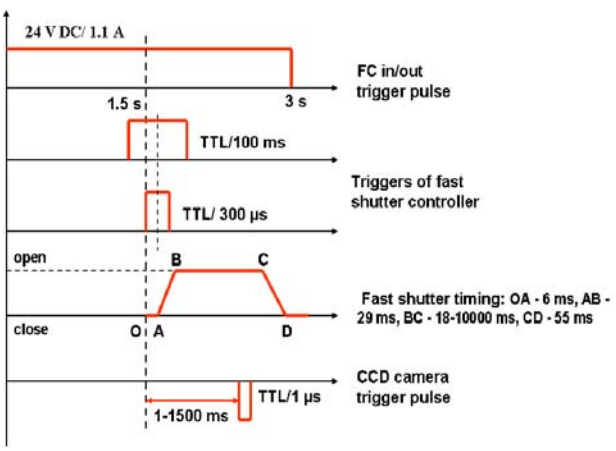

Figure 2: Emittance meter timing.

The operational cycle of the device consists of few steps. First, the Faraday Cup moves from the beamline axis to allow the beam to the closed iris of the fast shutter. Next, the shutter controller opens the iris for 100 msec to expose the scintillator to the beamlets from the PP plate. The image produced by the array of active beamlets on the crystal is acquired by CCD camera and sent to the control PC for analysis. The cycle is completed by closing the fast shutter iris and returning the Faraday Cup back into the beam line. The overall cycle period is about 3 seconds and restricted by the time delay for moving the massive FC body. The actual time of acquiring the beam signal is defined by the camera settings (66 ms for most measurements).

The results on emittance probe linearity and influence of pepper pot potential and scintillator pre-irradiation time on emittance measurements are presented in the paper "Development of a novel emittance probe and its application for ECR ion beam studies" submitted to Nuclear Instruments and Methods.

The emittance probe was used to measure the emittance of ion beams extracted from a high-intensity permanent magnet ECR ion source. The probe was placed at the end of the injector shown in Fig. 3.

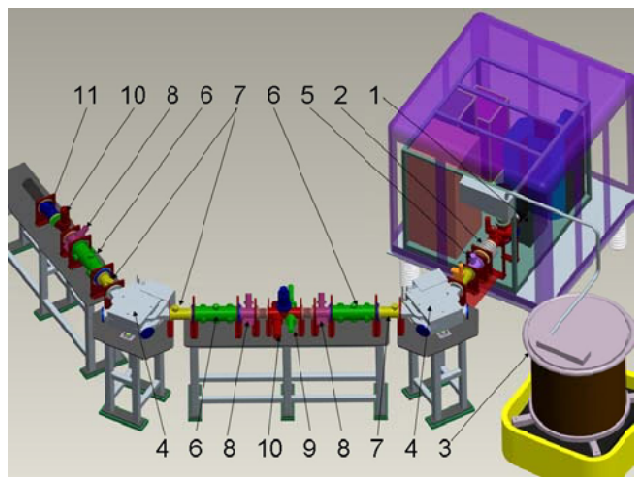

Figure 3: General view of the injector. 1- All permanent magnet ECRIS installed on HV platform, 2- 75-kV accelerating tube, 3- isolation transformer, 4- 60° bending magnet, 5- Einzel lens, 6- electrostatic triplet, 7- electrostatic steering plates, 8- rotating wire scanner, 9- horizontal slits, 10- Faraday cups, 11- emittance probe.

The injector consists of an ECR ion source, a 100-kV platform and an achromatic LEBT system based on two 60° bending magnets. The ECR ion source is built using all permanent magnets and it is described in more detail elsewhere [5]. The main parameters of the source are listed below:

- Axial peak field (injection region) – 13 kG
- Axial field at extraction – 6.6 kG
- Axial central magnetic field – 4.2 kG
- Maximum radial field (at chamber wall) – 11 kG
- Aluminum plasma chamber: length – 17.5 cm, diameter – 6.4 cm
- Extraction aperture – 8 mm
- Heating: 2 kW/14 GHz klystron + 700 W/12.75-14.5 GHz TWT RF amplifier
- Extraction potential – up to 25 kV

- HV platform potential – up to 75 kV

The high voltage (HV) platform accelerates all ion species extracted from the ECR source to higher energy to reduce the influence of space charge effects in the LEBT. Ion beam focusing along the LEBT is provided by electrostatic Einzel lenses and quadrupole triplets. Rotating wires are used for beam profile measurements and ion beam alignment. The injector allows us to accelerate all ion species up to q×100 keV total kinetic energy, where q is the charge state of the ion.

Our injector differs from any other ECR source on HV platform currently used in various applications worldwide. Specifically, we extract all ion species available from the ECR source and analyze them after acceleration by the platform potential. A bismuth ion beam was produced using an oven heated to about 550°C. The ECR is equipped with two RF amplifiers set to 12.8 GHz and 13.8 GHz with total available RF power up to 2.7 kW. Oxygen is used as a support gas to enhance the intensity of higher charge states of ^{209}Bi ions.

CURRENTS OF DIFFERENT ION SPECIES

For all the measurements described below the bismuth ion beam is first extracted by applying a 15 kV source potential and then accelerated by a 60 kV platform potential. To analyze the beam, a 36 mm aperture Faraday cup (FC1) equipped with a suppression ring is installed downstream of the first 60° magnet to record the beam current. After few days of source conditioning and tuning, we were able to obtain stable ion beam. Figs. 4 and 5 shows the currents of all ion species extracted from the source and zoomed currents of bismuth ions with different charge states respectively.

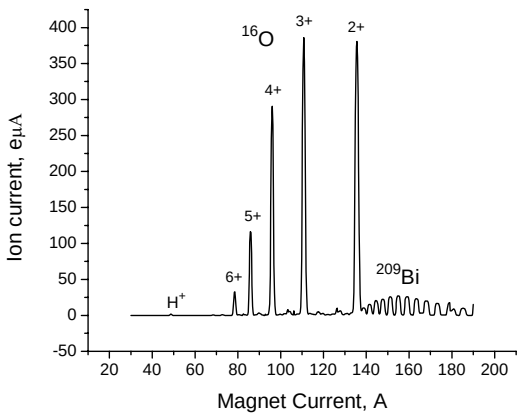

Figure 4: Currents of all ion species measured downstream the first bending magnet.

The currents of all ion species extracted from the source and measured downstream from the first magnet are summarized in Table I.

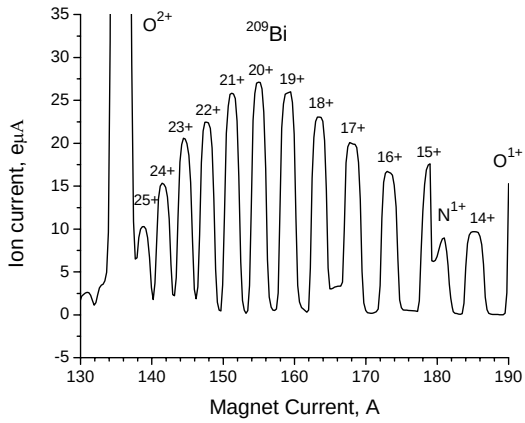

Figure 5: Currents of bismuth ions measured downstream the first bending magnet.

The sum of all currents in Table I is equal to 1.8 mA (current of O^{1+} ions is supposed to be 370 μA according to tendency of oxygen ions distribution). The total ion current extracted from the source is equal to 3.8 mA. It means that the total transmission from the source exit to FC1 can be estimated to be about 47%. Transmissions from FC1 to FC2 for all ion species extracted are shown in Fig. 6.

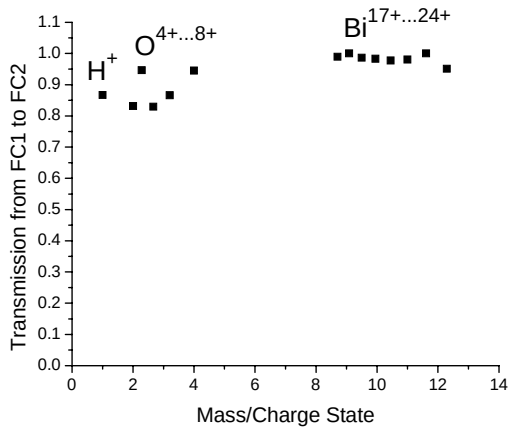

Figure 6: Transmission from FC1 to FC2 for different ion species.

FC2 is installed downstream of the second 60° magnet in front of the emittance probe. Using these data, the total transmission from the source exit to the emittance probe can be estimated to be in the range of 40 – 47% for all ion species. All the results of emittance measurements presented and discussed in this paper were obtained for these transmitted fractions of ions.

Table I: Currents of all ion species measured downstream the first bending magnet

El.	Hydrogen		Oxygen						Bismuth											
Ion	1+	2+	7+	6+	5+	4+	3+	2+	25+	24+	23+	22+	21+	20+	19+	18+	17+	16+	15+	14+
I, μA	2	0.6	1.0	32	118	292	387	378	10	15	21	23	26	27	26	23	20	17	12	10

EMITTANCE MEASUREMENTS FOR DIFFERENT ION SPECIES

The emittance was measured for all ion species listed in Table I. The following procedure was implemented for all ion species before each measurement:

- Beam was centered along LEBT by adjusting both bending magnets
- Slits were scanned to measure the spatial distribution of different ion species
- Slits were set to select a single ion specie.

An example of slit scan for Bi ions with charge states 22+ -24+ is presented in Fig. 7.

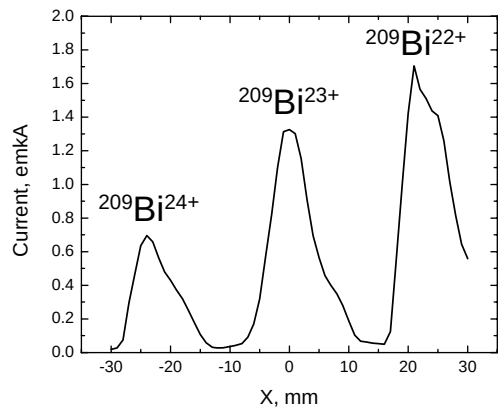

Figure 7: Slit scan for Bi ions with charge states 22+ -24+.

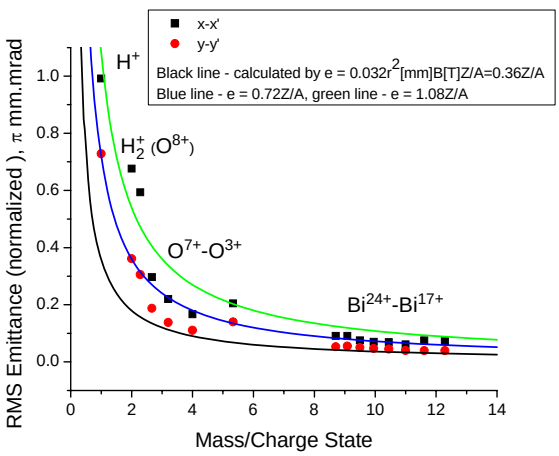

Figure 8: Dependences of normalized x-x' and y-y' rms emittance on mass to charge state ratio for all ion species extracted from the source.

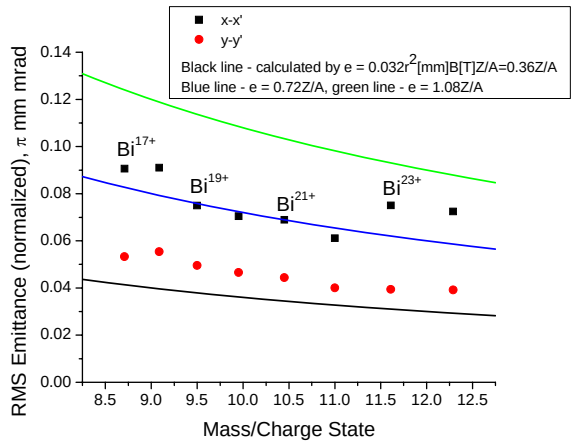

Figure 9: Enlarged fragment for highly charged Bi ions.

One can see that spatial resolution is good enough to select the single charge state (23+ in this case) by adjusting slit positions. The spatial resolution was better than the one shown in Fig. 7 for all other ion species extracted from the source. Each ion specie was easily separated from all others for emittance measurements.

The dependence of the normalized x-x' and y-y' rms emittances on the mass-to-charge ratio is presented in Fig. 8 for all ion species extracted from the source. An enlarged fragment of this dependence for highly charged Bi ions is shown in Fig. 9. Taking into account the transmission from source exit to the emittance meter estimated above, emittance of 40 – 48% of each ion species extracted from the source was measured. The black line in Fig. 8 shows the expected emittance dependence under the assumption that emittance is fully defined by beam rotation induced by the decreasing ion source magnetic field [7]. The blue and green lines are the results of multiplication of this dependence by factor 2 and 3. One can see that emittance decreases significantly with increasing ion mass or with decreasing ion charge state. The experimental dependence of emittance vs mass-to-charge state follows very well the dependence defined by beam rotation only. One can conclude that ion beam rotation has very strong influence on the emittance of ion beams extracted from ECR ion sources. But, the measured emittances are 2 – 3 times higher than predicted by ion beam rotation. The contributions to the emittance of ion temperature in plasma, non-linear electric fields and non-linear space charge are comparable or even higher than the contribution of ion beam rotation. The measured x-x' emittances are always higher than y-y' emittances for all ion species extracted from the source. This can be explained by both higher x-x' acceptance of the first bending magnet and asymmetric ion beam distribution at ECR exit.

DEPENDENCE OF EMITTANCE ON BIASED DISC POTENTIAL

The influence of biased disc potential on the emittance was studied for the Bi^{20+} ion beam. The dependences of emittance on biased disc potential are presented in Fig. 10.

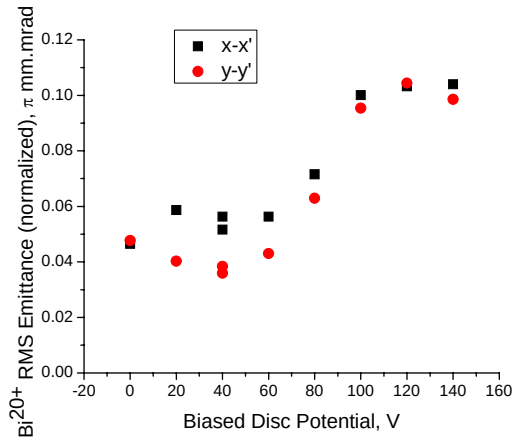

Figure 10: Dependences of Bi^{20+} ion beam emittance on biased disc potential.

The dependences of Bi^{20+} ion beam current at the entrance of emittance meter and total current extracted from the source on the biased disc potential are shown in Fig. 11. All values for biased disc potential equal to -40 V were measured twice: in the beginning and in the end of measuring cycle. The emittance is minimal and Bi^{20+} ion beam current is maximal for biased disc potential equal to -40 V. It means that the brightness of Bi^{20+} ion beam is well peaked for -40 V biased disc potential. The ratio of x-x' and y-y' emittance values depends on the biased disc potential as well.

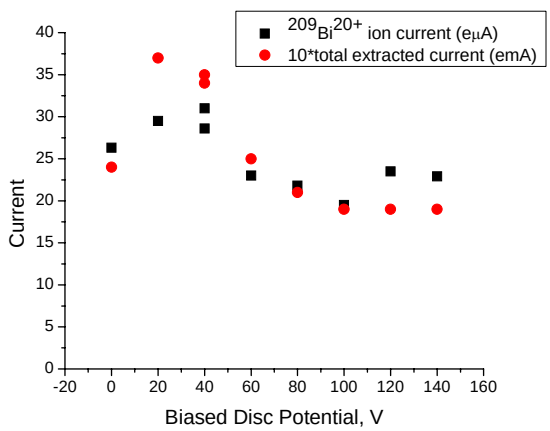

Figure 11: Dependences of Bi^{20+} ion beam at the entrance of emittance meter and total current extracted from the source on biased disc potential.

CONCLUSION

A 4D emittance meter based on pepper pot - scintillator screen was developed for on-line measurements and used to study the emittance of DC ion beams extracted from an ECR ion source.

The emittance was measured for about 40 – 48% of each ion species extracted from ECR ion source and it was found that:

- Dependence of emittance on ion mass over charge state ratio qualitatively follows very well the dependence due to beam rotation induced by decreasing ECR axial magnetic field
- Measured emittance values can not be explained by only ion beam rotation for all ion species and contributions to emittance of ion temperature in plasma, non-linear electric fields and non-linear space charge are comparable or even higher than the contribution of ion beam rotation
- Emittance increases with increasing of charge state for both oxygen and bismuth ions
- Emittance and brightness can be optimized by biased disc potential

ACKNOWELEDGEMENT

This work was supported by the U.S. Department of Energy, Office of Nuclear Physics, under Contract No. DE-AC02-06CH11357.

The authors are grateful to R. H. Scott for his help with the ECR ion source operation, to M. Anthony, P. Wilt and S. I. Sharamentov for their electronics support, and to A. Pikin for discussions about the pepper-pot technique.

REFERENCES

[1] P. Spadtke, K. Tinschert, R. Lang, J. Mader, J. Robbach, J. W. Stetson and L. Celona, Rev. Sci. Instr. 79, 02B716 (2008).

[2] R. Scrivens, Extraction of an Ion Beam from a Laser Ion Source, Ph.D. thesis, Physics Department, University of Wales Swansea, May 1999.

[3] A. Sidorov, M. Dorf, V. Zorin, A. Bokhanov, I. Izotov, S. Razin, V. Skalyga, J. Roßbach, P. Spädtke, and A. Balabaev, Rev. Sci. Instr. 79, 02A313 (2008).

[4] S. Kondrashev, A. Barsikowski, P. Ostroumov, R. Scott, S. Sharamentov. N. Vinogradov, Experimental results on multi-charge-state LEBT approach. Proceedings of PAC 2007, pp. 1658-1660, Albuquerque, U.S.A., 2007.

[5] D. Z. Xie, Rev. Sci. Instr., 73(2), 2002, p.531.

[6] A. Pikin, A. Kponou, J. Ritter, V. Zajic, Pepper pot emittance meter, BNL note C-A/AP/#244, July 2006.

[7] D. Leitner, C. M. Lyneis, S. R. Abbott, D. Collins, R. D. Dwinell, M. L. Galloway, M. Leitner and D. S. Todd, Nucl. Instr. And Meth. In Phys. Res. B, **235** (2005) 486–493

COMPARISON BETWEEN AN ALLISON SCANNER AND THE KVI-4D EMITTANCE METER*

H. R. Kremers#, J. P. M. Beijers, S. Brandenburg, S. Saminathan, V. Mironov, Kernfysisch Versneller Instituut, University of Groningen , Groningen, the Netherlands
T. Thuillier, LPSC, CNRS/IN2P3, UJF, INPG, Grenoble, France.

INTRODUCTION

The demand for intense highly-charged ion beams at the AGOR facility has triggered a study to improve the beam-line transport efficiency. In the framework of this study an emittance meter (KVI-4D) to measure the 4D phase-space of a beam has been developed. The device is also intended for use at GSI with the MS-ECRIS, which is being built in the framework of the EURONS-ISIBHI project.

The demand for intense beams is pushing the development of ECR ion sources to areas where the formation of ion beams in the extraction region is affected by the strong fringe field of the solenoids and extracted intense beams are influenced by space charge effects. With the KVI-4D emittance meter we hope to gain more understanding of beam formation and transport and thus to improve overall efficiency.

In the following we will describe the design and the main parameters characterizing the instrument. Measurements will be presented where we compare data taken with an Allison [1] scanner and with the KVI-4D [2] emittance meter for the same beam. An exploration of the 4D phase-space data shows how beam filamentation can be investigated.

THE MEASUREMENT CONCEPT AND MAIN CHARACTERISTICS

The emittance meter has been designed to analyze a low-energy ion beam at the image plane of an analyzing magnet. At the image plane, the beam has an estimated maximum waist of 5 mm in the horizontal direction and a beam size of 40 mm in the vertical direction. The corresponding divergences are about +/-50 mrad and +/-6 mrad respectively. The instrument is design such that it is able to accept beams with a power up to 150 W.

To measure the emittance in four dimensions the pepper pot method [3, 4] has been adopted. Implementation of this principle led to the basic design of a tantalum pepper pot plate (see Fig.1) with a thickness of 25 µm, machined with an array of 20 µm diameter holes with a pitch of 2 mm. Each hole position is accurately defined in the y-direction. The plate is mounted at a distance of 59.3 mm from a MCP-based position-sensitive detector which has been described in [2]. The pepper pot plate is stepped with a translation device in the x-direction through the beam. The accuracy of this movement is less than a micrometer. Images are recorded at each step and contain a row of spots in the y-direction. Each spot covers 500-3000 pixels of the CCD. Each pixel is defined accurately in a second coordinate system. By scanning a single row of holes over the beam area, overlap of the spots in the x-direction, where the divergence is large, is impossible. In the y-direction the divergence is much smaller, so that no overlap occurs for the 2 mm hole pitch, small compared to the 40 mm beam size.

From the measured positions of the ions and the exact position of the pepper pot plate we can reconstruct the rectilinear flight path of the particles and thus also the angular coordinates x' and y'. A 4D dataset $\rho(x,y,x',y')$ can be constructed that contains an intensity value proportional to the number of detected particles within a 4D volume-element dx, dy, dx', dy' at the phase-space position x, y, x', y'.

The dataset ρ can now be used to construct the various phasespace projections: x-x' (see Eq.1); y-y' and also x-y', y-x' by integrating over the other dimensions.

$$\rho(x,x') = \iint \rho(x,y,x',y')dydy' \quad (1)$$

By integrating over specific intervals of the other dimensions more detailed information can be obtained. An example of this will be discussed below.

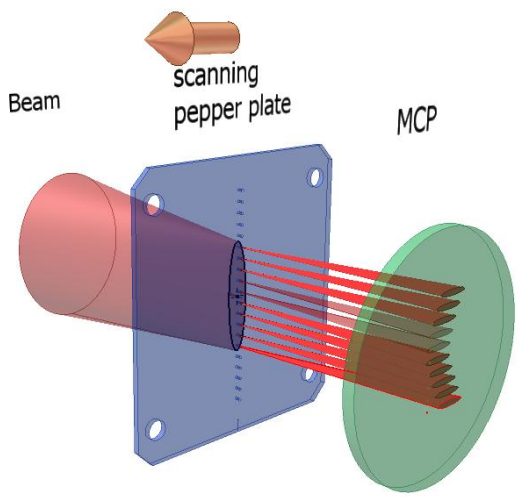

Figure 1: measurement concept of the KVI-4D emittance meter

* This work has been supported by the University of Groningen and by the European Union through EURONS, contract 506065. It has been performed as part of the research programme of the "Stichting voor Fundamenteel Onderzoek der Materie" (FOM), with support of the "Nederlandse Organisatie voor Wetenschappelijk Onderzoek" (NWO).

#kremers@kvi.nl

To be able to measure intense beams we need to reduce the beam power on the MCP surface as it is sensitive to sputtering effects. Here, the pepper pot principle has a clear advantage. It stops essentially the whole beam and the transmitted beamlets formed by the holes have a much lower power density because of their divergence. In our case the power density is reduced with a factor of $3x10^{-4}$. So a power deposition of 20 W/ cm^2 on the pepper pot plate results in a power deposition of 6 mW/cm^2 at the MCP surface. This decrease in power deposition makes it possible to measure intense low energy beams.

To optimize this reduction the hole diameter is minimized. To keep a large instrumental acceptance with respect to the beam emittance the thickness of the pepper pot plate needs to be reduced too. This decreases the heat conduction through the pepper pot plate material. Taking this into consideration in combination with the sputtering yields of a 150W beam on the tantalum pepper pot plate, a lower limit of the hole diameter is reached in the order of 5-10 µm.

DATA ANALYSIS

The dataset ρ(x, y, x', y') contains an intensity value obtained from a single pixel of the CCD camera and contains background, noise and beam related signal. The background and noise originate in both the MCP and CCD. The background is eliminated by subtracting an image taken without beam from the data. In order to determine the noise threshold the frequency distribution of the content of the pixels is constructed. The distribution (see Fig. 2) consists out of a bell shape part due to the noise and the tail part related to the beam. The threshold to separate the noise from the beam related signal is set by the 3 sigma of the Gaussian fit.

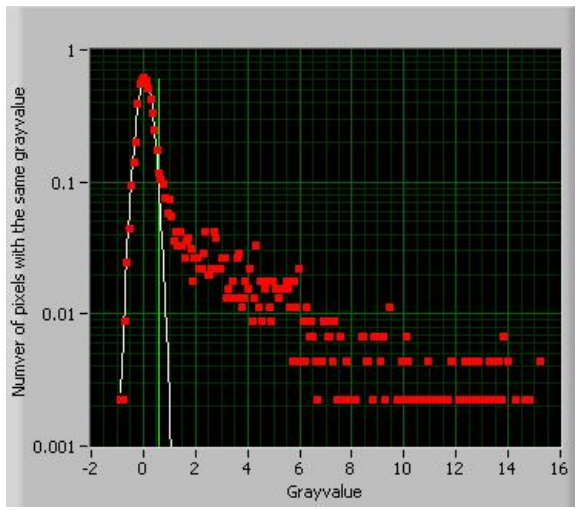

Figure 2: Frequency distribution of the dataset, white: Gaussian fit, green: 3 sigma threshold

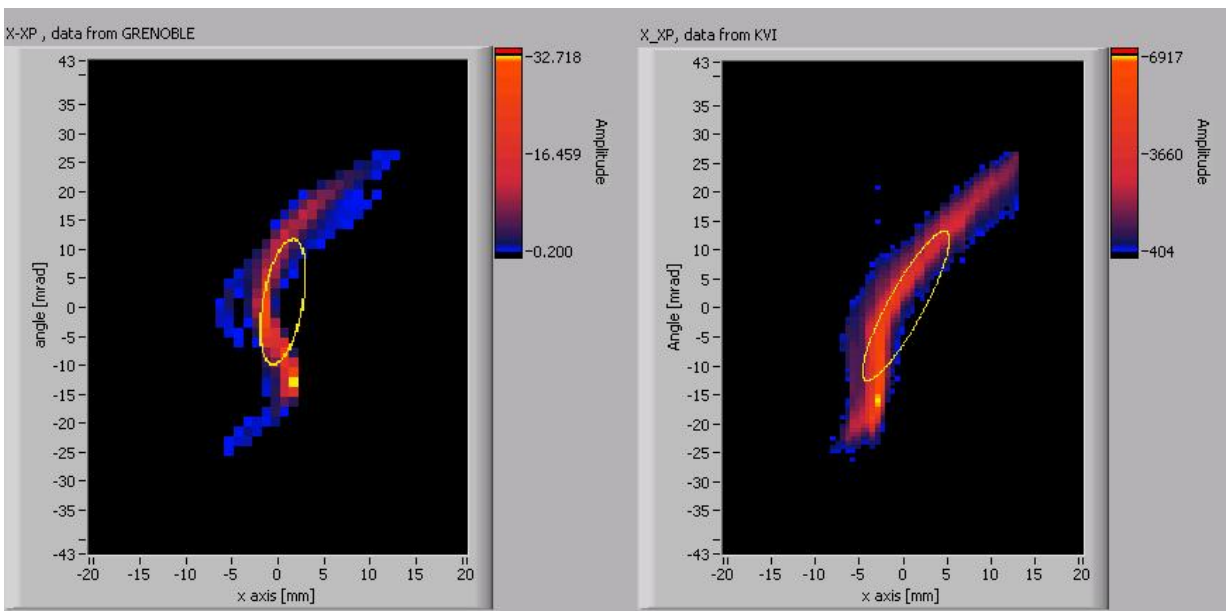

Figure 3: X-x' emittance measured with the KVI-4D emittance meter and the Allison scanner, both fitted with a 1σ RMS ellipse fit.

The beam related signal is used to calculate a RMS emittance [5]. The routine calculates the centre, the variance in both directions and plots the ellipse in an x-x' or y-y' coordinate system. The ellipse contains 68% of the intensity. To compare the outcome of the KVI-4D emittance meter with the 2D Allison scanner integration over the full dataset is needed

COMPARISON OF THE INSTRUMENTS

The KVI-4D emittance meter was installed 30 cm downstream a set of two Allison scanners at the test bench of A-Phoenix at LPSC Grenoble [6]. The emittance was measured with both devices subsequently. Measurements were made for different charge states and intensities of a Ne-beam at an extraction voltage of 35 kV. The influence of the MCP-gain on the measurements was also investigated. The data was analyzed with the above described RMS-fit routine.

From table 1, one can observe that with the Allison scanner a normalized emittance of 0.14 +/- 0.02 π mmmrad for the charge state 4+ has been found. With the KVI-4D emittance meter a value of 0.16+/-0.01 π mmmrad is obtained. So we conclude that the measurements with both instruments are consistent (see Fig. 3). The small effect of the increase of the RMS-emittance as a function of the MCP-gain will be investigated further.

Table 1: Normalized RMS emittance (1σ) as function of the charge, beam current, and high voltage on the MCP.

no	E	Beam cur	Charge	HV MCP	KVI-4D x-x'	Allison x-x‘
	keV	µA			π [mmmrad]	π [mmmrad]
A41	140	500	4+	5.1	0.17	0.15
A42	140	500	4+	4.8	0.16	
A43	140	500	4+	4.6	0.15	
A51	120	500	4+	5.2	0.16	0.13
A52	120	500	4+	4.9	0.15	
A61	210	180	6+	5.3	0.16	0.18
A62	210	200	6+	4.7	0.14	
A71	280	18	8+	5.7	0.19	0.13
A72	280	18	8+	5.1	0.16	

X – Y CORRELATIONS

The KVI-4D emittance meter measures the full four dimensional transverse phasespace density of the beam, thus allowing the analysis of correlations between the two transverse planes x-x' and y-y'. As an example of such an analysis we show in Fig. 4 the phasespace distribution ρ(x,x') extracted from the KVI-4D measurement shown in Fig. 3, by integrating over the full y-dimension and the interval -13<y'<-11 mrad. The phasespace distribution exhibits two more or less separated S-like structure. We observe that at certain angles y', the beam in the x-x' plane is split into two parts with similar focussing properties.

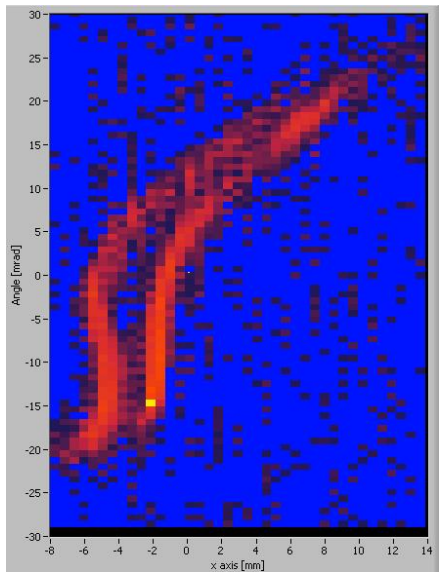

Figure 4: KVI-4D emittance x-x'(-20<y<20mm, -13<y'<-11 mrad)

Further analysis of the data shows that the left S-structure originates from the upper half of the beam, while the right S-structure originates from the lower half of the beam as can be seen from Fig.5. This illustrates how 2D-projections of the phasespace distribution obtained by integrating over a part of the full range for the orthogonal dimensions gives a more detailed insight in the structure of the phase space distribution.

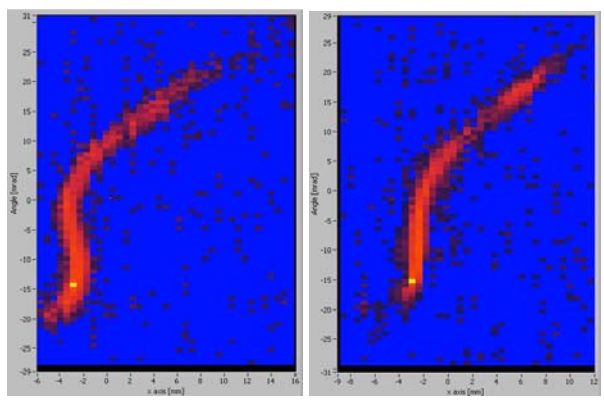

a) b)

Figure 5: KVI-4D, x-x' a)0<y<20, -13<y'<-11mrad, b)-20<y< 0, -13<y'<-11mrad

CONCLUSION

An instrument was developed to measure the full four dimensional phasespace distribution of low-energy highly-charged heavy ion beams. We have shown earlier [2] that it operates in a mode where we can detect single ions as well as with a beam current of 500 μA (20W) without damaging the detector. This is basically due to the dynamical range of the gain of the MCP. The emittances measured with the Allison scanner and the KVI-4D meter of the same beam are consistent with each other. Correlations between the transverse planes can be measured in detail. The complete 4D-structure of the phasespace distribution will help improving the understanding of beam formation and extraction in ECR-sources and in obtaining an optimum transport and matching of the beam to the accelerator.

REFERENCES

[1] P.W. Allison, J. D. Sherman, and D. B. Holtkamp, *IEEE Trans. Nucl. Sci.* **NS-30**, 2204-2206 (1983).

[2] H. R. Kremers, J. P. M. Beijers, S. Brandeburg, DIPAC'07, Venice, May 2007, TUPC24, (2007).

[3] L.E. Collins and P.T. Stroud, Nucl. Instr. and Meth. 26 (1964) 157.

[4] C. Lejeune and J. Aubert, Applied Charged Particle Optics,Ed. A. Septier (Academic Press, 1980) p. 159.

[5] J. Buon, CERN Accelerator School Proceedings (Editors : S. Turner) 94-01; vol. II p 89 (1994)

[6] T. Thuillier, T. Lamy, P. Sortais, P. Suominen, O. Tarvainen, and H. Koivisto, Rev. Sci. Instrum. 77, 03A323 (2006).

A METHOD OF TUNING ECRIS BEAM TRANSPORT LINES FOR LOW EMITTANCE*

J. W. Stetson#, NSCL/MSU, East Lansing, MI 48824, USA

Abstract

Heavy-ion beams from an ECR-type ion source have been shown to be structurally complex and to have a strong cross-correlation associated with their formation in and extraction from a high magnetic field with a strong sextupole content [1].

The emittances of such beams tend to be unavoidably large (compared to low magnetic field source types) yet because of cross-correlations, resistant to improvement by normal collimation methods [2].

Recent developments with beam from the 14 GHz room temperature ECRIS at the NSCL indicate that careful beam line tuning to pass specific parts of the beam structure can allow greatly reduced 4-dimensional emittances without losing a disproportionate amount of the total intensity.

INTRODUCTION

The National Superconducting Cyclotron Laboratory (NSCL) consists of two cyclotrons in series (the K500 and K1200) [3] which accelerate beams provided by one of two ECR Ion Sources. The primary source is ARTEMIS-A (Advanced Room Temperature Ion Source), which is a modification of the Berkeley AECR source and runs at 14 GHz using permanent sextupole magnets, radial ports and room temperature solenoids. A duplicate source, ARTEMIS-B, has been constructed and is installed on a separate test stand.

The primary operational mode of the accelerators is as a driver for operation of the A1900 particle separator, where stable-nuclei beams of 120-170 MeV/u are impacted on a solid target, with the resulting nuclear fragments collected, purified, and sent as a beam of exotic nuclei to the experimental areas.

MOTIVATION

Generally, from the point of view of the experimental program, the highest possible intensities are desired. The shielding of the production target area would allow for beams of up to 4 kW beam power. Presently, for some beams, final output is limited by the beam intensity from the ion sources. For others, beam powers are limited to about 800 W by losses and resulting heating of extraction elements in the cyclotrons. When the new high intensity ECRIS, SUSI, comes on line in 2009, the loss issue will become more pressing.

An important constraint on any solution to running with higher intensities is that the facility operates by user demand with a run of any particular beam seldom lasting more than a few days. The list of beams available for nuclear science contains 22 different stable isotopes [4]. This great variety of beam types and the short run times requires that tunes also be repeatable, reliable, and quick to optimize.

EXPERIENCE

From nearly the beginning of coupled cyclotron operation in 2001, it was clear that an increase of beam current from the source and subsequent injection did not lead to increased K500 output and overall transmission efficiencies were low. Simple collimation (apertures and a small (8 mm diameter) plasma chamber extraction hole) improved the situation but the resulting beam images seen on phosphor-coated plates inserted into the injection beam line had many undesirable features such as large variations in intensity within the image. Considerable effort on improving injection beam line performance was undertaken, including a major change from magnetic to electrostatic focusing in the initial part of the line and a higher-quality analysis magnet [5, 6]. Better performance through the cyclotrons was achieved as the emittance of the low-energy beam injected into the K500 was reduced.

Artemis-B Beam Tests

In August 2007, the Artemis-B test stand was configured to explore the possibility of making a full 2nd order correction of aberrations in the extracted ECRIS beam due to the sextupole radial confinement field.

The beam line with relevant devices is shown in Figure 1. An electrostatic double-doublet system (DDS) consisting of four quadrupoles and one octupole served as the focusing elements before the 90 degree analysis magnet. Vertical and horizontal steering control is done by offsetting the plate voltages of the first and fourth quadrupoles. A sextupole magnet, rotatable about the beam line axis, was placed between the DDS and the analysis magnet. Calculations had shown that with the DDS set to give a π phase-advance (essentially, a focus) between the source sextupole and the external sextupole, the desired correction could be achieved. An Allison-type scanner was used to measure beam emittances. However, since it is a 2-dimensional device, to achieve some gauge of the higher-order nature of the beam, a pepper-pot-like plate was made to insert into the beam after the analysis magnet, followed by a field-free drift and a viewer plate. (An uncorrelated beam will project an image of the grid hole unchanged except for size, depending on the optical conditions.) The test stand configuration is shown in Figure 1 and the beam used was $^{40}Ar^{7+}$ with an extraction voltage of 20 kV.

*Supported under National Science Foundation Grant PHY-0110253
#stetson@nscl.msu.edu

The correction scheme as tested did not work as anticipated. However, three interesting results were noted that led to a new method of tuning for the beam line injecting into the K500.

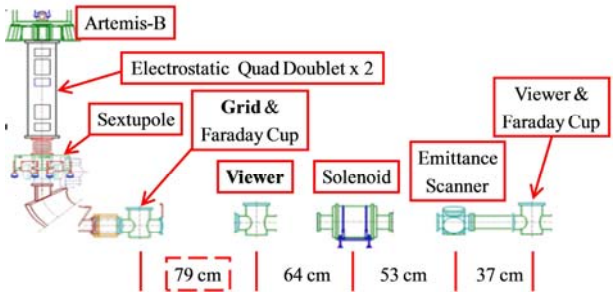

Figure 1: Artemis-B configuration for described tests (not to scale). The grid filters the beam into beamlets that drift 79 cm to a viewer, allowing x-y cross-correlations to be seen easily, as in Fig 2.

First to note is that when tuning the DDS quadrupoles to achieve maximum intensity on the first Faraday cup (without regard for beam quality), the downstream grid projections of the resultant beam were highly structured and contained large correlations. Some of these patterns are shown in Figure 2.

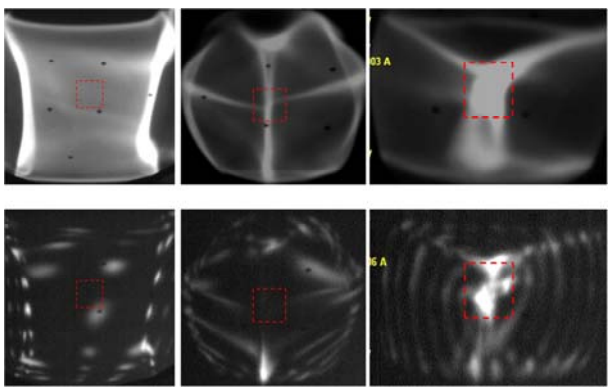

Figure 2: Some $^{40}Ar^{7+}$ beam patterns seen on the first viewer of the Artemis-B test line with various DDS quadrupole settings optimized only for beam intensity (about 120 eμA). The top row is without grid, the bottom row is with the grid inserted. The dashed-line square represents a 1 cm x 1 cm scale in this and subsequent figures.

Figure 3: The Artemis-B grid is placed behind a 25 mm diameter aperture. The grid holes are about 1.5 mm in diameter, and 4 mm between centers.

The grid used for these projections is shown in Figure 3. Hole sizes and spacing are larger than what is used in typical pepper-pot arrangements.

Secondly, it was noted that when the DDS quads were set to values near those calculated to achieve a π phase-advance at the location of the external sextupole, the resulting grid patterns were markedly different. An example is shown in Figure 4. In this case, a major portion of the beam projects the grid pattern 79 cm downstream without major distortion, even with the external sextupole turned off. This indicates that the transmitted portion of beam is without large x-y correlations, i.e. uncorrelated or what is sometimes referred to as laminar [7].

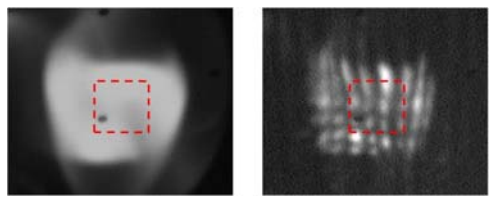

Figure 4: The left-hand image shows the "π phase-advance" tuned $^{40}Ar^{7+}$, 80 eμA beam on the first viewer, without the grid inserted. At right, the grid is inserted, showing a relatively undistorted pattern at the center of a dimmer "cloud".

Lastly, it was also noted that when the beam was tuned in this manner, raising the sextupole captured some of the halo beam, but did not change the "core" in any substantial way, qualitatively hinting that the 2nd order content of this selected part of the beam is low.

Artemis-A Beam Tests

A shutdown of operations in the summer of 2008 allowed an extensive set of tests to be conducted on the K500 injection line. The goal of these tests was to generate the same uncorrelated beam condition seen with Artemis-B, clean up beam tails around the main core of beam, and characterize the results with an Allison-type emittance scanner.

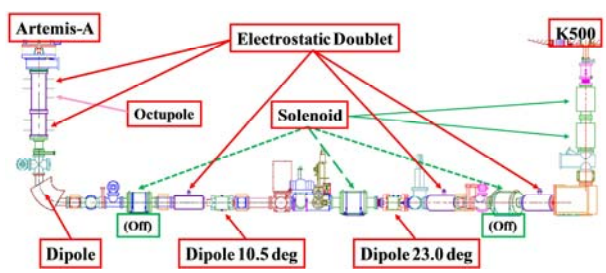

Figure 5: Artemis-A configuration showing the major optical elements.

The major optical elements are shown in Figure 5 and a view with relevant devices is given in Figure 6.

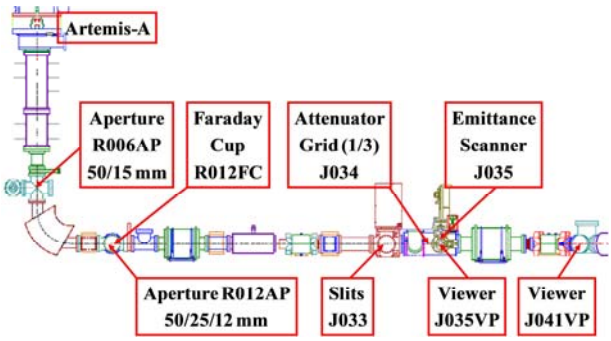

Figure 6: Artemis-A configuration showing the major devices. The 3-digit number within the device name indicates the relative position along the line.

The grid (Fig. 7) is located further downstream than for the Artemis-B line and the drift between the grid and the first viewer (J035VP) is shorter, about 30 cm compared to 79 cm, but still suffices as a qualitative display of beam correlations. In the 2.1 m path between J035VP and the second viewer, J041FP there is a dipole (J039DS) bending 23 degrees and a solenoid (J041SN). With the solenoid set to zero however, this represents an "almost-free" drift since the focusing effects of the dipole are small (negligible in the vertical direction) and the distance from J039DS to J041VP is short.

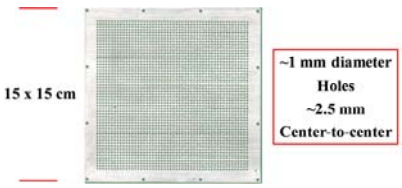

Figure 7: Artemis-A x1/3 attenuator grid, located ~30 cm upstream of the first viewer plate, J035VP.

Using the "π phase-advance" DDS settings from the studies on Artemis-B also gave uncorrelated beam patterns through the J034 grid in the Artemis-A line. Initially, considerable fine-tuning was needed to get both the uncorrelated patterns and low emittance. Accumulated experience with different beams now allows a standard setting for the two quad doublets of the DDS and the beam line quad doublet, J017QA/18QB that gives the desired low-emittance condition and a focus at J035.

The general tuning procedure is as follows:

- With the aperture R006AP in front of the analysis dipole R009DS closed to 15mm, tune the DDS quadrupoles to pass beam through this aperture.
- Use the quadrupole doublet downstream, J017QA/18QB, to focus the beam to a minimum size on viewer J035VP.
- Close R012AP, the aperture after R009DS. Use steering upstream of the aperture to select an intense-looking spot on J035VP.
- Insert the grid at J034 which will cast a pattern on the viewer plate. This pattern should reflect the hole pattern of the grid. If it does not, readjust the DDS quadrupoles and steering to select a different piece of beam that does cast such a pattern.
- With the intermediate solenoid J037SN set to zero, look at the beam on J041VP. Since the beam is a focus/waist at J035VP, the increase in spot size during the drift is directly related to the emittance.
- Opening and closing the apertures at R006 and R012 will show the degree of contamination of the selected beam by other parts following a different path.
- The grid image can be seen on J041VP by raising the J037SN solenoid. Since the grid and the slits at J033 are close together, cutting into the beam with these slits should result in a sharp cut of the grid image seen at J041VP.

Aspects and results of this process are noted below, starting with features in tuning a $^{124}Xe^{20+}$ beam. The first attempt resulted in a distorted grid pattern on J035VP as shown in Figure 8a-Left. (The quad doublet, J017QA/18QB is set to give the minimum spot size on J035VP.) After passing through the drift to J041VP, one sees in Figure 8a-Right a substantial increase in the beam size as well as a highly-structured beam spot.

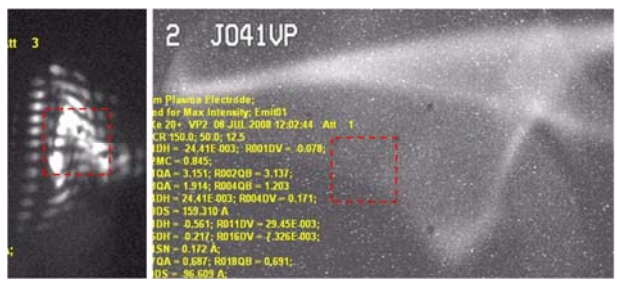

Figure 8a: Images of a $^{124}Xe^{20+}$ beam at J035VP and after the drift to J041VP.

Re-steering and focusing of the DDS quadrupoles, while attempting to keep an organized grid pattern, yet selecting a part of the beam that was small on both viewers, gave the images shown in Figure 8b. The rectilinear grid pattern is visible, the growth of the beam size in the drift is minimal, and the complicated structures seen above, absent.

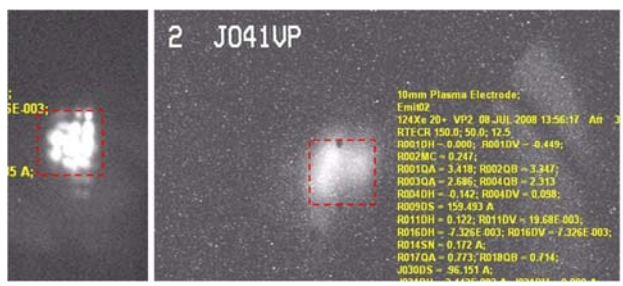

Figure 8b: $^{124}Xe^{20+}$ beam images at J035VP and J041VP as in Figure 8a, but tuned for low emittance.

The implication from the viewer data that the second attempt has reduced emittance in comparison to the first is confirmed by the corresponding emittance scans, given in Figures 9a and 9b.

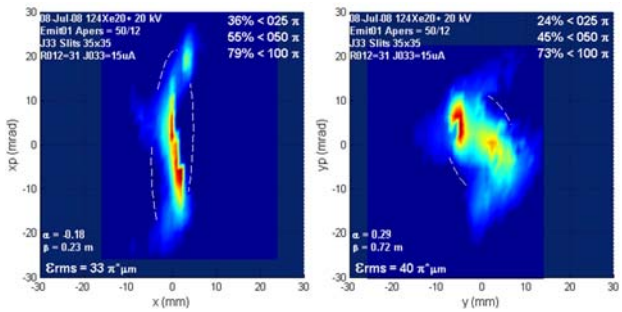

Figure 9a: Horizontal and vertical emittance scans at J035 with a $^{124}Xe^{20+}$ beam tuned as in Fig. 8a. Beam intensity is 31 eμA on the Faraday cup just after the analyzing bend (R012FC) and 15 eμA at the scanner location J033. Resulting emittances are 33 and 40π mm*mrad respectively.

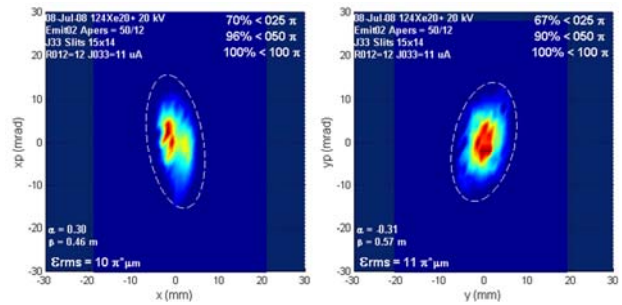

Figure 9b: Horizontal and vertical emittance scans at J035 with a $^{124}Xe^{20+}$ beam tuned as in Fig. 8b. Beam intensity is 12 eμA on R012FC and 11 eμA at J033. Resulting emittances are as calculated are 10 and 11π mm*mrad respectively.

Another test of beam quality is the response of that beam to focusing. In a normal tune transmitting maximum intensity, one manifestation of a cross-dimensional coupling that seems peculiar to ECRIS-produced beam, is that when such a beam is focused to a its smallest size by a solenoid, then over-focused slightly, a star appears [1, 5, 6]. An example of this behavior is shown in Figure 10.

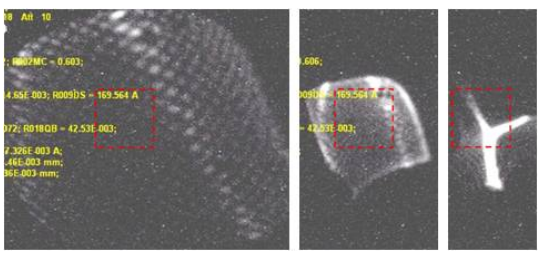

Figure 10: J041VP images. With a $^{40}Ar^{7+}$ beam tuned "normally" through the grid at J034 to a focus/waist at J035VP, the solenoid J037SN between the two viewers is raised from zero to ~110 A.

These low-emittance tunes respond very differently and in a much more desirable way as shown in Figure 11 for a $^{58}Ni^{11+}$ example tuned similarly to the example used for Figures 8b and 9b.

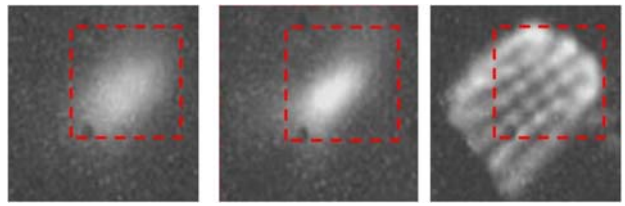

Figure 11a: J041VP images. A low-emittance tuned $^{58}Ni^{11+}$ is passed through the grid at J034 to a focus/waist at J035VP. The solenoid J037SN between the two viewers is raised from 0 to ~100 A. Left is the under-focused condition, center is the minimum spot size, and at right is an over-focused condition.

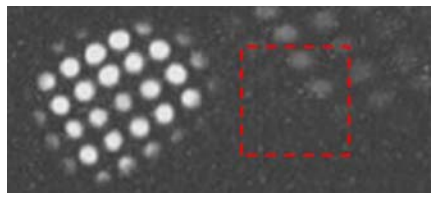

Figure 11b: A J041VP image with the above $^{58}Ni^{11+}$ beam strongly over-focused (J037SN ~ 120A). On the right, a $^{16}O^{3+}$ contaminant is distinctly separated from the main beam.

Because the J033 slits are located close to the grid at J034, a sharp rectilinear grid pattern infers that closing these slits will result in a clean cut. This is shown to be the case in Figure 11c.

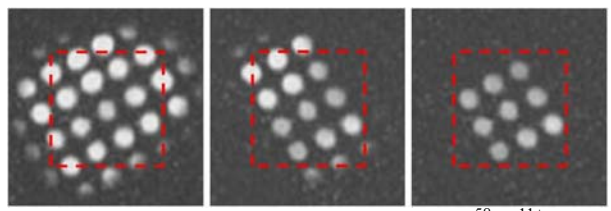

Figure 11c: A J041VP image of the above $^{58}Ni^{11+}$ beam, with the J033 slits open (left), with a vertical gap of 5 mm (middle), and with both the horizontal and vertical gaps set to 5 mm (right).

It is important to remark that if the best piece of the overall beam is selected through focusing and steering upstream of the analysis magnet, that piece is fundamentally uncorrelated and of low emittance. The cuts are not to improve this part of the beam, but serve to cut away other parts of the beam. An example is shown below in Figure 12.

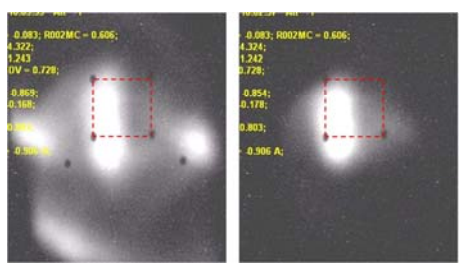

Figure 12: A J041VP image with a $^{40}Ar^{7+}$ beam tuned in the "low emittance" condition. At left, the aperture R012AP = 50 mm diameter, at right, R012AP = 12 mm. The horizontal core of the beam is unaffected; in the vertical direction the cut is a little too severe (which could be eliminated if adjustable slits were used at that location rather than apertures.)

Emittance Scanner Resolution

The resolution of the emittance scanner is given to be 0.5 mm in position and 6.7 mrad in angle [8]. The very low emittances of the beams being produced in these tests often are less than the resolution of this scanner. In particular, positional resolution is adequate given the 5-10 mm spot size typically found at the scanner location. However, when the beam emittances are smaller than about 15π mm*mrad, the measured angle no longer responds to changes in spot size made by focusing only. An example is given in Figure 13.

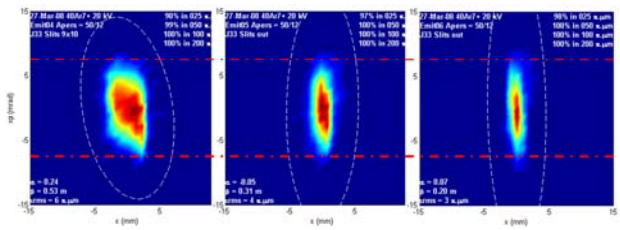

Figure 13: Three emittance scans of the same "low-emittance" tuned $^{40}Ar^{7+}$ beam (selecting about 20% of the maximum available intensity) with the horizontal spot size progressively reduced to a line focus using the quadrupole doublet upstream of the scanner. As the spot size is decreased, the calculated r.m.s. emittance is 8, 6, and 3π mm*mrad respectively. The measured angular divergence is not increasing as it should because it is smaller than what the scanner can presently resolve.

In such cases, common in the "low-emittance" tune mode, the real emittance value is lower than what is calculated from the measurement. Narrower scanner slits will be installed in the future to rectify this issue.

Beam Current

The "low-emittance" tunes result in 70-80% loss in beam intensity measured at the first Faraday cup (R012FC) in comparison to the case where the DDS quadrupole settings and steering are set to give maximum intensity. However, further downstream, this loss is reduced to 25-35% due to the higher losses incurred by the higher-emittance beam. To increase beam intensities, the 8 mm plasma diameter plasma chamber extraction electrode was replaced by one of 10 mm diameter. The beam output went up by about 30-40% and could still be tuned to low-emittance condition very similar to that in the 8 mm case. The net result is that the 10mm/low-emittance tune gives intensities comparable to the 8mm/normal (intensity maximized) tune at the last injection line faraday cup before the K500, but with much higher 2-d brightness. The improvement would be even greater if comparing 4-d volumes, since, as shown above, the normal beams exhibit complicated x-y coupling that are essentially absent in these low-emittance tunes.

CONCLUSIONS

Results of these tests can be summarized as follows:

- Beams of $^{40}Ar^{7+}$, $^{58}Ni^{11+}$, $^{78}Kr^{11+}$, and $^{124}Xe^{20+}$ were extensively tested and showed very similar optical properties.
- A bright beam core exists that has minimal, if any, cross-correlations.
- This core has about 20-30% of the intensity of a beam tuned for maximum current.
- Measured 2-d emittances are reduced by at least a factor of 3-5 over that of the full beam. Higher-resolution scans will be needed to fully quantify the improvements.
- Settings of the first quadrupole focusing elements scale by extraction voltage very precisely between the different ion beams.
- The minimal x,y beam correlations that result from this technique allow clean slit cuts.
- Changing the plasma chamber electrode diameter from 8mm to 10mm increased both overall and "low emittance" output by 30-40%, without significantly degrading the quality of the "low-emittance" tuned beam.

ACKNOWLEDGEMENTS

The author wishes to thank D. Cole, M. Doleans, G. Machicoane, L. Tobos, P. Zavodszky at NSCL and P. Spädtke at GSI for their contributions.

REFERENCES

[1] P. Spädtke, R. Lang, J. Mäder, J. Rossbach, K. Tinschert, J. Stetson, 17th Int. Workshop on ECR Ion Sources, Lanzhou, China (2007), p. 192.
[2] J. Stetson, P. Spädtke, IEEE Proc. of PAC07, Albuquerque, N.M., USA (2008).
[3] F. Marti, P. Miller, D. Poe, M. Steiner, J. Stetson, and X.Y. Wu, in Cyclotrons and their Applications 2001, AIP Conf. Proc. 600 (2001) p. 64.
[4] www.nscl.msu.edu/exp/propexp/beamlist .
[5] J. Stetson, G. Machicoane, P. Miller, M. Steiner, P. Zavodszky, in Proc. of LINAC06, 2007, p. 352.
[6] J. Stetson, G. Machicoane, P. Miller, M. Steiner, X. Wu at the 18th Intl. Conf. on Cyclotrons and their Applications, Catania, Italy, 2007, p. 340.
[7] S. Humphries, *Charged Particle Beams*, 1990, p. 80.
[8] G. Machicoane, M. Doleans, G. Humenik, P. Miller, M. Steiner, J. Stetson, X. Wu, P. Zavodszky, Q. Zhao, 17th Int. Workshop on ECR Ion Sources, Lanzhou, China (2007), p. 187.

Low Energy Beam Transport for Ion Beams created by an ECRIS

P. Spädtke, R. Lang, J. Mäder, J. Roßbach, K. Tinschert, GSI Darmstadt

Abstract

It has been shown previously that the emittance of an ion beam, extracted from an Electron Cyclotron Resonance Ion Source (ECRIS) is determined by magnetic field, applied electric potentials, geometry, and particle density distribution together with the initial properties of these particles[1],[2].

The model used for computer simulation seems to fit the experimental results: ions are extracted from the ion source if they are created (started) at places where magnetic field lines are going through the extraction aperture. Furthermore, the absolute value of magnetic flux density relative to the flux density at the extraction aperture defines, whether this ion can be extracted or not.

Due to coupling between the different subspaces of phase space because of the magnetic field, several assumptions used for beam transport issues are not valid any more: for example, two-dimensional emittance does not stay constant in every case; the six dimensional phase space does.

With increasing extracted ion currents, space charge compensation of the extracted beam becomes an important issue. The beam itself will create secondary particles which can serve for space charge compensation. This compensation will build up in a relatively short time, depending on the pressure, as long no leakage is present within the beam line.

ION BEAM EXTRACTION

Electron cyclotron resonance ion sources (ECRIS) are used more often, especially since several improvements of this type of ion source had increased the available intensities even for higher charge states. Nevertheless, extraction and beam transport is only partially comparable to the case of ion beam extraction not influenced by magnetic fields. It seems that the starting conditions of the ions within the plasma are essential for the process of beam formation. Because of the low ion temperature which is in the low eV range and the high magnetic flux density up to several T, the Larmor radius of ions is in the sub-mm range. Therefore, ion-ion collisions are minor important for the path of the ion. The magnetic field lines going through the extraction aperture show the possible path for the ions to be extracted. If the magnetic flux density is increasing along the field line, particles will transform energy in direction of the field line into rotational energy perpendicular to the field line and visa versa. Only if it is possible to create ions at these locations or to transport them to these places with a certain magnetic flux density, the ion can be extracted. The magnetic flux density in the plane of extraction is therefore a good approximation for the minimum required flux density from which ions can be extracted. This surface is shown in the following 2D-cuts for different ECRIS types, see Figures 1, 2, 4 - 10. Together with the information where the magnetic field lines going through the extraction aperture are coming from, the possible extraction area can be determined. It is assumed that the plasma generator is able to produce particles in the required charge state at these locations.

The model has been tested for different existing ion sources, and for ion sources which are still under design or in construction, and it has been found that the actual magnetic setting has to be taken into account, instead of using the design values only.

CAPRICE

This source, used at the accelerator facility at GSI, has been investigated together with the technique of viewing targets, to proof our estimates about beam extraction. The ion source has two normal conducting coils for the mirror trap and a hexapole, made of permanent magnets. Using different materials for these permanent magnets, we have tested three differently strong hexapolar fields: 0.8 T, 1.0 T, and 1.2 T, measured at the inner diameter of the plasma chamber. Whereas the transverse magnetic flux density is fixed when the hexapole has been installed, the mirror field for both mirror coils is variable up to 1.2 T on axis, see Fig. 1. Plasma heating is done by a 14.5 GHz klystron. By changing the mirror field on injection side or extraction side, the origin of extracted ions can be changed from the back side of the source to the radial location of the loss lines, starting at injection side and reaching the center between both coils, see as example Fig. 7 for the MS-ECRIS. Because the allowed starting conditions are determined by the magnetic settings, it is important for ECRIS extraction simulation to include the different possible magnetic fields.

SUPERNANOGAN ©

This commercially available ion source[3] is easier to simulate, because the magnetic flux density is frozen due to the only use of permanent magnets, which might be a disadvantage on the other side. The magnetic flux density has been calculated using the PANDIRA code[4], which calculates the rotational symmetric mirror field. Because of the usage of permanent magnets, the longitudinal field

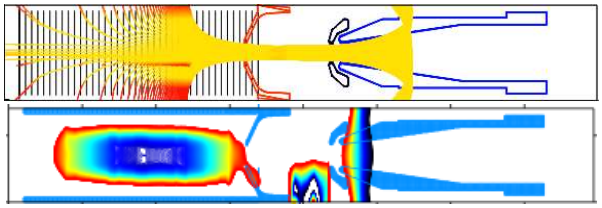

Figure 1: Magnetic field lines for Caprice, equipped with the 1.0 T hexapole, and corresponding lines of constant $|\vec{B}|$.

component changes sign within the extraction. The hexapolar component has been added in the 3D-map required for the KOBRA3 [5] simulation analytically, see Fig. 2. The extracted beam is shown in Fig. 3.

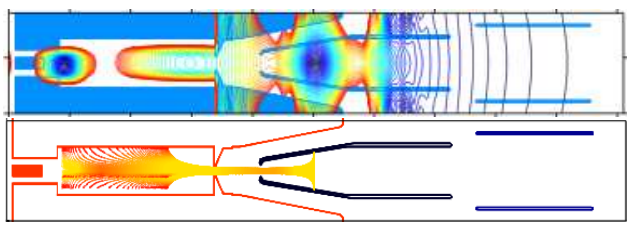

Figure 2: Magnetic flux density distribution in the SUPERNANOGAN: top: lines of constant $|\vec{B}|$ in mid-plane, bottom: magnetic field lines in projection.

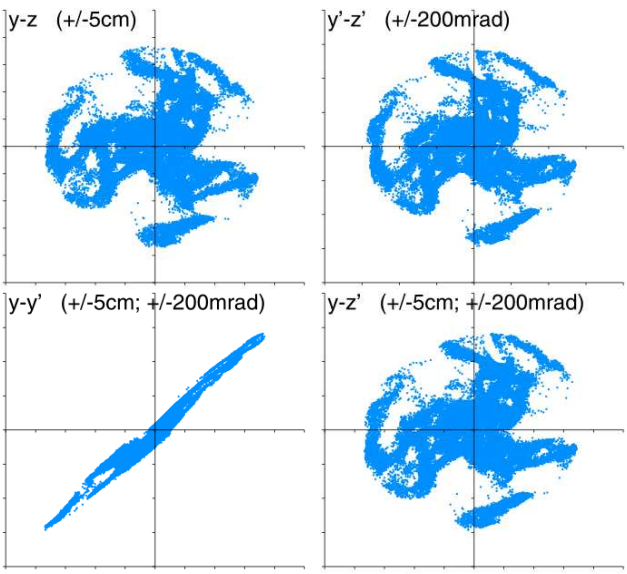

Figure 3: Different projections of the 6D phase space for the beam extracted from SUPERNANOGAN: top left: beam cross section, top right: momentum space, bottom left: emittance, bottom right: mixed phase space. Total current at 24 kV extraction voltage is 3 mA for oxygen, Only O^{3+} is shown here.

ARC-ECRIS

This is an old idea from plasma-fusion science [9], using a curved coil to produce the required magnetic configuration for a stable plasma confinement, which is reinvestigated for ion source application[8]. This device creates a minimum $|\vec{B}|$ structure with quadrupole like loss cones, see Fig. 4.

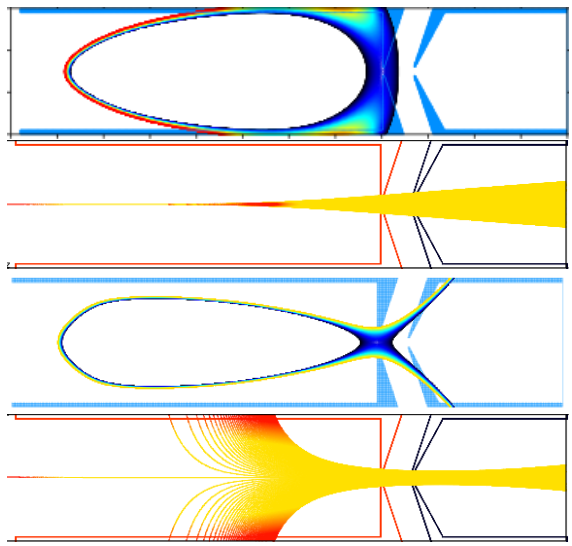

Figure 4: Magnetic structure of the arc-ecris: lines of constant $|\vec{B}|$ and magnetic field lines in horizontal and in vertical projection.

The extracted beam, shown in Fig. 5 favors a beam line with quadrupoles. If the properties of the plasma generator are as good as for regular ECRIS, this could be an interesting alternative.

MS-ECRIS

This superconducting source has been designed within a European collaboration[6]. It consists out of three solenoidal coils to produce the mirror field and a set of coils for the hexapole, designed to be 2.7 T at the plasma chamber. Because the magnetic structure is important for the possible starting conditions, simulations have to be made for all the different possible magnetic settings, see Fig. 6. Depending on the polarity and strength of the middle solenoid, the extraction area can be changed from the back side of the source (flat field mode) to the radial loss lines (high B mode). The question remains, whether the plasma generator is able to produce the ions which would be possible to extract. For plasma heating a 28 GHz gyrotron device is foreseen.

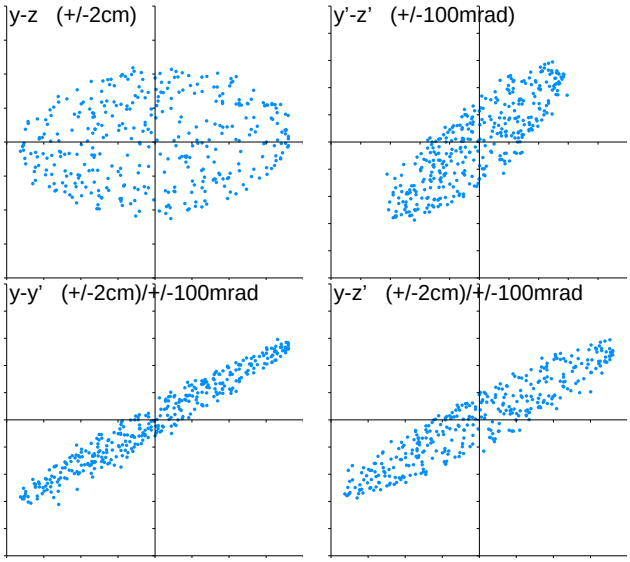

Figure 5: Different projections of the 6D phase space for the beam extracted from ARC-ECRIS: real space, momentum space, emittance, and a mixed phase space. In this solution, space charge effects are still neglected.

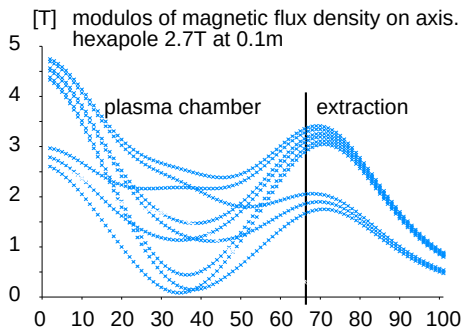

Figure 6: Different magnetic flux density on axis for the MS-ECRIS, used for the simulation necessary to determine extraction conditions for each hexapole setting.

A-PHOENIX

This source[7] has a hybrid set up: two superconducting coils form the mirror field. The minimum between both coils can be slightly modified by an additional normal conducting coil. The hexapole is made by permanent magnets. For this simulation we have used the standard hexapole design with 1.83 T at 65 mm diameter. The position of the extraction electrode is far away from the maximum field of the mirror coil on extraction side, see Fig. 8. Positioning of the electrode at that point selects a lower magnetic flux density on axis at extraction, having influence on the extractable ions. If the electrode would be close to the position of maximum flux density, the plasma chamber seems to be too small for an effective extraction.

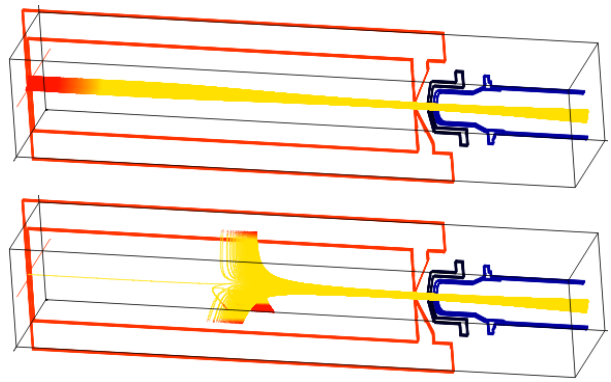

Figure 7: Magnetic field lines for different coil settings of the MS-ECRIS. Top: design value, middle coil switched off. Bottom: design values, injection field decreased to 60%. The red part of the field line indicates that the value of flux density is above that value at extraction aperture.

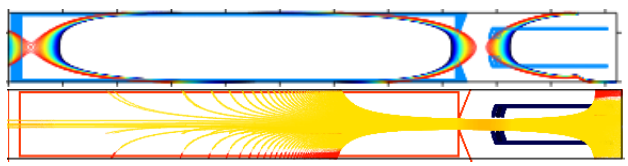

Figure 8: Magnetic field lines and magnetic flux density for the A-PHOENIX ion source.

SECRAL

This source[11] has a reversed radial position of solenoids and hexapole. Here the hexapole is outside the solenoids. This was decided for technical reasons, especially due to the forces between solenoid and hexapole.

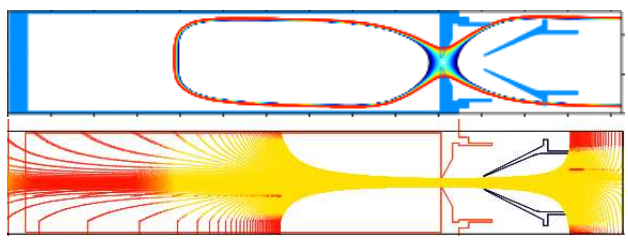

Figure 9: Magnetic field lines and magnetic flux density for the SECRAL ion source.

The magnetic flux density distribution shows good conditions for extraction, see Fig. 9.

RIKEN 28 GHz

The Riken version of a 28 GHz ECRIS [12] includes the possibility to bias the beam line, giving the opportunity to increase beam energy without having the source on extensive high potential, see Fig. 10. The advantage is the smaller emittance for the beam transport with higher en-

ergy, according to Liouville. The space charge compensation is not affected. When connecting the beam line again to ground, decelerating the beam, the emittance will increase again. Screening just before decelerating is required, otherwise the space charge compensation would be lost due to extracting electrons from the beam.

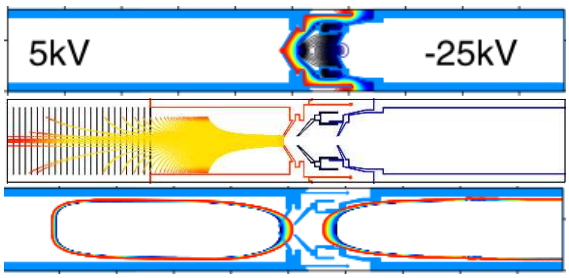

Figure 10: Superconducting ECRIS from Riken: top: electric potential, middle: magnetic field lines, bottom: lines of constant $|\vec{B}|$.

BEAM LINE SIMULATION

Different numerical methods can be used to simulate the transport of an ion beam. The choice is from simple matrix formalism to time dependent particle in cell codes with exact calculation of forces. It depends on the specific problem to be investigated which type of program has to be used. However, if the computational results represent the experimental observations, it can be concluded that the applied model describes the experimental observations sufficiently well. In the simulation of the beam line shown in Fig. 11 we use all phase space coordinates of each particle obtained from the extraction simulation.

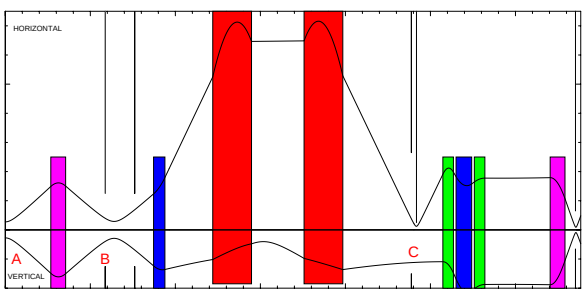

Figure 11: Beam line from left to right: solenoid, quadrupole singlet, split dipole, quadrupole triplet, solenoid. Top: horizontal dispersive plane, bottom: vertical. Envelope for 300π mm mrad, no correlation. A, B, C denotes the three locations where the beam is shown in figures 12 - 16.

Beam transport itself is made by a matrix formalism using the full 6×6 matrix, including coupling for the different optical elements, for each particle individually, not only for the ellipse parameter.

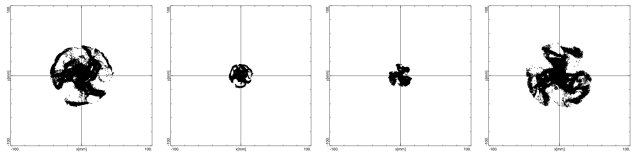

Figure 12: Beam cross sections from SUPERNANOGAN© behind the beam line solenoid (position B in Fig. 11) with increasing magnetic focusing strength from left to right.

The experimental results can be reproduced, using a linear transformation without space charge effects, see Fig. 13. From that fact we conclude a reasonable degree of space charge compensation.

Having shown that this transformation is consistent with experimental results, the same transformation can be applied to different ion sources or to different ion source operating conditions, see Fig. 15,16.

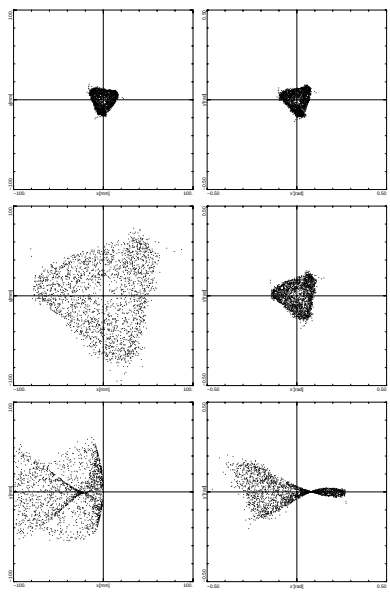

Figure 13: Beam from CAPRICE, equipped with the 1.0 T hexapole. Top: after extraction, starting conditions for MIRKO (position A in Fig. 11). Middle: behind the first beam line solenoid (position B in Fig. 11). Bottom: behind the dipole in the plane of resolving slits (position C in Fig. 11). Left column: real space ±100 mm full scale. Right column: momentum space ±500 mrad full scale.

Space Charge

The extracted positive ion beam creates a positive electric potential with a value given by the number of particles and their velocity. If the potential becomes high enough it will influence the path of the extracted beam itself. On the other side such a potential acts as a trap for electrons which are created in collisions of the primary beam ions

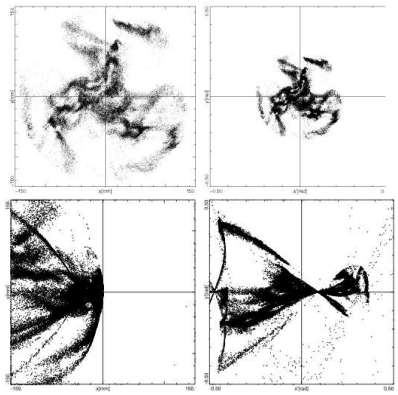

Figure 14: Beam from SUPERNANOGAN. Starting conditions are shown in Fig. 12). Top: behind the first beam line solenoid (position B in Fig. 11). Bottom: behind the dipole in the plane of resolving slits (position C in Fig. 11). Left column: real space $\pm$150 mm full scale. Right column: momentum space $\pm$500 mrad full scale.

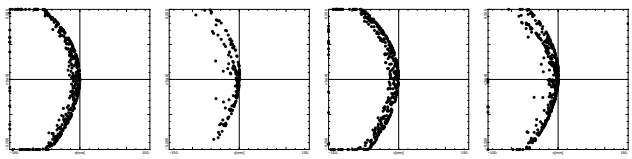

Figure 15: Unmatched emittances behind the dipole in the dispersive plane for different magnetic settings of MS-ECRIS. $\pm$150 mm, $\pm$200 mrad full scale.

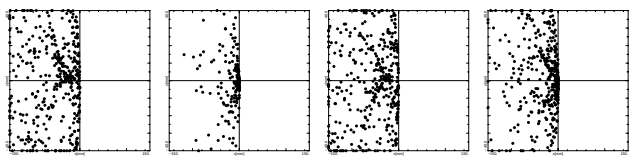

Figure 16: Beam cross sections behind the dipole for different magnetic settings of MS-ECRIS. horizontal $\pm$150 mm, vertical $\pm$40 mm full scale (position C in Fig. 11).

with residual gas atoms. The specific kind of trap might change along the beam line, as for example from a drift section with a pure electrostatic beam plasma to a bending section with a magnetic beam plasma. The movability of electrons within these elements is high only in the magnetic field direction, restricted in the transverse direction. If there are no leakages for electrons it is a question of time only until this potential will be compensated down to the range of the electron temperature. Leakages are given by electric fields similar to the extraction, or dc post-acceleration columns, but already a beam tube, which is not properly grounded, might remove electrons from the space charge compensation. These leakages have to be screened if they cannot be removed.

EXPERIMENTS

All experimental results have been described in [1]. One main result, which has been obtained with the CAPRICE, was that the cross section of each different extracted mass to charge ratio m/q changes from a hollow triangular ring to a three-wing structure when the specific m/q becomes over-focused with decreasing m/q in the stray field of the source, see Fig. 17.

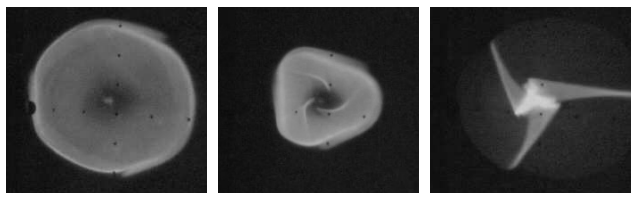

Figure 17: Measured beam profiles from CAPRICE at location B with increasing focusing strength of the beam line solenoid. Only one m/q is visible, all other are de- or over focused. Starting from m/q=1 all different ratios show the same behavior when focused.

Another result was that the cross-section of each m/q ratio, starting with m/q= 1 focused by a beam line solenoid located directly behind extraction shows similar behavior.

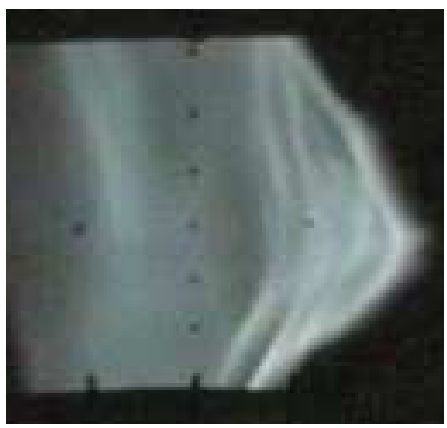

Figure 18: Measured beam profile from CAPRICE at location C.

CONCLUSION

We have shown, that the ion beam extracted from an ECRIS is affected by the magnetic field. The effects have been shown in experiment as well as in simulation. We do conclude that the effects observed with ECRIS beams are given by correlation of particles inside the plasma and by all resulting forces during extraction itself. The extraction can be simulated using a fully 3D code with the usual space charge compensation described by Self[14].

REFERENCES

[1] P. Spädtke, The Physics of Ion Beam Extraction from an Electron Cyclotron Resonance Ion Source, IEEE.

[2] P. Spädtke et al., Prospects of Ion Beam Extraction and Transport Simulations, RSI Vol. 79, Num. 2, 2008.

[3] C. Bieth, O. Tasset, S. Kantas, Pantechnik, Caen, France http://www.pantechnik.net.

[4] Los Alamos Computer Program Group http://laacg1.lanl.gov.

[5] KOBRA3-INP, INP, Junkernstr. 99, 65205 Wiesbaden, http://www.inp-dme.com.

[6] G. Ciavola, A Status Report on the Multipurpose Superconducting Electron Cyclotron Resonance Ion Source, RSI Vol. 79, Num. 2, 2008.

[7] T. Thuillier et al., High Intensity Ion Beam Prospects for Acceleration with PHOENIX 28GHz, Proceedings of the EPAC Conference, Paris (2002).

[8] P. Suominen anf F. Wenander, Electron Cyclotron Resonance Ion Source with Arc-shaped Coils, RSI Vol. 79, Num. 2, 2008.

[9] F. Cap, Einführung in die Plasmaphysik II, Wissenschaftliche Taschenbücher, Akademie Verlag Berlin, 1972.

[10] K. Tinschert, J. Bossler, S. Schennach, H. Schulte; Rev. Sci. Instr. 69 (1998) 709.

[11] H.W. Zhao et al., Intense Beam Production of Highly Charged Heavy Ions by the Superconducting Electron Cyclotron Resonance Ion Source SECRAL, RSI Vol. 79, Num. 2, 2008.

[12] T. Nakagawa et al., New superconducting electron resonance ion source for RIKEN RI beam factory project, Rev. Sci. Intstrum. 79, 02A327 (2008).

[13] http://mirko-optik.franczak.de

[14] S.A. Self, Exact Solution of the Collisionless Plasma Sheath Equation; Phys. Fluids 6, 1762, 1963

PAPER NOT RECEIVED

THREE DIMENSIONAL SIMULATION OF ION BEAM EXTRACTION FROM AN ECR ION SOURCE

S.M. Elliott, Lamplighter Technology Inc., Boulder, CO 80304 U.S.A
O. Delferrière, CEA-DSM/IRFU, 91191 Gif-sur-Yvette cedex, France
J. Simkin, Vector Fields Ltd., Oxford, OX5 1JE, UK
E.K. White, Lamplighter Technology Inc., Boulder, CO 80304 U.S.A.

Abstract

Accurate prediction of ECR ion extraction behavior is important for high current density operation and subsequent beam transport calculations. In this paper we review the combined electric and magnetic space charge beam simulation of ion beam formation from an ECR ion source with a multi-electrode extraction system. Included in the simulation is the influence of secondary charged particles generated by ion collisions in the residual gas on the space charge in the beam. The self-consistent space charge simulation uses a finite element method with mixed linear and quadratic elements, magnetic fields incorporating non-linear magnetic materials, a plasma free surface emission model, and the generation of secondary charged particles by sampling of the primary beam trajectories. This method is useful for predicting the ion beam behavior from the ECR ion source under conditions of varying current density, electrode potential, and background gas pressure, including the behavior of suppressed electron flow and the influence of magnetic fields.

INTRODUCTION

This simulation represents an electron cyclotron resonance (ECR) ion source for producing a proton beam. The source is similar to a CEA-Saclay ECR source [1], though with a much higher magnetic field. New Vector Fields SCALA software [2] simulation capabilities permit fast prediction of ion beam formation with automatically generated secondary charged particles from background gas. The model is used for a space charge simulation of ECR extraction system with an accel-decel extraction system from a plasma free surface in combined electric and magnetic fields. The simulation includes beam neutralization from gas secondary electrons.

MODEL

The finite element model is composed of a three-electrode accel-decel extraction system and two solenoid magnets with non-linear magnetic materials (Fig. 1). The ion source dimensions are as follows:

Extraction aperture diameter	3.0 mm
Accel and decel aperture diameters	4.0 mm
Extractor-accel gap	12.5 mm
Accel-decel gap	1.5 mm
Ion beam drift space length	84.0 mm
Solenoid coil center spacing	100.0 mm
Magnet pole inside diameter	150.0 mm

The magnetic field model is analyzed first and the magnetic field information added to the electrostatic space charge database before solving.

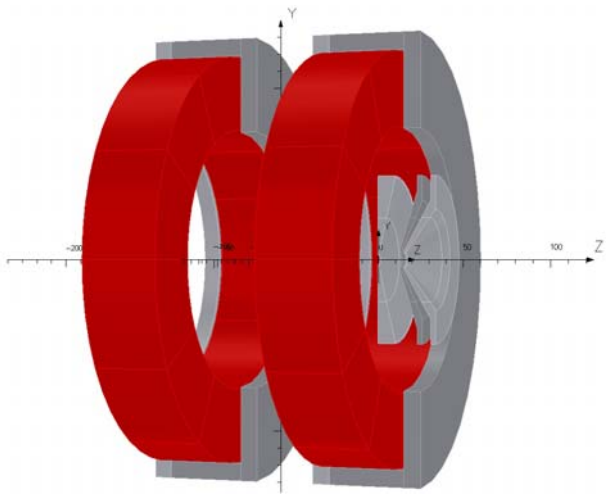

Figure 1: Source geometry with non-linear magnetic materials.

The model incorporates mixed linear and quadratic tetrahedral elements of varying size (Fig. 2).

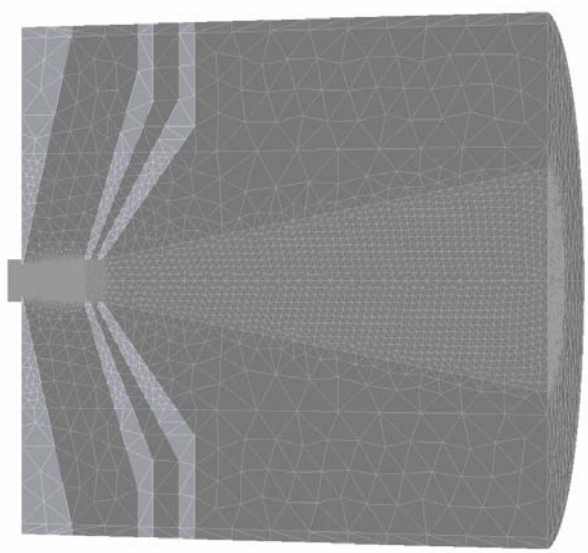

Figure 2: Tetrahedral mesh.

The source electrode (magenta) is held at 0 V, the extractor or accel electrode (blue) is biased at -12 kV, and the electron suppressor or decel electrode (aqua) is operated at -10 kV (Fig. 3).

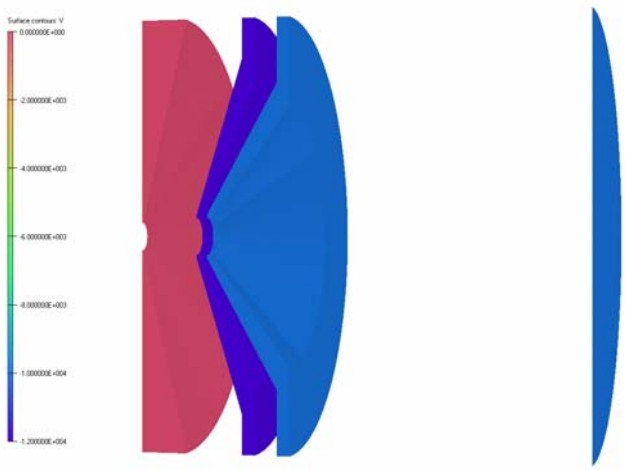

Figure 3: Boundary conditions, 0 V, -12 kV, -10 kV.

PRIMARY CHARGED PARTICLE EMISSION

The primary ion emitter is self consistently simulated, over a range of concave to convex meniscus, by Bohm current density ion emission from a free plasma surface. Concave to convex meniscus.

The primary emission model assumes an ion temperature much lower than the electron temperature. The user specifies the Bohm current density, particle mass and charge, electron temperature, and meniscus voltage. Parameters for the primary emitter are:

Ion species	Proton
$J_{Extraction}$	0.040 A·cm^{-2}
$T_{Electron}$	23209 K
$E_{Meniscus}$	-1.6022 x 10^{-12} V

BEAM INTERACTIONS

Secondary emission from background gas, with user specified energy and angular distributions, is automatically simulated.

Secondary particles can be generated from a volume representing the background gas, conductive surfaces, and lossy dielectric surfaces including the influence of beam induced insulator charging. Other behavior can include scattering, recombination, beam energy loss, and beam current loss. Beam current (Eq. 1) and energy loss (Eq. 2) (negative for losses) can be simulated by sampling the primary beam trajectories and generating yields along the primary trajectory paths.

$$\frac{dI}{ds} = \Gamma_I(x, y, z, \vec{E})I \quad (1)$$

$$\frac{dE}{ds} = \Gamma_E(x, y, z, \vec{E})E \quad (2)$$

where: I is primary beam current

E is primary beam energy

s is distance along trajectory

Ion beam neutralization from background gas volume secondaries (Eq. 3) can be simulated by sampling the primary beam trajectories and generating an emission fraction of electrons along the primary trajectory paths.

$$\frac{dn}{ds} = \Gamma_n(x, y, z, E)N \quad (3)$$

where: N is primary beam linear density

n is secondary particle linear density

A simple Gaussian energy distribution (Fig. 4) and a spherical angular distribution were used for the emission fraction in this model.

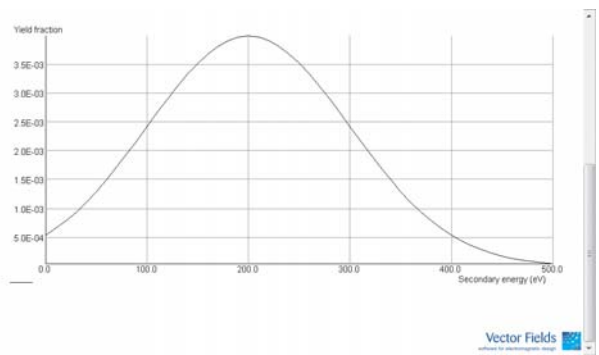

Figure 4: Gaussian secondary emission fraction used for simulations.

All volume secondaries are generated at a randomized, user-defined characteristic length along the primary beam trajectories.

RESULTS

Simulation of emission from a free plasma surface agrees well with Child's law space charge limited emission, both analytically and by simulation. In other work, we have seen good agreement to extraction from a glow discharge ion source. Magnetic field simulations, with non-linear materials, agree well with physical measurement. The magnetic flux density along the ion

source axis is shown in Fig. 5 with the extraction aperture located at Z = 0 mm.

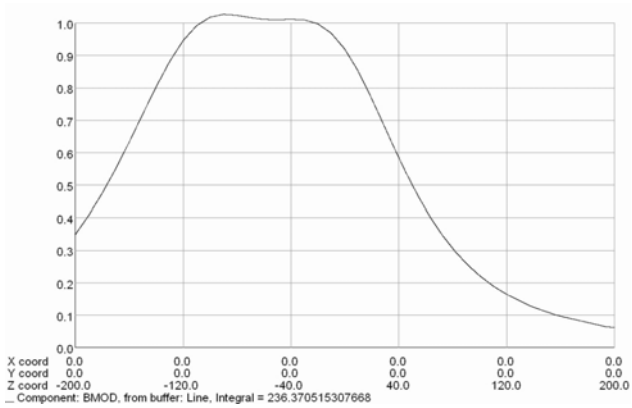

Figure 5: On-axis magnetic flux density.

The gas secondary electrons are highly magnetized and are confined near the ion beam by both the magnetic field and the ion beam space charge. The secondary electrons can be seen to orbit as expected around the magnetic flux lines in Fig. 6.

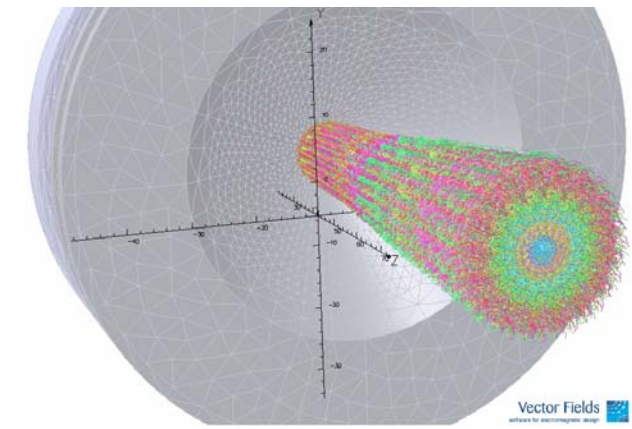

Figure 6: Magnetized secondary electrons.

The ion beam envelope divergence is reduced with neutralization (Figs. 7 and 8).

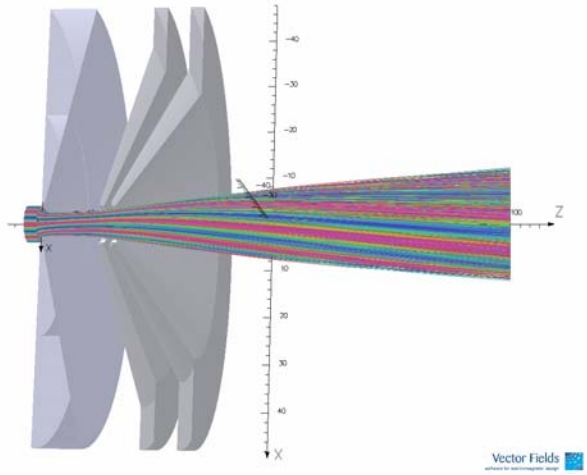

Figure 7: Ion beam without neutralization.

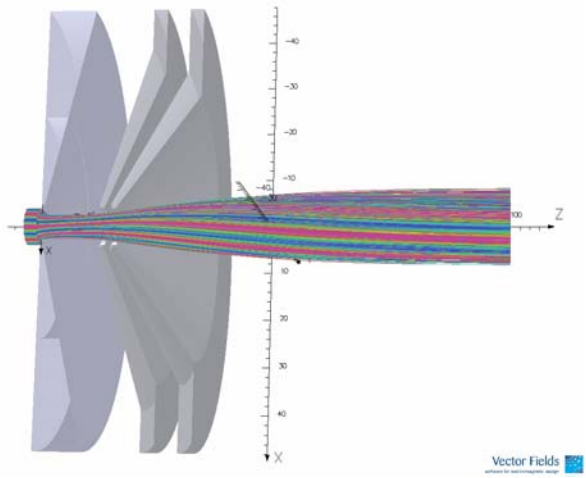

Figure 8: Ion beam with neutralization.

Figs. 9 and 10 further illustrate the beam envelope divergence with and without neutralization.

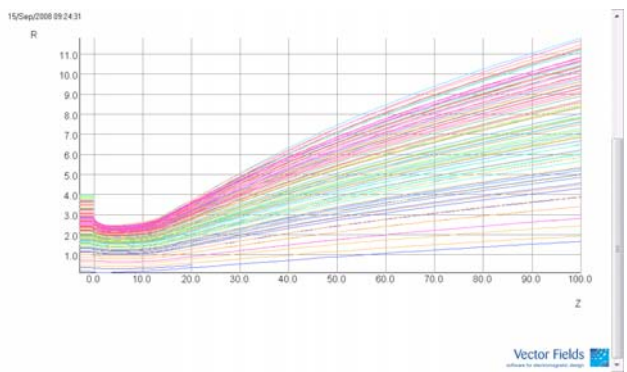

Figure 9: Ion beam without neutralization, note vertical scale.

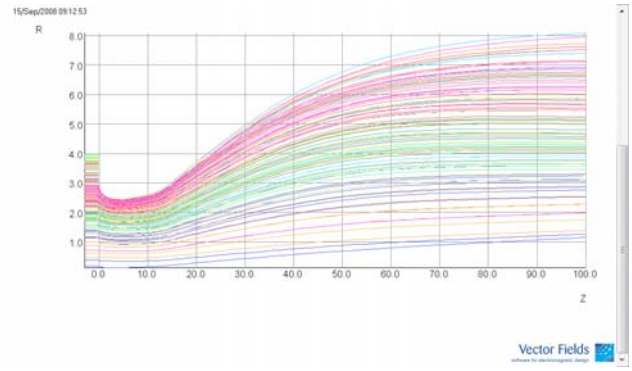

Figure 10: Ion beam with neutralization, note vertical scale.

The space charge, in Coulombs·mm^{-3}, is generally seen to be smaller with gas secondary electron neutralization, but varies spatially (Figs. 11 and 12).

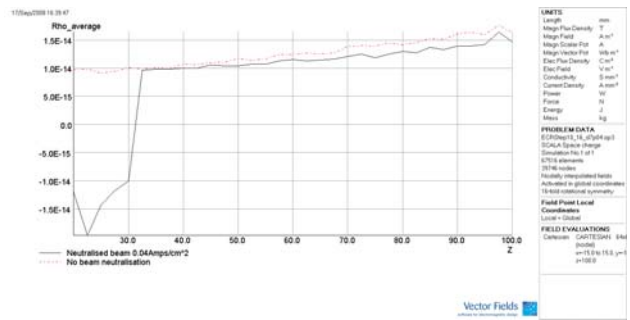

Figure 11: Average space charge across beam diameter.

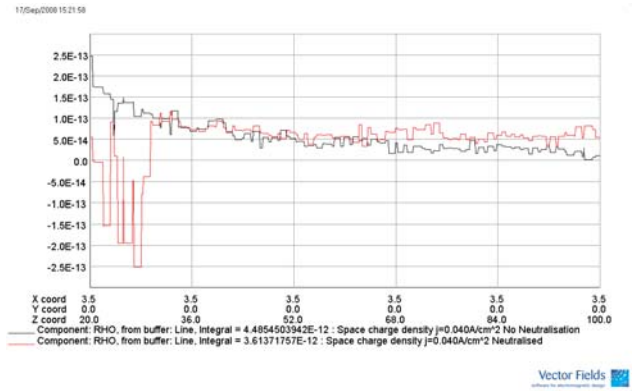

Figure 12: Space charge along a line, radius = 3.5 mm.

CONCLUSIONS

The extracted ion beam conditions are consistent with glow discharge ion source conditions, though this may not be a good approximation to low pressure ECR source operation [3] [4]. Simulation of ion beam neutralization by gas secondary electrons is demonstrated. Gas secondaries are simulated by automatic sampling of primary ion beam trajectories within a finite element environment without the need of particle-in-cell methods.

REFERENCES

[1] P-Y. Beauvais, P. Ausset, D. Bogard, O. Delferrière, J. Faure, R. Ferdinand, A. France, R. Gobin, P. Gros, J-M. Lagniel, P-A. Leroy, “First Beam of the CEA-Saclay CW-High Intensity Microwave Source”, PAC’07, Albuquerque, June 2007, p. 2720 (2007); http://www.JACoW.org.

[2] OPERA 3d, Vector Fields Ltd., Oxford, UK

[3] P. Spädtke, R. Lang, J. Mäder, J. Roßbach, K. Tinschert, J. Stetson, “Ion Beam Extracted from a 14 GHz ECRIS of CAPRICE Type”, ECRIS’06, Lanzhou, September 2006, (2006).

[4] J.W. Stetson and P. Spädtke, “Inhomogeneities in Beams Extracted from ECR Ion Sources”, PAC’07, Albuquerque, June 2007, FROBAB02, p. 3789 (2007).

EXTRACTION FROM ECR ION SOURCES: A NEW WAY TO INCREASE BEAM BRIGHTNESS

L, Maunoury[#,*] and C. Pierret, CIMAP, BP5133, Caen, France
J. Y. Pacquet, GANIL, BP552027, Caen, France

Abstract

One of the goals of work on ion sources is to provide the highest beam intensity in the smallest emittance. As computer power has increased so rapidly over the last few years, it is now possible to simulate the extraction from the ECR ion sources with greater accuracy, taking into account the physics of the several processes involved in the beam creation. In the last section of their paper, R. Leroy and co-workers [1] showed experimentally that the intensity of a beam can be improved significantly by biasing the plasma electrode. The idea was to use the isolated plasma electrode as a "biased disk". We have calculated the influence on the extracted ion trajectories of this additional potential (from 0 V down to -60 V). The simulations have been computed for the MONO1000 [2] and SUPERSHyPIE [3] ion sources. All the simulations showed an increase of the beam brightness with more or less important gain depending on the extraction voltage and the extraction conditions. A recent experiment performed on the MONO1000 ECRIS has confirmed the feasibility of this method: a gain of around 40% in terms of emittance has been obtained on an $^{84}Kr^{1+}$ beam.

Introduction

This work was performed in the framework of the ITSLEIF [4] network. One of the tasks deals with the improvement of the ECR ion source extraction. The goal is to get higher intensity in a smaller emittance for multi-charged ions of low energy (1–25 keV/q) used in the different facilities of the network. In previous work [1], Leroy and co-workers measured the evolution of the Ar^{4+} current with the polarisation of the plasma electrode at different bias of the coaxial tube. Each time, a maximum value of the current was obtained for a biased plasma electrode between -14 and -30 V. One of the major results was: "the plasma potential of the source is decreased when the coaxial tube voltage is increased". We have used this technique to investigate the extraction zone and the effect of this polarisation on the plasma electrode. Figure 1 shows the effect for negative potentials. This small polarisation will slightly modify the electric field lines in the extraction zone such that the divergence of the beam will be decreased. But at the same time ions from the edges of the beam will not be extracted. So to get a measurable effect, the emittance reduction should be larger than the diminution of the extracted ion current.

* Work supported by the ITS-LEIF project (RII3 – 026015)
# maunoury@ganil.fr

The relevant parameter in this process is the brightness of a beam. We will use the equation (1) where I_{beam} represents the beam current and ε_x and ε_y the emittances of the beam in the respective transverse planes of the beam propagation. In the following, we will deal only with geometric emittances.

$$B = \frac{2I_{beam}}{\pi^2 \varepsilon_x \varepsilon_y} \qquad (1)$$

The results will be shown by the relative brightness:

$$B_{rel} = \frac{B(V_{pe})}{B(V_{pe} = 0\text{V})} \qquad (2)$$

In the equation, V_{pe} corresponds to the difference between the voltage applied to the plasma electrode and the voltage applied to the ECRIS body: in our case this value will be negative and varies from 0 V down to -60 V. In this paper, V_{pe} = 0 V corresponds to the usual extraction case.

a)

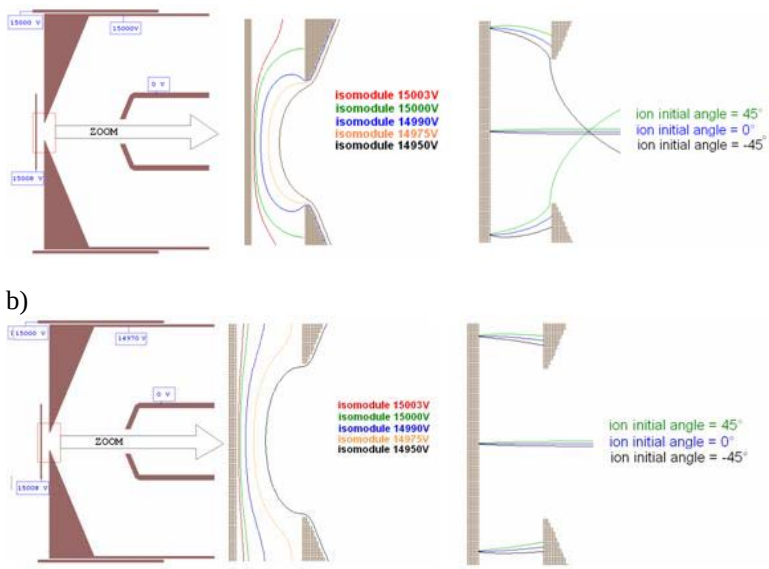

b)

Figure 1: Principle of the technique; case a) corresponds to a plasma electrode at source potential while b) corresponds to a plasma electrode biased at -30 V relative to the source potential.

In the following sections we present the beneficial effects of the idea, and not absolute values. First we will present calculations done with a singly charged ECRIS

called MONO1000 [2] and the first experimental results performed with this source. In the next section, we will present simulations done for a multicharged ECRIS named SUPERSHyPIE [3].

Simulations: general issue

In reference [5], C. Pierret and co-workers have already described the tools used for the extraction simulations. The RADIA [6] module which runs with the Mathematica program was used for calculating the magnetic field, especially in the extraction zone. For the trajectory calculations, the SIMION3D [7] and CPO [8] codes are used. With the first of these, the space-charge effect is not really effective but it is fast enough to perform many calculations and hence to get results for several configurations. The second reproduces the space-charge effect correctly (see the reference [5]) but it is slower. It will be used to re-compute solutions obtained from the SIMION3D calculations, with more accuracy. In these calculations, the space-charge compensation effect is not included. For both cases, the extraction is made in the following manner: the ions are generated on a plasma surface at the source potential added to the plasma potential. One way to get closer to a realistic spatial and energy distribution of the generated ions to be extracted, would be the application of a plasma simulation code (e.g. TrapCAD [9,10]) as pre-processor for the extraction calculations. For each case the ion distribution used is in accordance with the results from the reference [5]. The energy of the ions is 0.1 and 1 eV for MONO1000 and SUPERSHyPIE respectively. The angle of emission of the ion is within the range of 90°. No energy dispersion has been taken into account. The results of the simulation reflect the total beam extracted (summed over all charge states) and for the beam located in the middle of the puller electrode.

The singly-charged case: MONO1000 ECRIS

As this source is an axisymmetric source without a hexapole and a singly charged one, it is a simple case to simulate and test the technique described above.

Simulations

The MONO1000 ECRIS is mainly a singly charged ion source that can produce multicharged ions. It comprises a double ring of permanent magnets with the same magnetic field orientation and without a hexapole. It works with 2.45 GHz RF signal injected into the source via a coaxial wave-guide.

As it is a axi-symmetric source, the ion distribution is assumed to have the same symmetry. Moreover, a random ion distribution is generated a few mm from the plasma electrode and only the singly charged ions have been treated, which is a fairly good reproduction of reality. The plasma potential has been taken to be 8 V. In this case, the diameter of the plasma electrode is 7 mm and for the puller electrode it is 10 mm. The plasma electrode is located in a magnetic field of around 0.2 Tesla.

Figure 3 shows the relative brightness calculated with both SIMION3D and CPO codes applied to an Ar^{1+} extracted beam. Both curves increase with the diminution of the V_{pe} voltage without getting a plateau.

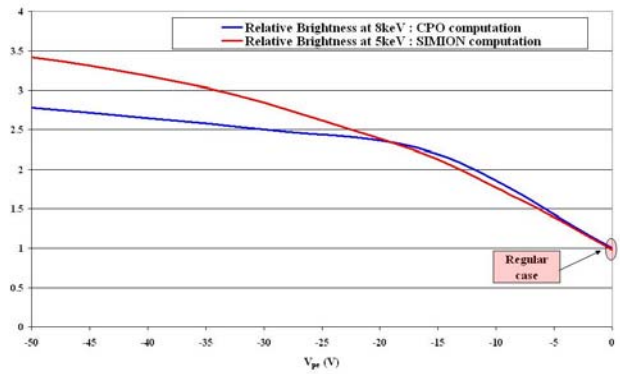

Figure 2: Relative brightness of an extracted Ar^{1+} beam at low energy calculated with the SIMION3D code (red) and with CPO (blue)

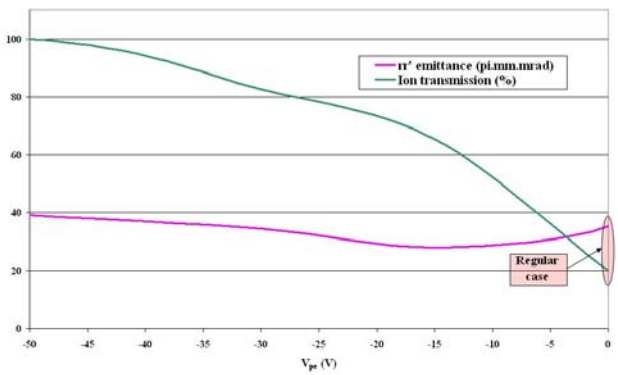

Figure 3: Ion transmission and emittance of an extracted Ar^{1+} beam at high energy (15 keV)

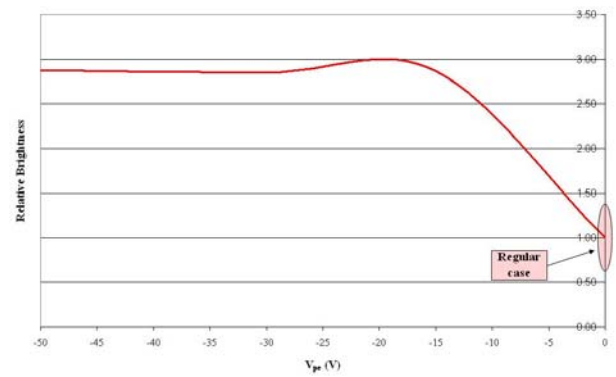

Figure 4: Relative brightness of an extracted Ar^{1+} beam at high energy (15 keV) calculated with the CPO code

Both curves are similar down to -20 V but below this SIMION3D overestimates the relative brightness

compared to the CPO code, which should give more realistic results. For a higher energy, e.g. 15 keV, the emittance of the beam and the ion transmission as well as the relative brightness are shown in figures 4 and 5. The ion transmission increases with reducing V_{pe} voltage while the emittance curve has a minimum value for V_{pe} = -15 V. The combination of these two parameters (ion transmission and emittance) is summarized with the curve displayed in figure 4. In this higher-energy case , the relative brightness increases up to a maximum and then hits a plateau which corresponds to the increase of the ion transmission and the emittance in the same range. In essence, the use of this bias plasma electrode improves the brightness of the beam. The next step is the comparison of this technique with the experiment.

Experiment

An experiment has been done to confirm or invalidate the method explained above. The MONO1000 ECRIS was used used with a simple test bench composed of an extraction box, a double focusing analyse dipole with a Br_{max} of 0.244 T.m, a faraday cup and an emittance meter of the type describes in reference [11]. This device can measure the emittance in both transverse planes of the

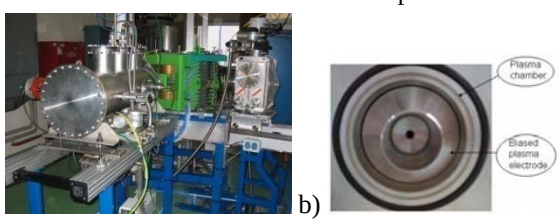

Figure 5: a) The test bench, and b) the extraction system with insulated plasma electrode.

beam. It is located beyond the analysing dipole and we focused our measurement on a specific beam: $^{84}Kr^{1+}$ in this case. Within the extraction box, there is an einzel lens and the plasma electrode is movable.

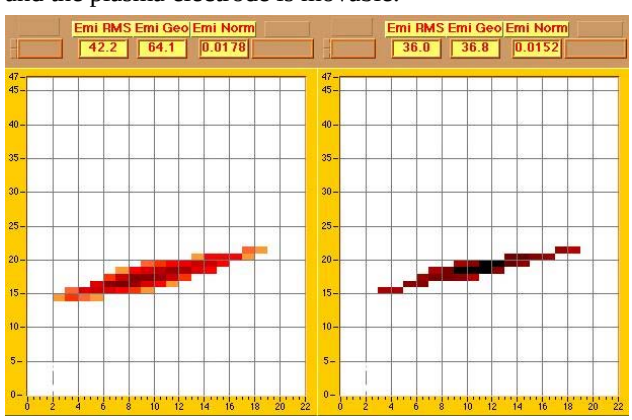

Figure 6: Vertical emittance of the $^{84}Kr^{1+}$ beam with V_{pe} = 0 V (left) and with V_{pe} = -30 V (right)

During the experiment, the total extracted current was 0.5 emA. The Kr gas was injected through a calibrated leak of 2.2 pμA value. All the atoms injected are ionized so there is 2 eμA of $^{84}Kr^{1+}$ and 0.4 eμA of $^{84}Kr^{2+}$. The source extraction was set to 7 kV to enable comparison for low-energy extraction. The source was tuned to get the maximum current of the $^{84}Kr^{1+}$ – in this case 2 eμA – and hence the emittance was recorded for different values of the V_{pe} without modifying the source parameters. Figure 6 shows emittances recorded and analysed after applying such a threshold, the emittance corresponds to 63% of the total current of $^{84}Kr^{1+}$ (in our case 1.26 eμA). The reduction of the emittance is evident from comparison of the case with V_{pe} = 0V and the case with V_{pe} = -30V. The gain, in terms of emittance reduction, is 42.6%. Figure 7 is a summary of the data recorded.

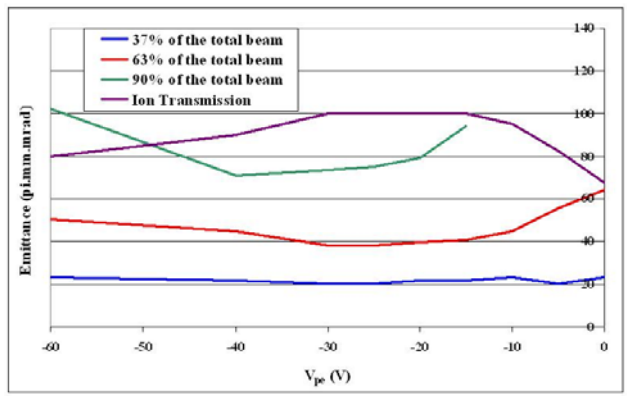

Figure 7: Emittance and ion transmission of the $^{84}Kr^{1+}$ beam asa function of V_{pe}.

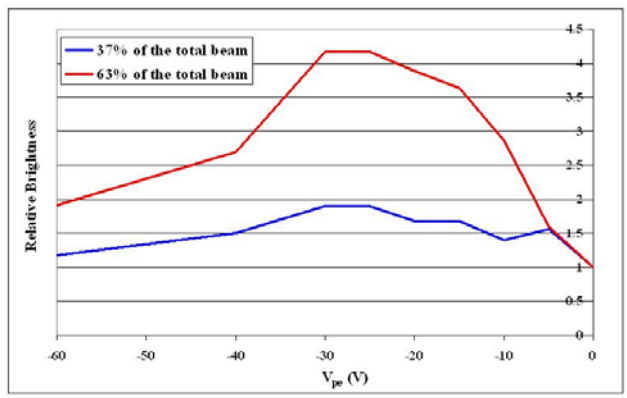

Figure 8: Variation of the relative brightness of the $^{84}Kr^{1+}$ beam with V_{pe}.

Each percentage curve corresponds to the values of an emittance for that percentage of the total beam. The blue curve is related to the core of the beam. It is slightly affected by the negative bias of the electrode plasma because in this region we can assume that the beam is a little divergent. The green curve corresponds to nearly the whole beam. In this case the negative bias modifies the emittance appreciably so as to give a real reduction for a value around -30 V. The figure 8 shows the experimental

result but in terms of relative brightness. Only the curves for 37% and 63% are displayed because it was not possible to get the emittance value at V_{pe} = 0V and for the 90% case. Again, a real improvement of the relative brightness of the beam for the value around -30 V can be seen. The enhancement is higher because a larger part of the beam is involved, so the negative bias can reduce the larger ion angles.

The multicharged case: SUPERSHyPIE ECRIS

The SUPERSHyPIE ECRIS is mainly a multicharged ion source that can produce beams with a high charge state, such as $O^{8+,}$ Ar^{17+}, Xe^{30+} [4]. After the promising result obtained with the singly charged ECRIS, it was encouraging to apply this technique to a multicharged ECRIS. Many simulations have been done but only that concerning a real case will be presented: it is the case of a plasma for producing Ar^{q+} beam with O_2 as a support gas.

Simulations

The SUPERSHyPIE ECRIS runs with a RF frquency of 14.5 GHz. It is composed of a combination of coils and permanent magnets and a hexapole for the axial and radial magnetic components, respectively. The scheme is the same as that discussed above: the ions are generated few mm from the plasma electrode (diameter of 13 mm) at the source potential added to the plasma potential of 8 V. Hence there is the puller electrode with a flat nose and a diameter of 20 mm. The plasma electrode is located in a

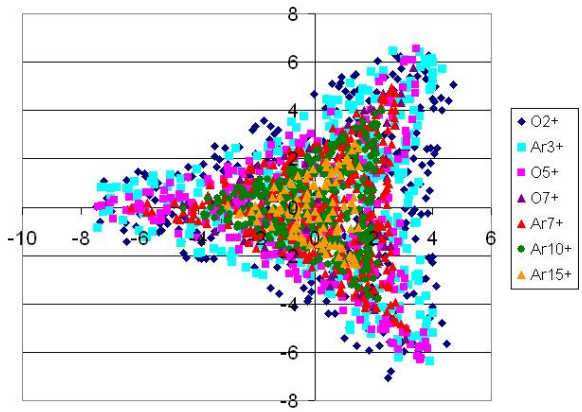

Figure 9: Initial ion distribution representing a real spectrum measured with the SUPERSHyPIE ECRIS

magnetic field of around 1 Tesla. Clearly the ion distribution should follow the shape of the plasma due to the total magnetic structure (star structure) and the charge distribution which has been chosen following the results in the reference [11]: the higher the charge, the more concentrated are the ions. Moreover, macro ions have been created in order to avoid slowing down the CPO calculation by gathering charges (table 1). The result of the ion distribution is shown in the figure 9. The star is within a 15-mm diameter circle. The calculations have been done using 15 kV of extraction.

Table 1: Average charge distribution

Average charge	Included charges	Equivalent intensity (emA)
O^{2+}	1,2,3	2,235
O^{5+}	4,5,6	2,369
O^{7+}	7,8	0,061
Ar^{3+}	1,2,3,4,5	0,231
Ar^{7+}	6,7,8	0,325
Ar^{10+}	9,10,11,12	0,938
Ar^{15+}	13,14,15,16	0,108

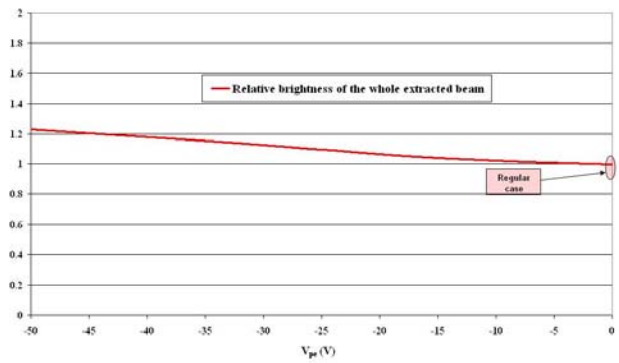

Figure 10: Relative brightness of an extracted beam (realistic case) at high energy (15 keV) calculated with the CPO code

voltage and with the CPO code. Figure 10 shows the relative brightness for the whole extracted beam (i.e. O^{q+} and Ar^{q+} beams). Again, there is an increase but much smoother compared with the MONO1000 case and with a

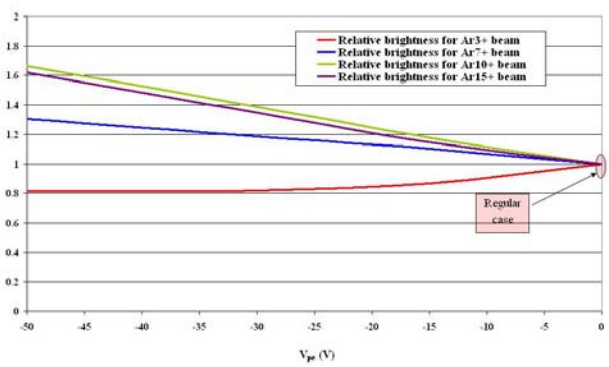

Figure 11: Relative brightness of the Ar^{q+} extracted beams at high energy (15 keV) calculated with the CPO code.

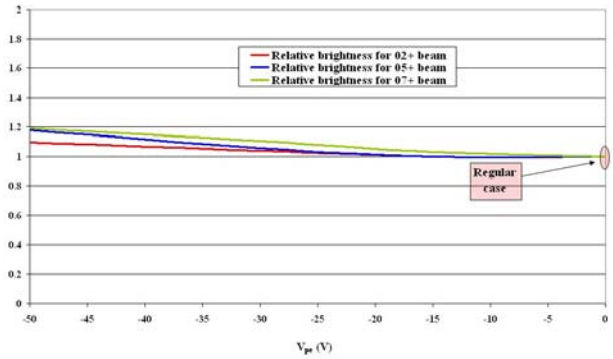

Figure 12: Relative brightness of the O^{q+} extracted beams at high energy (15 keV) calculated with the CPO code.

lower gain. Looking at the O and Ar beams, the results are somewhat different. For the Ar beams (figure 11), the method is unfavourable for the lower charge (3+) but positive for the others. This could be explained by the magnetic field gradient which is really strong (19 Tesla/m). For such low charge states, the new effect cannot compensate for the increase of the emittance due to this high gradient. For the O beams (figure 12), the method is favourable for all the charge states.

a) Discussion

We have shown that biasing the plasma electrode negatively over a small range of *V* works. The assumption that it is possible to modify the electric field lines in the extraction region slightly and hence to increase the brightness of a beam has been proved experimentally. Clearly, all the curves do not give the required gain but they encourage us to believe that this method could significantly improve the brightness of the beams extracted from ECR ion sources

The experiment has only been done for one case: low extraction voltage and for a singly charged extracted beam. It should also be done for a higher voltage (e.g. for 15 kV extraction voltage) and especially for other masses. Our measurements have been done after the analysing dipole. For the calculation of the relative brightness, it has been assumed that the vertical and horizontal emittances are equal which is not true due to the horizontal dispersion from analysing dipole. The relative brightness should be deduced from the measurements of the emittances in the both transverse plane but this was made impossible for us due to a failure in the movement of the horizontal slit set.

After the encouraging calculations done for the multi-charged case, measurements should be also performed in order to confirm this method applied to such an ECRIS. For this purpose, a new extraction box will be installed on the SUPERSHyPIE bench in order to be able to bias the plasma electrode, and also to move it. A movable plasma electrode experiment was already reported at the ATOMKI-ECRIS [12], however that electrode was not biased. We plan to apply the method described in this paper at the ATOMKI source in 2009. At GANIL, the experiment is scheduled for the first half of 2009 but not with the SUPERSHyPIE ECRIS. The GTS [13] ECRIS, which will be mounted at the beginning of 2009, will be our multicharged ECRIS to test this technique.

Finally, simulations should be continued to fit the experimental data and to provide the right ion distribution which characterises an ECRIS, and to allow us to predict the emittance and brightness of a beam extracted from an ECRIS.

REFERENCES

[1] R. Leroy et al., ECRIS'95, Riken, April 1995, Japan (1995)
[4] http://its-leif.org/
[2] P. Jardin et al., Rev. Sci. Instrum. **72** (2), 789 (2002)
[3] L. Maunoury et al., Rev. Sci. Instrum. **72** (2), 561 (2002)
[5] C. Pierret et al., Rev. Sci. Instrum. **79**, 02B703 (2008)
[6] http://www.esrf.eu/Accelerators/Groups/InsertionDevices/Software/Radia
[7] http://www.sisweb.com/simion.htm
[8] CPO programs, free versions available at www.electronoptics.com
[9] J. Vámosi, S. Biri Comp. Phys. Comm. 98 (1996) 215
[10] S. Biri S. , A. Derzsi, É. Fekete, I. Iván, High Energy Physics and Nuclear Physics - Chinese Edition Supplement **31** (2007)165
[11] J. Mandin, PhD-thesis, Caen University (1997)
[12] S. Biri, A. Valek, A. Kitagawa, M. Muramatsu M., Proc. 15. Int. Workshop on ECRIS (ECRIS'02). JYFL Research Report 4/2002, p. 49
[13] D. Hitz et al., Proc. 15. Int. Workshop on ECRIS (ECRIS'02). JYFL Research Report 4/2002

PAPER NOT RECEIVED

PAPER NOT RECEIVED

List of Authors

Italic papercodes indicate primary authors

Institutes List

AEC
Chiba
- Takasugi, W.
- Wakaisami, M.

ANL
Argonne, Illinois
- Barcikowski, A.
- Carr, J. R.
- Henderson, D.
- Jiang, C. L.
- Kondrashev, S. A.
- Maybury, D.
- Mustapha, B.
- Ostroumov, P. N.
- Pardo, R. C.
- Rehm, E.
- Scannell, M. M.
- Scott, R. H.
- Sharamentov, S. I.
- Spada, F. E.
- Vondrasek, R. C.

ANSTO
Menai
- Button, D.
- Hotchkis, M. A.C.

ATOMKI
Debrecen
- Biri, S.
- Ivan, I.
- Juhasz, Z.
- Sulik, B.

Bengal Engineering and Science University
Howrah
- Ray, P. K.

CEA
Gif-sur-Yvette
- Delferriere, O.
- Gobin, R.
- Harrault, F.
- Pottin, B.
- Tuske, O.

CERN
Geneva
- Kuchler, D.
- O'Neil, M.
- Scrivens, R.

CIMAP
Caen
- Maunoury, L.
- Pierret, C.

CPI
Palo Alto, California
- Blank, M.
- Cauffman, S.
- Felch, K.
- Jory, H.

Coimbra University
Coimbra
- do Carmo, S. J.C.

DAE/VECC
Calcutta
- Bhandari, R. K.
- Chakraborty, D. K.
- Mallik, C.
- Rashid, M. H.
- Sarma, P. R.
- Taki, Dr. G. S.

Far-Tech, Inc.
San Diego, California
- Bogatu, I. N.
- Cluggish, B.
- Galkin, S.
- Grubert, L.
- Kim, J. S.
- Zhao, L.

GANIL
Caen
- Alcantara Nunez, J. A.
- Alves Conde, R.
- Barue, C.
- Canet, C.
- Dubois, M.
- Dupuis, M.
- Flambard, J. L.
- Frigot, R.
- Jardin, P.
- Leboucher, C.
- Lecesne, N.
- Lecomte, P.
- Leherissier, P.
- Lemagnen, F.
- Pacquet, J. Y.
- Pichard, A.
- Saint|-|Laurent, M. G.

GHMFL
Grenoble
- Debray, F.
- Dumas, J. M.
- Sala, P.
- Trophime, C.

GSI
Darmstadt
- Lang, R.
- Maeder, J.
- Rossbach, J.
- Spaedtke, P.
- Tinschert, K.

HIT
Heidelberg
- Cee, R.
- Haberer, Th.
- Naas, B.
- Peters, A.
- Scheloske, S.
- Winkelmann, T.

IAP/RAS
Nizhny Novgorod
- Bokhanov, A.
- Bykov, Yu. V.
- Golubev, S.
- Izotov, I.
- Mansfeld, A.
- Razin, S.
- Sidorov, V.
- Skalyga, V.
- Zorin, V.

IEAP
Kiel
- Helmke, C.
- Panitzsch, L.
- Seimetz, L.
- Stalder, M.
- Wimmer|-|Schweingruber, R. F.

IFIN
Magurele- Bucuresti
- Dobrescu, S.
- Schachter, L.

IKF
Frankfurt am Main
- Enz, S.
- Kruppi, Th.
- Stiebing, K. E.

IMP
Lanzhou
- Sun, L. T.
- Zhao, H. W.

INFN/LNS
Catania
- Celona, L.
- Chines, F.
- Ciavola, G.
- Gallo, G.
- Gambino, N.
- Gammino, S.
- Maimone, F.
- Mascali, D.
- Miracoli, R.
- Passarello, S.

INSP
PARIS
- Lamour, E.
- Merot, J.
- Prignet, C.
- Rozet, J.-P.
- Trassinelli, M.
- Vernhet, D.

IUAC
New Delhi
- Kanjilal, D.
- Kumar, P.
- Lakshmy, P. S.
- Mandal, A.
- Rodrigues, G.

Institut fur Kernphysik, Westfalische Wilhelms-Universitat Munster
Munster
- Albers, B.
- Heinen, A.
- Hupe, L.
- Kahnt, M.
- Nowack, L.
- Ortjohann, H. W.
- Taschner, A.
- Vitt, Ch.
- Wolosin, S.

JAEA
Ibaraki-ken
- Ichikawa, S.
- Kabumoto, H.
- Matsuda, M.
- Osa, A.
- Otokawa, Y.

JYFL
Jyvaskyla
- Arje, J.
- Jones, P.
- Kalvas, T.
- Koivisto, H. A.
- Peura, P.
- Ropponen, T.
- Savonen, M.
- Toivanen, V. A.

KEK
Ibaraki
- Arai, S.
- Okada, M.
- Oyaizu, M.

KEK, Tokai Branch
Tokai, Naka, Ibaraki
- Fuchi, Y.
- Hirayama, Y.
- Imai, N.
- Ishiyama, H.
- Jeong, S. C.
- Miyatake, H.
- Watanabe, Y.

KVI
Groningen
- Beijers, J. P.M.
- Brandenburg, S.
- Drentje, A. G.
- Kremers, H. R.
- Mironov, V.
- Mulder, J.
- Saminathan, S.

LANL
Los Alamos, New Mexico
- Kurennoy, S. S.
- Tarvainen, O. A.

LBNL
Berkeley, California
- Benitez, J. Y.
- Caspi, S.
- Dietderich, D. R.
- Ferracin, P.
- Hannaford, R.
- Ji, Q.
- Kwan, J. W.
- Leitner, D.
- Leitner, M.
- Ludewigt, B. A.
- Lyneis, C. M.
- Noland, J. D.
- Prestemon, S.
- Regis, M. J.
- Sabbi, G. L.
- Todd, D. S.
- Trillaud, F.

LKB
PARIS
- Szabo, C. I.
- Attia, D.
- Gumberidze, A.
- Indelicato, P.
- Le Bigot, E.-O.
- Schlesser, S.

LLT
Boulder
- Elliott, S. M.
- White, E. K.

LPSC
Grenoble
- Angot, J.
- Fourel, C.
- Giraud, J.
- Lamy, T.
- Latrasse, L.
- Thuillier, T.

NIRS
Chiba-shi
- Kitagawa, A.
- Muramatsu, M.

NSCL
East Lansing, Michigan
- Cole, D.
- Doleans, M.
- Machicoane, G.
- Marti, F.
- Stetson, J. W.
- Wu, X.
- Zavodszky, P. A.

Northern Illinois University
DeKalb, Illinois
- Vinogradov, N.

Osaka University
Suita
- Kato, Y.

PU
Princeton, New Jersey
- Calaprice, F.
- Galbiati, C.

Prizztech Ltd, Magnet Technology Centre
Pori
- Suominen, P.

RCNP
Osaka
- Fukuda, M.
- Hatanaka, K.
- Kibayashi, M.
- Morinobu, S.
- Okamura, H.
- Tamii, A.
- Yorita, T.

RIKEN Nishina Center
Wako, Saitama
- Nakagawa, T.

SAIC
San Diego, California
- Cornelius, W. D.

SSolutions
San Diego CA
- Cornelius, W. D.

TRIUMF
Vancouver
- Ames, F.
- Baartman, R. A.
- Bricault, P. G.
- Jayamanna, K.
- Labrecque, F. S.
- McDonald, M.
- Schmor, P.

Tateyama Machine Co. Ltd.
Toyama-shi
- Asaji, T.
- Tanaka, K.

Tech-X
Boulder, Colorado
- Choi, Y.
- Fillmore, D. W.
- Messmer, P.
- Mullowney, P. J.
- Smithe, D. S.

Technische Universitat Munchen
Garching
- Yakushev, A.

Texas A&M University Cyclotron Institute
College Station, Texas
- May, D. P.

Texas A&M University, Cyclotron Institute
College Station
- Tabacaru, G.

The Hebrew University of Jerusalem, The Racah Institute of Physics
Jerusalem
- Paul, M.

Toyo University
Kawagoe-shi, Saitama
- Minezaki, H.
- Uchida, T.
- Yoshida, Y.

University Debrecen
Debrecen
- Hegedüs, Cs.
- Kokenyesi, S.
- Mojzes, I.
- Palinkas, J.

University of Notre Dame
Notre Dame
- Bowers, M.
- Collon, P.
- Robertson, D.
- Schmitt, C. J.

VERA
Wien
- Kutschera, W.

Vector Fields Ltd.
Oxford
- Simkin, J.

Westfaelische Wilhelms-Universität Muenster
Muenster
- Andrä, J. H.

iThemba LABS
Somerset West
- Thomae, R. W.

Participants List